UC San Diego
UC San Diego Electronic Theses and Dissertations

Title
Seismic Behavior of Cold-Formed Steel-Framed Wall-Line Systems in Mid-Rise Buildings

Permalink
https://escholarship.org/uc/item/8z183193

Author
Singh, Amanpreet

Publication Date
2023

Peer reviewed|Thesis/dissertation

eScholarship.org Powered by the California Digital Library
University of California

UNIVERSITY OF CALIFORNIA SAN DIEGO

Seismic Behavior of Cold-Formed Steel-Framed Wall-Line Systems in Mid-Rise Buildings

A dissertation submitted in partial satisfaction
of the requirements for the degree
Doctor of Philosophy

in

Structural Engineering

by

Amanpreet Singh

Committee in charge:

Professor Tara C. Hutchinson, Chair
Professor Joel P. Conte
Professor William Hodgkiss
Professor Machel L. Morrison
Professor Benjamin W. Schafer
Professor Pui-shum Shing

2023

Copyright

Amanpreet Singh, 2023

All rights reserved.

The Dissertation of Amanpreet Singh is approved, and it is acceptable in quality and form for publication on microfilm and electronically.

University of California San Diego

2023

DEDICATION

To my family

for their love and support, their patience and sacrifice.

EPIGRAPH

No matter where you are from, your dreams are valid.

Lupita Nyong'o

There is unexpected traffic ahead, but you're still on the right path.

Google Maps

Don't forget to be awesome.

Hank and John Green

TABLE OF CONTENTS

Dissertation Approval Page iii

Dedication iv

Epigraph v

Table of Contents vi

List of Figures ix

List of Tables xxi

Acknowledgements xxiii

Vita xxviii

Abstract of the Dissertation xxxi

Chapter 1 Introduction 1
1.1 Background 1
1.2 Previous Research on CFS-Framed Structures 3
1.2.1 Component-level Experiments of CFS-Framed Walls 3
1.2.2 System-level Experiments of CFS-Framed Buildings 14
1.2.3 Numerical Modeling of CFS-Framed Structures 19
1.3 Research Scope 28
1.4 Organization of Dissertation 30

Chapter 2 CFS-Framed Wall-Line Experimental Program 33
2.1 Introduction 33
2.2 CFS-NHERI Archetype Building 34
2.3 Shake Table Test Phase 36
2.3.1 Test Matrix and Specimen Details 36
2.3.2 Test Setup 41
2.3.3 Application of Finish Materials 46
2.3.4 Detailing around Window Opening 48
2.3.5 Motion Scaling Strategy and Test Protocol Development 51
2.3.6 Instrumentation and Monitoring Systems 63
2.4 Quasi-static Test Phase 69
2.4.1 Test Matrix 69
2.4.2 Test Setup 72
2.4.3 Instrumentation and Monitoring Systems 76
2.5 Summary Remarks 81

Chapter 3 Impact of Nonstructural and Structural Detailing on Wall-Line Lateral Behavior 83
3.1 Introduction 83
3.2 Baseline Specimen Performance 83
3.3 Finish Application 91
3.4 Window Opening 97
3.5 Asymmetric Shear Wall Location 103
3.6 Tie-down Detailing 111
3.7 Shear Wall Detailing 119
3.8 Sheet Fastener Pattern 126
3.9 Summary Remarks 128

Chapter 4 Physical Damage-Hysteretic Response Correlation for CFS-Framed Wall-Lines 132
4.1 Introduction 132
4.2 Physical Damage Progression 133
4.2.1 Unfinished Specimens 133
4.2.2 Finished Specimens 138
4.3 Evolution of Dynamic Characteristics 140
4.4 Hysteretic Energy Dissipation 146
4.5 Summary Remarks 153

Chapter 5 Design-Grade Numerical Model of CFS-Framed Mid-Rise Buildings 156
5.1 Introduction 156
5.2 CFS-HUD Experimental Program 157
5.3 Design-Grade Numerical Model 161
5.3.1 Modeling of Shear Walls 163
5.3.2 Modeling of Tension Tie-Rod and Compression Stud Pack Assembly . . 170
5.3.3 Modeling of Gravity Walls 172
5.3.4 Seismic Mass and Gravity Load Definition 174
5.4 Comparison between Numerical Predictions and Measured Experimental Response 176
5.4.1 Comparison of Natural Frequencies 177
5.4.2 Comparison of Nonlinear Response to Earthquake Motions 178
5.5 Summary Remarks 187

Chapter 6 Conclusions and Future Work 190
6.1 Motivation and Scope 190
6.1.1 Experimental Scope and Contributions 191
6.1.2 Numerical Modeling Scope and Contributions 193
6.2 Research Significance 194
6.3 Major Findings 195
6.3.1 Experimental Investigation of Cold-Formed Steel-Framed Wall-Lines in Mid-Rise Buildings 195

6.3.2 Numerical Modeling of Cold-Formed Steel-Framed Wall-Lines in Mid-Rise Buildings 200
6.4 Future Work 201
6.4.1 Component-level Test Needs 201
6.4.2 Complete Building Test Needs: CFS-NHERI 10-story Building 203
6.4.3 Numerical Modeling Needs 209

Appendix A Shop Drawings of Fabricated Wall-lines 212

Appendix B Material Tests and Certificates 233
B.1 Framing Member Coupon Tests 233
B.2 Finish Layer Stucco Compressive Strength Tests 236
B.3 Hold-down Manufacturer Catalog 236
B.4 Tension Tie-rods Uni-axial Tests 237

Appendix C Hysteretic Response of Wall-Line Specimens 245
C.1 Shake Table Test Phase 245
C.2 Quasi-Static Test Phase 258
C.2.1 Force-Displacement Response of Wall-Line Specimens 258
C.2.2 Equivalent Hysteretic Damping of Wall-Line Specimens 263

Appendix D Local Response of Wall-Line Specimens 265
D.1 Shake Table Test Phase 265
D.2 Quasi-Static Test Phase 282

Appendix E OpenSeesPy Code of Building Numerical Model 317

Bibliography 354

LIST OF FIGURES

Figure 1.1. CFS member manufacturing through roll-forming machines and commonly used CFS cross sections (source: www.buildsteel.org/) 1

Figure 1.2. CFS-framed building under construction (photo credit: Diego Rivera, Superior Wall Systems) 3

Figure 1.3. Schematic of CFS-framed shear wall 4

Figure 1.4. Different failure modes observed in shear walls tested by Yu et al. (2007): (a) steel sheet sheathing buckling and screw pullout (coarsely spaced fasteners at 152 mm o.c. edge), and (b) flange distortion of boundary studs (tightly spaced fasteners at 51 mm o.c. edge) 6

Figure 1.5. Failure observed in blocked shear walls tested by Yu and Chen (2009) 7

Figure 1.6. Construction details for mid-ply shear wall developed by Brière et al. (2018) 9

Figure 1.7. (a) Mid-ply shear wall tested by Brière et al. (2018) showing extensive shear buckling of steel sheet with no framing member damage, and (b) force-deformation response comparison for mid-ply and traditional shear wall Santos and Rogers (2017) 10

Figure 1.8. Illustration demonstrating the ideal tie-down force distribution in Type I and Type II shear walls by Peterman (2014) 13

Figure 1.9. (a) Continuous tie-rod system with floor-to-floor installation (Wang et al., 2018a), and (b) traditional hold-down installed at wall end stud (Madsen et al., 2011) 13

Figure 1.10. Building specimen tested by Peterman et al. (2016): (a) structural system only, and (b) complete with nonstructural components 15

Figure 1.11. Two-story building tested by Landolfo et al. (2018): (a) structural system only, and (b) complete with nonstructural components 16

Figure 1.12. CFS-HUD building tested by Hutchinson et al. (2021) 18

Figure 1.13. Six-story building tested by Zhou et al. (2022): (a) structural system only, and (b) complete with nonstructural components 19

Figure 1.14. Details of OpenSees model used by Buonopane et al. (2014) for OSB sheathed CFS-framed shear walls 21

Figure 1.15. Details of OpenSees model used by Singh and Hutchinson (2018) for steel sheet sheathed CFS-framed shear walls 22

Figure 1.16. Details of OpenSees model used by Kechidi and Bourahla (2016) for CFS-framed shear walls 22

Figure 1.17. Details of ABAQUS model used by Derveni et al. (2020) for CFS-framed shear walls 23

Figure 1.18. Details of numerical model for low-rise wood structures developed by Folz and Filiatrault (2004) 24

Figure 1.19. Numerical modeling of vertical stiffness elements by Pei and Van de Lindt (2009) 25

Figure 1.20. 3D OpenSees models for building analysis developed by Leng et al. (2017) 27

Figure 1.21. Comparison of P- and A- shear wall models developed by Leng et al. (2017) 27

Figure 1.22. 3D OpenSees model for building analysis developed by Campiche et al. (2020) 28

Figure 2.1. The unified archetype building plan (left), elevation (right) and shear wall layout (Torabian et al., 2016a) 35

Figure 2.2. Baseline specimen (SGGS-1) photograph as installed in test setup 39

Figure 2.3. Framing details of baseline specimen (SGGS-1) 41

Figure 2.4. Specimen fabrication photographs (taken at fabricator SWS Panel Inc. manufacturing facility in South Gate, CA) 42

Figure 2.5. Photographs demonstrating steps involved in test setup 44

Figure 2.6. Elevation view of tension tie-rod assembly 46

Figure 2.7. (a) Isometric and (b) top view of the test setup 47

Figure 2.8. Test setup for monotonic pull tests 48

Figure 2.9. Photographs demonstrating steps involved in finish application during shake table test phase 49

Figure 2.10. Jamb stud built-up section used around window opening 51

Figure 2.11. Framing details of shear wall specimen W21 (Santos and Rogers, 2017) . . 53

Figure 2.12. Framing details of shear wall specimen W2 (Rizk and Rogers, 2017) 54

Figure 2.13. Force displacement behavior of shear wall specimens (a) W21 (Santos and Rogers, 2017) and (b) W2 (Rizk and Rogers, 2017) 55

Figure 2.14. Test predictions for selected representative test specimens 55

Figure 2.15. Selected earthquake seed motions: (a) acceleration time histories and (b) elastic pseudo-acceleration spectra (ξ = 5%) 56

Figure 2.16. Pre-test scale factor selection 57

Figure 2.17. Scale factor calculations for EQ1 for test group 3 61

Figure 2.18. Scale factor calculations for EQ4 for test group 3 62

Figure 2.19. Scaled achieved earthquake motions for SGGG-1 and SGGS-2B: (a) acceleration time histories, (b) displacement time histories and (c) pseudo-acceleration spectra (ξ = 5%) 63

Figure 2.20. Layout and nomenclature of string potentiometers used for measuring wall and table displacements during dynamic tests 66

Figure 2.21. Layout and nomenclature of string potentiometers used for measuring wall panel distortion for specimen SGGS-1 67

Figure 2.22. Layout and nomenclature of linear potentiometers used for measuring wall uplift and slip for specimen SGGS-1XS 68

Figure 2.23. Layout and nomenclature of accelerometers used during dynamic tests . . . 69

Figure 2.24. Layout and nomenclature of strain gages for measuring axial strains in tension tie-rods 70

Figure 2.25. Specimen naming example: SGGS-2: (a) interior face and (b) exterior face 72

Figure 2.26. Framing details of specimen SGGS-2 73

Figure 2.27. Photographs demonstrating steps involved in finish application during quasi-static test phase 74

Figure 2.28. CUREE loading protocol (example shown for specimen SGGS-2) 76

Figure 2.29. Quasi-static cyclic test setup: (a) isometric view and (b) end view 77

Figure 2.30. Layout and nomenclature of: (a) displacement transducers and load cell on wall interior face for measuring lateral force and displacement and panel distortion; (b) and (c) linear potentiometers and strain gages for measuring wall uplift and slip, and tension tie-rod axial strain for specimen SWWS-2F 79

Figure 2.31. Layout and nomenclature of washer load cells used for measuring hold-down tension force for specimen SGGS-1HDF 80

Figure 3.1. Force-displacement response of baseline specimen SGGS-1 86

Figure 3.2. Physical damage to specimen SGGS-1 following the end of monotonic test ($\Delta_{res} = 1.86\%$): (a) tension field in steel sheets, (b) sheet pullover, (c) local buckling of gravity stud and (d) screw edge tearing 88

Figure 3.3. Schematic illustration of instrumentation for wall local response 88

Figure 3.4. Illustration of panel distortion calculations 89

Figure 3.5. SGGS-1 specimen local response during earthquake test EQ4:DE 91

Figure 3.6. Effect of finish application: (a) force-displacement response and (b) backbone curve comparison for Type I specimens; and (c) force-displacement response and (d) backbone curve comparison for Type II specimens 93

Figure 3.7. Effect of finish application on key parameters: (a) lateral strength, (b) elastic stiffness, (c) drift at strength, and (d) drift at 80% strength post-peak 95

Figure 3.8. Physical damage to specimen SGGS-1F following the testing sequence ($\Delta_{max} = 4.92\%; \Delta_{res} = 2.29\%$) 96

Figure 3.9. Effect of finish on tension-rod forces with increase in: (a) and (b) normalized drift, and (c) and (d) normalized lateral force 98

Figure 3.10. Effect of finish on wall end uplift with increase in: (a) and (b) normalized drift, and (c) and (d) normalized lateral force 99

Figure 3.11. Effect of finish on shear wall shear distortion with increase in: (a) and (b) normalized drift, and (c) and (d) normalized lateral force 100

Figure 3.12. Effect of window opening: force-displacement response for (a) Type II specimen pair, and (b) Type I specimen pair; and (c) backbone curve comparison for Type I and II specimens 101

Figure 3.13. Physical damage to specimen SWWS-1 at drift ratio $\Delta = +4.12\%$ 103

Figure 3.14. Effect of window opening on tension-rod forces with increase in: (a) and (b) normalized drift, and (c) and (d) normalized lateral force 104

Figure 3.15. Effect of window opening on wall end uplift with increase in: (a) and (b) normalized drift, and (c) and (d) normalized lateral force 105

Figure 3.16. Effect of window opening on shear wall shear distortion with increase in: (a) and (b) normalized drift, and (c) and (d) normalized lateral force 106

Figure 3.17. Effect of asymmetric shear wall location: (a) force-displacement response, and (b) backbone curve comparison 107

Figure 3.18. Pysical damage to specimen SGGG-1 following the dynamic testing sequence ($\Delta_{max} = 5.1\%; \Delta_{res} = 0.26\%$) 109

Figure 3.19. Effect of asymmetric shear wall location on tension-rod forces with increase in: (a) normalized drift and (b) normalized lateral force 110

Figure 3.20. Effect of asymmetric shear wall location on wall end uplift with increase in: (a) normalized drift and (b) normalized lateral force 110

Figure 3.21. Effect of asymmetric shear wall location on shear wall shear distortion with increase in: (a) normalized drift and (b) normalized lateral force 111

Figure 3.22. Effect of tie-down detailing: (a) force-displacement response, and (b) backbone curve comparison 112

Figure 3.23. (a)-(d) Damage to steel sheet and hold-downs used in specimen SGGS-1HD at drift ratio $\Delta = 4.0\%$, and (e) tie-down force time history of hold-downs installed on stud pack 114

Figure 3.24. Hold-down damage installed on chord stud pack at wall end in specimen SGGS-1HD at drift ratio (a) 3.0%: bottom track bending and prying action at hold-down, (b) 5.0% and (c) 6.0%: plate weld fracture, and (d) 7.0%: thread bar fracture. 115

Figure 3.25. Effect of tie-down detailing on anchor forces with increase in: (a) and (b) normalized drift, and (c) and (d) normalized lateral force 116

Figure 3.26. Effect of tie-down detailing on wall end uplift with increase in: (a) and (b) normalized drift, and (c) and (d) normalized lateral force 117

Figure 3.27. Effect of tie-down detailing on shear wall shear distortion with increase in: (a) and (b) normalized drift, and (c) and (d) normalized lateral force 118

Figure 3.28. Effect of shear wall detailing: (a) force-displacement response, and (b) backbone curve comparison 120

Figure 3.29. Physical damage to specimen SGGS-2 at drift ratio $\Delta_{max} = 4.08\%$ 121

Figure 3.30. Effect of shear wall detailing on tension-rod forces with increase in: (a) and (b) normalized drift, and (c) and (d) normalized lateral force 123

Figure 3.31. Effect of shear wall detailing on wall end uplift with increase in: (a) and (b) normalized drift, and (c) and (d) normalized lateral force 124

Figure 3.32. Effect of shear wall detailing on shear wall shear distortion with increase in: (a) and (b) normalized drift, and (c) and (d) normalized lateral force . . 125

Figure 3.33. Sheet fastener pattern for specimens: (a) SGGS-1 and (b) SGGS-1XS (all units in mm); and (c) force-displacement response of SGGS-1 and SGGS-1XS 127

Figure 3.34. Sheet fastener pattern for specimens: (a) SGGS-2B and (b) SGGS-2 (all units in mm); and (c) force-displacement response of SGGS-2 and SGGS-2B 128

Figure 3.35. Damage to steel sheet and fasteners at the end of monotonic pull tests for specimens: (a) SGGS-1 ($\Delta_{max} = 4.15\%; \Delta_{res} = 1.85\%$), and (b) SGGS-1XS ($\Delta_{max} = 4.6\%; \Delta_{res} = 2.8\%$) 129

Figure 3.36. Damage to steel sheet and fasteners at the end of testing for specimens: (a) SGGS-2B ($\Delta_{max} = 10\%; \Delta_{res} = -0.23\%$), and (b) SGGS-2 ($\Delta_{max} = 4.1\%$) 130

Figure 4.1. Envelope of lateral force versus drift for all tested configurations: (a) unfinished specimens and (b) finished specimens 133

Figure 4.2. Fastener damage statistics for identified failure modes in unfinished specimens: (a) quasi-static test phase, and (b) shake table test phase 136

Figure 4.3. Fastener connection damage in specimen SGGS-1HD at (a) undamaged state, (b) elastic ($\Delta = 0.40\%$), (c) quasi-elastic ($\Delta = 0.80\%$), (d) design ($\Delta = 1.99\%$), (e) above design ($\Delta = 3.0\%$) performance levels, and (f) and (g) drift ratio $\Delta = 4.0\%$ 137

Figure 4.4. Framing member damage in specimen SGGS-1HD at above design performance level ($\Delta = 3.0\%$): (a)-(c) views of steel sheet buckling from front and back, (d) and (e) bottom track bending near chord stud pack, and (f) bending in chord stud pack 138

Figure 4.5. Framing member damage in specimen SGGS-1HD at conclusion of testing ($\Delta_{res} = 1.93\%$) after larger drift cycles ($\Delta_{max} = 7.0\%$): (a) elevation view of wall-line, (b) gravity stud flange buckling, and (c) stud pack framing connection failure 139

Figure 4.6. EIFS layer damage in specimen SGGS-2F at (a) elastic ($\Delta = 0.21\%$) and (b) quasi-elastic ($\Delta = 0.62\%$), (c) and (d) design ($\Delta = 1.41\%$), (e) and (f) above design ($\Delta = 2.04\%$) performance levels, (g) and (h) at drift ratio $\Delta = 4.0\%$ 141

Figure 4.7. Gypsum damage in specimen SGGS-2F at (a) quasi-elastic ($\Delta = 0.62\%$) and (b) design ($\Delta = 1.41\%$), (c) above design ($\Delta = 2.04\%$) performance levels, (d)-(f) drift ratio $\Delta = 4.0\%$ 143

Figure 4.8. Evolution of (a) and (b) natural period, and (c) and (d) damping ratio for shake table test phase specimens 144

Figure 4.9. Illustration of the drift cycle qualification procedure for specimen SGGG-1 148

Figure 4.10. Comparison of (a) significant drift cycle distribution, and (b) fractional (normalized) significant drift cycle distribution for select wall specimens tested during shake table and quasi-static test phases 148

Figure 4.11. (a) Cumulative dissipated energy, and (b) energy dissipation rate for unfinished specimens 150

Figure 4.12. (a) Cumulative dissipated energy, and (b) energy dissipation rate for finished specimens 152

Figure 4.13. Cumulative dissipated energy comparison for select specimens from quasi-static test phase 153

Figure 4.14. Comparison of (a) equivalent hysteretic damping, (b) and (c) hysteretic loops at elastic and above design performance levels between SGGS-2 and SGGS-2F wall configurations 154

Figure 5.1. Isometric view and schematic floor plan of test building (Wang et al., 2018b) 158

Figure 5.2. (a) Corridor shear wall and longitudinal corner shear wall framing at level 2, and (b) Tie-rod connection details: tie-rod assembly, coupler and double nut connection, and bearing plate connection (Wang et al., 2018b) 160

Figure 5.3. (a) Elastic pseudo-acceleration spectra (ξ = 5%), and (b) acceleration time histories of achieved input motions 162

Figure 5.4. Elements considered in OpenSees numerical model 164

Figure 5.5. *Pinching4* uniaxial material model (Lowes and Altoontash, 2003) 165

Figure 5.6. Schematic of refined wall-line OpenSeesPy finite element model (Zhang, 2023). 166

Figure 5.7. Comparison of experimental and calibrated *pinching4* material response: (a) force-deformation response, (b) dissipated energy per cycle, and (c) cumulative dissipated energy 168

Figure 5.8. (a) Effect of framing details on shear wall response, and (b) backbone curves for west corridor shear walls 171

Figure 5.9. Methodology for deriving vertical element behavior: level 2 west corridor shear wall uplift versus tie-rod force at (a) service level and (b) design and MCE level earthquake intensities; and (c) general schematic of tension tie-rod material behavior. 173

Figure 5.10. Backbone curves for: (a) corner shear walls, and (b) interior and exterior gravity walls in longitudinal and transverse directions 173

Figure 5.11. Comparison of eigen analysis results with system ID results per Wang and Hutchinson (2020): natural frequency and mode shapes at undamaged state (S0) 179

Figure 5.12. Comparison of eigen analysis results with system ID results: elongation of mode 2 (longitudinal translation) natural period at different damage states 180

Figure 5.13. Roof drift ratio time history comparison for: (a) EQ2:CNP-25 (SLE), (b) EQ6:CNP-100 (DE) and (c) EQ7:CNP-150 (MCE) 181

Figure 5.14. Contribution of shear deformation towards inter-story drift for EQ6:CNP-100 earthquake 182

Figure 5.15. Story shear versus inter-story drift response comparison for EQ2:CNP-25 183

Figure 5.16. Story shear versus inter-story drift response comparison for EQ6:CNP-100 184

Figure 5.17. Story shear versus inter-story drift response comparison for EQ7:CNP-150 185

Figure 5.18. (a) Normalized peak base shear forces versus peak roof drift ratio, (b) peak roof drift ratios, (c) normalized peak base shear and (d) normalized peak overturning moment 186

Figure 5.19. Floor pseudo-acceleration response spectra ($\xi = 5\%$) comparison 187

Figure 5.20. Building peak response comparison: (a) peak floor acceleration, and (b) floor acceleration amplification 188

Figure 5.21. Building peak response comparison: peak inter-story drift ratio envelope . 189

Figure 6.1. Archetype building slice options (color regions overlaid with original archetype building plan set) 206

Figure 6.2. Floor plan of the 10-story CFS-NHERI test building 207

Figure 6.3. CFS-NHERI test building installed at the NHERI@UC San Diego LH-POST6 facility (rendering courtesy of Charlie Zhang) 207

Figure 6.4. Psuedo-acceleration response spectrum for selected site 208

Figure 6.5. Tie-down systems used in the longitudinal direction of the test building: (a) hold-down attached to built-up chord studs, (b) hold-down attached to HSS section, (c) plate hold-down attached to HSS section, and (d) HSS section welded to transfer plate on shake table 208

Figure B.1. Stress-strain curve of CFS coupons 236

Figure B.2. Hold-down catalog from manufacturer (source: www.mitek-us.com) 239

Figure B.3. Stress-strain curve for tension tie-rods 240

Figure B.4. Material certification for tension tie-rods provided by manufacturer 241

Figure C.1. Force displacement response of SGGS-1 specimen 246

Figure C.2. Force displacement response of SGGS-1XS specimen 247

Figure C.3. Force displacement response of SGGS-1F specimen 248

Figure C.4. Force displacement response of SGGS-1SB specimen 250

Figure C.5. Force displacement response of SGGS-2B specimen 252

Figure C.6. Force displacement response of SGGG-1 specimen 253

Figure C.7. Force displacement response of SWWS-2 specimen 254

Figure C.8. Force displacement response of SWWS-1 specimen 256

Figure C.9. Force displacement and energy dissipation response of specimen GGGG . 258

Figure C.10. Force displacement and energy dissipation response of specimen GGGG-F 258

Figure C.11. Force displacement and energy dissipation response of specimen SGGS-2 259

Figure C.12. Force displacement and energy dissipation response of specimen SGGS-2F 259

Figure C.13. Force displacement and energy dissipation response of specimen SWWS-2 260

Figure C.14. Force displacement and energy dissipation response of specimen SWWS-2F 260

Figure C.15. Force displacement and energy dissipation response of specimen SWWS-1 261

Figure C.16. Force displacement and energy dissipation response of specimen SGGG-1F 261

Figure C.17. Force displacement and energy dissipation response of specimen SGGS-1HD 262

Figure C.18. Force displacement and energy dissipation response of specimen SGGS-1HDF 262

Figure C.19. Equivalent hysteretic damping for specimens GGGG and GGGG-F 263

Figure C.20. Equivalent hysteretic damping for specimens SGGS-2 and SGGS-2F 263

Figure C.21. Equivalent hysteretic damping for specimens SWWS-2 and SWWS-2F . . . 264

Figure C.22. Equivalent hysteretic damping for specimens SGGG-1F and SWWS-1 . . . 264

Figure C.23. Equivalent hysteretic damping for specimens SGGS-1HD and SGGS-1HDF 264

Figure D.1. SGGS-1 specimen local response during design earthquake test 266

Figure D.2. SGGS-1 specimen local behavior evolution 267

Figure D.3. SGGS-1XS specimen local response during quasi-elastic earthquake test . 268

Figure D.4. SGGS-1XS specimen local behavior evolution 269

Figure D.5. SGGS-1F specimen local response during quasi-elastic earthquake test . . . 270

Figure D.6. SGGS-1F specimen local behavior evolution 271

Figure D.7. SGGS-1SB specimen local response during quasi-elastic earthquake test . 272

Figure D.8. SGGS-1SB specimen local behavior evolution 273

Figure D.9. SGGS-2B specimen local response during design earthquake test 274

Figure D.10. SGGS-2B specimen local behavior evolution 275

Figure D.11. SGGG-1 specimen local response during design earthquake test 276

Figure D.12. SGGG-1 specimen local behavior evolution 277

Figure D.13. SWWS-2 specimen local response during above design 2 earthquake test 278

Figure D.14. SWWS-2 specimen local behavior evolution 279

Figure D.15. SWWS-1 specimen local response during above design 1 earthquake test . 280

Figure D.16. SWWS-1 specimen local behavior evolution 281

Figure D.17. Wall uplift evolution for specimen GGGG with increase in lateral force and lateral drift 282

Figure D.18. Wall uplift evolution for specimen GGGG-F with increase in lateral force and lateral drift 283

Figure D.19. Tension tie-rod force evolution for specimen SGGS-2 with increase in lateral force and lateral drift 284

Figure D.20. Wall uplift evolution for specimen SGGS-2 with increase in lateral force and lateral drift: (a) Wall ends and (b) Gravity bay ends 285

Figure D.21. Shear wall shear distortion evolution for specimen SGGS-2 with increase in lateral force and lateral drift 287

Figure D.22. Tension tie-rod force evolution for specimen SGGS-2F with increase in lateral force and lateral drift 288

Figure D.23. Wall uplift evolution for specimen SGGS-2F with increase in lateral force and lateral drift: (a) Wall ends and (b) Gravity bay ends 289

Figure D.24. Shear wall shear distortion evolution for specimen SGGS-2F with increase in lateral force and lateral drift 291

Figure D.25. Tension tie-rod force evolution for specimen SWWS-2 with increase in lateral force and lateral drift 292

Figure D.26. Wall uplift evolution for specimen SWWS-2 with increase in lateral force and lateral drift: (a) Wall ends and (b) Window bay ends 293

Figure D.27. Shear wall shear distortion evolution for specimen SWWS-2 with increase in lateral force and lateral drift 295

Figure D.28. Tension tie-rod force evolution for specimen SWWS-2F with increase in lateral force and lateral drift 296

Figure D.29. Wall uplift evolution for specimen SWWS-2F with increase in lateral force and lateral drift: (a) Wall ends and (b) Window bay ends 297

Figure D.30. Shear wall shear distortion evolution for specimen SWWS-2F with increase in lateral force and lateral drift 299

Figure D.31. Tension tie-rod force evolution for specimen SWWS-1 with increase in lateral force and lateral drift: (a) Exterior rods and (b) Interior rods 300

Figure D.32. Wall uplift evolution for specimen SWWS-1 with increase in lateral force and lateral drift: (a) Wall ends and (b) Window bay ends 302

Figure D.33. Shear wall shear distortion evolution for specimen SWWS-1 with increase in lateral force and lateral drift 304

Figure D.34. Tension tie-rod force evolution for specimen SGGG-1F with increase in lateral force and lateral drift 305

Figure D.35. Wall uplift evolution for specimen SGGG-1F with increase in lateral force and lateral drift: (a) Wall ends and (b) Shear segment ends 306

Figure D.36. Shear wall shear distortion evolution for specimen SGGG-1F with increase in lateral force and lateral drift 308

Figure D.37. Hold-down tie-down force evolution for specimen SGGS-1HD with increase in lateral force and lateral drift 309

Figure D.38. Wall uplift evolution for specimen SGGS-1HD with increase in lateral force and lateral drift: (a) Wall ends and (b) Gravity bay ends 310

Figure D.39. Shear wall shear distortion evolution for specimen SGGS-1HD with increase in lateral force and lateral drift 312

Figure D.40. Hold-down tie-down force evolution for specimen SGGS-1HDF with increase in lateral force and lateral drift 313

Figure D.41. Wall uplift evolution for specimen SGGS-1HDF with increase in lateral force and lateral drift: (a) Wall ends and (b) Gravity bay ends 314

Figure D.42. Shear wall shear distortion evolution for specimen SGGS-1HDF with increase in lateral force and lateral drift 316

LIST OF TABLES

Table 2.1. Unit weight of dead load and live load 36

Table 2.2. Effective seismic weight of the building 37

Table 2.3. Design summary: 10 story archetype building 37

Table 2.4. Design summary: 4 story archetype building 38

Table 2.5. Test matrix and definition of specimens: shake table test phase 38

Table 2.6. Characteristics of selected seed motions 56

Table 2.7. Target performance level definition 56

Table 2.8. Motion scaling factors for test group 1 (specimens SGGS-1 and SGGS-1XS) 59

Table 2.9. Motion scaling factors for test group 2 (specimens SGGS-1F and SGGS-1SB) 59

Table 2.10. Motion scaling factors for test group 3 (specimens SGGG-1 and SGGS-2B) 59

Table 2.11. Motion scaling factors for test group 4 (specimens SWWS-2 and SWWS-1) 60

Table 2.12. Input earthquake sequence for specimens SGGS-1 and SGGS-1XS 64

Table 2.13. Input earthquake sequence for specimens SGGS-1F and SGGS-1SB 64

Table 2.14. Input earthquake sequence for specimens SGGG-1 and SGGS-2B 64

Table 2.15. Input earthquake sequence for specimens SWWS-1 and SWWS-2 64

Table 2.16. Test matrix and definition of specimens: quasi-static test phase 71

Table 3.1. Effect of finish application: results summary 94

Table 3.2. Effect of window opening: results summary 102

Table 3.3. Effect of asymmetric shear wall location: results summary 107

Table 3.4. Effect of tie-down detailing: results summary 113

Table 3.5. Effect of shear wall detailing: results summary 121

Table 3.6. Effect of sheet fastener pattern: results summary 128

Table 4.1. Hysteretic response measurements for unfinished specimens 134

Table 4.2. Hysteretic response measurements for finished specimens 134

Table 5.1. Summary of the shear wall and tie-down system detailing 159

Table 5.2. Summary of achieved pre-fire test sequence input motions 161

Table 5.3. Summary of wall specimens tested by Rizk and Rogers (2017) selected for analysis 170

Table 5.4. Vertical spring element parameters (tension and compression) used in the numerical model 174

Table 5.5. Calibrated *pinching4* backbone parameters 174

Table 5.6. *Pinching4* reloading, unloading and degradation parameters. 175

Table 5.7. *Pinching4* backbone parameters used for shear elements in numerical model 176

Table 5.8. Estimated building weight and floor distributions (in kN) 177

Table 5.9. Modal participation mass ratios for each mode 178

Table B.1. Batch source of framing members 234

Table B.2. Batch A1 material properties 234

Table B.3. Batch A2 material properties 234

Table B.4. Batch B2 material properties 234

Table B.5. Individual coupon test results 235

Table B.6. Stucco mix batches 237

Table B.7. Finish layer 1 compressive strength test 238

Table B.8. Finish layer 2 compressive strength test 238

Table B.9. Material properties of tension tie-rods 239

ACKNOWLEDGEMENTS

While this dissertation may bear my name as the author, the work presented in it has only been possible because of the input of many people and support of innumerable more. First and foremost, I would like to thank my advisor, Professor Tara Hutchinson. I am deeply indebted to her for her belief in my abilities, her constructive criticism of my work, for "playing devil's advocate" to force me to think further, and for her guidance to stop me before I "go down the rabbit hole". Her lengthy feedback and amazing suggestions have shown me what good quality work looks like, and I am immensely grateful for her example.

Along with my advisor, I would also like to thank Dr. Ben Schafer and Dr. Kara Peterman, for giving me the opportunity to a be part of the CFS-NHERI research team, providing insightful and meaningful input to enrich my work, trusting me with responsibilities, advocating for me and playing an active role in my academic progress. This journey was made fun and rewarding thanks to the hard-working graduate students I worked alongside on the CFS-NHERI project: Zhidong Zhang, Hernan Castaneda, Fani Derveni, Charlie Zhang, Mohammed Eladly.

I would like to express my sincere appreciation to the other members of my doctoral committee, Professors Joel Conte, William Hodgkiss, Machel Morrison and Pui-shum Shing, for their time, support and excellent suggestions for improving my research. I must also thank the faculty members of UC San Diego who taught me during my graduate studies. It was a privilege to be a part of your classes.

The experimental work presented herein was performed at NHERI@UC San Diego LHPOST facility and the Powell Laboratory. I am deeply thankful to the amazing lab staff: Alex Sherman, Jeremy Fitcher, Darren Mckay, Robert Beckley, Noah Aldrich, Abdullah Hamid, Dr. Christopher Latham, Michael Sanders, and Andrew Sander for their dedicated help executing the experiments and for showing patience with an inexperienced graduate student. I also gratefully acknowledge the undergraduate students: Kim-Chi Nguyen, Jesus Perez Castaneda, Tristen Gamboa, Roberto Furlan, Gustavo Ramirez Zarate, Jaysen Zapata; and visiting graduate students: Filippo Sirotti and Maryam Soltani who assisted with the experiments.

I shall always cherish the unexpected opportunity I had of being mentored by Dr. Xiang Wang. I would like to thank him for helping me hone my problem-solving abilities, for providing his wise counsel, for his unwavering support and his enthusiastic collaboration. Incredible people of the Structural Engineering department: Gloria Faraone, Elide Pantoli, Brandon Schiller, Angshuman Deb, Mukesh Kumar Ramancha, Mayank Chadha, Athul Prabhakaran Parayancode, Srikar Gunisetty, Rahul Hazra, Varun Bhatt, Michael Morano, Shokrullah Sorosh, Sneha Raj, Masood Inamdar, Aashka Vora, Soumabrata Dutta, Jenny Ni Zhan, Tiffany La, Krishna Anish Adusumilli, Maitreya Kurumbhati, Louis Lin, Kinal Bid, Divya Sharma, Daniel Kothoor, thank you for sharing in my journey. Staff of the Structural Engineering department: Lindsay Walton, Joana Halnez, Yvonne Wollmann, and Leslie Verfaillie, thank you for your thorough attention.

I must also thank my first academic mentor, Professor Durgesh Rai, from the Civil Engineering department of Indian Institute of Technology Kanpur (IITK), my undergraduate alma mater in India. My heartfelt appreciation and thanks go to him for showing a young student how appealing and exciting experiments can be. Speaking of IITK, shoutout to my friends who have continued to love and support from thousands of miles away: Aditya Jain, Shrey Verma, Mohit Sharma, Rakesh Kumar, Aaditya Verma, Amit Anand, Pranjal Verma, Shubham Singh, Manish Mehta.

I am enormously grateful to Tejas Baid, Elesh Lakhani, Aneri Sheth, Jay Sheth for their company during the distressing COVID pandemic. Even more enormously, if that is possible, to Sneha Jha and Dipendra Nath De. Their home was the safe haven I sought when things got tricky. And things used to get tricky a lot. Thank you for calling me family, for your kindness, for celebrating life in San Diego.

I cannot begin to express how lucky I am to have my wonderful partner, Devyani, by my side. Your intelligence constantly inspires me to be a better person. Nobody else I'd rather share with the humorous and lame parts of life but you. Last but not least I would like to thank my family, for letting me follow my dreams, supporting them without doubt or question. I am incredibly blessed to have encouraging, motivating and loving parents.

This dissertation research was supported by the National Science Foundation under Grant Nos. CMMI 1663569 and CMMI 1663348, "Collaborative Research: Seismic Resiliency of Repetitively Framed Mid-Rise Cold-Formed Steel Buildings". Dr. Tara C. Hutchinson is the principle investigator for the UCSD portion of the research project, alongwith Dr. Benjamin W. Schafer of Johns Hopkins University and Dr. Kara D. Peterman of University of Massachusetts, Amherst. The experiments were conducted at the Large High-Performance Outdoor Shake Table test facility at the University of California, San Diego, supported by the Natural Hazards Engineering Research Infrastructure (NHERI) program, and at the Structural Engineering Powell Laboratory. Specific to the wall-line systems tested within the experiments, the dissertation author appreciates ClarkDietrich Building Systems, California Expanded Metal Products Co. (CEMCO) and SWS Panel for their support in material donation and specimen fabrication. The above support is gratefully acknowledged. Opinions and findings of this dissertation are those of the author and do not necessarily reflect those of the sponsors.

****

Portions of the following paper and technical reports, for which the dissertation author was the primary investigator and author, are contained in Chapter 2:

Singh, A., Wang, X., Torabian, S., Hutchinson, T. C., Peterman, K. D., and Schafer, B. W. (2020). Seismic Performance of Symmetric Unfinished CFS In-Line Wall Systems. In *Structures Congress 2020* (pp. 629-642). Reston, VA. American Society of Civil Engineers.

Singh, A., Wang, X. and Hutchinson, T. C. (2021). *Lateral Response of Cold-Formed Steel Framed Steel Sheathed In-line Wall Systems Detailed for Mid-Rise Buildings. Part I: Shake Table Test Phase* (Structural Systems Research Report SSRP-19/05). University of California San Diego, La Jolla, CA.

Singh, A. and Hutchinson, T. C. (2022). *Lateral Response of Cold-Formed Steel Framed Steel Sheathed In-line Wall Systems Detailed for Mid-Rise Buildings. Part II: Quasi-Static Test*

Phase (Structural Systems Research Report SSRP-19/06). University of California San Diego, La Jolla, CA.

Portions of the following papers and technical reports, for which the dissertation author was the primary investigator and author, are contained in Chapter 3:

Singh, A., Wang, X., Zhang, Z., Derveni, F., Castaneda, H., Peterman, K. D., Schafer, B. W., and Hutchinson, T. C. (2022). "Steel Sheet Sheathed Cold-Formed Steel Framed In-line Wall Systems. I: Impact of Structural Detailing" *ASCE J. Struct. Eng.*, 148(12), 04022193.

Singh, A., Wang, X., Zhang, Z., Derveni, F., Castaneda, H., Peterman, K. D., Schafer, B. W., and Hutchinson, T. C. (2022). "Steel Sheet Sheathed Cold-Formed Steel Framed In-line Wall Systems. II: Impact of Nonstructural Detailing" *ASCE J. Struct. Eng.*, 148(12), 04022194.

Singh, A., Wang, X. and Hutchinson, T. C. (2021). *Lateral Response of Cold-Formed Steel Framed Steel Sheathed In-line Wall Systems Detailed for Mid-Rise Buildings. Part I: Shake Table Test Phase* (Structural Systems Research Report SSRP-19/05). University of California San Diego, La Jolla, CA.

Singh, A. and Hutchinson, T. C. (2022). *Lateral Response of Cold-Formed Steel Framed Steel Sheathed In-line Wall Systems Detailed for Mid-Rise Buildings. Part II: Quasi-Static Test Phase* (Structural Systems Research Report SSRP-19/06). University of California San Diego, La Jolla, CA.

Portions of the following manuscript and technical reports, for which the dissertation author was the primary investigator and author, are contained in Chapter 4:

Singh, A., Wang, X., Zhang, Z., Schafer, B. W., and Hutchinson, T. C. "Physical Damage-Hysteretic Response Correlation for Steel Sheet Sheathed Cold-Formed Steel-Framed Wall-Lines" *Earthq. Eng. Struct. Dyn.* In preparation for submission.

Singh, A., Wang, X. and Hutchinson, T. C. (2021). *Lateral Response of Cold-Formed Steel Framed Steel Sheathed In-line Wall Systems Detailed for Mid-Rise Buildings. Part I: Shake*

Table Test Phase (Structural Systems Research Report SSRP-19/05). University of California San Diego, La Jolla, CA.

Singh, A. and Hutchinson, T. C. (2022). *Lateral Response of Cold-Formed Steel Framed Steel Sheathed In-line Wall Systems Detailed for Mid-Rise Buildings. Part II: Quasi-Static Test Phase* (Structural Systems Research Report SSRP-19/06). University of California San Diego, La Jolla, CA.

Portions of the following manuscript, for which the dissertation author was the primary investigator and author, are contained in Chapter 5:

Singh, A., Zhang, Z., Wang, X., Schafer, B. W., and Hutchinson, T. C. "Development of a Design-Grade Numerical Model of Cold-Formed Steel-Framed Mid-Rise Buildings." *Eng. Struct.* In preparation for submission.

Portions of the following papers, for which the dissertation author was the primary investigator and author, are contained in Chapter 6:

Singh, A., Wang, X., Zhang, Z., Derveni, F., Castaneda, H., Peterman, K. D., Schafer, B. W., and Hutchinson, T. C. (2022). "Steel Sheet Sheathed Cold-Formed Steel Framed In-line Wall Systems. I: Impact of Structural Detailing" *ASCE J. Struct. Eng.*, 148(12), 04022193.

Singh, A., Wang, X., Zhang, Z., Derveni, F., Castaneda, H., Peterman, K. D., Schafer, B. W., and Hutchinson, T. C. (2022). "Steel Sheet Sheathed Cold-Formed Steel Framed In-line Wall Systems. II: Impact of Nonstructural Detailing" *ASCE J. Struct. Eng.*, 148(12), 04022194.

Singh, A., Hutchinson, T. C., Torabian, S., Schafer, B. W., Peterman, K. D., Padgett, L. and Jones, H. (2022). Structural Design Narrative of the CFS-NHERI 10-story Test Building for Multi-dimensional Shake Table Testing. In *Proceedings of Cold-Formed Steel Research Consortium Colloquium*. Baltimore, MD. Johns Hopkins University.

VITA

2016 Bachelor of Technology - Master of Technology (Dual Degree) in Civil Engineering, Indian Institute of Technology Kanpur, India

2023 Doctor of Philosophy in Structural Engineering, University of California San Diego

PUBLICATIONS

Peer-Reviewed Journal Articles

Singh, A., Wang, X., Zhang, Z., Derveni, F., Castaneda, H., Peterman, K. D., Schafer, B. W., and Hutchinson, T. C. (2022). "Steel Sheet Sheathed Cold-Formed Steel Framed In-line Wall Systems. I: Impact of Structural Detailing." *ASCE J. Struct. Eng.*, 148(12), 04022193.

Singh, A., Wang, X., Zhang, Z., Derveni, F., Castaneda, H., Peterman, K. D., Schafer, B. W., and Hutchinson, T. C. (2022). "Steel Sheet Sheathed Cold-Formed Steel Framed In-line Wall Systems. II: Impact of Nonstructural Detailing." *ASCE J. Struct. Eng.*, 148(12), 04022194.

Zhang, Z., **Singh, A.**, Derveni, F., Torabian, S., Peterman, K. D., Hutchinson, T. C., and Schafer, B. W. (2022). "Cyclic Experiments on Steel Sheet Connections for Standard CFS Framed Steel Sheet Sheathed Shear Walls." *ASCE J. Struct. Eng.*, 148(2), 04021261.

Zhang, Z., **Singh, A.**, Derveni, F., Torabian, S., Peterman, K. D., Hutchinson, T. C., and Schafer, B. W. (2021). "Cyclic Experiments on Isolated Steel Sheet Connections for CFS Framed Steel Sheet Sheathed Shear Walls with New Configurations." *Eng. Struct.*, 244(11), 112805.

Research Reports

Singh, A., and Hutchinson, T.C. (2022). *Lateral Response of Cold-Formed Steel Framed Steel Sheathed In-line Wall Systems Detailed for Mid-Rise Buildings. Part II: Quasi-Static Test Phase*, Structural Systems Research Report SSRP-19/06, University of California San Diego, La Jolla, CA.

Singh, A., Wang, X., and Hutchinson, T.C. (2021). *Lateral Response of Cold-Formed Steel Framed Steel Sheathed In-line Wall Systems Detailed for Mid-Rise Buildings. Part I: Shake Table Test Phase*, Structural Systems Research Report SSRP-19/05, University of California San Diego, La Jolla, CA.

Conference Papers

Singh, A., Hutchinson, T. C., Torabian, S., Schafer, B. W., Peterman, K. D., Padgett, L. and Jones, H. (2022). Structural Design Narrative of the CFS-NHERI 10-story Test Building for Multi-dimensional Shake Table Testing. *Proceedings of the Cold-Formed Steel Research Consortium Colloquium*, Baltimore, MD.

Singh, A., Zhang, Z., Castaneda, H., Peterman, K.D., Schafer, B.W., and Hutchinson, T. C. (2022). Correlating fastener damage to hysteretic response and performance levels in steel sheet sheathed CFS wall-lines. *Proceedings of the 12th National Conference in Earthquake Engineering*, Earthquake Engineering Research Institute, Salt Lake City, UT.

Singh, A., Wang, X., Zhang, Z., Derveni, F., Castaneda, H., Peterman, K. D., Schafer, B. W. (2020). Lateral Response of Cold-Formed Steel Framed Steel Sheathed In-line Wall Systems Detailed for Mid-Rise Buildings. *Proceedings of the Cold-Formed Steel Research Consortium Colloquium*, Baltimore, MD.

Singh, A., Wang, X., Torabian, S., Hutchinson, T. C., Peterman, K. D., and Schafer, B. W. (2020). Seismic Performance of Symmetric Unfinished CFS In-Line Wall Systems. In *Structures Congress 2020* (pp. 629-642), Reston, VA. ASCE.

Singh, A., and Hutchinson, T. C. (2018). Finite Element Modeling and Validation of Steel Sheathed Cold-Formed Steel Framed Shear Walls. *CCFSS Proceedings of International Specialty Conference on Cold-Formed Steel Structures*. 5.

Zhang, J., **Singh, A.**, Hutchinson, T. C., and Wang, X. (2022). Seismic Analysis of the 10-Story CFS-NHERI Building. *Proceedings of the Cold-Formed Steel Research Consortium Colloquium*, Baltimore, MD.

Zhang, Z., Speicher, M.S., **Singh, A.**, Hutchinson, T. C., and Schafer, B. W. (2022). Effects of Modeling Decisions on the Lateral Performance of Cold-Formed Steel Framed Walls. *Proceedings of the Cold-Formed Steel Research Consortium Colloquium*, Baltimore, MD.

Zhang, Z., Speicher, M.S., **Singh, A.**, Hutchinson, T. C., and Schafer, B. W. (2022). Impact of detailing on the lateral performance of cold-formed steel framed walls. *Proceedings of the 12th National Conference in Earthquake Engineering*, Earthquake Engineering Research Institute, Salt Lake City, UT.

Zhang, Z., **Singh, A.**, Derveni, F., Torabian, S., Peterman, K. D., Hutchinson, T. C., and Schafer, B. W. (2020). Cyclic Performance of Steel Sheet Connections for CFS framed Steel Sheet Sheathed Shear Walls. *Proceedings of the Cold-Formed Steel Research Consortium Colloquium*, Baltimore, MD.

Dataset DOIs

Singh, A., Hutchinson, T., Wang, X., Zhang, Z., Schafer, B., Castaneda, H., Derveni, F., Peterman, K. (2022) "Wall Line Tests: Phase 2 – Quasi-Static Tests", in CFS-NHERI: Seismic Resiliency of Repetitively Framed Mid-Rise Cold-Formed Steel Buildings. DesignSafe-CI. DOI: 10.17603/ds2-encf-vj32.

Singh, A., Hutchinson, T., Wang, X., Zhang, Z., Schafer, B., Derveni, F., Castaneda, H., Peterman, K. (2021) "Wall Line Tests: Phase 1 – Shake Table Tests", in CFS-NHERI: Seismic Resiliency of Repetitively Framed Mid-Rise Cold-Formed Steel Buildings. DesignSafe-CI. DOI: 10.17603/ds2-mvj8-8386.

Zhang, Z., Torabian, S., **Singh, A.**, Derveni, F., Peterman, K., Hutchinson, T., Schafer, B. (2021) "Cyclic Experiments on Isolated Steel Sheet Connections for CFS Framed Steel Sheet Sheathed Shear Walls", in CFS-NHERI: Seismic Resiliency of Repetitively Framed Mid-Rise Cold-Formed Steel Buildings. DesignSafe-CI. DOI: 10.17603/ds2-y1wv-yz51.

ABSTRACT OF THE DISSERTATION

Seismic Behavior of Cold-Formed Steel-Framed Wall-Line Systems in Mid-Rise Buildings

by

Amanpreet Singh

Doctor of Philosophy in Structural Engineering

University of California San Diego, 2023

Professor Tara C. Hutchinson, Chair

Cold-formed steel (CFS) framing offers many benefits to buildings in seismically active regions. Amongst the most notable CFS attributes include its low fabrication and maintenance costs, noncombustible and corrosion resistant nature, high durability and ductility. These benefits have made CFS framing a popular choice for construction of low-rise and mid-rise structures. From a seismic performance perspective, the light weight and ductility offered by a CFS-framed structure aligns with system resiliency needs in moderate to high seismic zones. Although experimental data exists documenting the performance of isolated CFS-framed shear walls, the structural lateral force resisting systems (LFRS) in CFS-framed buildings are constructed and integrally attached to non-designated systems, such as gravity walls as well as various nonstructural components. The contribution of the non-designated systems and the

nonstructural components towards the response of wall-lines within the building system under high intensity earthquake shaking is not well understood. Moreover, experimental data to support code guidelines in current North American standards for design of CFS-framed shear walls, which meet the seismic demands for mid-rise buildings (>6 stories) are lacking. Indeed, the paucity of full-scale test data documenting the behavior of wall-line systems detailed for mid-rise buildings has been a barrier to bringing the potential benefits of CFS framing to the community.

To address these limitations, a two-phased experimental program was undertaken in this dissertation to advance the understanding of CFS-framed steel sheet sheathed shear walls placed in-line with gravity walls. Referred to herein as "wall-lines", these test specimens were detailed to support the lateral load demands anticipated of mid-rise buildings in high seismic zones. In the first phase, wall-line assemblies were tested at full-scale on a shake table, first under a sequence of increasing amplitude (in-plane) earthquake input motions, and subsequently under slow monotonic pull conditions (for select specimens). In the second phase, wall-line assemblies were tested under quasi-static reverse cyclic displacement-controlled loading using a simulated floor-load imposed via hydraulic actuators. Steel sheet sheathed shear walls offered energy dissipation primarily through structural member-to-sheathing connections and yielding of the steel sheet. All specimens demonstrated a tension field that spread across the entirety of the steel sheet at failure. The impact of different test variables governing the structural and nonstructural detailing on the seismic performance of the CFS-framed wall-line specimens is quantified by careful systematic comparison between different configurations. Wall-line assemblies with interior and exterior finish demonstrated substantially increased strength and stiffness without any decrease in drift capacity or change in failure mode. Specimens with hold-downs offered a larger lateral strength compared to specimens with tension tie-rods. However, hold-downs reached their capacity at higher drift demands whereas tension tie-rods remained linear elastic, even though both wall-lines with the different tie-down systems were designed for same overstrength force levels.

The second part of this work involved a comprehensive numerical modeling effort, using

prior experimental findings, both of the wall-line experiments discussed herein as well as a previous mid-rise six-story building specimen tested at full-scale using a suite of earthquake excitations. The developed finite element model takes into consideration the major assemblies, beyond just the isolated shear walls, which influence the dynamic response of the system, such as the strength and stiffness contribution from gravity walls as well as nonstructural components such as exterior and interior finishes installed over the shear wall and gravity wall segments. In this phase, as is common in west coast practice in the United States, a continuous tie-rod system is also modeled to capture the cumulative floor displacements caused by the axial elongation in the steel rods. The effect of built-up stud packs on strength, stiffness and drift parameters of a shear wall is also considered in the nonlinear hysteretic material model of shear walls. Very good agreement between numerical predictions and available experimental seismic response data of the six-story test building demonstrates that the proposed numerical model scheme can be employed to predict the seismic response of mid-rise CFS-framed buildings. Development of such a numerical model is an essential tool for enabling performance-based seismic design of cold-formed steel structures in this rapidly growing industry.

Chapter 1

Introduction

1.1 Background

Cold-formed steel (CFS) is structural quality steel sheet, 0.5-3 mm thick, that is gradually bent via a roll-forming process through series of dies into desired cross sections. Since, no heat is required to form the cross-section, the resulting light steel members formed during this manufacturing process are called cold-formed steel members. These members may be used as wall studs, joists, headers, jamb studs, chord studs etc. and then assembled into a wall panel or a floor diaphragm. The roll-forming machines and commonly used CFS cross sections are shown in Figure 1.1.

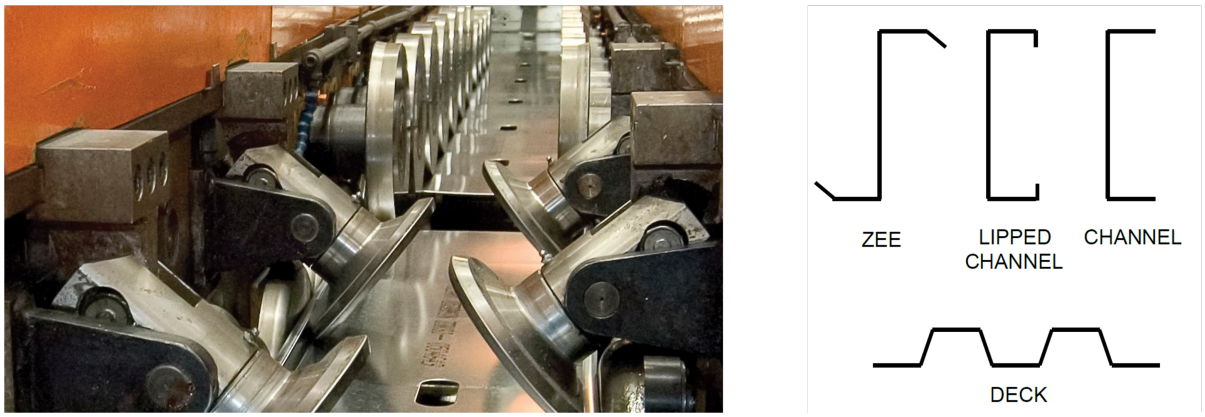


Figure 1.1. CFS member manufacturing through roll-forming machines and commonly used CFS cross sections (source: www.buildsteel.org/)

CFS-framed construction has seen a substantial growth in the North American construc-

tion industry in recent years. CFS-framed construction is rapidly becoming a popular construction choice due to an urgent need for low cost, multi-hazard resilient buildings. CFS framing provides many benefits for low and mid-rise structures. The framing components are produced from recycled materials by roll-forming steel coil or plate material into finished products at room temperatures. By the nature of their production, they are thin and easily workable. As a result, CFS framing has low installation costs since the components of their framed subsystems can be assembled quickly and with relative ease into prefabricated panels for use in wall or floor arrangements. CFS framing also has low maintenance costs due to its resistance to corrosion. In addition to the significant cost benefits, CFS framing also leads to lightweight structures, which have high durability and ductility. Moreover, it exhibits consistent material behavior and offers a high strength-to-weight ratio (Schafer, 2011). Owing to these many benefits, in particular, the light-weight construction of CFS-framed structures continues to make them increasingly common, notably in high seismic regions of the United States. From a seismic performance perspective, the ductile nature of a CFS-framed structure also aligns with system resiliency needs in moderate to high seismic zones. An added benefit, CFS is inherently non-combustible and therefore, CFS-framed buildings can potentially reduce fire spread. From a post-earthquake fire performance perspective, the non-combustible nature of CFS makes it a natural winner, specifically compared with wood framed buildings, its closest and most viable competition. Taken in totality, there are many beneficial attributes leading to a system that can meet the need for a highly sustainable, multi-hazard resilient infrastructure leading to safer communities.

Figure 1.2 shows a CFS-framed building under construction. Notably visible is the repetitively placed CFS studs within buildings framed with CFS walls, which develop lateral resistance through sheathing attached to the wall framing members. CFS shear walls have commonly used Oriented Strand Board (OSB), plywood or gypsum panels as sheathing on one or both sides of the wall, see Figure 1.3. Use of steel sheet as sheathing is relatively new and offers potential benefits over other sheathing options such as higher lateral capacity and development of well defined ductile zones along diagonal struts prior to fastener failure. Current

North American standards, AISI S240-20 and AISI S400-20, provide information to design cold-formed steel-framed steel sheet shear walls. The structural lateral force resisting systems (LFRS) in CFS-framed buildings are pragmatically constructed, and integrally attached to, non-designated systems, such as gravity walls or window/door openings as well as a significant number of nonstructural components. In the case of exterior shear walls, architectural finishes such as stucco or veneer are applied; attachments that add inertial mass and stiffness and provide additional inter-connection between shear walls and gravity walls.

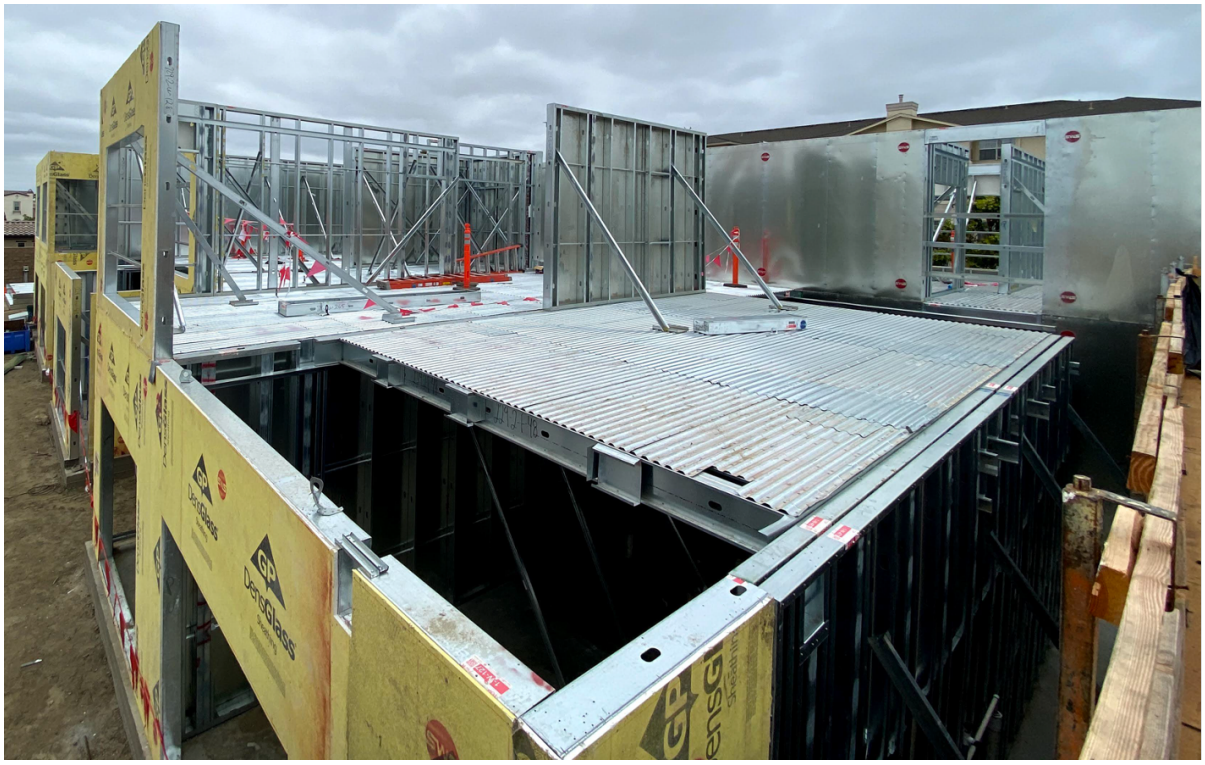


Figure 1.2. CFS-framed building under construction (photo credit: Diego Rivera, Superior Wall Systems)

1.2 Previous Research on CFS-Framed Structures

1.2.1 Component-level Experiments of CFS-Framed Walls

CFS framing has been used extensively in nonstructural applications such as interior partition walls and non-load bearing walls. However, research into use of CFS framing for

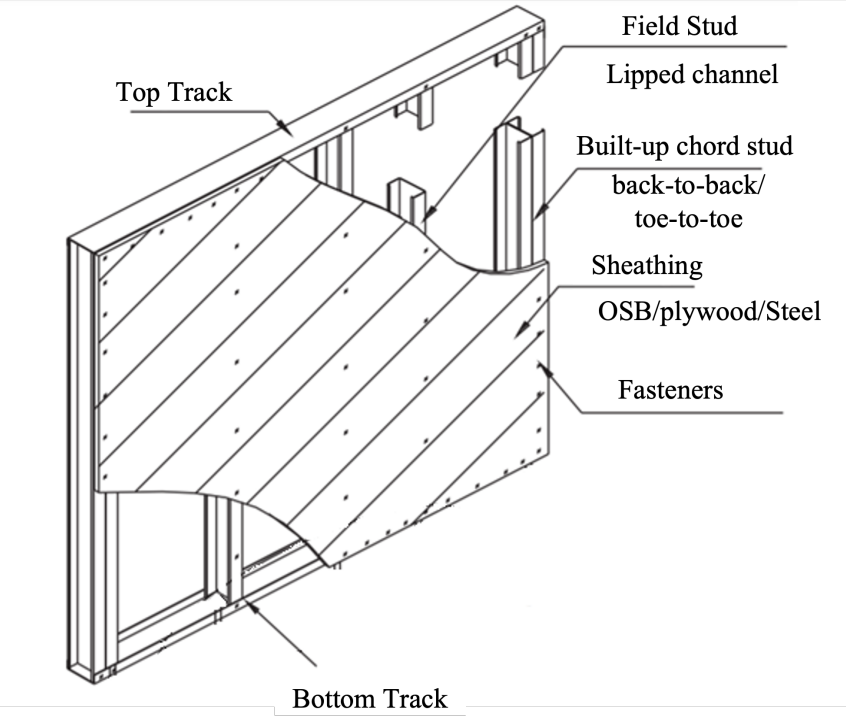


Figure 1.3. Schematic of CFS-framed shear wall

structural applications, namely, lateral force and gravity load resisting, has been growing over the last two decades. This research has supported the development of design codes, e.g. AISI S100-20, AISI S240-20, and AISI S400-20, and led to adoption of CFS in model codes such as ASCE/SEI 7-22 and International Building Code (IBC, 2018b). Several studies have examined the impact of gypsum panel sheathing on the walls lateral resistance, e.g. Nguyen et al. (1996); Morgan et al. (2002); Morello (2009); Liu et al. (2014); Lu (2015). Similarly, Serrette et al. (1997) and Liu et al. (2014) investigated OSB-sheathed shear walls with different construction details and their effect on wall lateral capacity. Indeed, the use of OSB as a structural sheathing overlay to CFS framing was observed to offer notable strength and stiffness enhancement and facilitate design goals of shear walls in seismic and wind (lateral) load needs. Serrette (1997) was the first to investigate 0.46 mm (0.018") and 0.68 mm (0.027") thick steel sheet as sheathing options for shear walls. Tested shear wall specimens were 1.22 m (4 ft) or 0.61 m (2 ft) long and 2.44 m (8 ft) high, with sheathing edge fastener spacing of 152 mm, 102 mm or 51 mm

(6”, 4” or 2”) on center (o.c.). These walls were loaded via a quasi-static cyclic sequential phase displacement-controlled protocol. These tests indicated that CFS shear walls using thicker sheathing resulted in larger lateral strength with walls failing through a combination of screw fasteners pulling out of the framing and tearing at the edge of the sheathing due to extensive bearing. Yu et al. (2007) and Yu (2010) expanded and improved upon this and provided design values for 0.76 mm (0.030”), and 0.84 mm (0.033”) thick steel options for CFS-framed shear walls. Tested shear wall specimens were 1.22 m or 0.61 m long and 2.44 m high, with sheathing edge fastener spacing of 152 mm, 102 mm or 51 mm. The test matrix consisted of a total of fifteen shear walls. These tests also showed an undesirable failure mode in some cases where specimens were detailed with a tight fastener spacing, and flange distortion of the boundary studs occured when the studs were not capacity-designed to carry higher shear forces. Figure 1.4 shows the two different failure modes observed in shear walls detailed with coarser and tighter edge fastener spacing for sheathing. It was also observed that staggering the fasteners at the edge sheathing-to-stud regions helped prevent chord stud damage and improved the shear strength and ductility of the walls. Yu and Chen (2009) subsequentyl, developed a special seismic detailing for CFS-framed shear walls to increase their lateral strength as well as improve their ductility. This was achieved by installing blocking and strapping at wall mid-height, which restricted the flexural buckling of the studs. Tested shear wall specimens were 1.22 m or 0.61 m long and 2.44 m high, with sheathing edge fastener spacing of 152 mm or 51 mm. The test matrix consisted of a total of fourteen shear walls, with ten configurations using 0.68 mm thick steel sheet and four configurations using 0.46 mm thick steel sheet. The tests demonstrated the effect special blocking detail at mid-height had on the failure mode being changed back to damage at sheathing fastener locations, see Figure 1.5

Complementary efforts of Ong-Tone (2009) and Balh et al. (2014) tested a total of 54 steel sheet sheathed CFS-framed shear walls, with 0.61 m or 1.22 m or 1.83 m or 2.44 m long and 2.44 m high, with sheathing edge fastener spacing varying betweem 50 mm or 100 mm or 150 mm. Steel sheet sheathing thickness options of 0.46 mm and 0.76 mm were considered in



(a)



(b)

Figure 1.4. Different failure modes observed in shear walls tested by Yu et al. (2007): (a) steel sheet sheathing buckling and screw pullout (coarsely spaced fasteners at 152 mm o.c. edge), and (b) flange distortion of boundary studs (tightly spaced fasteners at 51 mm o.c. edge)



Figure 1.5. Failure observed in blocked shear walls tested by Yu and Chen (2009)

these tests. Additionally, different CFS framing member thickness options were included in the test matrix. It was found that found that tighter fastener edge spacing led to an increase in shear strength. Moreover, shear walls with thicker steel sheet sheathing and framing members developed greater lateral resistance with the main failure mode being sheathing to framing connection failure. Complementing efforts of Yu et al. (2007), DaBreo et al. (2014) tested a total of fourteen shear walls and demonstrated that an improved chord stud design through introduction of blocking members, that reduced stud twisting, and increased wall lateral strength by 40-80%.

Research conducted by these and several other authors have contributed to the development of the current North American standards, AISI S100-20, AISI S240-20 and AISI S400-20, providing guidelines for design of shear walls with steel sheet sheathing. Nonetheless, despite availability of experimental data documenting the strength and damage characteristics of isolated CFS shear walls, the understanding of the structural behavior of steel sheet sheathed shear wall is still fairly limited. Case in point, while these current standards can be used to design CFS shear walls to meet the seismic demands for low-rise (3-6 story) buildings, experimental data to

support code guidelines for taller mid-rise (>6 stories) and high-rise buildings (>10 stories), where large lateral load resistance is required, are lacking.

Recent studies by Rizk and Rogers (2017), Santos and Rogers (2017) and Briere and Rogers (2017) have attempted to bridge the gap between the lateral capacities of steel sheet sheathed CFS-framed and hot-rolled steel shear walls through development of center-sheathed specimens, termed "mid-ply" shear walls in which a single piece of steel sheathing is sandwiched between built-up studs and tracks, see Figure 1.6. These specimens attained shear resistances as high as 165 kN/m (11.3 klf), more than four times the largest strength values for design available in AISI S400-20, while also demonstrating ductile behavior at large lateral drifts (up to 7%), see Figure 1.7. The higher shear resistance found in the center-sheathed wall design was attributed to avoiding sheathing pull-through within the fastener connection. This aligns well with the findings from a recent study by Zhang et al. (2021) on the performance of fastener connections adopted in center-sheathed steel sheathing assemblies under cyclic loading.

Despite the available experimental data and advancement of design standards, additional limitations exist. Notably, most prior research programs have involved testing isolated shear walls under quasi-static monotonic or reversed cyclic loading, and thus far, only one component level experimental program described by Shamim et al. (2013), prior to the research conducted within this dissertation, has aimed to shed light on the seismic performance of CFS-framed shear walls. Shamim et al. (2013) conducted dynamic tests on single- and double-story CFS-framed steel sheet sheathed shear walls and observed that the hysteretic response of the walls (strength and drift at strength) is not significantly affected when tested using dynamic loading or reversed-cyclic displacement-controlled loading protocols. Additionally, observed failure modes were consistent with observations from monotonically and reverse cyclically tested shear walls in the literature. These were the first experiments, which evaluated the seismic performance of steel sheet sheathed CFS-framed shear walls through shake table testing. This paucity of dynamic testing data, at component level for CFS-framed assemblies detailed for mid-rise CFS-buildings, as well as at full-scale, system-level, has been a barrier to bringing the potential benefits of this

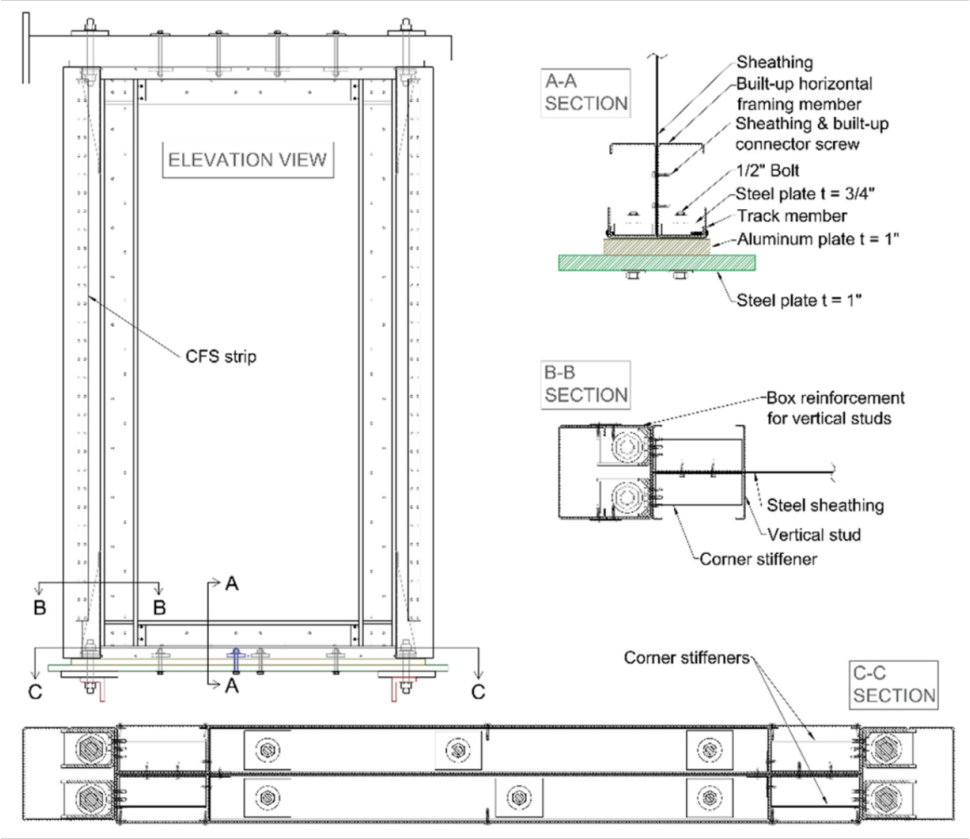


Figure 1.6. Construction details for mid-ply shear wall developed by Brière et al. (2018)

system to the community. As a result, a correlation of the evolution of dynamic characteristics with the observed physical damage has not been addressed in the literature. Juxtapose however to these findings of consistent failure modes and lateral wall strength from testing of CFS-framed shear walls, testing of wood-framed shear walls using different loading protocols conducted by Gatto and Uang (2003) showed that hysteretic dissipated energy, an essential feature of improved seismic performance of components, is highly dependent on loading protocol. This would imply that a comparison of energy dissipation characteristics across specimens tested using different loading protocols would require a procedure, which can mitigate the protocol-induced bias in structural performance evaluation. Despite that, even when the testing involved consistent application of the same loading protocol for all specimens, a correlation of the energy dissipation characteristics with the observed physical damage and structural performance metrics has not been addressed in the literature. Literature on structural performance evaluation has often been

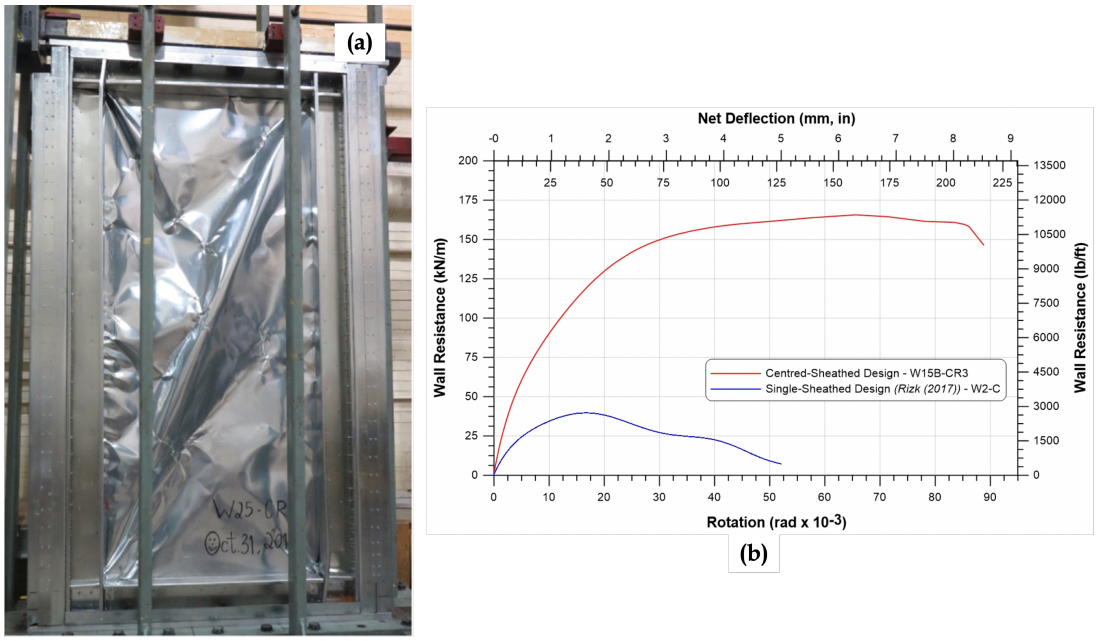


Figure 1.7. (a) Mid-ply shear wall tested by Brière et al. (2018) showing extensive shear buckling of steel sheet with no framing member damage, and (b) force-deformation response comparison for mid-ply and traditional shear wall Santos and Rogers (2017)

limited to considering CFS-framed partition walls sheathed with gypsum panels, e.g. McMullin and Merrick (2007); Lee et al. (2007); Restrepo and Bersofsky (2011); Peterman et al. (2013); Petrone et al. (2015); Pali et al. (2018). These studies have evaluated the progression of damage in partition walls at defined damage limit states. However, similar research on performance evaluation of CFS-framed shear walls has been limited to a few studies such as Haghpanah and Schafer (2021). There is a lack of well documented damage progression considering wall detailing and nonstructural variations common to CFS-framed structural walls.

An additional and equally important limitation within the experimental literature is that the previous studies have considered shear walls and gravity walls separately. However, these wall components are generally placed along the same line for architectural purposes and have finishes installed (exterior and interior) for insulation purposes, and thus, may be subject to similar kinematic demands. Due to the inherent lightweight of CFS-framed assemblies, their structural performance is impacted by the architectural components and nonstructural detailing. The response of CFS-framed assemblies and, in particular, the contribution of the

nonstructural components not specifically designated by the design engineers, to resist high intensity earthquake shaking are not well understood.

The need to understand the combination of structural and nonstructural finish materials for light-weight framing has been addressed to some extent for wood framed shear walls, and thus, this literature offers insight to the CFS community. For example, Uang and Gatto (2003) examined the effects of gypsum wallboard and stucco finish materials on the lateral behavior of wood framed shear walls with OSB or plywood as sheathing. Testing results showed that finish materials have a substantial effect on the shear wall performance. Usually ignored in design applications, the nonstructural finish application increased the wall strength. To evaluate at a system level, Filiatrault et al. (2002) tested a two-story wood framed house structure with and without interior (gypsum board) and exterior (stucco) wall finish. Application of finish materials again led to an increase in lateral strength and stiffness of the wood framed structure, accompanied with a decrease in deformation capacity. In concurrence with prior test program findings, these effects on performance were deemed significant and recommended to be considered in design. Based on several such component and system level tests, ASCE/SEI 41-17 Table 12-1 provides the expected strength values for different types of finishes for wood framed shear walls. Despite advancement in the wood-framed literature, limited investigations on the impact of finishes on CFS-framed shear walls have been undertaken. In one study, Liu et al. (2014) reported that using gypsum panels on the interior face of OSB sheathed CFS shear walls increased the wall initial stiffness and may also slightly increase wall strength. The impact of finishes on the lateral resistance of shear walls with steel sheet sheathing has not been explored in the literature. As a result, definitive strength predictions for finish systems are not widely available. In contrast to wood-framed structures, no summarized strength data exists for CFS-framed walls to aid the designer when such walls are finished. Thus, the current design codes do not take into account the effect of finish application on wall behavior.

Another nonstructural element whose impact on CFS wall behavior has not been adequately considered in research, is the presence of openings, such as windows and doors. Design

of typical CFS-framed shear walls includes fully sheathed shear walls with tie-downs at each end. Such shear walls are referred to as Type I shear walls, see Figure 1.8. However, walls often have doors and windows openings, which are permitted provided details are incorporated to account for force transfer around openings. Structurally accounting for window or door openings involves assuming a load path around the opening, thus creating frame action. In this situation, the tension and compression developed during lateral loading is resolved at the extreme wall ends. This concept, referred to as Type II shear wall detailing emerged from testing of 12 m long shear walls with openings (NAHB Research Center, 1997). Openings of varying areas were considered as perforations in the sheathing, and thus walls with larger opening areas demonstrated greater reduction in wall lateral strength. Similarly, Salenikovich et al. (2000) compared the performance of 12 m long CFS-framed walls with and without openings, again, considering openings as perforations in the designated lateral force resisting system. Despite these and other prior studies on walls with window openings, their impact as a nonstructural component in-line with multiple shear walls has not been systematically evaluated. Additionally, current design provisions for CFS-framed shear walls available in the AISI standards are largely based on data obtained from static tests on Type I shear walls. However, Type II shear walls have not been investigated at the component level through experiments in the existing literature.

In addition, continuous tie-rod systems have emerged as popular tie-down systems in mid-rise CFS-framed buildings. This tie-down system provides a continuous load path from the floors to the walls and into the foundation. A continuous tie-down system can be used in a multi-story building to resist overturning forces and ensure structural stability and integrity, see Figure 1.9. While the construction industry has moved ahead with its adoption, testing to support code provisions for their inclusion has lagged. Current design provisions for CFS-framed shear walls have instead focussed on design variables such as sheathing and framing thicknesses and fastener spacing. In such prior CFS shear walls testing have been employed hold-downs as the traditional tie-down system. To the author's knowledge, shear walls with tension rods as tie-down systems have not been tested at the component level within the existing literature.

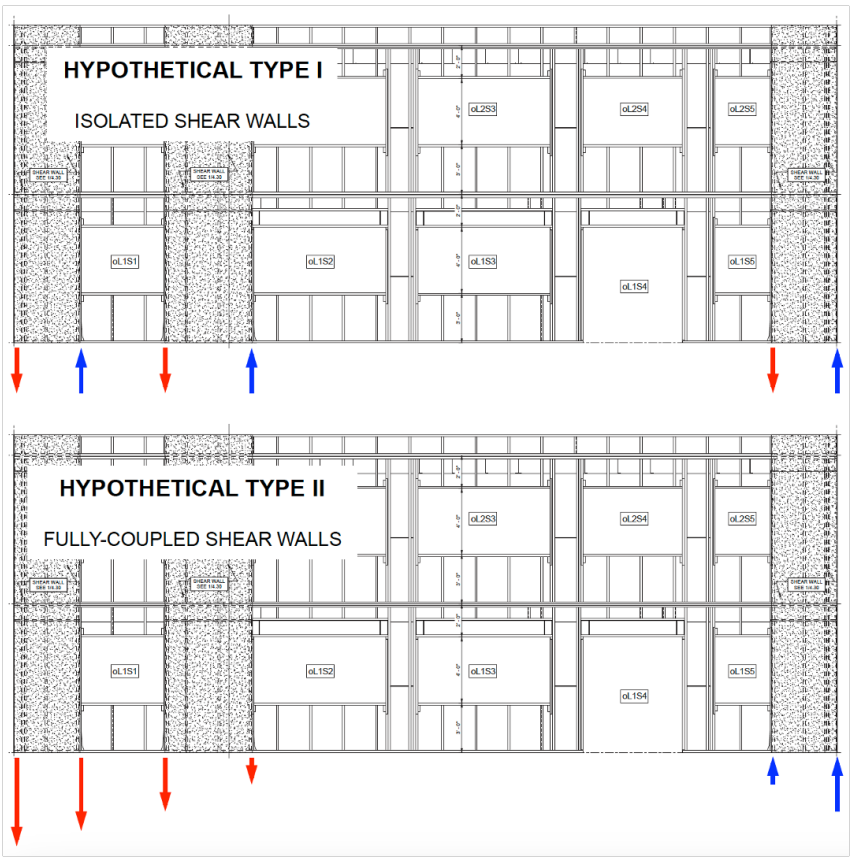


Figure 1.8. Illustration demonstrating the ideal tie-down force distribution in Type I and Type II shear walls by Peterman (2014)

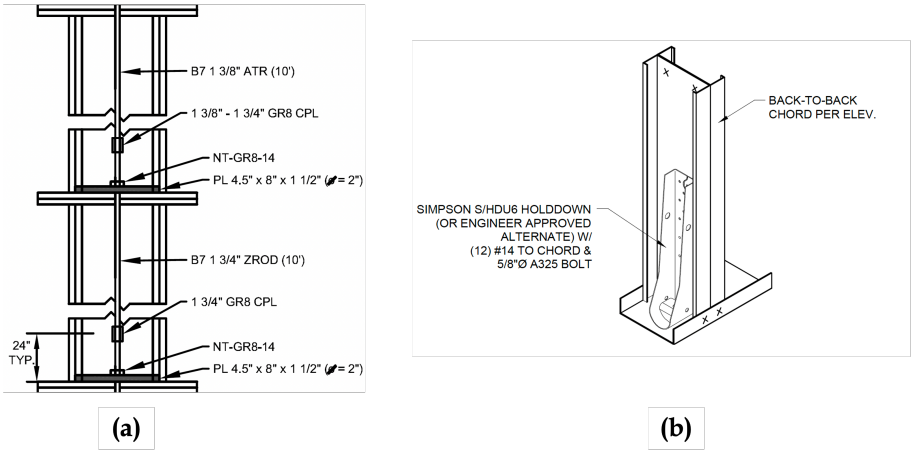


Figure 1.9. (a) Continuous tie-rod system with floor-to-floor installation (Wang et al., 2018a), and (b) traditional hold-down installed at wall end stud (Madsen et al., 2011)

1.2.2 System-level Experiments of CFS-Framed Buildings

Research on understanding the system-level seismic performance of CFS-framed buildings through shake table testing of full-scale test specimens has only recently emerged in the last decade, due in part to the availability of large-scale shake table facilities. One important notable research program, coined CFS-NEES, undertaken by Peterman et al. (2016) involved the first shake table tests in the U.S. on a CFS-framed building. The CFS-NEES building was a two-story CFS-framed building with OSB-sheathed Type I shear walls and floor and roof diaphragms. A modification to this specimen further included exterior weatherproof sheathing of the perimeter gravity walls as well as gypsum board sheathing of the interior of the perimeter gravity and shear walls among other nonstructural components such as partition walls, ceilings and staircase. Figure 1.10 shows the bare structural and complete with nonstructural components building specimens (15.2 m $\times$ 7.0 m plan area, 5.8 m height; 50 ft $\times$ 23 ft plan area, 19 ft height) on the three-axis shake tables at the Structural Engineering and Earthquake Simulation Laboratory (SEESL) at the University of Buffalo. The CFS-NEES building used ledger framing, wherein the joists are hung from the interior face of the top of the wall using a ledger track and a clip angle. Each shear wall was connected to the foundation through a hold-down and threaded bar assembly at the chord stud locations. Complete design details of the CFS-NEES building can be found in Madsen et al. (2011). The specimens examined the performance of the structural system solely and then the whole building system complete with nonstructural elements at different stages of construction. The building specimens were subjected to white-noise system identification tests and earthquake tests of increasing intensity. These tests indicated that the system performance of CFS-framed buildings is far more influential than the isolated shear wall performance, even under large excitations. Importantly, the stiffness, damping, and response of the building are significantly altered by the architectural finish systems. The nonstructural systems significantly altered the dynamic characteristics of the building, while also increasing the lateral load capacity of the building. The fundamental period decreased from 0.32s and 0.36s to 0.15s and 0.26s in

the long and short directions of the building, respectively.



(a)



(b)

Figure 1.10. Building specimen tested by Peterman et al. (2016): (a) structural system only, and (b) complete with nonstructural components

A similar strategy of testing a two-story building in phases, first as the structural system only and subsequently as the complete building system with nonstructural components added, was utilized by Fiorino et al. (2017) within the ELISSA (Energy Efficient LIghtweight-Sustainable-SAfe-Steel Construction) project at the Laboratory of Structures for Engineering and Architecture Department of the University of Naples Federico II. This building had a smaller foot-print of 4.7 m $\times$ 2.7 m (15.4 ft $\times$ 8.8 ft) plan area, and 5.3 m (17.4 ft) building height. Figure 1.11 shows the isometric view of the six-story building. The wall-lines used impact resistant gypsum board panels as sheathing on both exterior and interior faces. Similarly, the floor and roof diaphragms were sheathed with high density gypsum board panels. The complete building system was evaluated for its seismic performance by subjecting it to a motion from the 2009 Aquila earthquake with different scale factors along the short direction of the building. Seismic performance evaluation by Landolfo et al. (2018) demonstrated the influence of finish application, resulting in a 20% reduction of the fundamental period compared to the bare structural system only.

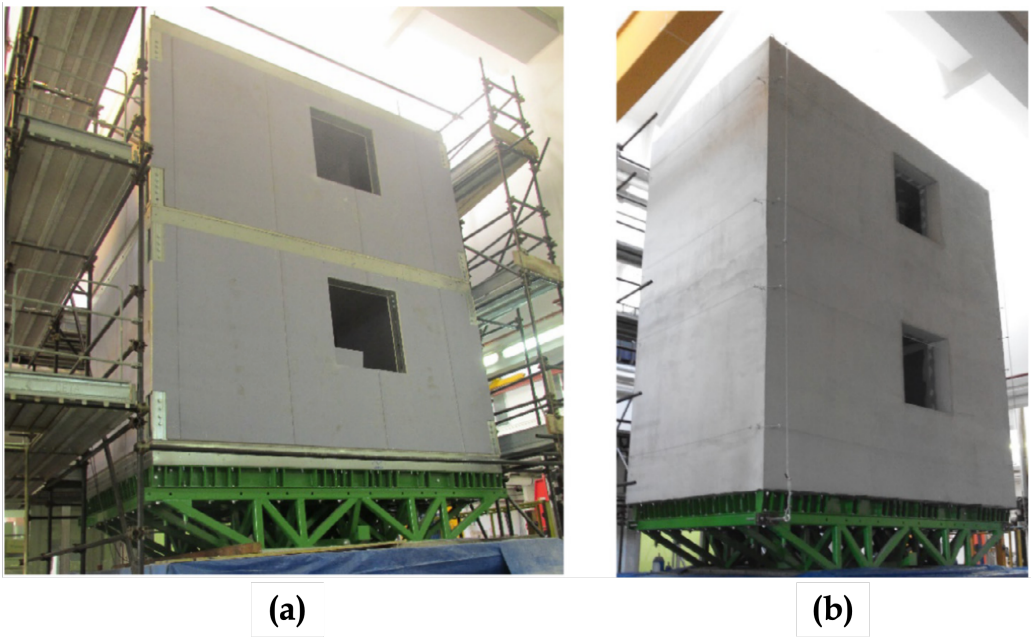


Figure 1.11. Two-story building tested by Landolfo et al. (2018): (a) structural system only, and (b) complete with nonstructural components

Hutchinson et al. (2021) tested a six-story CFS-framed building at NHERI (Natural Hazards Engineering Research Infrastructure) Large High Performance Outdoor Shake Table (LHPOST) at the University of California San Diego within the CFS-HUD project. The test building had a 10.4 m $\times$ 7.3 m (34 ft $\times$ 24 ft) floor plan. It had a 3.05 m (10 ft) floor-to-floor height with a 1.2 m (4 ft) tall roof parapet, for a total building height of 19.5 m (64 ft). Figure 1.12 shows the isometric view of the building. Shear walls in the CFS-HUD building utilized structural panels, fabricated using thick gypsum boards bonded with steel sheet, as sheathing. In addition, regular gypsum boards were also installed on the interior side of the walls. To resist seismic overturning moment and uplift forces, the test building adopted continuous tie-rods and built-up compression stud pack assembly at the ends of each individual shear walls. Complete discussion of building design and construction can be found in Wang and Hutchinson (2021). The building was subjected to seven earthquake tests of increasing motion intensity along the longitudinal direction of the building. Subsequently, live fire tests were conducted on the earthquake-damaged building at two select floors. Finally, the test building was subjected two post-fire earthquake tests, including an extreme near-fault target MCE-scaled motion. Even though the extreme near-fault earthquake test caused the building to develop a full soft story mechanism and caused severe damage to the buildings structural system, the building resisted collapse due to redistribution of loads and framing action of the building rod tie-down system. Wang and Hutchinson (2020) report the evolution of modal characteristics for the CFS-HUD building during phases of construction and increasing earthquake intensity scaled shaking. Installation of gypsum panels on the interior face of wall framing during construction increased the natural frequency in the longitudinal translation mode of the test building by approximately 10%. Assessment at different performance targets demonstrated that the evolution of identified modal parameters correlated well with the progression of observed physical, with increases in both damping ratio and natural period.

Recently concluded experimental program by Zhou et al. (2022) at Chongqing University, China, tested a full-scale six-story building under bi-directional ground motion input to evaluate



Figure 1.12. CFS-HUD building tested by Hutchinson et al. (2021)

the effects of the nonstructural components and structural members on the seismic performance. The test building had a 5.6 m $\times$ 4.2 m floor plan, and a 2.7 m floor-to-floor height. Figure 1.13 shows the isometric view of the six-story building. In this study, two different shear wall detailing were employed, namely, the clamped steel sheet detail and the sheathed steel sheet detail. This building adopted hold-downs as tie-down system. However, due to the high overturning moment demand of a mid-rise building, the end studs were replaced by square HSS (hollow structural section) steel tubes. The building demonstrated good seismic performance with maximum inter-storey displacement angle of 1/100 under maximum considered earthquake (PGA = 0.4g) that satisfied local code requirements of elastic inter-storey displacement angle of 1/250. These system-level tests have demonstrated the excellent seismic performance of such CFS-framed structures, and also highlighted the existing knowledge gap between our understanding of component level performance and observed system-level performance. Such

tests, and an industry need for low-cost multihazard-resilient construction, have stimulated further research to realize mid-rise CFS-framed buildings, such as development of ductile lateral framing system which can offer high shear resistance (Brière et al., 2018), contributions from non-designated systems on lateral performance and use of modern construction details, discussed in this dissertation, as well as further system-level seismic tests of full-scale mid-rise test building, such as the CFS-NHERI 10-story test building (Singh et al., 2022a).



Figure 1.13. Six-story building tested by Zhou et al. (2022): (a) structural system only, and (b) complete with nonstructural components

1.2.3 Numerical Modeling of CFS-Framed Structures

Numerical modeling of CFS-framed assemblies has progressed alongside the experimental research in a similar fashion. Several research studies have focused on modeling the cyclic lateral response of isolated CFS assemblies, e.g. CFS-framed shear walls, most commonly by

fitting the test data using a phenomenological material model. Such a concept is alluring for ready implementation into analysis packages such as SAP2000 or ETABS, since these strategies boast computational efficiency. OpenSees (Open System for Earthquake Engineering Simulation) (McKenna, 2011) has often been used to develop phenomenological models due to its capability of facilitating research-grade analysis. It should be noted that efficient phenomenological models are often limited to the behavior captured in the underlying testing used for validation. Explicit models, as implemented in robust finite element softwares such as ABAQUS, may be more successful in capturing subtle behaviors observed in the testing.

Numerical modeling of OSB sheathed CFS-framed shear walls, such as Liu et al. (2012), Buonopane et al. (2014) and Bian et al. (2015), have employed a fastener-based modeling approach where each fastener is modeled as a non-linear, in-plane, radially-symmetric zero length (CoupledZeroLength) spring element, see Figure 1.14. The fastener elements used a *pinching4* material model which is defined using a softening multi-linear backbone curve, pinching, and loading and unloading parameters. This model assumed that significant deformation which occurs locally around the fasteners in an OSB sheathing can be captured by the non-linear properties assigned to the fastener elements. The CFS framing members, studs, tracks and ledger, were modeled using displacement beam-column elements, and the sheathing was modeled as a rigid diaphragm. This OpenSees model provided a way to efficienty model OSB sheathed CFS-framed shear walls and characterize their nonlinear hysteretic response under a multitude of different design details. Bian et al. (2015) also pursued high fidelity simulations in ABAQUS where the CFS framing members and sheathing were modeled as four-node shell elements, while the sheathing connections were modeled as axial spring elements. Results from the OpenSees and ABAQUS models were found to be in good agreement with one another.

Similarly, numerical modeling of steel sheet sheathed CFS-framed shear walls has been performed in OpenSees and ABAQUS. Singh and Hutchinson (2018) developed an efficient numerical model in OpenSees to capture the in-plane cyclic response of steel sheet sheathed shear walls, where the sheathing and connections were modeled as truss elements assigned

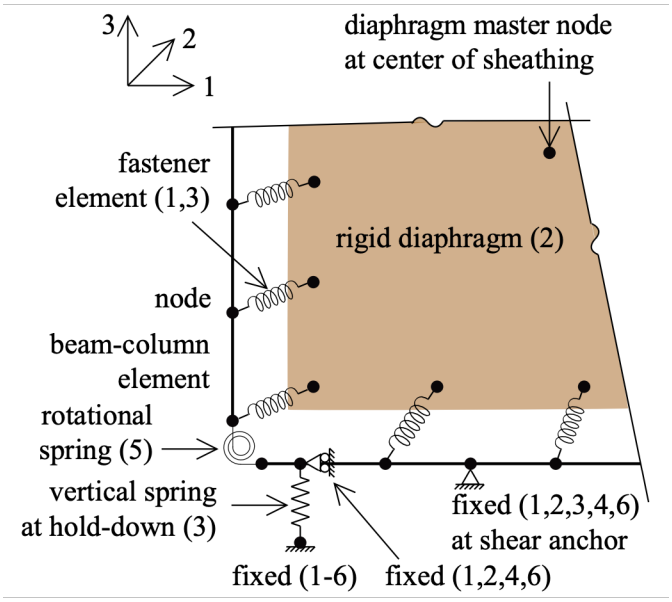


Figure 1.14. Details of OpenSees model used by Buonopane et al. (2014) for OSB sheathed CFS-framed shear walls

with a *pinching4* material, see Figure 1.15. The CFS framing members were modeled using displacement beam-column elements. The X-brace type numerical model was able to capture the severely pinched hysteretic response as well as the energy dissipated through displacement cycles.

Dynamic response of multi-story CFS-framed steel sheet sheathed shear walls was modeled by Shamim and Rogers (2013) using a similar approach of lumping the nonlinear behavior into diagonal truss elements using the *pinching4* material model in OpenSees. The numerical model was able to achieve a good agreement with the test results in terms of shear resistance versus drift behavior and dissipated energy, as well as the time history responses. As an alternative of *pinching4* material model, Kechidi and Bourahla (2016) developed a new material models called CFSWSWP (Cold-Formed Steel Wood Sheathed Shear Wall Panel) and CFSSSWP (Cold-Formed Steel Steel Sheathed Shear Wall Panel) uniaxialMaterial implemented in OpenSees, which can simulate the deteriorating behavior, strength and stiffness degradation and pinched hysteretic response of wood sheathed and steel sheet sheathed cold-formed steel shear walls, respectively. Figure 1.16 shows the details of the details of the developed OpenSees

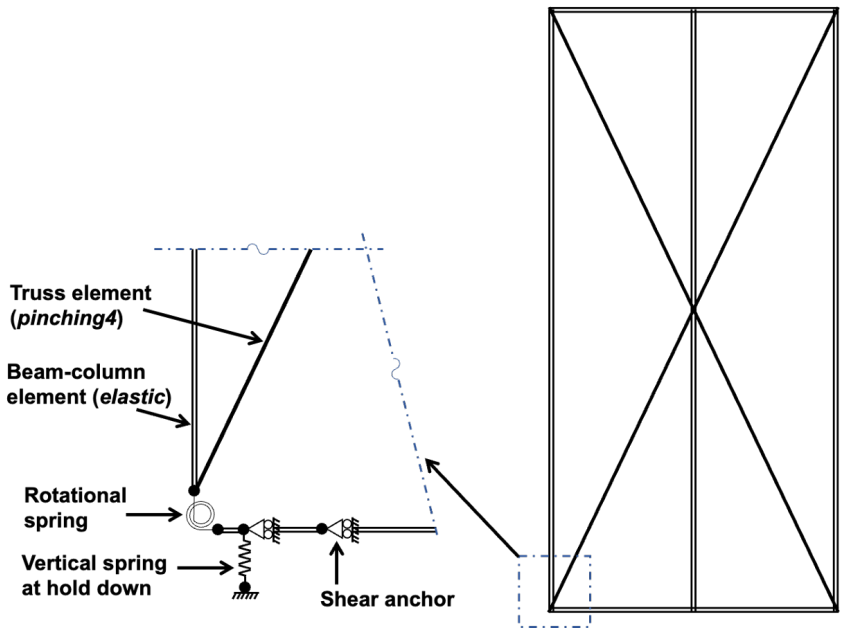


Figure 1.15. Details of OpenSees model used by Singh and Hutchinson (2018) for steel sheet sheathed CFS-framed shear walls

model. The proposed model is able capture the influence of design parameters on the lateral stiffness, strength and ductility of wood or steel sheet sheathed shear walls.

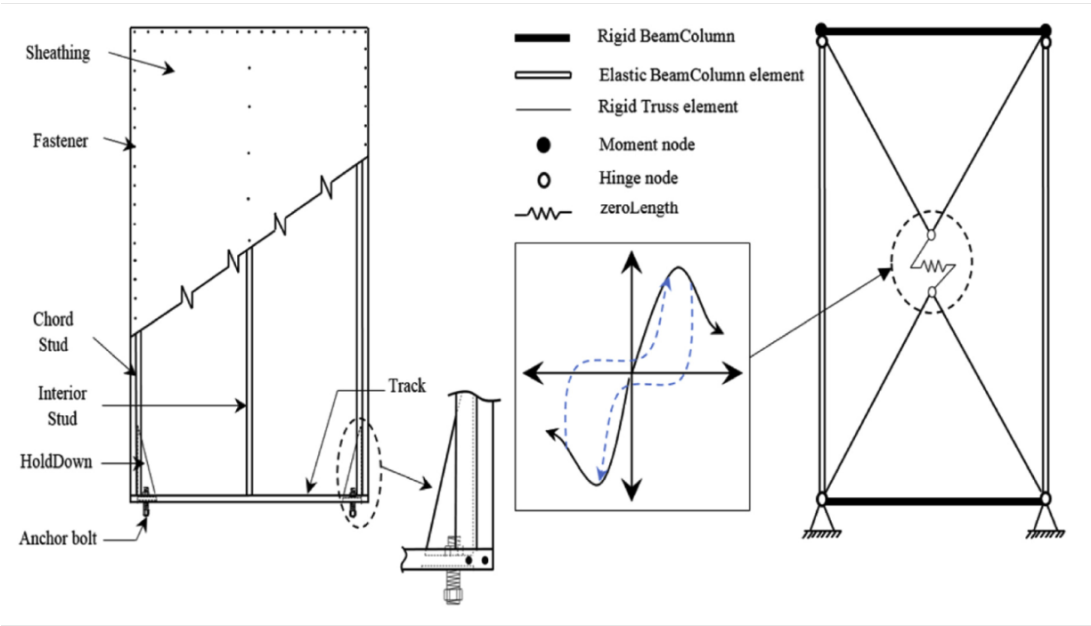


Figure 1.16. Details of OpenSees model used by Kechidi and Bourahla (2016) for CFS-framed shear walls

Derveni et al. (2020) and Zhang and Schafer (2019) pursued high fidelity finite element shell models with fastener-based modeling in ABAQUS to focus on the steel-gypsum composite and steel sheet sheathing behavior, respectively. Framing-to-framing connections were modeled as multi-point constraint pin connections, while framing-to-sheathing connections were modeled as nonlinear spring elements, see Figure 1.17. These models emphasized the importance of characterizing connection behavior for modeling shear walls. However, it should be noted that it is computationally very expensive to perform nonlinear time history analyses for a CFS-framed structure which employs these high fidelity models as building blocks due to the large number of degrees-of-freedom. Computational demand for whole building model can be significantly reduced by using equivalent nonlinear phenomenological models of the various components of the building.

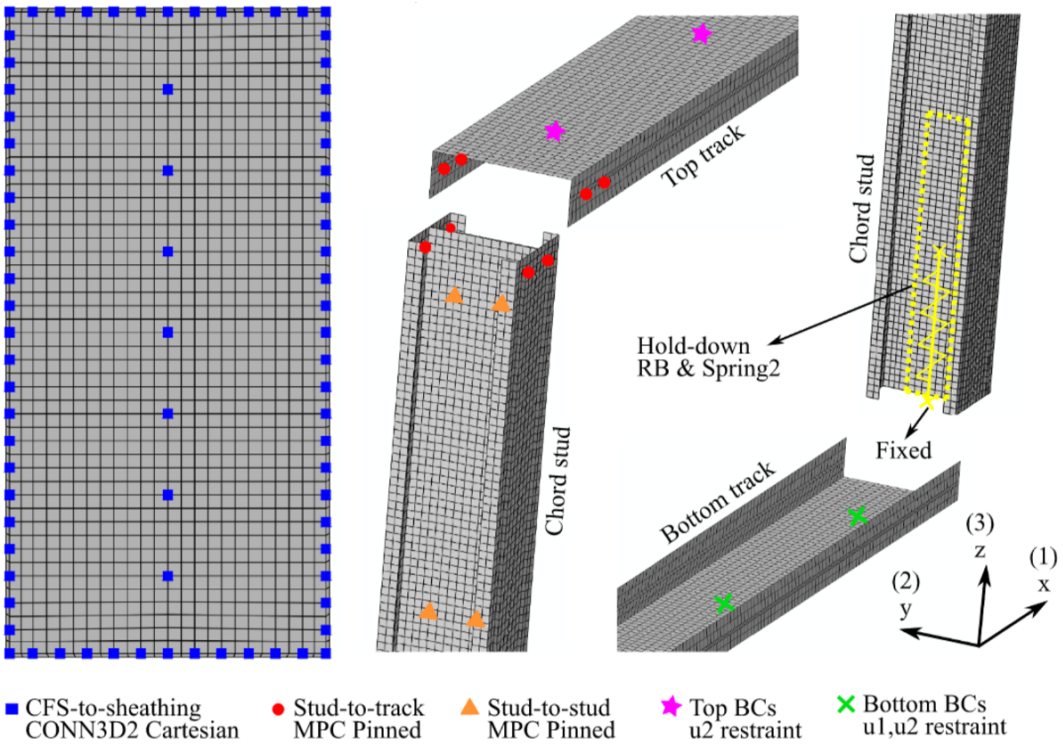


Figure 1.17. Details of ABAQUS model used by Derveni et al. (2020) for CFS-framed shear walls

Modeling the seismic response of whole CFS-framed building systems has been explored

to a much lesser extent, especially compared to modeling work of wood-framed buildings, which has existed for a longer time. For example, an effort by Folz and Filiatrault (2004) within the CUREE-Caltech Woodframe Project was undertaken to develop a computationally efficient biaxial shear model which could be used to accurately to predict the lateral seismic response of low-rise wood-frame buildings. This "pancake" model neglected story-to-story height of building and assumed rigid body in-plane diaphragm. Single degree of freedom (SDOF) shear springs, calibrated using the companion numerical program CASHEW (cyclic analysis of shear walls) or by fitting a hysteretic model to full-scale cyclic wall experimental data, represented the load-resistance behavior of shear walls, as shown in Figure 1.18.

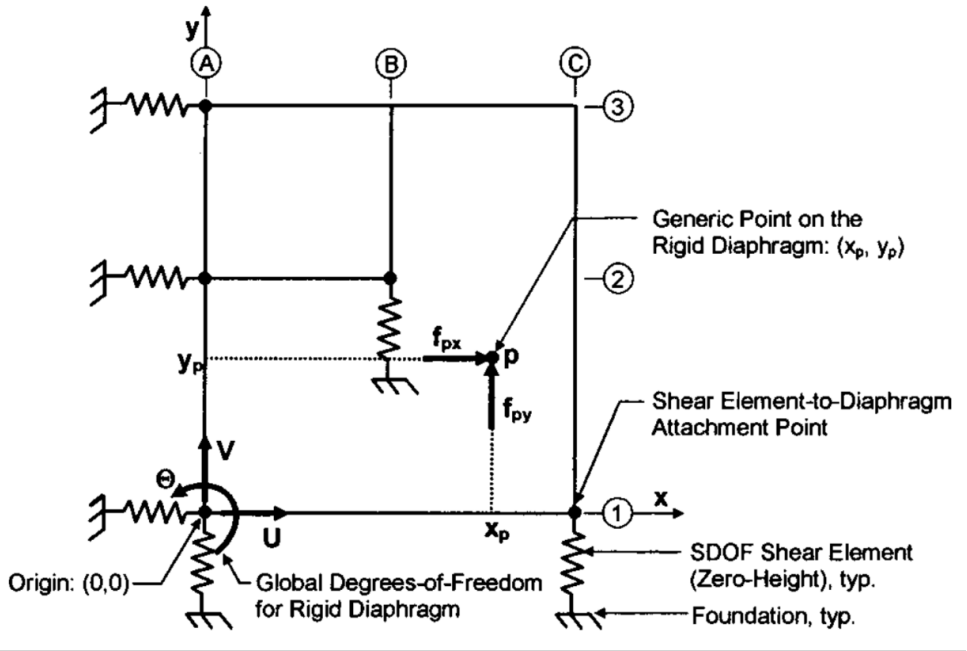


Figure 1.18. Details of numerical model for low-rise wood structures developed by Folz and Filiatrault (2004)

Taller wood-framed structures often use continuous rods as overturning moment and uplift restraint system. The cumulative elongation of such hold-down systems over several stories can have a significant contribution to the out-of-plane floor diaphragm deformation. A "pancake" numerical model which only considers shear deformation cannot be used to adequately capture floor lateral displacement in taller structures. Pei and Van de Lindt (2009) extended

this pure shear deformation formulation and developed a coupled shear-bending formulation that could be used for seismic analysis of multi-story wood-framed structures. Within this formulation, the shear walls are modeled similarly as hysteretic shear spring elements. However, the vertical stiffness from hold-down system, vertical studs etc. is combined and represented using a simplified piecewise-linear model, as shown in Figure 1.19. Through consideration of both pure shear deformation and the out-of-plane rotation in diaphragm, this numerical formulation was able to accurately predict response of multi-story wood-framed structures. This formulation has been incorporated into the software Seismic Analysis Package for Wood-frame Structures (SAPWood) (Pei and van de Lindt, 2010). Numerical predictions from SAPWood models have been validated against experimental seismic responses of a full-scale two-story wood-framed townhouse building (van de Lindt et al., 2010) and a full scale six-story, wood-framed apartment building (Pei and Van de Lindt, 2011). The availability of such a tool has made possible performance-based seismic design of mid-rise wood-framed buildings.

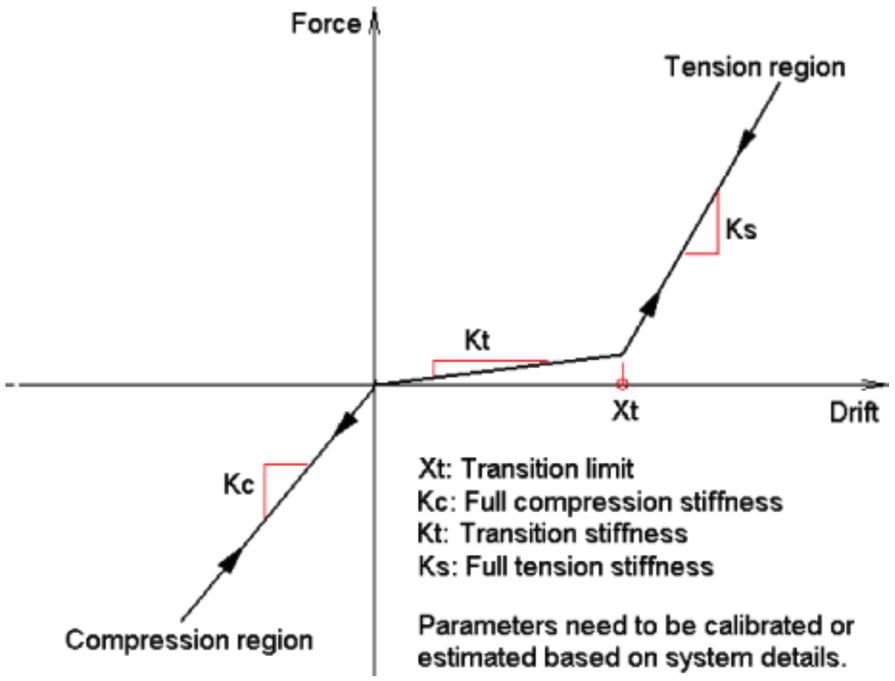


Figure 1.19. Numerical modeling of vertical stiffness elements by Pei and Van de Lindt (2009)

As discussed in the previous subsection, full-scale system-level testing of CFS-framed

buildings has begun quite recently and available test data is very limited. Nevertheless, these recent tests have produced vital datasets which can be used for developing finite element models for CFS-framed buildings. For example, Leng et al. (2017) was the first study aimed at developing numerical modeling protocol for CFS-framed building. High fidelity OpenSees models of the two-story CFS-NEES building were developed at different phases of construction and validated against the measured response from shake table tests. Figure 1.20 shows the state-of-the-practice (P-) and state-of-the-art (A-) models for the CFS-NEES building. P-models used a pair of diagonal trusses with nonlinear material, elastic-perfectly-plastic (EPP) or *pinching4*, for modeling the OSB-sheathed shear walls with framing members modeled with elastic beam-column elements. Modeling the shear wall in this fashion means that lateral forces have to carried through the top or bottom track. However, in actual shear walls, shear transfer happens through the closely spaced fasteners around the perimeter along the length of the stud and track. Therefore, A-model shear walls included sub-division of the sheathing board into subpanels, modeled as diagonal trusses with *pinching4* material, and introducing intermediate members such as ledger track and framing around window or door opening. This sub-division allows for secondary load paths for shear within in the model. The framing members were also explicitly included by incorporating the their individual failure modes through nonlinear uniaxial materials. Another important distinction between the P-models and A-models was the connection to the foundation at the hold-down locations. The P-model used pin connections at hold-down locations, while the A-model used non-linear axial springs with stiffness based on manufacturer reported testing. Figure 1.21 shows the shear wall modeling strategy within the state-of-the-practice and state-of-the-art models. It was demonstrated that P-models could not adequately predict the response of actual building. However, P-model were able to adequately predict the stiffness, strength, and local response as measured through building tests.

Franklin et al. (2019) proposed a modeling method for elastic analysis of CFS-framed buildings at serviceability limit state, and verified the predictions from the method against the CFS-NEES building results under low-intensity earthquake tests. High efficiency and good

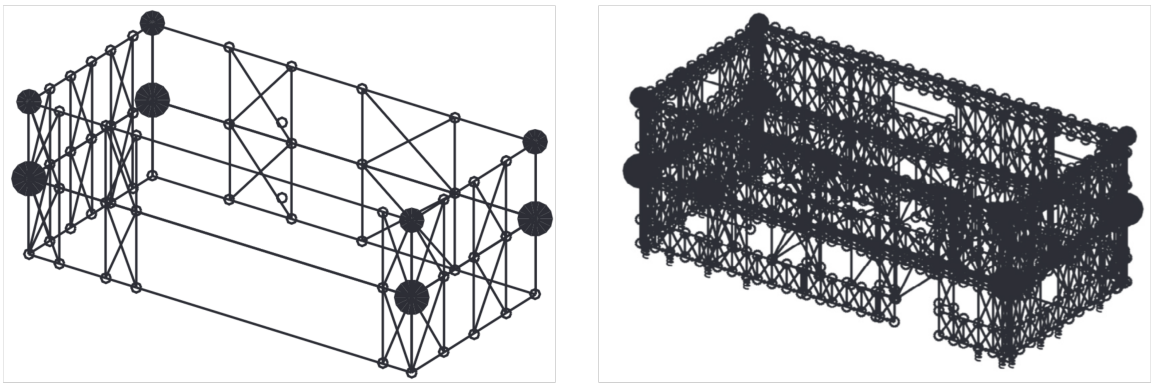


Figure 1.20. 3D OpenSees models for building analysis developed by Leng et al. (2017)

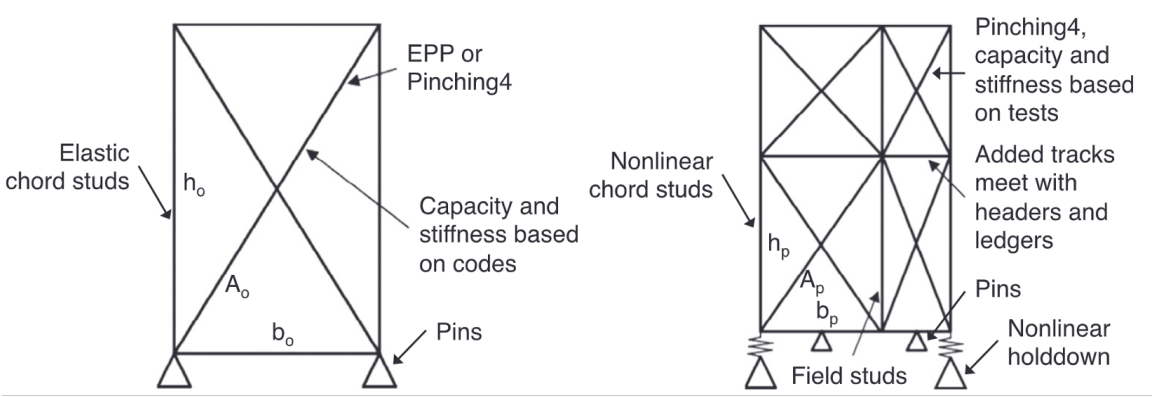


Figure 1.21. Comparison of P- and A- shear wall models developed by Leng et al. (2017)

accuracy could be acheived through reduction of degrees of freedom by modeling of all shear and gravity walls using orthotropic shell elements in ETABS (2023). Another efficient numerical modeling procedure was developed in OpenSees by Campiche et al. (2020), which evaluated building models of varying complexity. These models were compared against shake-table tests performed on the full-scale two-story CFS-framed building sheathed with gypsum panels, as part of the ELISSA project. The developed OpenSees model used similar strategy as the A-model described by Leng et al. (2017), without the sub-division of the panels. Using a full-panel approach for walls was observed to be sufficient for obtaining accurate numerical predictions while keeping the computational cost low.

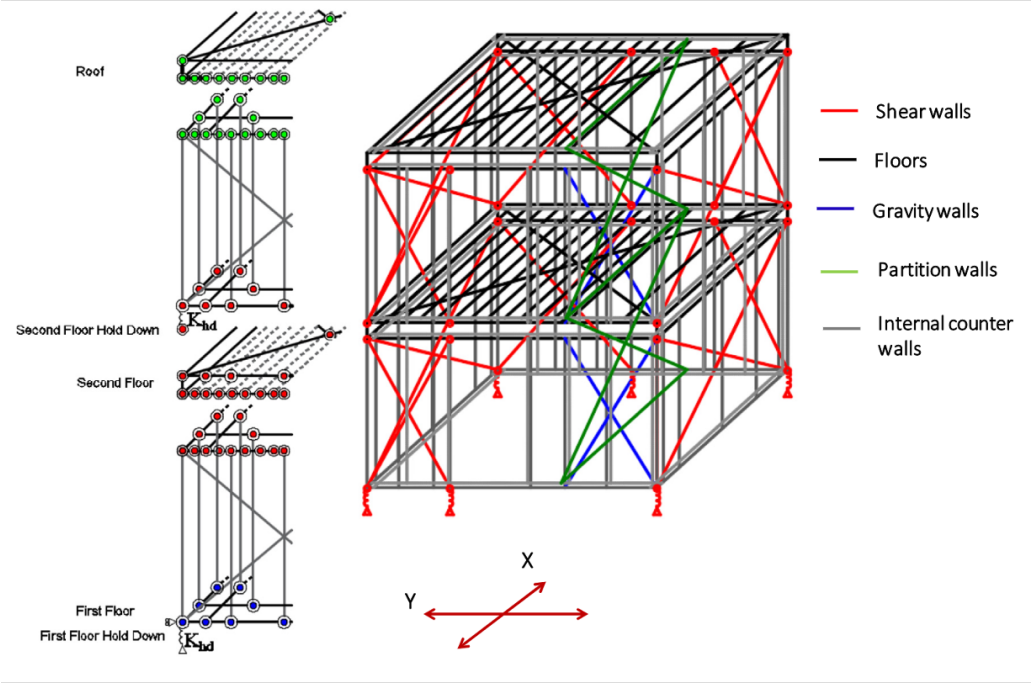


Figure 1.22. 3D OpenSees model for building analysis developed by Campiche et al. (2020)

1.3 Research Scope

Upon identifying the gaps in the current understanding of CFS-framed wall behavior and current North American Standards, AISI S240-20 and AISI S400-20, and the paucity in experimental data to support design of CFS-framed shear walls that are capable of developing lateral resistance suitable for mid-rise buildings, a two-phased experimental effort was designed to address the shortcomings and advance the understanding of CFS-framed steel sheet sheathed shear walls placed in-line with gravity walls. The experimental program in the current research project was designed to include test variables that address several of the limitations discussed in the previous section. CFS-framed wall-lines with distinctly different detailing variations, namely structural detailing such as shear wall symmetry, tie-down detailing, as well as nonstructural detailing, such as finishes and openings were included within the test matrix. The first phase of the experimental program was conducted at LHPOST (NHERI@UC San Diego). Wall-line assemblies were tested at full-scale, first under a sequence of increasing amplitude (in-plane)

earthquake ground motions, and subsequently under slow monotonic pull conditions (for select specimens). The second phase of the experimental program was conducted at the UC San Diego Structural Engineering Powell Laboratory where wall-line configurations were tested under quasi-static reverse cyclic displacement controlled loading imposed at the top of the wall. The impact of different detailing variables on wall-line lateral behavior is discussed by comparing across specimens systematically in terms of key global response parameters as well as local measurements. This dissertation also documents and quantifies the progressively incurred physical damage observed in the tested wall-line assemblies, and correlates it with the evolution of dynamic characteristics and hysteretic energy dissipation characteristics at different defined performance levels.

Even though numerical modeling of CFS-framed assemblies for building response prediction under earthquake motions has been limited to low-rise buildings, and none have considered steel sheet sheathed shear walls, numerical modeling literature shows the promise of reduced-scale, simplified finite element modeling approaches towards capturing full-scale CFS-framed building seismic response courtesy of validation against test data. There is a need to develop different strategies and extend them to modeling of mid-rise and high-rise CFS-framed buildings. Following the experimental investigation of CFS-framed wall-lines detailed for mid-rise buildings, this dissertation also presents a design-grade numerical modeling strategy developed in OpenSeesPy for CFS-framed wall-lines. This modeling strategy can be used for numerical response predictions for mid-rise CFS buildings under seismic inputs to support design engineer needs. The numerical model is validated against the measured response of the mid-rise CFS-HUD building described in Wang et al. (2018b). The model aims to provide a robust, yet computationally efficient approach, with minimal degrees-of-freedom, while also capturing the salient features of seismic response of mid-rise CFS-framed buildings suitable for design-grade predictions of response. A detailed discussion of the modeling strategies adopted in the development of the numerical model is provided, followed by validation of the model through comparison with measured response from shake table tests.

1.4 Organization of Dissertation

This dissertation is organized into six chapters, as follows:

- Chapter 2: CFS-Framed Wall-Line Experimental Program.

  This chapter provides a general overview of the two-phased experimental program undertaken to advance the understanding of CFS-framed wall-lines: shake table test phase conducted at the NHERI Large High-Performance Outdoor Shake Table, and quasi-static test phase conducted at the Structural Engineering Powell Laboratory. This chapter also provides background for selection of wall details for the experimental program. Testing protocols used during the two phases to capture wall performance at different performance levels have been described in this chapter. Complete details of the specimen fabrication, test setup, instrumentation and monitoring systems used in the two test phases are described in this chapter.

- Chapter 3: Impact of Nonstructural and Structural Detailing on Wall-Line Lateral Behavior.

  The impact of different variables within the test matrix which govern the nonstructural and structural detailing of CFS-framed walls have been discussed in this chapter. The impact of test variables is discussed by discussing the performance of the baseline specimen in detail, and then comparing select groups of specimens systematically. Based on measured response, the findings are presented in terms of force-displacement backbone curves, key performance parameters, wall local behavior and observed physical damage evidence.

- Chapter 4: Physical Damage-Hysteretic Response Correlation for CFS-Framed Wall-Lines.

  This chapter documents the quantification of the progressively incurred physical damage observed in wall-line assemblies, and its correlation with the evolution of dynamic characteristics and hysteretic energy dissipation characteristics at different performance levels. Dynamic characteristics of the wall-lines are identified using the data recorded from white noise base excitation tests performed during the shake table test phase. A procedure which

allows comparison of dissipated energy for specimens tested using different loading protocols between the shake table and quasi-static test phases has been presented. Progression of damage within the framing members, fastener connections and nonstructural finish layers for various specimens is presented in this chapter.

- Chapter 5: Design-grade Numerical Model of CFS-Framed Mid-Rise Buildings.
  This chapter presents a finite element modeling approach for CFS-framed mid-rise buildings. Discussion about modeling the different major assemblies such as shear walls, gravity walls, seismic overturning moment and uplift restraint system has been provided within this chapter. Comparison of numerical model predictions with measured experimental response of a six-story CFS-framed building through non-linear time-history and eigenvalue analyses are presented in this chapter.

- Chapter 6: Conclusions and Future Work.
  This chapter summarizes major findings and contributions of the work presented in this dissertation and provides recommendations for future work within the cold-formed steel research area. This chapter also includes an introduction to the 10-story CFS-framed building which will be subjected to multi-dimensional shake table testing.

Appendices provide supplemental materials, supporting the main body of the dissertation, as follows:

- Appendix A: Shop Drawings of Fabricated Wall-lines.
  This appendix provides the shop drawings of the tested wall-line configurations used for fabrication.

- Appendix B: Material Tests and Certificates.
  This appendix provides the material properties of all framing members, tie-down components and finish stucco as obtained from the manufacturer and from conducted tests.

- Appendix C: Hysteretic Response of Wall-Line Specimens.

  This appendix provides the force-displacement response for all the wall-line specimens tested across the two phases of the CFS-NHERI wall-line experimental program. The calculated equivalent hysteretic damping for the specimens tested during the quasi-static test phase of the CFS-NHERI wall-line experimental program are also provided in this appendix.

- Appendix D: Local Response of Wall-Line Specimens.

  This appendix provides the wall local response for all the specimens tested across the two phases of the CFS-NHERI wall-line experimental program.

- Appendix E: OpenSeesPy Code of Building Numerical Model.

  This appendix provides the OpenSeesPy code of a mid-rise CFS-framed building numerical model used for eigenvalue and nonlinear time history analyses.

Chapter 2

CFS-Framed Wall-Line Experimental Program

2.1 Introduction

A two-phased experimental program was undertaken to advance the understanding of CFS-framed steel sheet sheathed shear walls. Coined the CFS-NHERI project, this experimental program within the project had the following primary objectives: (a) characterize the dynamic performance of CFS walls that include shear walls and gravity walls, i.e. wall lines; (b) understand the effect of finishes on wall behavior; (c) compare the behavior of Type I and Type II wall lines; (d) compare the wall behavior with steel tension tie-rods assembly to that of hold-down tie-down systems; (e) compare the behavior of symmetrical and unsymmetrical wall lines; (f) understand the effect of openings on wall behavior; and (g) examine lateral load sharing between shear walls placed in-line with gravity walls. The first phase of the experimental program was conducted at the NHERI Large High Performance Outdoor Shake Table (LHPOST) at the University of California San Diego (nheri.ucsd.edu). Shear walls placed in-line with gravity walls carrying tributary mass were tested at full-scale, first under a sequence of increasing amplitude (in-plane) earthquake motions, and subsequently under slow monotonic pull conditions (for select specimens). The second phase of the experimental program was conducted at the UC San Diego Structural Engineering Powell Laboratory. In this phase, ten single wall-line configurations were tested under quasi-static cyclic displacement controlled loading conditions.

The selection of wall details was motivated by the design of the CFS archetype building that used available experimental data in addition to guidelines provided by current design standards. This chapter provides a summary of the archetype building design and selection of wall detailing, which led to the test matrix. Complete details of the specimen fabrication, test setup, instrumentation and monitoring systems used in the two test phases are described in the various sections of this chapter.

2.2 CFS-NHERI Archetype Building

Cold-formed steel framing is a cost-effective solution for low-rise structures, where it is often used as the gravity and lateral force resisting system (LFRS). However, as the height of the building increases, other materials/systems such as reinforced concrete shear walls may have to be used as the LFRS in conjunction with CFS-framing as gravity framing. This reduces the efficiency and favorability of CFS construction. To this end, a complete archetype building using only CFS framing helps advance new CFS detailing and evaluation of buildings constructed entirely using these systems. The archetype mid-rise CFS building discussed by Torabian et al. (2016a) was used as the basis for the CFS-NHERI archetype building. Specifically, this building used CFS framing exclusively for its entire gravity and lateral force resisting systems, including ledger framing similar to the CFS-NEES building (Peterman et al., 2016). The typical floor plan of this archetype building was selected as 35.4 m $\times$ 14.6 m (116 ft $\times$ 48 ft) and is shown in Figure 2.1. This floor plan was based on the plan provided in Example-1 of the IBC SEAOC Structural/Seismic Design Manual Vol. 2: Four story wood light-frame structure (IBC, 2018a). The hypothetical site of the CFS NHERI archetype building was located in the high seismic region of southern California, namely in Orange County (coordinates: 33.79°N, -117.86°W and site class: D). As a result, the following design parameters were assumed in accordance with ASCE/SEI 7-16: spectral acceleration at short periods, S_s=1.39g, spectral acceleration at a period of 1s, S_1=0.57g, and design spectral accelerations, S_{DS} = 0.927g and S_{D1} = 0.57g.

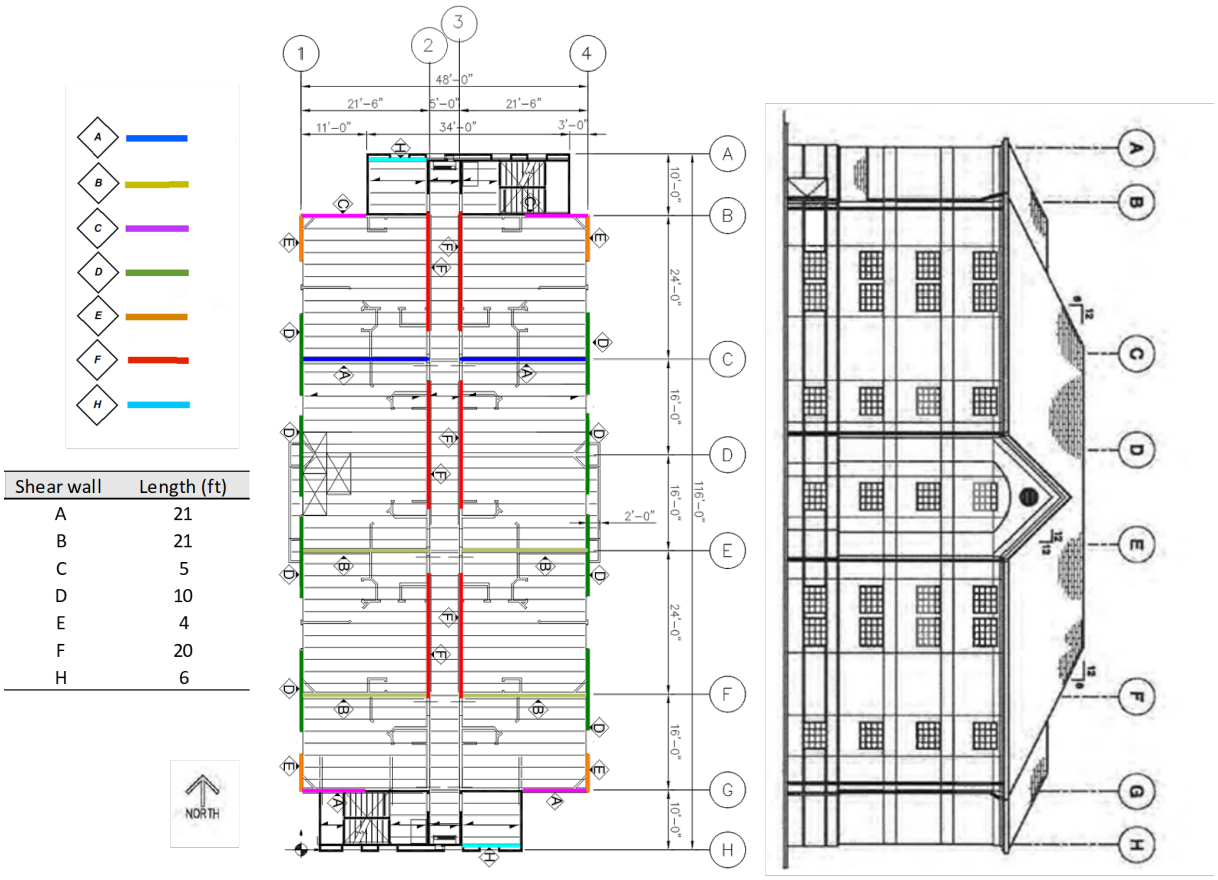


Figure 2.1. The unified archetype building plan (left), elevation (right) and shear wall layout (Torabian et al., 2016a)

The LFRS of the archetype building consisted of Type I steel sheet sheathed shear walls anchored with tension tie-rods and compression stud packs at wall ends. The seismic design parameters R (response modification coefficient), Ω_o (over-strength factor) and C_d (deflection amplification factor) for light-frame (cold-formed steel) walls sheathed with wood structural panels rated for shear resistance or steel sheets are as 6.5, 3 and 4, respectively ASCE/SEI 7-16. It should be noted that current code provisions restrict such structural systems to a height limit of 65 ft ($\sim$6 story building). Utilizing this floor plan and codified seismic design details, a 4-story and a 10-story CFS building were designed. Assumed gravity loads were 1.44 kPa (30 psf) dead load and 1.92 kPa (40 psf) live load for typical floor, and 0.96 kPa (20 psf) dead load and live load for roof, as shown in Table 2.1. The effective seismic weight calculated based on estimated

weights of the floor, roof and walls was 940.8 kN (211.5 kips) for a typical floor and 470.6 kN (105.8) kips for the roof, as shown in Table 2.2. The 4-story building, which meets the code height limitations, could be designed with existing AISI S400-20 steel sheet shear wall capacities. However, the 10-story building, which exceeds code height limitations, could only be designed by extending the shear wall capacities beyond AISI S400-20 and using available experimental data which document the larger capacity available with steel sheet sheathed shear walls (Rizk and Rogers, 2017; Santos and Rogers, 2017; Briere and Rogers, 2017). The selection of wall details for the experimental program were motivated from the designed buildings. Selected shear wall details reflected the detailing from approximately the mid-height floors (5-7 stories) within the 10-story archetype building. These wall details are highlighted in Table 2.3 which provides a summary of the 10-story building design. Similarly, Table 2.4 provides a summary of the 4-story archetype building design. The design process highlighted current design code limitations: large compression stud packs (consisting of eight or more studs) and tight fastener spacing required in the lower floors to resist high shear demand.

Table 2.1. Unit weight of dead load and live load

Roof weights	(psf)	Floor Weights	(psf)
Roofing + re-roof	5.0	Flooring	1.0
Sheathing	2.5	Lt. wt. concrete	14
Trusses	3.0	Sheathing	2.8
Insulation + sprinklers	2.5	Joist	4.0
2 layers gypsum + misc	7.0	2 layers gypsum + misc	8.2
Dead load	20.0	Dead load	30.0
Live load	20.0	Live load	40.0

2.3 Shake Table Test Phase

2.3.1 Test Matrix and Specimen Details

The CFS-NHERI wall line shake table test phase consisted of eight wall configurations tested at LHPOST at UCSD. A pair of nominally identical walls were tested for each config-

Table 2.2. Effective seismic weight of the building

Level	Height of each floor (ft)	Assembly	Dead load (Included in effective weight)				Live load (Not included)	
			Unit weight (psf)	Area (ft^2)	Weight (kips)	Story weight (kips)	Unit weight (psf)	Story weight (psf)
Roof	9.44	Roof	20	5288	105.8	158.5	20.0	105.8
		Exterior wall	15	1350	20.3			
		Interior wall	10	2644	26.4			
		Rooftop MEP			6.0			
Typical Floor	9.44	Floor	30	5288	158.6	258.0	40.0	211.5
		Exterior wall	15	3096	46.4			
		Interior wall	10	5288	52.9			

Table 2.3. Design summary: 10 story archetype building

	Level	Steel sheet thickness	Fastener spacing	Stud blocking	Stud pack	Chord stud	Gravity stud	Tie rod
Transverse	Roof	(1) 0.027”	#8@6”	No	2	600S200-54	600S137-33	ϕ0.5”
	9	(1) 0.033”	#8@3”	No	4	600S200-54	600S137-33	ϕ0.75”
	8	(1) 0.033”	#8@2”	No	4	600S200-97	600S137-33	**ϕ1.125”**
	7	(1) 0.030”	#10@2”	Yes	**4**	**600S250-97**	600S137-33	ϕ1.375”
	6	**(1) 0.030”**	**#10@2”**	**Yes**	6	600S250-97	600S137-33	ϕ1.75”
	5	(2) 0.014”	#10@2”	Yes	6	600S250-97	600S137-33	ϕ2.0”
	4	(2) 0.019”	#10@2”	Yes	6	600S250-97	600S137-33	ϕ2.0”
	3	(2) 0.019”	#10@2”	Yes	10	600S250-97	600S137-43	ϕ2.25”
	2	(2) 0.019”	#10@2”	Yes	10	600S250-97	600S137-43	ϕ3.0”
	1	(2) 0.019”	#10@2”	Yes	12	600S250-97	600S137-43	ϕ3.5”
Longitudinal	Roof	(1) 0.018”	#8@6”	No	2	600S200-43	600S137-33	ϕ0.5”
	9	(1) 0.030”	#8@6”	No	4	600S200-54	600S250-43	ϕ0.75”
	8	(1) 0.033”	#8@2”	No	4	600S200-68	600S250-54	ϕ1.0”
	7	(1) 0.033”	#8@2”	No	**4**	600S250-97	600S250-54	ϕ1.375”
	6	(1) 0.033”	**#10@2”**	**Yes**	6	**600S250-97**	**600S250-68**	ϕ1.75”
	5	**(1) 0.030”**	#10@2”	Yes	6	600S250-97	600S250-68	ϕ2.0”
	4	(1) 0.030”	#10@2”	Yes	6	600S250-97	600S250-68	ϕ2.0”
	3	(1) 0.030”	#10@2”	Yes	10	600S250-97	600S250-97	ϕ2.25”
	2	(2) 0.014”	#10@2”	No	10	600S250-97	600S250-97	ϕ2.75”
	1	(2) 0.014”	#10@2”	No	10	600S250-97	600S250-97	ϕ3.0”

Note: Highlighted terms indicate the selected wall details.

uration, amounting to 16 walls tested in total. Table 2.5 shows the eight wall configurations tested during the shake table test phase. It should be noted that the specimen names refer to the characteristics of each 4 ft quadrant length of the 16 ft long specimen appended with a number indicating whether it is a Type I or Type II wall system, as defined by AISI S400-20, specifying

Table 2.4. Design summary: 4 story archetype building

	Level	Steel sheet thickness	Fastener spacing	Stud blocking	Stud pack	Chord stud	Gravity stud	Tie rod
Transverse	Roof	(1) 0.027”	#8@6”	No	4	600S162-33	600S137-33	ϕ0.5”
	3	(1) 0.033”	#8@4”	No	4	600S162-54	600S137-33	ϕ0.75”
	2	(1) 0.033”	#8@2”	No	4	600S200-68	600S137-33	ϕ1.0”
	1	(1) 0.033”	#8@2”	No	4	600S200-97	600S137-33	ϕ1.25”
Longitudinal	Roof	(1) 0.018”	#8@6”	No	4	600S162-33	600S137-33	ϕ0.5”
	3	(1) 0.030”	#8@6”	No	4	600S162-54	600S137-54	ϕ0.625”
	2	(1) 0.033”	#8@4”	No	4	600S200-54	600S137-68	ϕ1.0”
	1	(1) 0.033”	#8@2”	No	4	600S200-68	600S137-97	ϕ1.0”

the locations of tension tie-rods. Thus, for example, SGGS-1 (baseline specimen) was a Type I Shear-Gravity-Gravity-Shear wall line specimen with a pair of tie-rods at each shear wall segment end; and SWWS-2 is a Type II Shear-Window-Window-Shear wall line specimen with tie-rods located at the wall ends (Figure 2.2).

Table 2.5. Test matrix and definition of specimens: shake table test phase

Specimen	Description	Tie-down detailing	Shear wall detailing	Finish	
				Exterior face	Interior face
SGGS-1	Baseline specimen. Symmetrical shear segments on both wall ends	Tension tie-rods	Type I	-	-
SGGS-1XS	SGGS-1 with finer steel sheet fastener pattern	Tension tie-rods	Type I	-	-
SGGS-1F	SGGS-1 with finish	Tension tie-rods	Type I	EIFS	Gypsum
SGGS-1SB	SGGS-1 with composite steel sheet glass-mat panels	Tension tie-rods	Type I	EIFS	Gypsum
SGGS-2B	SGGS-2 with coarser steel sheet fastener pattern	Tension tie-rods	Type II	-	-
SGGG-1	Unsymmetrical wall: shear segment on one wall end only	Tension tie-rods	Type I	-	-
SWWS-1	SGGS-1 with window opening in the middle bays	Tension tie-rods	Type I	-	-

Note: Specimen names indicate characteristics of each quadrant length appended with a number for shear wall detailing and additional characters for differences in finish, fastener detail, tie-down detail.

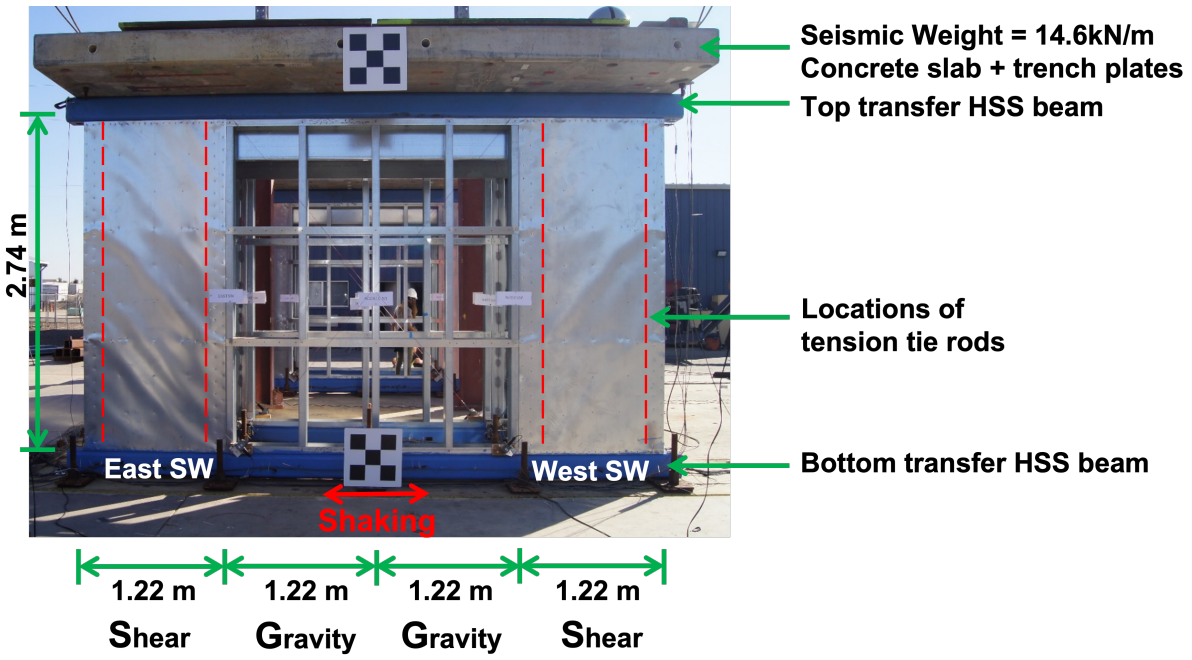


Figure 2.2. Baseline specimen (SGGS-1) photograph as installed in test setup

Individual walls were 4.88 m (16 ft) long and 2.74 m (9 ft) high. The baseline specimen was a symmetric, unfinished wall with a 2.44 m (8 ft) gravity wall segment in the middle and 1.22 m (4 ft) Type I shear wall segments on each end. Each shear wall segment was detailed with a pair of tie-down assemblies consisting of compression stud packs built up by arc welding toe-to-toe 600S250-97 studs and a ϕ29 mm (ϕ1-1/8") Grade B7 tension tie rod (theoretical yield strength 442 kN, 99 kips) in the middle of the stud packs on each end. Built-up compression stud packs required intermittent flare groove welds of 4.76 mm (3/16") grove depth, with 2.54 cm (1") weld length and 30.5 cm (12") pitch. The all-thread tie-rods were provided with a Grade 8 29 mm (1-1/8") coupler at approximately mid-height of the wall. The wall sheathing was made of 0.76 mm (0.030") thick steel sheet of ASTM A653 Grade 33 ksi (230 MPa) nominal yield strength. The steel sheet was attached to one side (exterior face) of the shear wall framing using No. 12 gauge 22 mm (7/8") flat pan head screws at 51 mm (2") on center (o.c.) edge and 305 mm (12") o.c. field spacing. The gravity wall framing utilized 600S250-68 vertical studs placed at 610 mm (2 ft) o.c. The top and bottom tracks used 600T250-97 members. Additionally,

a 1200T250-97 ledger track was attached to the top 0.3 m (12") height of the interior face of the wall with six rows of screws at 51 mm (2") o.c. (Figure 2.3). The bottom four rows used No. 12 gauge 22 mm (7/8") flat pan head screws, while the top two rows used No. 12 gauge 38 mm (1-1/2") hex head screws as those screws were required to penetrate a longer distance due to the presence of three layers of steel framing. Flat straps which were 64 mm (2-1/2") wide and 1.4 mm (0.054") thick were used for bracing. Walls were fully blocked, with blocking and bracing installed at third height points of the wall. Two different types of clips were used to connect the blocking with the vertical studs: 102 mm $\times$ 38 mm $\times$ 76 mm, 1.77 mm thickness (4" $\times$ 1-1/2" $\times$ 3", 0.068" thickness) and 38 mm $\times$ 38 mm $\times$ 76 mm, 1.77 mm thickness (1-1/2" $\times$ 1-1/2" $\times$ 3", 0.068" thickness). It should be noted that these specimens were fabricated off-site and shipped to the testing facility. Only, the installation of ledger track and tension tie-rods was performed on-site prior to testing. All framing members were ASTM A653 Grade 50 ksi (345 MPa) nominal strength and were assembled using No. 10 gauge 19 mm (3/4") flat pan head screws. These framing details for specimen fabrication, selected based on the archetype building design, are same as those highlighted in Table 2.3, except for the size of screws used. Taking into consideration the thickness of the steel sheet and framing members, No. 12 screws were deemed more suitable compared to No. 10 for attaching the steel sheet to the CFS framing. Shop drawings of all the tested configurations are provided in Appendix A

Figure 2.3 show the framing details of the baseline wall specimen (SGGS-1). Same components were used for the fabrication of the other wall specimens. Figure 2.4 shows the various steps involved in the fabrication of specimens on the shop floor. All the individual structural components belonging to the different walls were cut to the correct length. The built-up members such as chord studs requiring arc-welding and window framing members including jamb studs and sill tracks were assembled first as per drawings. Next, the tracks and studs were connected together while applying pre-compression to properly seat the members and prevent any gaps. Next, the blocking and bracing was installed, followed by installation of the steel sheet as the last step on the shop floor. Tension tie-rod assembly and ledgers were

installed in field during test setup. For specimens requiring finish application, gypsum boards on the interior face and glass-mat sheathing panels with Exterior Insulation Finish System (EIFS) on the exterior face were installed in the field using No. 8 gauge 44 mm (1-3/4") flat head screws at 152 mm (6") o.c. edge and 406 mm (16") o.c. field spacing. Installed gypsum boards were 1.22 m × 2.44 m × 16 mm (4 ft × 8 ft × 5/8 in) Firecode Type X, while glass-mat sheathing panels were 1.22 m × 2.74 m × 16 mm (4 ft × 9 ft × 5/8 in) Firecode Type X. Material properties of the framing members, tension tie-rods, finish stucco etc. as obtained from the manufacturer and from material tests are provided in Appendix B.

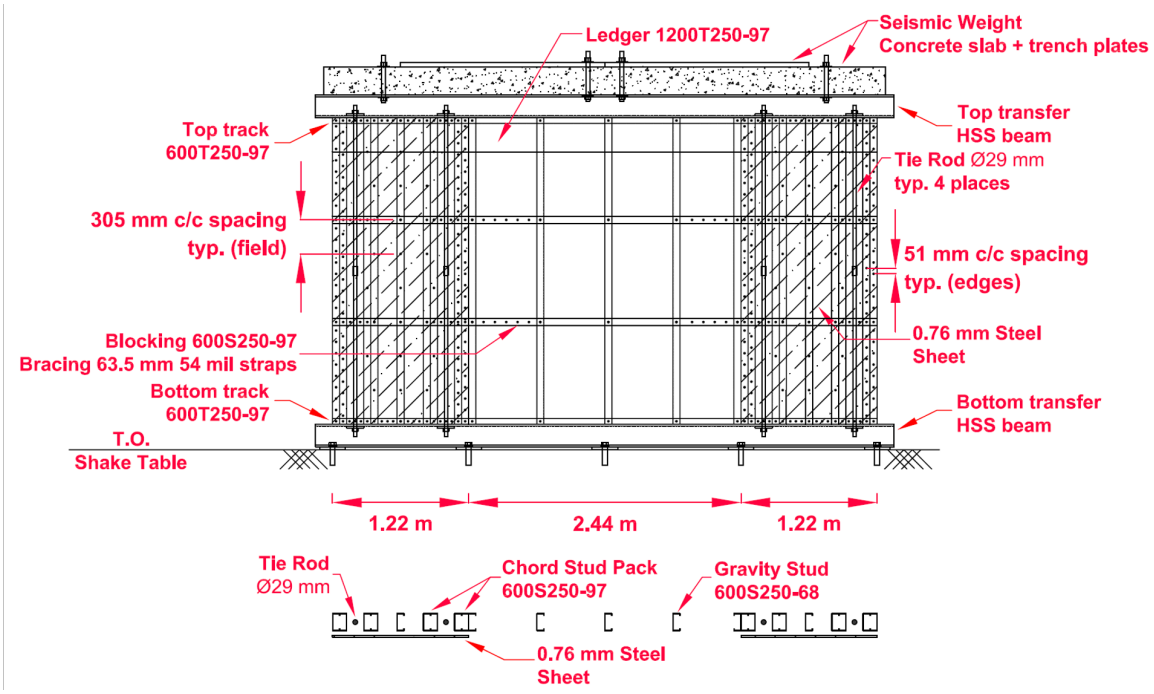
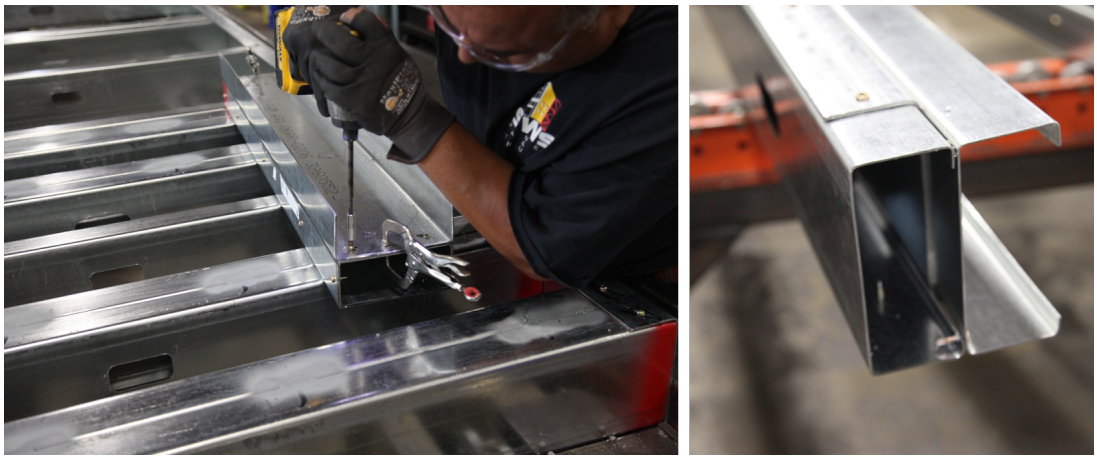


Figure 2.3. Framing details of baseline specimen (SGGS-1)

2.3.2 Test Setup

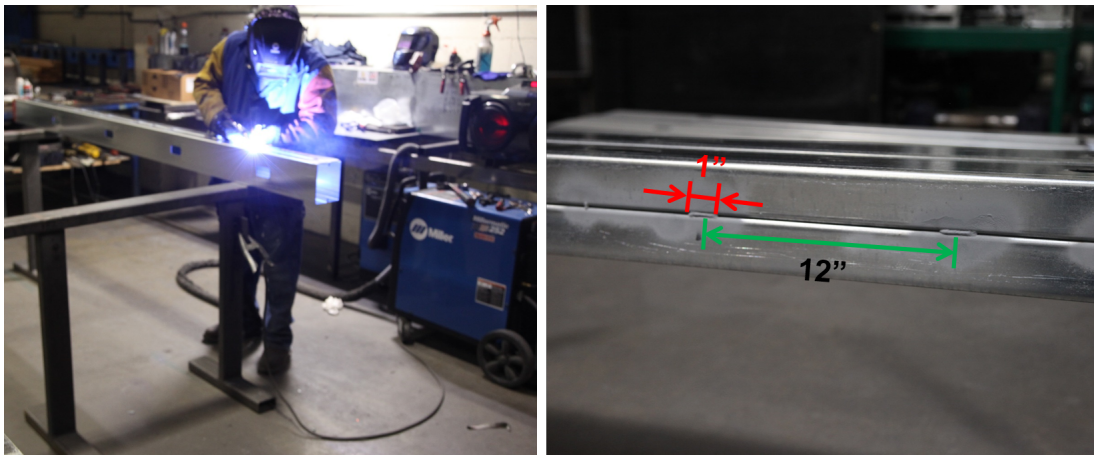
Figure 2.5 shows the various steps involved in the test setup. The NHERI @ UC San Diego shake table footprint of 12.2 m × 7.6 m (40 ft × 25 ft) allowed for two pairs of nominally identical walls to be tested simultaneously. Five base plates were welded to each bottom transfer beam (hollow steel section) at 1.22 m (4 ft) spacing. These bottom transfer beams alongwith

safety columns on and along the edge of the shake table were post-tensioned to the strong floor. The specimens were dropped in to the test setup and attached to the bottom transfer beam using two rows of 12.7 mm (1/2") A325 shear bolts. The two wall pairs were provided with temporary out-of-plane bracing to ensure the walls remain vertical when the top mass is installed. The top transfer beams were also installed using two rows of 12.7 mm A325 shear bolts. Before the installation of top mass, the tension tie-rods were installed and tightened using the access holes in the transfer beams with the nut-plate assembly bearing against the inside surfaces of the top and bottom beams. Figure 2.6 shows the elevation view of the tension tie-rod assembly when installed in the test setup. The concrete mass slabs were dropped in above the wall pairs and post-tensioned to the top transfer beams. Safety cables ran from safety towers on one edge to the other edge of the shake table through D-rings installed on the concrete slabs. Additionally, two steel trench plates were installed and post-tensioned to the concrete slab on each wall pair to achieve the desired seismic weight. The seismic weight for the wall pairs consisted of a concrete slab (16.5 ft × 10 ft × 10 in, 5.0 m × 3.0 m × 254 mm), two steel plates (6 ft × 10 ft × 1.5 in, 1.8 m × 3.0 m × 38 mm) and the top transfer beams themselves, resulting in a total weight of 14.6 kN/m (1000 plf) per wall. This gravity load was estimated to be typical for



(a) Built-up members for window framing

Figure 2.4. Specimen fabrication photographs (taken at fabricator SWS Panel Inc. manufacturing facility in South Gate, CA)



(b) Arc-welding of chord studs



(c) Pre-compression for seating framing members



(d) Blocking and steel sheet installation

Figure 2.4. Specimen fabrication photographs (taken at fabricator SWS Panel Inc. manufacturing facility in South Gate, CA) (cont.)

CFS-framed buildings and also fell in the range of gravity loads [8.3 kN/m (570 plf) to 18.2 kN/m (1,250 plf)] considered in past research on combined gravity and lateral loading of shear walls (Hikita, 2006). The steel frames to the east of shake table were used as reference frames for global displacement measurements for dynamic tests. It should be noted that the earthquake input motions were applied in the east-west direction using the single axis shake table, which aligned with the long axis of the wall specimens. Figure 2.7 shows the top and isometric view of the completed test setup.

A similar setup was used for the monotonic pull tests performed only on few select wall pairs: SGGS-1, SGGS-1XS, SGGS-1F and SGGS-1SB. The steel frames to the east of shake table were used as reaction frames to pull against. A column placed to the west of the wall pair on the shake table was used as reference column for local displacement measurements, as shown in Figure 2.8. The two walls within the pair were connected from the top transfer beams to the reaction frame using cables with turnbuckles at the end. Two 222.4 kN (50 kip) load cells connected to the reaction frame measured the wall pair lateral resistance during the monotonic pull test. At the beginning of each pull test, the turnbuckles were adjusted such that the two load cells carried approximately the same amount of load and prevent any eccentricity in loading.



(a) Welding of base plates on bottom transfer beam; bottom transfer beams and safety towers post-tensioned to shake table floor

Figure 2.5. Photographs demonstrating steps involved in test setup



(b) Installation of wall pairs into test setup with temporary out-of-plane bracing



(c) Installation of top transfer beams; installed tension tie-rods; installation of concrete slab mass



(d) Safety cables running from tower to tower through D-rings on concrete slab; installation of trench plates as mass

Figure 2.5. Photographs demonstrating steps involved in test setup (cont.)

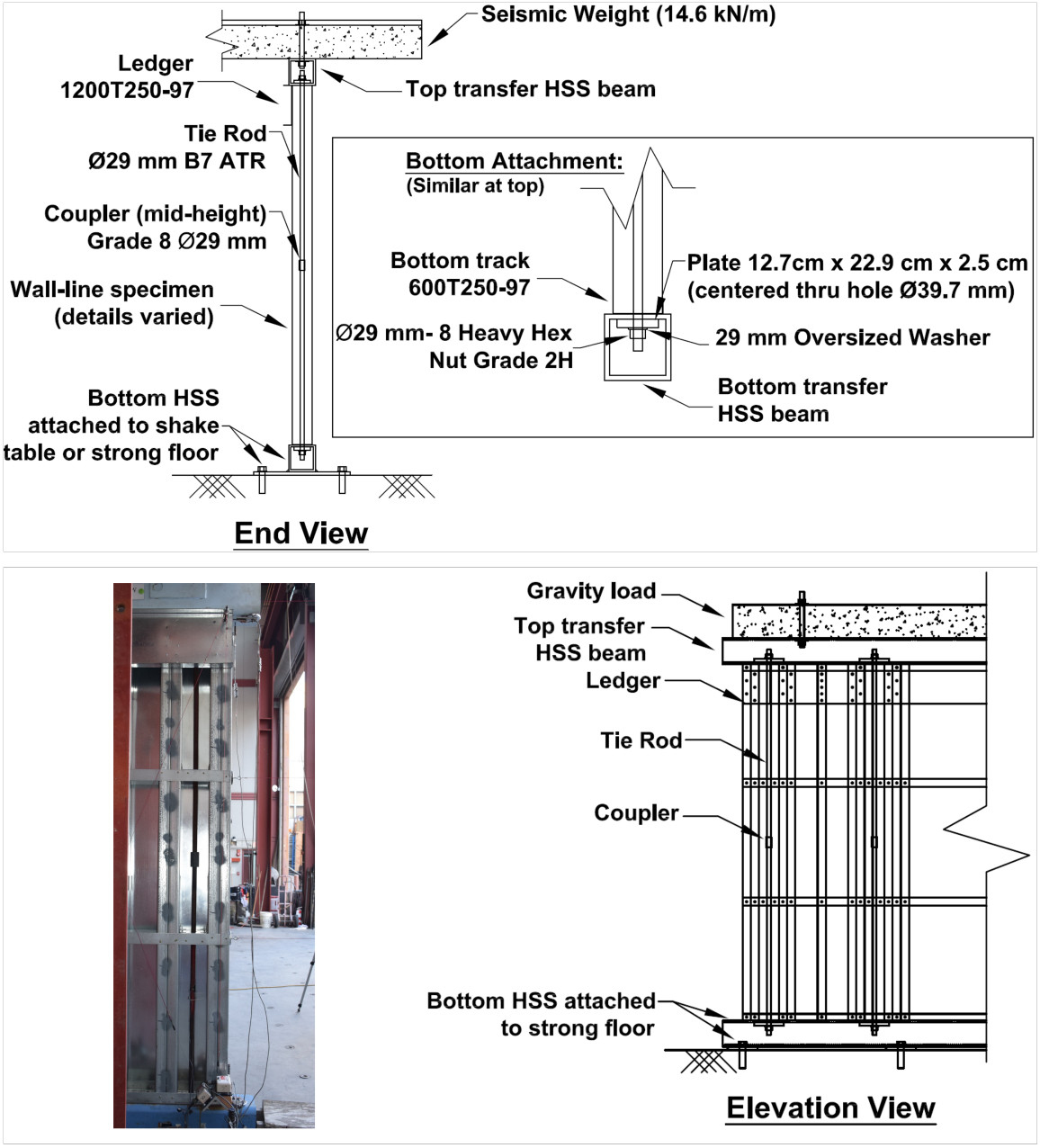


Figure 2.6. Elevation view of tension tie-rod assembly

2.3.3 Application of Finish Materials

Finish application for the two wall pairs in the test matrix was performed after installing both wall pairs into the test setup and the mass installed on top. Gypsum boards were attached on the interior face and glass-mat sheathing panels were attached on the exterior face. Figure

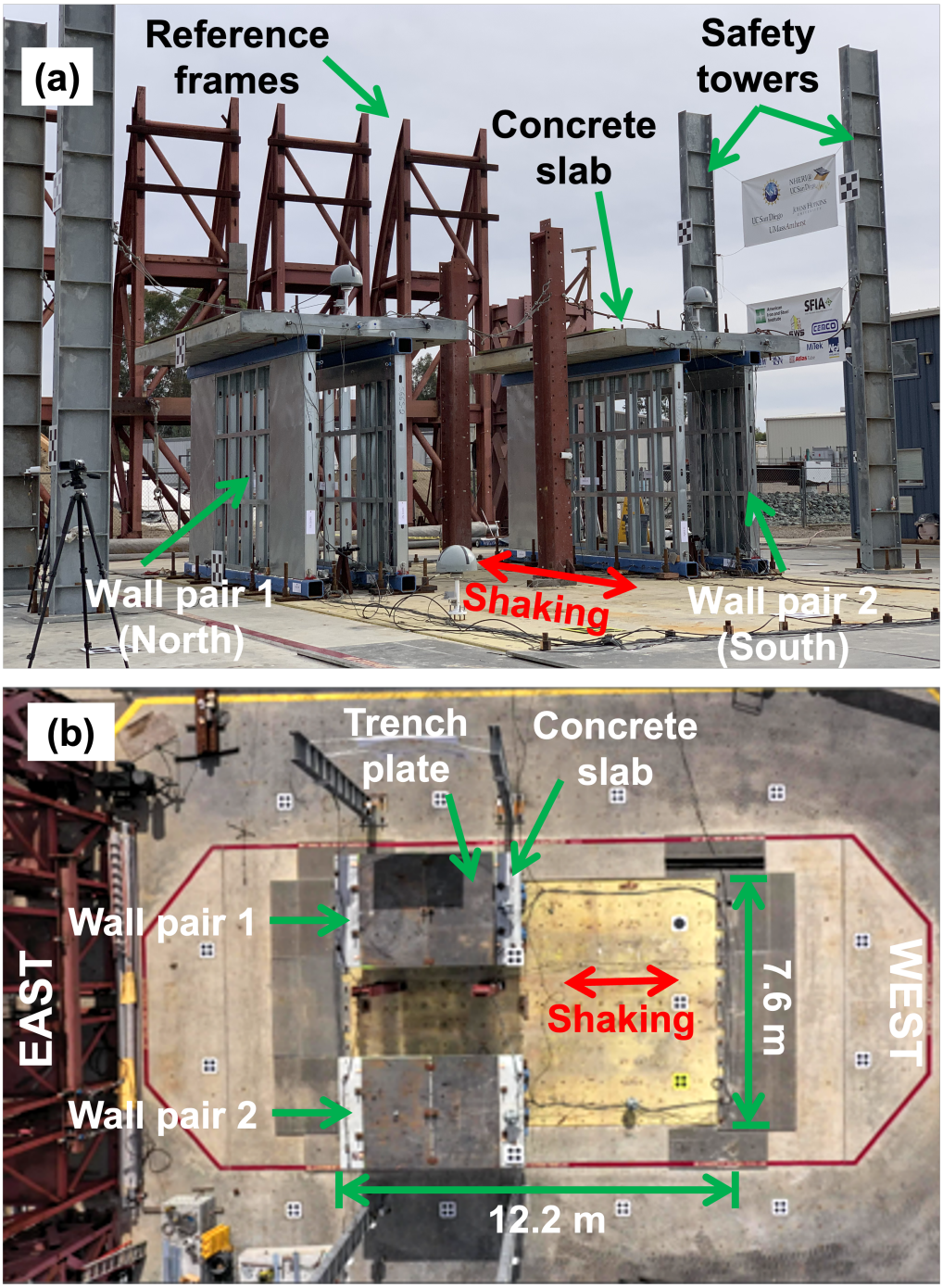


Figure 2.7. (a) Isometric and (b) top view of the test setup

2.9 show the various steps involved in finish application. First, 25.4 mm (1") thick Expanded Polystyrene (EPS) foam boards were attached onto the glass-mat sheathing or Sure-Board® panel as substrate using cement adhesive. Next, the foam boards were rasped down before applying

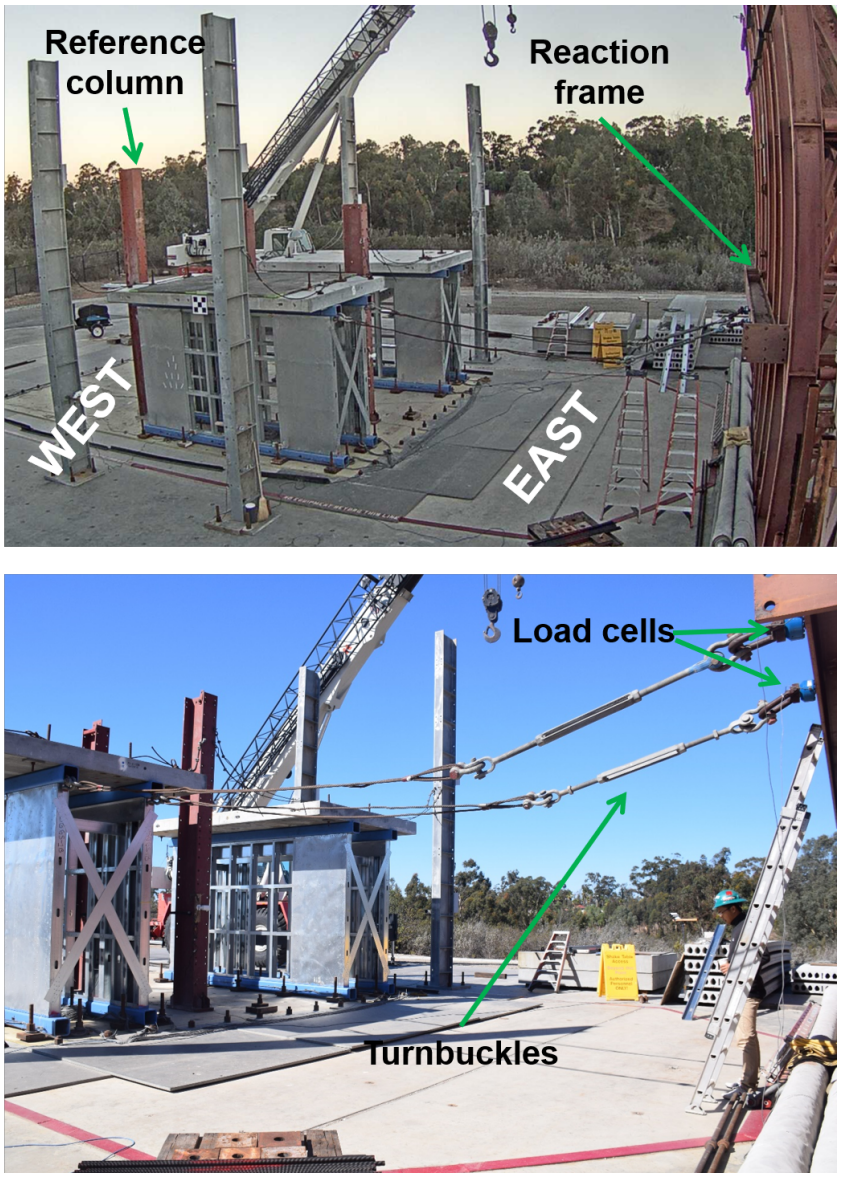


Figure 2.8. Test setup for monotonic pull tests

the base coat. The reinforcing mesh was embedded into the base coat during its application. A second coat was applied over the mesh-base coat before applying the finish coat as the last step. The different layers of EIF system were applied over a period of three days.

2.3.4 Detailing around Window Opening

To support the force transfer around window openings, jamb studs, sill and header tracks were sized per design codes AISI S400-20 andAISI S100-20. A window opening 2.18 m (7 ft

2 in) wide and 1.22 m (4 ft) tall with a sill height 0.76 m (2 ft 6 in) was installed within the middle 2.44 m (8 ft) long bay. This opening would occupy the same space as the gravity bay in the baseline specimen, and hence would similarly have one 1.22 m (4 ft) long shear wall segment at each end. Jamb studs were built-up members, which utilized 600S250-68 stud and 600T250-97 track members as shown in Figure 2.10. Similarly, the header track was also a built up member using the same framing members, while the sill track used a single 600T250-97 track member and the cripple region utilized 600S250-68 studs.



(a) Installation of glass-mat sheathing panels



(b) Application of EPS foam boards using adhesive onto panel substrate

Figure 2.9. Photographs demonstrating steps involved in finish application during shake table test phase



(c) Rasping of foam boards before application of base coat



(d) Embedded reinforcing mesh in base coat and application of second layer



(e) Application of finish coat

Figure 2.9. Photographs demonstrating steps involved in finish application during shake table test phase (cont.)

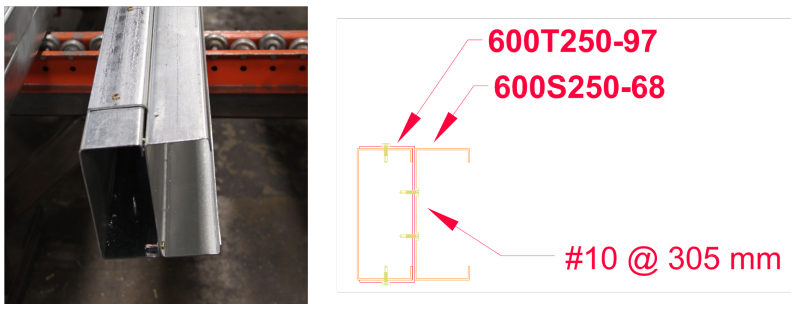


Figure 2.10. Jamb stud built-up section used around window opening

2.3.5 Motion Scaling Strategy and Test Protocol Development

To facilitate measurement and observation of the seismic behavior of the specimens and obtain their dynamic characteristics at different performance levels, a unique scaling strategy was developed. The two pair of specimens to be tested simultaneously were selected such that they had similar expected lateral strength and initial stiffness. This was done aiming that the scaled earthquake motions subjected the two wall pairs to the same target performance level. However, such pairing of specimens was not always possible. Due to this, developed motion scaling strategy was also required to take into account the strength and stiffness differences between the two wall pairs that were going to be tested simultaneously on the shake table. This section explains the development of the motion scaling strategy and its application in the test protocol used for shake table tests. The pre-test numerical simulations based on available literature and details of the test protocol used are documented in this section.

Selection of Representative Specimens

To determine the intensity of individual earthquake tests, three wall specimens, representative of the breadth of expected strength for the entire test matrix, were modeled as single degree of freedom systems with damping ratio $\xi = 5\%$. First of these three representative wall specimens was the baseline specimen SGGS-1. Since the framing details used in the construction of the baseline specimen fell outside the provisions of design code AISI S400-20, available tests of steel sheet shear wall specimens were utilized for strength and stiffness predictions.

Specifically, experimental data from the shear wall test of specimen W21 from Santos and Rogers (2017) and specimen W2 from Rizk and Rogers (2017) were considered for obtaining material modeling parameters for the baseline specimen for benchmark model predictions.

Shear wall specimen W21 was a 1.22 m (4 ft) long and 2.44 m (8 ft) tall specimen with 0.35 mm (0.014") thick double side steel sheet attached using No. 10 gauge self-drilling pan head screws at 51 mm (2") o.c edge and 305 mm (12") o.c field spacing. Stud members of size 600S300-97 were used for field and built-up back-to-back chord studs. In contrast, the top and bottom track members were 600T200-97 members. Wall W21 did not use any blocking members. Simpson Strong-Tie S/HD15S hold-downs were used to resist uplift forces. Similarly, shear wall specimen W2 was a 1.22 m long and 2.44 m tall specimen with 0.76 mm (0.030") thick single side steel sheet attached using No. 8 gauge self-drilling pan head screws at 51 mm o.c edge and 305 mm field spacing. Stud members of size 362S162-97 were used for field as well as built-up back-to-back chord studs. Top and bottom track members were 362T125-97. Wall W2 was fully blocked at quarter points using 362T125-54 members. Simpson Strong-Tie S/HD10S hold-downs were used to resist uplift forces. Figures 2.11 and 2.12 show the dimensions and framing details of shear wall specimens W21 and W2. Figure 2.13 shows the force-displacement response of the shear wall specimens W21 and W2. Interested readers are directed to the referenced reports to obtain further information about the wall specimens.

The other two representative wall specimens included SGGS-2 (lowest expected strength) and SGGS-1F (highest expected strength). A strength scale factor of 1.3 and 0.5 was applied to SGGS-1 material model parameters for SGGS-1F and SGGS-2 SDOF systems, respectively. In the end, specimen W21 was chosen for material model definition in benchmark models. Figure 2.14 shows the force-displacement responses of the three selected representative test specimens.

Seed Motion Characteristics and Pre-test Scale Factor Selection

Two test motions from two earthquake events, namely the: (a) 1994 $M_w = 6.7$ Northridge earthquake (Canoga Park record component ID: CNP196) and (b) 2010 $M_w = 8.8$ Maule earth-

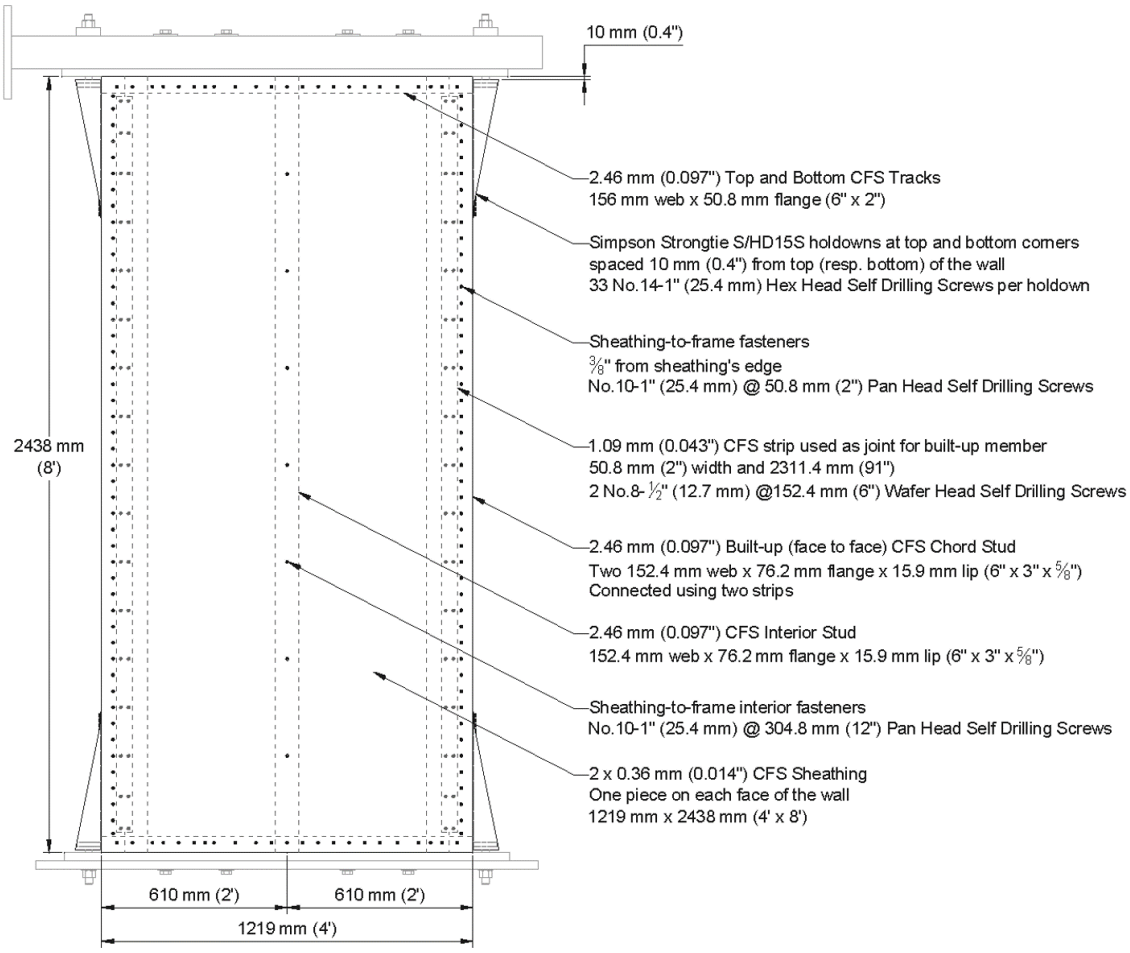


Figure 2.11. Framing details of shear wall specimen W21 (Santos and Rogers, 2017)

quake in Chile (Curicó record component ID: CUR EW) were selected as seed motions in this test phase. These motions were selected in part to assure representative strong earthquakes from past California events, while also including events with a long duration of strong shaking (Hutchinson et al. (2017)). The characteristics of the selected seed motions are shown in Table 2.6 and Figure 2.15.

During the earthquake motion test sequence, scale factors for subsequent earthquake tests on the various specimen pairs were determined based on the measured natural period of the two wall pairs within the test group, as determined from the 3%g RMS white noise test conducted immediately prior to the earthquake motion. As part of pre-test preparations, On-Line iterations (OLI) of the selected seed motions at defined scale factors (SF_{OLI}) were performed

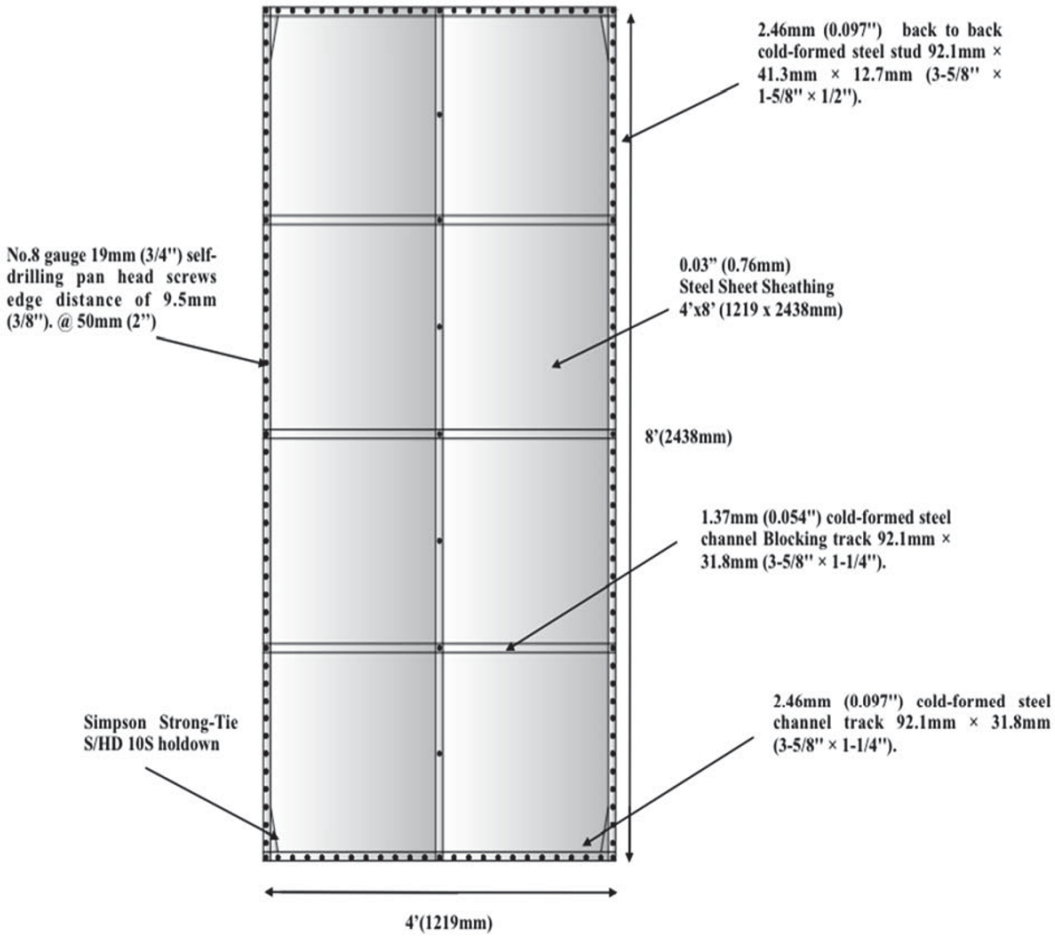


Figure 2.12. Framing details of shear wall specimen W2 (Rizk and Rogers, 2017)

on the bare table. These OLI motions are motion iterations conducted on bare table platen until convergence on desired target scale factors of seed motions is achieved. Table 2.6 lists the scale factors (SF_{OLI}) used during the shake table test phase.

Based on the four performance levels, defined in Table 2.7, scale factor (SF_{desired}) for a desired performance level was determined as explained here. Figure 2.16 shows the pre-test scale factor selection. The green, blue and orange colored regions denote the lateral force, F (as fraction of strength, F_{p}) and drift, Δ (as fraction of drift at strength, $\Delta_{\text{F}_{\text{p}}}$) ranges for elastic, quasi-elastic and design performance levels, as defined in Table 2.7. It should be noted that scale factor for above design performance level is not predicted using pre-test benchmark model. The yellow range bars indicate the range of scale factors that can be achieved using the OLI motion

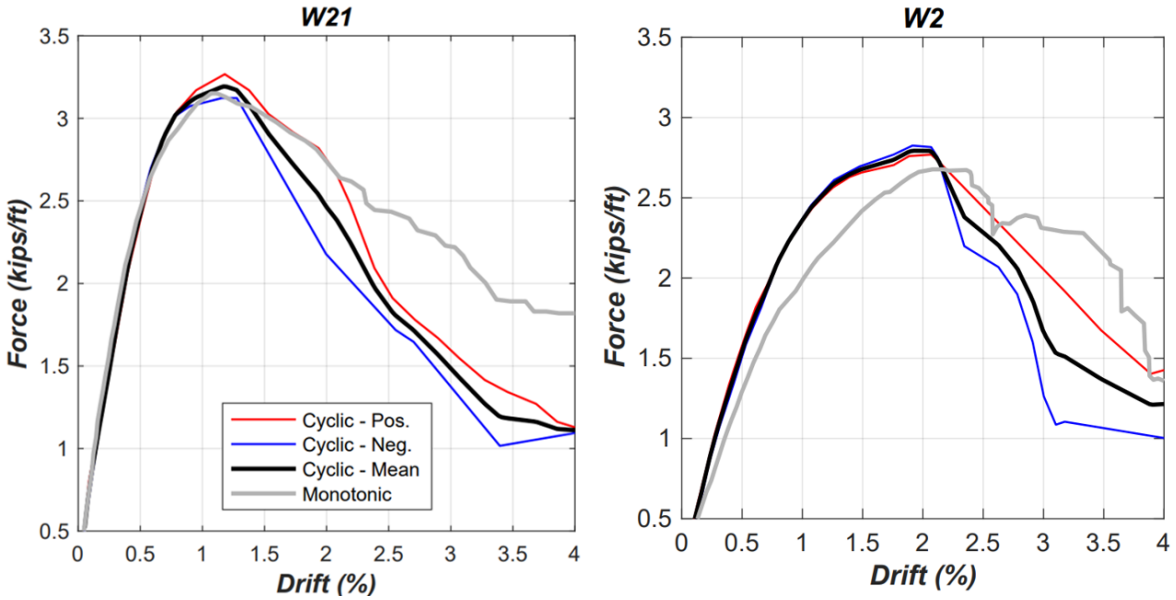


Figure 2.13. Force displacement behavior of shear wall specimens (a) W21 (Santos and Rogers, 2017) and (b) W2 (Rizk and Rogers, 2017)

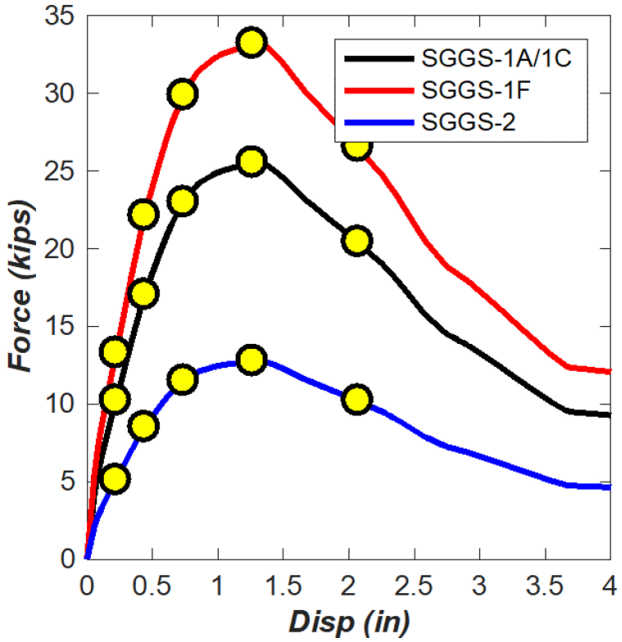


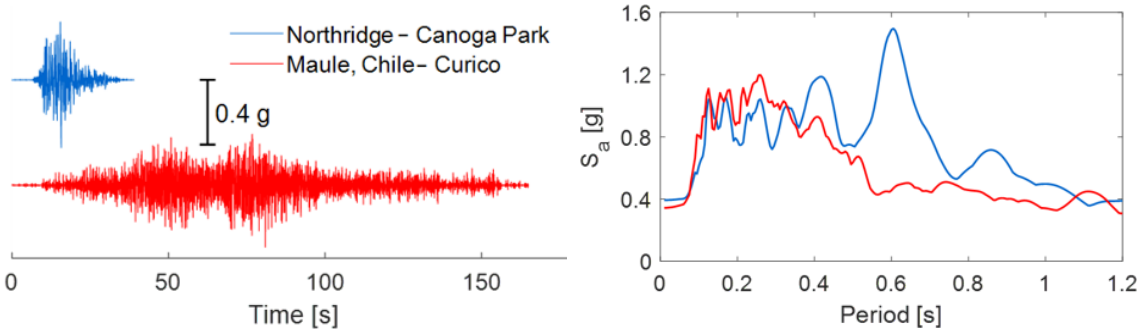
Figure 2.14. Test predictions for selected representative test specimens

with that specific SF_{OLI} (see Table 2.6) and PGA value. For example, an earthquake motion with scale factor between 0.5 and 0.8 is predicted to yield an elastic response from SGGS-1 specimen.

Table 2.6. Characteristics of selected seed motions

Record ID	Earthquake Event	Year	M_w	Station	R_{rup} (km)	PGA (g)	PGV (in/s)	PGD (in)	Ds_{5-95} (s)	Selected scale factors, SF_{OLI}
CNP196	Northridge	1994	6.7	Canoga Park	14.7	0.39	23.8	4.9	10.6	0.4, 0.7, 1.4, 2.5, 3.25
CUR-EW	Maule, Chile	2010	8.8	Curicó	N/A	0.41	12.8	2.0	51.6	0.7

PGA: Peak ground acceleration, PGV: Peak ground velocity, PGD: Peak ground displacement.



(a) **(b)**

Figure 2.15. Selected earthquake seed motions: (a) acceleration time histories and (b) elastic pseudo-acceleration spectra ($\xi = 5\%$)

The available CNP196 OLI motion with $SF_{\text{OLI}} = 0.7$, which has a target PGA = 0.27 g, can be employed to obtain that elastic response from SGGS-1 specimen. However, this OLI motion could have been scaled used a scaling procedure to produce an earthquake motion with a scale factor between 0.45 and 0.95, as also indicated by the yellow range bar. This ground motion scaling procedure is explained next.

Table 2.7. Target performance level definition

Target performance level	Response characteristics	Force target, V_{target} ($\%V_u$)	Drift target, Δ_{target} ($\%\Delta_{\text{Vu}}$)	Damage
Elastic	Linear	20%-40%	~20%	Minimal
Quasi-elastic	Quasi-linear	60%-70%	30%-40%	Minor (cosmetic)
Design	Nonlinear	Near strength	75%-95%	Moderate
Above design (optional)	Noticeable pinching	<20% strength deterioration	125%-150%	Major; uncompromised structural integrity

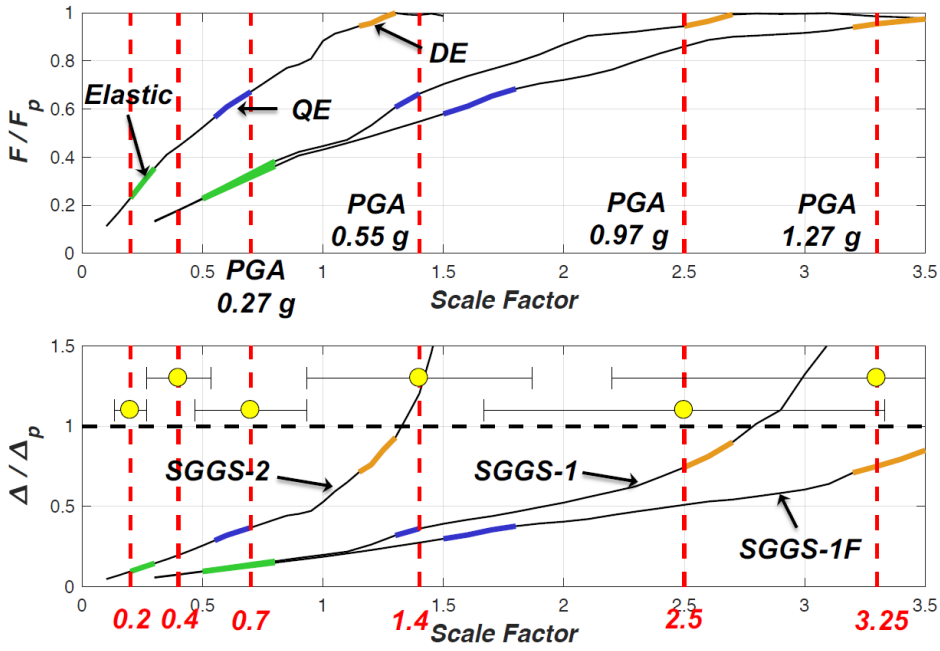


Figure 2.16. Pre-test scale factor selection

Ground Motion Scaling Procedure

Scaling of the seed motions aimed to achieve the intended target performance levels (as defined in Table 2.7) that progressively damage the wall specimens. The motion scaling procedure was carried out using the steps explained next. It should be noted that the procedure presented here is in its final form, after modifications that were made as the testing proceeded.

1. Determine scale factor (SF_{desired}) for a desired performance level using pre-test benchmark model prediction results.

2. Calculate performance adjustment coefficient (SF_1) based on selected performance level and specific OLI motion (SF_{OLI}).

$$SF_1 = \frac{SF_{\text{desired}}}{SF_{\text{OLI}}} \tag{2.1}$$

3. Calculate motion spectra adjustment coefficient (SF_2) based on measured (or estimated) period of specimen at different damage stages during the test sequence.

$$SF_2 = \frac{\tilde{S}_{\text{a,target}}}{\tilde{S}_{\text{a,OLI}}} \tag{2.2}$$

where $\tilde{S}_{\text{a,target}}$ and $\tilde{S}_{\text{a,OLI}}$ are the average spectral acceleration of the scaled target motion and achieved bare table OLI motion within the period interval of interest, respectively. This period interval of interest is determined using the natural period identified from a 3% g RMS white-noise test conducted before the earthquake test and an estimated earthquake induced period elongation.

For elastic and quasi-elastic performance level tests, period interval of interest is chosen as $T_{1,min}$ - $\alpha T_{1,max}$, where $T_{1,min}$ and $T_{1,max}$ are the natural periods of the stiffer and flexible wall pairs, respectively, associated with their undamaged state measured from a 3% g RMS white-noise test; and α is a coefficient considering the uncertainty related to period elongation, taken as 1.25. The wall pairs within the test group were chosen such that they have similar strength and stiffness. However, for test group 4 (specimens SWWS-1 and SWWS-2), such a pairing was not possible. Hence, during scale factor calculation, period interval of interest was chosen as T_1 - αT_1, where T_1 is the natural period of the control wall pair, in this case chosen as the wall pair with the lower expected strength.

For design performance level test, period interval of interest is chosen as $T_{2,min}$ - $\beta T_{1,max}$, where $T_{2,min}$ is the natural period of the stiffer wall pair associated with its damaged state identified from the 3% g RMS white noise test conducted before the design level earthquake test and $T_{1,max}$ is same as defined above. β is a coefficient considering the uncertainty related to period elongation, taken as 2.0, assuming a maximum period elongation of 100% when the specimen reaches its lateral strength. Specifically for specimens in test group 4, for scale factor calculation, the period interval of interest was chosen as T_2 - βT_1, where T_2 and T_1 are the natural periods of the control wall pair associated with its damaged and undamaged states, respectively.

4. Compute final adjusted coefficient (SF_{final}). This coefficient is applied to the selected OLI motion and input to the shake table to achieve the desired target performance level.

$$SF_{final} = SF_1 \times SF_2 \tag{2.3}$$

Tables 2.8-2.11 report the calculated factors at each step following the procedure as explained above for each of the four test groups. Step by step calculations for EQ1 and EQ4 for test group 3 have been shown as an example following Table 2.11. It should be noted that target performance reported in Table 2.11 is only for the control wall pair, and not for both wall pair specimens within test group 4.

Table 2.8. Motion scaling factors for test group 1 (specimens SGGS-1 and SGGS-1XS)

Test motion	Target performance	Bare table motion (SF_{OLI})	SF_{desired}	SF_1	SF_2	SF_{final}	Period range (sec)	$S_{\text{a,target}}$ (g)	$S_{\text{a,OLI}}$ (g)
EQ1	Elastic	CNP196 (0.7)	0.64	0.914	1.169	1.069	0.145 - 0.185	0.661	0.566
EQ2	Elastic	CUR-EW (0.7)	0.64	0.914	1.010	1.006	0.145 - 0.185	0.729	0.663
EQ3	Quasi-Elastic	CNP196 (1.4)	1.35	0.964	1.035	0.998	0.145 - 0.185	1.323	1.278
EQ4	Design	CNP196 (2.5)	2.5	1.0	1.098	1.098	0.16 - 0.35	2.252	2.051

Table 2.9. Motion scaling factors for test group 2 (specimens SGGS-1F and SGGS-1SB)

Test motion	Target performance	Bare table motion (SF_{OLI})	SF_{desired}	SF_1	SF_2	SF_{final}	Period range (sec)	$S_{\text{a,target}}$ (g)	$S_{\text{a,OLI}}$ (g)
EQ1	Elastic	CNP196 (0.7)	0.7	1.0	0.821	0.821	0.075 - 0.095	0.36	0.44
EQ2	Elastic	CUR-EW (0.7)	0.7	1.0	0.623	0.623	0.075 - 0.095	0.422	0.677
EQ3	Quasi-Elastic	CNP196 (1.4)	1.6	1.143	0.966	1.104	0.1 - 0.125	1.095	1.133
EQ4	Design	CNP196 (2.5)	2.5	1.0	1.06	1.06	0.11 - 0.14	2.276	2.146
EQ5	Above Design	CNP196 (3.25)	3.25	1.0	1.128	1.128	0.16 - 0.32	2.886	2.558

Table 2.10. Motion scaling factors for test group 3 (specimens SGGG-1 and SGGS-2B)

Test motion	Target performance	Bare table motion (SF_{OLI})	SF_{desired}	SF_1	SF_2	SF_{final}	Period range (sec)	$S_{\text{a,target}}$ (g)	$S_{\text{a,OLI}}$ (g)
EQ1	Elastic	CNP196 (0.4)	0.3	0.75	1.17	0.877	0.18 - 0.30	0.346	0.296
EQ2	Elastic	CUR-EW (0.7)	0.3	0.429	1.163	0.498	0.18 - 0.30	0.738	0.635
EQ3	Quasi-Elastic	CNP196 (0.7)	0.6	0.857	1.175	1.007	0.18 - 0.30	0.606	0.516
EQ4	Design	CNP196 (1.4)	1.2	0.857	1.108	0.95	0.19 - 0.36	1.24	1.12
EQ5	Above Design	CNP196 (1.4)	1.8	1.286	1.117	1.436	0.31 - 0.48	1.39	1.25

Table 2.11. Motion scaling factors for test group 4 (specimens SWWS-2 and SWWS-1)

Test motion	Target performance	Bare table motion (SF_{OLI})	SF_{desired}	SF_1	SF_2	SF_{final}	Period range (sec)	$S_{\text{a,target}}$ (g)	$S_{\text{a,OLI}}$ (g)
EQ1	Elastic	CNP196 (0.4)	0.3	0.75	1.15	0.866	0.145 - 0.20	0.362	0.313
EQ2	Elastic	CUR-EW (0.7)	0.3	0.429	1.109	0.475	0.145 - 0.20	0.703	0.634
EQ3	Quasi-Elastic	CNP196 (0.7)	0.6	0.857	1.166	1.0	0.145 - 0.20	0.633	0.543
EQ4	Design	CNP196 (1.4)	1.2	0.857	1.093	0.937	0.16 - 0.33	1.252	1.145
EQ5	Above Design 1	CNP196 (1.4)	1.5	1.07	1.093	1.17	0.16 - 0.33	1.252	1.145
EQ6	Above Design 2	CNP196 (2.5)	2.0	0.8	1.107	0.885	0.18 - 0.33	2.197	1.985

The two wall pairs in test group 3, SGGS-2B and SGGG-1, had very similar expected strength and stiffness. Hence, the benchmark prediction model for SGGS-2 could be appropriately utilized for both wall pairs. Calculations for EQ1 for test group 3 have been shown next.

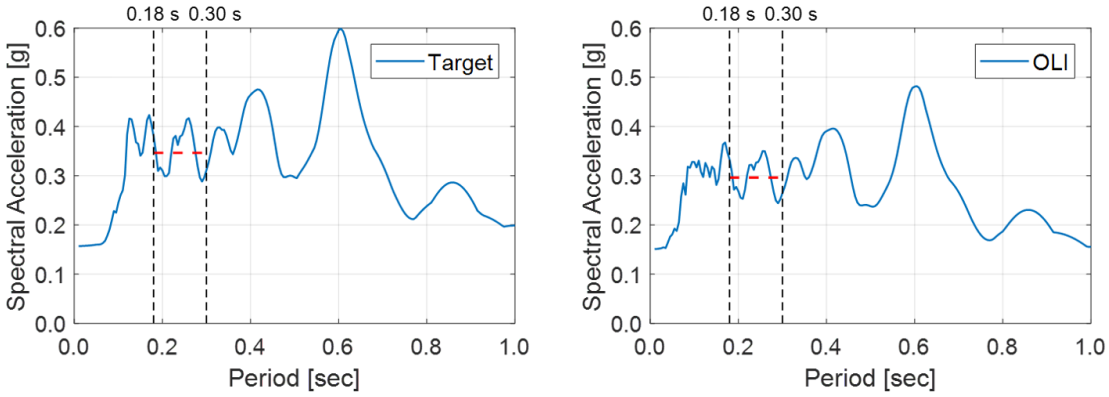
1. For an elastic level target performance, $SF_{\text{desired}} = 0.3$ is chosen (green colored region for SGGS-2 in Figure 2.16). This can be achieved by scaling OLI motion with $SF_{\text{OLI}} = 0.4$ for 1994 Northridge (CNP196) ground motion record (yellow range bars for SGGS-2 in Figure 2.16).

2. Performance adjustment coefficient is calculated as: (SF_1)

$$SF_1 = \frac{SF_{\text{desired}}}{SF_{\text{OLI}}} = \frac{0.3}{0.4} = 0.75 \tag{2.4}$$

3. From the 3% g RMS white-noise test conducted before the earthquake test, natural periods of the flexible and stiff wall pairs, $T_{1,min}$ and $T_{1,max}$ are determined as 0.18 s and 0.24 s respectively. Period interval of interest is calculated as $T_{1,min}$ - $\alpha T_{1,max}$ = 0.18 s - 0.30 s. For the determined period interval of interest, $\tilde{S}_{\text{a,target}}$ (average spectral acceleration of the scaled target motion) and $\tilde{S}_{\text{a,OLI}}$ (average spectral acceleration of the achieved bare table OLI motion) are calculated, as shown in Figure 2.17, as 0.346 g and 0.296 g, respectively. Motion spectra adjustment coefficient (SF_2) is calculated as:

$$SF_2 = \frac{\tilde{S}_{\text{a,target}}}{\tilde{S}_{\text{a,OLI}}} = \frac{0.346}{0.296} = 1.17 \tag{2.5}$$



(a) $\tilde{S}_{a,target}$ calculation **(b)** $\tilde{S}_{a,OLI}$ calculation

Figure 2.17. Scale factor calculations for EQ1 for test group 3

4. Final adjusted coefficient (SF_{final}) is computed as:

$$SF_{final} = SF_1 \times SF_2 = 0.75 \times 1.17 = 0.877 \tag{2.6}$$

Similarly, calculations for EQ4 for test group 3 are shown below.

1. For a design level target performance, SF_{desired} = 1.2 is chosen. This was achieved by scaling OLI motion with SF_{OLI} = 1.4 for 1994 Northridge (CNP196) ground motion record.

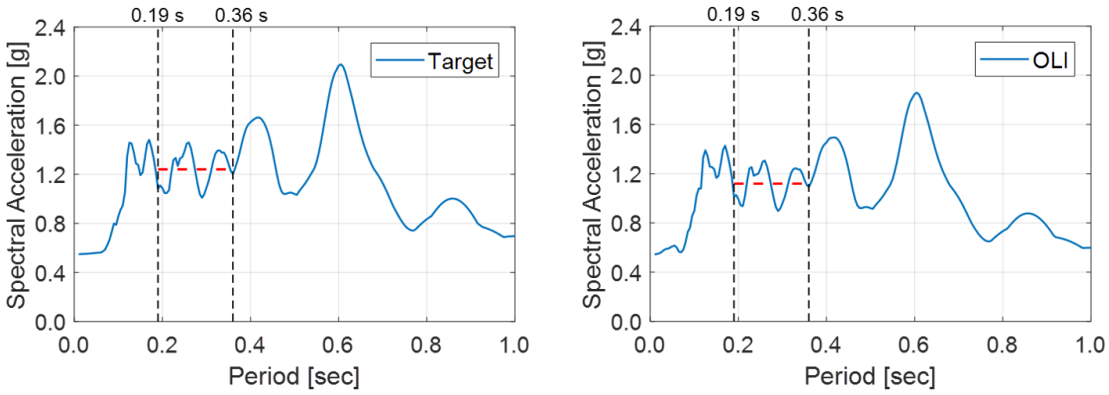
2. Performance adjustment coefficient is calculated as: (SF_1)

$$SF_1 = \frac{SF_{\text{desired}}}{SF_{\text{OLI}}} = \frac{1.2}{1.4} = 0.857 \tag{2.7}$$

3. From the 3% g RMS white-noise test conducted before the earthquake test, natural period of the flexible wall pair associated with its damaged state, $T_{2,min}$ is determined as 0.19 s. Period interval of interest is calculated as $T_{2,min}$ - $\beta T_{1,max}$ = 0.19 s - 0.36 s. For the determined period interval of interest, $\tilde{S}_{a,target}$ (average spectral acceleration of the scaled target motion) and $\tilde{S}_{a,OLI}$ (average spectral acceleration of the achieved bare table OLI

motion) are calculated, as shown in Figure 2.18, as 1.24 g and 1.12 g, respectively. Motion spectra adjustment coefficient (SF_2) is calculated as:

$$SF_2 = \frac{\tilde{S}_{\text{a,target}}}{\tilde{S}_{\text{a,OLI}}} = \frac{1.24}{1.12} = 1.108 \tag{2.8}$$



(a) $\tilde{S}_{\text{a,target}}$ calculation **(b)** $\tilde{S}_{\text{a,OLI}}$ calculation

Figure 2.18. Scale factor calculations for EQ4 for test group 3

4. Final adjusted coefficient (SF_{final}) is computed as:

$$SF_{final} = SF_1 \times SF_2 = 0.857 \times 1.08 = 0.95 \tag{2.9}$$

Figure 2.19 shows the test sequence used for specimens SGGG-1 and SGGS-2B, tested simultaneously during the shake table test phase. Tables 2.12-2.15 summarize the peak input acceleration (PIA) and peak input displacement (PGD) of the achieved input motions used for pairs of tested specimens. It should be noted that the target performance level was not the achieved performance level in a few cases. Wang et al. (2023) assesses the effectiveness and limitations of the motion scaling strategy.

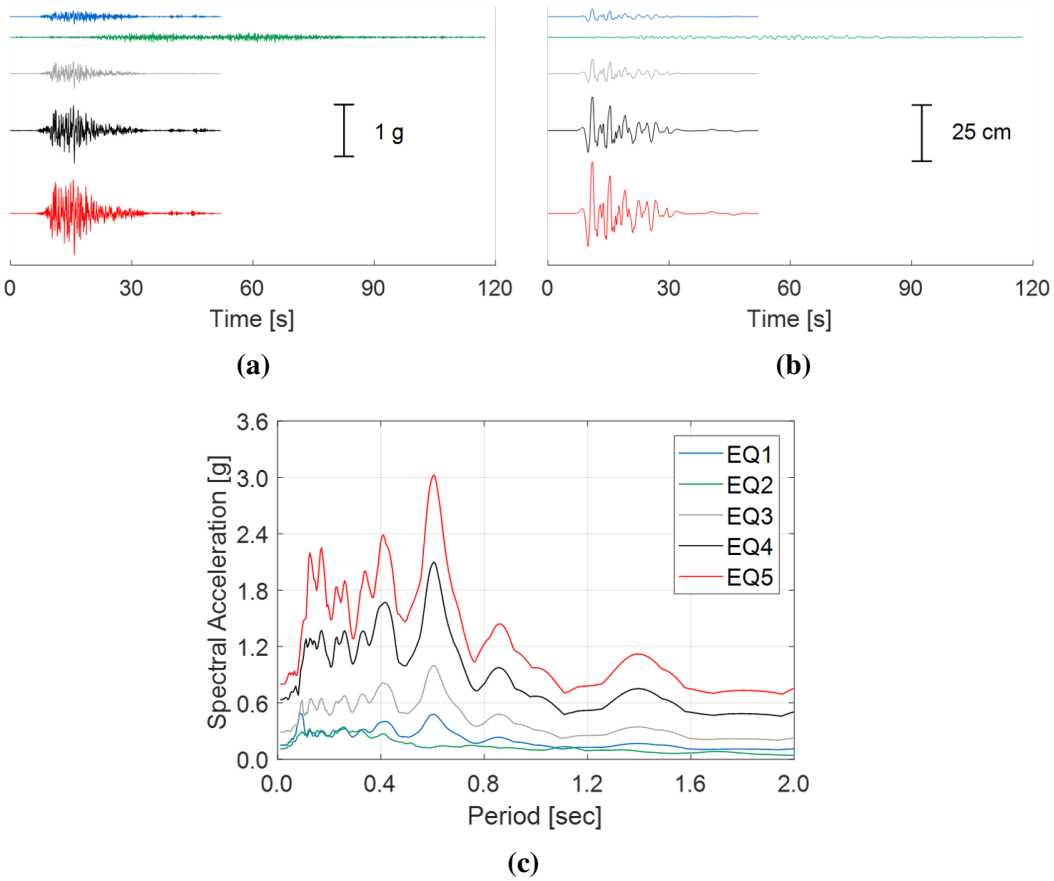


Figure 2.19. Scaled achieved earthquake motions for SGGG-1 and SGGS-2B: (a) acceleration time histories, (b) displacement time histories and (c) pseudo-acceleration spectra (ξ = 5%)

2.3.6 Instrumentation and Monitoring Systems

The two pairs of wall specimens were densely instrumented with over 170 analog sensors and an array of 15 cameras to record the wall response during the tests. These analog sensors included: (a) accelerometers, (b) string potentiometers, (c) strain gages, and (d) linear potentiometers. All analog sensors were connected to a multi-node distributed data acquisition system that sampled signals at a rate of 256 samples/sec. During the dynamic tests, a Global Positioning System (GPS) system and unmanned aerial vehicles (UAVs) were also used as monitoring systems. Additionally, a light detection and ranging (LiDAR) system was employed to collect data during the construction phase.

Table 2.12. Input earthquake sequence for specimens SGGS-1 and SGGS-1XS

Test motion	Target performance level	PIA (g)	PID (cm)
EQ1: CNP196	Elastic (E1)	0.31	7.69
EQ2: CUR-EW	Elastic (E2)	0.24	2.32
EQ3: CNP196	Quasi-Elastic (QE)	0.66	17.66
EQ4: CNP196	Design event (DE)	1.20	35.0

Table 2.13. Input earthquake sequence for specimens SGGS-1F and SGGS-1SB

Test motion	Target performance level	PIA (g)	PID (cm)
EQ1: CNP196	Elastic	0.25	5.98
EQ2: CUR-EW	Elastic	0.15	1.41
EQ3: CNP196	Quasi-Elastic (QE)	0.66	19.51
EQ4: CNP196	Design event (DE)	1.20	33.77
EQ5: CNP196	Above Design	1.56	48.23

Table 2.14. Input earthquake sequence for specimens SGGG-1 and SGGS-2B

Test motion	Target performance level	PIA (g)	PID (cm)
EQ1: CNP196	Elastic	0.15	3.61
EQ2: CUR-EW	Elastic	0.11	1.16
EQ3: CNP196	Quasi-Elastic (QE)	0.29	7.20
EQ4: CNP196	Design event (DE)	0.63	16.45
EQ5: CNP196	Above Design	0.80	25.14

Table 2.15. Input earthquake sequence for specimens SWWS-1 and SWWS-2

Test motion	Target performance level	PIA (g)	PID (cm)
EQ1: CNP196	Elastic	0.14	3.39
EQ2: CUR-EW	Elastic	0.11	1.05
EQ3: CNP196	Quasi-Elastic (QE)	0.30	7.24
EQ4: CNP196	Design event (DE)	0.62	16.63
EQ5: CNP196	Above Design 1	0.75	21.35
EQ6: CNP196	Above Design 2	0.93	28.49

Displacement Transducers

Each wall pair was instrumented with a pair of string potentiometers, attached to the top transfer beams, to measure the displacement of the two walls within the pair in the longitudinal direction (East-West direction). Additionally, one string potentiometer was used to measure the shake table platen displacement in the longitudinal direction. Figure 2.20 shows the layout of these displacement transducers measuring wall global response and their nomenclature. In total, five string potentiometers were installed during the dynamic tests on the reference frame. Together, these displacement transducers were used to measure wall pair lateral story drift. These five transducers were not used during the monotonic tests. Instead, one displacement transducer, installed on a reference column placed adjacent to wall pair on the shake table, was used to directly measure the relative displacement of the wall pair. Unlike the dynamic tests where the two wall pairs were tested simultaneously, the monotonic tests were performed sequentially. Hence, only one test column with one displacement transducer was sufficient.

Two different types of displacement transducers were used for measuring local wall response, namely string potentiometers and liner potentiometers. The shear and the gravity segments of each wall were instrumented with up to ten string potentiometers and seven linear potentiometers to measure the panel distortion and the uplift/slip displacements of the wall. All the string potentiometers were mounted directly on the interior face of wall on the CFS framing using aluminum brackets. This required cut outs at the corners of gypsum boards in case of finished specimens for mounting the aluminum brackets directly on the framing underneath. Out of the seven linear potentiometers, three were employed per wall to measure (a) slip between table platen and bottom transfer beam, (b) wall slip along bottom HSS transfer beam, and (c) slip between concrete slab and top HSS transfer beam. Figures 2.21 and 2.22 show the layout of displacement transducers used for measuring wall local response and their nomenclature. In total, 40 string potentiometers and 28 linear potentiometers were installed during the testing phase. The procedure for using a pair of two vertical and two diagonal string potentiometers

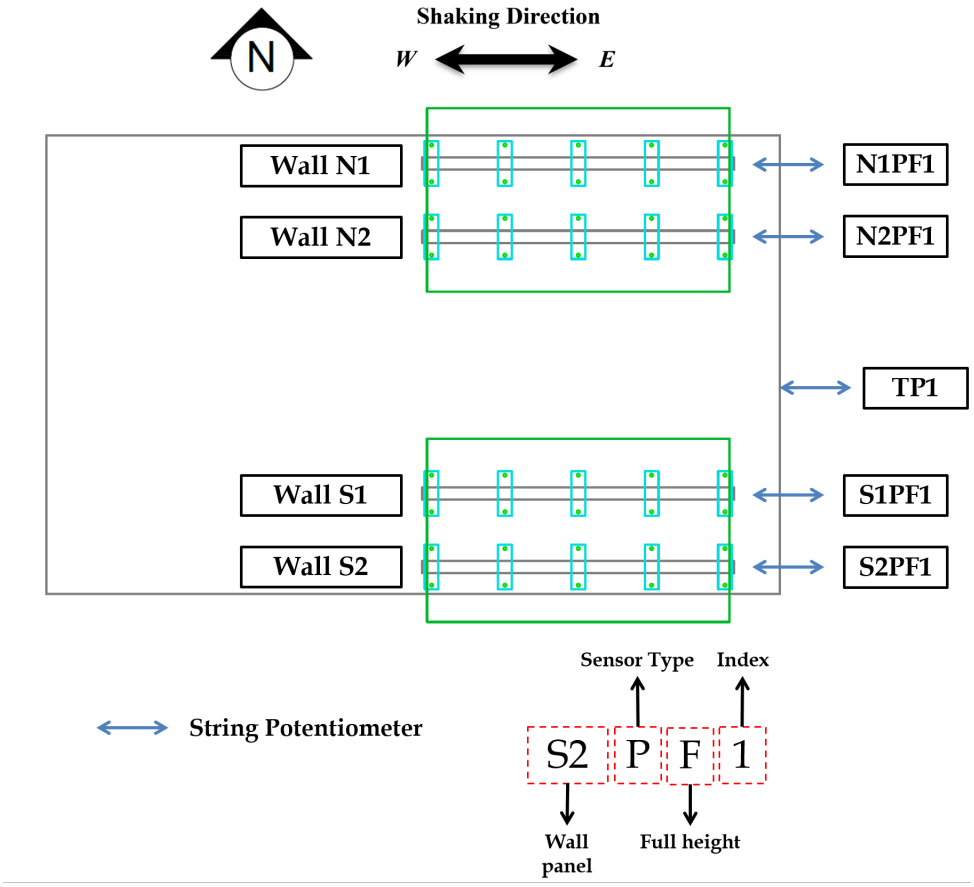


Figure 2.20. Layout and nomenclature of string potentiometers used for measuring wall and table displacements during dynamic tests

in a double-triangle configuration to evaluate the wall shear distortion for each wall segment is explained in section 3.2.

Load Cells

Two 222.4 kN (50 kip) load cells mounted on the reaction frame were used to measured the wall pair lateral resistance during the monotonic pull tests. Similar to the reference column, the two load cells locations could be moved to test the two different wall pairs.

Accelerometers

Each wall pair was instrumented with five uniaxial MEMS accelerometers, mounted atop the concrete slab. These accelerometers measured the seismic weight accelerations: (a) two in

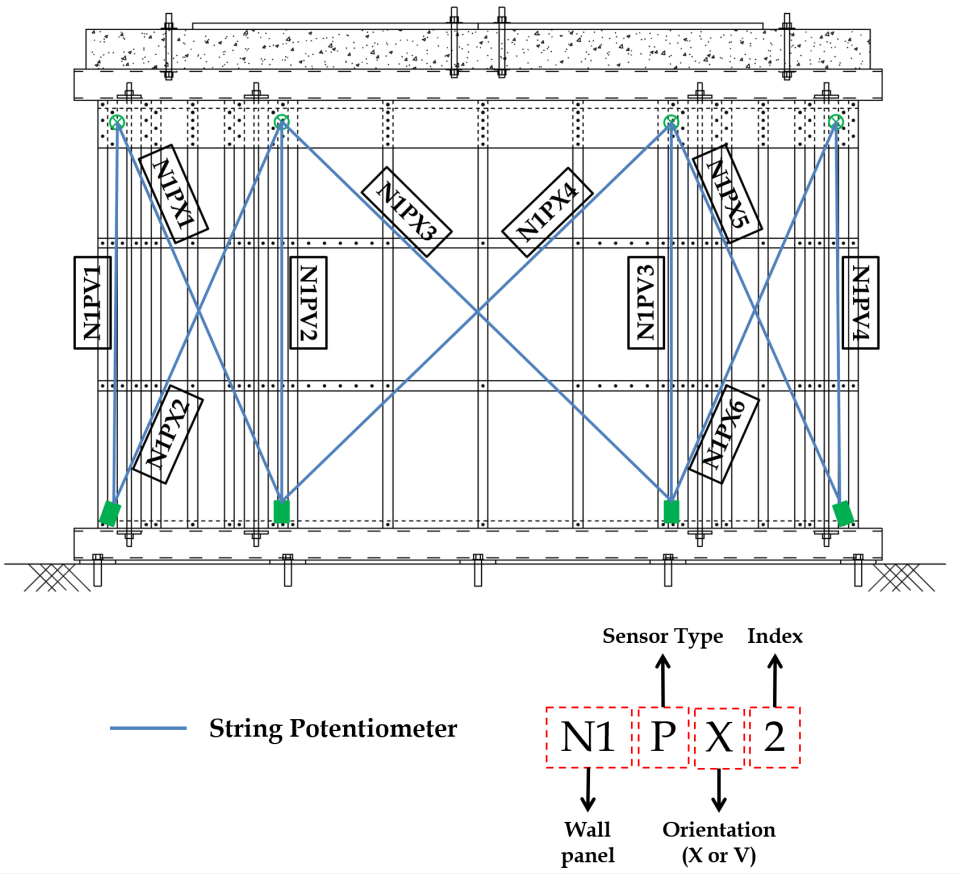


Figure 2.21. Layout and nomenclature of string potentiometers used for measuring wall panel distortion for specimen SGGS-1

the longitudinal direction (East-West direction), (b) one in the transverse direction (North-South direction), and (c) two in the vertical direction. Additionally, three accelerometers were used to measure the shake table platten accelerations: (a) two in the longitudinal direction (East-West direction), (b) one in the transverse direction (North-South direction). Figure 2.23 shows the layout and nomenclature of the accelerometers. In total, 13 accelerometers were installed during the testing phase. The accelerometers mounted on concrete slab were used to measure wall pair lateral resistance. In some cases, where issues with displacement transducers measuring global response were encountered, accelerometers measuring response in longitudinal direction of the slab and table platen were double integrated to obtain wall story drift time histories.

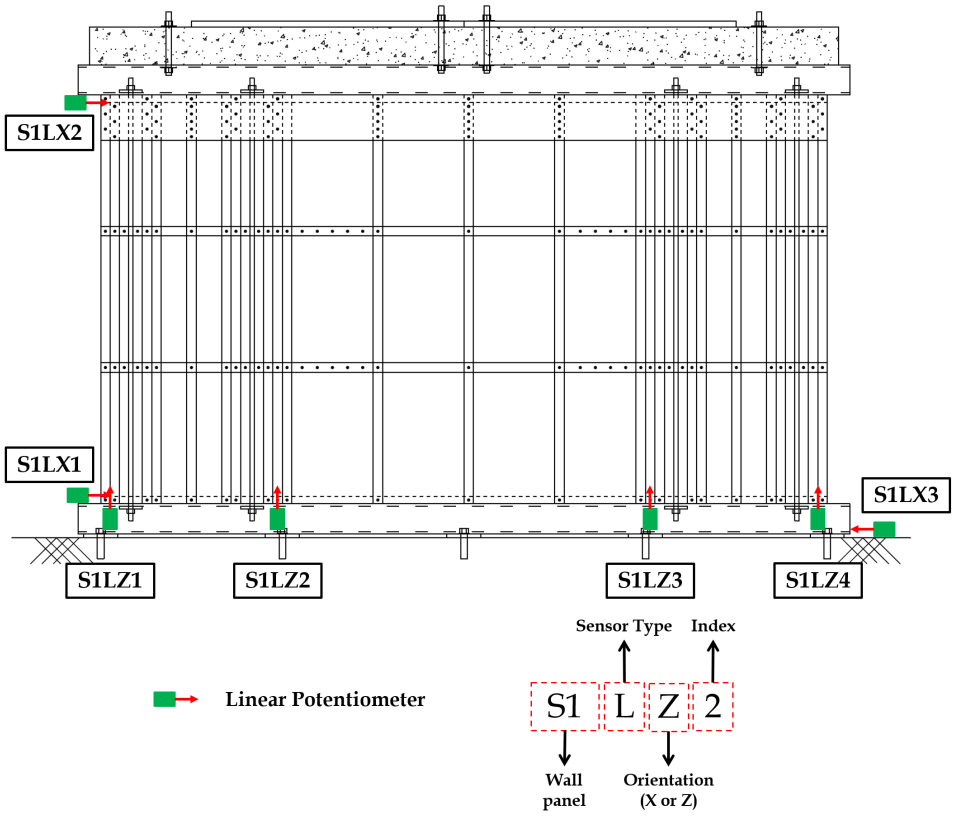


Figure 2.22. Layout and nomenclature of linear potentiometers used for measuring wall uplift and slip for specimen SGGS-1XS

Strain Gages

A pair of strain gages (Type FLA) were installed on every shear wall tension tie-rod by grinding away the threads at mid-height of the rod to obtain the axial strain and estimate the axial force in each rod. For two Type I wall pairs simultaneously on the table (e.g. SGGS-1 and SGGS-1XS), a total of 32 strain gages were installed. Additionally, the bottom HSS transfer beams were also instrumented to understand the shear distribution between the different segments of a wall. Each transfer beam had 12 strain gages in the longitudinal direction (East-West direction). A total of 80 strain gages were installed for measuring response during the tests. Figure 2.24 shows the layout of these strain gages and their nomenclature.

Two commercial UAVs were also deployed to record the dynamic responses of the test specimens during the earthquake tests. Theses UAVs were equipped with high-resolution

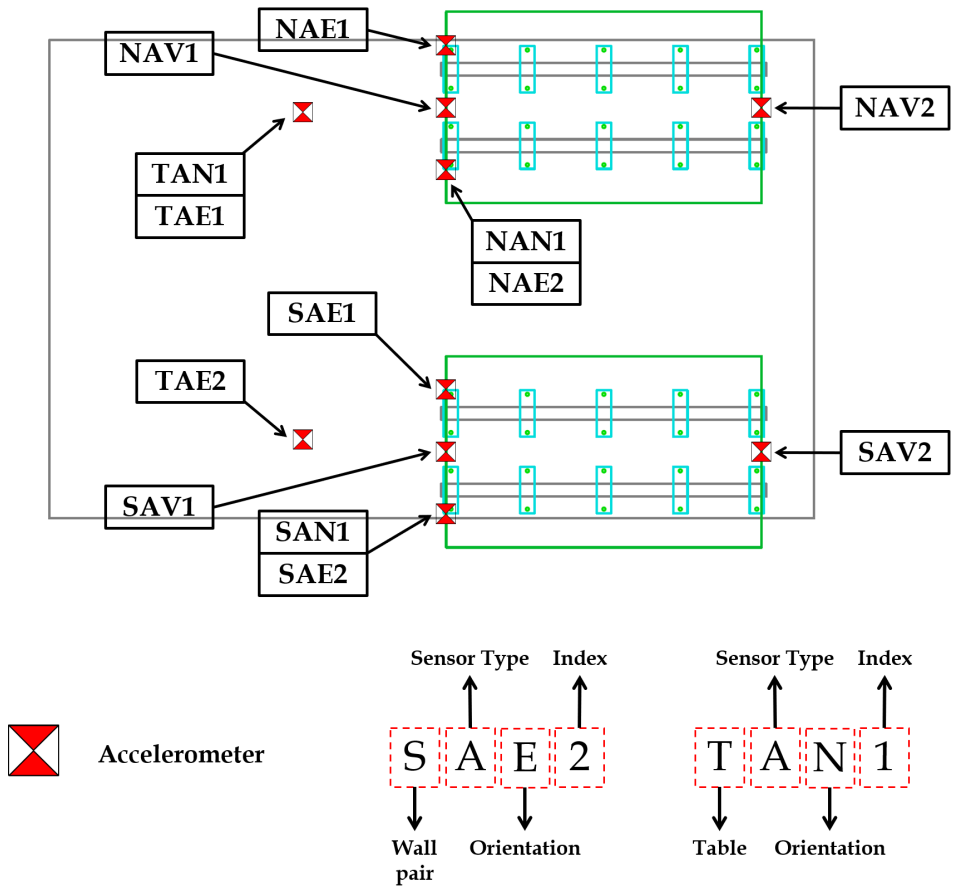


Figure 2.23. Layout and nomenclature of accelerometers used during dynamic tests

video recording built-in camera. Another two camera views were strategically placed for video recordings which focused on specific targets attached on the wall specimens. These measurements were used as auxiliary systems for measuring wall specimen displacements. Complete details of target detection, motion tracking and comparison with physical transducer output can be found in Wang et al. (2022).

2.4 Quasi-static Test Phase

2.4.1 Test Matrix

The CFS-NHERI wall-line quasi-static cyclic test phase consisted of ten wall configurations tested at the UC San Diego Structural Engineering Powell Laboratory. The wall details

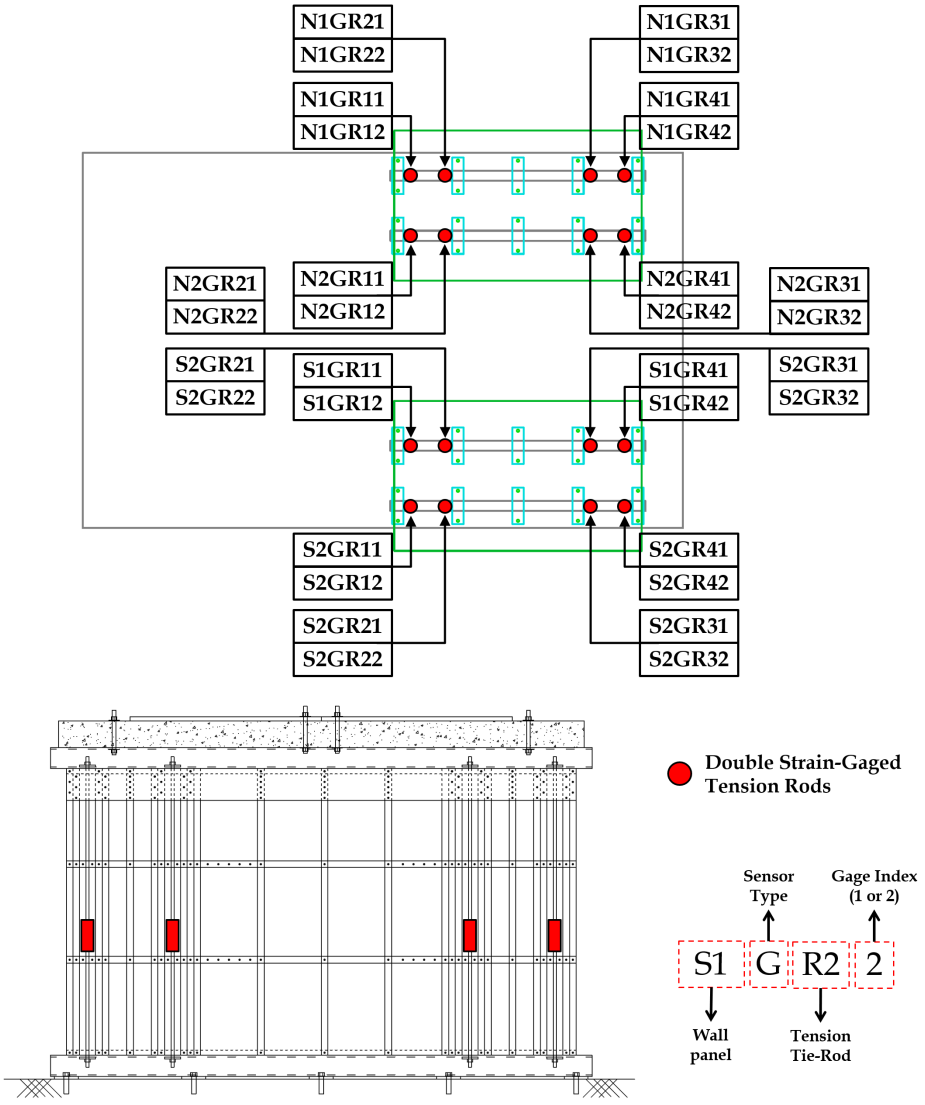


Figure 2.24. Layout and nomenclature of strain gages for measuring axial strains in tension tie-rods

were similar to those in shake table test phase, motivated by the design of the CFS-NHERI archetype building. Table 2.16 shows the ten wall configurations included in the test matrix. Specimen names followed the same naming convention explained in section 2.3. Thus, for example, SGGS-2 is a Type II Shear-Gravity-Gravity-Shear wall line specimen with tie-rods located at the wall ends; and SWWS-1 is a Type I Shear-Window-Window-Shear wall line specimen with a pair of tie-rods at each shear wall segment end (Figure 2.25). Generally, all

wall configurations used tension tie-rods for shear wall tie-down detailing (both Type I and Type II). However, two configurations in the test phase, namely SGGS-1HD and SGGS-1HDF, used hold-downs instead. The configurations GGGG and GGGG-F, as the naming convention suggests, were detailed as gravity walls with no tie-downs.

Table 2.16. Test matrix and definition of specimens: quasi-static test phase

Specimen	Description	Tie-down detailing	Shear wall detailing	Finish	
				Exterior face	Interior face
SGGS-2	Symmetrical: shear segments on both wall ends	Tension tie-rods	Type II	-	-
SGGS-2F	SGGS-2 with finish	Tension tie-rods	Type II	EIFS	Gypsum
SWWS-1	SGGS-1 with window opening in the middle bays	Tension tie-rods	Type I	-	-
SWWS-2	SGGS-2 with window opening in the middle bays	Tension tie-rods	Type II	-	-
SWWS-2F	SWWS-2 with finish	Tension tie-rods	Type II	EIFS	Gypsum
SGGG-1F	SGGG-1 with finish	Tension tie-rods	Type I	EIFS	Gypsum
SGGS-1HD	SGGS-1 with hold-downs	Hold-downs	Type I	-	-
SGGS-1HDF	SGGS-1HD with finish	Hold-downs	Type I	EIFS	Gypsum
GGGG	Gravity frames in all bays	None	N/A	-	Gypsum
GGGG-F	GGGG with exterior finish	None	N/A	EIFS	Gypsum

Note: Specimen names indicate characteristics of each quadrant length appended with a number for shear wall detailing and additional characters for differences in finish, fastener detail, tie-down detail.

Wall-line specimens used the same framing details as during the shake table test phase. The SGGS-2 specimen, as an example, was a symmetric, unfinished wall with a 2.44 m (8 ft) gravity wall segment in the middle and 1.22 m (4 ft) Type II shear wall segments on each end detailed with a pair of tie-rods located at the wall ends. Figure 2.26 shows the framing details of one of the tested specimens: SGGS-2 wall line. Same components used in framing of this specimen were used in the fabrication of other specimens. Finish application for the five wall configurations in the test matrix was performed after installing the walls into the test setup. Gypsum boards were attached on the interior face and glass-mat sheathing panels were attached on the exterior face. Figure 2.27 show the various steps involved in finish application.

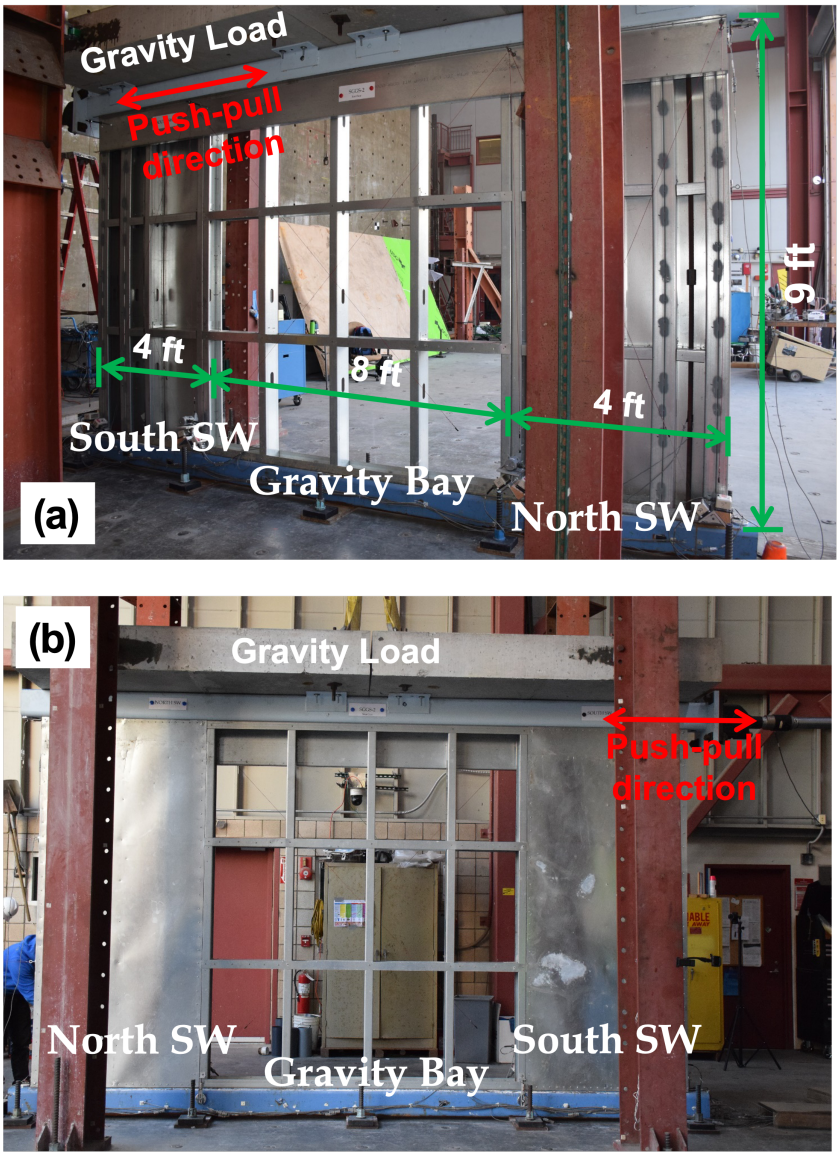


Figure 2.25. Specimen naming example: SGGS-2: (a) interior face and (b) exterior face

2.4.2 Test Setup

The quasi-static wall-line test setup top loaded wall-lines using a displacement-controlled loading protocol. The top and bottom HSS transfer beams used in the dynamic test phase were used, with minor adjustments, for installing the walls into the setup. Two concrete slabs (8 ft × 5 ft × 12 in, 2.44 m × 1.52 m × 305 mm each), together with the top HSS transfer beam, were used to apply a total of 12.4 kN/m (850 plf) gravity load. Out-of-plane columns with roller

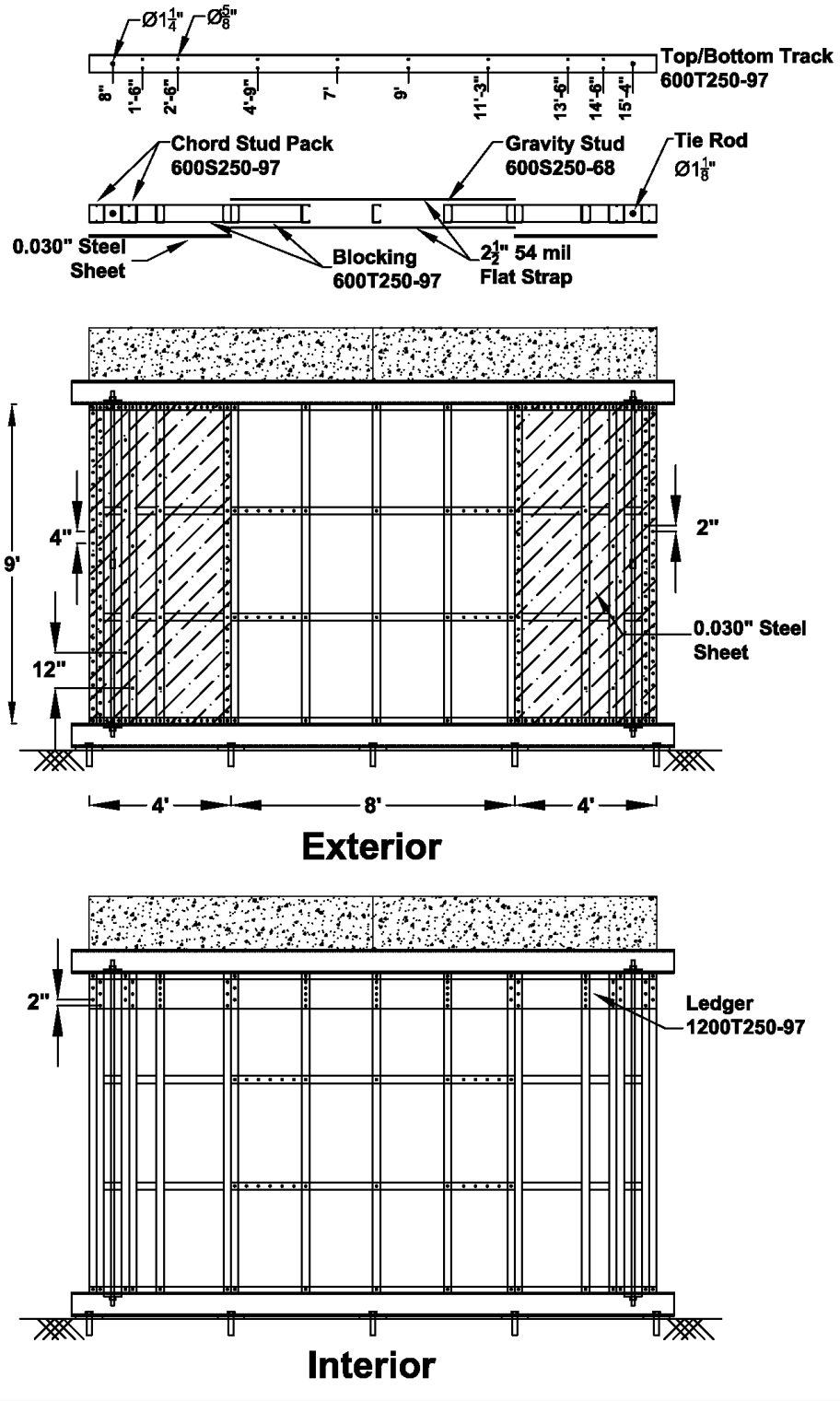


Figure 2.26. Framing details of specimen SGGS-2



(a) Installation of glass-mat sheathing panels and application of EPS foam boards using adhesive onto panel substrate



(b) Rasping of foam boards



(c) Embedment of reinforcing mesh in base coat

Figure 2.27. Photographs demonstrating steps involved in finish application during quasi-static test phase



(d) application of second layer and finish coat

Figure 2.27. Photographs demonstrating steps involved in finish application during quasi-static test phase (cont.)

guides provided the required restraint preventing top mass movement in the transverse direction. The bottom transfer beam and columns were post-tensioned to the strong floor. The specimens were dropped into the test setup and attached to the bottom transfer beam using two rows of A325 shear bolts. The wall specimens were provided with temporary out-of-plane bracing to ensure the walls remain vertical when the top mass is installed. The top transfer beam was also installed using two rows of A325 shear bolts. Figure 2.26 shows the sizes and locations of the drilled holes (done in field) in top and bottom track for connection between specimen and transfer beams. Before the installation of top mass, the tension tie-rods were installed and tightened using the access holes in the transfer beams with the nut-plate assembly bearing against the inside surfaces of the top and bottom beams. The concrete mass slabs were dropped in above the wall pairs and attached to the top transfer beams.

The walls were subjected to a displacement controlled cyclic CUREE protocol (Krawinkler et al., 2001) as shown in Figure 2.28. Two hydraulic 220 kN (50 kip) actuators with $\pm$60 cm ($\pm$24") stroke, were used in-line with the wall specimen to push (north direction) and pull (south direction) along the wall longitudinal axis. The reference displacement required to define the protocol was obtained from the wall-line behavior measured during the shake table experiments.

The reference displacement for defining the CUREE protocol for all configurations, with the exception of GGGG and GGGG-F specimens, was adopted as 2% drift ratio. For the two wall configurations GGGG and GGGG-F, 1.4% drift ratio was adopted instead because those specimens were expected to have lower drift capacity. The specimens were reverse cyclically tested until a 60% post-peak strength degradation was observed. Subsequently, the test was concluded and the specimen was brought to zero applied lateral force. Figure 2.29 shows the isometric view and end view of the test setup.

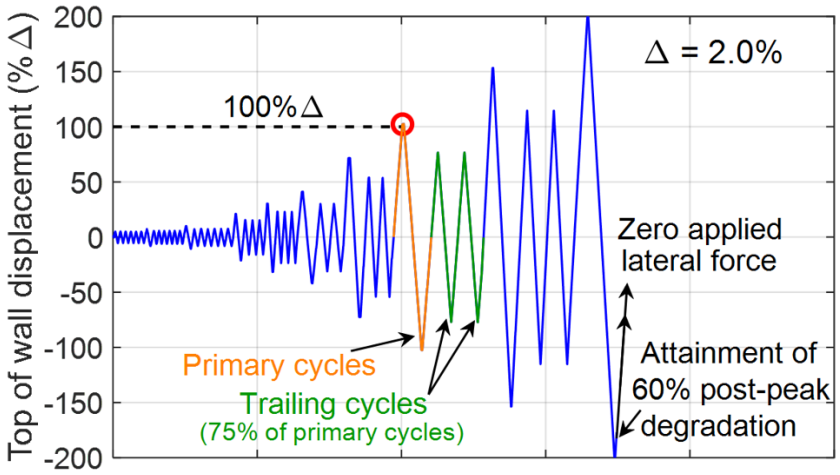


Figure 2.28. CUREE loading protocol (example shown for specimen SGGS-2)

2.4.3 Instrumentation and Monitoring Systems

The wall specimens were densely instrumented with more than 40 analog sensors and five cameras to continuously record the wall response during the tests. The analog sensors measured wall lateral drift and load as well as wall local measurements such as sheathing panel shear distortion, tension tie-rod strains, and wall uplift.

Displacement Transducers

Each wall was instrumented with three string potentiometers, attached at 1/3rd, 2/3rd and full height, to measure the lateral displacement profile of the wall along the loading (in-plane) direction. For measuring local wall response, the shear segment(s) and the gravity/window

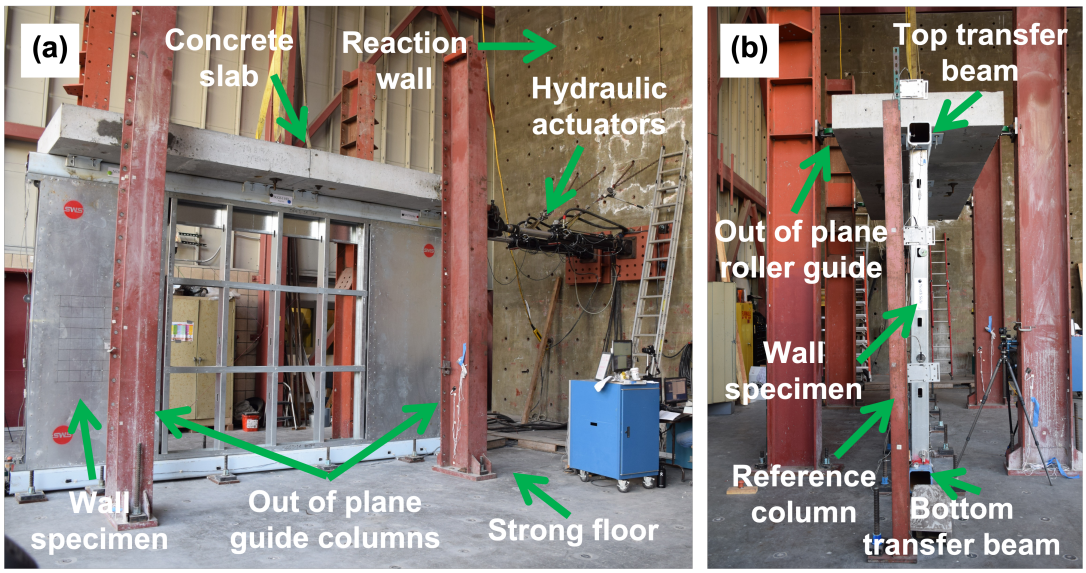


Figure 2.29. Quasi-static cyclic test setup: (a) isometric view and (b) end view

segments in each wall were instrumented with string potentiometers, LVDTs (Linear Variable Differential Transformer) and linear potentiometers to measure the shear distortion and the uplift displacements of each segment. All distortion measuring displacement transducers were mounted directly on the CFS framing using aluminum brackets. This required cutouts at the corners of gypsum boards in case of finished specimens for mounting the aluminum brackets directly on the framing underneath. Additional linear potentiometers were employed to measure slip between the strong floor and bottom transfer beam, wall slip along the top and bottom HSS transfer beams, and the planar movement of the EIFS layer. Figure 2.30 shows the layout of displacement transducers used for measuring wall local and global response and their nomenclature. In total, up to 13 string potentiometers, 9 linear potentiometers and 4 LVDTs were installed.

Actuator Load Cells

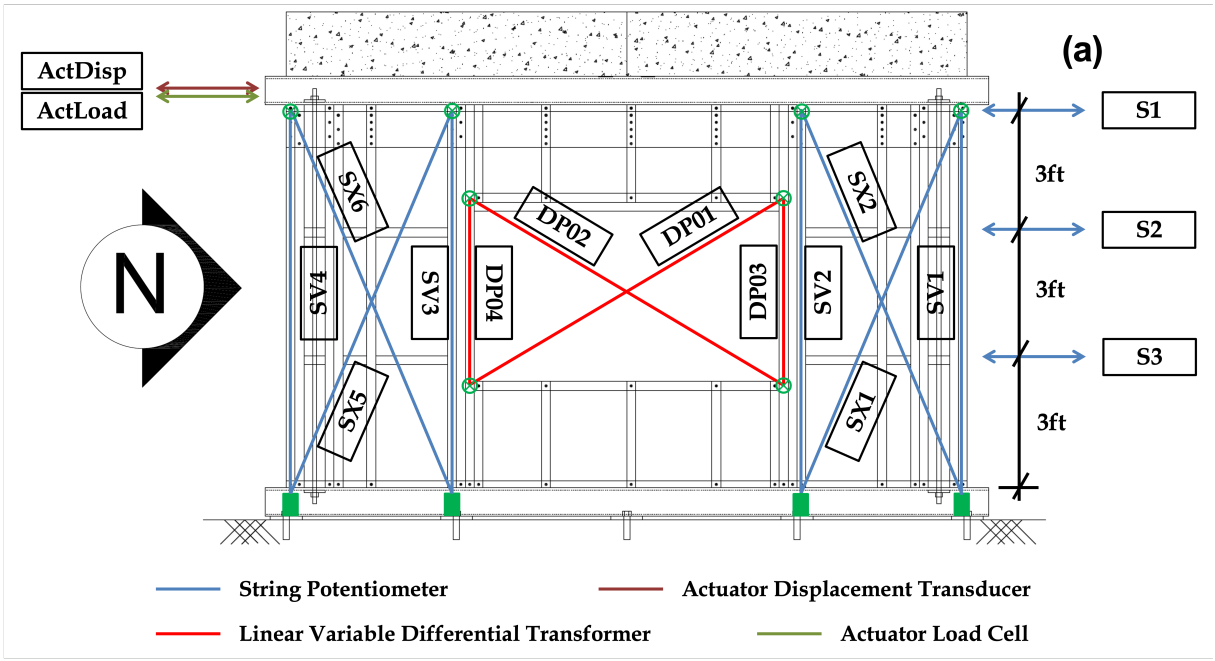
Two hydraulic 220 kN (50 kip) actuators with ±60 cm (±24”) stroke were used in parallel (total lateral load capacity of 440 kN) configuration. These were attached to the top of the wall to push and pull along the wall longitudinal axis. Figure 2.30 shows the nomenclature used for actuator load cell(s).

Strain Gages

A pair of standard strain gages (Type FLA) were installed on every shear wall tension tie-rod by grinding away the threads at mid-height of the rod to obtain the axial strain and allow estimation of the axial force in each rod. For Type I wall-lines, a total of 8 strain gages were installed. Additionally, the bottom HSS transfer beam was instrumented with 12 strain gages to understand the shear distribution between the different segments of a wall in the longitudinal direction. Up to a total of 20 strain gages were employed for measuring response during the tests. Figure 2.30 shows the layout of the strain gages and their nomenclature as installed on the tie-rods.

Washer Load Cells

Used specifically in wall-lines with hold-downs, washer load cells were installed on the hold-down anchor rod to measure the hold-down tension force. Up to 12 washer load cells, each with a 130 kN (30 kip) capacity, were installed during the testing. Figure 2.31 shows the layout of the washer load cells and their nomenclature installed on the hold-downs.



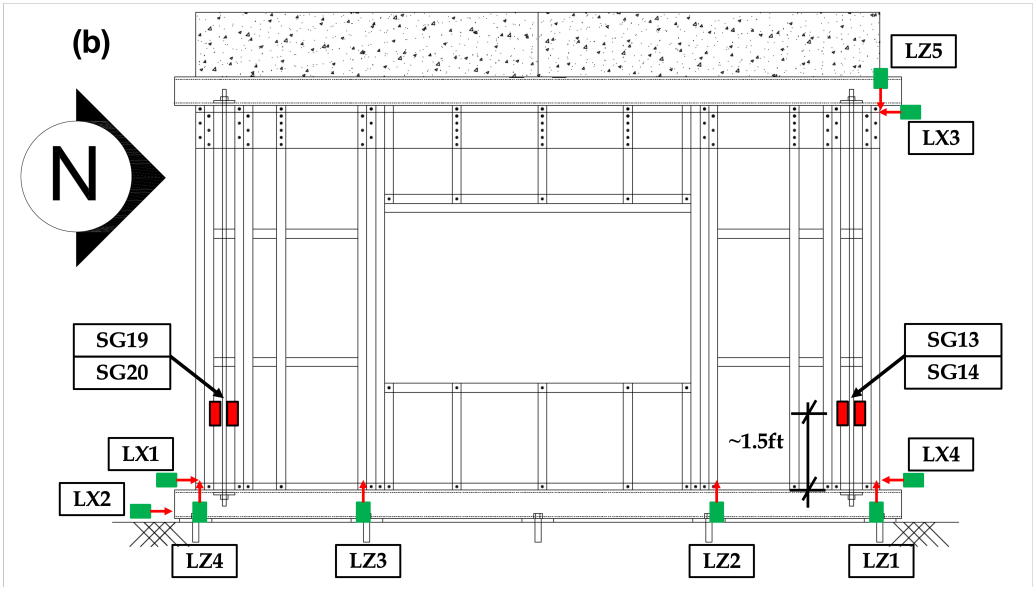


Figure 2.30. Layout and nomenclature of: (a) displacement transducers and load cell on wall interior face for measuring lateral force and displacement and panel distortion; (b) and (c) linear potentiometers and strain gages for measuring wall uplift and slip, and tension tie-rod axial strain for specimen SWWS-2F

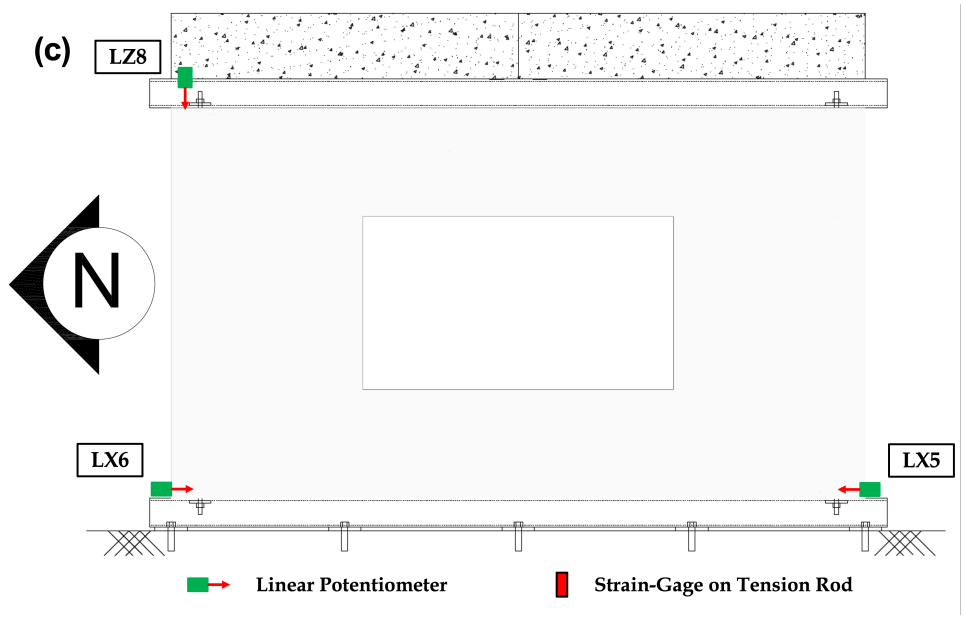


Figure 2.30. Layout and nomenclature of: (a) displacement transducers and load cell on wall interior face for measuring lateral force and displacement and panel distortion; (b) and (c) linear potentiometers and strain gages for measuring wall uplift and slip, and tension tie-rod axial strain for specimen SWWS-2F (cont.)

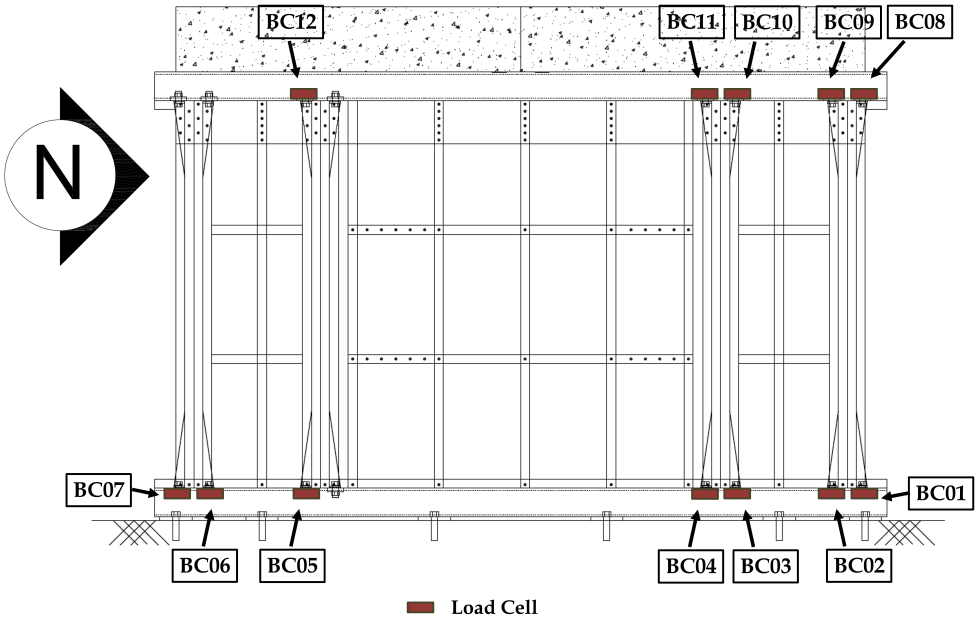


Figure 2.31. Layout and nomenclature of washer load cells used for measuring hold-down tension force for specimen SGGS-1HDF

2.5 Summary Remarks

A two-phased experimental program was undertaken to advance the understanding of CFS-framed wall-lines, steel sheet sheathed shear walls placed in-line with gravity walls. Eight pairs of wall configurations were tested at the NHERI Large High-Performance Outdoor Shake Table under a sequence of increasing intensity earthquake motions. Ten single wall-line configurations were tested under quasi-static cyclic loading conditions at the Structural Engineering Powell Laboratory. An overview of this unique CFS wall-line experimental program as distributed into the two test phases has been presented in this chapter. Selection of wall details for the experimental program were based on the design of a 4-story and 10-story archetype buildings. Wall detailing was selected to represent wall design from approximately the mid-height floors within a 10-story building.

Particularly for the shake table test phase, a motion scaling strategy and testing protocol was developed to capture wall performance at pre-defined target performance levels. To determine the intensity of individual earthquake tests, three wall specimens, representative of the breadth of expected strength for the entire test matrix were modeled as SDOF systems. Scale factors for earthquake motions were determined based on the measured natural period of the two wall pairs on the shake table platen being tested simultaneously. This scaling of seed motions aimed to achieve the intended target performance levels that progressively damage the wall specimens. The steps involved in motion scaling procedure have been explained in this chapter.

One of the main objectives of the experimental effort was to characterize the performance of CFS-framed walls, detailed for mid-rise construction in high intensity seismic zones. The test matrix was also designed to examine the impact of several variables on wall-line behavior. Instrumentation and monitoring systems employed to record the wall responses during the tests have been explained in this chapter. Using the measured response, the impact of test variables on CFS-framed wall-line behavior has been discussed in the next chapter.

The CFS-NHERI wall-line experimental program is discussed in further detail within

the technical reports Singh et al. (2021b) and Singh and Hutchinson (2022). High-quality data generated from the many analog sensors in addition to digital still cameras, several video cameras, and GPS and UAV monitoring systems during the testing of wall-line specimens is publicly available within the DesignSafe-CI repository (designsafe-ci.org, Rathje et al., 2017) through data sets Singh et al. (2021a) and Singh et al. (2022b).

Acknowledgment of Publications

Portions of the following paper and technical reports, for which the dissertation author was the primary investigator and author, are contained in Chapter 2:

Singh, A., Wang, X., Torabian, S., Hutchinson, T. C., Peterman, K. D., and Schafer, B. W. (2020). Seismic Performance of Symmetric Unfinished CFS In-Line Wall Systems. In *Structures Congress 2020* (pp. 629-642). Reston, VA. American Society of Civil Engineers.

Singh, A., Wang, X. and Hutchinson, T. C. (2021). *Lateral Response of Cold-Formed Steel Framed Steel Sheathed In-line Wall Systems Detailed for Mid-Rise Buildings. Part I: Shake Table Test Phase* (Structural Systems Research Report SSRP-19/05). University of California San Diego, La Jolla, CA.

Singh, A. and Hutchinson, T. C. (2022). *Lateral Response of Cold-Formed Steel Framed Steel Sheathed In-line Wall Systems Detailed for Mid-Rise Buildings. Part II: Quasi-Static Test Phase* (Structural Systems Research Report SSRP-19/06). University of California San Diego, La Jolla, CA.

Chapter 3

Impact of Nonstructural and Structural Detailing on Wall-Line Lateral Behavior

3.1 Introduction

The previous chapter introduced the two phases of the CFS-NHERI wall-line experimental program: the shake table test phase and the quasi-static test phase. In this chapter, the impact of test matrix variables on wall-line lateral behavior is discussed by comparing select groups of specimens systematically. This chapter provides key comparisons between specimens tested in the two phases, and quantifies the impact of test variables governing the structural detailing and architectural variations of CFS-framed walls on wall-line behavior. First, however the performance of the baseline specimen SGGS-1 is discussed. This wall-line specimen had an unfinished symmetric configuration, a 2.44 m (8 ft) gravity wall segment in the middle and 1.22 m (4 ft) Type I shear wall segments on each end which use compression chord stud packs with a steel tension tie-rods assembly.

3.2 Baseline Specimen Performance

The baseline specimen SGGS-1 wall pair was subjected to four earthquake motions with increasing intensity, as listed in Table 2.12, as well as a sequence of low amplitude white noise tests before and after each earthquake test. Following the completion of the dynamic

test sequence, this wall pair was also subjected to static monotonic displacement loading by restraining the top of the specimen, and moving the base of the shake table slowly, in an effort to capture its post-peak behavior at large displacements. Figure 3.1 shows the force-displacement responses of the wall specimen during the earthquake tests and the subsequent monotonic pull test. This specimen's response was essentially linear for the first three earthquake tests, with less than 0.4% achieved drift ratio and a lateral force below 50% of strength. Physical damage to the wall specimen was also very minimal during these lower intensity elastic (EQ1: E1 and EQ2: E2) and quasi-elastic (EQ3: QE) level earthquake tests as the walls underwent low drift demands. Less than 2% of the screw fasteners showed incipient bearing into the steel sheet with only a minor low tilt angle. No damage was seen in any framing members. Nonetheless, transient elastic sheet buckling could be observed and heard as it cycled within the tension field during the dynamic shaking. The specimen demonstrated nonlinearity during the design earthquake test (EQ4: DE) when the drift demand reached 1% and the specimen experienced lateral forces up to 85% of its strength. Buckling of the steel sheet with a widely distributed tension field and readily observable lines of plastic deformation were visible at the end of this test. Fastener tilting and bearing onto the steel sheet was evident in approximately 20% of the screws following the test, with most clustered at the corners of the steel sheet directly along the main diagonals of the tension field.

During the monotonic pull test, the specimen reached strength V_u at 160.2 kN (36.0 kip) at a drift ratio Δ_{Vu} of 1.95% and during continued pull demonstrated a post-peak degradation of 40% at 4.15% drift ratio. The elastic stiffness of the specimen K, defined as the secant stiffness at 40% strength, was measured as 83.0 kN/cm (47.4 kip/in). Compared to a 1.22 m long Type I isolated shear wall with 0.76 mm (0.030") thick steel sheet sheathing and 51 mm (2") o.c. fastener edge spacing from AISI S400-20, the baseline specimen SGGS-1 demonstrated 3.3 times higher lateral strength. Most of the damage in the SGGS-1 wall pair occurred during the monotonic pull, when extensive shear buckling of the steel sheet was observed as the width of the tension field increased with increasing drift demand, widening to include most of the steel

sheet sheathing. At the end of the monotonic pull test, local buckling of the gravity stud adjacent to the shear segment compression stud pack at diagonally opposite locations of the gravity wall segment was observed. However, the compression stud packs and track framing members did not experience any visible damage. At the end of the test, most steel sheet screws showed some form of damage. Sheet pull over or edge tearing had spread from the corner to quarter height of the chord studs and a third of the length of the top and bottom tracks, with damage also to a few field screws in the middle of the sheet. Outside of the heavily damaged diagonal tension field, fasteners along the off diagonals showed some tearing of the sheet steel as screws tilted to large angles. Fasteners furthest away from the plastic tension field region showed bearing/tilting damage accumulated primarily during the earthquake tests. Photographs documenting these physical damage observations are shown in Figure 3.2. The accumulation of damage through the earthquake test sequence led to an elongation of the fundamental period from 0.157s in its undamaged state to 0.199s following the design level earthquake test EQ4. Similarly, the damping ratio increased from 2.1% in its undamaged state to 5.3% after earthquake test EQ4. It should be noted that based on the results of the baseline specimen, 2% drift ratio was adopted as the reference displacement for defining the CUREE protocol used during the quasi-static test program.

Axial force in the tension tie-rods were measured using a pair of strain gages installed on the rods. Since, the tension force demands on the rods remained in the elastic zone, well below their yield strength, during the test sequence, axial force could be calculated by multiplying the measured strain with the elastic modulus of steel and cross-sectional area of the rod. Through material tests, the yield point and tensile strength of the tie-rods were obtained as 876.7 MPa and 985.2 MPa, respectively. The modulus of elasticity was measured as 202.3 GPa. A pair of two vertical and two diagonal string potentiometers in a double-triangle configuration were used to evaluate the wall lateral distortion by measuring the change in angles of the triangles. Figure 3.3 presents a schematic illustration of the various instrumentation used for measuring wall local response. Wall lateral drift can be approximated as the sum of contributions from the

pure shear of the steel sheet sheathing and wall end uplift. Figure 3.4 presents an illustration of calculating the two parts of lateral drift using the string potentiometers and linear potentiometers. For single story structures, most of the lateral drift is from the shear distortion of the sheathing panel. However for taller structures, the contribution from wall end uplift can add up to be a significant portion of lateral drift at higher stories. Final expressions for the derived quantities are presented here:

$$\gamma = \theta_1 - \theta_o \tag{3.1}$$

$$\Delta^{\gamma} = b_o \cos(\theta_o + \alpha) - b_1 \cos(\theta_1 + \alpha) \tag{3.2}$$

$$\Delta^{\delta_y} = b_o \cos(\theta_o) - b_o \cos(\theta_o + \alpha) \tag{3.3}$$

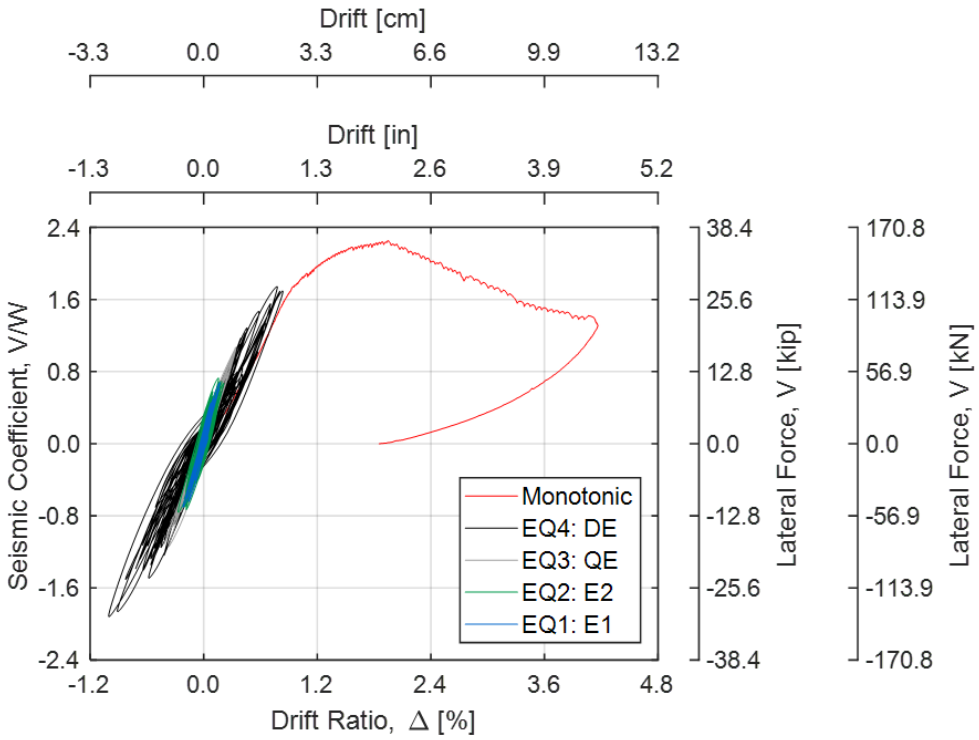


Figure 3.1. Force-displacement response of baseline specimen SGGS-1

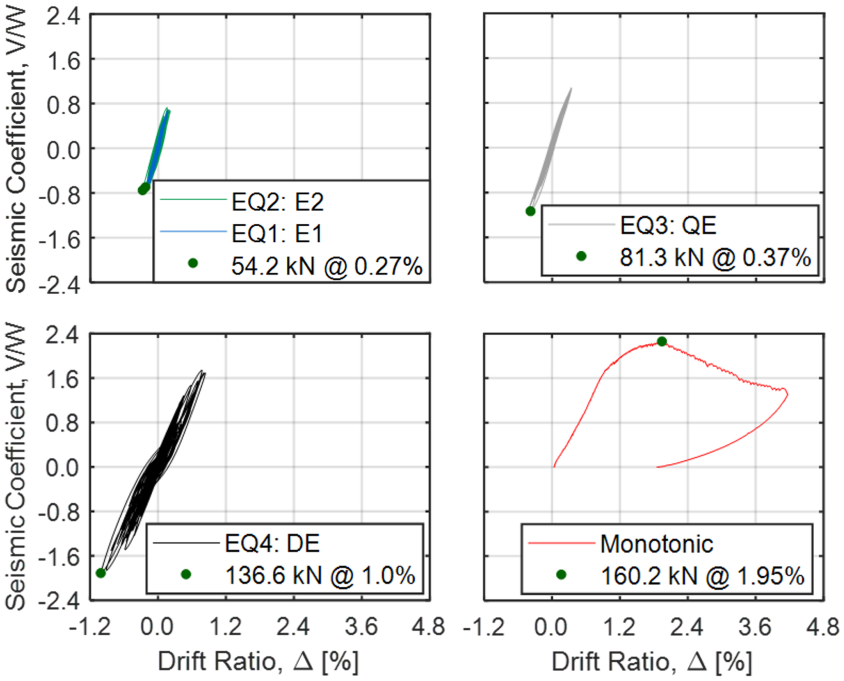


Figure 3.1. Force-displacement response of baseline specimen SGGS-1 (cont.)

where, γ is the shear distortion, and Δ^{γ} and Δ^{δ_y} are the contributions to lateral movement due to shear distortion and uplift, respectively. Figure 3.5 shows the wall local response for earthquake test EQ4: DE, which targeted a design level performance. This plot documents the end of the wall segment uplift, tie-rod forces F^t and wall shear distortion γ, compared with the global drift ratio and lateral force histories. Comparing wall lateral drift with the end of wall uplift, note that as the wall moves towards the east (positive) direction, wall uplift is observed on the west ends of both shear wall segments, while the east ends of the shear segments bore into the bottom HSS. Similarly, when the wall drift is to the west (negative) direction, uplift on the east ends of both shear wall segments and bearing in compression on the west ends of the shear wall segments is observed. The green and purple circles represent the time instances when each response parameter attains its peak values in positive drift and negative drift direction, respectively. It can be observed that the time instances of peak measurement for these responses occur simultaneously with peak global drift and lateral force.

The axial force response of the tension tie-rods was quite similar to wall uplift measure-

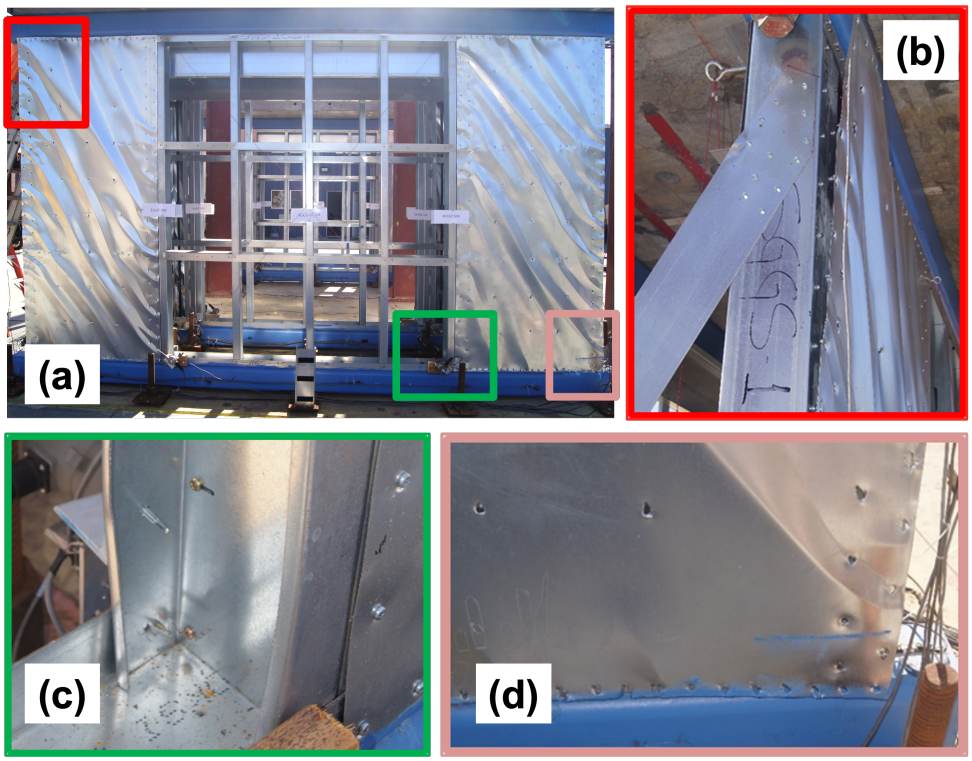


Figure 3.2. Physical damage to specimen SGGS-1 following the end of monotonic test ($\Delta_{res} = 1.86\%$): (a) tension field in steel sheets, (b) sheet pullover, (c) local buckling of gravity stud and (d) screw edge tearing

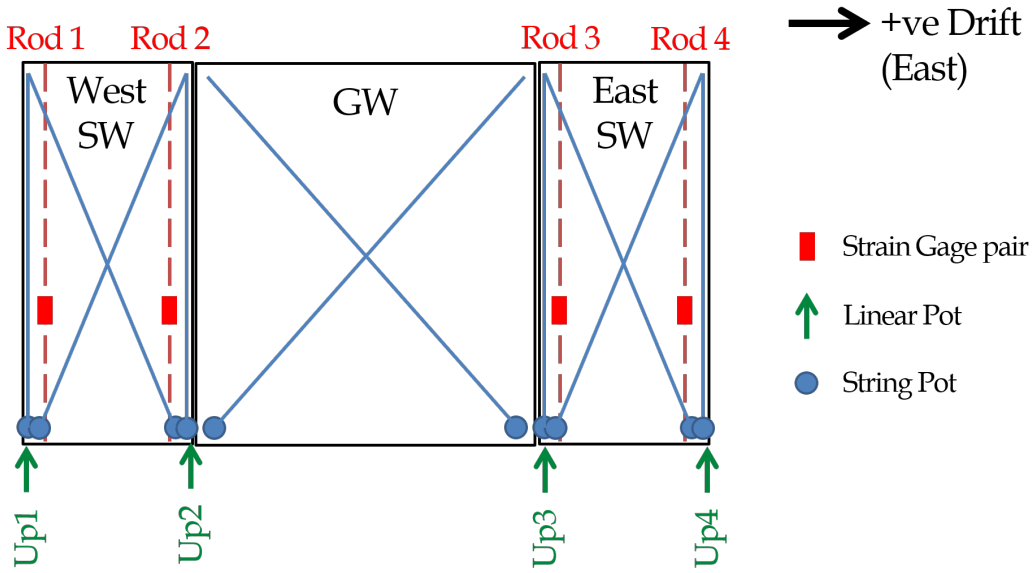
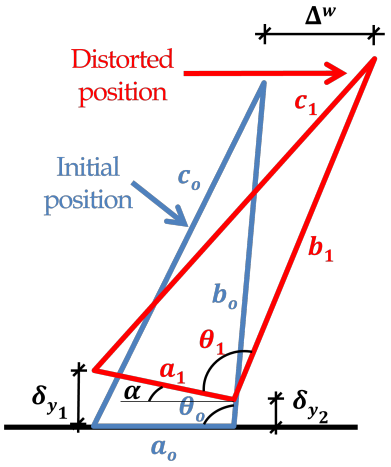


Figure 3.3. Schematic illustration of instrumentation for wall local response

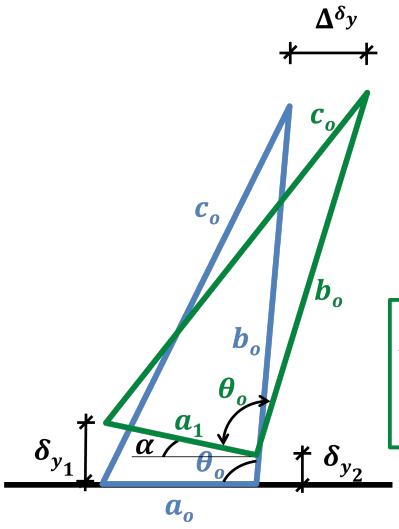


$$a_1^2 = a_o^2 + \left(\delta_{y_1} - \delta_{y_2}\right)^2 \qquad \tan\alpha = \frac{\delta_{y_1} - \delta_{y_2}}{a_o}$$

$$\Delta_1 = b_1 - b_o \qquad \Delta_2 = c_1 - c_o$$

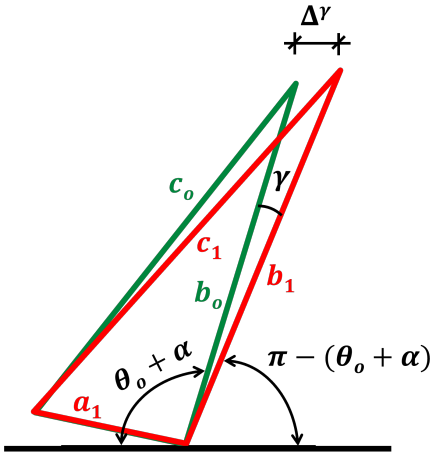
$$\cos\theta_o = \frac{a_o^2 + b_o^2 - c_o^2}{2a_o b_o} \qquad \cos\theta_1 = \frac{a_1^2 + b_1^2 - c_1^2}{2a_1 b_1}$$

$$\Delta^w = b_1\cos\left(\pi - \left(\theta_1 + \alpha\right)\right) - b_o\cos\left(\pi - \theta_o\right)$$
$$= b_o\cos\left(\theta_o\right) - b_1\cos\left(\theta_1 + \alpha\right)$$



Contribution to lateral movement due to **uplift** only

$$\Delta^{\delta_y} = b_o\cos\left(\pi - \left(\theta_o + \alpha\right)\right) - b_o\cos\left(\pi - \theta_o\right)$$
$$= b_o\cos\left(\theta_o\right) - b_o\cos\left(\theta_o + \alpha\right)$$



Contribution to lateral movement due to **shear distortion** only

$$\gamma = \theta_1 - \theta_o$$

$$\Delta^{\gamma} = \Delta^{w} - \Delta^{\delta_y}$$
$$= b_o\cos\left(\theta_o + \alpha\right) - b_1\cos\left(\theta_1 + \alpha\right)$$

Figure 3.4. Illustration of panel distortion calculations

ments with respect to wall drift in the positive and negative direction, as those uplift measurements were located near the tension rod locations. Notably, all tie-rod forces remained below 20% yield strength. However, all rods reported a low axial force when its surrounding stud packs were expected to be in compression. Tension rods placed closer to the ends of walls consistently reported higher axial forces as compared to rods placed towards the interior of the walls. This indicates that the two shear wall segments did not behave strictly as individual Type I segments. This observation was inconsistent with the tension tie-rod behavior observed in a prior full-scale building shake table test program (Wang and Hutchinson, 2021). This discrepancy may be attributed to the different wall boundary elements in the two test programs. Namely, in the present program, the concrete mass at the top of the in-line wall specimens essentially acted as a rigid floor diaphragm. In contrast, a CFS floor system in the building tests of Wang and Hutchinson (2021) offered nominal diaphragm flexibility. Additionally, the wall layout and wall end boundary conditions were significantly different in the building test, which may have also affected the local behavior. It is also noted that the tension rods experienced pre-tension loss due to repetitive shaking. The rods were pre-tensioned prior to the shaking sequence, however, due to the subsequent seismic motion, invariably a reduction in pre-tension occurred during the tests.

The measured panel distortion of different segments of the wall in both directions are also presented in Figure 3.5. It can be seen that the gravity wall segment underwent 1.8-2.3 times larger panel distortion, when compared with its adjacent shear wall segments, as kinematic constraints were maintained between them. The shear distortion histories of the two shear wall segments show that even though they drift the same amount laterally, the two segments did not undergo the same amount of shear distortion, uplift and stud/track bending. The east shear wall segment underwent greater shear distortion when the wall drift was eastwards, while the west shear wall segment underwent greater shear distortion when the wall drift was westwards. This is also, similarly, observed in the contribution of wall uplift to its lateral drift. When the wall drift was eastwards, there is a larger contribution of wall uplift to the lateral drift for the west shear wall segment, and hence, lower shear distortion. These relative contributions of shear distortion

and wall uplift to lateral drift for all segments evolve as specimen damage progresses. Similarly, the wall lateral resistance is influenced by the tension tie-rod axial forces. The evolution of these responses for different specimens is discussed in subsequent sections.

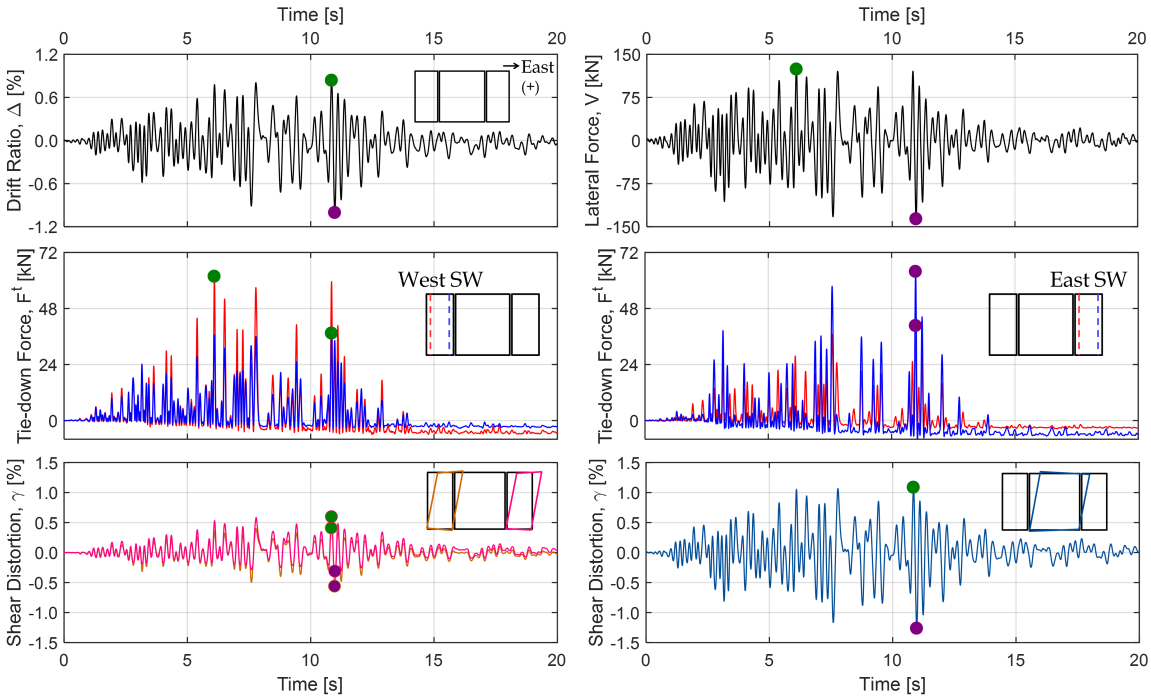


Figure 3.5. SGGS-1 specimen local response during earthquake test EQ4:DE
Note: Schematics within subplots indicate location and type of response plotted. Symbols denote peak in the two drift directions.

3.3 Finish Application

There were five pairs of finished-unfinished wall configurations among the suite of tested wall specimens. Figures 3.6a and 3.6c show the force-displacement response comparison of two such pairs, namely SGGS-1 and SGGS-1F, and SGGS-2 and SGGS-2F. It is noted that the Type I specimen pair was tested at the shake table, while the Type II specimen pair was tested within the quasi-static test setup. Nonetheless, the impact of loading history is not pronounced as it can be seen that the finish application consistently increases the lateral capacity of the specimen (V_u) without significant change in the drift at which strength is achieved (Δ_{Vu}). Elastic stiffness (K) is also consistently increased due to finish application. Figures 3.6b and 3.6d show

backbone curve comparisons of the five pairs of unfinished and finished wall configurations further corroborating the aforementioned conclusions across all considered variables. Finally, a summary of key response measurements is provided in Table 3.1 with a visualization of these parameters provided in Figure 3.7. Using a single additive strength model (Eq. 3.4), and using linear regression, it was measured that the finish application added 14.66 kN/m (1005 plf) to wall lateral strength.

$$V_{u,\text{finished}} = V_{u,\text{unfinished}} + \left(\Delta v_{\text{EIFS}} + \Delta v_{\text{gypsum}}\right) \times L \tag{3.4}$$

where, L is the length of a wall, and $V_{u,\text{finished}}$ and $V_{u,\text{unfinished}}$ are the wall lateral strengths for a finished and unfinished specimen, respectively. Assuming that 5.4 kN/m (370 plf) was contributed by gypsum panels $\left(\Delta v_{\text{gypsum}}\right)$ attached to CFS framing at 150 mm perimeter spacing (Schafer et al., 2020), from the EIFS layer, the estimated increase in strength $\left(\Delta v_{\text{EIFS}}\right)$ is calculated as 9.3 kN/m (635 plf). The slope of the best-fit line from linear regression being close to unity indicates that the increase in lateral strength is independent of the similar underlying wall framing details. This is consistent with an additive strength model hypothesis. Note that the elastic stiffness (K) was also 1.5-3 times higher for finished wall specimens compared to unfinished specimens, see Figure 3.7b. Finally, in no case was the drift at strength (Δ_{Vu}) or the drift at 80% post-peak strength ($\Delta_{0.8\text{Vu}}$) negatively affected due to the application of finishes.

For finished specimens, damage observations during the test were limited to the damage in the EIFS layer and gypsum panels, as the underlying framing members were not visible. Here, the damage observed in a finished specimen SGGS-2F is described. Initially, hairline cracks in the EIFS layer began to appear at approximately 0.6% drift ratio. Minor crushing along gypsum panel edges and partial screw pull-through was also observed at this drift ratio. Appreciable visible separation of the EIFS layer from the CFS framing was observed at wall corners at 1.4% drift ratio. This was also accompanied by almost full height vertical surface cracks in the EIFS where the glass-mat sheathing panel edges existed, see photograph in Figure 3.7c. The majority

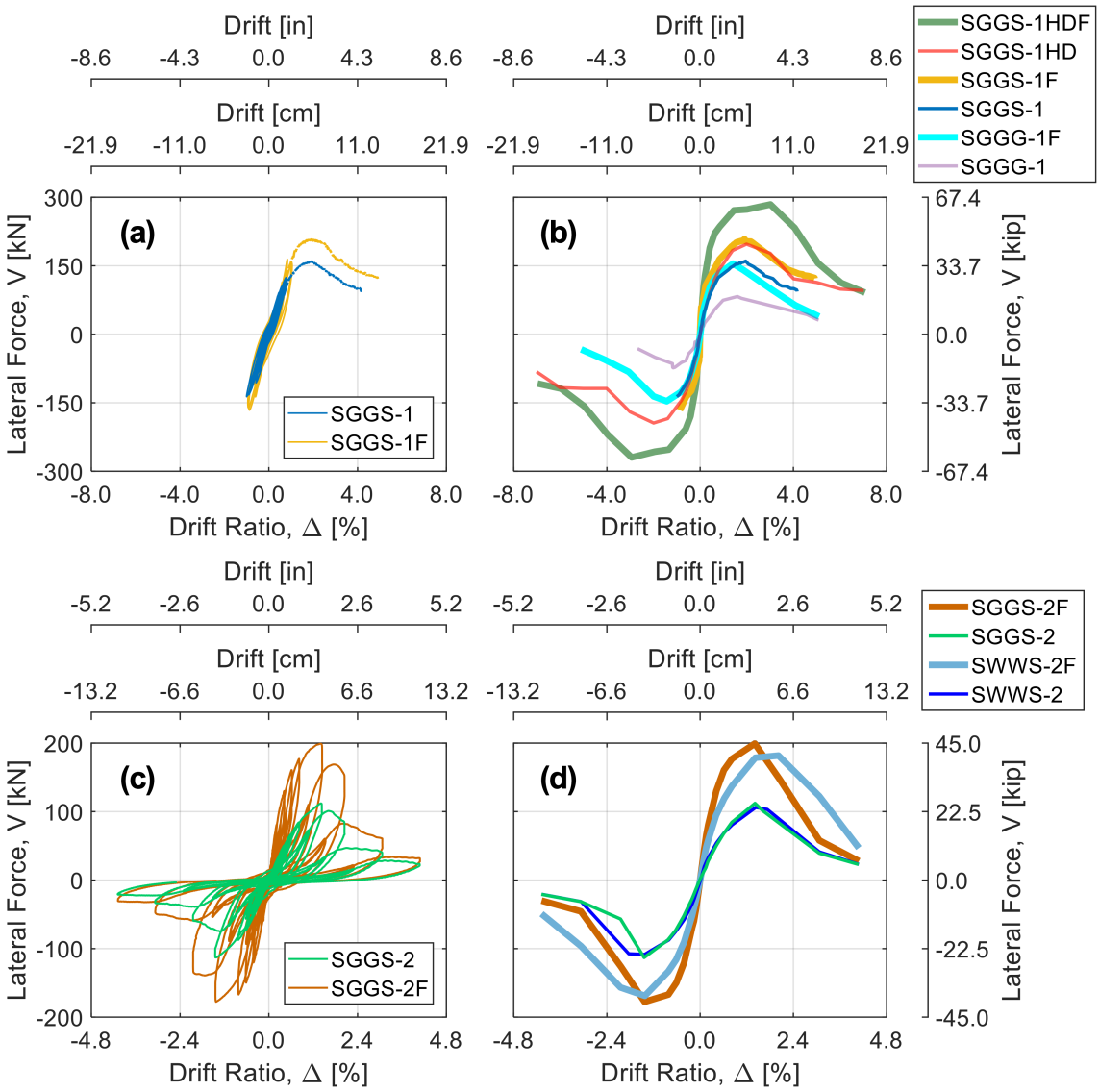


Figure 3.6. Effect of finish application: (a) force-displacement response and (b) backbone curve comparison for Type I specimens; and (c) force-displacement response and (d) backbone curve comparison for Type II specimens

of the gypsum panel screws along the entire wall height also showed some degree of screw pull-through at this stage. At about 2% drift ratio, separation at the wall ends of the EIFS from the framing was visible, particularly along the bottom, but detachment extended approximately half the wall height. By 3% drift ratio, the EIFS layer could be seen warped out-of-plane as the layer separation from steel sheet and framing had propagated towards the middle from both wall ends. At this stage, gypsum panels had completely detached along one panel edge or fallen off.

Table 3.1. Effect of finish application: results summary

	Specimen	Wall strength V_u (kN)	Drift ratio at $0.4V_u$ (pre-peak) $\Delta_{0.4Vu}$ (%)	Drift ratio at V_u (peak) Δ_{Vu} (%)	Drift ratio at $0.8V_u$ (post-peak) $\Delta_{0.8Vu}$ (%)	Elastic stiffness[1] K (kN/cm)
Shake table	SGGS-1	160.2	0.28	1.95	2.79	84.5
		–	-0.29	–	–	81.5
	SGGS-1F	208.2	0.15	1.90	3.14	198.1
		–	-0.14	–	–	210.9
	SGGG-1	82.7	0.32	1.60	2.76	37.1
		-72.3	-0.26	-1.08	-1.53	41.0
Quasi-static	SGGG-1F	156.8	0.17	1.41	2.35	74.7
		-144.5	-0.23	-1.43	-2.36	53.1
	SGGS-2	113.3	0.36	1.41	1.89	46.2
		-111.8	-0.37	-1.44	-1.68	44.4
	SGGS-2F	199.2	0.20	1.41	1.90	141.9
		-177.7	-0.21	-1.43	-1.85	121.7
	SWWS-2	107.2	0.30	1.43	2.13	52.6
		-107.3	-0.29	-1.43	-2.17	54.1
	SWWS-2F	181.8	0.29	2.01	2.66	91.9
		-169.0	0.29	-1.42	-2.41	84.7
	SGGS-1HD	197.4	0.35	1.99	3.36	82.9
		-194.3	-0.32	-2.00	-3.57	89.5
	SGGS-1HDF	284.7	0.17	3.01	4.13	237.3
		-269.2	-0.18	-2.94	-4.03	223.9

Notes: 1. When information about wall strength is not available in the negative direction, for stiffness calculations, the strength is assumed to be the same as in the positive direction.

The EIFS layer had also almost entirely detached from the CFS framing as the drift demand increased to 5%. The detachment of finish layer allowed inspection for damage to any framing members. Notably, gravity studs adjacent to the shear wall segment compression stud packs had buckled locally. Select framing screws attaching the compression stud packs failed in shear at their head resulting in the stud packs slipping and damaging the bottom track locally. It should be noted that the damage to framing members observed in finished specimens is consistent with the damage observed in unfinished specimens. However, it is expected that the adherence of glass-mat panels to the steel sheet may have stabilized sheet buckling initially and delayed damage to fasteners. Even though the damage observations presented here are from a particular specimen, the progression of damage was similar for all finished specimens. Figure 3.8 provides examples of the aforementioned damage observed in the finished specimen SGGS-1F after

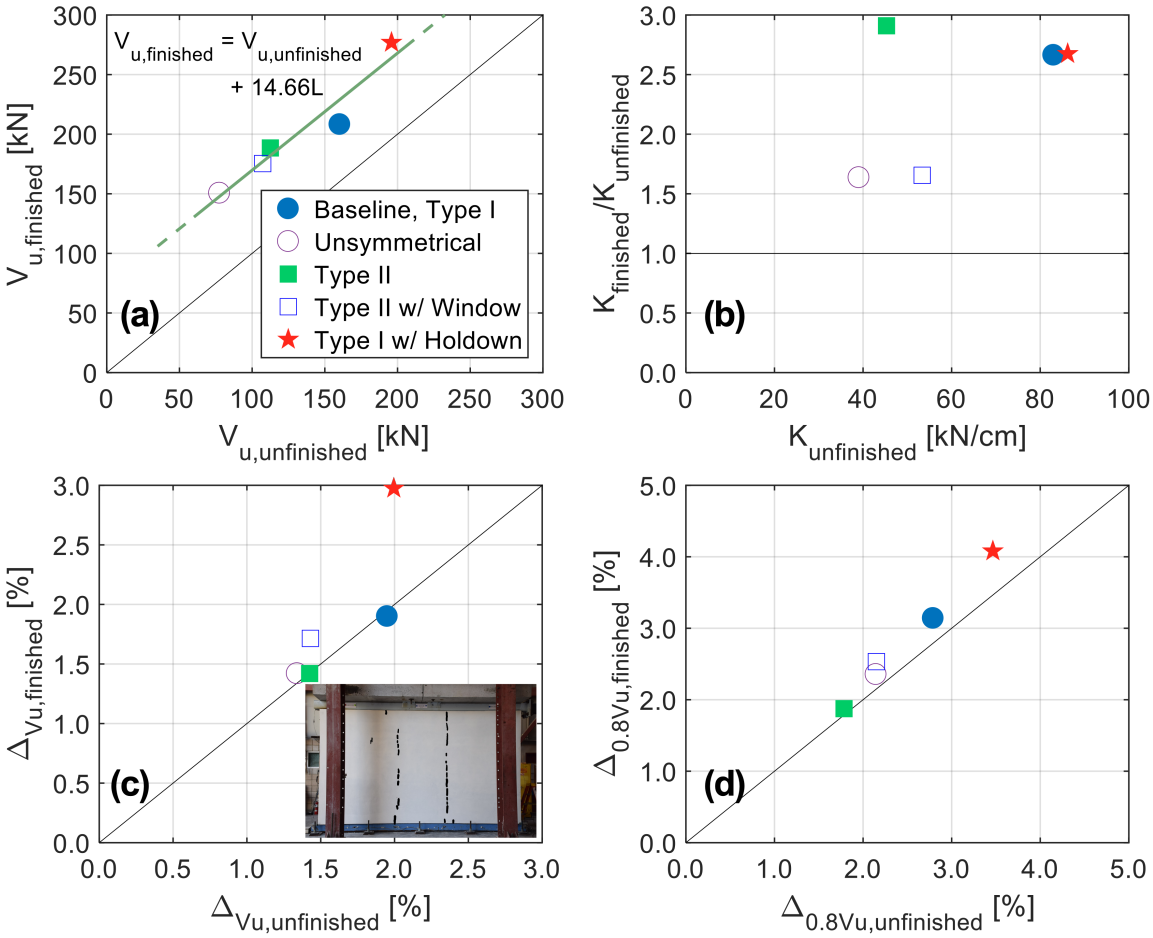


Figure 3.7. Effect of finish application on key parameters: (a) lateral strength, (b) elastic stiffness, (c) drift at strength, and (d) drift at 80% strength post-peak

removing it from the test setup following its attainment of a maximum drift ratio Δ_{max} of 4.92%.

Figure 3.9 shows the comparison of tension tie-rod force evolution between two finished and unfinished wall configuration pairs, namely the SGGS-2 and SGGS-2F pair, and the SWWS-2 and SWWS-2F pair. Tie-rod forces are plotted against increases in lateral force (V/V_u) and lateral drift (Δ/Δ_{Vu}). It should be noted that for each measurement, response in only the direction of interest (push or pull) has been shown through colored traces, while response in the opposing direction is grayed out. Schematics above the figure indicate location and type of response plotted. For the same amount of normalized lateral drift, tension rods in finished specimens experienced larger axial forces when compared to unfinished specimens, see Figure 3.9a-b.

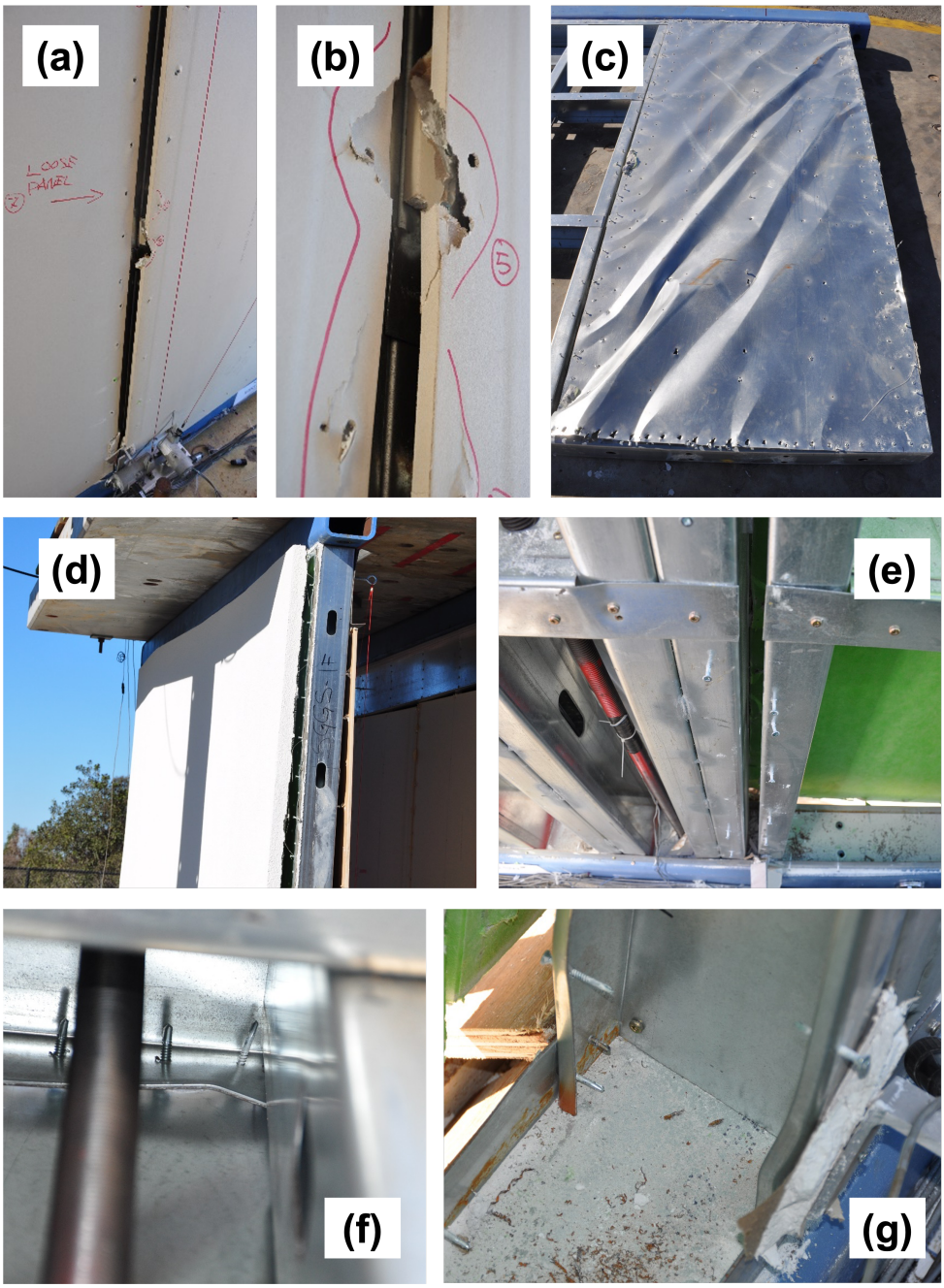


Figure 3.8. Physical damage to specimen SGGS-1F following the testing sequence ($\Delta_{max} = 4.92\%; \Delta_{res} = 2.29\%$)
Note: EIFS finish was manually removed to inspect the state of steel sheathing, which articulated a well defined plastic diagonal tension zone, in part c.

However, when normalized for individual specimen strengths, difference in tension tie-rod force evolution is not as pronounced, even though finished specimens are nominally subjected to larger

axial forces, see Figure 3.9c-d. Due to the larger stiffness of the finished specimens, SGGS-2F and SWWS-2F experienced greater lateral force as compared to SGGS-2 and SWWS-2 for the same lateral drift, resulting in larger axial force carried by the tension tie-rods.

Comparison of wall end uplift evolution between finished and unfinished wall specimens with increasing normalized lateral force and drift is presented in Figure 3.10. These analyses show that finished specimens experience only slightly larger wall uplift at their ends when compared with unfinished counterparts. Though small, the increased wall end uplift at comparable normalized lateral load may explain variations in shear distortion amongst finished and unfinished pairs. Since the contribution towards drift due to uplift is larger for finished walls, the contribution of panel shear distortion towards drift (Δ^{γ}) is lower, see Figure 3.11.

3.4 Window Opening

Three unique wall configurations included a window opening in the middle 2.44 m bay rather than a gravity bay. This allowed for direct comparison between walls with and without openings, the later referred to as a gravity bay. Figure 3.12a shows a force-displacement response comparison between wall specimens SGGS-2 and SWWS-2, while Table 3.2 summarizes key response measurements of the tested specimen pairs. From the figure, it can be seen that the presence of an opening did not have a significant impact on the global hysteresis response. Moreover, the lateral strengths for the two specimens were within 10% of each other. Additional specimen pairs shown in Figure 3.12c comparing the backbones of varying window-no window wall pairs consistently showed that the lateral strengths are within 10% of each other. In general, there was little to no impact on lateral strength, drift at strength and elastic stiffness due to the presence of a window opening.

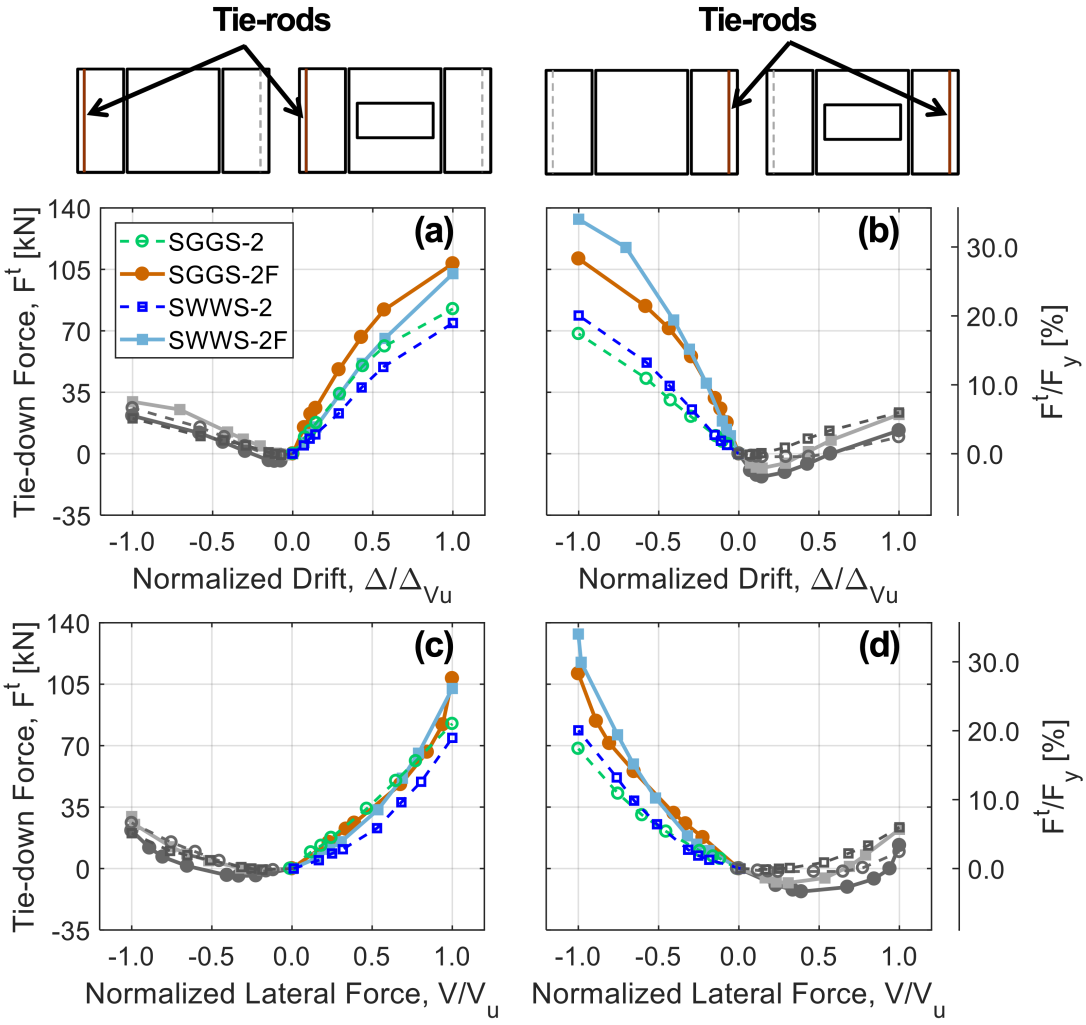


Figure 3.9. Effect of finish on tension-rod forces with increase in: (a) and (b) normalized drift, and (c) and (d) normalized lateral force

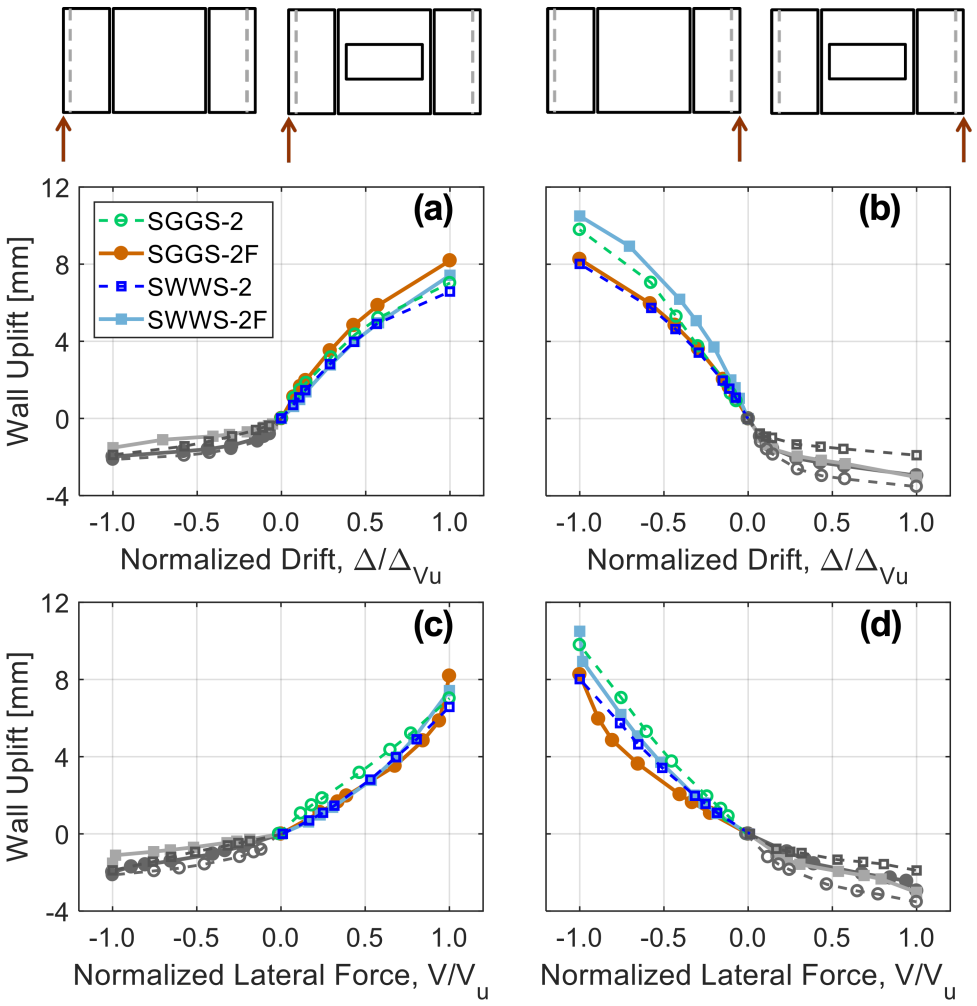


Figure 3.10. Effect of finish on wall end uplift with increase in: (a) and (b) normalized drift, and (c) and (d) normalized lateral force

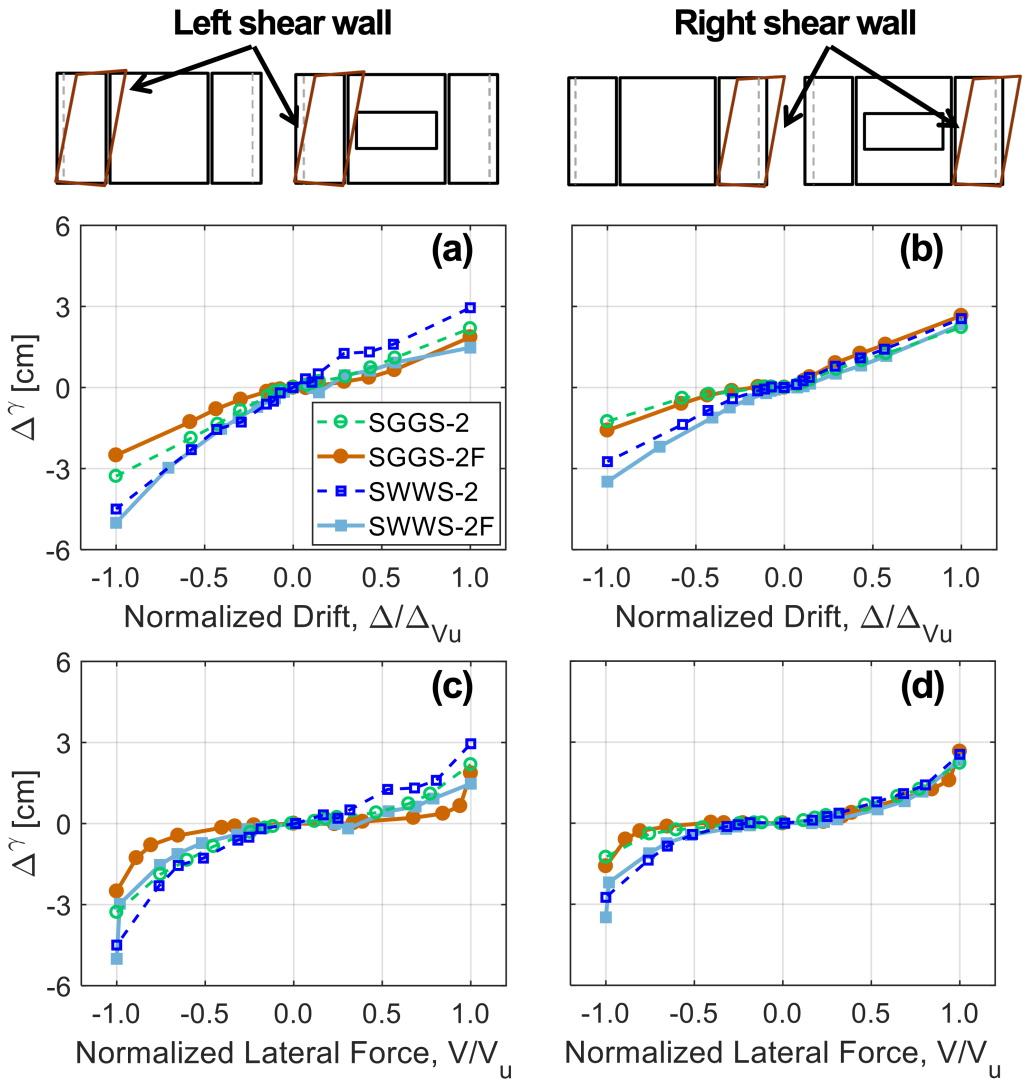


Figure 3.11. Effect of finish on shear wall shear distortion with increase in: (a) and (b) normalized drift, and (c) and (d) normalized lateral force

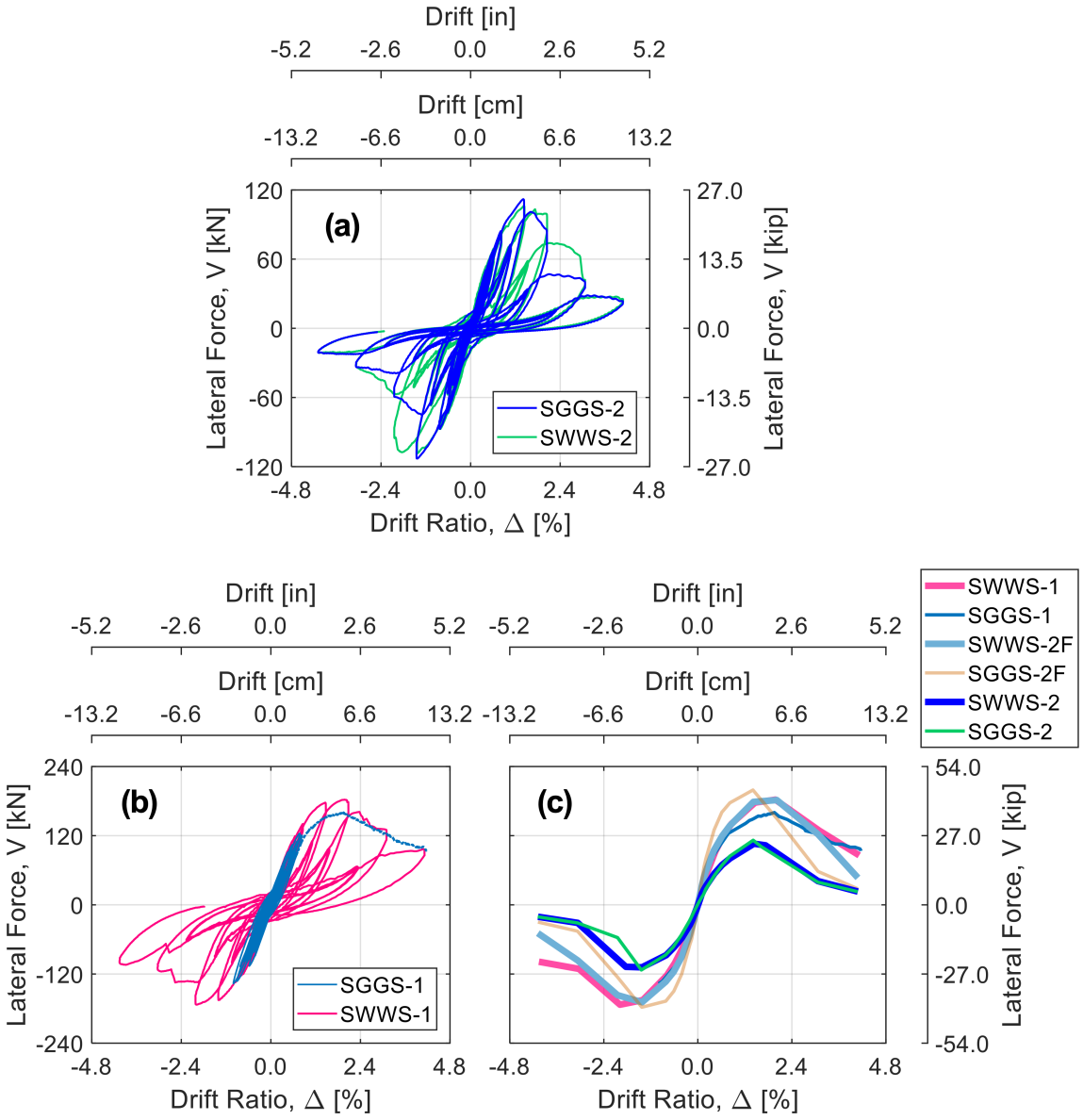


Figure 3.12. Effect of window opening: force-displacement response for (a) Type II specimen pair, and (b) Type I specimen pair; and (c) backbone curve comparison for Type I and II specimens

Damage to specimens with a wall opening developed initially with a well defined tension field in the steel sheets. Yielding within the steel sheet progressed with increasing drift demand similar to that which manifest in specimens without a window opening. However, damage to framing members differed significantly for the two configurations. At approximately 1% drift ratio, a small gap became visible at the corners of the window as the rectangular opening

Table 3.2. Effect of window opening: results summary

	Specimen	Wall strength V_u (kN)	Drift ratio at $0.4V_u$ (pre-peak) $\Delta_{0.4Vu}$ (%)	Drift ratio at V_u (peak) Δ_{Vu} (%)	Drift ratio at $0.8V_u$ (post-peak) $\Delta_{0.8Vu}$ (%)	Elastic stiffness K (kN/cm)
Shake table	SGGS-1	160.2	0.28	1.95	2.79	84.5
		–	-0.29	–	–	81.5
Quasi-static	SWWS-1	182.5	0.34	1.97	2.74	79.1
		-173.3	-0.36	-2.00	-2.58	70.4
	SGGS-2F	199.2	0.20	1.41	1.90	141.9
		-177.7	-0.21	-1.43	-1.85	121.7
	SWWS-2F	181.8	0.29	2.01	2.66	91.9
		-169.0	0.29	-1.42	-2.41	84.7
	SGGS-2	113.3	0.36	1.41	1.89	46.2
		-111.8	-0.37	-1.44	-1.68	44.4
	SWWS-2	107.2	0.30	1.43	2.13	52.6
		-107.3	-0.29	-1.43	-2.17	54.1

deformed. Due to force transfer around the opening, compression stud packs adjacent to the opening experienced higher stresses. This resulted in an approximately 1 cm wide gap developing between the stud packs and window jamb stud. These additional stresses led to failure in shear of the screws attaching the compression stud packs to the bottom track at 3% drift ratio. As drift demand increased, the now detached stud packs slipped along the bottom track and began to bear against the tension tie-rod. In addition, the bottom track suffered local buckling along its flange. Figure 3.13 presents the aforementioned damage as observed in specimen SWWS-1 at a drift ratio of 4.12%.

Figure 3.14 provides a comparison of the tension tie-rod forces for walls with and without a window opening with increasing normalized lateral force and drift. These plots demonstrate that the tension tie-rod force amongst window-no window pairs is nominally unaffected, irrespective of whether the wall had a window opening. Comparison of wall end uplift and panel shear distortion evolution of the shear segment with growth in lateral force and lateral drift were also unaffected by presence of window opening. These are presented in Figures 3.15 and 3.16.

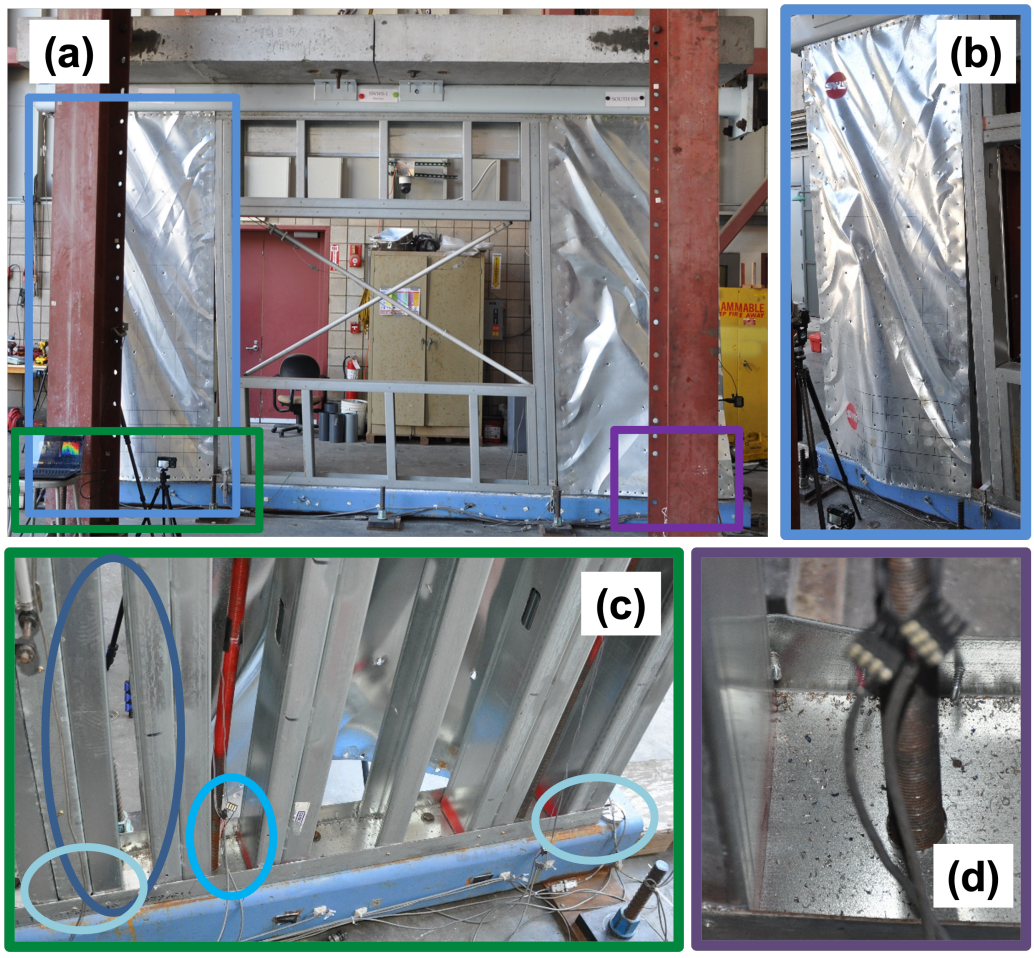


Figure 3.13. Physical damage to specimen SWWS-1 at drift ratio $\Delta = +4.12\%$

3.5 Asymmetric Shear Wall Location

Two wall configurations included shear wall segments laid out in an asymmetric fashion. These walls had a 1.22 m long shear segment in-line with a 3.66 m long gravity bay. As a result, a direct comparison between walls with asymmetrical or symmetrical shear wall locations was possible. Figure 3.17 shows the force-displacement response comparison between wall specimens SGGS-1F and SGGG-1F, while Table 3.3 summarizes key response measurements. Results show that the asymmetric specimen reports lower lateral strength as compared to the symmetrical specimen. Figure 3.17 also shows the backbone curve comparisons of the two pairs of asymmetrical and symmetrical wall configurations (total of four specimen backbone

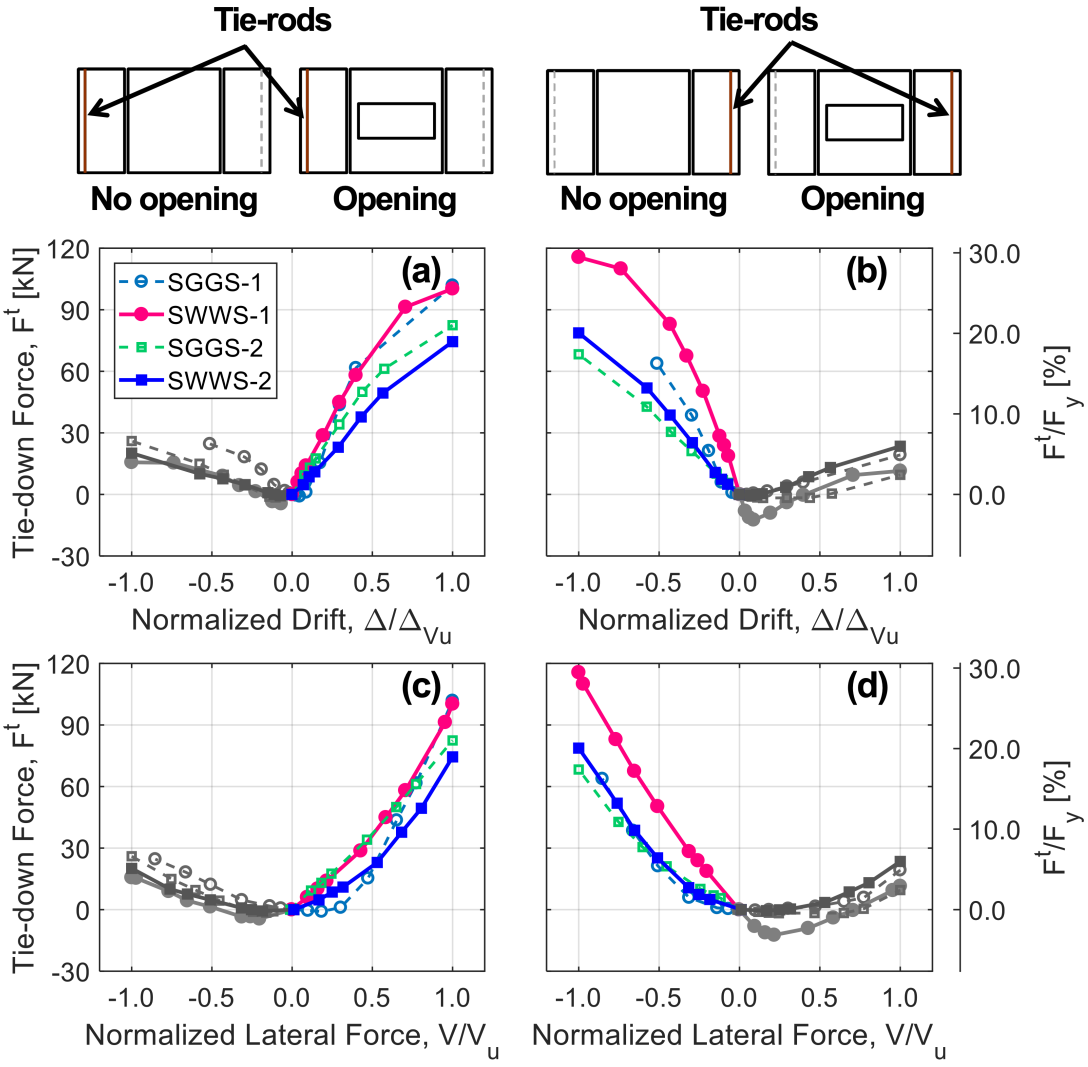


Figure 3.14. Effect of window opening on tension-rod forces with increase in: (a) and (b) normalized drift, and (c) and (d) normalized lateral force

curves). After removing the additive effect of finishes, the asymmetric walls demonstrate 54% of the lateral strength of the symmetrical walls. While the asymmetric walls had 50% of the shear segments as compared to symmetrical walls, the 4% extra strength over the 50% may be anticipated due to be the contribution of the additional 1.22 m gravity segment. Note as well that the elastic stiffness decreased by 53% for SGGG-1 compared to SGGS-1, and drift at strength was also lower for the asymmetric specimens.

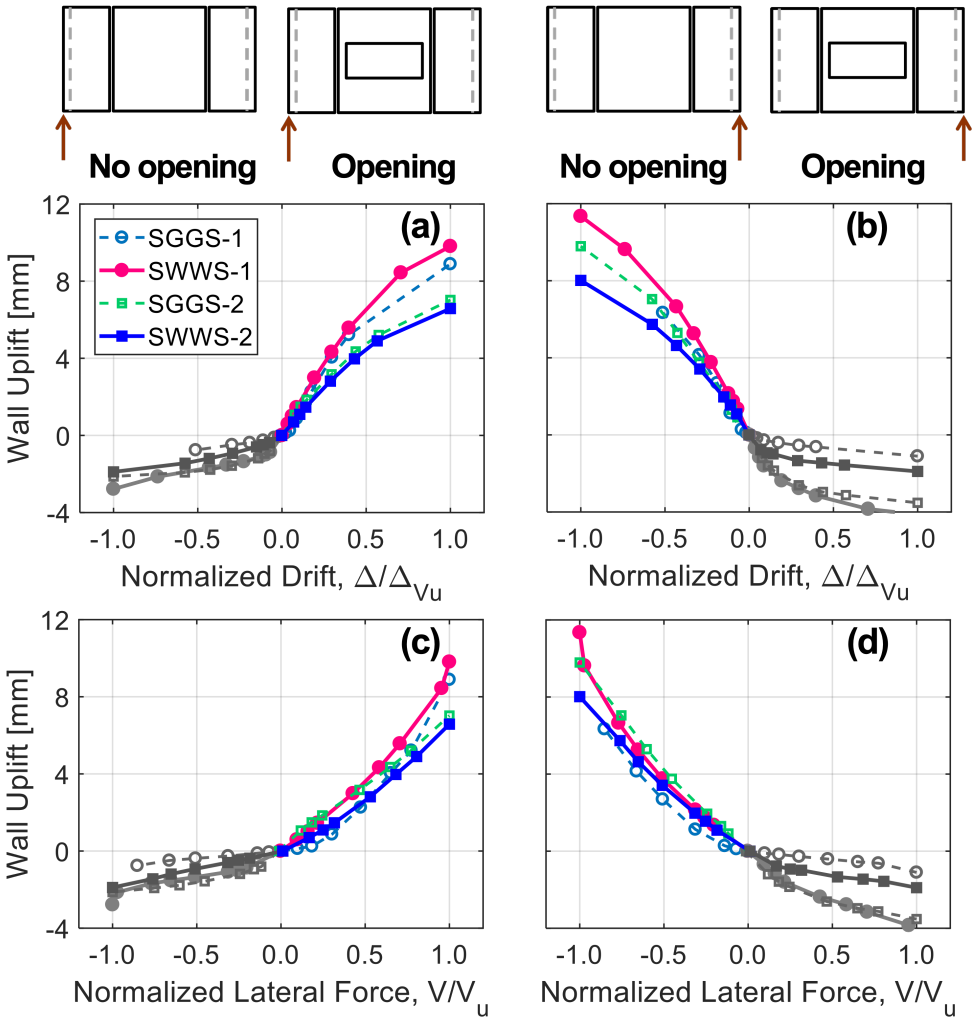


Figure 3.15. Effect of window opening on wall end uplift with increase in: (a) and (b) normalized drift, and (c) and (d) normalized lateral force

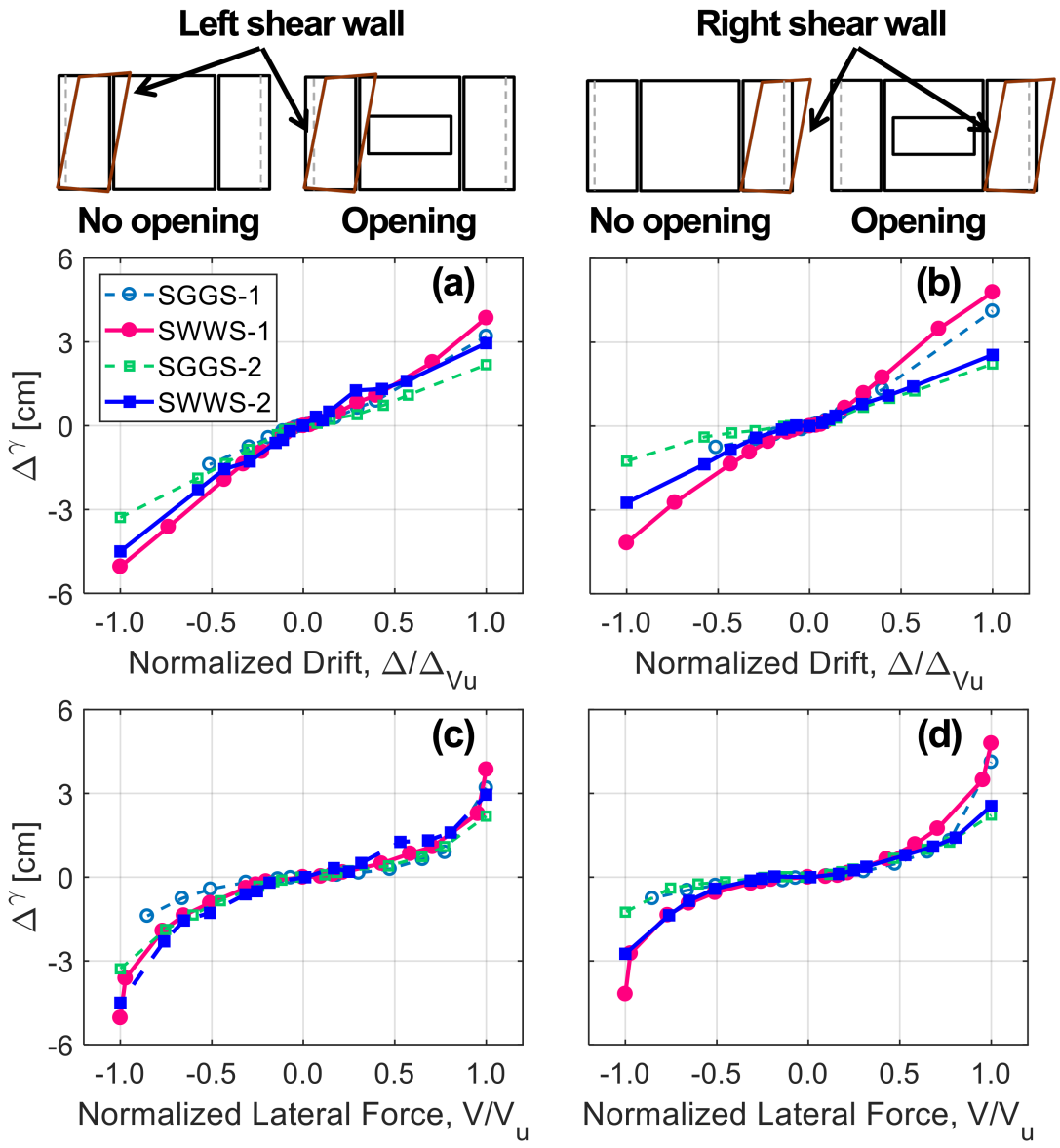


Figure 3.16. Effect of window opening on shear wall shear distortion with increase in: (a) and (b) normalized drift, and (c) and (d) normalized lateral force

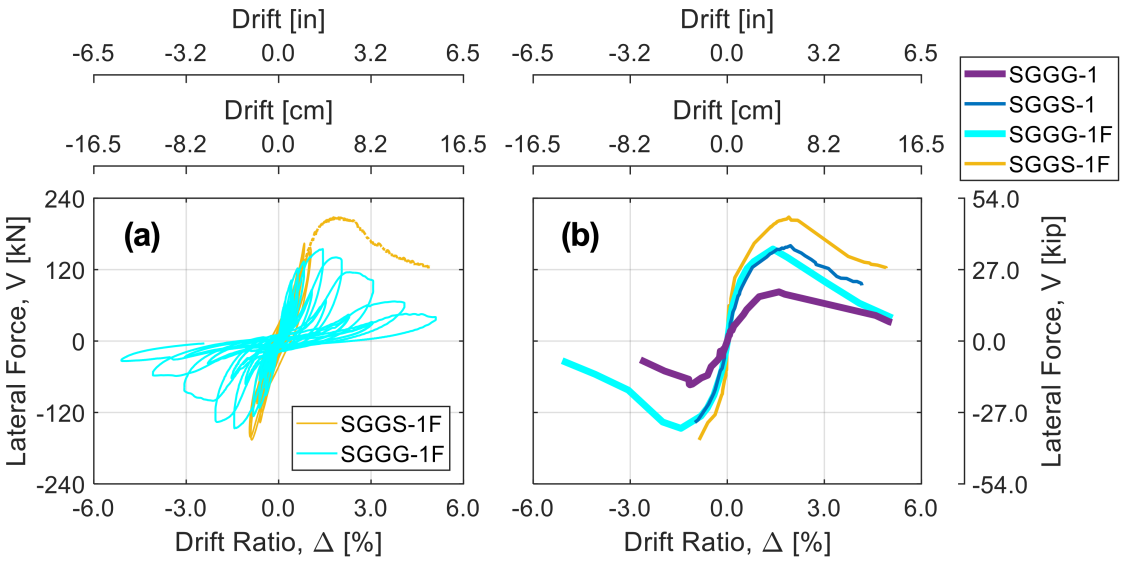


Figure 3.17. Effect of asymmetric shear wall location: (a) force-displacement response, and (b) backbone curve comparison

Table 3.3. Effect of asymmetric shear wall location: results summary

	Specimen	Wall strength V_u (kN)	Drift ratio at $0.4V_u$ (pre-peak) $\Delta_{0.4Vu}$ (%)	Drift ratio at V_u (peak) Δ_{Vu} (%)	Drift ratio at $0.8V_u$ (post-peak) $\Delta_{0.8Vu}$ (%)	Elastic stiffness K (kN/cm)
Shake table	SGGS-1	160.2	0.28	1.95	2.79	84.5
		–	-0.29	–	–	81.5
	SGGG-1	82.7	0.32	1.60	2.76	37.1
		-72.3	-0.26	-1.08	-1.53	41.0
	SGGS-1F	208.2	0.15	1.90	3.14	198.1
		–	-0.14	–	–	210.9
Quasi-static	SGGG-1F	156.8	0.17	1.41	2.35	74.7
		-144.5	-0.23	-1.43	-2.36	53.1

Asymmetric walls demonstrated a failure mode similar to their symmetrical counterparts. However, the failure, and any damage to framing members, were observed at lower drift ratio values for the asymmetric walls. Figure 3.18 shows the damage observed in specimen SGGG-1 following the final event in the dynamic testing sequence during which it was pushed to a maximum drift ratio of 5.0%. During the low intensity events, transient elastic sheet buckling was observed developing within a diagonal tension field as repeated cycles of relatively low drift demand were imposed. As drift demand increased to 1%, the width of the tension field and

buckling of the steel sheet became more distributed with lines of plastic deformation remaining prominently visible following a test. Fastener tilting and bearing onto the steel sheet was visible in 20% of screws at test end for specimen SGGG-1. Most of these were edge screws clustered at corners of sheet and mid height of field studs, which fell directly along the main diagonal of tension field. At the end of the dynamic testing sequence, the steel sheet had pulled over 40% of the fastener heads. The remaining screws also showed tearing or bearing due to tilting at a significant angle. The framing suffered extensive damage, including gravity studs adjacent to the shear segment and bottom track, which suffered local buckling. The chord stud packs and field stud framing connections suffered head shear failure, which caused the chord stud packs to slip along the bottom track.

Figure 3.19 shows a comparison of the tension tie-rod force for the two pairs of asymmetrical and symmetrical wall specimens with increasing normalized lateral force and drift. At similar lateral force, the tension rods in the asymmetrical walls were subjected to larger axial forces, as compared to their symmetrical counterparts. However, when normalized by the individual specimen strengths, the tension rod forces is similar for the two pairs. Tension tie-rod force evolution is also similar for the two pairs when normalized for lateral drift. Due to their increased stiffness, the symmetrical walls experience larger lateral force when compared to the asymmetrical walls at similar lateral drift amplitudes, which results in larger axial forces in the tension tie-rods. Consistent with tension tie-rod forces, normalizing for individual specimen strengths or drift at strength, the evolution of wall uplift and panel shear distortion for the two pairs is quite similar. Figures showing the evolution of wall uplift and panel shear distortion with increase in lateral force and drift are not shown here for brevity.

Comparison of wall end uplift evolution between wall specimens SGGS-1 and SGGG-1 with increasing normalized lateral force and lateral drift is presented in Figure 3.20. Consistent with tension tie-rod forces, asymmetrical walls experience greater wall uplift as compared to symmetrical walls for the same lateral force. However, after normalizing for individual specimen strengths or drift at strength, the evolution of wall uplift for the two pairs is quite similar. Figure

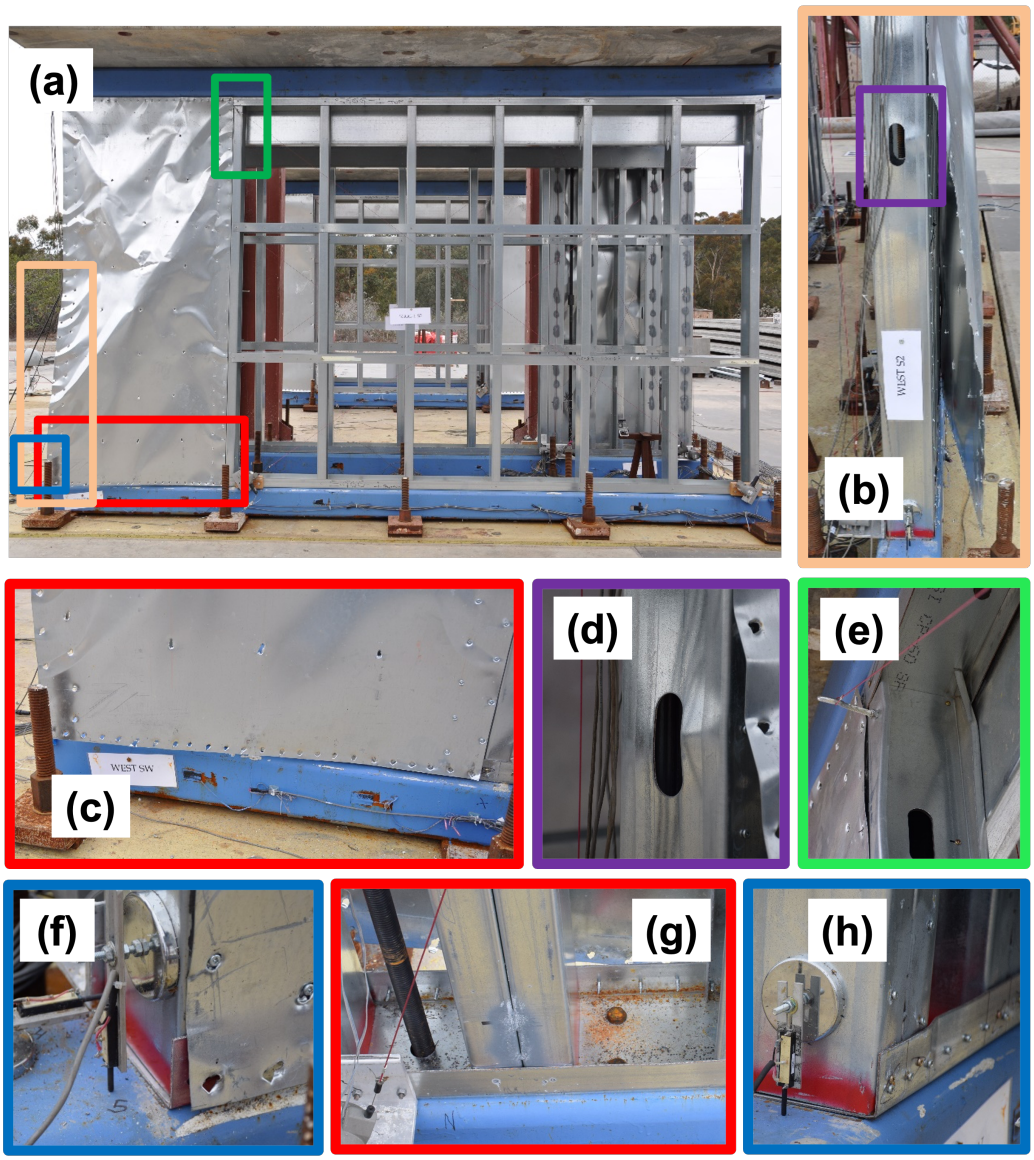


Figure 3.18. Pysical damage to specimen SGGG-1 following the dynamic testing sequence ($\Delta_{max} = 5.1\%; \Delta_{res} = 0.26\%$)

3.21 shows the comparison of panel shear distortion evolution of the shear segment between symmetrical and asymmetrical walls. Normalized for lateral force or drift, the differences between the two pairs are minimal.

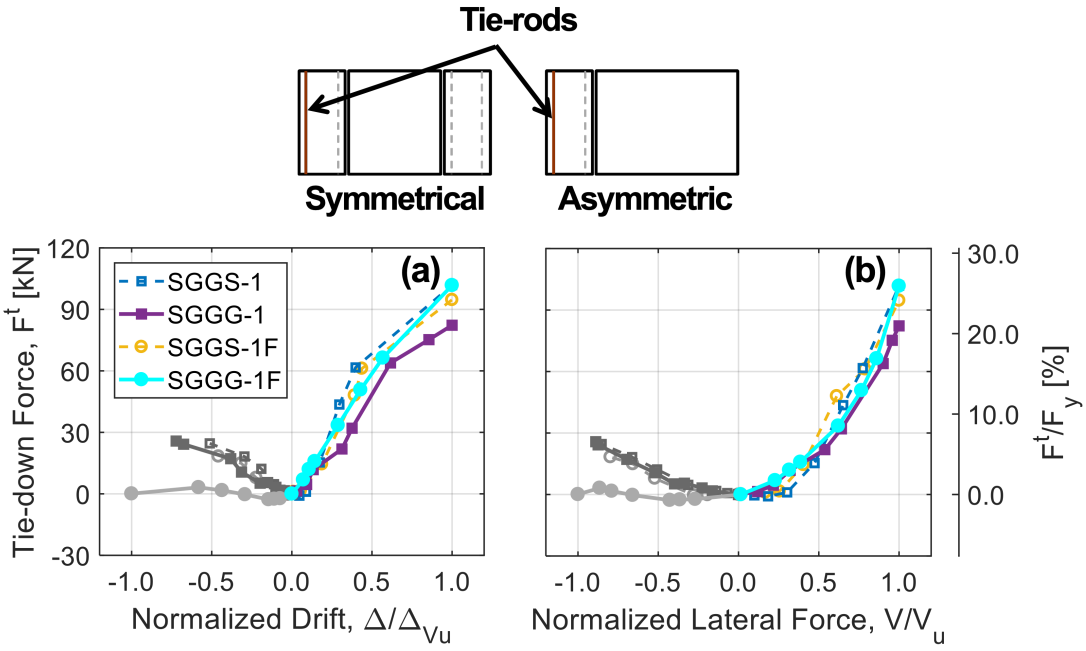


Figure 3.19. Effect of asymmetric shear wall location on tension-rod forces with increase in: (a) normalized drift and (b) normalized lateral force

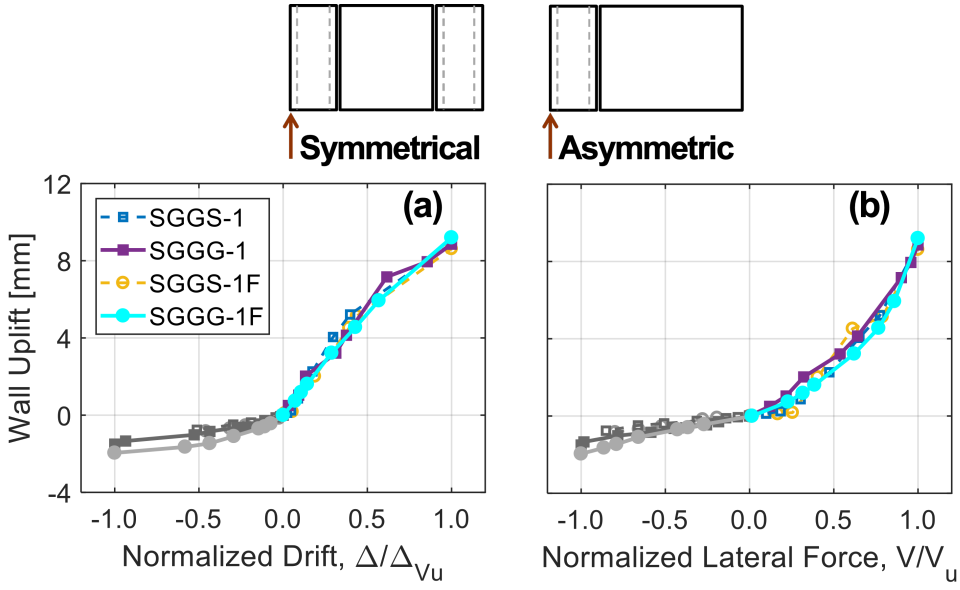


Figure 3.20. Effect of asymmetric shear wall location on wall end uplift with increase in: (a) normalized drift and (b) normalized lateral force

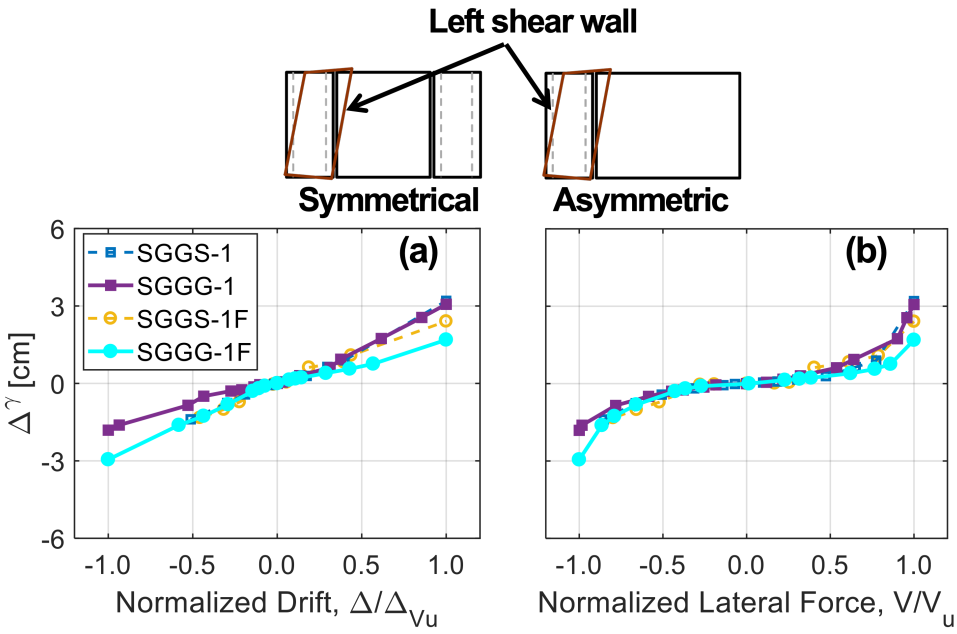


Figure 3.21. Effect of asymmetric shear wall location on shear wall shear distortion with increase in: (a) normalized drift and (b) normalized lateral force

3.6 Tie-down Detailing

As noted, most wall configurations tested during the experimental program used tension tie-rods for shear wall detailing, either of the Type I or Type II configurations. However, prior experimental programs on CFS-framed shear walls has generally involved use of hold-downs as the tie-down systems. Thus, it was considered important to include configurations in the test matrix, which compared the effect of these two different tie-down details on wall behavior. Two configurations, namely, SGGS-1HD (unfinished) and SGGS-1HDF (finished), in the quasi-static test phase used hold-downs instead of tension tie-rods. Figure 3.22a shows the force-displacement response comparison between wall specimens SGGS-1 (tension tie-rods) and SGGS-1HD (hold-downs), while Table 3.4 summarizes important response measurements. These results show that specimens detailed with tie-rods compared with nominally identical specimens detailed with hold-downs demonstrate considerably lower strength and moderately lower stiffness, irrespective of the presence of finish or not. Notably, however, the drift at which strength is achieved is

similar for the two specimens. The exception to this was the finished specimen SGGS-1HDF, which attained strength at 3.0% drift ratio, as seen from the backbone curves in Figure 3.22b. The elastic stiffness of the walls with tension tie-rods was slightly lower (5%) than similarly framed specimens with hold-downs, on average. Specimens with hold-downs also demonstrated 20-30% larger lateral strength. This is mostly attributed to the 20% larger over-turning moment lever arm provided when hold-downs were utilized as they were placed outside of the chord stud packs. In contrast, tie-rods were sandwiched between the chord stud packs, and hence, had a smaller over-turning moment lever arm.

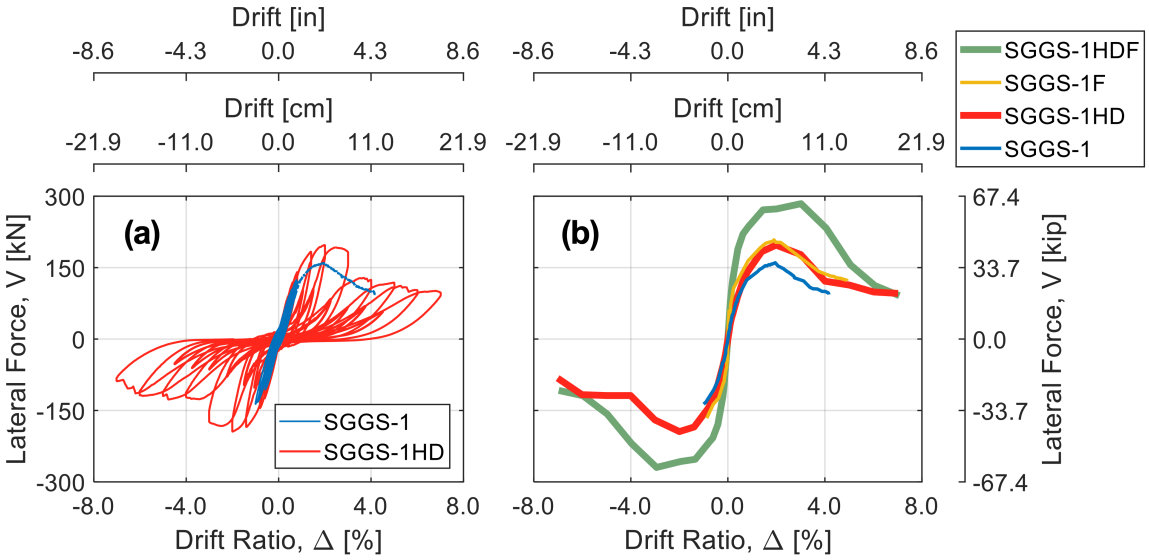


Figure 3.22. Effect of tie-down detailing: (a) force-displacement response, and (b) backbone curve comparison

Prior to 2% drift ratio, damage to the specimen was limited to the steel sheet and the screws connecting the sheet to wall framing. Most of the screw damage was concentrated around the corners of the sheet. No damage to framing members was observed up to these drift demands. This was followed by sheet pullover around 4% drift ratio. This damage is similar to what was observed in specimens with tension tie-rods. However, between 3% and 4% drift ratios, significant damage to the hold-downs at the wall ends was observed due to prying action at the thread bar centerline leading to a weld failure. Figure 3.23 shows the damage to the hold-downs

Table 3.4. Effect of tie-down detailing: results summary

	Specimen	Wall strength V_u (kN)	Drift ratio at $0.4V_u$ (pre-peak) $\Delta_{0.4Vu}$ (%)	Drift ratio at V_u (peak) Δ_{Vu} (%)	Drift ratio at $0.8V_u$ (post-peak) $\Delta_{0.8Vu}$ (%)	Elastic stiffness K (kN/cm)
Shake table	SGGS-1	160.2	0.28	1.95	2.79	84.5
		–	-0.29	–	–	81.5
	SGGS-1F	208.2	0.15	1.90	3.14	198.1
		–	-0.14	–	–	210.9
Quasi-static	SGGS-1HD	197.4	0.35	1.99	3.36	82.9
		-194.3	-0.32	-2.00	-3.57	89.5
	SGGS-1HDF	284.7	0.17	3.01	4.13	237.3
		-269.2	-0.18	-2.94	-4.03	223.9

Notes: 1. When information about wall strength is not available in the negative direction, for stiffness calculations, the strength is assumed to be the same as the positive direction.

at 4% drift ratio. Between 4% and 7% drift ratio, several hold-down thread bars failed as they experienced excessive tie-down forces, beyond their ultimate capacity. Figure 3.24 shows the damage observed in hold-downs and thread bars. Damage to the hold-downs began in the form of local buckling of the flanges below the hold-down plate and bearing against the bottom track and transfer beam. This caused the weld around the hold-down plate to fracture at 5.0% drift ratio. As drift demand increased, one-by-one beginning from the hold-downs at wall ends, the hold-down thread bars started to fracture. Each bar fracture was accompanied by a sudden drop in the lateral force resistance of the wall. It should be noted that even though as the hold-down thread bars fractured, the wall-line continued to show significant residual strength as the load path changed.

In contrast, the tie-rods remained linear-elastic when the specimens with tension rods were subjected to similar drift demands. This is of particular concern, since the hold-downs and tie-rods were designed for the same over-strength level forces $\Omega_o = 3.0$ Singh et al. (2021b). A pair of hold-downs, having a combined nominal capacity $(2 \times F_u)$ of 400 kN, were installed at every chord stud pack location. Despite this, several hold-downs suffered extensive damage. It should also be noted that the two hold-downs installed on the same stud pack did not experience equal amounts of force. Due to the difference in the overturning lever arm, there was an

imbalance in the load sharing between the two hold-downs with the outer most hold-down experiencing significantly larger axial forces. As seen in Figure 3.23, the outer hold-down was already experiencing more then 50% of its individual nominal capacity and 3-4 times larger force compared to the other hold-down before the specimen reached strength. It is expected that due to this imbalance, the outer hold-downs on both ends of the wall reached their capacity earlier and failed during the large drift demand cycles.

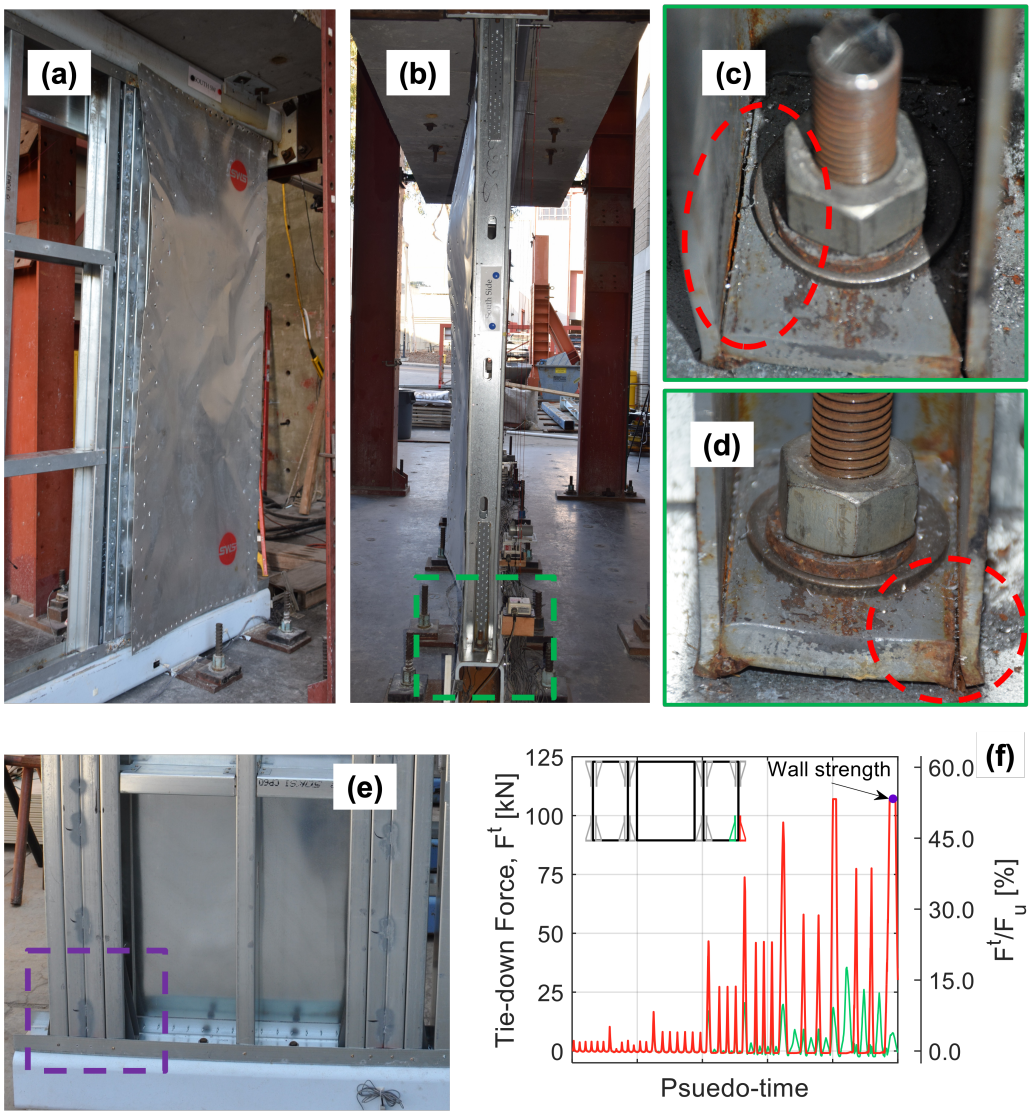


Figure 3.23. (a)-(d) Damage to steel sheet and hold-downs used in specimen SGGS-1HD at drift ratio $\Delta = 4.0\%$, and (e) tie-down force time history of hold-downs installed on stud pack

Figure 3.25 shows the comparison of tie-down force evolution between two pairs of

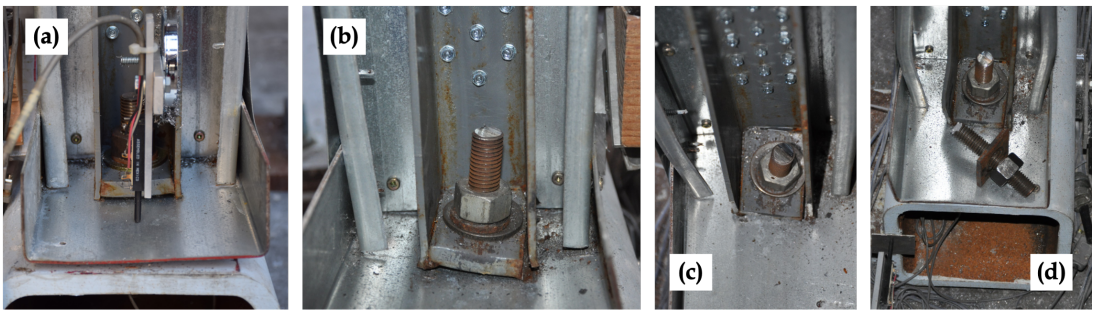


Figure 3.24. Hold-down damage installed on chord stud pack at wall end in specimen SGGS-1HD at drift ratio (a) 3.0%: bottom track bending and prying action at hold-down, (b) 5.0% and (c) 6.0%: plate weld fracture, and (d) 7.0%: thread bar fracture.

wall configurations, one employing hold-downs and the other employing tension tie-rods, with increasing lateral force (V/V_u) and lateral drift ($\Delta/\Delta_{\text{Vu}}$). It should be noted that the compression only button type load cells employed for measuring hold-down forces were pre-compressed before beginning of test. During cyclic testing, some of the hold-downs became loose, which showed up as negative tie-down force in Figure 3.25. Similar to what was observed from damage photographs of SGGS-1HD, hold-downs experienced significantly larger axial forces compared to tension tie-rods. With eight hold-downs connected to the bottom transfer beam, wall configurations employing hold-downs had a more rigid connection to the base as compared to wall configurations with tie-rods, which had only four such connections. As a result, the wall end uplift was significantly lower when hold-downs were employed. Comparison of wall end uplift evolution with increasing lateral force and lateral drift is presented in Figure 3.26. This also explains the panel shear distortion evolution of the shear segments. Since the contribution towards drift due to uplift is low for walls with hold-downs, the contribution of panel shear distortion to the drift $\left(\Delta_\gamma\right)$ is higher. These can be seen by studying Figure 3.27, which shows the comparison of panel shear distortion evolution of the shear segments between the same pairs of wall configurations, with increasing lateral force and lateral drift.

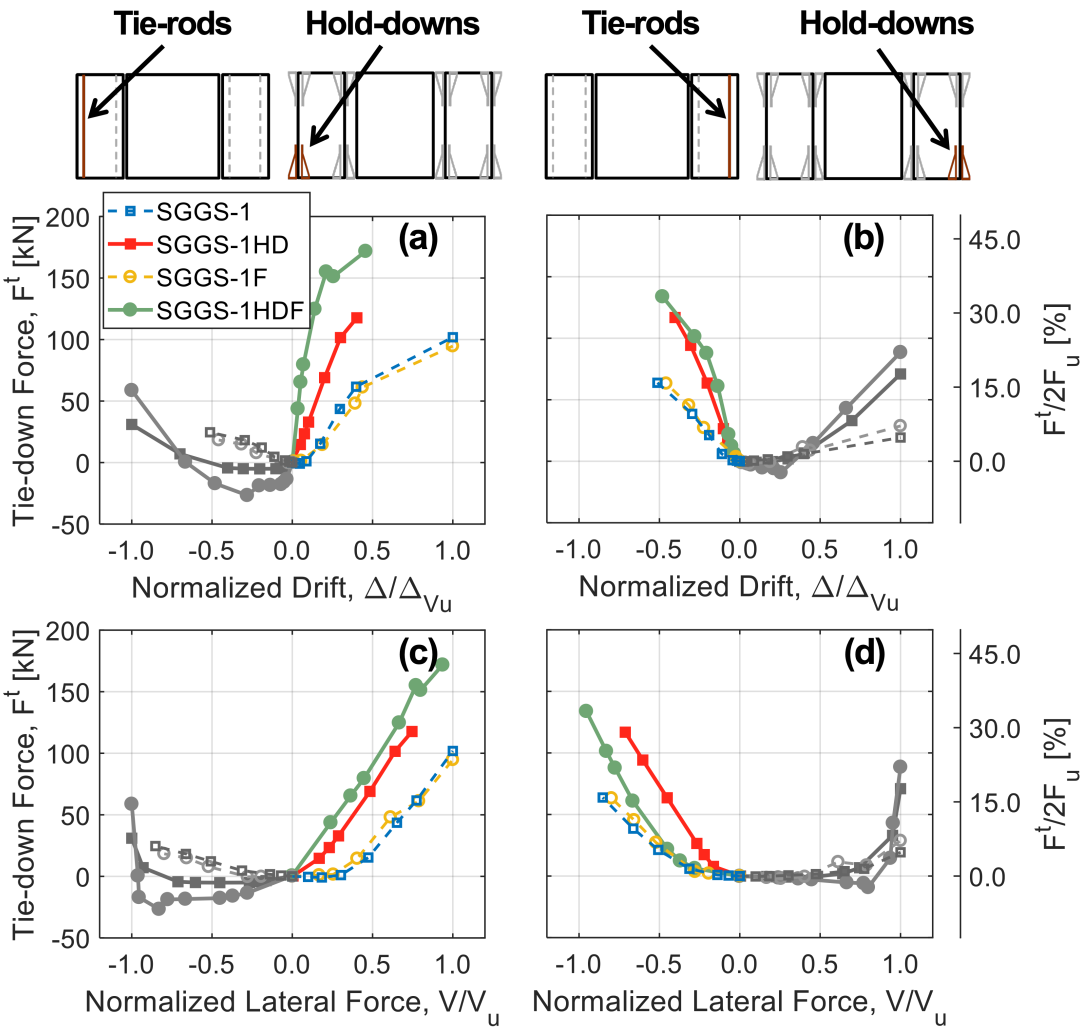


Figure 3.25. Effect of tie-down detailing on anchor forces with increase in: (a) and (b) normalized drift, and (c) and (d) normalized lateral force

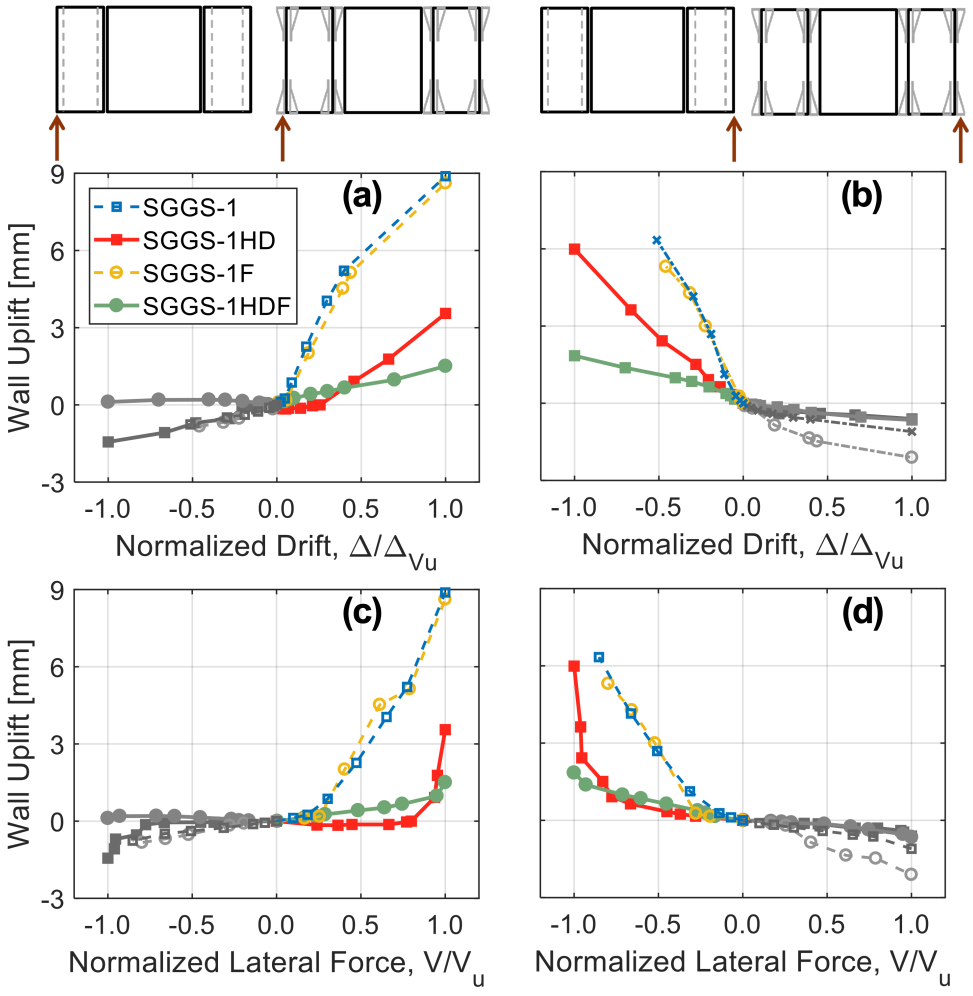


Figure 3.26. Effect of tie-down detailing on wall end uplift with increase in: (a) and (b) normalized drift, and (c) and (d) normalized lateral force

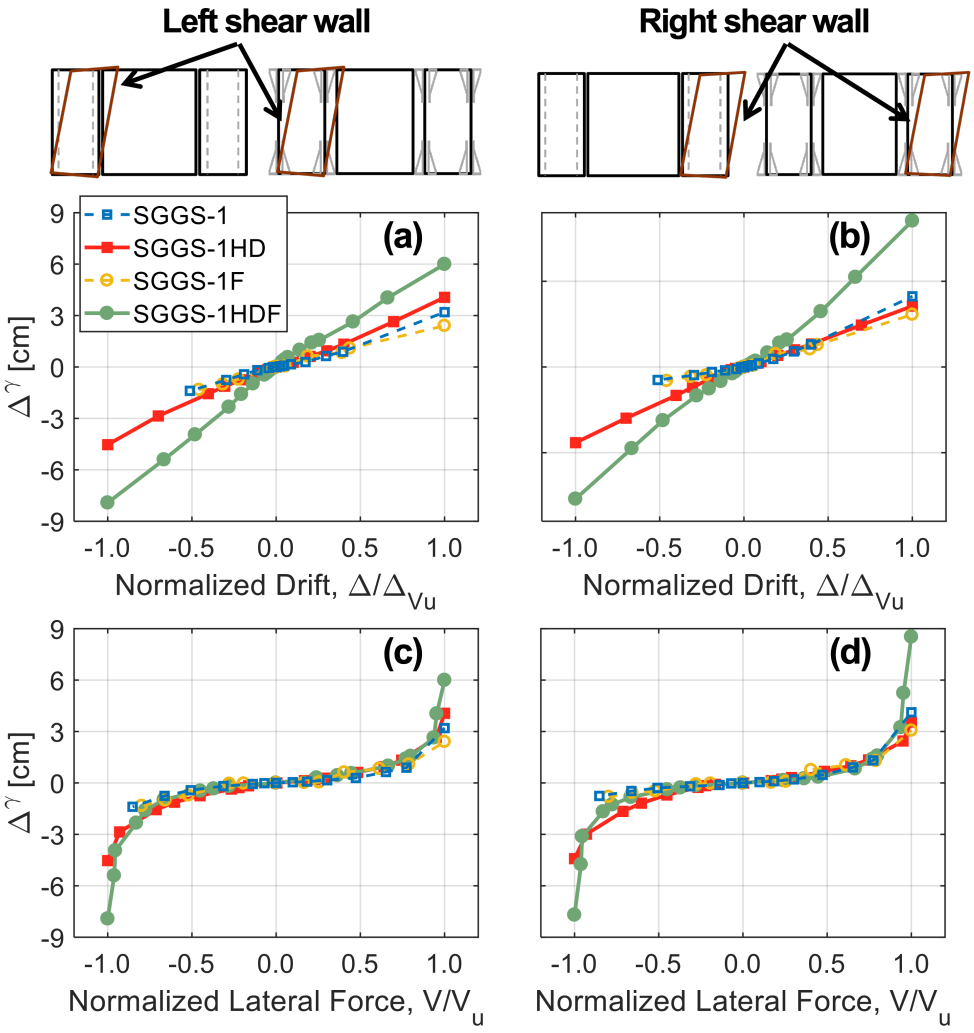


Figure 3.27. Effect of tie-down detailing on shear wall shear distortion with increase in: (a) and (b) normalized drift, and (c) and (d) normalized lateral force

3.7 Shear Wall Detailing

Amongst the 16 wall configurations tested, five configurations were detailed as Type II shear walls. Consistent with AISI S400-20, tie-downs and compression posts for Type II shear walls were provided at the ends of the wall only. However, it should be noted that these Type II specimens were not designed and detailed with any members collecting and carrying the shear to the shear wall segments at the ends. As such, these specimens were not code compliant Type II shear walls as defined in AISI S400-20. Nonetheless, they shared the most salient characteristic of Type II walls. Figure 3.28 shows the force-displacement response comparison between wall specimens SGGS-1 and SGGS-2, while Table 3.5 summarizes important response measurements. From this figure, it can be seen that the Type II specimen achieved about 30% lower strength when compared with the Type I specimen. Additionally, the drift at which strength is achieved, as well as the elastic stiffness, is also lower for the Type II specimen. Figure 3.28 also shows the backbone curves of three Type II wall configurations compared with a similarly framed Type I wall configurations (total of six specimen backbone curves). These aggregate backbone curve comparisons consistently demonstrate that the Type II specimens have about 70% of the strength of a similarly framed Type I wall, on average. Elastic stiffness for a Type II wall is also similarly about 60% of the elastic stiffness of a similarly framed Type I wall, on average. Drift at strength for Type II walls was always lower than its Type I counterpart. Due to the reduced tension tie-rods and steel sheet fasteners, the Type II specimens were naturally anticipated to have a lower strength and stiffness. It should be noted that for such Type II walls, AISI S400-20 suggests a 50% reduction in lateral strength. However, experimental results indicate that these reductions are not as high as suggested by the code.

Type II wall-lines demonstrated a failure mode similar to Type I wall-lines. Similar to lower strength and stiffness unsymmetrical wall-lines, Type II wall-lines also incurred failure and any damage to framing members at lower drift ratio values. Damage in specimens began with development of tension field in the steel sheets, which lead to yielding within the steel sheet

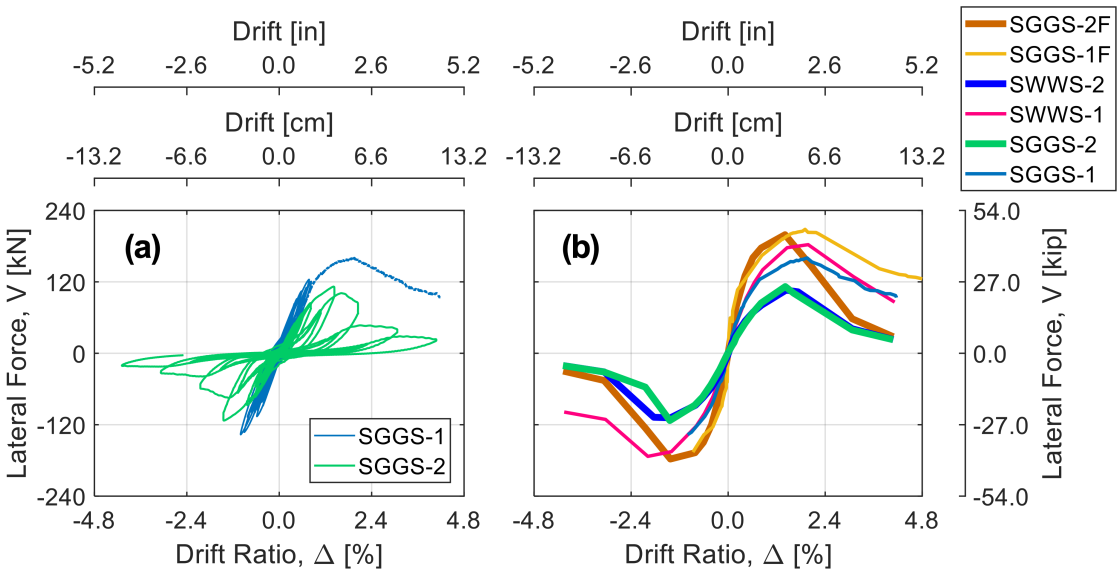


Figure 3.28. Effect of shear wall detailing: (a) force-displacement response, and (b) backbone curve comparison

with increased drift demand up to 1.41% drift ratio. Similar to Type I specimens, sheet tearing and screw pull-through could be observed along the top and bottom edges of the steel sheet for Type II specimens. In addition, the bottom track suffered local buckling in the shear wall segment. Screw head shear failure was also observed at one gravity stud framing connection in the middle of the wall-line. Figure 3.29 presents the aforementioned damage as observed in specimen SGGS-2 at the end of testing ($\Delta_{max} = 4.08\%$).

Figure 3.30 shows the comparison of tension tie-rod force evolution between two Type II and Type I wall configuration pairs, SGGS-2 & SGGS-1 and SWWS-2 & SWWS-1, with increasing lateral force and lateral drift. For the same amount of lateral force, tension rods in Type II specimens experience larger axial forces when compared with Type I specimens. Because of the lower number of steel sheet fasteners in Type II walls, a greater portion of lateral force has to flow through the tension tie-rods. However, when normalized for lateral force or drift at strength, Type I specimens show higher axial forces. Due to higher stiffness, Type I specimens experience higher lateral force as compared to Type II specimens for the same normalized lateral drift, which shows up as greater axial force in the tension tie-rods. Comparison of wall end uplift

Table 3.5. Effect of shear wall detailing: results summary

	Specimen	Wall strength V_u (kN)	Drift ratio at $0.4V_u$ (pre-peak) $\Delta_{0.4Vu}$ (%)	Drift ratio at V_u (peak) Δ_{Vu} (%)	Drift ratio at $0.8V_u$ (post-peak) $\Delta_{0.8Vu}$ (%)	Elastic stiffness K (kN/cm)
Shake table	SGGS-1	160.2	0.28	1.95	2.79	84.5
		–	-0.29	–	–	81.5
	SGGS-2B	84.1	0.17	1.22	1.77	70.7
		-73.8	-0.15	-0.79	-1.39	70.7
	SGGS-1F	208.2	0.15	1.90	3.14	198.1
		–	-0.14	–	–	210.9
Quasi-static	SGGS-2	113.3	0.36	1.41	1.89	46.2
		-111.8	-0.37	-1.44	-1.68	44.4
	SGGS-2F	199.2	0.20	1.41	1.90	141.9
		-177.7	-0.21	-1.43	-1.85	121.7
	SWWS-1	182.5	0.34	1.97	2.74	79.1
		-173.3	-0.36	-2.00	-2.58	70.4
	SWWS-2	107.2	0.30	1.43	2.13	52.6
		-107.3	-0.29	-1.43	-2.17	54.1
	SWWS-2F	181.8	0.29	2.01	2.66	91.9
		-169.0	0.29	-1.42	-2.41	84.7

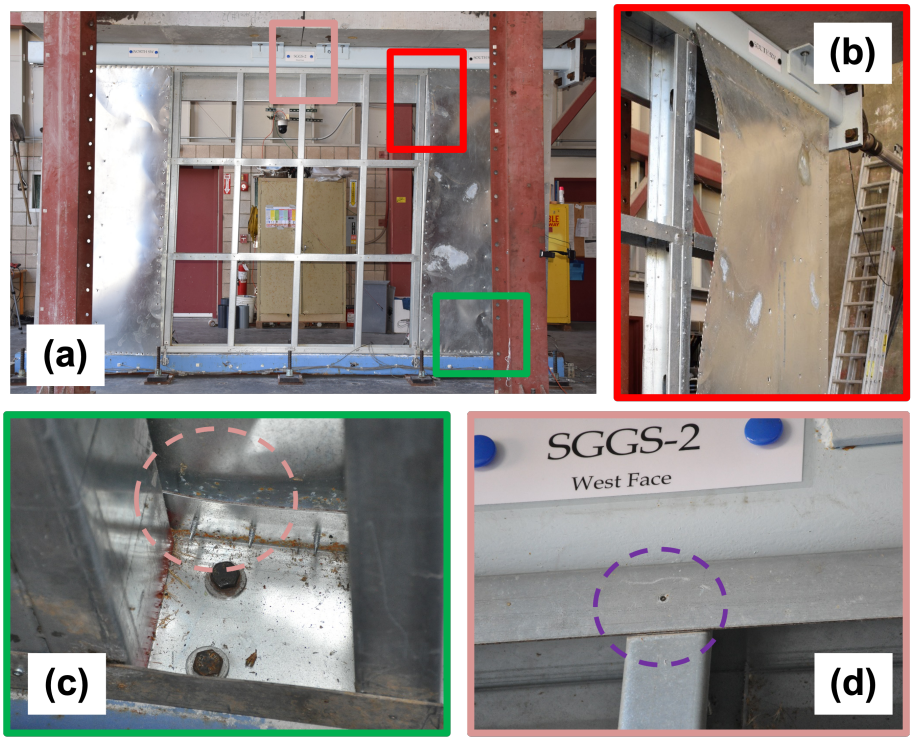


Figure 3.29. Physical damage to specimen SGGS-2 at drift ratio $\Delta_{max} = 4.08\%$

evolution between Type II and Type I wall specimens with growth in lateral force and lateral drift remained consistent with tension tie-rod forces. Type II specimens experiences greater wall uplift as compared to Type I specimens for the same lateral force, since Type II specimens have lower stiffness. However, when normalized for lateral force or drift at strength, Type I specimens show greater wall uplift.

Comparison of wall end uplift evolution between Type II and Type I wall specimens with increase in lateral force and lateral drift is presented in Figure 3.31. Consistent with tension tie-rod forces, Type II specimens experiences greater wall uplift as compared to Type I specimens for the same lateral force, since Type II specimens have lower stiffness. However, when normalized for lateral force or drift at strength, Type I specimens show greater wall uplift. A comparison of panel shear distortion evolution of the shear segments between the same pairs of Type II and Type I wall configurations, with growth in lateral force and lateral drift showed that for the same lateral force, the different segments of Type II specimens underwent greater panel distortion as compared to Type I specimens, see Figure 3.32. This is expected since Type II specimens have lower stiffness. However, after normalizing for individual lateral force at strength, the differences are not as significant, with distortion in Type I specimens being slightly higher only at high applied lateral forces. Looking at this evolution in terms of growth in normalized lateral drift, the difference in wall stiffness explains the greater panel distortion in Type I specimens.

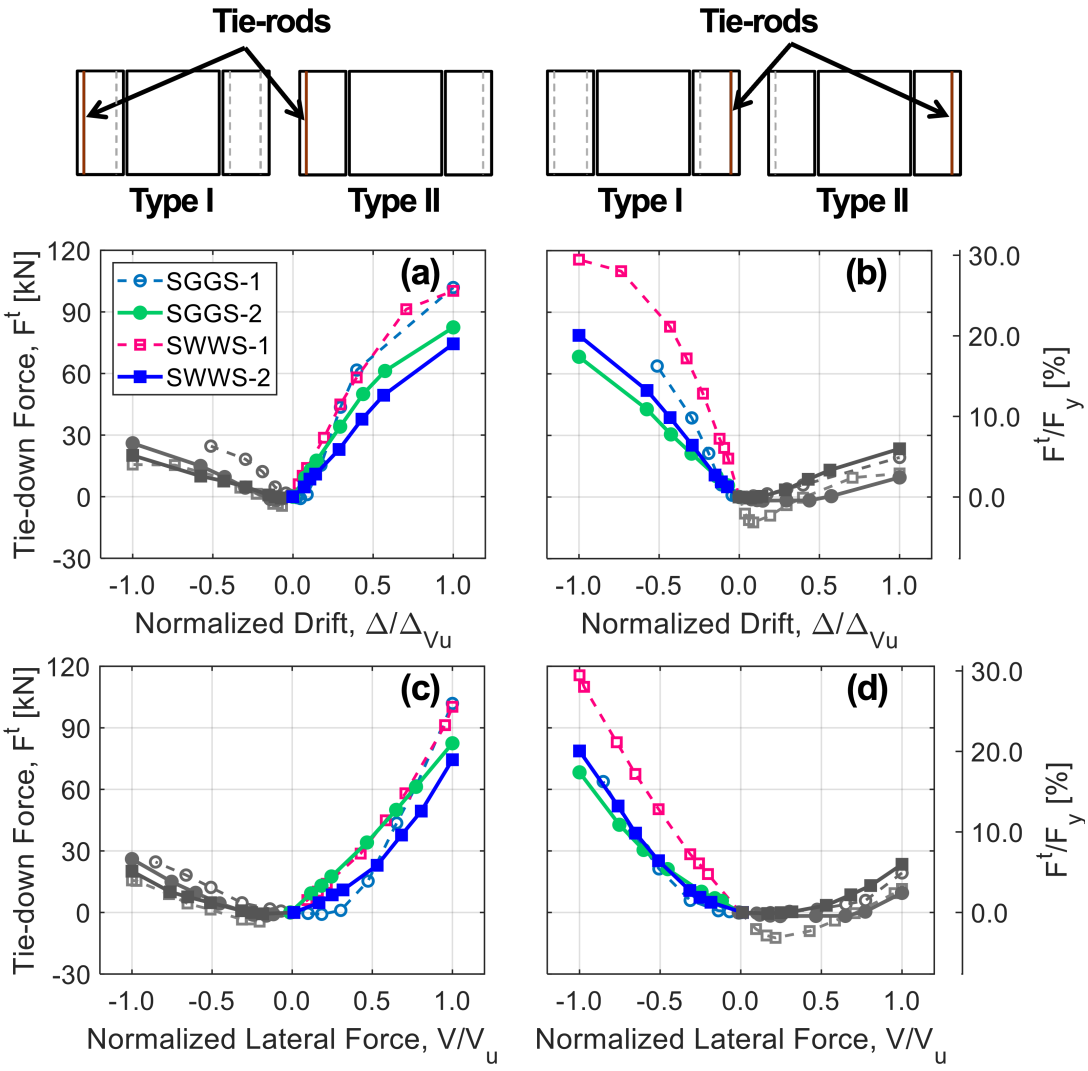


Figure 3.30. Effect of shear wall detailing on tension-rod forces with increase in: (a) and (b) normalized drift, and (c) and (d) normalized lateral force

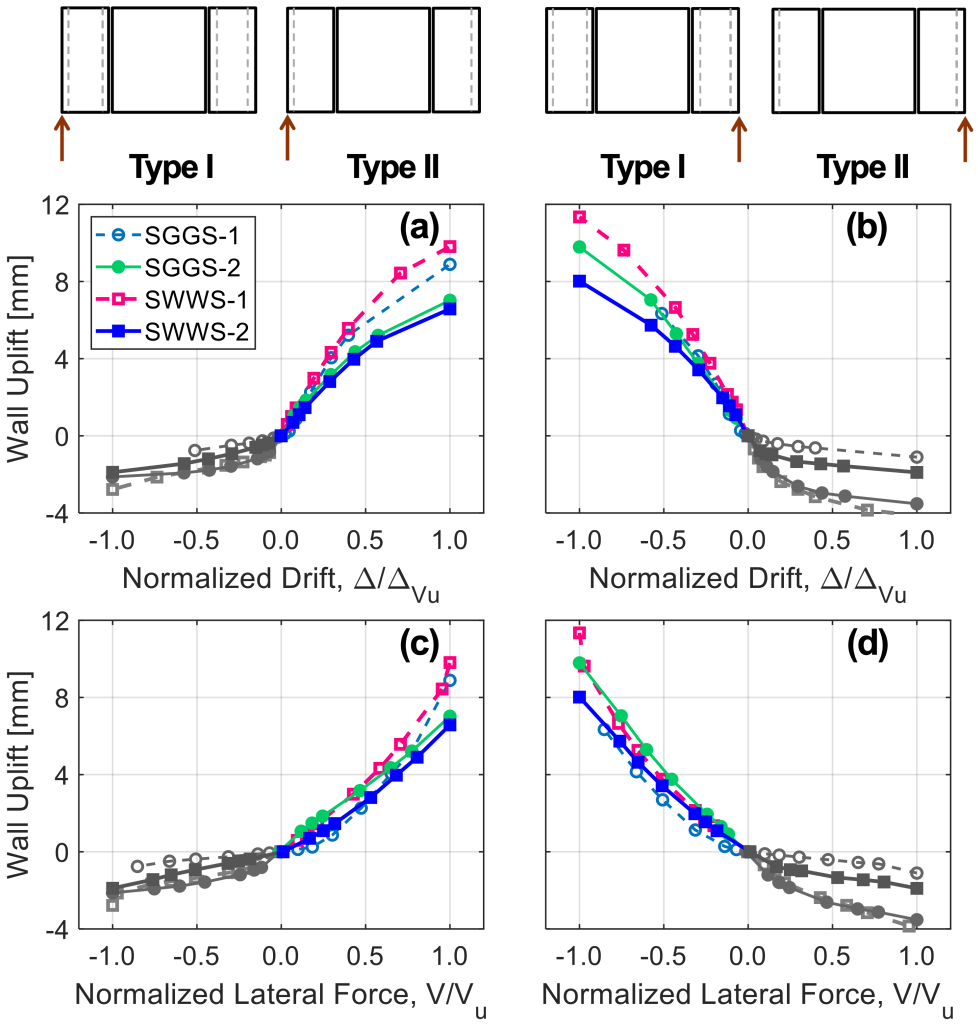


Figure 3.31. Effect of shear wall detailing on wall end uplift with increase in: (a) and (b) normalized drift, and (c) and (d) normalized lateral force

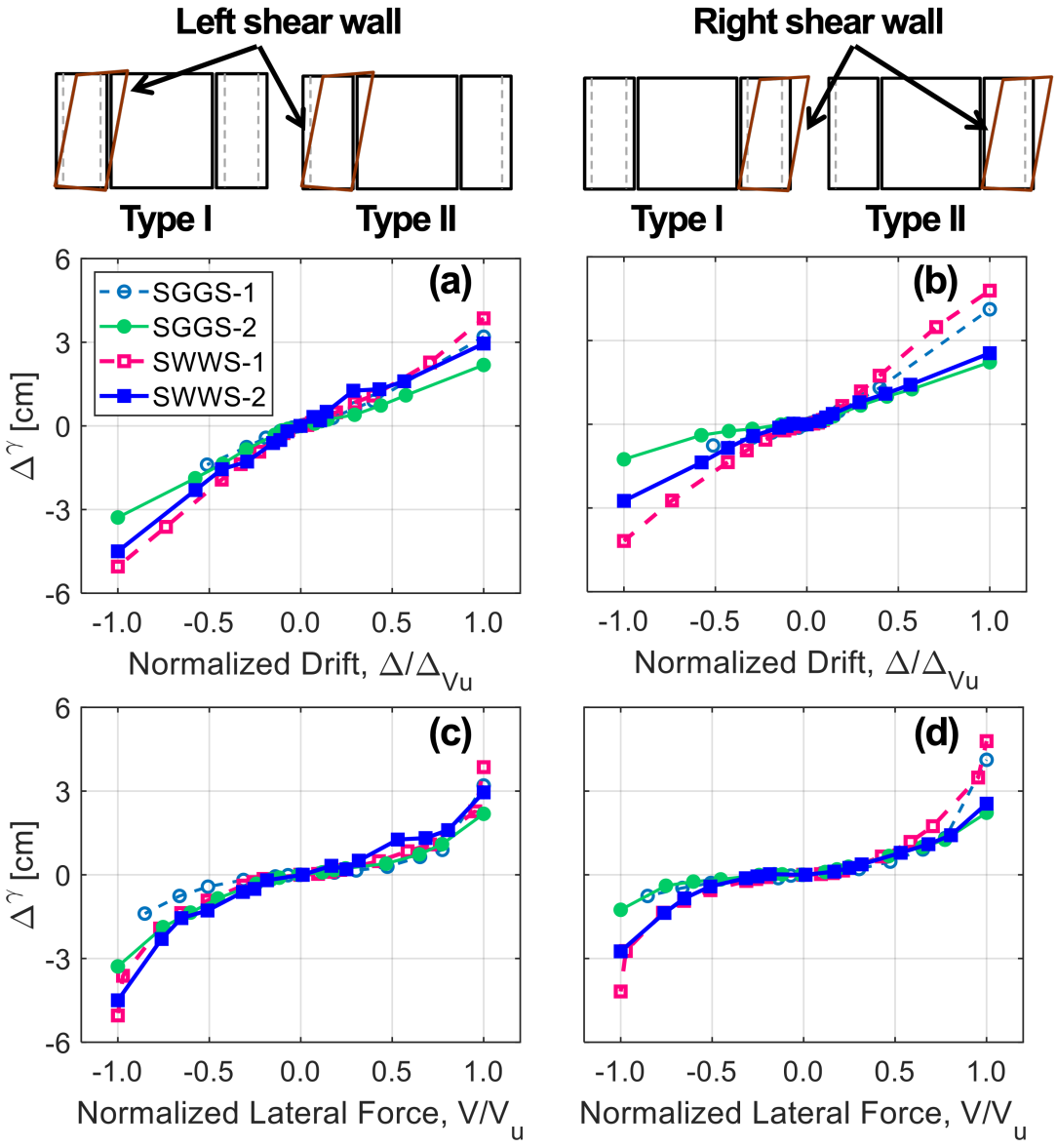


Figure 3.32. Effect of shear wall detailing on shear wall shear distortion with increase in: (a) and (b) normalized drift, and (c) and (d) normalized lateral force

3.8 Sheet Fastener Pattern

There is some reported literature such as Yu et al. (2007) suggesting that use of staggered screw pattern for attaching steel sheet to built-up chord stud members of (Type I) shear walls improved their shear strength. Generally, however, there is a lack of experimental data regarding the variation of screw pattern on shear walls that use stud packs as boundary element. Similarly, there is no experimental data on the variation of fastener spacing along the edge of steel sheet adjacent to any perforations, like next to a gravity bay. These were taken into account by adding wall specimens in the test matrix which allowed evaluating the effect of sheet fastener pattern. One wall configuration, SGGS-1XS with a sheet fastener pattern different to the typical pattern used in SGGS-1 and other Type I specimens was present in the test matrix. Generally for all Type I configurations, steel sheet was attached to the shear wall framing with 51 mm (or 102 mm staggered) o.c. spacing at the outer chord stud packs and 305 mm o.c. spacing at the field stud and interior chord stud packs. For SGGS-1XS, the steel sheet was attached to the shear wall framing with 51 mm o.c. spacing at the outer and inner chord stud packs and 305 mm o.c. spacing at the field stud. This difference is shown in Figure 3.33a-b. Similarly, generally for all Type II configurations, the steel sheet was attached to the shear wall framing with 51 mm (or 102 mm staggered) o.c. spacing at the outer chord stud pack, 305 mm o.c. spacing at the field stud, and 102 mm o.c. at the chord stud (not a built-up member) located at the interior edge of steel sheet. For SGGS-2B, the steel sheet was attached to the shear wall framing with 51 mm o.c. spacing at the outer chord stud pack, and 305 mm o.c. spacing at the field stud and the chord stud located at the interior edge of steel sheet. This difference is shown in Figures 3.34a-b.

Figures 3.33c and 3.34c show the force-displacement curve comparisons between configurations SGGS-1 and SGGS-1XS, and configurations SGGS-2 and SGGS-2B. It can be seen from the hysteresis response, in both cases, that the use of additional fasteners for attaching steel sheet led to increase in specimen strength and elastic stiffness. SGGS-1XS showed a modest 13% increase in strength and 8% increase in elastic stiffness over SGGS-1. However, the presence

of additional screws increased the drift at strength for SGGS-1XS specimen up to 2.29%, from 1.95% for SGGS-1. The post-peak strength drop behavior is also significantly different due to the larger number of fasteners being engaged. A 30% reduction in lateral strength was observed for SGGS-2B compared to SGGS-2. Drift at strength for SGGS-2B was also lower at 1.22%, compared to 1.41% for SGGS-2. The post-peak behavior is quite similar since the failure mode for both specimens was bearing/tilting or tearing around fastener heads leading to eventual sheet pull over fastener heads. A summary of the important response measurements is provided in Table 3.6.

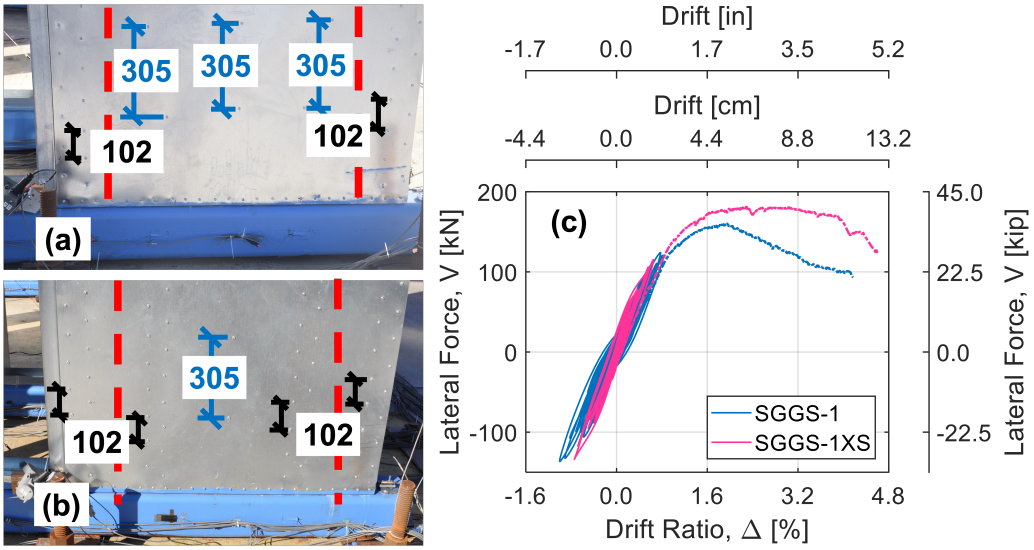


Figure 3.33. Sheet fastener pattern for specimens: (a) SGGS-1 and (b) SGGS-1XS (all units in mm); and (c) force-displacement response of SGGS-1 and SGGS-1XS
Note: Field spacing in blue, edge spacing in black font.

Figure 3.35 compares the damage to the steel sheet and fasteners at the end of monotonic pull tests for specimens SGGS-1 and SGGS-1XS. In both cases, steel sheet screws governed the wall response. Using more screws did not lead to change in the failure mode. Wall local behavior such as tension tie-rod forces also remained similar between the two configurations. Figure 3.36 shows the damage to the steel sheet and fasteners at the end of tests for specimens SGGS-2 and SGGS-2B, with full height steel sheet pull over fastener heads along the edge with coarser fastener edge spacing.

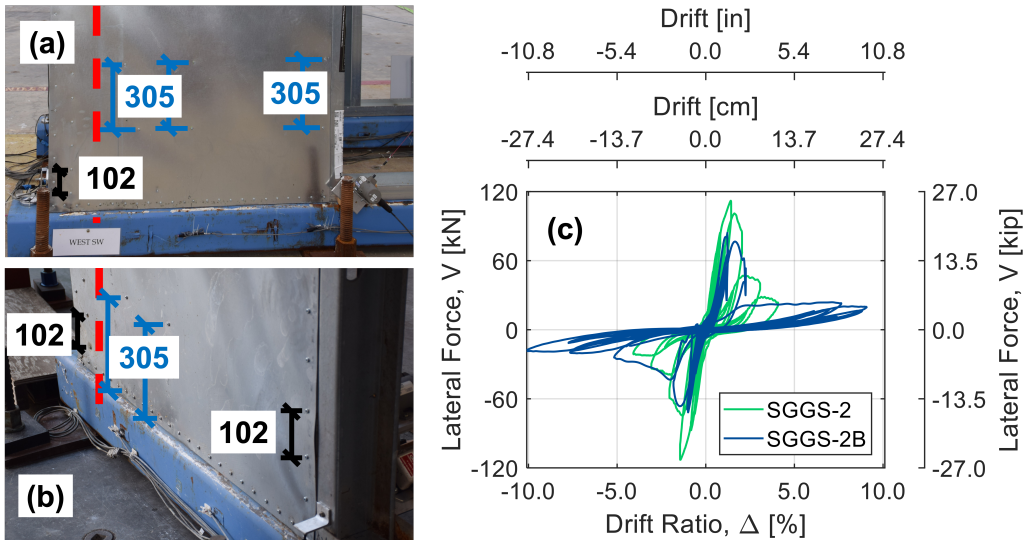


Figure 3.34. Sheet fastener pattern for specimens: (a) SGGS-2B and (b) SGGS-2 (all units in mm); and (c) force-displacement response of SGGS-2 and SGGS-2B

Table 3.6. Effect of sheet fastener pattern: results summary

	Specimen	Wall strength V_u (kN)	Drift ratio at $0.4V_u$ (pre-peak) $\Delta_{0.4Vu}$ (%)	Drift ratio at V_u (peak) Δ_{Vu} (%)	Drift ratio at $0.8V_u$ (post-peak) $\Delta_{0.8Vu}$ (%)	Elastic stiffness K (kN/cm)
Shake table	SGGS-1	160.2	0.28	1.95	2.79	84.5
		–	-0.29	–	–	81.5
	SGGS-1XS	181.5	0.31	2.29	4.13	86.2
		–	-0.28	–	–	93.3
	SGGS-2B	84.1	0.17	1.22	1.77	70.7
		-73.8	-0.15	-0.79	-1.39	70.7
Quasi-static	SGGS-2	113.3	0.36	1.41	1.89	46.2
		-111.8	-0.37	-1.44	-1.68	44.4

3.9 Summary Remarks

The impact of variables governing the nonstructural detailing of CFS-framed walls, namely: finish application, window opening, and asymmetric shear wall location, and structural detailing of CFS-framed walls, namely: tie-down detailing, shear wall detailing, and sheet fastener detailing have been discussed in this chapter. The impact of test variables is evaluated by discussing the performance of the baseline specimen SGGS-1 first, and then comparing select groups of specimens systematically. The findings are presented in terms of force-displacement

backbone curves, key measured parameters, such as lateral strength and stiffness, drift at strength; wall local behavior, such as tie-down force, wall uplift and shear distortion; and observed physical damage evidence. Force-displacement response for all individual wall-lines, tested during the

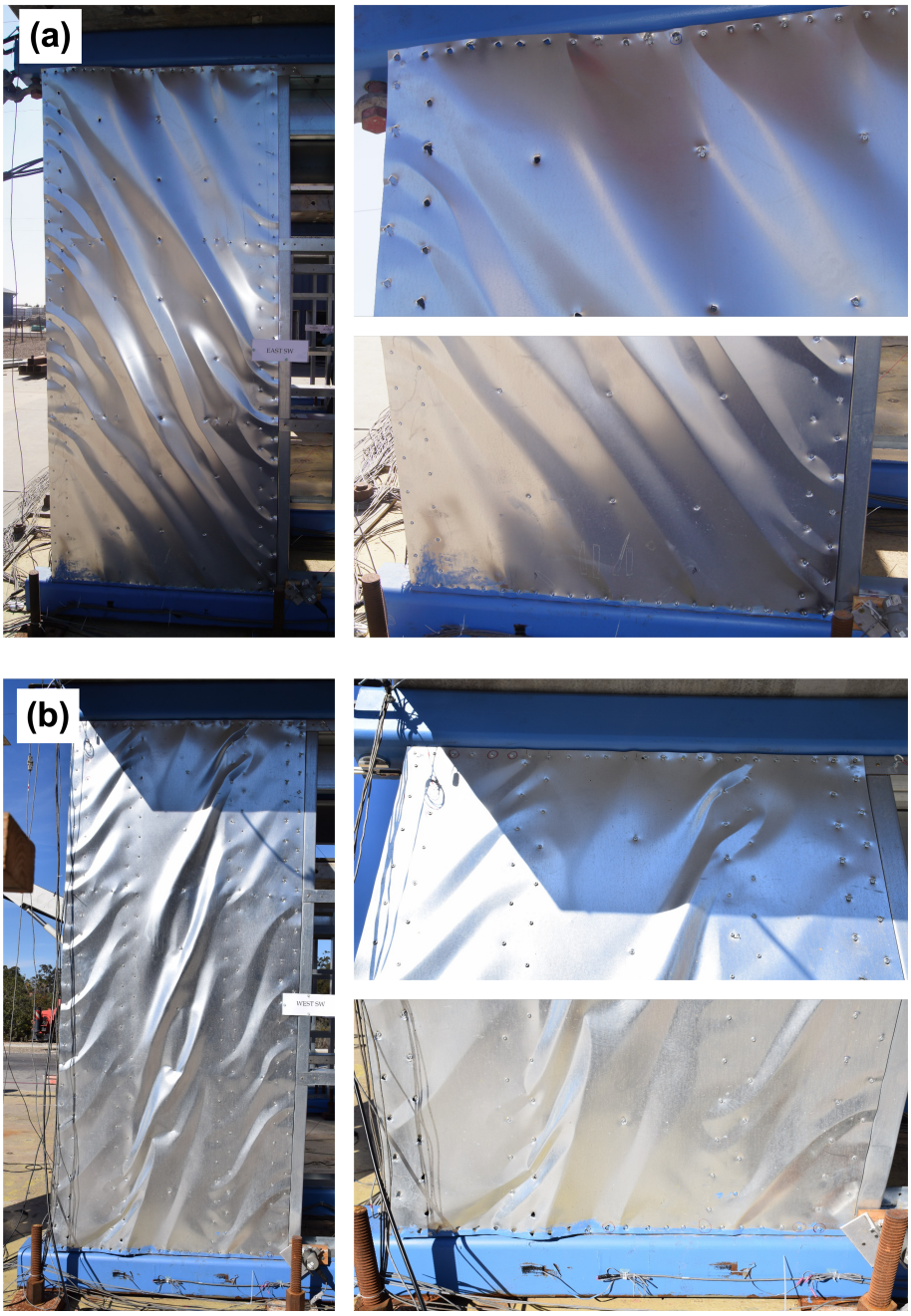


Figure 3.35. Damage to steel sheet and fasteners at the end of monotonic pull tests for specimens: (a) SGGS-1 ($\Delta_{max} = 4.15\%; \Delta_{res} = 1.85\%$), and (b) SGGS-1XS ($\Delta_{max} = 4.6\%; \Delta_{res} = 2.8\%$)

two phases, are provided in Appendix C. Local response, i.e. tie-down force, wall uplift, and panel shear distortion, for all individual wall-lines, tested during the two phases, are provided in Appendix D.



Figure 3.36. Damage to steel sheet and fasteners at the end of testing for specimens: (a) SGGS-2B ($\Delta_{max} = 10\%; \Delta_{res} = -0.23\%$), and (b) SGGS-2 ($\Delta_{max} = 4.1\%$)

Acknowledgment of Publications

Portions of the following papers and technical reports, for which the dissertation author was the primary investigator and author, are contained in Chapter 3:

Singh, A., Wang, X., Zhang, Z., Derveni, F., Castaneda, H., Peterman, K. D., Schafer, B. W., and Hutchinson, T. C. (2022). "Steel Sheet Sheathed Cold-Formed Steel Framed In-line Wall Systems. I: Impact of Structural Detailing" *ASCE J. Struct. Eng.*, 148(12), 04022193.

Singh, A., Wang, X., Zhang, Z., Derveni, F., Castaneda, H., Peterman, K. D., Schafer, B. W., and Hutchinson, T. C. (2022). "Steel Sheet Sheathed Cold-Formed Steel Framed In-line Wall Systems. II: Impact of Nonstructural Detailing" *ASCE J. Struct. Eng.*, 148(12), 04022194.

Singh, A., Wang, X. and Hutchinson, T. C. (2021). *Lateral Response of Cold-Formed Steel Framed Steel Sheathed In-line Wall Systems Detailed for Mid-Rise Buildings. Part I: Shake Table Test Phase* (Structural Systems Research Report SSRP-19/05). University of California San Diego, La Jolla, CA.

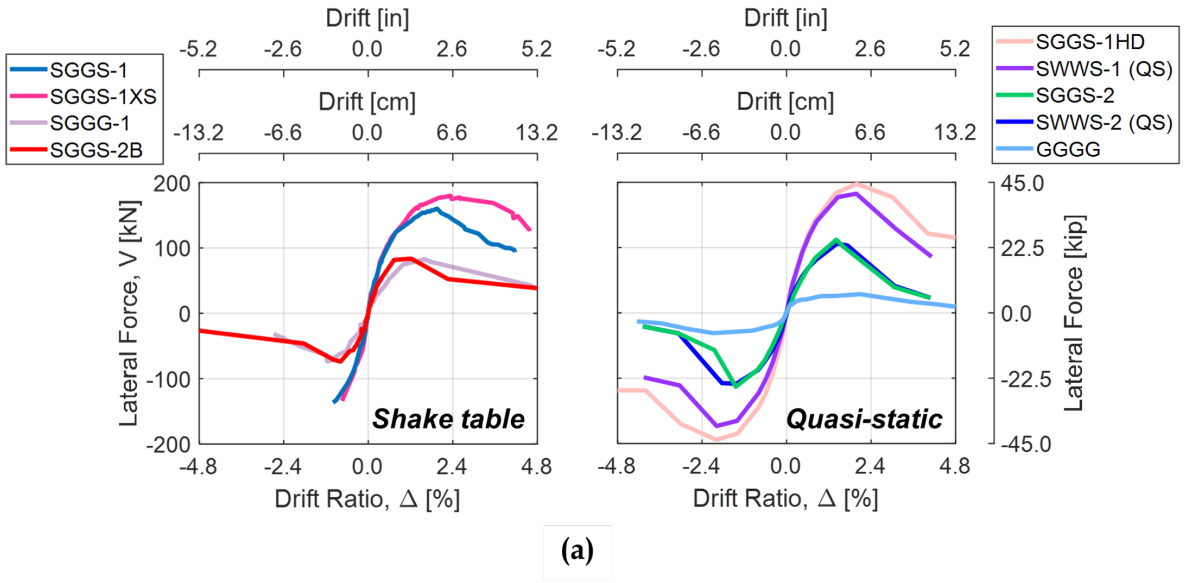
Singh, A. and Hutchinson, T. C. (2022). *Lateral Response of Cold-Formed Steel Framed Steel Sheathed In-line Wall Systems Detailed for Mid-Rise Buildings. Part II: Quasi-Static Test Phase* (Structural Systems Research Report SSRP-19/06). University of California San Diego, La Jolla, CA.

Chapter 4

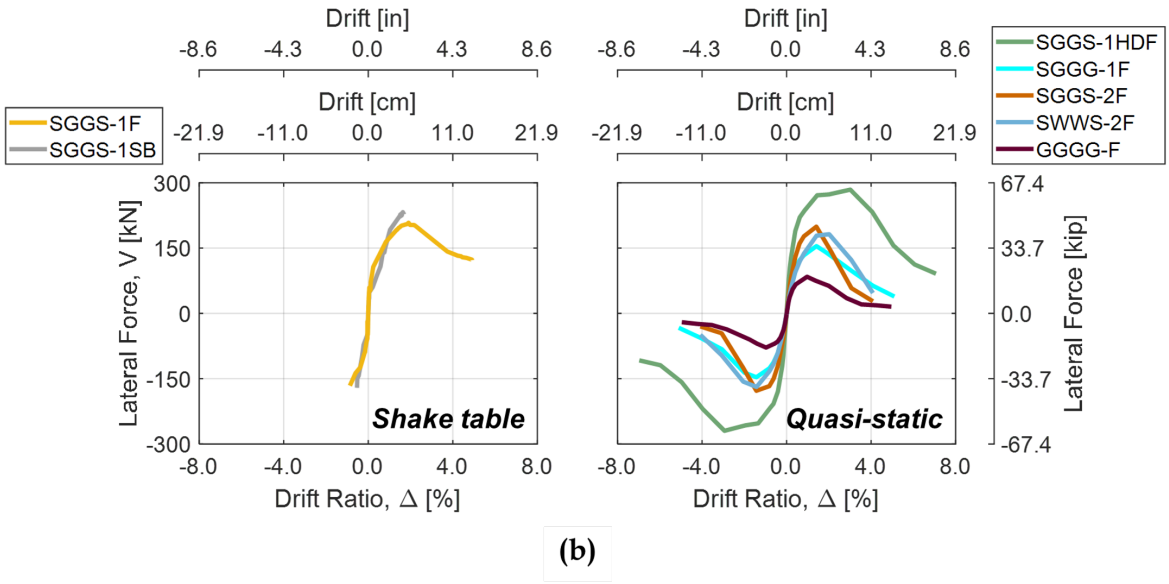
Physical Damage-Hysteretic Response Correlation for CFS-Framed Wall-Lines

4.1 Introduction

Failure mechanism in several wall-lines was discussed in Chapter 3. This chapter documents and quantifies the progressively incurred physical damage observed in wall-line assemblies, and correlates it with the evolution of dynamic characteristics and hysteretic energy dissipation characteristics at different performance levels. Unfinished and finished configurations tested within the two test phases are systematically examined. Figure 4.1 shows the envelope of lateral force versus drift, while Tables 4.1 and 4.2 summarize the hysteretic response measurements for these specimens. It should be noted that testing of configurations SWWS-1 and SWWS-2 could not be completed during the shake table test phase, and hence, were tested during both test phases. Results presented in the next section pertaining to these two configurations are marked with ”ST” for shake table or ”QS” for quasi-static to indicate the test phase from which the results were obtained. Observed physical damage in the tested wall-line assemblies is discussed and correlated with the evolution of dynamic characteristics and hysteretic energy dissipation characteristics in the following sections.



(a)



(b)

Figure 4.1. Envelope of lateral force versus drift for all tested configurations: (a) unfinished specimens and (b) finished specimens

4.2 Physical Damage Progression

4.2.1 Unfinished Specimens

Steel sheet sheathed cold-formed steel shear walls dissipate energy primarily through structural member-to-sheathing connections and yielding of the steel sheet. Even at low drift levels, tension field action is visible and manifests via buckling of the steel sheet sheathing.

Table 4.1. Hysteretic response measurements for unfinished specimens

	Specimen	Wall strength V_u (kN)	Drift ratio at $0.4V_u$ (pre-peak) $\Delta_{0.4Vu}$ (%)	Drift ratio at V_u (peak) Δ_{Vu} (%)	Drift ratio at $0.8V_u$ (post-peak) $\Delta_{0.8Vu}$ (%)	Elastic stiffness K (kN/cm)
Shake table	SGGS-1	160.2	0.28	1.95	2.79	84.5
		–	-0.29	–	–	81.5
	SGGS-1XS	181.5	0.31	2.29	4.13	86.2
		–	-0.28	–	–	93.3
	SGGG-1	82.7	0.32	1.60	2.76	37.1
		-72.3	-0.26	-1.08	-1.53	41.0
	SGGS-2B	84.1	0.17	1.22	1.77	70.7
		-73.8	-0.15	-0.79	-1.39	70.7
	SWWS-2 (ST)	119.1	0.26	1.49	–	67.3
		-116.3	-0.24	-1.27	–	72.0
	SWWS-1 (ST)	–	–	–	–	–
Quasi-static	SGGS-1HD	197.4	0.35	1.99	3.36	82.9
		-194.3	-0.32	-2.00	-3.57	89.5
	SWWS-1	182.5	0.34	1.97	2.74	79.1
		-173.3	-0.36	-2.00	-2.58	70.4
	SGGS-2	113.3	0.36	1.41	1.89	46.2
		-111.8	-0.37	-1.44	-1.68	44.4
	SWWS-2	107.2	0.30	1.43	2.13	52.6
		-107.3	-0.29	-1.43	-2.17	54.1
	GGGG	28.8	0.12	2.09	2.79	35.3
		-30.9	-0.15	-2.09	-2.78	30.7

Table 4.2. Hysteretic response measurements for finished specimens

	Specimen	Wall strength V_u (kN)	Drift ratio at $0.4V_u$ (pre-peak) $\Delta_{0.4Vu}$ (%)	Drift ratio at V_u (peak) Δ_{Vu} (%)	Drift ratio at $0.8V_u$ (post-peak) $\Delta_{0.8Vu}$ (%)	Elastic stiffness K (kN/cm)
Shake-table	SGGS-1F	208.2	0.15	1.90	3.14	198.1
		–	-0.14	–	–	210.9
	SGGS-1SB	233.2	–	1.62	–	163.0
		–	–	–	–	–
Quasi-static	SGGS-1HDF	284.7	0.17	3.01	4.13	237.3
		-269.2	-0.18	-2.94	-4.03	223.9
	SGGG-1F	156.8	0.17	1.41	2.35	74.7
		-144.5	-0.23	-1.43	-2.36	53.1
	SGGS-2F	199.2	0.20	1.41	1.90	141.9
		-177.7	-0.21	-1.43	-1.85	121.7
	SWWS-2F	181.8	0.29	2.01	2.66	91.9
		-169.0	0.29	-1.42	-2.41	84.7
	GGGG-F	84.2	0.13	0.97	1.78	96.8
		-78.4	-0.11	-0.97	-1.65	101.5

As drift demand increases, yielding in the steel sheet and damage at the sheathing fastener locations becomes prominent. For unfinished specimens across the test phases, steel sheet fastener damage in the wall-lines was readily observable. Damage in fasteners initiates in the form of bearing/tilting of screw heads, which leads to enlargement of the hole around the screw head as the angle of tilting increases. As drift amplitude increases, this hole becomes large enough for the sheet to pull-over the screw head. If the screw edge distance is insufficient, tear-out at sheathing edges may also occur. For wall-lines tested in the current experimental program, fastener damage modes observed included initial bearing/tilting, which progressed to sheet pull-over. The observed failure modes are consistent with those in other CFS-framed shear wall tests (Zhang et al., 2022b).

Figure 4.2 shows the fastener damage statistics for the modes observed at drift amplitudes associated with the different performance levels for unfinished specimens from the two test phases. Specifically, the number of steel sheet fasteners experiencing the tilting/bearing or sheet pullover mechanism as a percentage of total sheet fasteners are summarized. Beyond the defined performance levels, a Δ=4% drift level was the highest drift amplitude at which screw damage assessment could be performed consistently across quasi-static test phase specimens. For shake table test specimens, the statistics are provided based on damage observations following an earthquake test achieving a specific performance level. Since some specimens were tested to strength using a monotonic pull test, the fastener damage statistics could not be collected consistently as the drift demands varied for different specimens. Due to this, the damage statistics at the end of the testing sequence are provided collectively and reported as a post-peak level, which can be considered equivalent to damage at above design performance level and beyond. Consistently, approximately 20% fasteners demonstrated tilting/bearing damage in the elastic and quasi-elastic performance levels. A gradual increase to 40-60% damaged fasteners was observed in the unfinished specimens at design performance level. The transition in damage mode to sheet pullover was observed post-peak at above design performance level irrespective of loading protocol. The total percentage of screws damaged reached 75-85% for all specimens at

the end of testing.

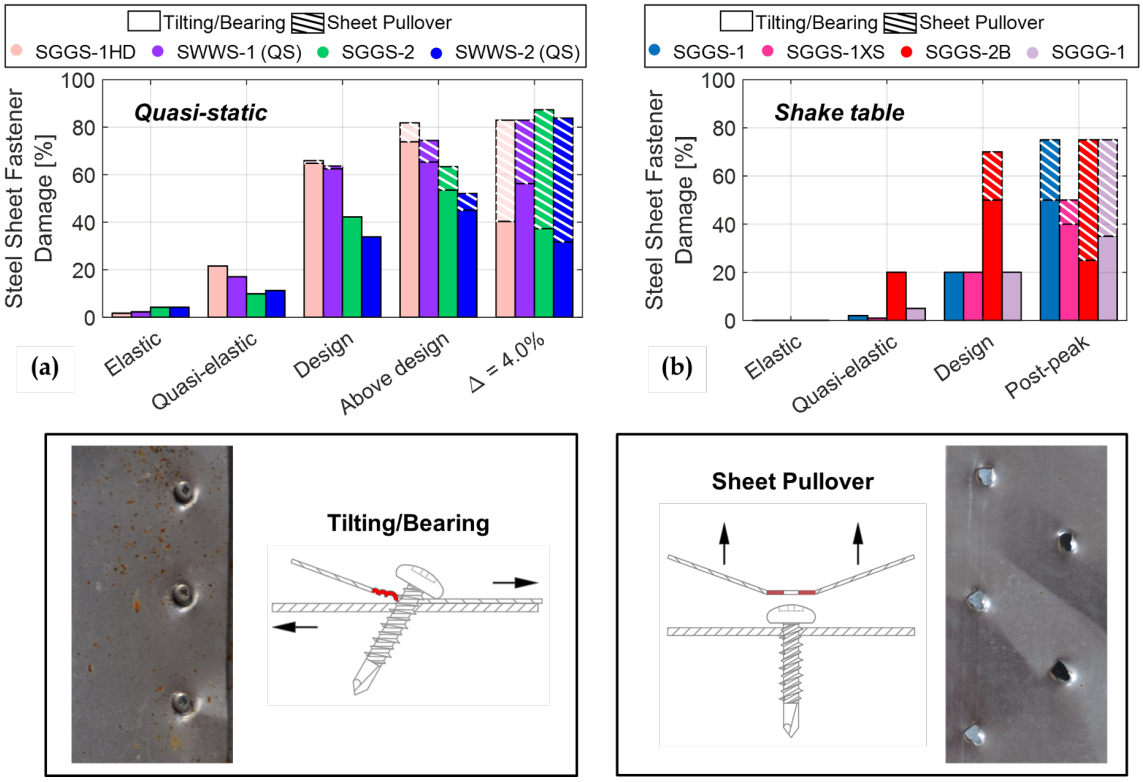


Figure 4.2. Fastener damage statistics for identified failure modes in unfinished specimens: (a) quasi-static test phase, and (b) shake table test phase

Figure 4.3 shows photographs from specimen SGGS-1HD to demonstrate the damage in the fasteners at the different performance levels for a typical unfinished wall-line. It should be noted that the damage progression described herein is for a specimen tested during quasi-static loading, however, the progression of damage was independent of loading protocol. Elastic buckling of the steel sheet was observed at the elastic performance level when the specimen response was essentially linear. The width of the tension field, measured across the sheet diagonal, became 61 cm (24”) and approximately 20% screw heads showed tilting/bearing damage at the quasi-elastic level. Specimens began to demonstrate nonlinearity beyond this performance level. As drift demand increased, the angle of screw head tilting visibly increased, with enlarged holes in the steel sheet observed surrounding the screw heads at the design performance level. During the drift cycles, a 125 cm (49”) wide tension field distributed across the steel sheet with lines

of plastic deformation were clearly visible. However, no significant damage in any framing members was observed. At above design performance level, holes around few screw heads had become enlarged enough for the sheet to pull-over the screw head during the drift cycles. In this manner, the damage mode for a significant fraction of screws demonstrating bearing/tilting initially changed to sheet pull-over later. Due to the high lateral and overturning demands at this performance level, bending in chord stud packs, bottom track and ledger track could be observed. During high drift demand cycles ($\Delta > 4\%$), the steel sheet detached from framing due to screw pull-through at a majority of fastener locations. This was also accompanied by local buckling of gravity studs within the gravity wall segment, and failure of many chord stud framing connections in head shear. Figures 4.4 and 4.5 show the framing damage observed in specimen SGGS-1HD at the above design performance level ($\Delta = 3.0\%$) and at conclusion of testing ($\Delta_{max} = 7.0\%; \Delta_{res} = 1.93\%$), respectively.

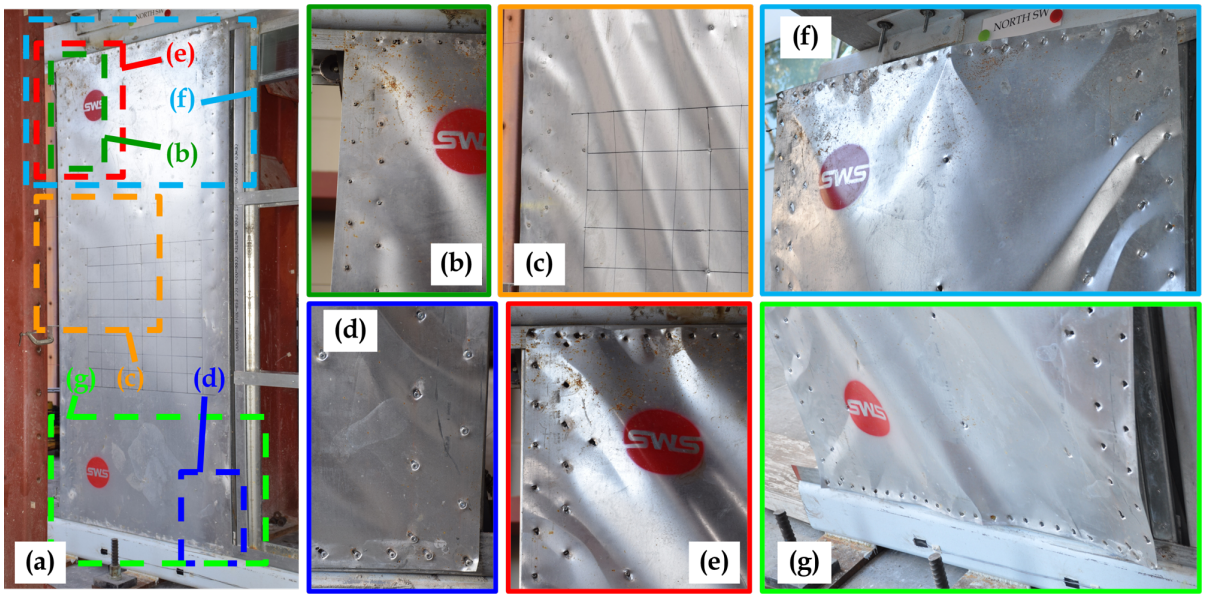


Figure 4.3. Fastener connection damage in specimen SGGS-1HD at (a) undamaged state, (b) elastic ($\Delta = 0.40\%$): sheet buckling, (c) quasi-elastic ($\Delta = 0.80\%$): tilting/bearing damage, (d) design ($\Delta = 1.99\%$): enlarged holes around screw heads, (e) above design ($\Delta = 3.0\%$) performance levels: pullover at sheet corners, and (f) and (g) drift ratio $\Delta = 4.0\%$: sheet pullover at majority fastener locations

Note: Colored boxed regions in part (a) show location of damage presented in other subfigures with like outline color.

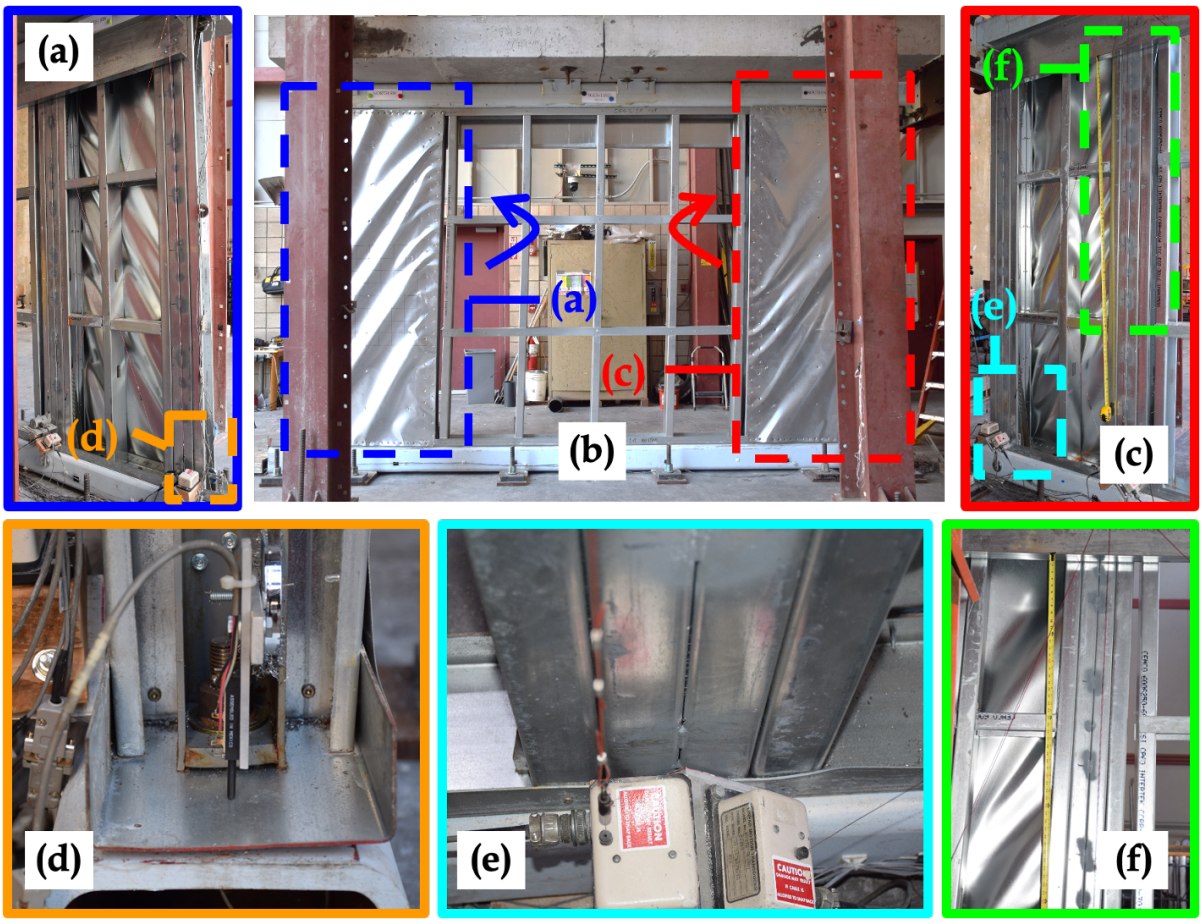


Figure 4.4. Framing member damage in specimen SGGS-1HD at above design performance level ($\Delta = 3.0\%$): (a)-(c) views of steel sheet buckling from front and back, (d) and (e) bottom track bending near chord stud pack, and (f) bending in chord stud pack

Note: Colored boxed regions and arrows show location of damage presented in other subfigures with like outline color.

4.2.2 Finished Specimens

Although yielding of steel sheet and sheathing fastener failure remained the mode of failure in finished wall-lines (Uang and Gatto, 2003), it can be seen from Figure 4.1 that the presence of finish layers increased the wall lateral strength and stiffness. In addition, the presence of the finish layers suppressed damage development within the structural components of the wall-line specimens. Figures 4.6 and 4.7 show photographs from specimen SGGS-2F to demonstrate the progression of damage in the exterior and interior finishes in a typical finished wall-line specimen at different performance levels. Damage in the finished specimens were observable

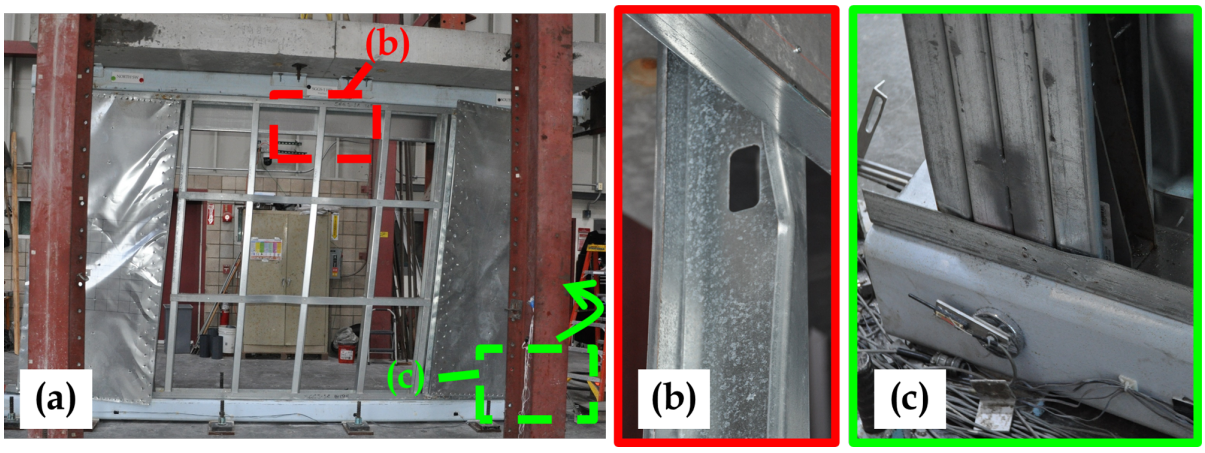


Figure 4.5. Framing member damage in specimen SGGS-1HD at conclusion of testing ($\Delta_{res} = 1.93\%$) after larger drift cycles ($\Delta_{max} = 7.0\%$): (a) elevation view of wall-line, (b) gravity stud flange buckling, and (c) stud pack framing connection failure
Note: Colored boxed regions and arrow in part (a) show location of damage presented in other subfigures with like outline color.

within the gypsum panels and in the EIFS layer, as the framing members were not visible. CFS framing deformed as a parallelogram under shear, while the attached gypsum and glass-mat panels rotated rigidly (Macillo et al., 2017). This difference in kinematic behavior induced damage in the gypsum panels at fastener heads, as well as caused crushing at panel edges on the interior face. On the exterior face of the specimens, this difference resulted in vertical surface cracks at glass-mat panel interfaces in the middle of the wall, and detachment from the underlying CFS framing. As damage progressed, the gypsum panels and EIFS layer detached, allowing for observation of damage to framing members.

For a typical finished specimen, physical damage was limited to small hairline cracks in EIFS layer at the end of wall-line at the elastic performance level. At the quasi-static performance level, approximately 25 cm long thin cracks in the EIFS layer were observed at both ends of the wall where the separation from framing began. A pair of 10 cm long surface cracks were also observed on the EIFS layer surface at locations of the underlying glass-mat panel interfaces. This was accompanied by damage in the gypsum panels in the form of minor crushing along panel edges and partial screw pull-through. EIFS damage exacerbated at the design performance level with an appreciable visible separation from the steel sheet and framing accompanied by

full-height surface cracks. The EIFS layer is beneficial since it delays the damage to fasteners and stabilizes the sheet buckling on the exterior face (Singh et al., 2022d). Although the steel sheet was not entirely visible at this stage, the development of tension field action was audible and attributed to the cyclic buckling of the sheet. A wide tension field is expected to have developed in the steel sheet, part of which was visible at wall-line ends where the EIFS layer had separated. Extensive damage in gypsum board fasteners was also observed with 70-80% of the screws pulling through the panels. At the above design performance level, the EIFS layer had separated by about a quarter of the wall height from each corner, and a few glass-mat panel fasteners failed in head shear. Additionally, the EIFS layer had warped out-of-plane as the layer separation began at the wall-line perimeter and propagated towards the middle. Severe gypsum board crushing against the ledger was also observed. During the large drift demand cycle ($\Delta = 4\%$), the EIFS layer separated along the entire height and was only connected to the gravity segment framing in the middle of the wall-line. The exposed steel sheet of the shear wall segments, having gone through several cycles of plastic deformation, exhibited enlarged holes around screw heads along the edges of the steel sheet. Gypsum panels at both wall-line ends ultimately fractured due to crushing against the ledger. For specimen SGGS-2F, one panel detached along one edge. However, complete detachment of gypsum panels at this drift was also observed in other finished specimens. At the end of testing, the finish layers were removed to observe the underlying framing member damage. Notably, studs in the gravity segment suffered local buckling, and framing screws connecting stud packs and tracks had failed in head shear. This observed damage in framing members of finished specimens was quite similar to the framing member damage observed in unfinished specimens.

4.3 Evolution of Dynamic Characteristics

The progression of damage in wall specimens can also be observed through the evolution of their dynamic properties as characterized through their natural period and damping ratio of

the fundamental mode. Low-amplitude white noise tests with RMS intensity of 3%g and four minutes duration were performed before and following each earthquake test, achieving a specific performance level, to determine the dynamic properties of the wall-line specimens. The natural periods and damping ratios of the wall-line were identified using the time-domain optimization method with the assumption that they behave as single degree-of-freedom linear oscillators in response to earthquake input excitation. In the optimization algorithm, the objective function is defined as the RMS error between the simulated acceleration of the linear oscillator and the

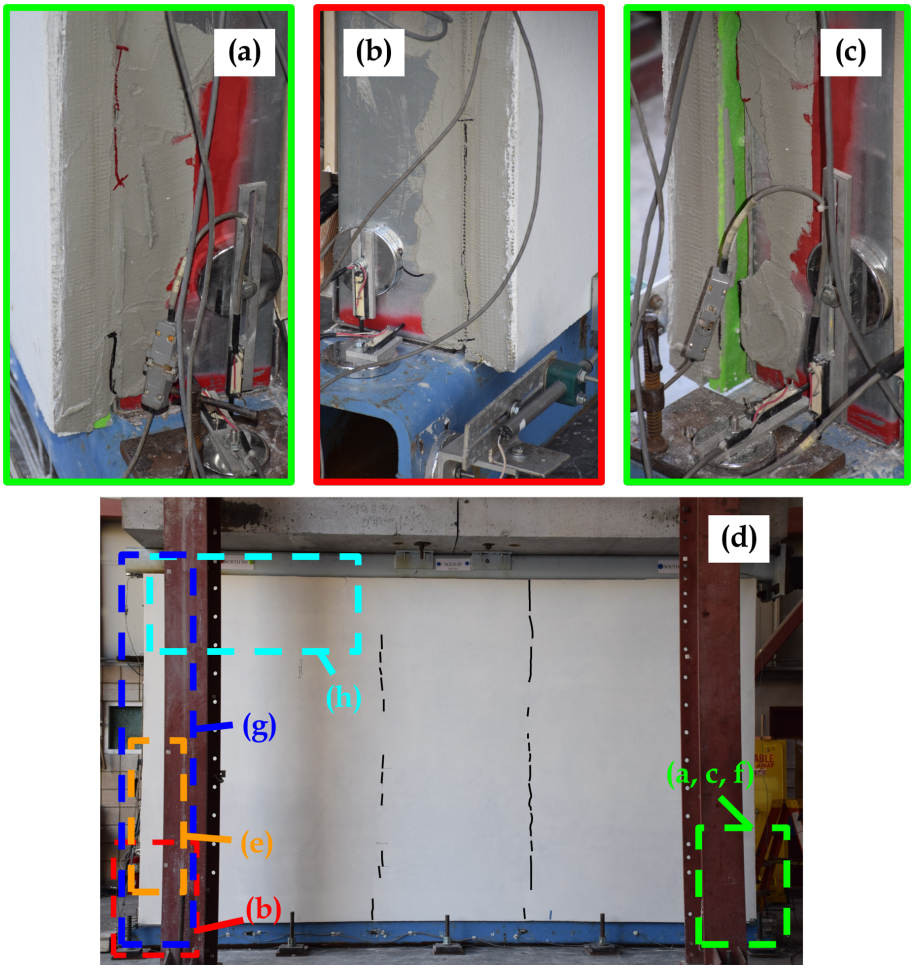


Figure 4.6. EIFS layer damage in specimen SGGS-2F at (a) elastic ($\Delta = 0.21\%$) and (b) quasi-elastic ($\Delta = 0.62\%$): thin EIFS cracks at wall-line corners, (c) and (d) design ($\Delta = 1.41\%$): visible separation from framing and full-height EIFS surface cracks, (e) and (f) above design ($\Delta = 2.04\%$) performance levels: EIFS detachment from corners towards mid-height, (g) and (h) at drift ratio $\Delta = 4.0\%$: full-height separation and steel sheet pullover damage

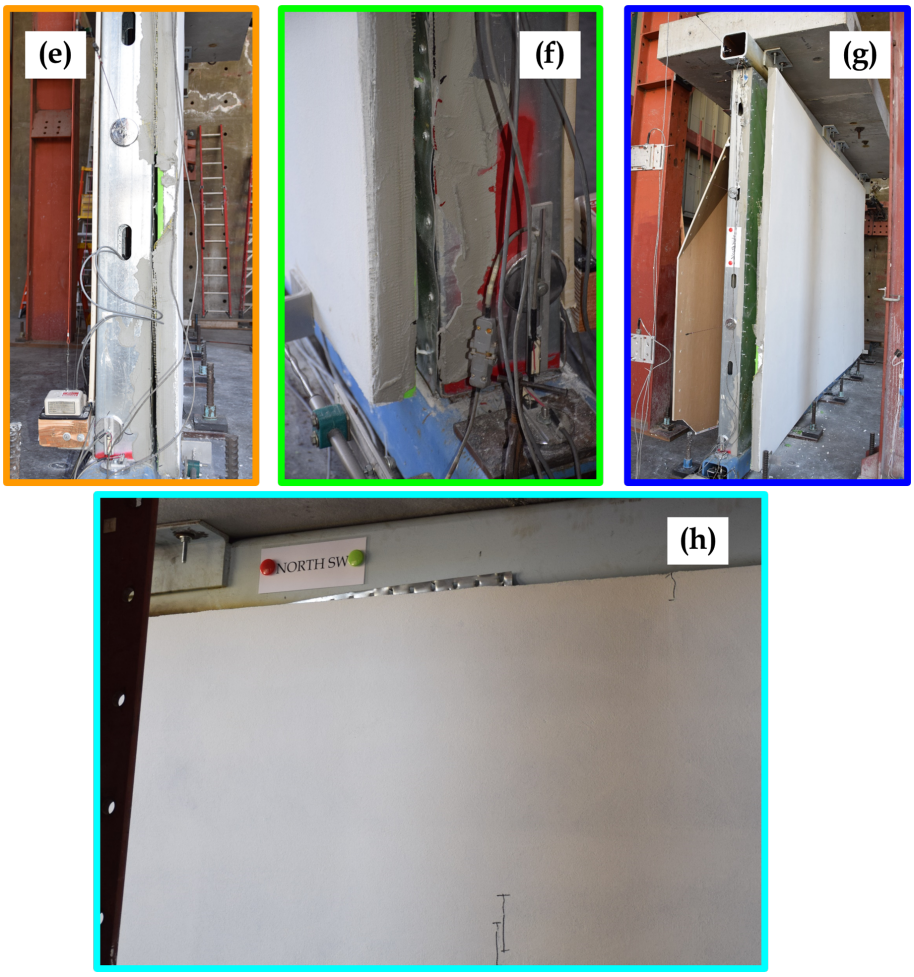


Figure 4.6. EIFS layer damage in specimen SGGS-2F at (a) elastic $(\Delta = 0.21\%)$ and (b) quasi-elastic $(\Delta = 0.62\%)$: thin EIFS cracks at wall-line corners, (c) and (d) design $(\Delta = 1.41\%)$: visible separation from framing and full-height EIFS surface cracks, (e) and (f) above design $(\Delta = 2.04\%)$ performance levels: EIFS detachment from corners towards mid-height, (g) and (h) at drift ratio $\Delta = 4.0\%$: full-height separation and steel sheet pullover damage (cont.)

Note: Colored boxed regions in part (D) show location of damage presented in other subfigures with like outline color.

measured acceleration response within the significant motion duration window (5% - 95% Arias intensity). Figure 4.8 shows the evolution of these dynamic properties with normalized lateral force (V/V_u), identified at different damage stages, for all shake table test phase specimens except SWWS-1 (ST). As mentioned earlier, testing of configuration SWWS-1 could not be completed during the shake table test phase. Only the fundamental natural period identified at the undamaged state (T_o) is presented in the discussion. In the discussion that follows, the

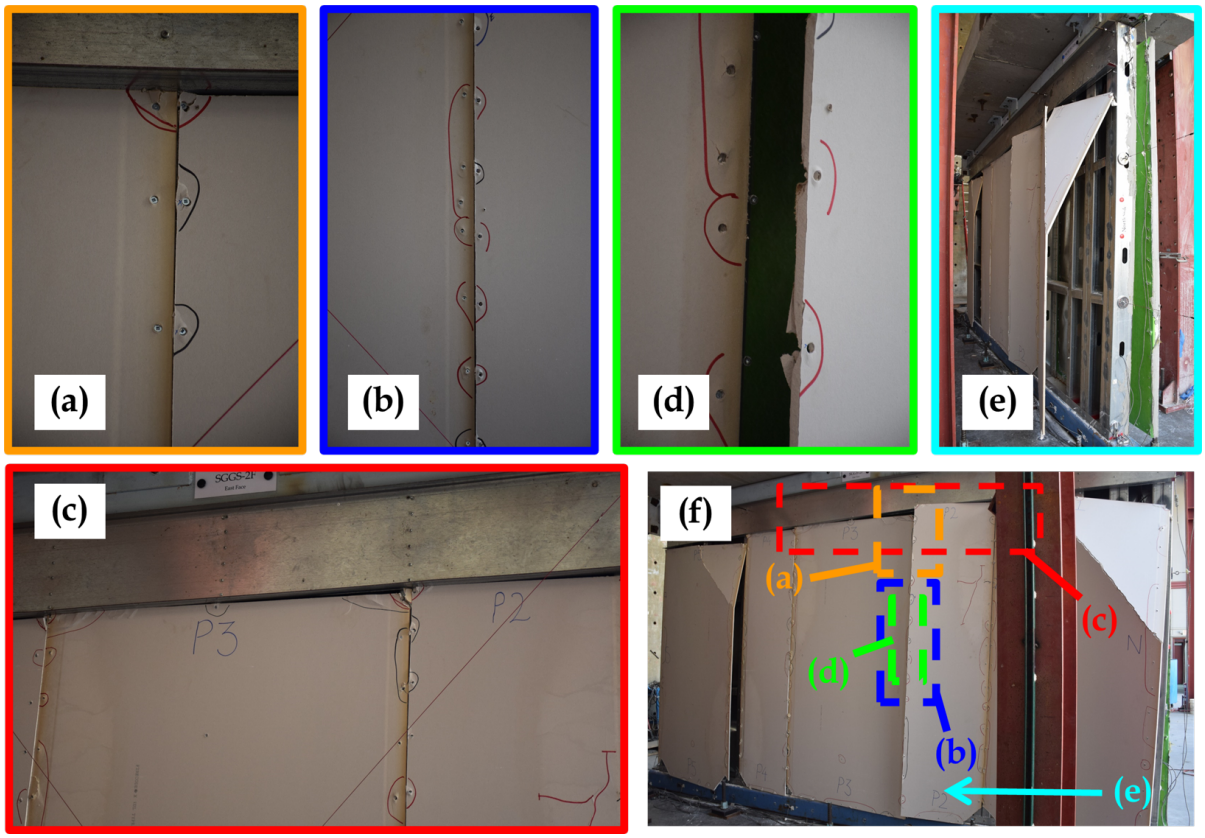


Figure 4.7. Gypsum panel damage in specimen SGGS-2F at (a) quasi-elastic ($\Delta = 0.62\%$) and (b) design ($\Delta = 1.41\%$): partial screw pull-through, (c) above design ($\Delta = 2.04\%$) performance levels: crushing against ledger track, (d)-(f) drift ratio $\Delta = 4.0\%$: screw pull-through along entire height and gypsum board fracture

Note: Colored boxed regions and arrow in part (f) show location of damage presented in other subfigures with like outline color.

dynamic properties of unfinished specimens are presented, followed by the finished specimens within the shake table test phase.

For reference, it is noted that the baseline specimen SGGS-1 natural period is 0.157s in its undamaged state. The natural period at the elastic performance level increased by less than 5% following EQ2: CUR-EW, and subsequently elongated by 10% from its undamaged state at the quasi-elastic performance level following EQ3. At the design performance level, the natural period for specimen SGGS-1 elongated to 0.199s following earthquake test EQ4, an increase of 27%, while the wall lateral resistance reached 85% of strength ($0.85V/V_u$). Specimen SGGS-1 offered a ζ_o = 2.1% fundamental mode damping in its undamaged state. This increased to 3.1%

and 5.3% at the quasi-elastic and design performance levels, respectively. Evolution of the natural period progressed similarly for specimen SGGS-1XS, as its natural period elongated from 0.143s in its undamaged state to 0.171s following earthquake test EQ4. The natural period elongated by 7% at the quasi-elastic level, and by 20% at the design performance level when the lateral force demand reached 75% strength following test EQ4. The damping available in this specimen increased from 1.6% in its undamaged state to 3.3% at the design performance level.

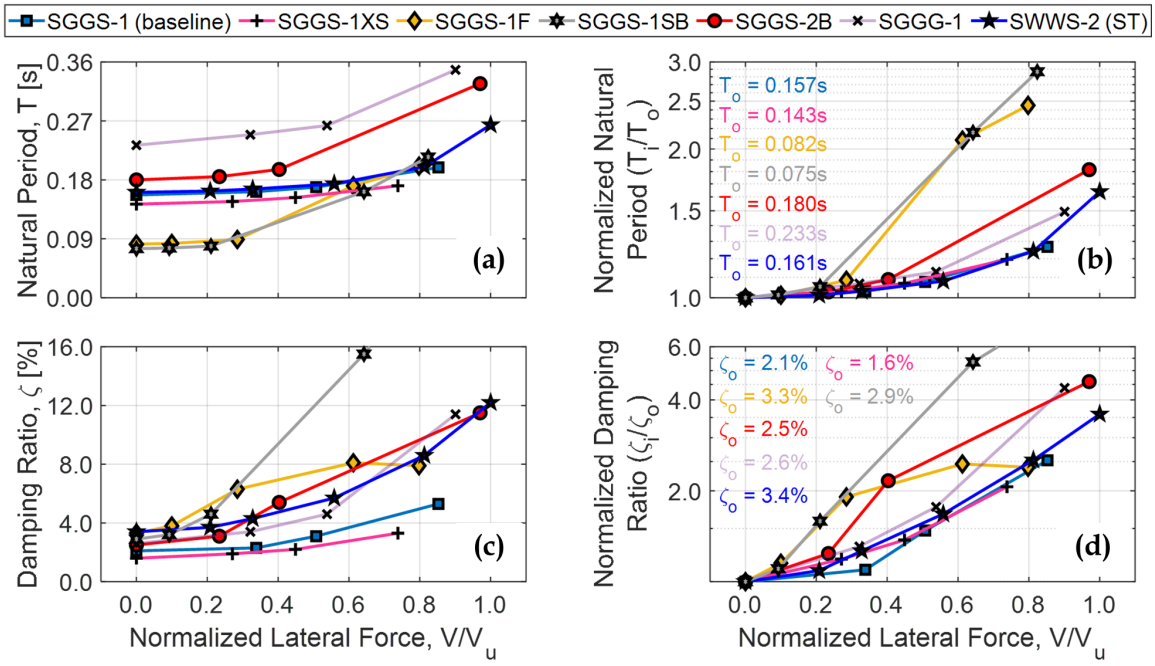


Figure 4.8. Evolution of (a) and (b) natural period, and (c) and (d) damping ratio for shake table test phase specimens

Note: T_o = natural period and ζ_o = damping ratio in initial (undamaged) state of specimen.

Specimens SGGS-2B and SGGG-1 both used fewer tension rods and fewer screw fasteners for attaching the steel sheet sheathing to the CFS framing, the former being a Type II specimen with tension tie-rods only at the wall-line ends, and the later being a specimen with only one asymmetrically placed shear wall segment placed at one end. As a result, these specimens demonstrated significantly lower strength and stiffness compared to the baseline specimen. For both these specimens, the natural period elongated less than 10% at the elastic and between 15-25% at the quasi-elastic performance levels. At the design performance level, the natural

period for specimen SGGS-2B increased from 0.180s to 0.327s. Similarly, the natural period for specimen SGGG-1 increased from 0.233s to 0.348s at the design performance level. The natural period elongated by 80% and 50% for specimens SGGS-2B and SGGG-1 respectively. Despite the variation in detailing compared to a typical symmetric, Type I wall-line, the rate of increase in damping with increasingly damaged specimen progressed in a similar manner. The damping ratio increased from 2.5% in the undamaged state, to 3.2% at elastic, 5.8% at quasi-elastic, and 11.5% at the design performance levels. These specimens demonstrated a larger damping ratio after incurring heavy damage to their framing during earthquake test EQ4.

The natural period and damping ratio for specimen SWWS-1 were 0.148s and 3.5% in its undamaged state, respectively. The difference in the dynamic properties in undamaged state between specimen SWWS-1 and baseline specimen SGGS-1 can be attributed to the additional framing detailing (jamb studs and sill track) to support the force transfer around window opening. Specimen SWWS-2 was also a Type II specimen, similar to SGGS-2B, however with tighter fastener edge spacing. The natural period for specimen SWWS-2 increased from 0.161s in undamaged state to 0.264s following test EQ6. Similarly, the damping ratio increased from 3.4% in the undamaged state to 12.2% following test EQ6.

Specimens SGGS-1F and SGGS-1SB were the stiffest amongst those tested during the shake table test phase, with a natural period of T_o = 0.082s and 0.075s in their undamaged state, respectively. This approximate four times increased stiffness compared to baseline specimen was due to the application of interior and exterior finishes. Specimen SGGS-1F reported less than a 10% natural period elongation at the elastic performance level following test EQ3: CNP196. It should be noted that although test EQ3: CNP196 was scaled to target the quasi-elastic performance level, the wall lateral resistance reached only 30% of the wall-line lateral strength, which is within the elastic performance level. However, as the specimen incurred progressive damage, in the form of the finish layer lose of adherence to the wall framing, its natural period approached that of its unfinished counterpart SGGS-1. The natural period elongated to 0.201s following test EQ5: CNP196 during which lateral force demand reached 80% strength. However,

in like fashion, it is noted that test EQ5: CNP196 targeted an above design performance level, however, the wall-line performance was closer to that of the design performance level. Specimen SGGS-1F reported a ζ_o = 3.3% damping in its undamaged state, which increased to 6.3% at the elastic and 8% at the quasi-elastic and design performance levels. Higher damping offered by SGGS-1F can be attributed to the use of significantly greater number of fasteners for gypsum and glass-mat panel installation. Evolution of the natural period progressed similarly for specimen SGGS-1SB, as its natural period elongated from 0.075s in its undamaged state to 0.215s following earthquake test EQ5: CNP196. Both specimens SGGS-1F and SGGS-1SB demonstrated abrupt changes in their dynamic properties when the finish layers began to detach.

4.4 Hysteretic Energy Dissipation

Progression of damage also manifests in the form of dissipation of hysteretic energy of the wall-line specimens, calculated as the area enclosed within the hysteresis loops of the force-displacement response. Similar to the presentation in the previous sections, the hysteretic energy dissipation of unfinished specimens is discussed first, followed by for the finished specimens. The reasoning for selection of the subset of wall-line configurations considered for analysis in each category is also provided.

For unfinished specimens under consideration, see Table 4.1, specimens SGGS-1 and SGGS-1XS were tested during the shake table test phase under slow monotonic pull conditions to obtain their post-peak behavior. Due to this, dissipated energy could not be calculated, and hence specimens SGGS-1 and SGGS-1XS are excluded from the hysteretic energy dissipation discussion. Additionally, specimen SWWS-1 (ST) is also excluded due to lack of complete testing data. Comparison of energy dissipation characteristics of the remaining wall-line specimens, however, is not feasible directly as they were tested under different loading protocols across the two test phases. To facilitate such a comparison, a two-step drift cycle qualification procedure is applied to the lateral drift histories of the wall-line specimens to remove the low-amplitude drift

cycles from those specimens tested within the shake table test sequence. The energy dissipated by the specimens during these low-amplitude drift cycles can be considered negligible (Hancock and Bommer, 2005). Implementation of this procedure is illustrated in Figure 4.9. The first step intends to determine the first instance when the specimen achieves or exceeds a drift demand greater than 40% of drift at strength Δ_{Vu}. The specimen is assumed to remain essentially linear with negligible energy dissipation prior to attaining this drift threshold, however, it is expected to behave nonlinearly during subsequent, increasing intensity tests. As such, the second step aims at identifying the significant half cycles of drift whose dissipated energy exceeds 2.5% of the sum of energy dissipated in the half cycles during which peak strength is attained in the positive and negative directions. A low threshold of 2.5% ensures that the total energy dissipated during the identified significant drift cycles is more than 95% of total energy dissipated during the entire testing protocol, and yet still, any drift cycles with negligible energy dissipation are removed.

The number of significant drift cycles is used as a metric to validate the procedure. In the cycle number counting, drift bins are defined in compliance with the distinct target drifts for the prescribed performance levels, see Table 2.7. Figure 4.10 compares the number of significant drift cycles for the wall specimens tested in the shake table and quasi-static test phases. Specifically, two specimens in the quasi-static test phase, namely, SGGS-2 and SWWS-2 (QS), and comparable specimens SGGG-1 and SGGS-2B from the shake table test phase are chosen for the purpose of comparison. It can be seen from Figure 4.10 that although the shake table test sequence imposed more drift cycles than those under the quasi-static loading tests, in particular within the moderately nonlinear drift response range (i.e., 0.3-0.7 Δ_{Vu} bin), the testing protocols remained consistent in terms of the fractional (normalized) drift cycle distribution within individual drift bins.

Following the drift cycle qualification procedure, the energy dissipation characteristics of the unfinished wall specimens tested under different loading protocols can be quantified. Figure 4.11 compares the evolution of cumulative hysteretic energy versus cumulative drift for unfinished wall specimens. Figure 4.11 also presents the energy dissipation rate with cumulative

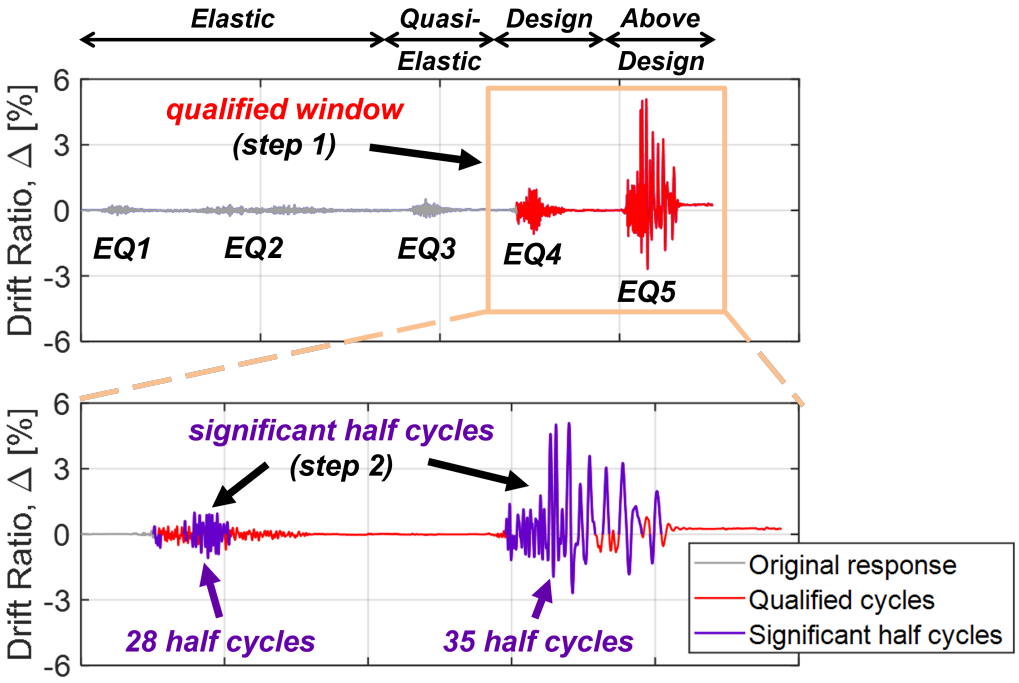


Figure 4.9. Illustration of the drift cycle qualification procedure for specimen SGGG-1

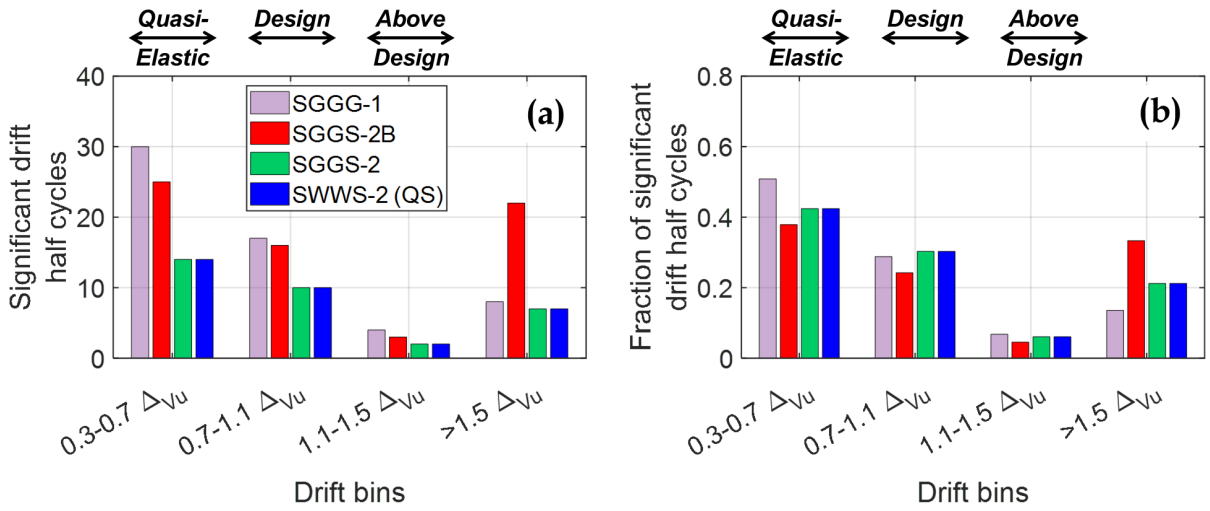


Figure 4.10. Comparison of (a) significant drift cycle distribution, and (b) fractional (normalized) significant drift cycle distribution for select wall specimens tested during shake table and quasi-static test phases

drift normalized by the average cumulative drift at strength in the two directions ($\Sigma\Delta/\Sigma\Delta_{Vu}$). The energy dissipation rate is calculated as the slope of the cumulative dissipated energy versus the cumulative drift for the primary cycles of the CUREE loading protocol. It should be noted

that the two-step drift cycle qualification procedure is applied to both the shake table and quasi-static protocols, and thus the cumulative hysteretic energy accounts for the energy contribution from significant drift cycles in both loading cases. The results reveal that the evolution of hysteretic energy is highly consistent for specimens with similar lateral strength and stiffness up to the above design performance level, and provides validation for the procedure. The energy dissipation discrepancies in the post-peak region can be attributed to the large variability of the hysteretic behavior of individual specimens when their damage becomes intensive.

Figure 4.11 shows that Type I symmetric specimens SGGS-1HD and SWWS-1 had significantly larger dissipated energy compared with Type II symmetric specimens SGGS-2, SGGS-2B and SWWS-2 (QS and ST), as well as Type I unsymmetrical specimen SGGG-1. Rate of energy dissipation calculation is also presented for the quasi-static phase specimens in Figure 4.11. The rate of energy dissipation increased until the specimens reached post-peak region (above design performance level), and started decreasing in the next drift cycle for the unfinished specimens. This is directly correlated to the number of engaged sheathing fasteners at different performance levels. As the width of the tension field increased and engaged more fasteners from the undamaged state to the above design performance level, the rate of energy dissipation increased. However, as the sheet pull over screw heads began at the above design performance level, the number of engaged sheathing fasteners began to decrease, and hence, the rate of energy dissipation also decreased. At the design performance level, specimens SGGS-1HD and SWWS-1 demonstrated 0.38 kN-m/cm rate of energy dissipation. At elastic and quasi-elastic performance levels, the rate of energy dissipation was 75% and 55% lower on average respectively. At the above design performance level, the rate of energy dissipation was 6% higher on average. Specimens SGGS-2 and SWWS-2 (QS) demonstrated 0.24 kN-m/cm rate of energy dissipation at design performance level. At elastic and quasi-elastic performance levels, the rate of energy dissipation was 85% and 65% lower on average respectively. At the above design performance level, the rate of energy dissipation was approximately the same as that at the design performance level. Gravity wall-line specimen GGGG demonstrated substantially lower

energy dissipation rates, with gypsum panel fasteners as the only source of energy dissipation. At the design performance level, specimen GGGG reported 0.11 kN-m/cm rate of energy dissipation, beyond which it started to reduce as the gypsum panels detached from CFS framing. At quasi-elastic and above design performance levels, the rate of energy dissipation was 30% and 20% lower on average, respectively.

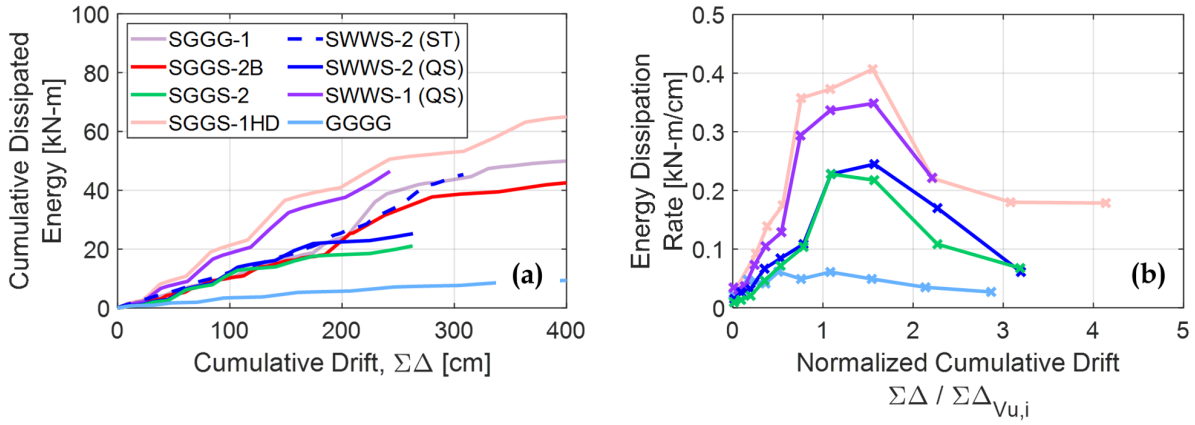


Figure 4.11. (a) Cumulative dissipated energy, and (b) energy dissipation rate for unfinished specimens
Note: Energy and drift are calculated for significant drift cycles only in Part a.

Among the finished specimens under consideration, see Table 4.2, specimens SGGS-1F and SGGS-1SB were tested during the shake table test phase under slow monotonic pull conditions to obtain their post-peak behavior. Due to this, dissipated energy could not be calculated. Hence, specimens SGGS-1F and SGGS-1SB are not considered in the hysteretic energy dissipation discussion for finished specimens. Since the other finished specimens were subjected to the same loading protocol during the quasi-static test phase, their energy dissipation characteristics can be cross compared at different performance levels directly. Figure 4.12 shows the cumulative dissipated energy and energy dissipation rate for finished specimens. It can be observed from Figure 4.12 that the specimen SGGS-1HDF, which was a Type I symmetric wall-line with hold-downs at its shear wall ends, had significantly larger dissipated energy compared with Type II symmetric specimens SGGS-2F and SWWS-2F, as well as the Type I asymmetrical specimen SGGG-1F. The rate of energy dissipation followed a similar trend. It can also be

seen that the rate of energy dissipation increased until the specimens attained its lateral strength. Beyond which, the rate of energy dissipation reduced steadily for all specimens. Compared to unfinished specimens, finished specimens demonstrated a larger rate of energy dissipation, since the finished specimens used additional fasteners at the gypsum and glass-mat panel installation locations. The rate of energy dissipation correlates well with the observed EIFS and gypsum panel damage at different performance levels. Beginning from the undamaged state to the design performance level, the number of sheathing and finish layer fasteners dissipating hysteretic energy increased and hence, the rate of energy dissipation increased. However, as the EIFS layer and gypsum panels detached from framing and sheet pull over sheathing screw heads began at the above design performance level, the rate of energy dissipation also decreased. At the design performance level, specimen SGGS-1HDF reported 0.59 kN-m/cm rate of energy dissipation. At elastic and quasi-elastic performance levels, the rate of energy dissipation was 40% and 15% lower respectively. At above design performance level, the rate of energy dissipation was also 15% lower. Specimens SGGS-2F, SWWS-2F and SGGG-1F demonstrated 0.31-0.42 kN-m/cm rate of energy dissipation. At elastic, quasi-elastic and above design performance levels, the rate of energy dissipation was 70%, 50% and 10% lower on average, respectively. Gravity wall-line specimen GGGG-F demonstrated substantially lower energy dissipation rates, due to the lack of steel sheet sheathing fasteners as sources of hysteretic energy dissipation. At the design performance level, specimen GGGG-F reported 0.19 kN-m/cm rate of energy dissipation, beyond which the EIFS layer and gypsum panels became detached from CFS framing. At elastic, quasi-elastic and above design performance levels, the rate of energy dissipation was 70%, 35% and 20% lower on average, respectively.

In particular, since the specimens in the quasi-static test phase were subjected to the same loading protocol, the energy dissipation results can be further synthesized by performance level and aggregated based on their common specimen variable, as shown in Figure 4.13. These figures show that wall configurations with finish application were consistently capable of dissipating about 2-3 times more energy as compared to their unfinished counterparts. The equivalent

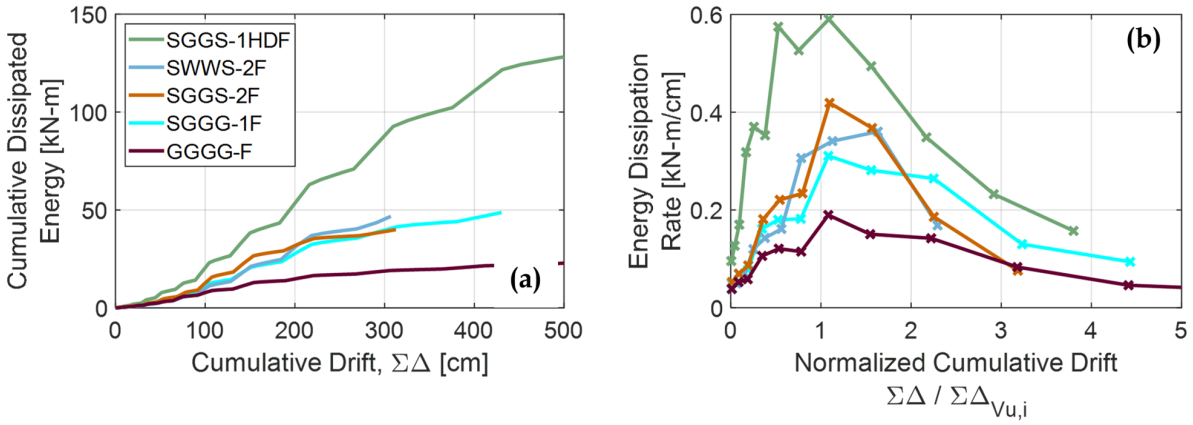


Figure 4.12. (a) Cumulative dissipated energy, and (b) energy dissipation rate for finished specimens

hysteretic damping ζ can also be computed on a per cycle basis using the global hysteretic response, as shown in Eq. 4.1.

$$\zeta = \frac{A_{\text{loop}}}{2\pi F_{\text{max}} D_{\text{max}}} \tag{4.1}$$

where, A_{loop} is the energy dissipated within a cycle in the hysteretic response, and F_{max} and D_{max} are the maximum absolute force and the maximum absolute displacement in the cycle, respectively. Figure 4.14 shows the comparison of equivalent hysteretic damping ζ with respect to cumulative drift ratio normalized by the average cumulative drift ratio at strength in the two directions for the Type II specimen pair, SGGS-2 and SGGS-2F. It can be observed from this figure that the equivalent hysteretic damping is larger for finished specimens at lower drift cycles and up to strength. Beyond strength, the equivalent hysteretic damping is similar for the two specimens. This same behavior is also observed for a Type II with window opening wall pair and a Type I with hold-downs wall specimen pair. A comparison of the hysteretic loops at elastic and above design performance levels is also shown in Figures 4.14b-c, respectively. These isolated full cycles articulate that the pinched behavior of the loops, and not the dissipated energy, governs the relative difference between the finished and unfinished configuration. Calculated equivalent hysteretic damping for the specimens tested during the quasi-static test phase of the CFS-NHERI

wall-line experimental program are provided in Appendix C.

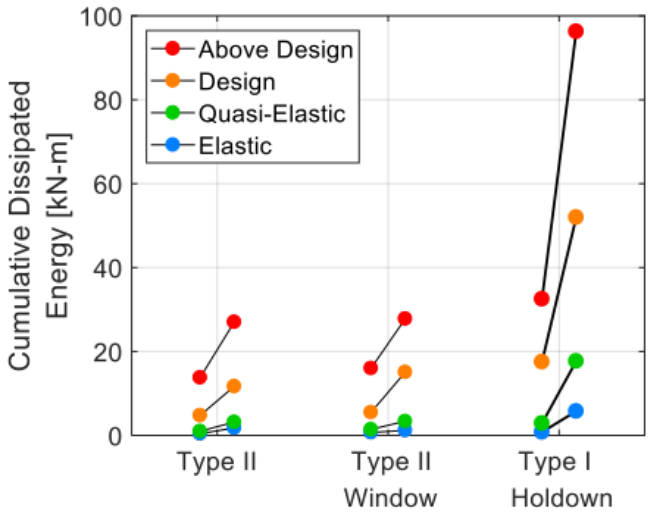


Figure 4.13. Cumulative dissipated energy comparison for select specimens from quasi-static test phase

4.5 Summary Remarks

The two-phased experimental program examined CFS-framed wall-line assemblies with varying arrangements and considered a wide range of variables, which govern the structural and nonstructural detailing. This chapter systematically documents the progressively incurred physical damage observed in the tested wall-line assemblies at different performance levels. A cross-comparison of physical damage with hysteretic energy dissipated and the evolution of the dynamic properties was also studied. The damage in fastener connections between steel sheet sheathing and CFS framing in unfinished wall-lines was examined and the number of fasteners demonstrating the two identified predominant damage modes were quantified. Damage statistics were accompanied with photographs showing the fastener and framing member damage progression in an unfinished wall-line. For finished specimens, the progression of damage in EIFS and gypsum panel layers was presented.

An important objective of the experimental program was to characterize the dynamic performance of CFS-framed wall-lines. To this end, the evolution of dynamic characteristics at

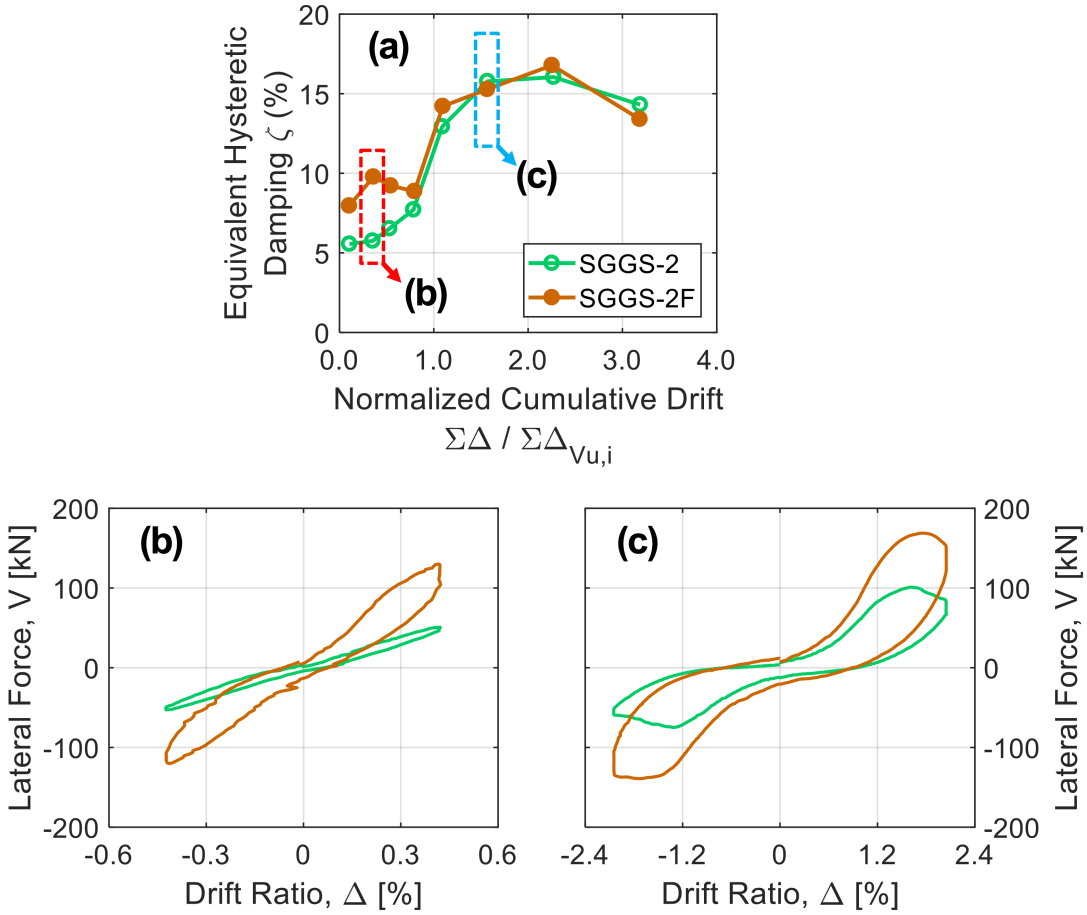


Figure 4.14. Comparison of (a) equivalent hysteretic damping, (b) and (c) hysteretic loops at elastic and above design performance levels between SGGS-2 and SGGS-2F wall configurations

different performance levels for specimens tested during the shake table test phase were discussed. Progression of damage was also correlated with hysteretic energy dissipation characteristics of the wall-line specimens at different performance levels. A two-step procedure, which aimed at identifying drift cycles with significant dissipated energy, was adopted to allow for energy dissipation comparisons for specimens tested using different loading protocols between the shake table and quasi-static test phases. The hysteretic energy dissipation of unfinished and finished specimens was discussed within this chapter.

Acknowledgment of Publications

Portions of the following manuscript and technical reports, for which the dissertation author was the primary investigator and author, are contained in Chapter 4:

Singh, A., Wang, X., Zhang, Z., Schafer, B. W., and Hutchinson, T. C. "Physical Damage-Hysteretic Response Correlation for Steel Sheet Sheathed Cold-Formed Steel-Framed Wall-Lines" *Earthq. Eng. Struct. Dyn.* In preparation for submission.

Singh, A., Wang, X. and Hutchinson, T. C. (2021). *Lateral Response of Cold-Formed Steel Framed Steel Sheathed In-line Wall Systems Detailed for Mid-Rise Buildings. Part I: Shake Table Test Phase* (Structural Systems Research Report SSRP-19/05). University of California San Diego, La Jolla, CA.

Singh, A. and Hutchinson, T. C. (2022). *Lateral Response of Cold-Formed Steel Framed Steel Sheathed In-line Wall Systems Detailed for Mid-Rise Buildings. Part II: Quasi-Static Test Phase* (Structural Systems Research Report SSRP-19/06). University of California San Diego, La Jolla, CA.

Chapter 5

Design-Grade Numerical Model of CFS-Framed Mid-Rise Buildings

5.1 Introduction

Previous chapters have discussed the experimental investigation of the seismic behavior of CFS-framed wall-line assemblies. The impact of structural and nonstructural variables within the test matrix on wall-line lateral behavior was discussed through comparisons between select groups of specimens. This chapter builds on the learnings from the experimental program to numerically model CFS-framed wall-lines assemblies. This numerical model, developed in OpenSeesPy (Zhu et al., 2018), can be used for numerical response predictions of seismic response of mid-rise CFS buildings to support a design engineers needs. The numerical model has been validated against the measured response of a full-scale 3D mid-rise CFS-framed building tested at the Large High-Performance Outdoor Shake Table (LHPOST) at the University of California, San Diego (UCSD). Section 5.2 presents a brief overview of the experimental program, named in short as CFS-HUD. Section 5.3 provides detailed discussion of the modeling strategies adopted in the development of the test building numerical model. Validation of the model through comparison with measured response from shake table tests is included in Section 5.4. The model aims to provide a robust, yet computationally efficient approach, with minimal degrees-of-freedom, while also capturing the salient features of seismic response of mid-rise CFS-framed buildings suitable for design-grade predictions of response.

5.2 CFS-HUD Experimental Program

The CFS-HUD experimental program involved system-level earthquake and live fire testing of a full-scale six-story CFS-framed building at the NHERI LHPOST facility at UC San Diego. Complete discussion of building design and construction, framing details and the tie-rod and compression stud pack assemblies details can be found in Wang et al. (2018b) and Wang et al. (2018a). In addition, a concise summary of the findings of this experimental program is available in Hutchinson et al. (2021) and Wang and Hutchinson (2021). The essential features of the experimental program are described herein. The CFS-HUD test building was designed per existing code provisions within design standards ASCE/SEI 7-10, AISI S100-12 and AISI S213-07 at an assumed hypothetical location in high seismic region near downtown Los Angeles, CA. The test building had a 10.4 m $\times$ 7.3 m (34 ft $\times$ 24 ft) floor plan, which occupied almost the entire 12.2 m $\times$ 7.6 m (40 ft $\times$ 25 ft) shake table footprint. It had a 3.05 m (10 ft) floor-to-floor height with a 1.2 m (4 ft) tall roof parapet, for a total building height of 19.5 m (64 ft). Figure 5.1 shows the isometric view of the building and the schematic floor plan. The building had a symmetric floor plan with a 1.2 m (4 ft) wide corridor along the longitudinal centerline with a room in each quadrant of the floor.

Two longitudinal shear walls of 3.96 m (13 ft) length were placed at the west end and two longitudinal shear walls of 3.35 m (11 ft) length were placed at the east end along the corridor (west and east corridor shear walls). Additionally, short shear walls with a length of 1.63 m (5 ft 4 in.) in the longitudinal direction and 2.13 m (7 ft) in the transverse direction were placed at the four corners of the building (corner shear walls). All shear walls utilized structural panels, fabricated using 16 mm (5/8 in.) thick gypsum boards bonded with a 0.686 mm (0.027") thick steel sheet, as sheathing installed over CFS framing members. The structural panels on the corridor shear walls were attached to framing using No. 8 gauge self-tapping metal screws at a fastener spacing of 406 mm (16") o.c. in field but a varying fastener spacing on the boundary: 76 mm (3") o.c. for the lower three levels, 102 mm (4") for level 4, and 152 mm (6") o.c. for

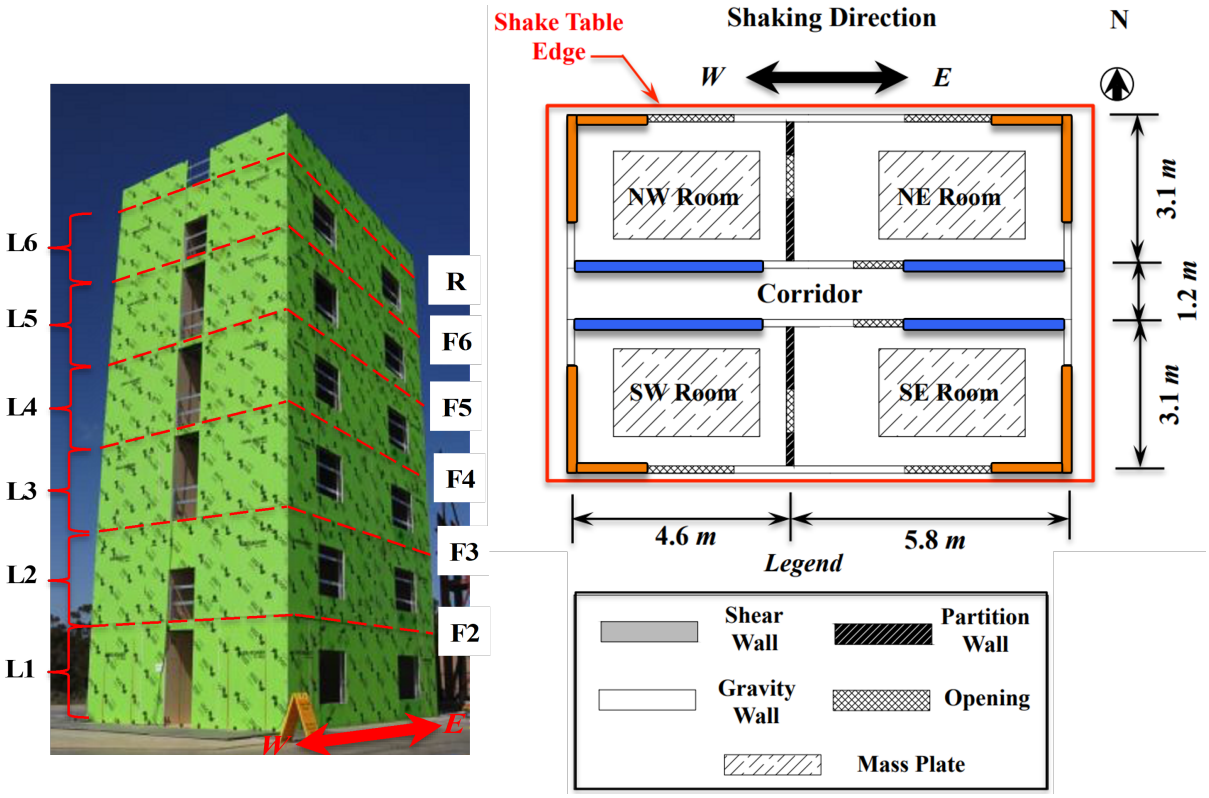


Figure 5.1. Isometric view and schematic floor plan of test building (Wang et al., 2018b)
Note: Corridor and corner shear walls are shown in blue and orange color respectively.

the upper two levels. The structural panels on the corner shear walls were attached at a fastener spacing of 406 mm (16") o.c. in field and 152 mm (6") o.c. at all levels. In addition, 16 mm (5/8") thick regular gypsum boards were installed on the interior (room) side of the shear walls using No. 8 gauge drywall screws at a fastener spacing of 152 mm (6") o.c. on boundary and 406 mm (16") o.c. in the field. The corridor shear walls served as the primary lateral force resisting system (LFRS) in the direction of shaking, while the corner shear walls were assumed to resist any transverse and torsion loads during the earthquake tests. Gravity wall segments, which were present in between openings on the perimeter of the building as well as in between corridor shear walls, were sheathed with gypsum panels on both sides of framing using No. 8 gauge drywall screws at a fastener spacing of 152 mm (6") o.c. on boundary and 406 mm (16") o.c. in the field.

To resist seismic overturning moment and uplift forces, the test building adopted con-

tinuous tie-rods and built-up compression stud pack assembly at the ends of each individual shear walls as the restraint system. These shear wall tie-down system components were capacity designed for the minimum of overstrength amplified seismic load or the maximum load the shear wall can deliver. The size of the built-up compression stud pack and tie-rod diameter changed from floor-to-floor for the corridor and corner shear walls. Photographs of the shear wall framing and tie-rod connection detailing are shown in Figure 5.2. Table 5.1 provides a summary of the shear wall and tie-down system detailing for each floor. The building construction largely involved the use of prefabricated structural wall and floor and roof diaphragm panels. The joists in the diaphragms spanned in the transverse direction. The diaphragm panels were connected to the wall panels by attaching the diaphragm end joist to the wall stud flange as a ledger framing system.

Table 5.1. Summary of the shear wall and tie-down system detailing

Shear wall	Level	Tie-rod specification[a]	Compression stud pack specification	Fastener spacing (mm)
Corridor (aspect ratio[b]= 0.91, 0.77)	6	ASTM A36 ϕ16 mm	(4) 600S200-54	152/406
	5	ASTM A36 ϕ29 mm	(8) 600S200-54	152/406
	4	ASTM A193 (Grade B7) ϕ29 mm	(8) 600S200-97	102/406
	3	ASTM A36 ϕ36 mm	(8) 600S200-97	76/406
	2	ASTM A193 (Grade B7) ϕ43 mm	(8) 600S200-97	76/406
	1	ASTM A722 (Grade 150) ϕ46 mm	(10) 600S200-97	76/406
Corner (aspect ratio = 1.88, 1.43)	6	ASTM A36 ϕ16 mm	(4) 600S200-54	152/406
	5	ASTM A36 ϕ16 mm	(4) 600S200-54	152/406
	4	ASTM A36 ϕ19 mm	(4) 600S200-54	152/406
	3	ASTM A36 ϕ25 mm	(4) 600S200-54	152/406
	2	ASTM A36 ϕ29 mm	(4) 600S200-54	152/406
	1	ASTM A722 (Grade 150) ϕ46 mm	(4) 600S200-68	152/406

[a] Elastic modulus of all steel rods is assumed to be 200 GPa.

[b] Aspect ratio is defined as the ratio of shear wall height and length.

The test building was subjected to seven pre-fire earthquake tests of increasing intensity, followed by post-earthquake live fire tests, and finally, two post-fire earthquake tests. Four seed

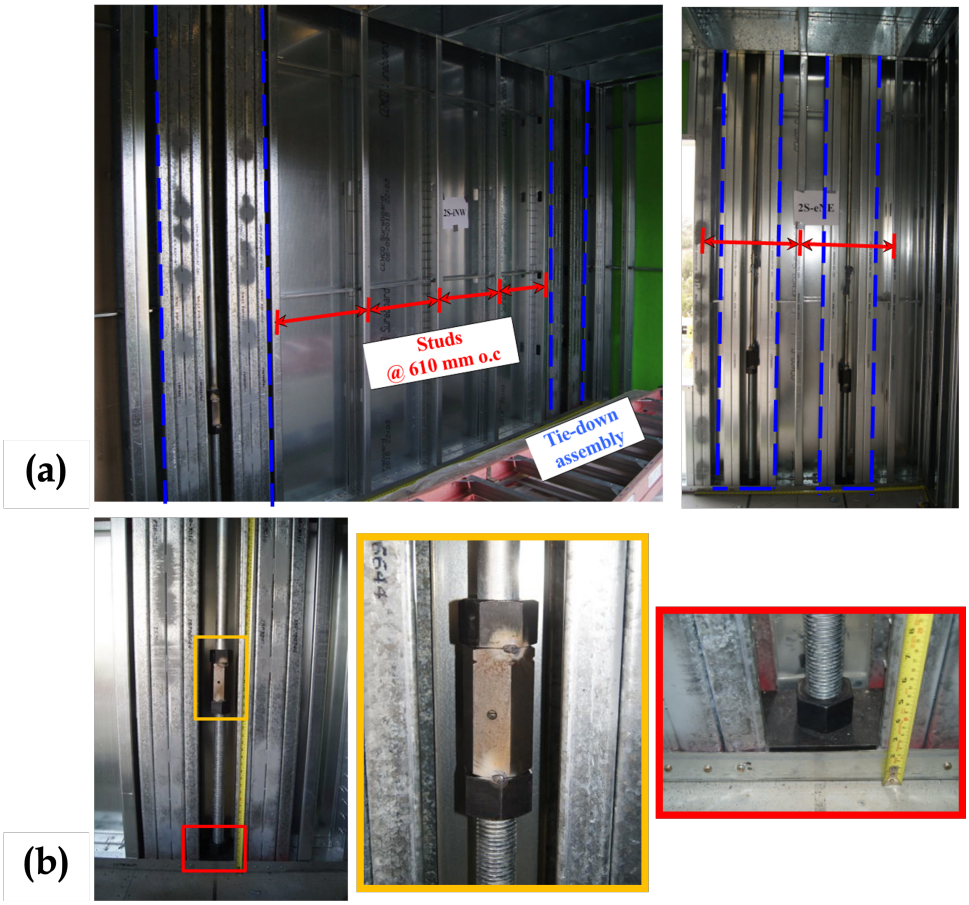


Figure 5.2. (a) Corridor shear wall and longitudinal corner shear wall framing at level 2, and (b) Tie-rod connection details: tie-rod assembly, coupler and double nut connection, and bearing plate connection (Wang et al., 2018b)

motions were selected for the earthquake tests, namely RIO from the 1992 Cape Mendocino earthquake (M_w=7.0), CNP and RRS from the 1994 Northridge earthquake (M_w=6.7), and CUR from the 2010 Maule earthquake (M_w=8.8) in Chile. The seed motions were scaled to measure and observe the seismic behavior of the test building at different performance levels, namely serviceability, design, and maximum considered (Wang et al., 2018b). Figure 5.3 and Table 5.2 provides a summary of the pre-fire test sequence, for which the experimental response of the building is compared with numerical model predictions in Section 5.4. Low-amplitude white-noise base excitation tests were conducted before and after the earthquake tests to investigate the evolution of dynamic characteristics at different damage states of the test building. To measure

the seismic response, a dense array of more than 250 analog sensors consisting of accelerometers, displacement transducers and strain gauges were installed on the test building. In addition, a Global Positioning System (GPS), more than 40 video cameras, unmanned aerial vehicles (UAVs) and light detection and ranging (LiDAR) systems were also employed to monitor the behavior of the building during the earthquake tests (Wang et al., 2020).

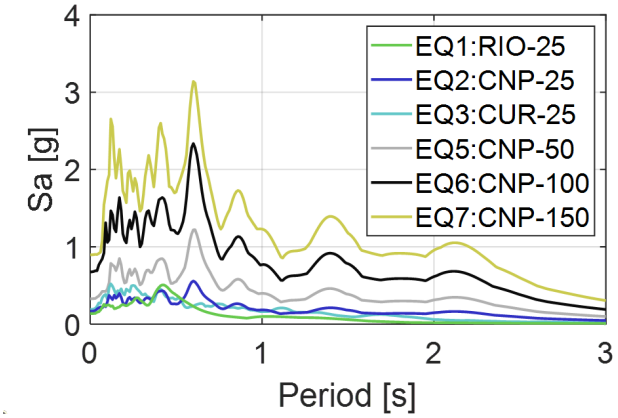
Table 5.2. Summary of achieved pre-fire test sequence input motions

Test Motion	Earthquake Event	Year	Station	Performance target	PIA (g)	PIV (cm/s)	PID (cm)
			Damage State S0				
EQ1:RIO-25	Cape Mendocino	1992	Rio Dell Overpass	SLE	0.14	10.98	1.29
EQ2:CNP-25	Northridge	1994	Canoga Park	SLE	0.17	22.14	4.68
			Damage State S2				
EQ3:CUR-25	Maule, Chile	2010	Curicó	SLE	0.19	11.39	1.90
EQ4:CNP-25	Northridge	1994	Canoga Park	SLE	0.17	23.41	5.00
EQ5:CNP-50	Northridge	1994	Canoga Park	50% DE	0.33	45.96	10.05
			Damage State S5				
EQ6:CNP-100	Northridge	1994	Canoga Park	DE	0.69	90.61	19.77
			Damage State S6				
EQ7:CNP-150	Northridge	1994	Canoga Park	MCE	0.91	131.90	31.00
			Damage State S7				

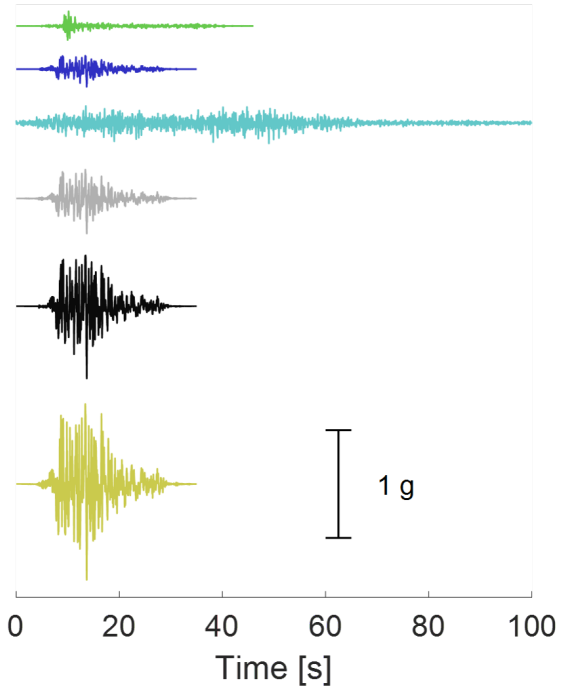
Note: PIA = peak input acceleration; PIV = peak input velocity; PID = peak input displacement;
SLE = service level earthquake; DE = design earthquake; MCE = maximum considered earthquake.
White-noise test after each earthquake test were used to estimate dynamic properties at damage states.

5.3 Design-Grade Numerical Model

A numerical model, which can accurately predict the seismic behavior of a CFS-framed building, while also optimizing the degrees-of-freedom to facilitate computational efficiency and support multiple ground motion analyses in the design phase, requires consideration of the major assemblies beyond the isolated shear walls. Thus, a refined numerical model would also need to include the strength and stiffness contribution from gravity walls as well as nonstructural components such as exterior and interior finishes installed over the shear wall and gravity wall segments. All of these components resist the shear deformation between the story diaphragms. For taller CFS-framed buildings, including the vertical stiffness components such as hold-downs or continuous tension tie-rod systems and built-up compression stud packs in the numerical model



(a)



(b)

Figure 5.3. (a) Elastic pseudo-acceleration spectra (ξ = 5%), and (b) acceleration time histories of achieved input motions

is also vitally important. The cumulative elongation of the tie-down systems over several stories can induce significant out-of-plane diaphragm rotation. The effect of diaphragm rotation on floor lateral displacement cannot be adequately captured by a numerical model for taller structures, which only considers shear deformation. Further refinement may be achieved by including

non-load bearing partition walls and explicitly modeling the in-plane diaphragm rigidity. The numerical model presented herein takes into account several of these features and interacting assemblies as they influence the dynamic behavior of multi-story CFS-framed buildings.

The CFS-HUD test building numerical model was developed using the OpenSeesPy framework. The model aimed to keep computational cost low by using only 181 nodes and 44 nonlinear elements (227 elements total) per floor. Figure 5.4 conceptually illustrates the elements considered in the model and their location overlaid on the building floor plan. It also provides an elevation view schematic of the corridor wall-line as modeled in OpenSees. The floor and roof diaphragms were considered as axially rigid in-plane, consistent with the observed behavior during the shake table tests. The partition walls on the two sides of the corridor separating the rooms on east and west side, as well as the framing around door and window openings were not considered in this numerical model. Modeling strategies adopted for the various lateral and vertical stiffness components considered is explained next.

5.3.1 Modeling of Shear Walls

As shown in Figure 5.4, the force-displacement behavior of shear walls is modeled using zero-length elements with a uniaxial material response defined using the *pinching4* material model (Lowes and Altoontash, 2003). The *pinching4* material model can capture a pinched global load-displacement response and exhibits damage through strength and unloading and reloading stiffness degradation under cyclic loading. Figure 5.5 shows the parameters required to define this material model in OpenSees. These parameters influence the force-displacement envelope as well as the degradation factors. The wall-line top track is modeled using rigid elements to ensure deformation compatibility of the shear and gravity segments along the same wall-line. The connection to the foundation is modeled as a pin connection. A zero-length rigid truss element is used to provide a similar pin connection between shear walls on adjacent floors. Two rigid elements connect the zero-length element to the top track and the rigid truss element. The length of these rigid elements was selected as half of the story height. The *pinching4* material

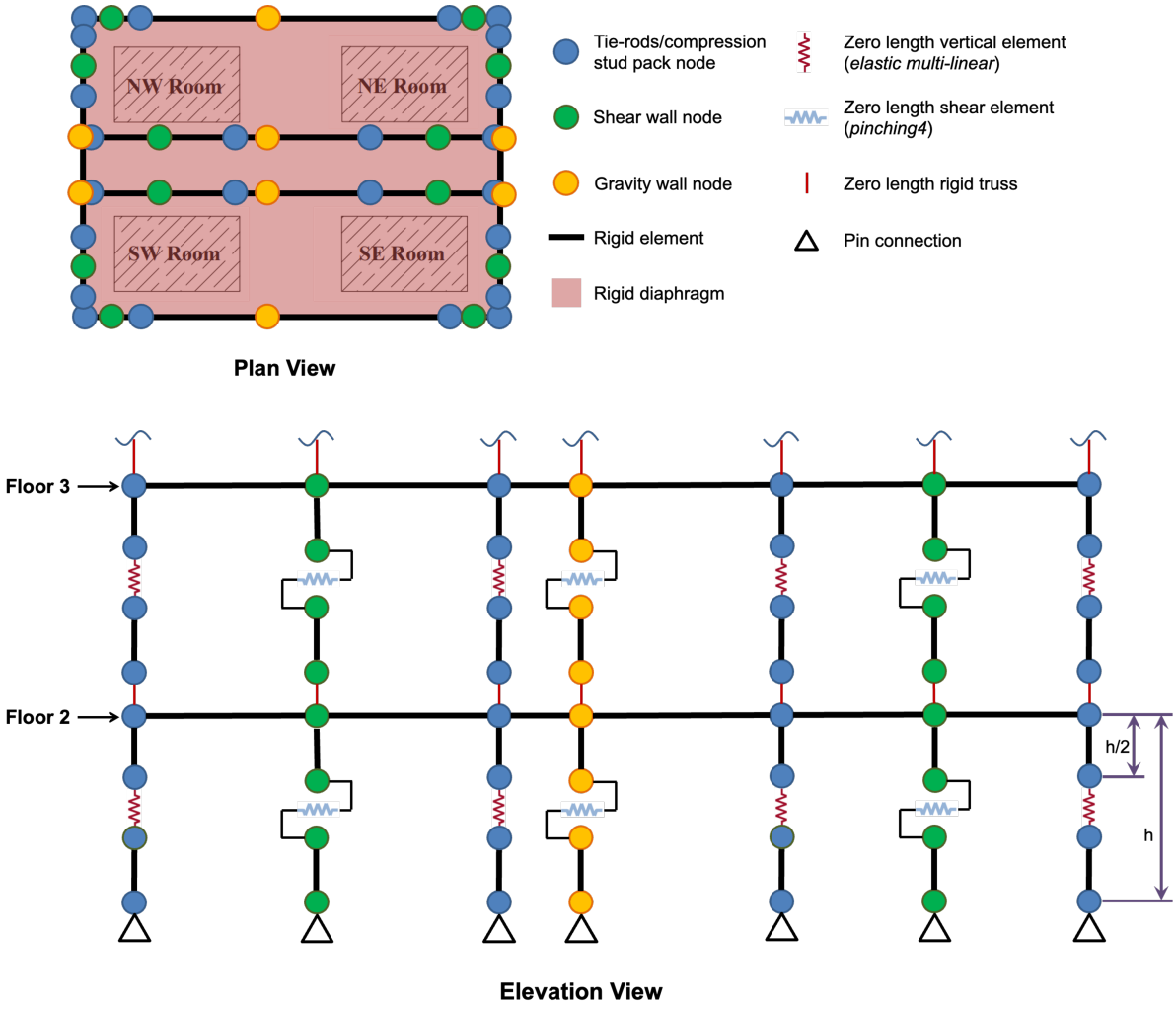


Figure 5.4. Elements considered in OpenSees numerical model

model parameters, assigned to the horizontal spring in the center of the zero-length element, represented the lateral force-displacement behavior in the longitudinal and transverse directions of the test building.

The *pinching4* material model parameters were defined using shear wall component test data from wall tests conducted by Hoehler et al. (2017) at the National Fire Research Laboratory (NFRL) at the National Institute of Standards and Technology (NIST) in Gaithersburg, Maryland. These specimens were designed in consultation with details adopted in the design of the CFS-HUD test building and constructed by the same panelizer. Shear wall specimens, 3.7 m (12 ft) long and 2.7 m (9 ft) tall, designed to mimic the lateral behavior of shear walls along the second

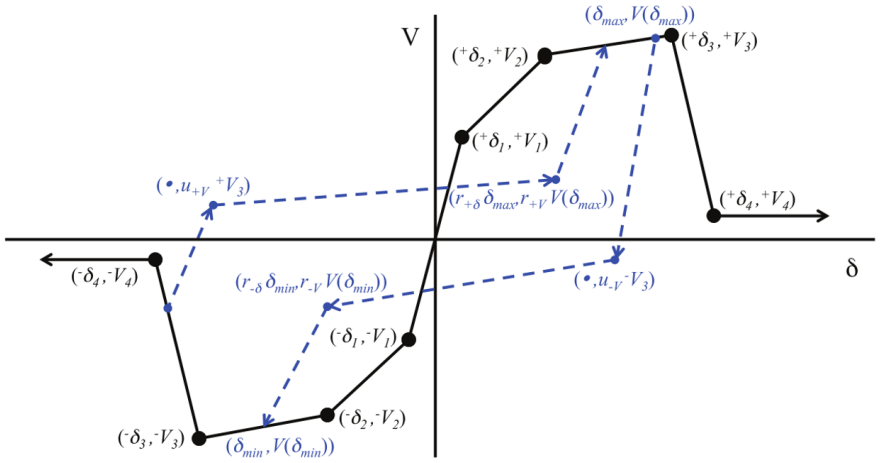


Figure 5.5. *Pinching4* uniaxial material model (Lowes and Altoontash, 2003)

floor corridor of the six-story test building were tested to investigate the influence of fire loads on lateral load resistance of shear walls. The shear walls were subjected to a displacement controlled cyclic CUREE protocol. Force-displacement behavior of test specimen CFS02, which represented the strength and stiffness of the wall under ambient conditions (non-fire loading sequence), was used to derive *pinching4* material model parameters.

The CFS02 test specimen consisted of CFS-framed shear walls sheathed with the same structural panel and gypsum board panel on the two sides as used in CFS-HUD test building. The fastener spacing to attach the structural and gypsum panels was also consistent with the fastener spacing used for level 2 corridor shear walls in the test building. However, there were a few key differences between the CFS02 test specimen and test building shear walls: (a) CFS02 used (4) 600S200-68 studs compared with (8) 600S200-97 studs in level 2 corridor shear wall as compression stud packs; (b) the 1000T200-54 ledger track attached along the top of the corridor shear wall was not considered in the fabrication of CFS02 specimen. Both of these details impact the lateral strength and stiffness of CFS-framed steel sheet sheathed shear walls. Additionally, the CFS02 specimen was 2.7 m tall to facilitate the load setup at the NIST laboratories, while the CFS-HUD test building had a 3.05 m floor-to-floor height. The steps involved in deriving the *pinching4* parameters for all corridor and corner shear walls attempt to account for these

variations, as described next.

Refined Wall-Line Model

A refined wall-line modeling strategy employing OpenSeesPy was adopted to investigate the effects of CFS framing components on shear wall lateral strength and stiffness, particularly the walls with significantly bigger compression stud packs (Zhang et al., 2022d,c). All framing components, such as studs, tracks and ledger, were simulated with displacement-based beam-column line elements. The axial and flexural behaviors of the beam-column elements were defined individually using the section aggregator command. To accurately represent the nonlinear axial and flexural behavior of studs and tracks, an elastic-perfectly plastic (EPP) material model was used, scaled to actual nominal strengths. The top and bottom track was simulated with loading beam properties. The OpenSeesPy model schematic is shown in Figure 5.6.

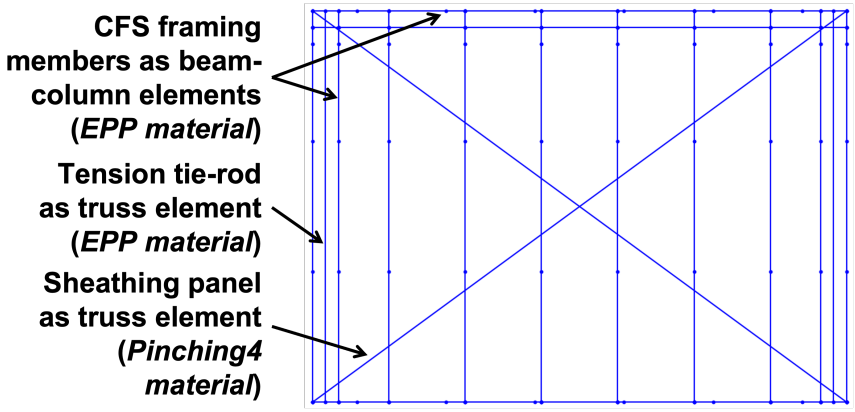


Figure 5.6. Schematic of refined wall-line OpenSeesPy finite element model (Zhang, 2023).

Per AISI S100-20, the actual framing component nominal strength was calculated by taking into account local buckling, distortional buckling, and yielding. The section elastic buckling critical loads used for nominal strength calculation were obtained using either AISI D100-17 or CUFSM software (Schafer, 2019). The discretization of the framing components into various beam-column parts over the unbraced length captured the global buckling behavior. The axial stiffness and strength of built-up sections were calculated by adding up single section

stiffness and strength, assuming each framing component within the built-up section can behave independently under compression. The flexural stiffness of built-up sections was calculated assuming that the whole section works as a single section. However, the flexural strength of built-up sections is calculated more conservatively assuming that each framing component within the built-up section works independently.

A *pinching4* hysteretic model was assigned to two diagonal truss elements to simulate the sheathing panel. This model was calibrated using CFS02 specimen cyclic test data. Tie rods were modeled with truss elements and EPP material model to capture tensile yielding and compression buckling explicitly. Therefore, the steel tie-rod elongation effects on the shear wall lateral drift were removed assuming that tie-rods have elastic elongatation. Force-displacement behavior of specimen CFS02 was adjusted by removing the contribution tie-rod elongation on wall lateral displacement to obtain the pure shear deformation of the sheathing panel. The *pinching4* parameter calibration procedure started by extracting the experimental backbone from the adjusted force-displacement behavior of CFS02. Material parameters were calibrated to achieve a match between experimental and simulation hysteresis backbone, as well as cumulative and per cycle dissipated energy of the hysteretic loops. Figure 5.7 shows the results of the calibration procedure overlaid with the experimental response of the CFS02 specimen. Table 5.5 lists the calibrated *pinching4* backbone curve parameters, and the strength and stiffness degradation parameters are provided in Table 5.6. Because of height difference between CFS02 shear wall and test building shear walls, the calibrated parameters of the backbone were adjusted based on the assumptions that lateral drift per unit height response and shear wall resistance per unit length response remains the same for the simulated wall and tested wall.

Based on the aforementioned modeling strategy, the contribution from cold-formed steel framing system, the sheathing panel and the steel tie-rod anchorage system on wall lateral performance have been modeled separately. It should be noted that the effect of CFS framing on the lateral performance in particular relies predominantly on the modeling assumptions and strategies for the framing connection. The modeling strategy adopted herein aimed to fully

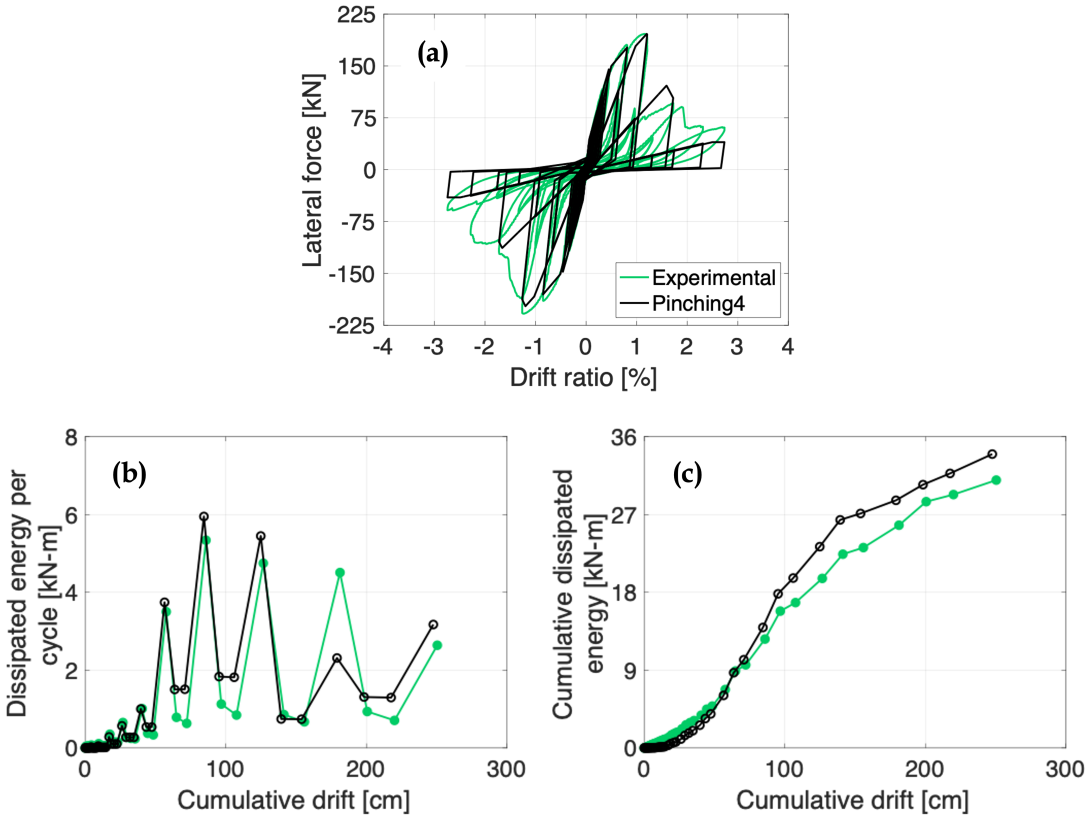


Figure 5.7. Comparison of experimental and calibrated *pinching4* material response: (a) force-deformation response, (b) dissipated energy per cycle, and (c) cumulative dissipated energy

capture the framing flexural strength contribution to the shear wall lateral performance. Since the chord stud packs have a large contact area with the top and bottom tracks due to their large cross-section depth, and are also connected to the tracks using many fasteners, the chord stud-to-track connections were modeled as fix connections. Furthermore, the ledger track web height was explicitly simulated with additional beam elements, with the beam element length equal to web height, coupled with the horizontal beam element modeling the long ledger track itself. This resulted in a more realistic transfer of moment between these elements by enabling the ledger-to-stud link to transfer moment across the entire depth of the ledger, as opposed to just a single point location. The majority of the framing components, with the exception of ledger track, employed centerline beam-column definitions.

To quantitatively investigate the impact of CFS framing components on shear wall lateral strength and stiffness, following the aforementioned modeling strategy, three numerical models were developed, which used the piching4 parameters derived for a 3.7 m $\times$ 3.05 m CFS02 shear wall. All three models included the ledger track but different compression stud pack configurations: (10) 600S200-97 studs, (8) 600S200-97 studs, and (4) 600S200-54 studs. Figure 5.8 shows the pushover results from displacement-controlled analysis for the three models. This modeling effort demonstrates the effect of chord stud pack size and ledger track on wall strength and stiffness, which were different from the CFS02 wall details in the NIST shear wall testing. It should be noted that the effect of a bigger compression stud pack on wall ductility had to be estimated from existing CFS-framed wall testing database (Zhang et al., 2022a). Shake table tests on wall-line assemblies conducted during the CFS-NHERI experimental program, described in Chapter 2, shared several key features with the test building corridor shear walls, namely: Type I shear walls that used steel sheet sheathing with gypsum panel on their exterior face, ordinary gypsum panel on their interior face, tension tie-rods, a tight fastener spacing on the shear wall perimeter, and heavier compression stud packs. In particular, specimens SGGS-1SB and SGGS-1F attained peak strength at drift ratios 1.6% and 1.9%, respectively. It is expected that the corridor shear walls which employed larger built-up compression stud packs would demonstrate a drift ratio at strength closer to 1.6%, and certainly higher than the 1.2% drift ratio at strength demonstrated by the CFS02 specimen. Due to this, the drift parameters of the backbone for two cases of the refined numerical model, (10) 600S200-97 studs and (8) 600S200-97 studs, were amplified to 1.6% drift ratio.

Another issue that requires further attention is that the corridor and corner shear walls on different levels of the building use different fastener spacing at their shear wall perimeter. The pushover response obtained from the refined wall-line modeling requires scaling for perimeter fastener spacing options other than 76 mm o.c., i.e. the 102 mm o.c. and 152 mm o.c. spacing options. This was also estimated using existing CFS-framed wall testing database. Namely, results from three sets of three wall specimens tested by Rizk and Rogers (2017) were analyzed for

wall strength and stiffness. Table 5.3 provides a summary of hysteretic response measurements for the wall specimens selected for this analysis of wall strength and stiffness. The three sets were defined based on walls with aspect ratios = 4.0, 1.33 and 1.0. Each set consisted of one shear wall each with 76 mm or 102 mm or 152 mm o.c. perimeter fastener spacing. The results from the third set (aspect ratio = 1.0) were used for scaling of corridor shear walls (aspect ratio = 0.91, 0.77), while the other two sets were used for scaling of corner shear walls (aspect ratio = 1.88, 1.43). The final step involves scaling the strength parameters for the actual shear wall length. The *pinching4* backbone parameters for all shear wall elements, obtained after following all the steps explained in this section, used in the building numerical model are provided in Table 5.7. Figure 5.8 shows the final backbone curves for the west corridor shear walls on all levels. Similarly, Figure 5.10 shows the final backbone curves for the longitudinal and transverse corner shear walls on all levels.

Table 5.3. Summary of wall specimens tested by Rizk and Rogers (2017) selected for analysis

Aspect ratio	Dimensions length × height	Wall specimen	Fastener spacing (mm)	Wall strength V_u (kN)	Elastic stiffness[1] K (kN/mm)
4.0	0.6 m × 2.4 m	W4-C	76	17.2	0.48
		W5-C	102	16.2	0.70
		W6-C	152	12.0	0.56
1.33	1.8 m × 2.4 m	W8-C	76	52.4	4.14
		W9-C	102	45.7	3.49
		W10-C	152	36.4	4.08
1.0	2.4 m × 2.4 m	W12-C	76	72.2	6.50
		W13-C	102	59.2	4.69
		W14-C	152	45.5	4.85

1. Elastic stiffness is measured as secant stiffness at $0.4V_u$

5.3.2 Modeling of Tension Tie-Rod and Compression Stud Pack Assembly

A vertical zero-length element at the story mid-height represents the vertical stiffness of the combined tension tie-rod and compression stud pack assembly on each end of the every shear wall, see Figure 5.4. The zero-length element is assigned a simplified multi-linear elastic

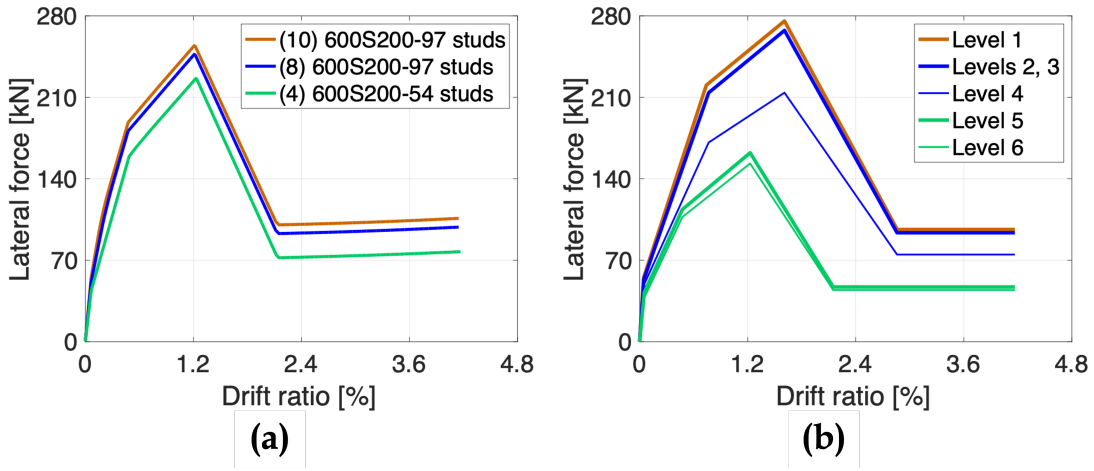


Figure 5.8. (a) Effect of framing details on shear wall response, and (b) backbone curves for west corridor shear walls

uniaxial material model. The force-deformation relationship of this material model is defined by a simplified piecewise-linear curve that is calibrated based on assembly detailing. Similar to the shear element, the connection to the foundation is modeled as a pin connection. A zero-length rigid truss element is used to provide a similar pin connection between vertical elements on adjacent floors. Two rigid elements connect the zero-length element at story mid-height to the top track and rigid truss element. It should be noted that for an isolated two-dimensional wall model, this modeling strategy of shear and vertical elements simulates the lateral behavior of a typical Type I shear wall, as defined by AISI S400-20, where the zero-length shear element develops the lateral resistance, while the zero-length vertical elements develop a force couple to resist the overturning moment.

Figure 5.9 shows the tension tie-rod versus wall end uplift behavior for the west corridor shear wall on level 2 of the test building. Complete details about the local shear wall behavior may be found in Wang and Hutchinson (2021). It can be seen that the observed stiffness aligns well with the theoretical axial stiffness k_e, calculated as $Area \times Elastic\ Modulus/Length$, for lower intensity earthquakes as the tension tie-rods remain in their pre-tension state, as provided since the construction of the building. However, during the subsequent higher intensity earthquake, a

reduction in pretension in the tie-rods was observed. The evolved behavior can be observed for the higher intensity earthquakes, where there is a transition region x_t that delays the engagement of tie-rods in tension. During this transition region, a lower transition stiffness k_t is observed, beyond which a higher tension stiffness k_s is observed. This behavior was also observed in wall-lines with tension tie-rods during the shake table test phase of CFS-NHERI experimental program (Singh et al., 2022c), see Chapter 3. Based on observed behavior of the tie-rods in the test building, two different elastic material models were defined for the zero-length vertical elements in the numerical model. The estimated elastic stiffness was assigned for service level earthquakes, while an elastic multi-linear behavior was assigned for above service level earthquakes. This strategy is similar to the modeling strategy described in Pei and Van de Lindt (2009) and implemented in SAPWood. It should be noted that using different material models for the vertical elements in tension did not affect the lateral stiffness of the building as observed through the eigen analysis results of the building numerical model. The material models used for the zero-length vertical elements are shown in Figure 5.9. A high compressive stiffness k_c is assumed for built-up stud packs in bearing. Material model parameters for tie-rods and stud pack assembly for corridor and corner shear walls at each level used in the building numerical model are provided in Table 5.4.

5.3.3 Modeling of Gravity Walls

Gravity walls were modeled similar to the shear walls employing a zero-length element assigned with a *pinching4* material model, connected to the top track and rigid truss element using rigid elements, see Figure 5.4. The connection to the foundation is modeled as a pin connection. The *pinching4* material model parameters were derived from the CFS-NHERI wall-line testing results. The quasi-static test phase included two specimens which examined the lateral behavior of exterior and interior gravity walls, see Chapter 2. Specifically, test results from specimens GGGG and GGGG-F were used to determine the *pinching4* material model parameters, see Tables 5.5 and 5.6. The strength parameters were scaled for the actual gravity

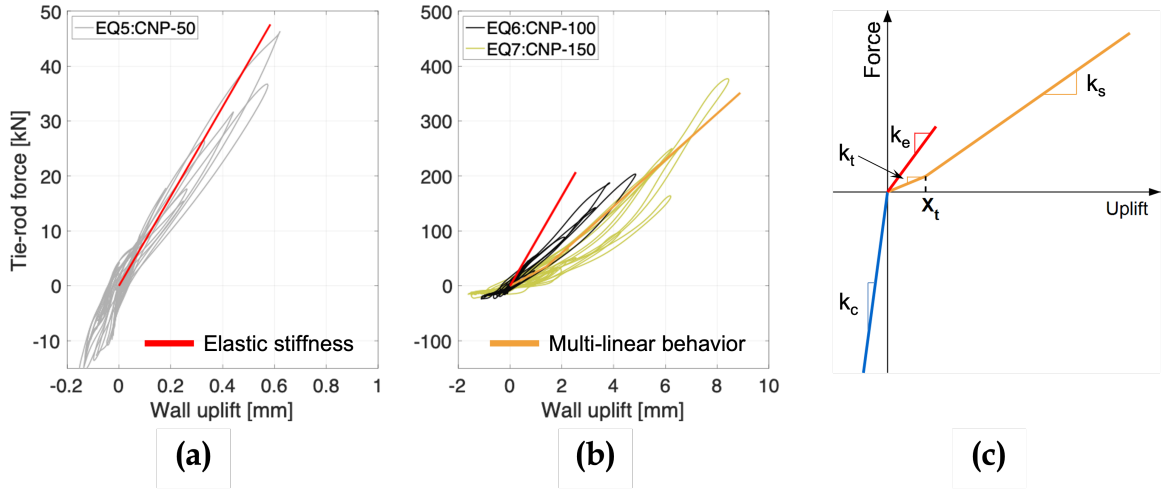


Figure 5.9. Methodology for deriving vertical element behavior: level 2 west corridor shear wall uplift versus tie-rod force at (a) service level and (b) design and MCE level earthquake intensities; and (c) general schematic of tension tie-rod material behavior.

wall length for use in the building numerical model. Figure 5.10 shows the final backbone curves for the exterior and interior gravity walls on all levels in the longitudinal and transverse directions of the test building. The *pinching4* backbone parameters for all gravity wall elements used in the building numerical model are provided in Table 5.7.

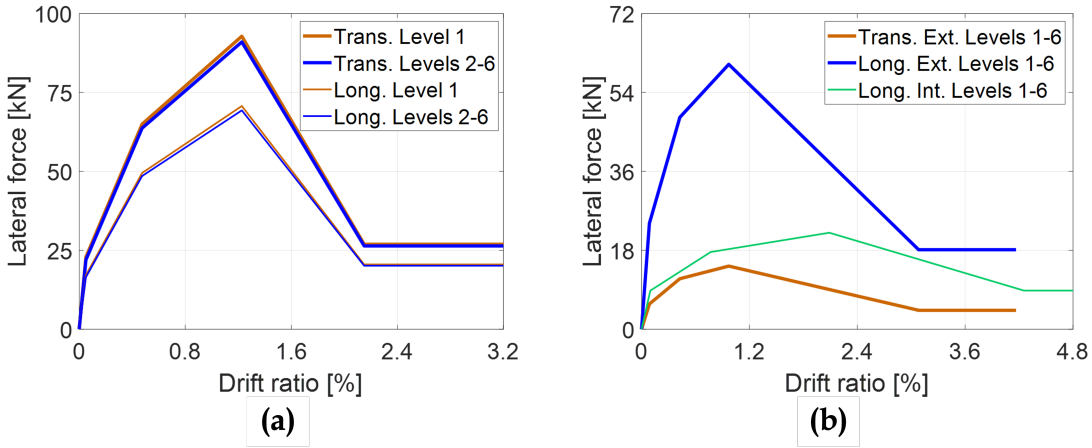


Figure 5.10. Backbone curves for: (a) corner shear walls, and (b) interior and exterior gravity walls in longitudinal and transverse directions

Table 5.4. Vertical spring element parameters (tension and compression) used in the numerical model

Level	k_e (kN/mm)	k_c (kN/mm)	x_t (mm)	k_t (kN/mm)	k_s (kN/mm)
Corridor shear walls (east-west)					
Level 1	86.9	482.3	1.4	26.5	45.1
Level 2	81.5	452.4	1.4	24.8	42.3
Level 3	53.0	294.4	1.4	16.2	27.5
Level 4	35.1	194.9	1.4	10.7	18.2
Level 5	35.1	194.9	1.4	10.7	18.2
Level 6	10.6	58.6	1.4	3.2	5.5
Corner shear walls (both directions)					
Level 1	86.9	482.3	1.4	26.5	45.1
Level 2	35.1	194.9	1.4	10.7	18.2
Level 3	27.8	154.4	1.4	8.5	14.4
Level 4	15.5	85.8	1.4	4.7	8.0
Level 5	10.6	58.6	1.4	3.2	5.5
Level 6	10.6	58.6	1.4	3.2	5.5

Table 5.5. Calibrated *pinching4* backbone parameters

Wall specimen	Dimensions	$^{+}V_1$ (kN)	$^{+}V_2$ (kN)	$^{+}V_3$ (kN)	$^{+}V_4$ (kN)	$^{+}\delta_1$ (mm)	$^{+}\delta_2$ (mm)	$^{+}\delta_3$ (mm)	$^{+}\delta_4$ (mm)
CFS02	3.7 m × 2.7 m	43.29	151.50	216.43	60.60	1.65	12.73	32.93	58.26
GGGG	4.9 m × 2.7 m	12.52	25.04	31.30	12.52	2.68	21.09	57.30	116.76
GGGG-F	4.9 m × 2.7 m	34.14	68.28	85.35	25.60	2.40	11.69	26.62	84.57

Note: Symmetric wall behavior is assumed. Provided parameters also apply for negative branch of backbone.

5.3.4 Seismic Mass and Gravity Load Definition

Table 5.8 summarizes the estimated weight of the components at each floor of the building. In the numerical model, self-weight of the components was assigned to the corresponding node on the top track at each floor. Since the floor joists in the test building spanned in the transverse direction, the floor weight was distributed based on the tributary area and assigned to the shear wall and gravity wall nodes on the top track of longitudinal wall-lines at each floor. The entire estimated seismic weight of the test building was accounted for in the numerical model. However, it should be noted that for gravity analysis, only the building weight carried by the stud pack

Table 5.6. *Pinching4* reloading, unloading and degradation parameters.

CFS02							
$r_{+\delta}$	0.165	gK_1	0.1	gD_1	0.5	gF_1	0.4
$r_{-\delta}$	0.165	gK_2	0.4	gD_2	0.25	gF_2	0.4
r_{+V}	0.11	gK_3	2.0	gD_3	1.0	gF_3	1.75
r_{-V}	0.11	gK_4	2.0	gD_4	2.0	gF_4	2.0
u_{+V}	-0.022	gK_{lim}	0.7	gD_{lim}	0.5	gF_{lim}	0.5
u_{-V}	-0.022	gE	10.0	Damage type		Energy	
GGGG							
$r_{+\delta}$	0.35	gK_1	0.1	gD_1	0.1	gF_1	0.4
$r_{-\delta}$	0.35	gK_2	0.5	gD_2	0.5	gF_2	0.4
r_{+V}	0.15	gK_3	3.0	gD_3	3.0	gF_3	3.0
r_{-V}	0.15	gK_4	1.2	gD_4	1.1	gF_4	1.2
u_{+V}	-0.075	gK_{lim}	0.6	gD_{lim}	0.6	gF_{lim}	0.5
u_{-V}	-0.075	gE	10.0	Damage type		Energy	
GGGG-F							
$r_{+\delta}$	0.35	gK_1	0.1	gD_1	0.1	gF_1	0.4
$r_{-\delta}$	0.35	gK_2	0.5	gD_2	0.5	gF_2	0.4
r_{+V}	0.16	gK_3	3.0	gD_3	3.0	gF_3	3.0
r_{-V}	0.16	gK_4	1.2	gD_4	1.1	gF_4	1.2
u_{+V}	-0.065	gK_{lim}	0.6	gD_{lim}	0.6	gF_{lim}	0.5
u_{-V}	-0.065	gE	10.0	Damage type		Energy	

assembly, calculated based on tributary area, was applied as vertical load at the tie-rod nodes. This was done because of the following two reasons:

1. The vertical elements in the numerical model represent the tie-rods, which carry the tension load as well as the coincident compression stud packs, which carry the gravity load. As a result, the entire building weight will be transferred through the vertical elements. However, in the test building, much of the gravity load was transferred through other vertical studs in the gravity and shear walls.

2. Tension tie-rods were tightened mechanically during building construction to ensure their vertical continuity. A portion of the tie-rod axial tension was lost as construction of upper stories progressed. The initial tension or loss of tension in tie-rods during construction was not measured. However, resisting the entire building weight will induce a large compressive force in the vertical elements in the numerical model.

Table 5.7. *Pinching4* backbone parameters used for shear elements in numerical model

Level	$^{+}V_1$ (kN)	$^{+}V_2$ (kN)	$^{+}V_3$ (kN)	$^{+}V_4$ (kN)	$^{+}\delta_1$ (mm)	$^{+}\delta_2$ (mm)	$^{+}\delta_3$ (mm)	$^{+}\delta_4$ (mm)
West corridor shear wall (east-west)								
Level 1	55.1	220.5	275.6	96.5	1.35	22.57	49.02	87.17
Levels 2, 3	53.5	214.0	267.5	93.6	1.41	23.36	49.02	87.12
Level 4	48.6	171.2	214.0	74.9	1.41	23.36	49.02	87.12
Level 5	42.2	113.6	162.3	47.1	1.55	14.46	37.39	65.52
Level 6	37.7	107.2	153.2	44.4	1.55	14.46	37.39	65.52
East corridor shear wall (east-west)								
Level 1	46.6	186.5	233.2	81.6	1.35	22.57	49.02	87.17
Levels 2, 3	45.3	181.1	226.4	79.2	1.41	23.36	49.02	87.12
Level 4	41.2	144.9	181.1	63.4	1.41	23.36	49.02	87.12
Level 5	35.7	96.2	137.4	39.9	1.55	14.46	37.39	65.52
Level 6	31.9	90.7	129.6	37.6	1.55	14.46	37.39	65.52
Corner shear wall (east-west)								
Level 1	17.1	49.5	70.7	20.5	1.55	14.46	37.39	65.52
Levels 2-6	16.5	48.5	69.3	20.1	1.55	14.46	37.39	65.52
Corner shear wall (north-south)								
Level 1	22.9	65.0	92.8	26.9	1.55	14.46	37.39	65.52
Levels 2-6	22.0	63.7	91.0	26.4	1.55	14.46	37.39	65.52
Corridor gravity wall (east-west)								
Levels 1-6	8.8	17.6	22.0	8.8	2.98	23.43	63.67	129.73
Exterior gravity wall (east-west)								
Levels 1-6	24.2	48.3	60.4	18.1	2.67	12.99	29.58	93.97
Exterior gravity wall (north-south)								
Levels 1-6	5.8	11.5	14.4	4.3	2.67	12.99	29.58	93.97

Note: Symmetric wall behavior is assumed. Provided parameters also apply for negative branch of backbone.

Due to this modeling decision, this developed modeling strategy may be incapable of producing reasonable predictions under vertical excitations.

5.4 Comparison between Numerical Predictions and Measured Experimental Response

In this section, the aforementioned numerical model response results are compared to the experiment results. It should be noted however, that although the input earthquake excitation was along the longitudinal direction of the building, any accidental excitation in the transverse

Table 5.8. Estimated building weight and floor distributions (in kN)

Floor	Wall	Floor diaphragm	Mass plate	Tie rods	Weight
Roof	58.4	47.2	65.8	0.0	171.5
6	78.3	29.0	65.8	1.3	174.5
5	78.3	29.0	65.8	2.0	175.1
4	78.3	29.0	65.8	2.7	175.9
3	79.5	47.2	65.8	4.2	196.7
2	78.3	29.0	65.8	6.9	180.0
1	39.1	0.0	0.0	22.00	70.4
Total	490.3	210.5	395.0	38.9	1134.7

direction, as measured by accelerometers installed on the shake table platen, in addition to the longitudinal achieved input acceleration were used as the bi-directional acceleration input for non-linear time-history analyses. Note as well that the service level earthquake (EQ2:CNP-25) was analyzed as an isolated event since it was not expected to have any residual effects on the numerical model. However, to capture the accumulating drift and stiffness degradation during higher intensity motions, non-linear time history analyses for the above service level earthquakes, EQ5:CNP-50, EQ6:CNP-100 and EQ7:CNP-150 were analyzed sequentially. A 5% Rayleigh damping for modes 1 (transverse translation) and 2 (longitudinal translation) was used to define the damping matrix for time history analyses, matching the 5% damping usually used in specifications and the design spectrum.

5.4.1 Comparison of Natural Frequencies

Figure 5.11 shows the mode shapes for the first two modes of the three primary DOF and compares the eigen analysis results with the system identification (ID) of the test building in the undamaged state (S0). The system ID results were obtained prior to the earthquake tests, using white-noise input excitation by Wang and Hutchinson (2020). It can be seen that the numerical model predicts the building stiffness in state S0 in the two orthogonal directions very well, with only 3% error. The torsional mode is not predicted as well by the numerical model, with an approximate 15% error. The interaction of wall-lines at building corners not being

considered in the numerical model may explain this disparity. The spatial distribution of seismic weight and assignment to different nodes on each floor may also contribute to this nominal error. However notably, higher modes are reasonably well predicted with the numerical model. Table 5.9 provides the modal participation mass ratios (%) for each mode. The first two modes in each of the three primary DOF have a cumulative 95% mass participation. Figure 5.12 shows the elongation of natural period for mode 2 (longitudinal translation) as predicted by the numerical model compared with measured natural period after different earthquake tests: S2 after EQ2, S5 after EQ5, S6 after EQ6 and S7 after EQ7, as defined in Wang and Hutchinson (2020). The progression of damage as seen through elongation of natural period is adequately captured by the numerical model.

Table 5.9. Modal participation mass ratios for each mode

Mode	X-Translational		Y-Translational		Z-Rotational	
	(%)	Cumulative (%)	(%)	Cumulative (%)	(%)	Cumulative (%)
1	0	0	83.4	83.4	0	0
2	82.4	82.4	0	83.4	0	0
3	0	82.4	0	83.4	86.5	86.5
4	0	82.4	11.9	95.3	0	86.5
5	12.3	94.8	0	95.3	0	86.5
6	0	94.8	0	95.3	9.3	95.8

5.4.2 Comparison of Nonlinear Response to Earthquake Motions

Figure 5.13 shows the roof drift ratio (RDR) time history comparison between the numerical model and experiments during the service level (EQ2:CNP-25), design (EQ6:CNP-100), and maximum considered earthquake (EQ7:CNP-150) tests. It can be seen that the numerical model adequately captures the experimental response, particularly for the design earthquake (EQ6:CNP-100) test. The inter-story drift ratio time histories obtained from the numerical model for each level during the design earthquake event EQ6:CNP-100 are shown in Figure 5.14. This figure also shows the pure shear deformation of each floor obtained directly from the shear element in the model. Assuming that the total inter-story drift is the sum of

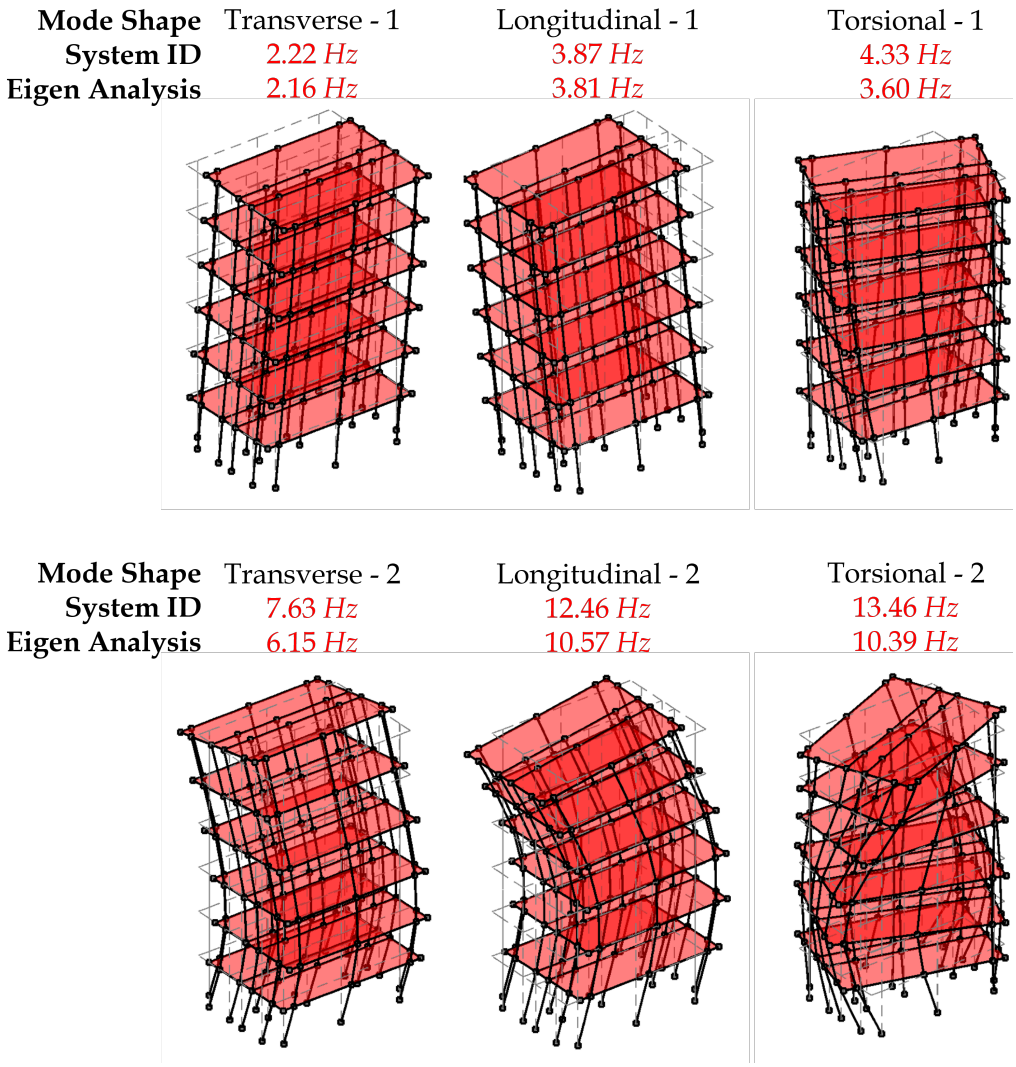


Figure 5.11. Comparison of eigen analysis results with system ID results per Wang and Hutchinson (2020): natural frequency and mode shapes at undamaged state (S0)

pure shear deformation and the contribution from wall uplift towards drift, it can be seen from Figure 5.14 that the ratio of shear deformation to inter-story drift decreases along the height of the building. This behavior suggests that the drift at the higher levels is dominated by the cumulative uplift and rod elongation, and not the pure shear deformation of the higher levels. This observation is consistent with the behavior observed in SAPWood model of stacked wood-framed shear walls (Pei and Van de Lindt, 2009).

Figures 5.15-5.17 present the comparison between numerical model prediction and the

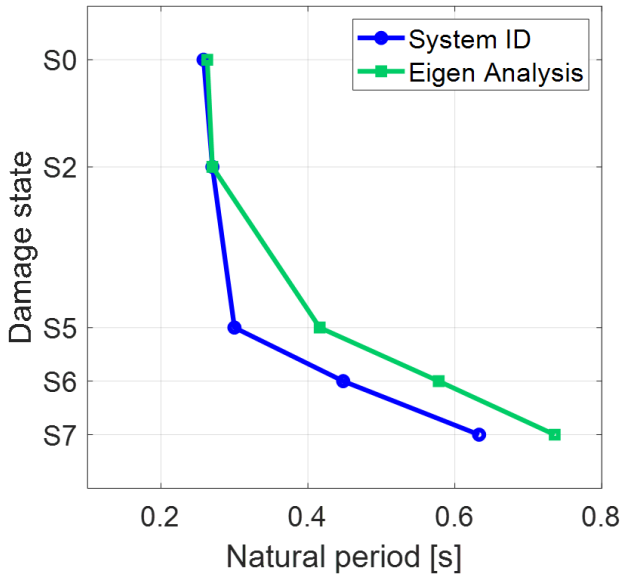


Figure 5.12. Comparison of eigen analysis results with system ID results: elongation of mode 2 (longitudinal translation) natural period at different damage states

experimental measured story shear versus inter-story drift (IDR) hysteretic responses at each level during the service level (EQ2:CNP-25), design (EQ6:CNP-100), and maximum considered earthquake (EQ7:CNP-150) tests. The numerical model adequately captured the story initial stiffness during the SLE event. It also adequately captured the secant stiffness, shear resistance and inter-story drift during the design earthquake. However, the predicted story shear versus IDR response did not capture the experimental results as well for the MCE event. Large shear resistance is provided at the lower level of the numerical model, reaching IDR close to drift at strength for corridor shear walls. This behavior was not observed in the test building, where shear strength was better distributed along the height of the building, even during the MCE test. This discrepancy may be due to the assumptions made in estimating the shear strength and the associated need to define the drift at strength for corridor shear walls at the lower four floors.

The peak roof drift ratio (PRDR), normalized peak base shear $\left(\tilde{V}_b\right)$, and normalized peak overturning moment $\left(\tilde{M}_o\right)$ obtained from the numerical analyses and measured from the experiments are compared in Figure 5.18. The normalized peak base shear and normalized peak

overturning moment associated with seismic loads are calculated as follows:

$$\tilde{V}_b = \frac{\sum_{i=2}^{N} -m_i a_i(t)}{\sum_{i=2}^{N} w_i} \tag{5.1}$$

$$\tilde{M}_o = \frac{\sum_{i=2}^{N} -m_i h_i a_i(t) + w_i \delta_i(t)}{\sum_{i=2}^{N} w_i h_i} \tag{5.2}$$

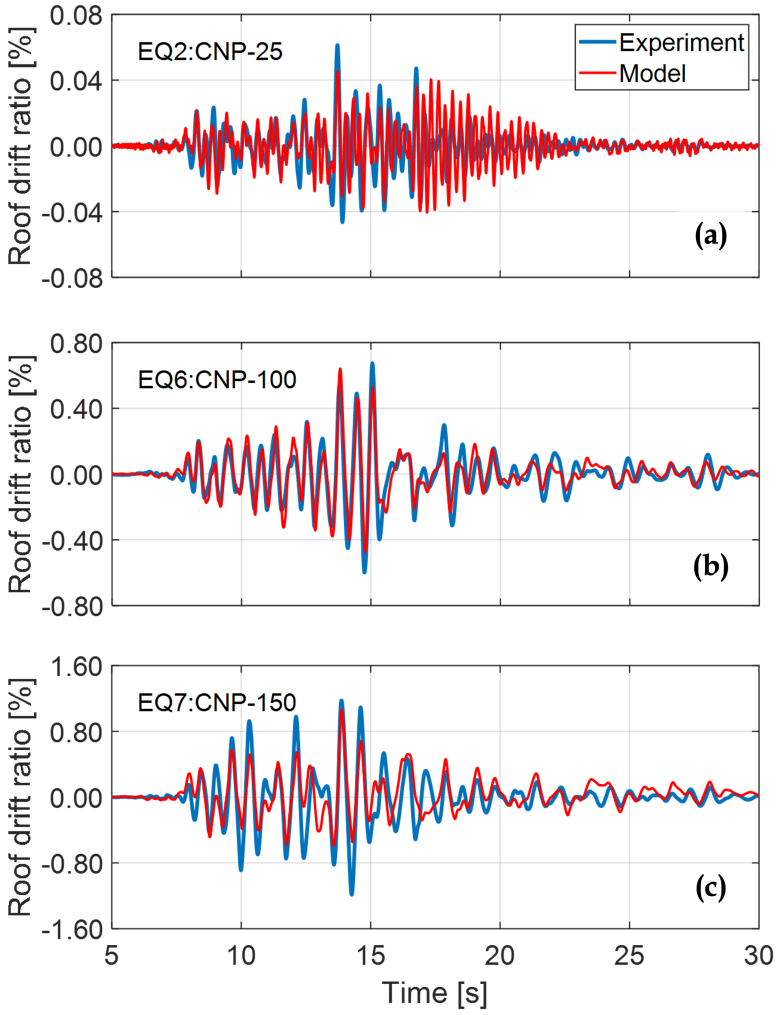


Figure 5.13. Roof drift ratio time history comparison for: (a) EQ2:CNP-25 (SLE), (b) EQ6:CNP-100 (DE) and (c) EQ7:CNP-150 (MCE)

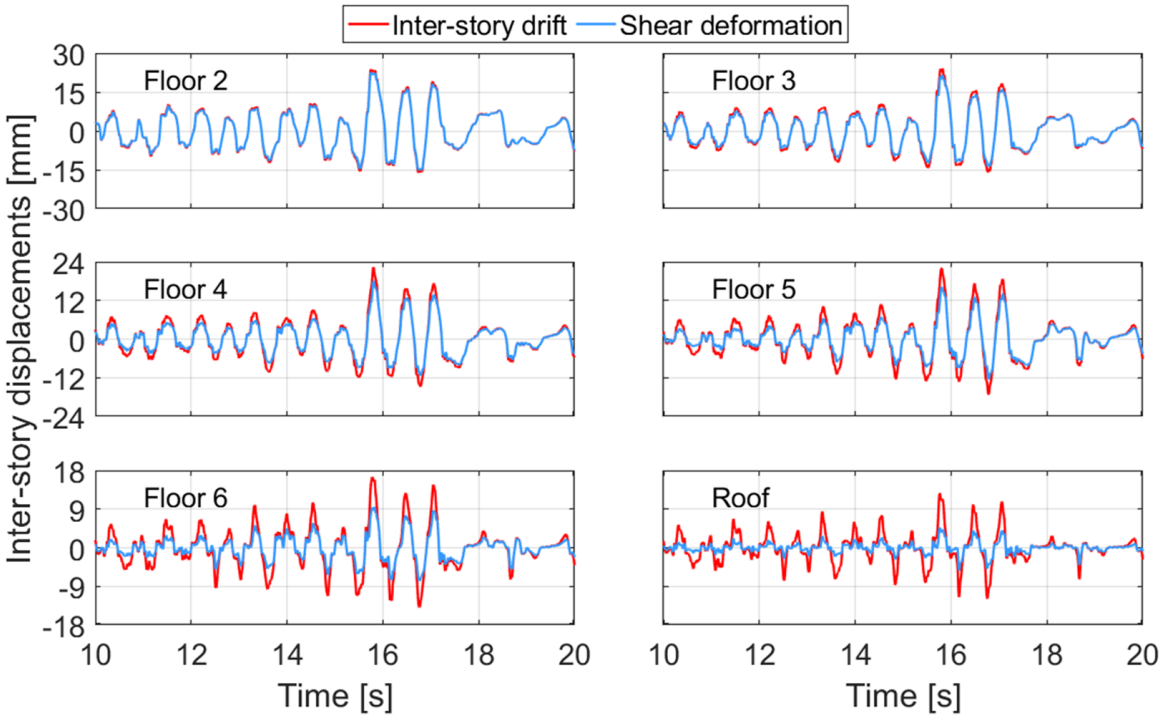


Figure 5.14. Contribution of shear deformation towards inter-story drift for EQ6:CNP-100 earthquake

where m_i and w_i denote the lumped floor mass and weight of the i^{th} floor at a height h_i from the ground, $a_i(t)$ and $\delta_i(t)$ denote the absolute floor acceleration and relative floor displacement histories of the i^{th} floor, and N is the total number of floors. Results in Fig. 5.18 show that the numerical model was able to adequately predict the PRDR value up to and including the design earthquake, however, it underpredicted the PRDR for MCE event. Similarly, the global base shear and overturning moment were well predicted up to the design earthquake, but overpredicted for the MCE event.

Comparison of floor response spectra (FRS) from predicted and measured acceleration responses for the three earthquake tests, namely EQ2:CNP-25, EQ6:CNP-100 and EQ7:CNP-150 are shown in Figure 5.19. In this case, the FRS is defined as the 5% damped elastic pseudo-acceleration spectra calculated using the floor acceleration in the longitudinal direction at each floor. A good match between the FRS was observed for all earthquake events at all floors. Figure 5.20 shows the peak floor acceleration (PFA) envelope and floor acceleration

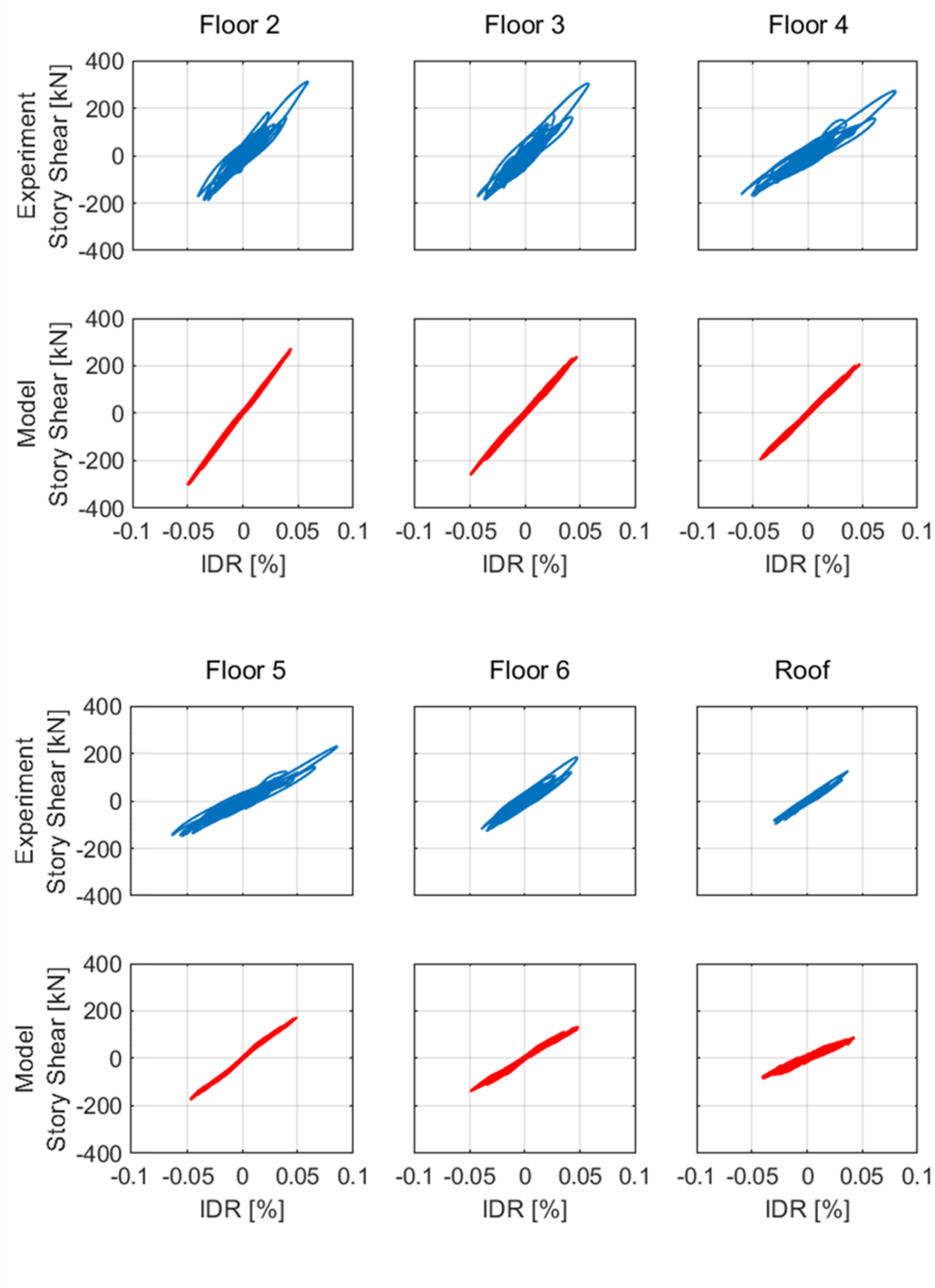


Figure 5.15. Story shear versus inter-story drift response comparison for EQ2:CNP-25

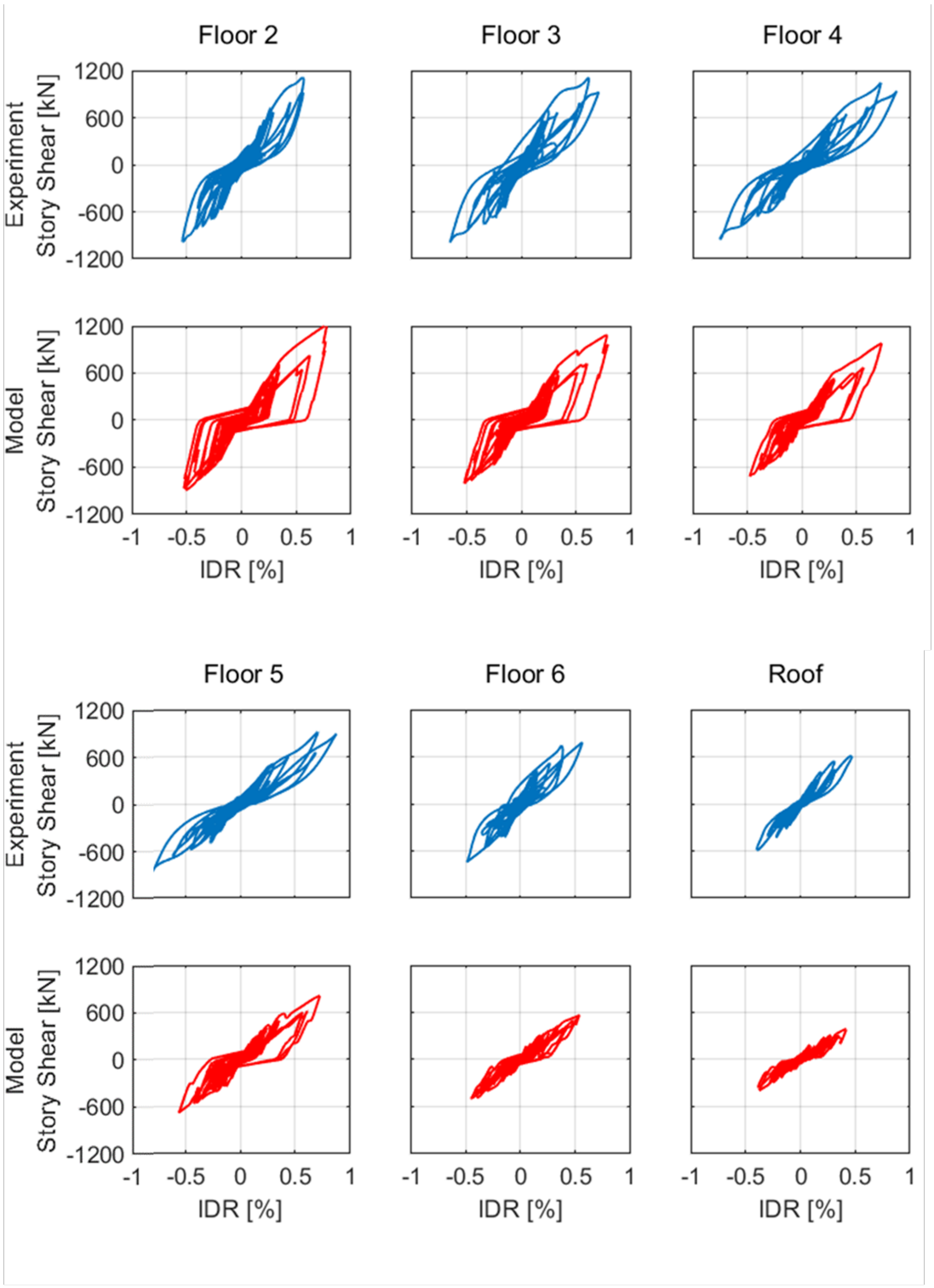


Figure 5.16. Story shear versus inter-story drift response comparison for EQ6:CNP-100

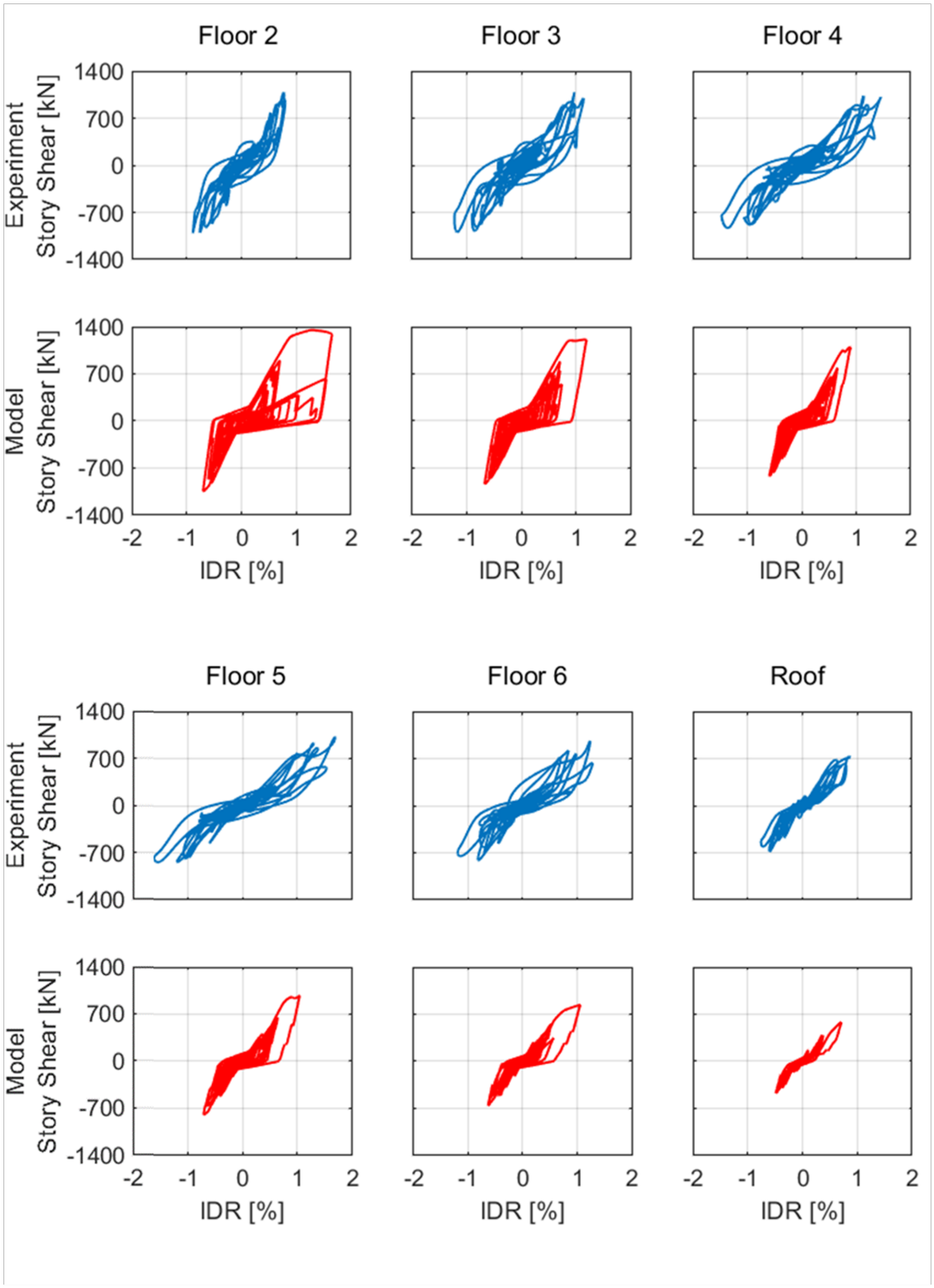


Figure 5.17. Story shear versus inter-story drift response comparison for EQ7:CNP-150

amplification comparisons. The floor acceleration amplification is determined as the ratio between the peak acceleration achieved at each floor and the peak input acceleration achieved by the table platen. According to ASCE/SEI 7-22 code provisions, the amplification factor is empirically defined as $1+2z/h$, where z/h denotes the normalized building height. This assumes a linear distribution along the building height from 1.0 at the base to 3.0 at the roof. The floor acceleration amplification is also compared to the code provisions in Figure 5.20. Similarly, Figure 5.21 shows the peak inter-story drift ratio (PIDR) envelope comparison. These plots also demonstrate the ability of the numerical model to adequately predict the PIDR response up to the design event. However, the predicted peak floor accelerations and floor acceleration amplification showed significant deviation from measured response.

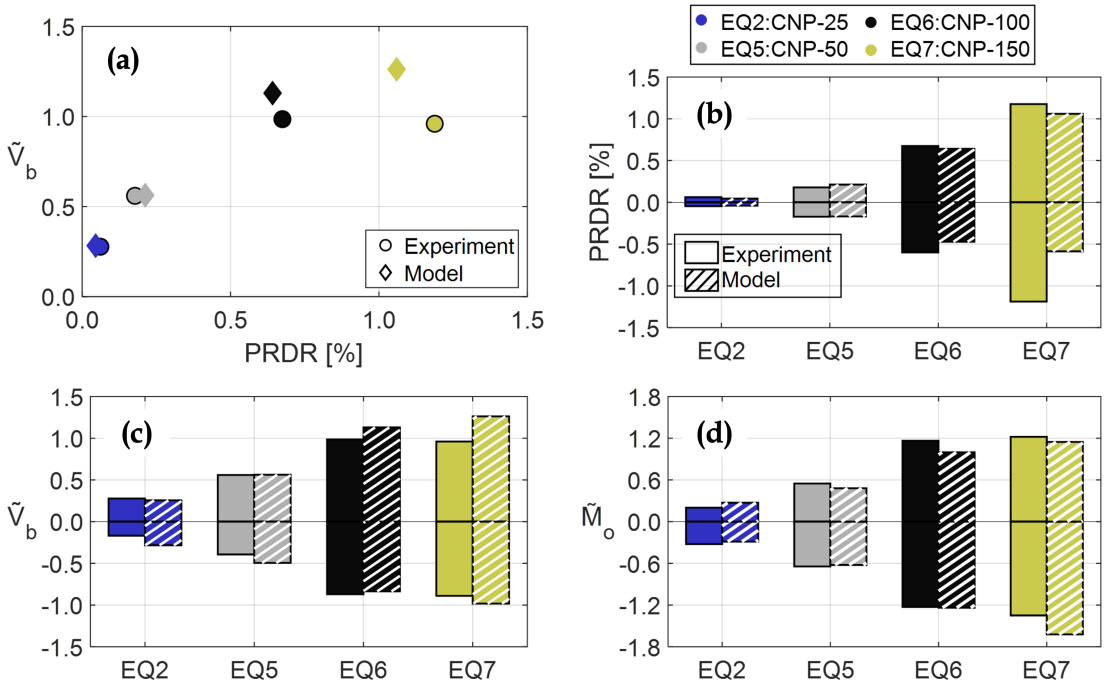


Figure 5.18. (a) Normalized peak base shear forces versus peak roof drift ratio, (b) peak roof drift ratios, (c) normalized peak base shear and (d) normalized peak overturning moment

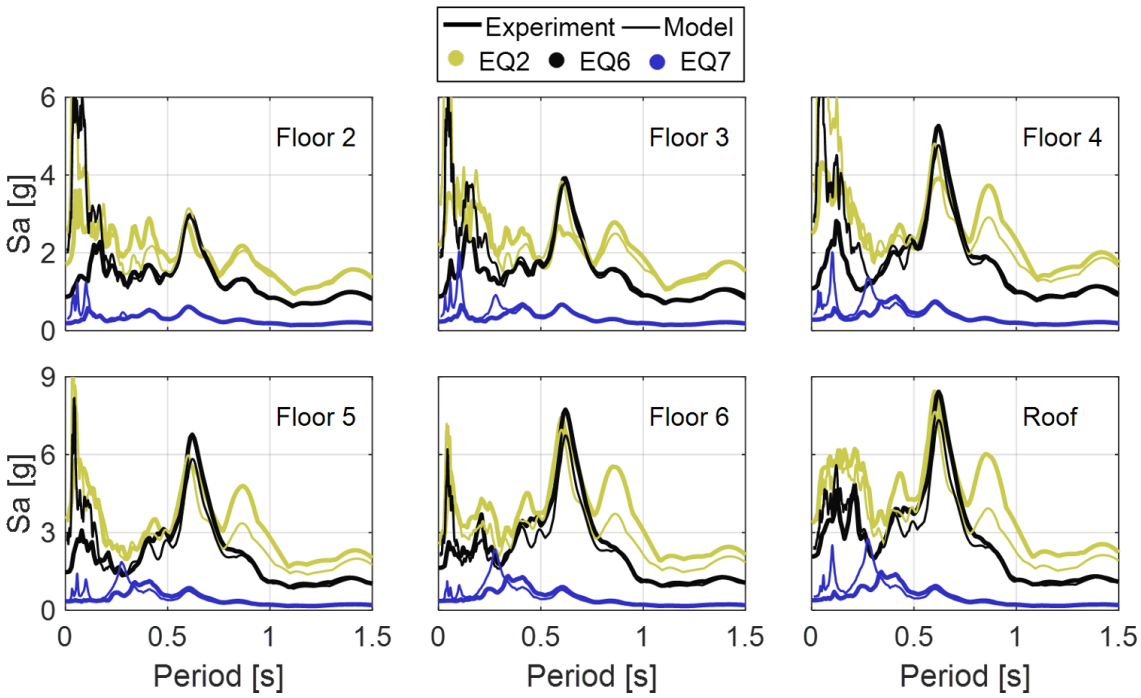


Figure 5.19. Floor pseudo-acceleration response spectra ($\xi = 5\%$) comparison

5.5 Summary Remarks

This chapter presents a finite element modeling approach for CFS-framed mid-rise buildings and compares the predictions from the numerical model against the measured seismic response of a six-story CFS-framed building. A brief description of the CFS-HUD test building has been provided, which adopted the use of continuous tie-rods with built-up compression stud pack assembly in shear walls. Discussion about modeling the different major assemblies such as shear walls, gravity walls, tension tie-rods and compression stud-pack assemblies are provided within this chapter. Detailed steps undertaken during modeling to take into consideration the effect of built-up stud packs and different fastener spacing in the nonlinear material model of shear walls are presented. Additionally, modeling of the continuous tie-rod system to capture the cumulative elongation over multiple stories is explained. Comparison between the numerical model predictions and measured experimental response is provided to evaluate the robustness of the proposed numerical modeling approach in predicting the seismic response of mid-rise

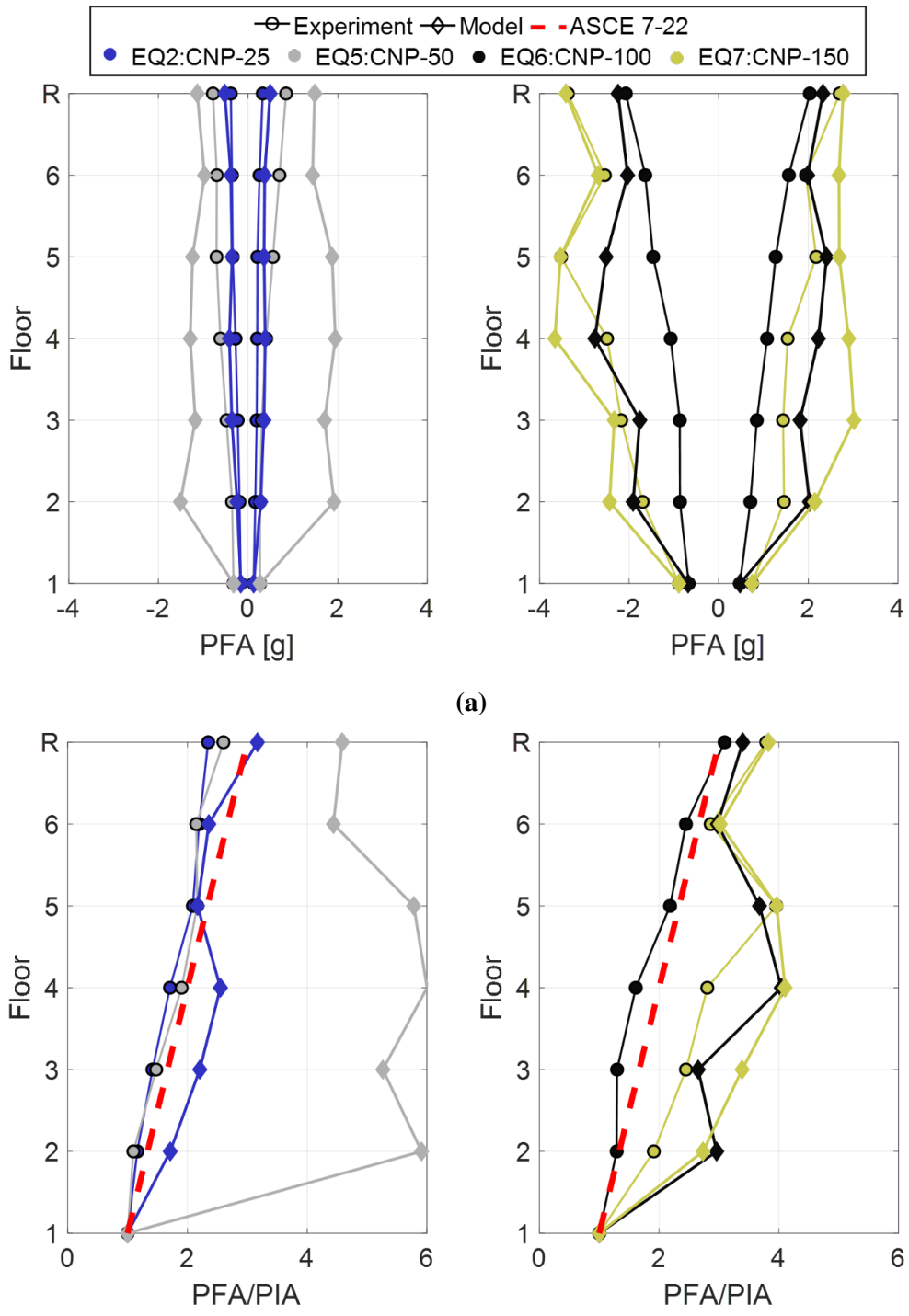


Figure 5.20. Building peak response comparison: (a) peak floor acceleration, and (b) floor acceleration amplification

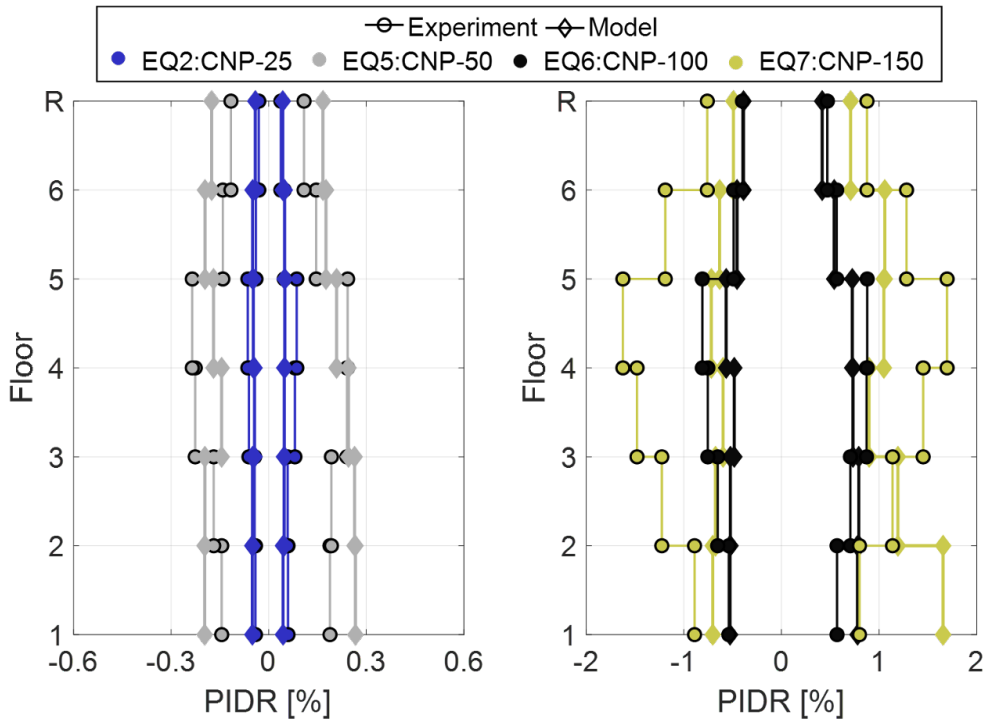


Figure 5.21. Building peak response comparison: peak inter-story drift ratio envelope

CFS-framed buildings. The complete OpenSeesPy code of the CFS-HUD test building numerical model is provided in Appendix E.

Acknowledgment of Publications

Portions of the following manuscript, for which the dissertation author was the primary investigator and author, are contained in Chapter 5:

Singh, A., Zhang, Z., Wang, X., Schafer, B. W., and Hutchinson, T. C. "Development of a Design-Grade Numerical Model of Cold-Formed Steel-Framed Mid-Rise Buildings" *Eng. Struct.* In preparation for submission.

Chapter 6

Conclusions and Future Work

6.1 Motivation and Scope

Cold-formed steel-framed assemblies use members produced from structural quality steel sheet gradually bent into desired cross sections via a roll-forming process. These cold-formed steel members are used as wall studs, joists, headers, jamb studs, chord studs etc. in wall panel or floor diaphragm assemblies. CFS-framed construction is rapidly becoming a popular construction choice as it provides many benefits such as low installation and maintenance costs, efficient construction using prefabricated panels, and high durability and ductility. CFS framing also leads to lightweight structures and their ductile nature aligns with system resiliency needs in moderate to high seismic zones, such as the high seismic regions of the United States.

CFS-framed shear walls develop lateral resistance through sheathing attached to the wall stud and track framing members. Sheathed CFS shear walls have commonly used OSB (Oriented Strand Board) or plywood panels as sheathing. Steel sheet is a relatively new sheathing option and offers potential benefits such as higher lateral capacity, ductile failure mechanism as well as higher energy dissipation capacity. Previous experiments have shown that CFS shear walls with thicker steel sheet as sheathing and a small edge fastener spacing demonstrate larger lateral strength. However, these tests focused on testing isolated shear walls loaded via a quasi-static cyclic displacement-controlled protocol. Experimental literature thus far has not considered wall-line specimens, where wall components, shear wall and gravity walls, are

placed along the same line. Moreover, the effect of wall openings, necessary for doors and windows, and installed finishes has not been explored. Only one study has considered the seismic evaluation of CFS-framed walls using dynamic loading protocol. In addition, there is a need to develop steel sheet sheathed CFS-framed detailing solutions, which can offer high lateral resistance required for shear walls in taller mid-rise and high-rise CFS-framed buildings. To support the aforementioned gaps in knowledge, a two-phased experimental effort was designed and executed within this dissertation in an effort to advance the understanding of CFS-framed steel sheet sheathed shear walls placed in-line with gravity walls. Complementary numerical modeling is subsequently performed using a design-grade phenomenological model with key features identified as important to capturing the wall-line response as observed from the full-scale component level experiments. Finally, a full-scale shake table building test data set is used to evaluate the robustness of the phenomenological model and used for seismic response simulations.

6.1.1 Experimental Scope and Contributions

The two-phased experimental program examined wall-line assemblies with varying arrangements of steel sheet sheathed shear wall segments with gravity or window segments in-line with each other. An important objective of the experimental effort was to characterize the performance of long CFS-framed wall-lines, particularly detailed for mid-rise construction in high intensity seismic zones. Wall detailing was selected to represent wall design from approximately the mid-height floors within the 10-story archetype building. The dimensions of the individual walls were 4.88 m length and 2.74 m height with varying configurations of 1.22 m long shear and gravity segments. Shear wall segments were detailed with compression stud packs studs and either tension tie rods or hold-downs at wall ends. The wall sheathing steel sheet, attached to the shear wall framing using closely spaced pan head screws along sheathing edges. Gravity wall segments, top and bottom tracks, and a ledger track were incorporated in all specimens and framed of CFS stock members. A few configurations were installed with

stucco-based exterior finish (EIFS) and gypsum board interior finish. The gypsum boards and glass-mat sheathing panels underlying the EIFS layer were installed using flat head screws. Notably, a few configurations had window opening rather than a gravity bay. A window opening 2.18 m wide and 1.22 m tall with a sill height 0.76 m was installed within the middle bay centered between equal length shear wall segments. Jamb studs and sill and header tracks were provided to support the force transfer around window openings.

The test matrix consisted of several variables governing the nonstructural detailing of CFS-framed walls, namely: finish application, window opening, and asymmetric shear wall location, and structural detailing of CFS-framed walls, namely: tie-down detailing, shear wall detailing, and sheet fastener detailing. The impact of test variables was quantified through full-scale shake table and quasi-static cyclic tests. In total, 16 unique wall configurations were tested between the two test phases. In particular for the shake table test phase, a motion scaling strategy and testing protocol was developed to capture wall performance at pre-defined target performance levels. Scale factors for input earthquake motions were determined based on pre-test SDOF numerical predictions as well as the measured natural period of the two wall pairs on the shake table being tested simultaneously. This scaling was performed to achieve the intended target performance levels that progressively damage the wall specimens. During the quasi-static test phase, the wall-lines were subjected to a displacement controlled cyclic protocol, using two hydraulic 220 kN actuators with a $\pm$60 cm stroke. A 2% drift ratio was adopted as the reference displacement to define the protocol based on the wall-line behavior of a baseline specimen from the shake table test phase. The specimens were reverse cyclically tested under displacement control until a 60% post-peak strength degradation was observed. All specimens in both phases were simultaneously loaded vertically to using a rigid mass to simulate anticipated gravity conditions of the mid-level of a mid-rise archetype building.

The impact of test variables is evaluated by comparing groups of specimens systematically in terms of their force-displacement backbone envelopes, global response, namely, lateral strength and stiffness, drift at strength; wall local behavior, such as tie-down force, wall uplift and

shear distortion; and observed physical damage characteristics. The progression of physical damage within the framing members, fastener connections and nonstructural finish layers is also correlated to the evolution of dynamic characteristics and hysteretic energy dissipation. Dynamic characteristics of the wall-lines are identified using the data recorded from white noise base excitation tests performed during the shake table test phase. Since the wall-line specimens were tested under different loading protocols across the two test phases, a drift cycle qualification procedure is applied to compare the energy dissipation characteristics.

6.1.2 Numerical Modeling Scope and Contributions

Following the wall-line experimental program, a design-grade numerical model was developed in OpenSeesPy. The model seeks computational efficiency by focusing on only the key mechanisms of response, such that it can be employed by design engineers to predict the seismic response of cold-formed steel-framed mid-rise buildings to earthquake motions. Efforts at numerical modeling of CFS-framed building have been severely restricted due to lack of full-scale system-level experimental data. Modeling the seismic response of complete CFS-framed building systems has been explored to a much lesser extent, compared to wood-framed buildings, where similar research work has already led to development of analysis software tools enabling performance-based seismic design of mid-rise wood-framed buildings. Recent shake table testing of a full-scale six-story CFS-framed wall braced building, tested at the Large High-Performance Outdoor Shake Table (LHPOST) at the University of California, San Diego (UCSD), produced valuable data describing the building response at service, design, and maximum credible earthquake level demands. This test building also adopted a unique restraint system to resist seismic overturning moment and uplift forces of the building through the use of continuous tie-rods and built-up compression stud pack assembly at the ends of individual shear walls. The developed finite element model takes into consideration the different major assemblies, which influence the dynamic response of the system, such as shear walls, gravity walls, tension tie-rod and compression stud-pack assembly. Utilizing data gathered

during the wall-line experimental program, key features of the mid-rise shake table building specimen model were advanced. The numerical model also considers the effect of built-up stud packs on the nonlinear material response of shear walls. The continuous tie-rod system is modeled to capture the cumulative elongation over several stories, which can induce significant out-of-plane diaphragm rotation. The numerical model response predictions were evaluated by comparing them with against the measured experimental seismic response of the full-scale six-story CFS-framed wall-braced test building.

6.2 Research Significance

Use of steel sheet as a sheathing material in CFS shear walls is relatively recent, and as such, understanding the structural behavior of steel sheet sheathed shear walls remains limited. At the same time, there is a demand to design all-steel shear walls capable of developing higher lateral resistance. Results from the two-phased test program enrich the experimental database by documenting the performance of CFS-framed wall assemblies, and in particular by quantifying the impact of structural and nonstructural detailing variations commonly required for practicing engineers. Steel sheet sheathed shear walls tested in this experimental program improve on the current understanding of CFS wall-line seismic behavior, demonstrate lateral resistance beyond current code provisions and provide important data for advancing modeling tools and design code provisions. Outcomes pertaining to the impact of design variables on wall performance add valuable information to the ongoing development of design codes and seismic systems for buildings framed with CFS. In particular, the contribution from non-designated lateral systems and portions of the building system not specifically designated by design engineers, has not been substantially investigated through experiments and, as a result, is not well understood. Based on the results of finished wall-line specimens, the contribution to lateral strength from exterior stucco-based finish has been adopted into the commentary section of AISI S400-20 design code.

The configuration of specimens and the methods utilized in the experimental program

to add to the body of knowledge regarding the behavior of cold-formed steel wall components is unique. No such wall-line configuration, namely incorporating both gravity and lateral wall framing lines; as well as subjecting such components to earthquake excitation, white noise, and quasi-static simulated seismic loading have yet to be conducted. An assessment of the extent of physical damage at different performance levels has been made to understand the structural integrity of CFS-framed wall-lines. These results will help researchers and design engineers understand the correlation between progressively incurred physical damage in wall-line and its dynamic characteristics and hysteretic energy dissipation characteristics.

Building upon the learnings from the experimental program, a design-grade numerical model of CFS-framed wall-lines assemblies which can be used for numerical response predictions for mid-rise buildings was developed in OpenSeesPy. Development of such numerical models is an essential analysis tool for the rapidly growing CFS industry, where a dedicated analysis software is currently not available for practicing engineers. The aim of the design-grade numerical model is to validate the finite element modeling approach that employs a suite of phenomenological elements that are able capture the most important mechanisms. The model is intentionally computationally simple, to allow its basic approach adoption in design-grade numerical platforms such as SAP2000, ETABS or others readily used in practice by design engineers. Furthermore, the availability of such tools is necessary to enable performance-based seismic design of multi-story cold-formed steel structures.

6.3 Major Findings

6.3.1 Experimental Investigation of Cold-Formed Steel-Framed Wall-Lines in Mid-Rise Buildings

The test matrix was designed to examine the impact of test variables on lateral behavior of CFS-framed wall-lines. The impact of variables governing the nonstructural and structural detailing of CFS-framed walls can be summarized as follows:

Finish application

- Finishes on a wall-line assembly substantially increase the wall strength without changing the wall failure mode. The additional strength from finish application has been quantified as 9.3 kN/m (635 plf) for an exterior EIFS layer, and 5.4 kN/m (370 plf) for an interior gypsum panel layer. This increase was found to be independent of the underlying wall framing details.

- The current design code AISI S400-20 does not take into account the effect finish application has on wall behavior, particularly the increase in lateral load capacity. It is recommended that overstrength be considered during the design of CFS framed systems.

- The elastic stiffness also increased between 1.5-3 times when walls were finished on both faces. However, the drift at strength and the drift at 80% post-peak strength were not affected by the application of finishes.

- The equivalent hysteretic damping was larger for finished specimens up to strength, beyond which the effect of finishes was negligible.

Window openings

- Window openings detailed per design codes AISI S240-20 and AISI S100-20 did not significantly effect wall seismic performance. Wall lateral strength, elastic stiffness as well as drift at strength for specimens with window opening were within 10% of that for configurations with similar framing but absent a window opening.

- Nonetheless, the force transfer around the window opening resulted in larger stresses on adjacent chord stud packs. This led to failure of framing connection screws and slipping of stud packs, which is a cause for concern for maintaining structural integrity. This detailing issue needs further attention.

Asymmetric shear wall location

- Wall strength and stiffness were anticipated to reduce by 50% due to the explicit use of half the amount of shear walls in the asymmetric specimens. Measurements of both strength and stiffness are nominally consistent with this anticipated reduction.

- Asymmetric walls demonstrated similar failure mode as symmetrical walls. However, failure and damage to framing members were observed at lower drift ratios for asymmetric walls, due to the overload imposed on a single shear wall segment within a wall line.

Tie-down detailing

- Specimens with hold-downs demonstrated 20-30% larger lateral strength. This was because installation of hold-downs led to a larger overturning lever arm compared to tension tie-rods.

- Several hold-downs reached their capacity at higher drift demands while tension tie-rods remained linear elastic, even though both hold-downs and tie-rods were designed for same over-strength force levels. The failure of this capacity-designed component of the lateral force resisting system is undesirable. The hold-downs reaching their nominal capacity showed that all of the overstrength in this type of wall system was realized.

- The difference in the overturning lever arm led to an imbalance in load sharing between the pair of hold-downs installed on the same stud pack. It is expected that this led to the outer hold-down reaching its nominal capacity earlier and failing.

- The lateral capacity of shear walls can often be limited due to hold-down capacity available for design. Such an issue is usually not encountered while designing with tension tie-rods, which offer increased flexibility to the wall system.

Shear wall detailing

- Symmetric Type I specimens reached 60-65 kN/m (4100-4400 plf) range of resistance for the shear wall segment, which is more than two times the highest available strength for design in AISI S400-20, and approximately 50% higher than a 1.22 m long and 2.44 m tall isolated shear wall tested by Rizk and Rogers (2017), which employed similar framing members and fastener spacing.

- Type II specimens had approximately 60% lower strength as compared to similarly-framed Type I specimens. This was due to the reduced number of tension rods and steel sheet fasteners used. However, the reduction in lateral strength was not as large as suggested by AISI S400-20.

- The elastic stiffness was 65% lower for Type II specimens. Drift at strength was also consistently lower for Type II specimens compared to Type I specimens.

Sheet fastener pattern

- Use of additional fasteners for steel sheet installation led to a modest increase in strength, stiffness and drift at strength.

- Fastener detailing change did not alter local wall response measurements or observed physical failure mode.

The progressively incurred physical damage observed in wall-line assemblies has been systematically documented at different performance levels. The damage in fastener connections between steel sheet sheathing and CFS framing in unfinished wall-lines was accessed. Two damage modes, tilting/bearing and sheet pullover, were identified and the quantity of fasteners which demonstrated that damage was quantified. Damage in fasteners began as tilting/bearing of fastener head, which spread to other screws as width of tension field increased, followed by sheet pull-over the heads for 40-50% of the fasteners at very large amplitude drift cycles ($\Delta = 4\%$).

Well detailed code-compliant wall systems showed tilting/bearing damage in 30-60% of fasteners, but no sheet pull-over damage at design performance level. Interestingly, the presence of a window opening next to shear wall segment had no apparent effect on the quantity of steel sheet fasteners damaged. Damage statistics were accompanied with photographs showing the fastener and framing member damage progression in an unfinished wall-line. The use of toe-to-toe built-up box section for chord studs augmented with blocking at every third height protected the stud packs against plastic deformations from twisting due to the eccentric forces placed on them from single sided sheathing. This has been a common damage observation in previous tests on CFS framed shear walls, especially when thicker steel sheet was used. Progression of damage in tie-down system specific to wall-line assemblies employing traditional hold-downs, beginning at 3% drift ratio, was also discussed. For finished specimens, the progression of damage in EIFS and gypsum panel layers was presented. It was also observed that the damage to framing members observed in finished and unfinished specimens was quite similar.

One important objective of experimental program was to characterize the dynamic performance of CFS-framed wall-lines. The evolution of dynamic characteristics at different performance levels for specimens tested during the shake table test phase were discussed. The accumulation of damage in baseline specimen SGGS-1 through the test sequence led to an elongation of the fundamental period from 0.157s in its undamaged state to 0.199s following the design level earthquake test. The damping ratio also increased from 2.1% in its undamaged state to 5.3% during the earthquake test sequence. Finished specimen SGGS-1F had the highest stiffness and damping ratio in its undamaged state, owing to the applied finishes. However, as damage progressed, its natural period approached that of its unfinished counterpart SGGS-1.

Progression of damage was also correlated with hysteretic energy dissipation characteristics of the wall-line specimens at different performance levels. A two-step procedure, which aimed at identifying drift cycles with significant dissipated energy, was adopted to allow for energy dissipation comparisons for specimens tested using different loading protocols between the shake table and quasi-static test phases. The procedure showed that the testing protocols were

consistent in terms of the fractional drift cycle distribution within different drift bins. Results also revealed that the evolution of hysteretic energy was highly consistent for specimens with similar lateral strength and stiffness up to the above design performance level. Finished specimens demonstrated higher rate of energy dissipation compared to their unfinished counterparts, since the finished specimens used additional fasteners for gypsum and glass-mat panel installation. Specimens with window opening in the middle showed very similar energy dissipation characteristics as similarly detailed wall-line specimens with gravity wall segment in the middle. The rate of energy dissipation increased until strength, and then dropped steadily for all finished specimens. This correlates well with the observed EIFS and gypsum panel damage at different performance levels. For unfinished specimens, the rate of energy dissipation did not see an immediate drop-off in the drift cycle following the cycle during which strength was achieved. This is directly correlated to the number of engaged sheathing fasteners at different performance levels.

6.3.2 Numerical Modeling of Cold-Formed Steel-Framed Wall-Lines in Mid-Rise Buildings

A finite element modeling approach for mid-rise CFS-framed buildings was presented and the predictions from this design-grade numerical model were compared against the measured seismic response of the six-story CFS-HUD test building. Comparison of eigen analysis results with system identification results showed that the numerical model captures the lateral stiffness of the test building in the two orthogonal directions, even though the torsional mode was not as well predicted. Higher modes were reasonably well predicted by the numerical model. The elongation of natural period for longitudinal translation mode as damage accumulated in the building was also adequately captured by the numerical model.

Comparisons between the numerical model predictions and measured experimental response, in terms of story shear versus inter-story drift hysteretic response, floor response spectra, PIDR and PFA envelopes, were presented. The numerical model adequately captured

the experimental response, particularly for the design earthquake test. The initial stiffness during service level earthquake event at different floors, as well as the secant stiffness, shear resistance and inter-story drift during the design earthquake were well captured by the numerical model. Peak roof drift ratios, global base shear and overturning moment up to design earthquake were also well predicted by the numerical model. The cumulative contribution from wall uplift and rod elongation towards story drift was evaluated at different levels. The numerical model was able to capture the higher contribution from cumulative uplift and rod elongation, compared to pure shear deformation of shear elements, towards lateral drift at higher levels of the building. Overall, a good agreement between the numerical model predictions and experimental response offer substantial validation for the proposed design-grade numerical modeling approach.

6.4 Future Work

While significant progress has been made in understanding the behavior of CFS-framed wall-line assemblies, further experimental and numerical investigations are needed to support code development for seismic detailing in mid-rise and high-rise CFS-framed buildings.

6.4.1 Component-level Test Needs

The wall-line experimental program undertaken in this dissertation was only the second research effort at evaluating the seismic performance of CFS-framed walls through dynamic testing, and further dynamic testing is imperative. In this regard, the following experimental investigations are recommended to advance the understanding of their seismic behavior:

- Wall-line specimens tested in the current experimental program were variations of the baseline specimen SGGS-1 configuration, a 2.44 m gravity wall segment in the middle and 1.22 m Type I shear wall segments on each end. Wall-lines observed in a wide range of archetypes from different seismic regions and building occupancy types can be considered to develop wall-line configurations with lengths of shear, gravity and opening segments,

typically seen in CFS-framed buildings, in-line with each other.

- The current experimental program used EIFS as an exterior finish layer. Dynamic characteristics of finished specimens were evaluated from the test results of a single specimen: SGGS-1F. Additional wall-line assemblies should be tested under dynamic loading. Other popular finish options such as Structural Insulated Panels (SIPs) typically installed over wood-sheathed shear walls, warrant exploration in future test programs.

- Tension tie-rod are becoming a common detail in multi-story CFS-framed buildings. The wall-lines considered in the experimental program herein were all single-story walls. Dynamic testing of stacked wall-lines can provide insight into the tie-rod behavior in multi-story buildings.

- The impact of window framing instead of gravity framing was explored in the current experimental program. Though the sizes and locations of wall openings were selected to be representative of configurations observed in practice, wall-lines with a typical door opening or different sized window openings are of interest. Furthermore, installing doors and glazing within the window space may also impact the wall lateral behavior, offering additional lateral resistance, particularly at low drift amplitudes.

- The lateral load sharing between shear and gravity wall segments within the wall-line was estimated through linear regression analysis between results of finished and unfinished specimens. This should be determined experimentally by measuring the base shear under different segments.

- The progression of damage observed for the different wall-line specimens was reported in this dissertation. Fragility functions for different damage states can be developed and related to level of repair required.

- Future experiments can include testing, repairing and re-testing wall-line specimens. The

recovered lateral strength from different repair options can be quantified and related to the cost of various options.

6.4.2 Complete Building Test Needs: CFS-NHERI 10-story Building

To complement component level investigations undertaken to advance our understanding of the seismic behavior of CFS-framed wall-line assemblies, full-scale building shake table tests of taller CFS-framed specimens are essential. To this end, future efforts within the CFS-NHERI project intend to advance the knowledge of the seismic performance of mid-rise CFS framed building systems and to use this knowledge to support improvements in the seismic design codes for such systems. As seen from the design of the archetype building, details required for these CFS-framed systems to move from a few stories to full mid-rise (>6 stories), with emphasis on details not designated by engineer, are not universally agreed upon as well as traditional details, e.g. the use of large built-up shear wall chord stud packs, are known to be inefficient. Additionally, the important impacts of architectural finishes and the contribution of gravity framing towards lateral force resistance, which have been evaluated at the component level through the wall-line experimental program, require understanding at the system level. To this end, a 10-story CFS-framed capstone building has been designed, with planning underway for construction and testing at the newly upgraded NHERI 6-DOF Large High Performance Outdoor Shake Table Facility (LHPOST6) in 2024. This experimental program will provide a unique opportunity to evaluate the post-earthquake fire performance of an earthquake damaged building. Notably unique to this building will be the integration of architectural finishes and a building height of 30.5 m which exceeds the 19.8 m height limitation set by the ASCE/SEI 7-22 design standard. This building height was selected to push the limits of current engineering practice and eliminate barriers for mid-rise CFS buildings. The experiments will provide vital full-scale system-level benchmark test data for a state-of-the-art CFS building under multidirectional seismic inputs.

The 35.4 m $\times$ 14.6 m CFS-NHERI archetype floor plan serves as the basis for the typical

floor plan for the 10-story building (Torabian et al., 2016a). Given the size limitations of the shake table, a slice of the archetype building that may be accommodated within the shake table platen area of 12.2 m × 7.6 m was selected and redesigned as the test building. Multiple slices of the archetype building were considered as potential options to be the test building. Figure 6.1 shows the different slice options of the archetype building. The selection was based on the following criterion: symmetric floor plan to prevent intentional introduction of torsion into the building; a mix of interior, exterior and corridor shear walls; and minimal changes to floor plan in order to adapt to the shake table. Based on these criterion, option 2 (shown in green) was chosen as the floor plan for the test building slice. Figure 6.2 shows the floor plan of the test building, after some modifications to the chosen floor plan. In its present design, the 10-story test building has a plan area of 11.6 m × 6.9 m , which occupies the entire usable area of the shake table. Figure 6.3 shows a three-dimensional rendering of the CFS-NHERI test building.

The 10-story test building is designed as a CFS-framed building at a hypothetical location in a high seismic region near Irvine, California (coordinates: 33.69°N, -117.83°W) and a corresponding NEHRP Site Class: C (very dense soil and soft rock) condition. Gravity and lateral loads were determined as per the International Building Code 2018 edition (IBC) based on this location. As a result, the following design parameters were assumed in accordance with ASCE/SEI 7-16: risk category: II, spectral acceleration at short periods, S_s=1.261g, spectral acceleration at a period of 1s, S_1=0.452g, and design spectral accelerations, S_{DS} = 1.009g and S_{D1} = 0.452g. Figure 6.4 shows the pseudo-acceleration elastic response spectrum for the selected site. The LFRS of the test building consisted of Type I shear walls with single sided steel sheet sheathing and ledger framing for floor-to-wall connections. The seismic design parameters R (response modification coefficient), Ω_o (over-strength factor) and C_d (deflection amplification factor) for light-frame (cold-formed steel) walls sheathed with steel sheets were taken as 6.5, 3.0 and 4.0, respectively as per ASCE/SEI 7-16.

Increasing the height of the building results in larger shear and overturning moment demands on the shear walls. This imposes the need for large built-up chord stud packs, even for

6-story buildings. Similarly, the shear wall seismic shear demands for a 10-story building require tight fastener spacing for shear walls at mid-height levels and are often beyond the tabulated steel sheet shear wall capacities provided in AISI S400-20 for lower levels. These issues are addressed in the test building design by using recently available experimental data on larger capacity shear walls with steel sheet sheathing (Rizk and Rogers, 2017; Santos and Rogers, 2017; Briere and Rogers, 2017). Additionally, to overcome the chord stud capacity limitation for taller CFS buildings, the lower stories of the test building use HSS sections as chord members to meet the overturning moment demand.

Traditionally, hold-downs are used in light-frame construction as the overturning and uplift restraint system. However, design of shear walls can often be limited due to hold-down capacity available where large lateral capacity is required. In such cases, a plate hold-down can be used to transfer chord stud forces through the building floor by welding the plate to the chord members of two adjacent stories. Another option could be to use continuous tension tie-rod system as the overturning and uplift restraint system. CFS-NHERI wall-line experimental program demonstrated that wall-lines using hold-downs achieved higher lateral strength. However, this was accompanied by undesirable failure in hold-downs at larger drift demands, while tension tie-rods remained linear elastic. Due to the importance of determining their viability in mid-rise construction, the test building is designed to incorporate both tie-down systems. The LFRS in the longitudinal direction is detailed with shear walls with hold-downs or plate hold-downs, see shear walls SW2 on lines 1 and 2 in Figure 6.2, while the LFRS in the transverse direction is detailed with shear walls with floor-to-floor continuous tension tie-rod system, see shear walls SW1 and SW3 on lines C, D and E. Figure 6.5 shows the different tie-down detailing systems used in the longitudinal direction at different levels of the building.

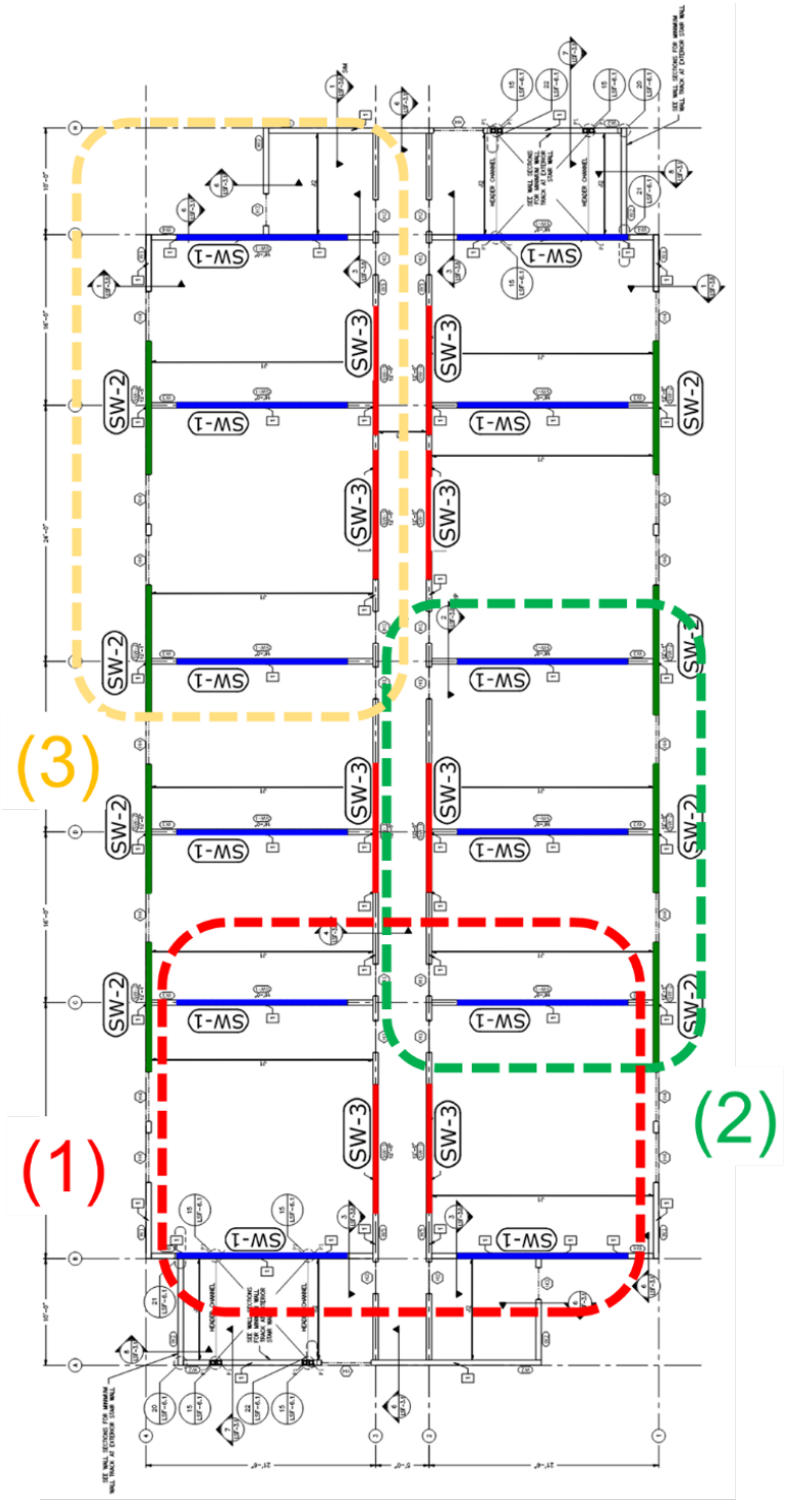


Figure 6.1. Archetype building slice options (color regions overlaid with original archetype building plan set)

Note: Slice option 2 in green was selected to derive the basis layout of the future building test specimen.

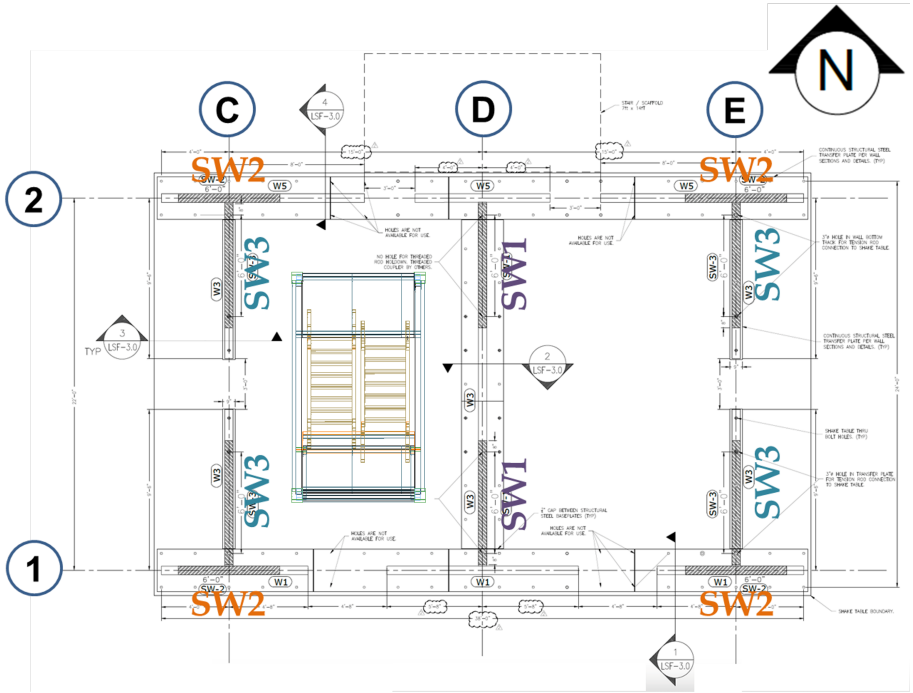


Figure 6.2. Floor plan of the 10-story CFS-NHERI test building (construction drawings courtesy of ClarkDietrich Building Systems)



Figure 6.3. CFS-NHERI test building installed at the NHERI@UC San Diego LHPOST6 facility (rendering courtesy of Charlie Zhang)

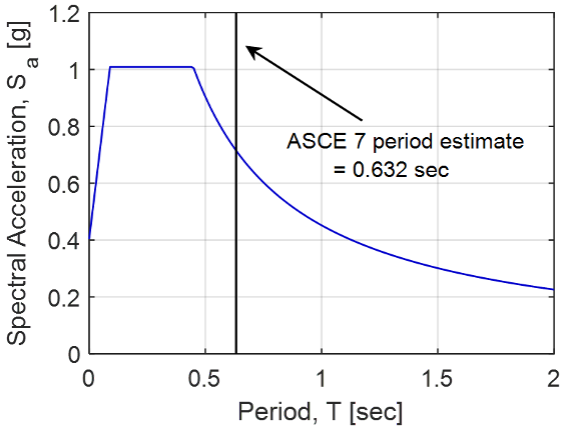


Figure 6.4. Psuedo-acceleration response spectrum for selected site

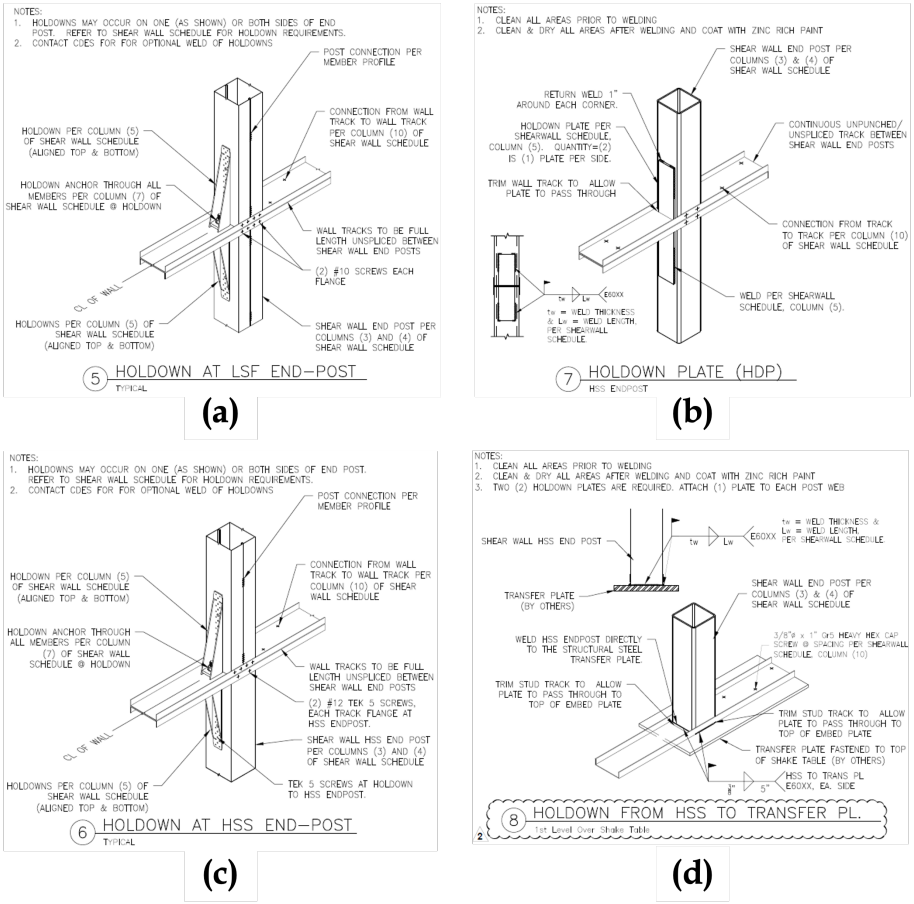


Figure 6.5. Tie-down systems used in the longitudinal direction of the test building: (a) hold-down attached to built-up chord studs, (b) hold-down attached to HSS section, (c) plate hold-down attached to HSS section, and (d) HSS section welded to transfer plate on shake table (construction details courtesy of ClarkDietrich Building Systems)

Wall lines C, D, E and 2 will have fire rated gypsum board finish, typical of interior walls. Similarly, wall line 1 will have EIFS exterior finish, similar to the wall-lines tested in the CFS-NHERI wall-line experimental program. The test building will also adopt a light gauge steel frame (LSF) floor system, built using CFS channel section joists with fire resistant cement board subfloor panels. It is notable that the test building will adopt use of prefabricated CFS wall-lines and floor diaphragms for rapid construction at the test site. The structural design narrative, which included in depth discussion of the different design decisions, can be found in Singh et al. (2022a).

The test protocol for the system-level shake table experimental program will consist of a sequence of earthquake tests of increasing intensity, which progressively damage the test building. The approach for numerical modeling of CFS-framed building presented in this dissertation can be used to develop a test protocol for the CFS-NHERI test building. Such pre-test numerical modeling can be used to obtain predictions of the test building seismic behavior, which can guide earthquake motion selection and a motion scaling strategy for defining the test protocol that allows for assessment of seismic performance of structural and nonstructural components at multiple pre-defined performance levels, for example: elastic (service), quasi-elastic, design, and maximum considered levels.

6.4.3 Numerical Modeling Needs

The research presented in this dissertation on the modeling of different components of wall-lines and analysis of the CFS-HUD building presents a numerical modeling approach for mid-rise CFS-framed buildings. However, the developed model has several limitations. In this regard, the following numerical investigations are recommended to improve the numerical model predictions:

- The vertical load path needs further consideration and improvement, especially to enable analysis under vertical excitation. This can be enabled by modeling the individual gravity studs as pin-connected vertical elements, allowing them to naturally carry gravity load.

- The floor and roof diaphragms within the building model were assumed to be axially rigid in-plane. A more appropriate approximation may model the diaphragm as a rigid plate. However, modeling of the in-plane stiffness of diaphragms, based on experimental results, should also be pursued for greater accuracy in numerical predictions. This is particularly important when a flexible diaphragm can impact the out-of-plane kinematics of the wall-line.

- The CFS-HUD building used tension tie-rods as the uplift restraint system. As evaluated in wall-line tests, wall-line assemblies in CFS-framed buildings can also employ hold-downs. Characterizing the hold-down behavior in multi-story buildings for use in numerical models should be pursued. Hold-downs offer a more rigid floor-to-floor connection depending upon the way they are installed, welded or bolted, and require due consideration.

- For the nonlinear time-history analyses, the damping ratio was set to 5% based of the adoption of 5% damping in codes and standards and recommended provisions. Damping ratio as measured from the CFS-HUD building indicates 8-10% may be attainable, and thus should be used in the service-level intensity time-history analyses, and then reduced accordingly for higher intensity motions when the building has incurred some damage. The choice of damping ratio has an impact on the numerical model response prediction, especially the floor acceleration response. It is important to understand how the simulated responses are affected by the variation of damping ratio.

- The numerical model predicted the natural period of the building in the translation modes very well. However, the natural period associated with torsional modes was not well predicted. The interaction of wall-lines at building corners can be modeled as a rotational spring to improve the three-dimensional building response prediction.

- A refined wall-line modeling strategy was employed to investigate the effects of compression stud packs on shear wall lateral strength and stiffness. Large compression stud packs

are typically used in mid-rise buildings. However, high-rise buildings might be detailed with HSS hot-rolled steel sections to provide against large overturning moment demands. The modeling strategy developed in this dissertation should be extended to HSS steel compression posts to allow application to high-rise CFS-framed buildings.

- The CFS-HUD building was subjected to post-fire aftershock earthquakes. However, the time-history analyses in this dissertation were restricted to the pre-fire earthquake events. Based on the observed damage in the CFS-HUD buildings, the properties of appropriate shear and gravity elements can be altered. Numerical prediction of the post-fire building response can be pursued by extending the numerical modeling strategy in such a manner.

Acknowledgment of Publications

Portions of the following papers, for which the dissertation author was the primary investigator and author, are contained in Chapter 6:

Singh, A., Wang, X., Zhang, Z., Derveni, F., Castaneda, H., Peterman, K. D., Schafer, B. W., and Hutchinson, T. C. (2022). "Steel Sheet Sheathed Cold-Formed Steel Framed In-line Wall Systems. I: Impact of Structural Detailing" *ASCE J. Struct. Eng.*, 148(12), 04022193.

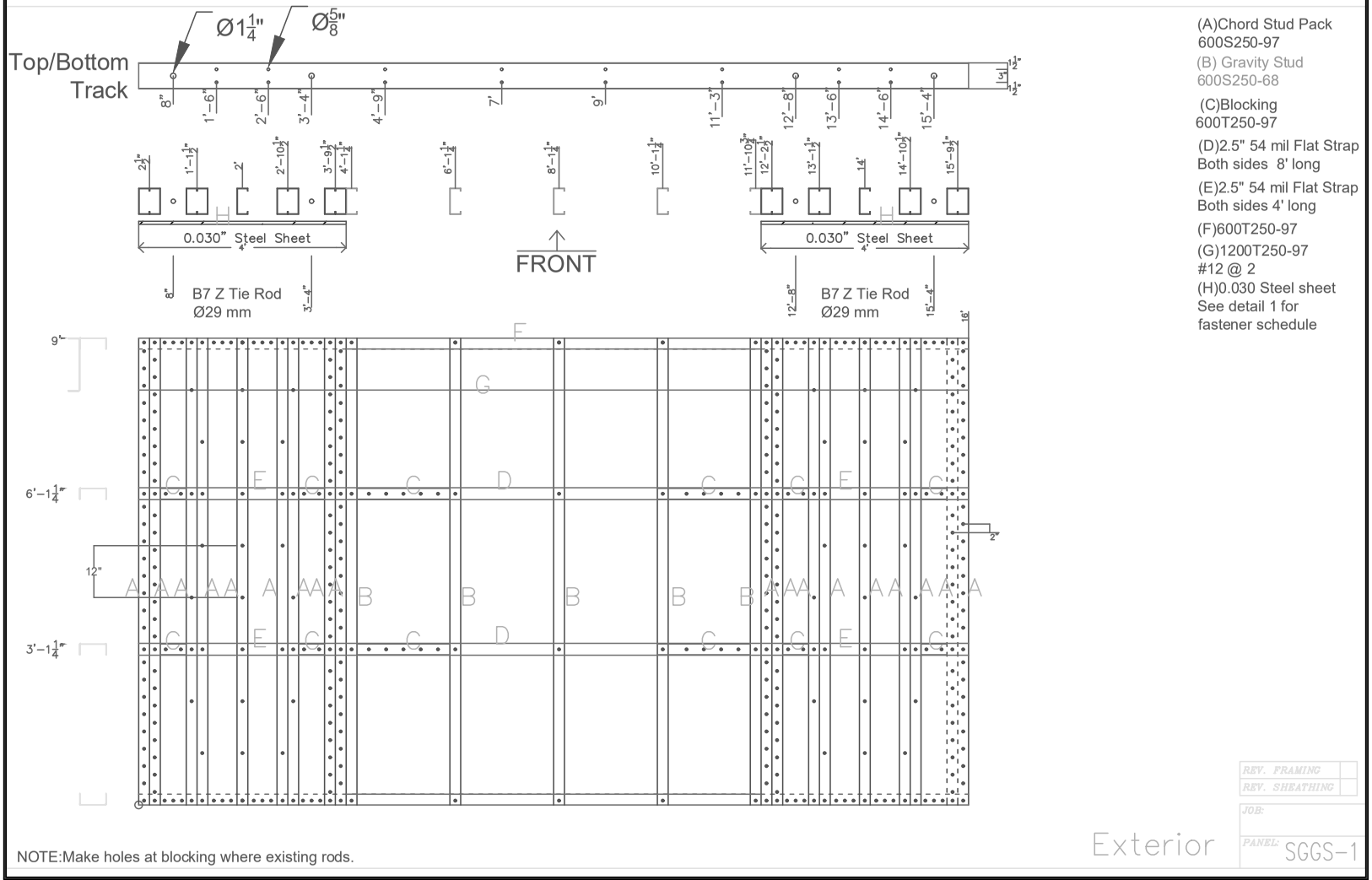
Singh, A., Wang, X., Zhang, Z., Derveni, F., Castaneda, H., Peterman, K. D., Schafer, B. W., and Hutchinson, T. C. (2022). "Steel Sheet Sheathed Cold-Formed Steel Framed In-line Wall Systems. II: Impact of Nonstructural Detailing" *ASCE J. Struct. Eng.*, 148(12), 04022194.

Singh, A., Hutchinson, T. C., Torabian, S., Schafer, B. W., Peterman, K. D., Padgett, L. and Jones, H. (2022). Structural Design Narrative of the CFS-NHERI 10-story Test Building for Multi-dimensional Shake Table Testing. In *Proceedings of Cold-Formed Steel Research Consortium Colloquium*. Baltimore, MD. Johns Hopkins University.

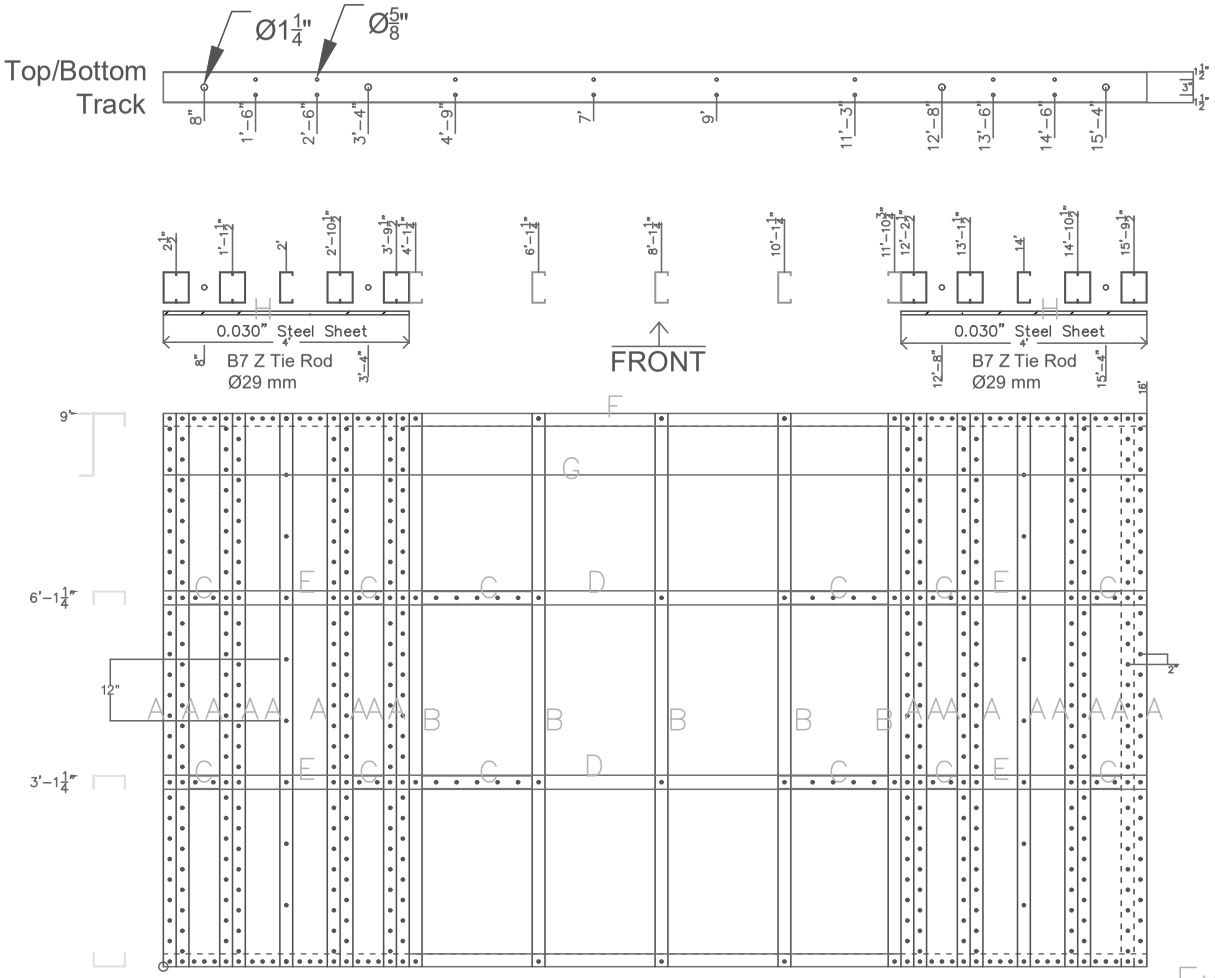
Appendix A

Shop Drawings of Fabricated Wall-lines

Shop drawings of all the tested configurations used for fabrication have been provided here.



UCSD	No. Date Revisions	CFS-NHERI Wall Tests	Amanpreet Singh
University of California, San Diego Department of Structural Engineering La Jolla, California 92093-0085			Graduate Student Researcher
Project No. Date:			

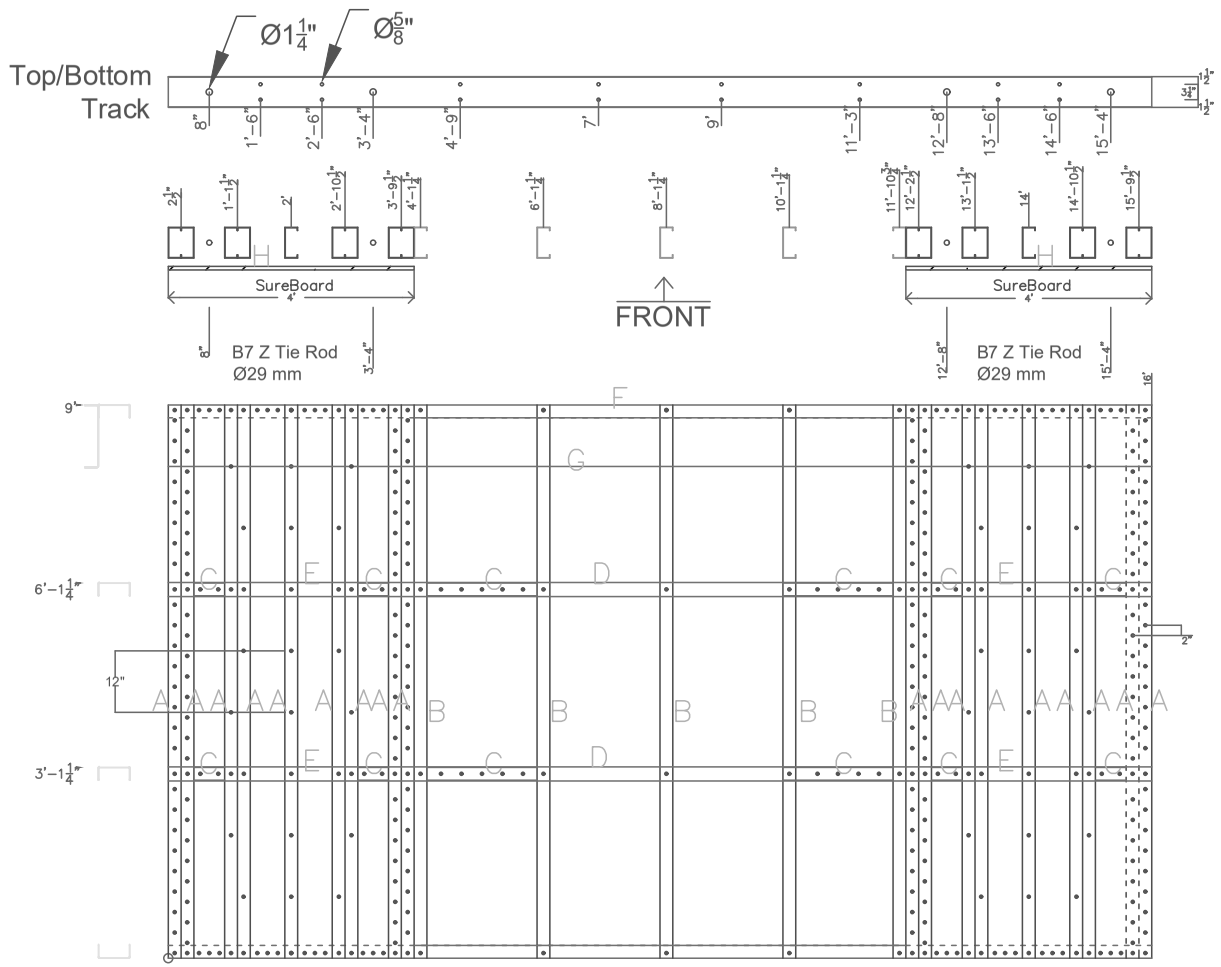


(A)Chord Stud Pack
600S250-97
(B) Gravity Stud
600S250-68
(C)Blocking
600T250-97
(D)2.5" 54 mil Flat Strap
Both sides 8' long
(E)2.5" 54 mil Flat Strap
Both sides 4' long
(F)600T250-97
(G)1200T250-97
#12 @ 2
(H)0.030 Steel sheet
See detail A for
fastener schedule

REV. FRAMING
REV. SHEATHING
JOB:
PANEL: SGGS-1XS

NOTE:Make holes at blocking where existing rods.

U C S D University of California, San Diego Department of Structural Engineering La Jolla, California 92093-0085 Project No. Date:	No. Date Revisions	CFS-NHERI Wall Tests	Amanpreet Singh Graduate Student Researcher



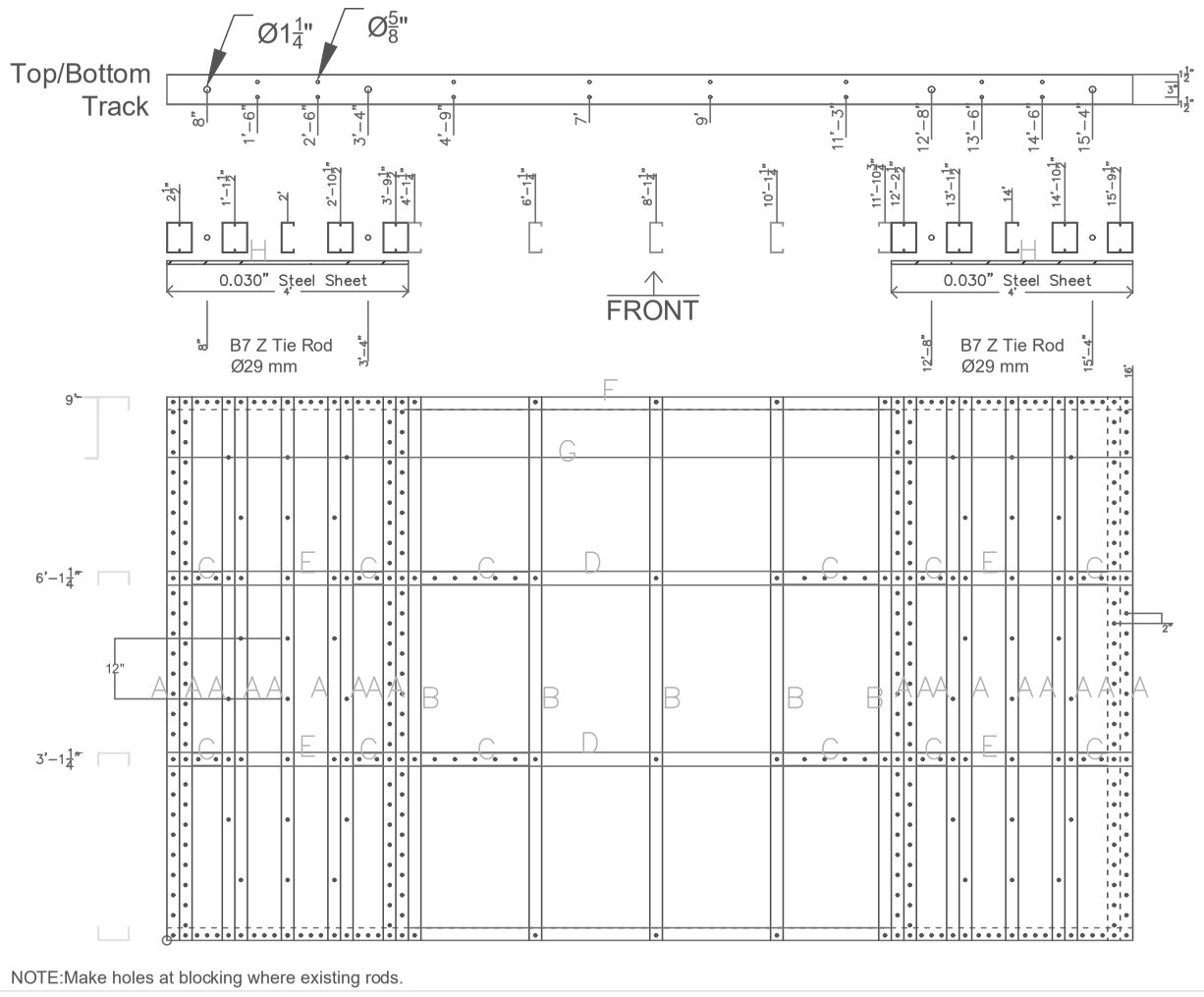
(A)Chord Stud Pack 600S250-97 detail 6
(B) Gravity Stud 600S250-68
(C)Blocking 600S250-68
(D)2.5" 54 mil Flat Strap Both sides 8' long
(E)2.5" 54 mil Flat Strap Both sides 4' long
(F)600T250-97
(G)1200T250-97 #12 @ 2
(H) SureBoard type 200 See detail 4 for fastener schedule

NOTE:Make holes at blocking where existing rods.

Exterior

REV. FRAMING
REV. SHEATHING
JOB:
PANEL SGGS-1SB

UCSD	No. Date Revisions	CFS-NHERI Wall Tests	Amanpreet Singh
University of California, San Diego Department of Structural Engineering La Jolla, California 92093-0085			Graduate Student Researcher
Project No. Date:			



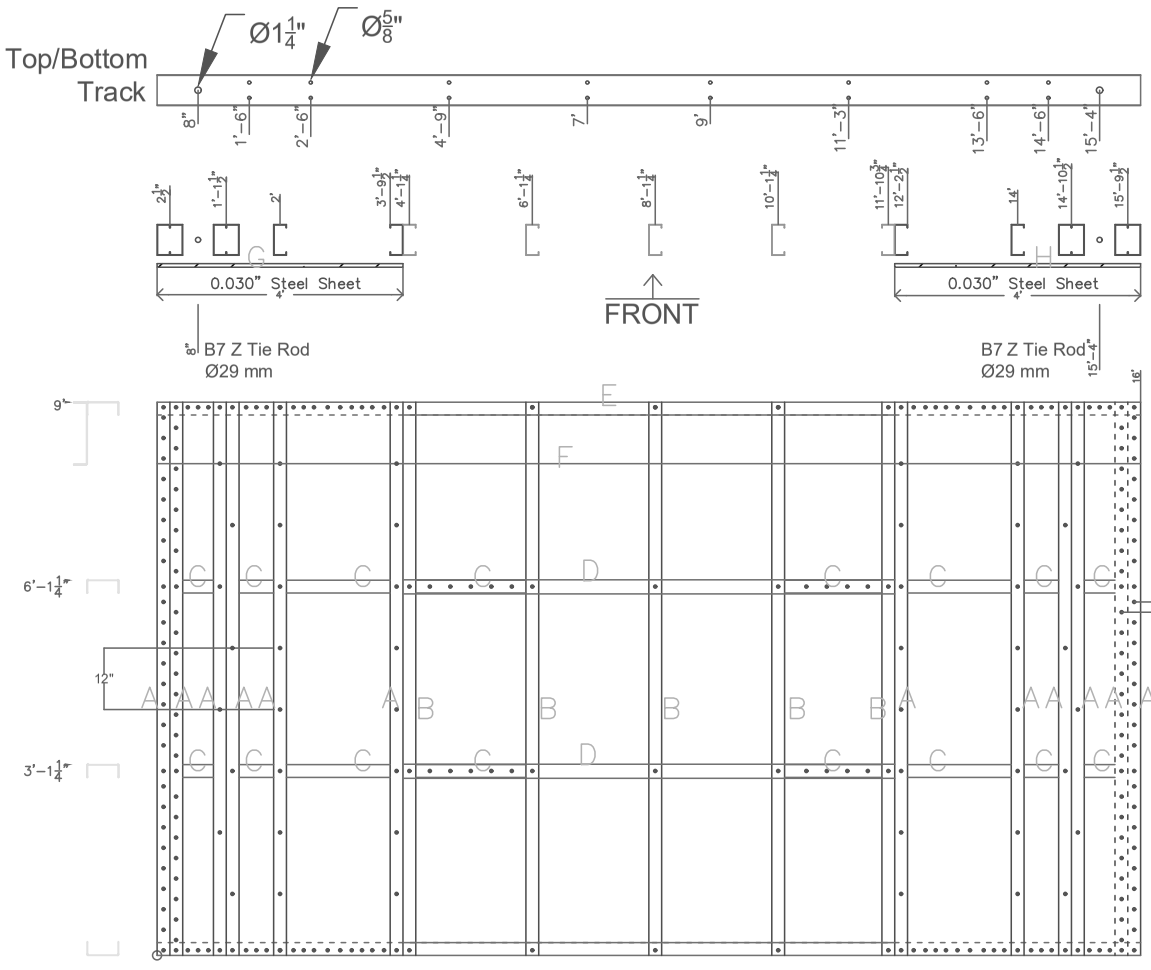
(A)Chord Stud Pack
600S250-97
(B) Gravity Stud
600S250-68
(C)Blocking
600T250-97
(D)2.5" 54 mil Flat Strap
Both sides 8' long
(E)2.5" 54 mil Flat Strap
Both sides 4' long
(F)600T250-97
(G)1200T250-97
#12 @ 2
(H)0.030 Steel sheet
See detail 1 for
fastener schedule

NOTE:Make holes at blocking where existing rods.

Exterior

REV. FRAMING
REV. SHEATHING
JOB:
PANEL: SGGS-1F

UCSD	No. Date Revisions	CFS-NHERI Wall Tests	Amanpreet Singh
University of California, San Diego Department of Structural Engineering La Jolla, California 92093-0085			Graduate Student Researcher
Project No. Date:			



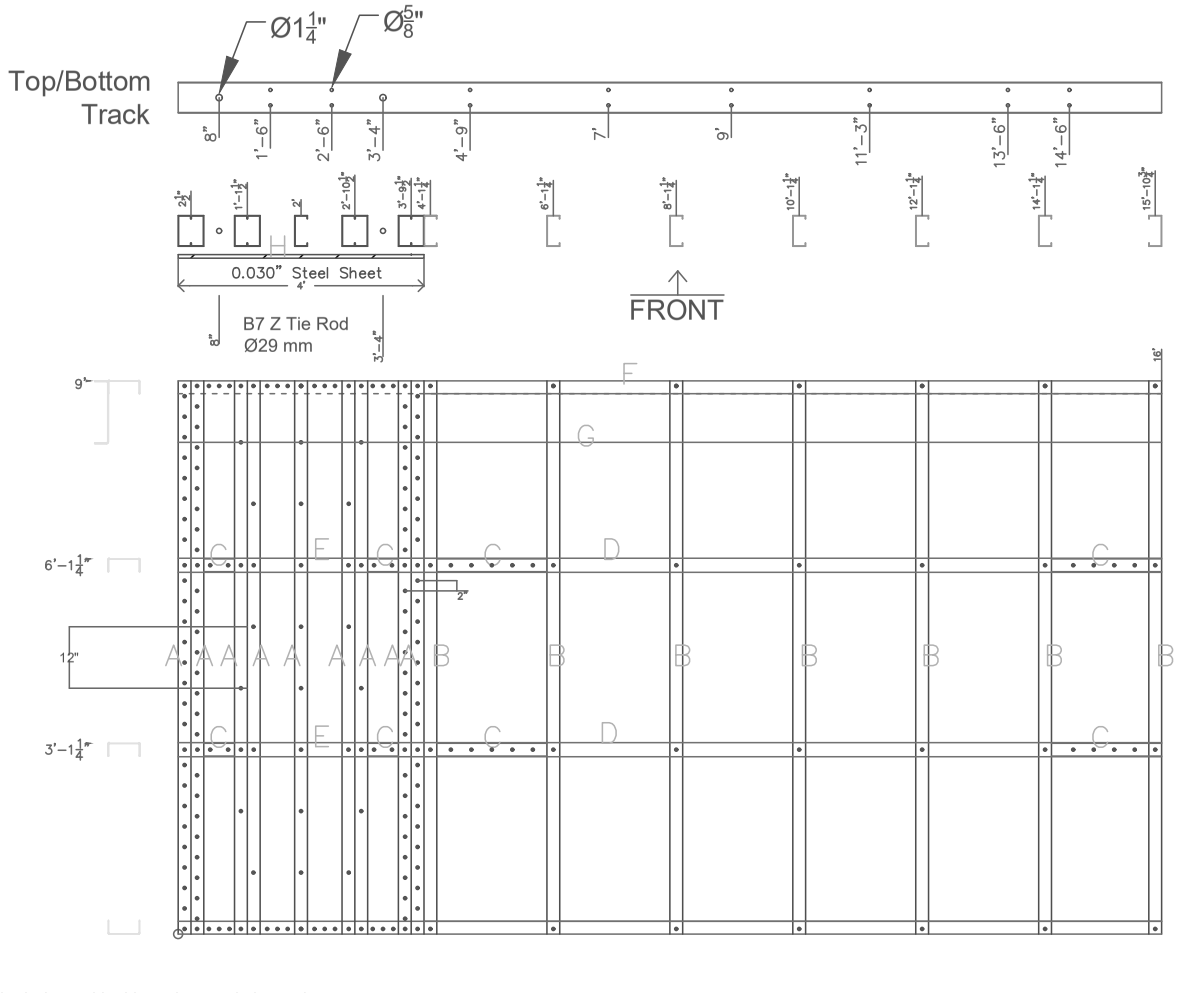
(A)Chord Stud Pack 600S250-97
(B) Gravity Stud 600S250-68
(C)Blocking 600T250-97
(D)2.5" 54 mil Flat Strap Both sides 8' long
(E)600T250-97
(F)1200T250-97 #12 @ 2
(G)0.030 Steel sheet See detail A for fastener schedule
(H)0.030 Steel sheet See detail 2 for fastener schedule

NOTE:Make holes at blocking where existing rods.

Exterior

REV. SHEATHING
JOB:
PANEL: SGGS-2

UCSD	No. Date Revisions	CFS-NHERI Wall Tests	Amanpreet Singh
University of California, San Diego Department of Structural Engineering La Jolla, California 92093-0085			Graduate Student Researcher
Project No. Date:			



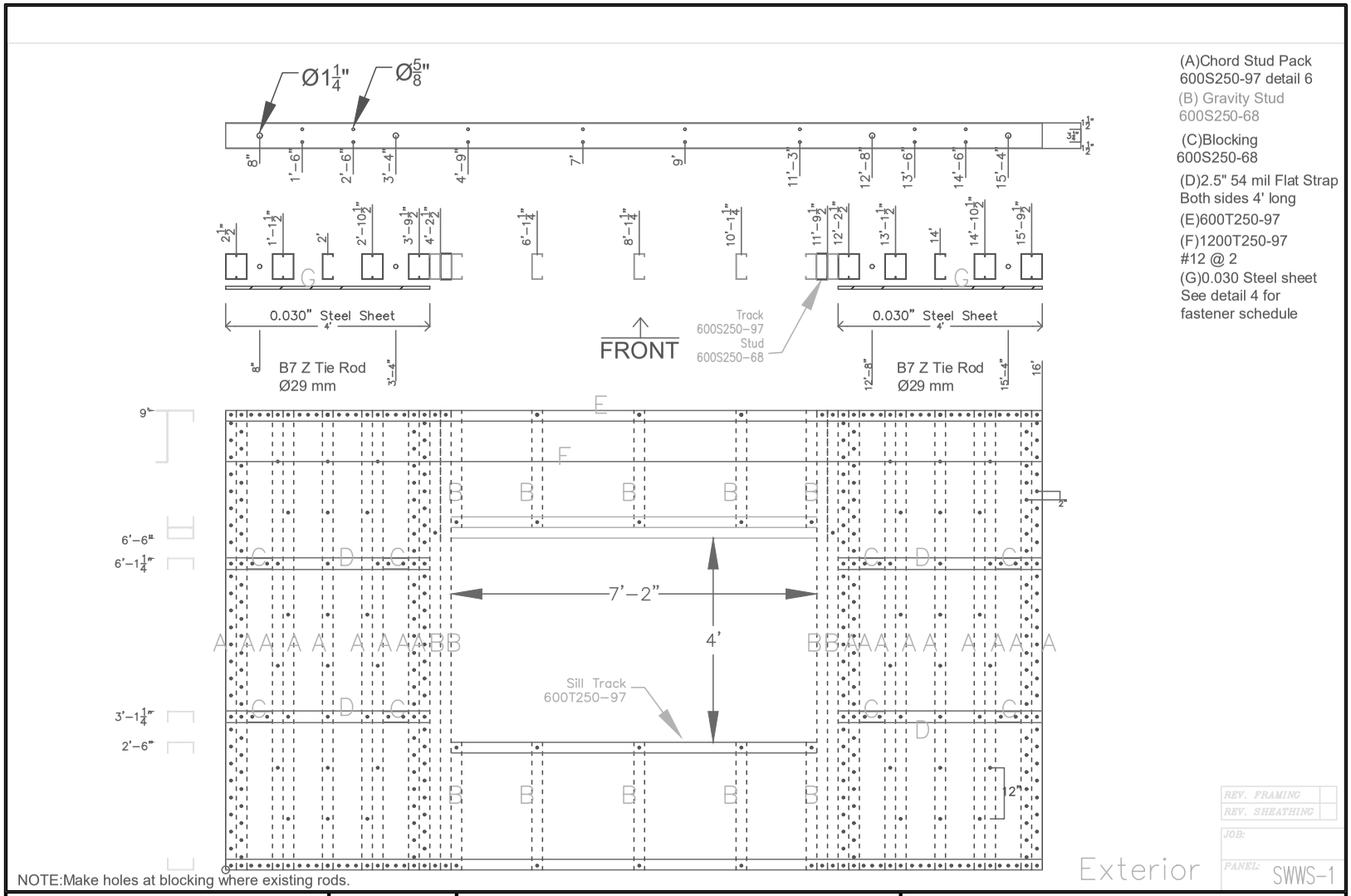
(A)Chord Stud Pack
600S250-97
(B) Gravity Stud
600S250-68
(C)Blocking
600T250-97
(D)2.5" 54 mil Flat Strap
Both sides 12' long
(E)2.5" 54 mil Flat Strap
Both sides 4' long
(F)600T250-97
(G)1200T250-97
#12 @ 2
(H)0.030 Steel sheet
See detail 1 for
fastener schedule

NOTE:Make holes at blocking where existing rods.

Exterior

REV. FRAMING
REV. SHEATHING
JOB:
PANEL: SGGG-1

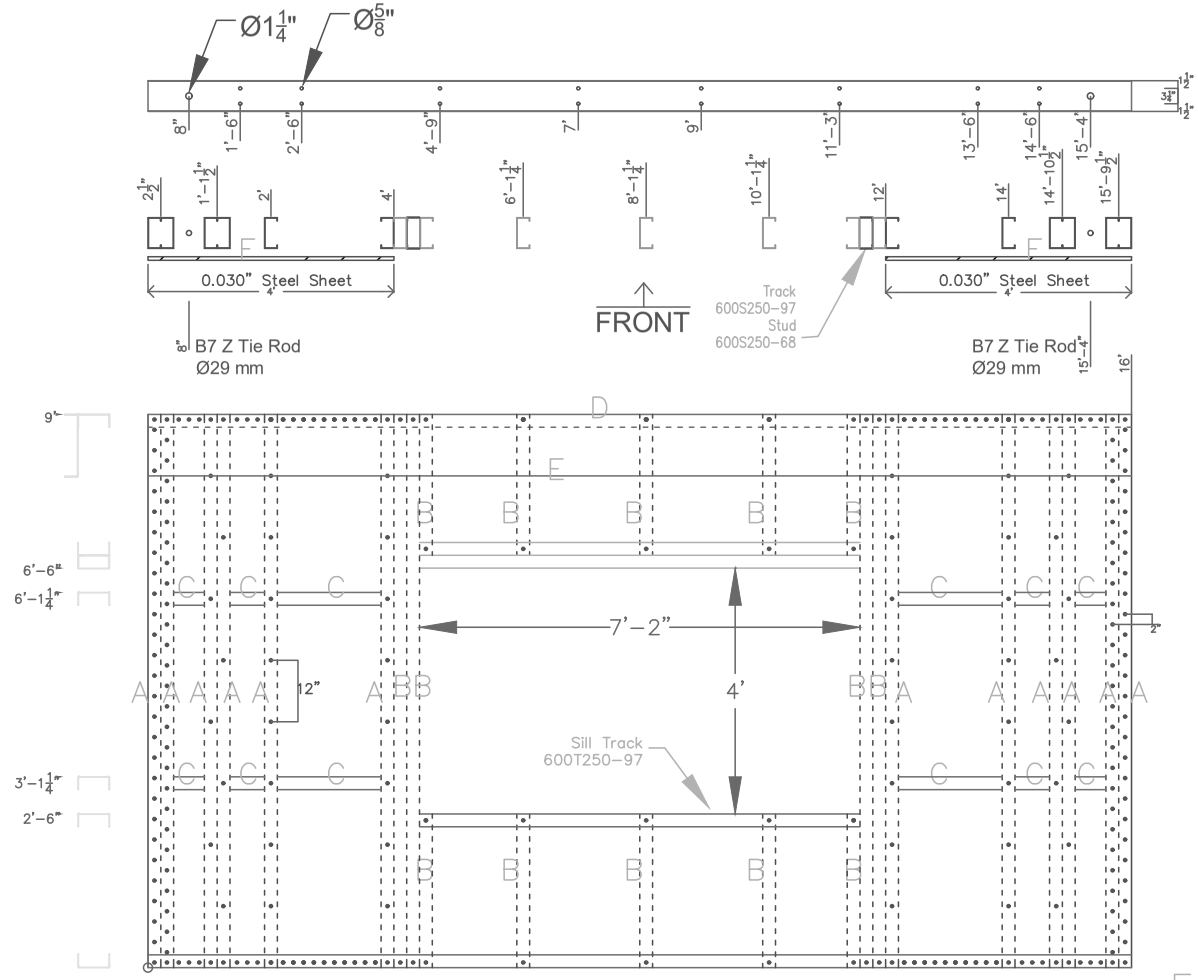
UCSD	No. Date Revisions	CFS-NHERI Wall Tests	Amanpreet Singh
University of California, San Diego Department of Structural Engineering La Jolla, California 92093-0085			Graduate Student Researcher
Project No. Date:			



(A)Chord Stud Pack
600S250-97 detail 6
(B) Gravity Stud
600S250-68
(C)Blocking
600S250-68
(D)2.5" 54 mil Flat Strap
Both sides 4' long
(E)600T250-97
(F)1200T250-97
#12 @ 2
(G)0.030 Steel sheet
See detail 4 for
fastener schedule

REV. FRAMING
REV. SHEATHING
JOB:
PANEL: SWWS-1

UCSD	No. Date Revisions	CFS-NHERI Wall Tests	Amanpreet Singh
University of California, San Diego Department of Structural Engineering La Jolla, California 92093-0085			Graduate Student Researcher
Project No. Date:			

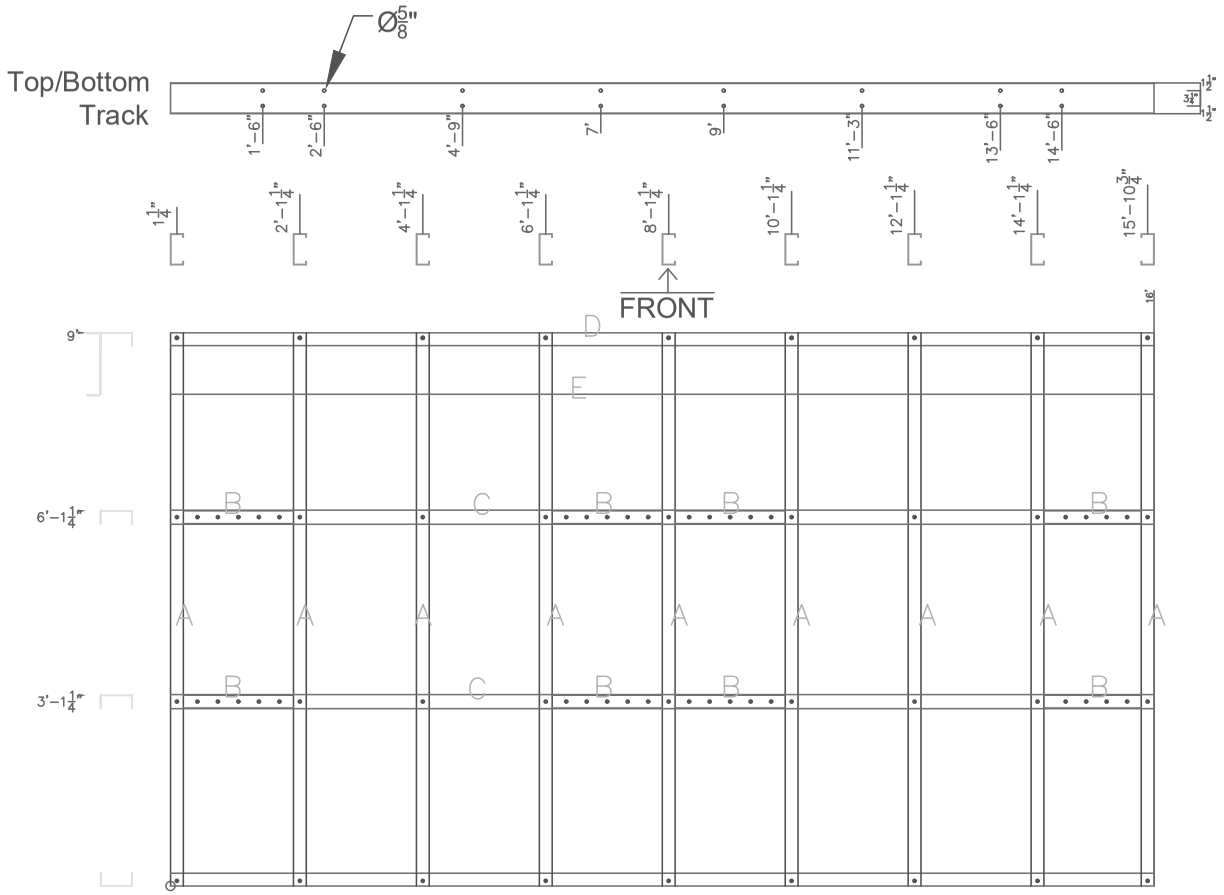


(A)Chord Stud Pack 600S250-97 detail 6
(B) Gravity Stud 600S250-68
(C)Blocking 600S250-68
(D)600T250-97
(E)1200T250-97 #12 @ 2
(F)0.030 Steel sheet See detail 2 for fastener schedule

NOTE:Make holes at blocking where existing rods.

REV. FRAMING
REV. SHEATHING
JOB:
PANEL: SWWS-2

UCSD	No. Date Revisions	CFS-NHERI Wall Tests	Amanpreet Singh
University of California, San Diego Department of Structural Engineering La Jolla, California 92093-0085			Graduate Student Researcher
Project No. Date:			



(A) Gravity Stud
600S250-68

(B)Blocking
600S250-68

(C)2.5" 54 mil Flat Strap
Both sides

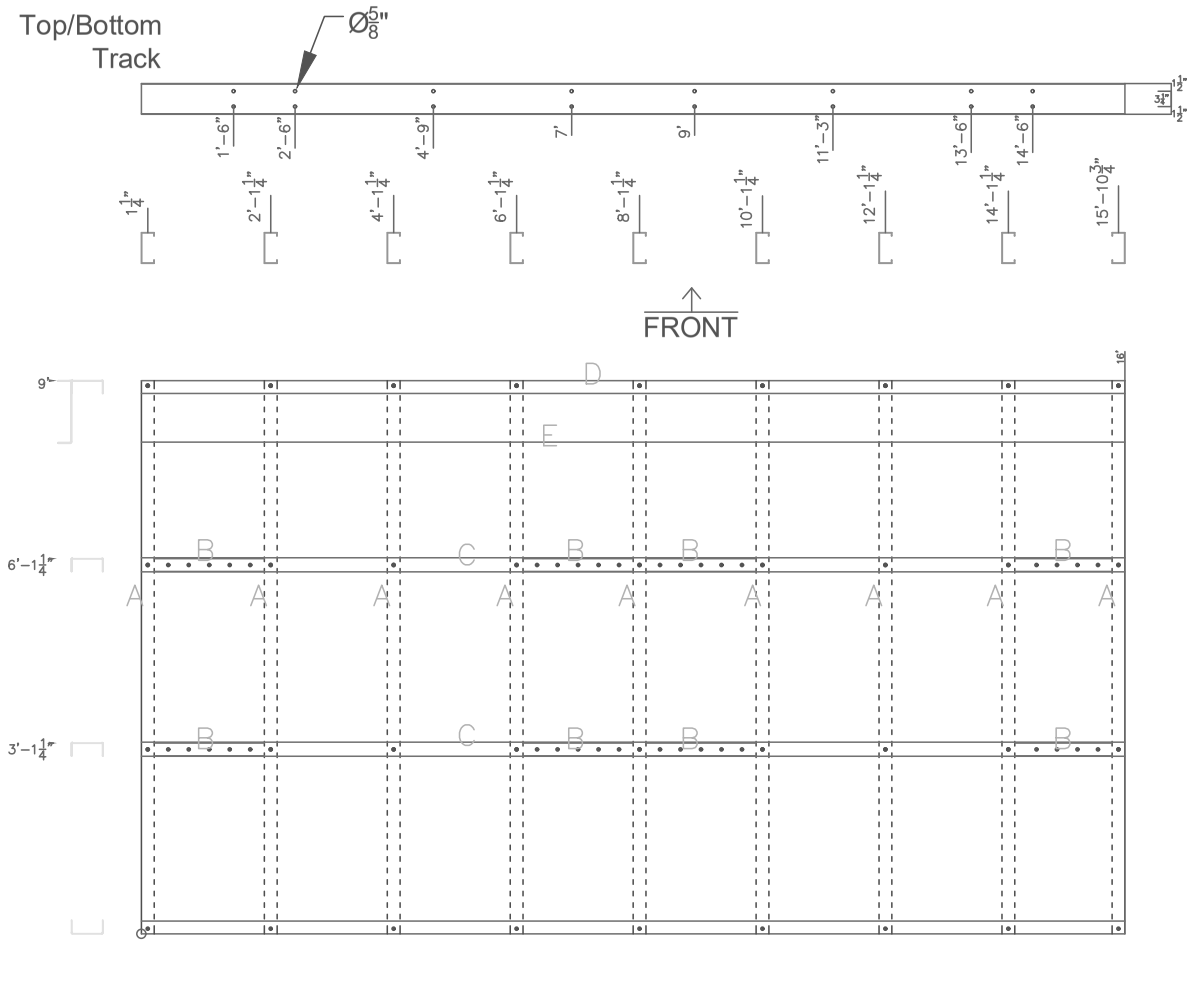
(D)600T250-97

(E)1200T250-97
#12 @ 2

Exterior

REV. FRAMING
REV. SHEATHING
JOB:
PANEL: GGGG

UCSD	No. Date Revisions	CFS-NHERI Wall Tests	Amanpreet Singh
University of California, San Diego Department of Structural Engineering La Jolla, California 92093-0085			Graduate Student Researcher
Project No. Date:			



(A) Gravity Stud
600S250-68

(B)Blocking
600S250-68

(C)2.5" 54 mil Flat Strap
Both sides

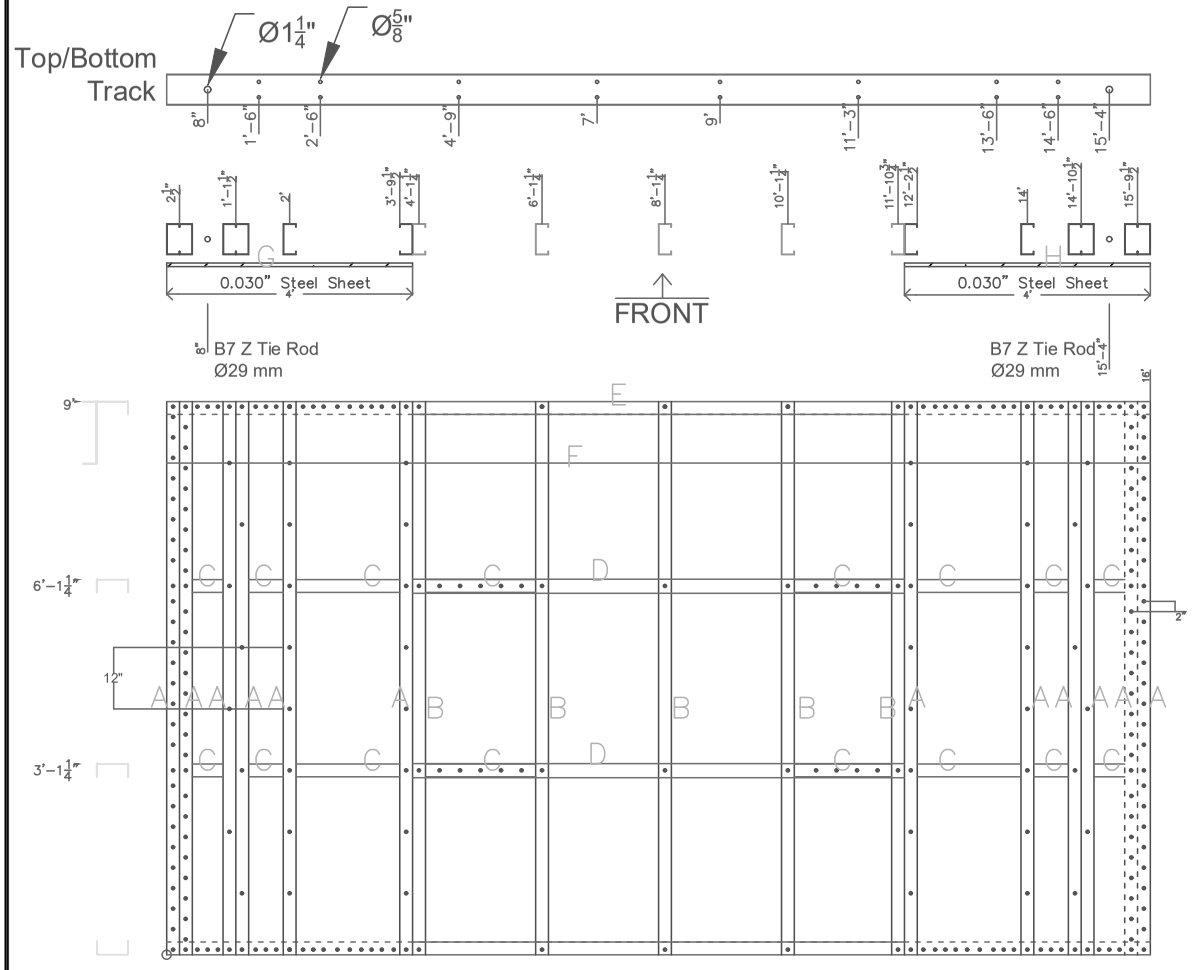
(D)600T250-97

(E)1200T250-97
#12 @ 2

Exterior

REV. FRAMING
REV. SHEATHING
JOB:
PANEL GGGG-F

UCSD	No. Date Revisions	CFS-NHERI Wall Tests	Amanpreet Singh
University of California, San Diego Department of Structural Engineering La Jolla, California 92093-0085			Graduate Student Researcher
Project No. Date:			



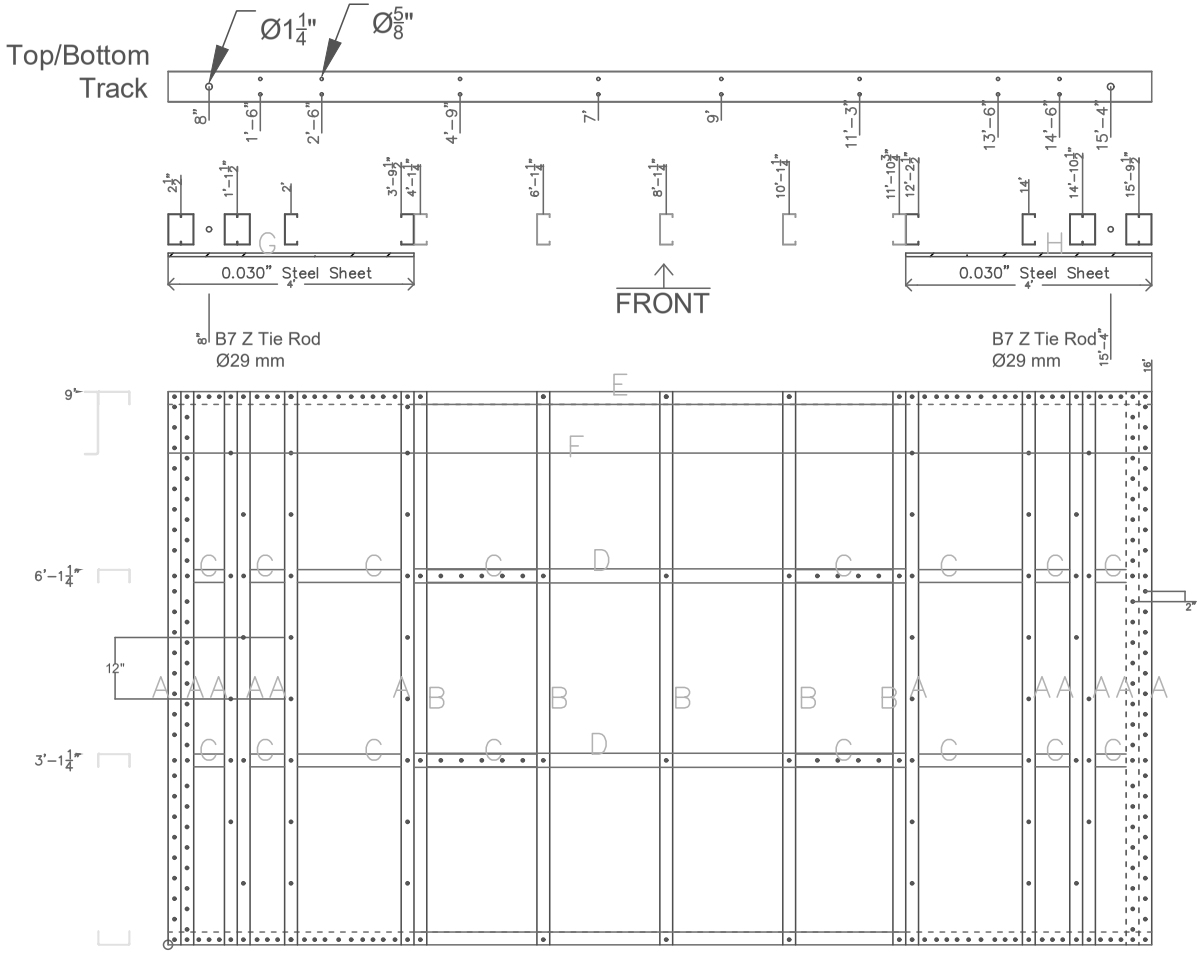
(A)Chord Stud Pack
600S250-97
(B) Gravity Stud
600S250-68
(C)Blocking
600T250-97
(D)2.5" 54 mil Flat Strap
Both sides 8' long
(E)600T250-97
(F)1200T250-97
#12 @ 2
(G)0.030 Steel sheet
See detail A for
fastener schedule
(H)0.030 Steel sheet
See detail 2 for
fastener schedule

NOTE:Make holes at blocking where existing rods.

REV. SHEATHING
JOB:
PANEL SGGS-2

Exterior

U C S D University of California, San Diego Department of Structural Engineering La Jolla, California 92093-0085 Project No. Date:	No. Date Revisions	CFS-NHERI Wall Tests	Amanpreet Singh Graduate Student Researcher



(A)Chord Stud Pack
600S250-97
(B) Gravity Stud
600S250-68
(C)Blocking
600T250-97
(D)2.5" 54 mil Flat Strap
Both sides 8' long
(E)600T250-97
(F)1200T250-97
#12 @ 2
(G)0.030 Steel sheet
See detail A for
fastener schedule
(H)0.030 Steel sheet
See detail 2 for
fastener schedule

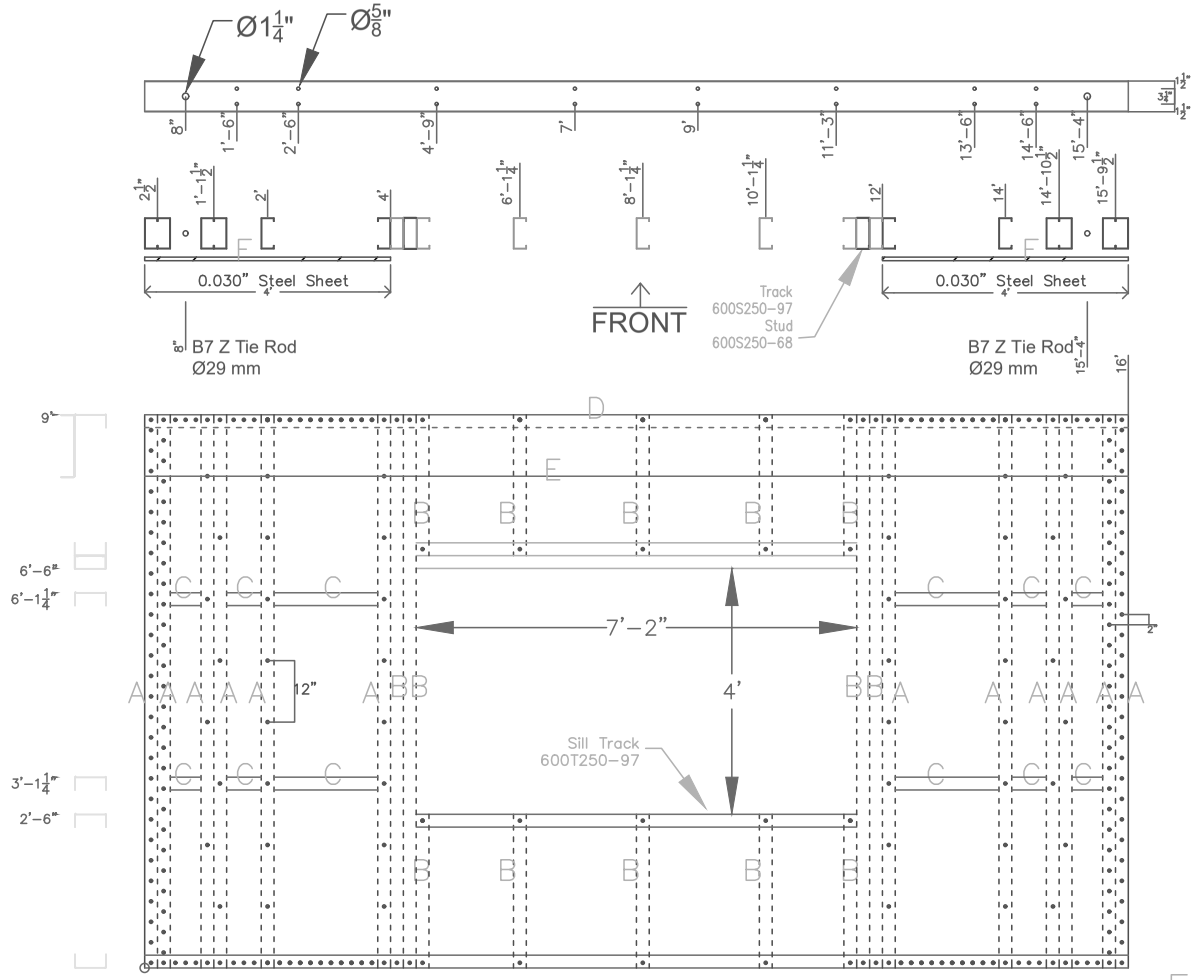
NOTE:Make holes at blocking where existing rods.

REV. SHEATHING

Exterior

PANEL: SGGS-2F

U C S D University of California, San Diego Department of Structural Engineering La Jolla, California 92093-0085 Project No. Date:	No. Date Revisions	CFS-NHERI Wall Tests	Amanpreet Singh Graduate Student Researcher



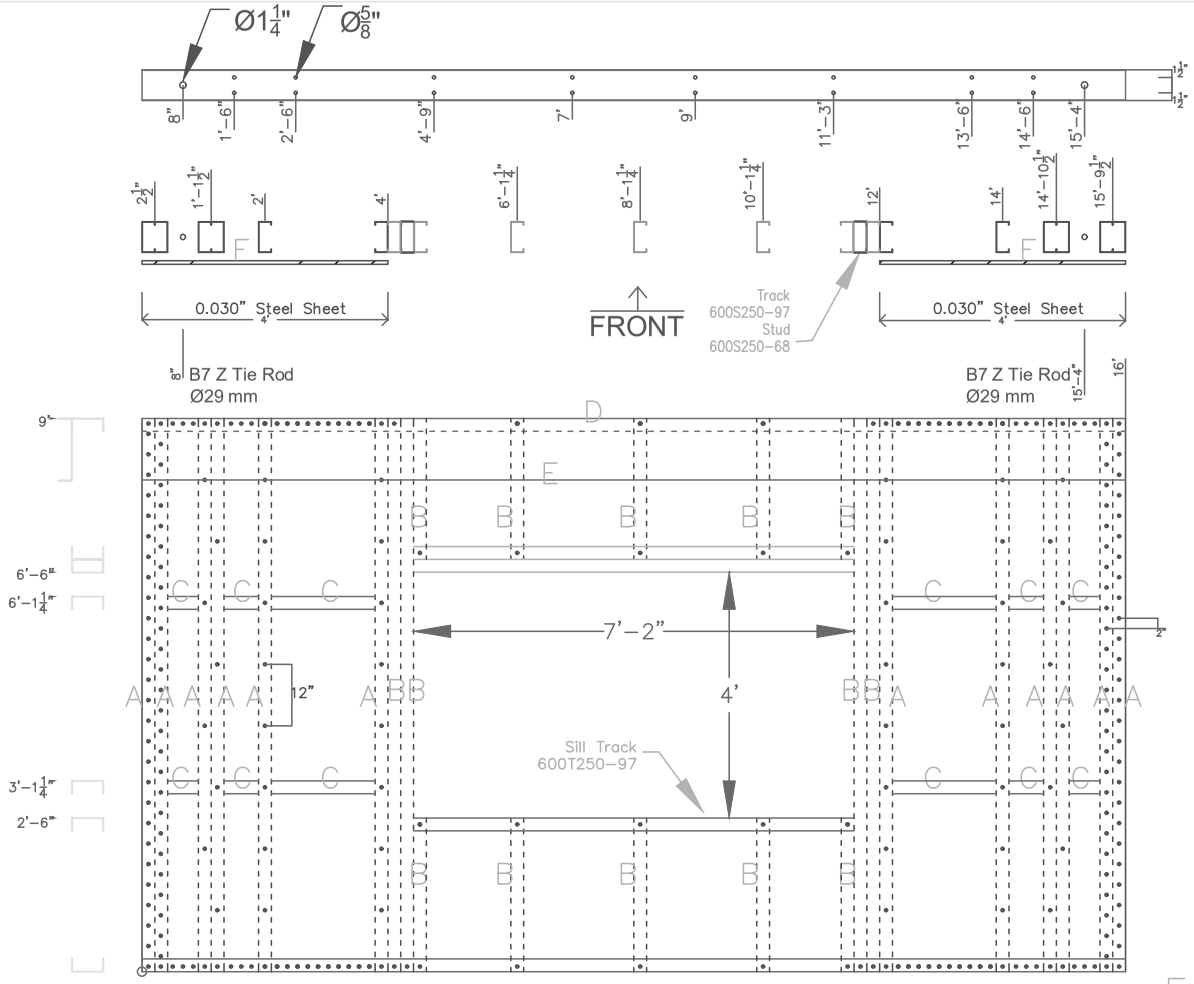
(A)Chord Stud Pack 600S250-97 detail 6
(B) Gravity Stud 600S250-68
(C)Blocking 600S250-68
(D)600T250-97
(E)1200T250-97 #12 @ 2
(F)0.030 Steel sheet See detail 2 for fastener schedule

NOTE:Make holes at blocking where existing rods.

Exterior

REV. FRAMING
REV. SHEATHING
JOB:
PANEL: SWWS-2

UCSD	No. Date Revisions	CFS-NHERI Wall Tests	Amanpreet Singh
University of California, San Diego Department of Structural Engineering La Jolla, California 92093-0085			Graduate Student Researcher
Project No. Date:			

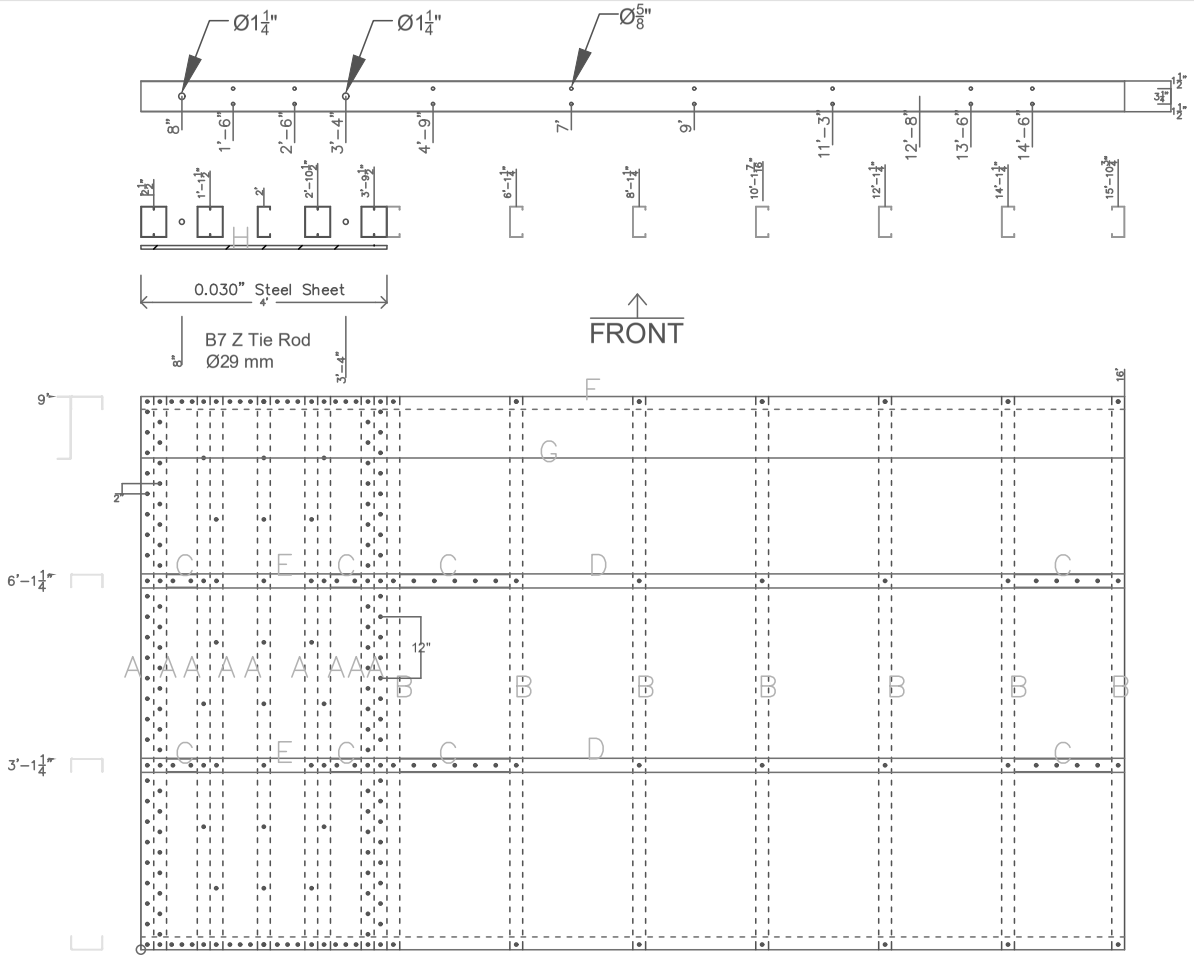


(A)Chord Stud Pack 600S250-97 detail 6
(B) Gravity Stud 600S250-68
(C)Blocking 600S250-68
(D)600T250-97
(E)1200T250-97 #12 @ 2
(F)0.030 Steel sheet See detail 2 for fastener schedule

NOTE:Make holes at blocking where existing rods.

REV. FRAMING
REV. SHEATHING
JOB:
PANEL: SWWS-2F

UCSD	No. Date Revisions	CFS-NHERI Wall Tests	Amanpreet Singh
University of California, San Diego Department of Structural Engineering La Jolla, California 92093-0085			Graduate Student Researcher
Project No. Date:			



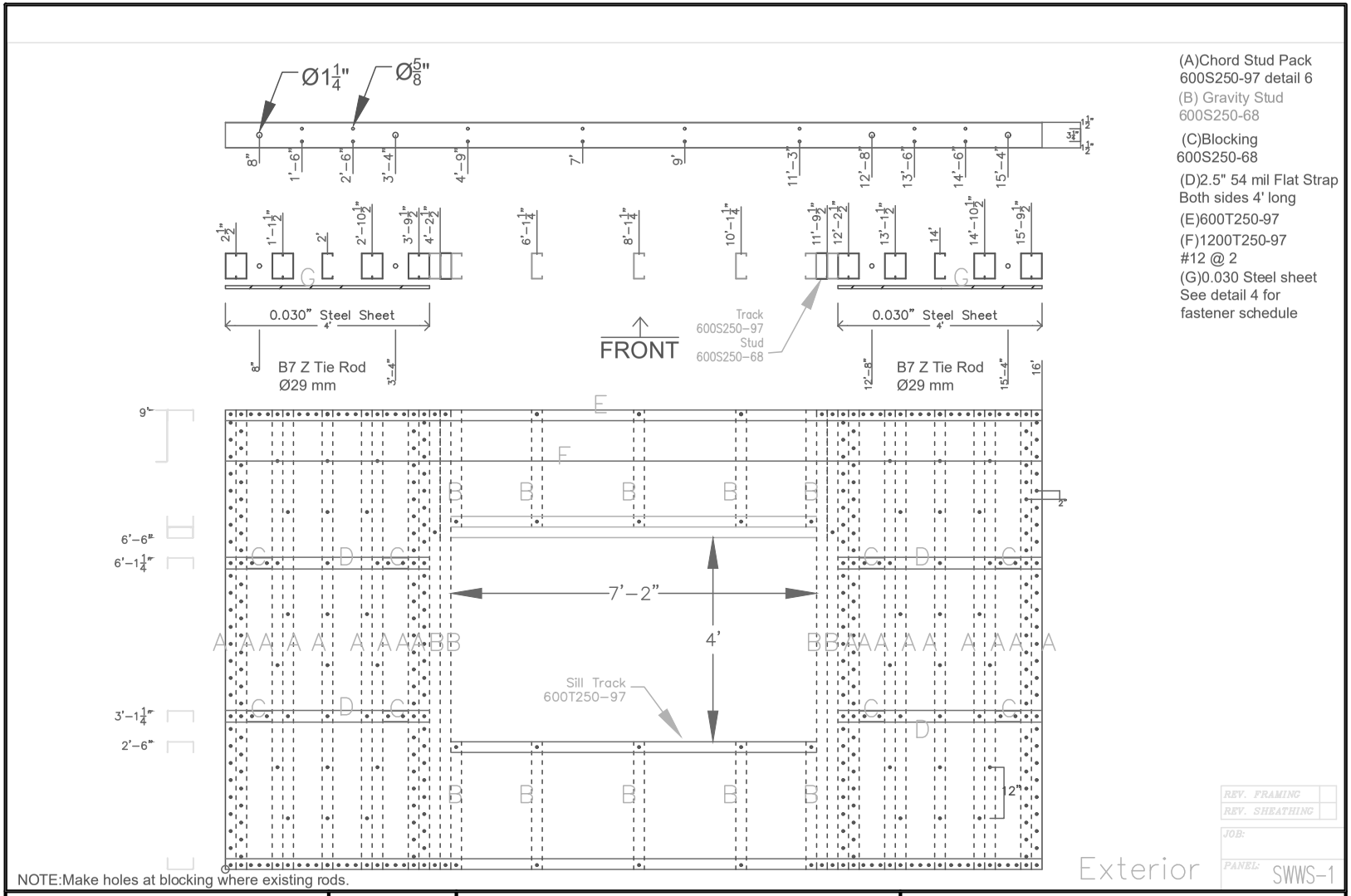
(A)Chord Stud Pack
600S250-97 detail 6
(B) Gravity Stud
600S250-68
(C)Blocking
600S250-68
(D)2.5" 54 mil Flat Strap
Both sides 12' long
(E)2.5" 54 mil Flat Strap
Both sides 4' long
(F)600T250-97
(G)1200T250-97
#12 @ 2
(H)0.030 Steel sheet
See detail 4 for
fastener schedule

NOTE:Make holes at blocking where existing rods.

REV. FRAMING
REV. SHEATHING
JOB:
PANEL: SGGG-1F

Exterior

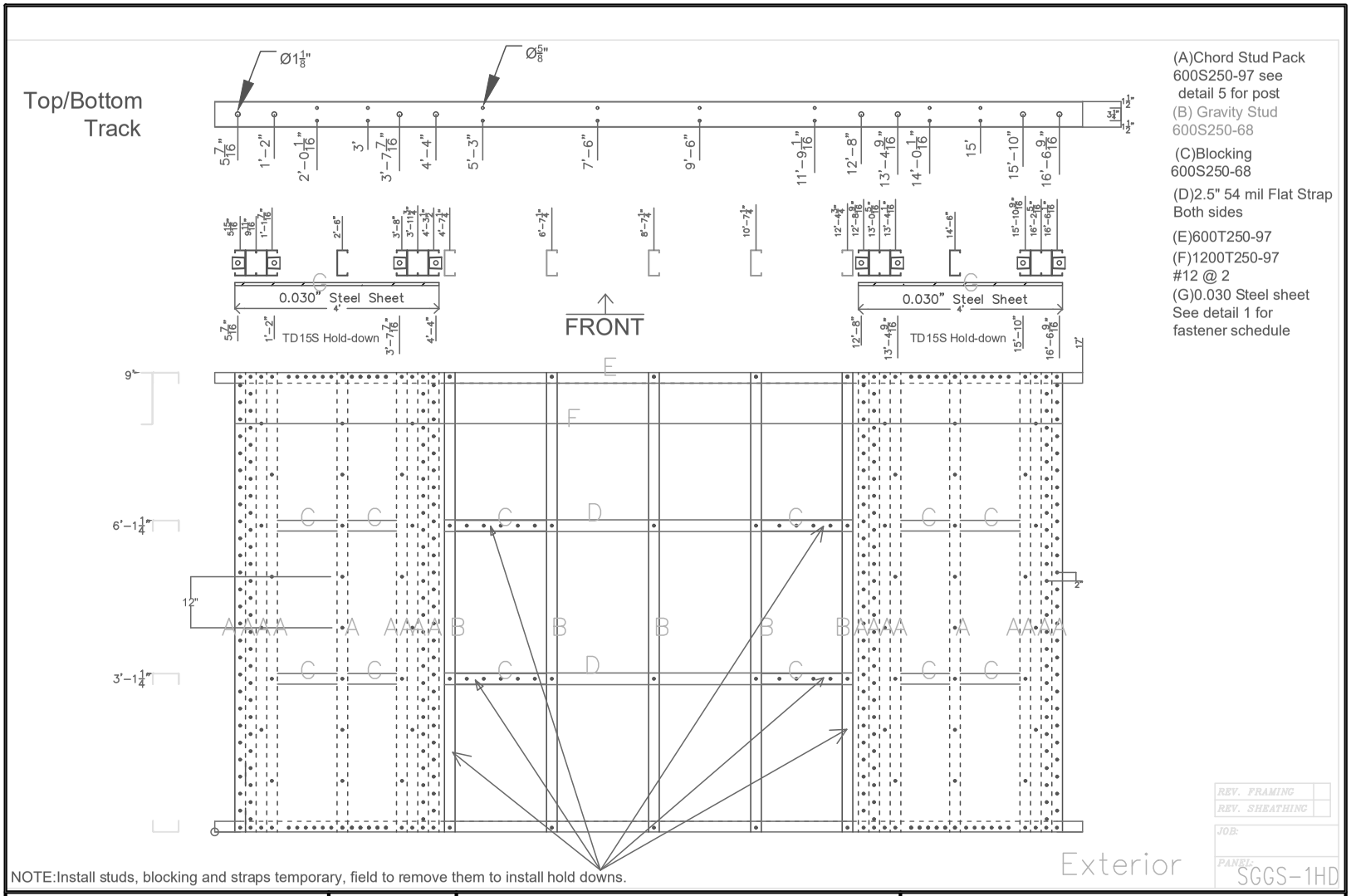
U C S D University of California, San Diego Department of Structural Engineering La Jolla, California 92093-0085 Project No. Date:	No. Date Revisions	CFS-NHERI Wall Tests	Amanpreet Singh Graduate Student Researcher



(A)Chord Stud Pack
600S250-97 detail 6
(B) Gravity Stud
600S250-68
(C)Blocking
600S250-68
(D)2.5" 54 mil Flat Strap
Both sides 4' long
(E)600T250-97
(F)1200T250-97
#12 @ 2
(G)0.030 Steel sheet
See detail 4 for
fastener schedule

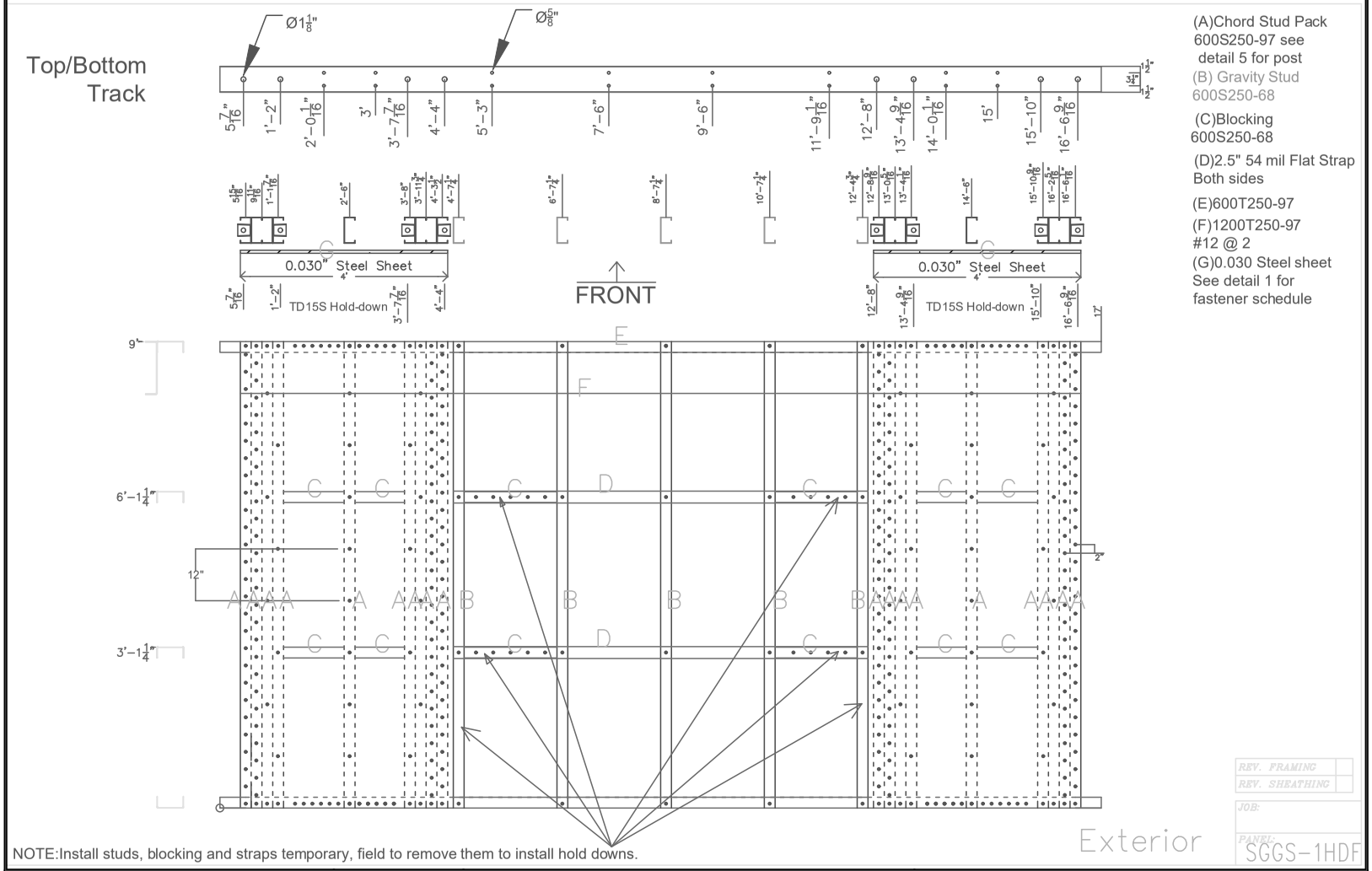
REV. FRAMING
REV. SHEATHING
JOB:
PANEL: SWWS-1

UCSD	No. Date Revisions	CFS-NHERI Wall Tests	Amanpreet Singh
University of California, San Diego Department of Structural Engineering La Jolla, California 92093-0085			Graduate Student Researcher
Project No. Date:			



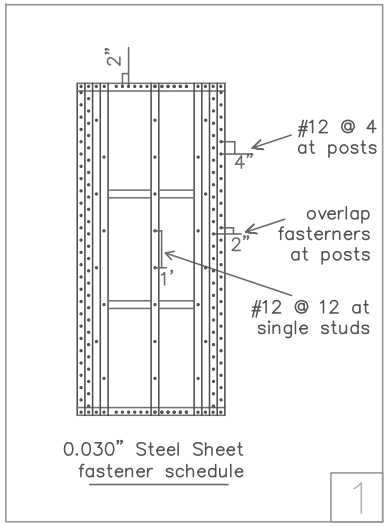
NOTE:Install studs, blocking and straps temporary, field to remove them to install hold downs.

U C S D University of California, San Diego Department of Structural Engineering La Jolla, California 92093-0085 Project No. Date:	No. Date Revisions	CFS-NHERI Wall Tests	Amanpreet Singh Graduate Student Researcher



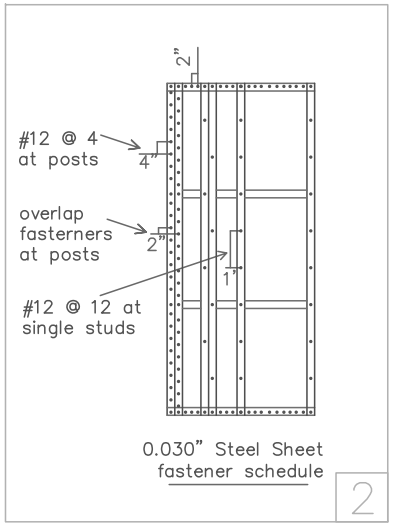
NOTE:Install studs, blocking and straps temporary, field to remove them to install hold downs.

U C S D University of California, San Diego Department of Structural Engineering La Jolla, California 92093-0085 Project No. Date:	No. Date Revisions	CFS-NHERI Wall Tests	Amanpreet Singh Graduate Student Researcher



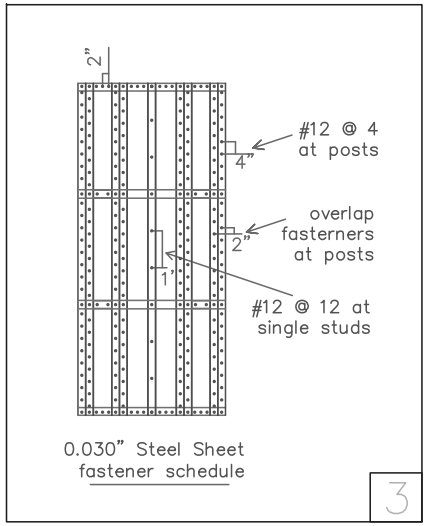
0.030" Steel Sheet
fastener schedule

1



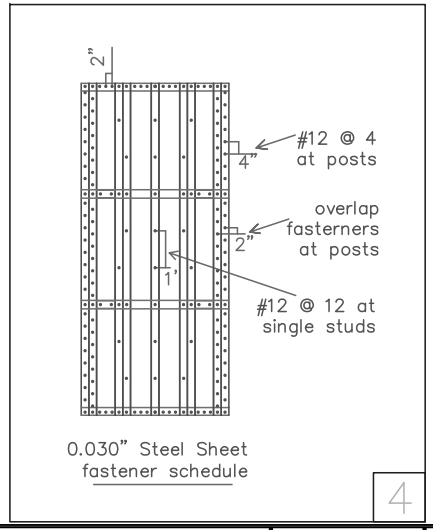
0.030" Steel Sheet
fastener schedule

2



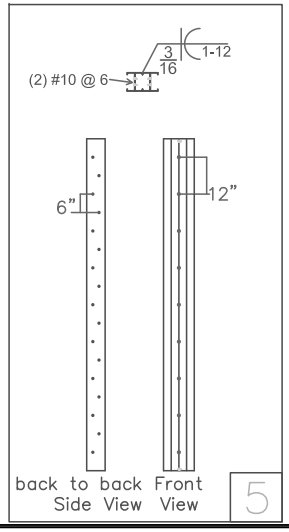
0.030" Steel Sheet
fastener schedule

3

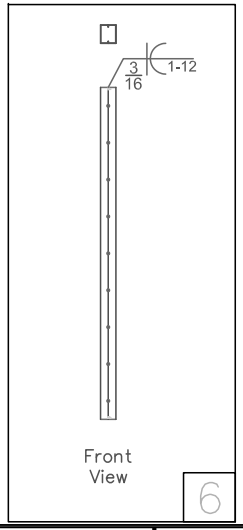


0.030" Steel Sheet
fastener schedule

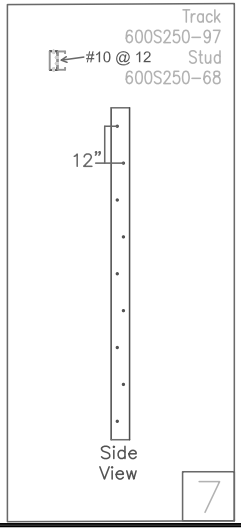
4



5

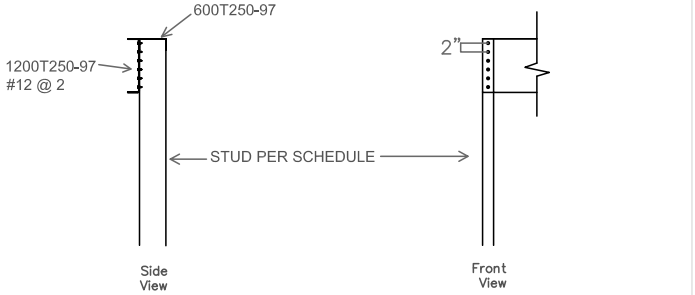


6

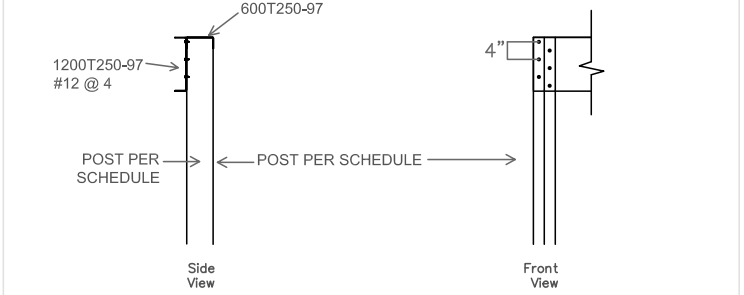


7

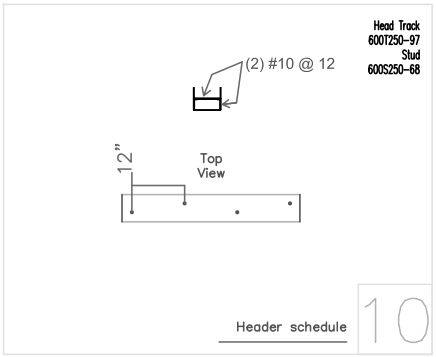
UCSD	No. Date Revisions	CFS-NHERI Wall Tests	Amanpreet Singh
University of California, San Diego Department of Structural Engineering La Jolla, California 92093-0085			Graduate Student Researcher
Project No. Date:			



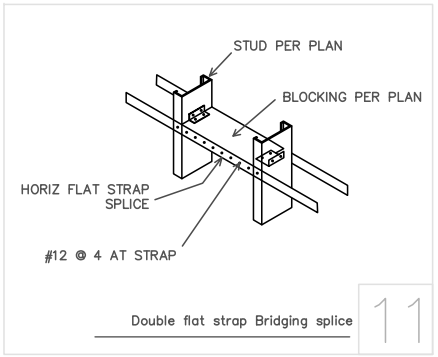
Ledger fastener schedule at single studs – 8



Ledger fastener schedule at existing posts – 9



Header schedule 10



Double flat strap Bridging splice 11

UCSD	No. Date Revisions	CFS-NHERI Wall Tests	Amanpreet Singh
University of California, San Diego Department of Structural Engineering La Jolla, California 92093-0085			Graduate Student Researcher
Project No. Date:			

Appendix B

Material Tests and Certificates

Material properties of the framing members, tension tie-rods, hold-downs and finish stucco as obtained from the manufacturer and from material tests are provided here.

B.1 Framing Member Coupon Tests

Material donations from industry partners for framing members were obtained from multiple sources and in multiple batches. Table B.1 provides information regarding the batch source of each framing component. Tables B.2-B.4 provide material properties of the framing components received in those batches obtained from tensile coupon tests Torabian et al. (2016b), performed on a MTS Axial Test System with 500 kN maximum capacity. These coupons were obtained from cutouts from the framing members used in wall specimen fabrication. Test protocol started as a force controlled test initially at a defined rate up to a defined load limit, and then switched to a displacement controlled test. The rate of machine head movement was increased by the operator to a pre-defined faster test (head movement) rate when the coupon has gone beyond yield point. Individual coupon stress-strain behavior is provided in the subsequent Table B.5.

Table B.1. Batch source of framing members

Wall specimen	Framing members				Steel sheet
	Chord stud	Track	Gravity stud	Ledger	
GGGG	B2	B2	B2	A2	-NA-
GGGG-F	B2	B2	B2	A2	-NA-
SGGS-2	A1	A1	A1	A1	A1
SGGS-2F	A1	A1	A1	A1	A1
SWWS-2	B2	B2	B2	A2	A2
SWWS-2F	B2	B2	B2	A2	A2
SWWS-1	A1	A1	A1	A2	A1
SGGG-1F	A1	A1	A1	A2	A1
SGGS-1HD	B2	B2	B2	A2	A2
SGGS-1HDF	B2	B2	B2	A2	A2

Table B.2. Batch A1 material properties

Material property		Chord stud	Track	Gravity stud	Steel Sheet
Yield stress (MPa)	Avg.	373.2	406.1	388.0	264.6
	Std. Dev.	14.4	35.6	6.3	4.8
	COV (%)	3.87	8.76	1.63	1.81
Tensile stress (MPa)	Avg.	483.8	520.1	532.8	315.6
	Std. Dev.	15.5	33.0	7.0	2.8
	COV (%)	3.20	6.34	1.31	0.88

Table B.3. Batch A2 material properties

Material property		Steel Sheet
Yield stress (MPa)	Avg.	285.1
	Std. Dev.	7.8
	COV (%)	2.74
Tensile stress (MPa)	Avg.	326.7
	Std. Dev.	4.2
	COV (%)	1.30

Table B.4. Batch B2 material properties

Material property		Chord stud	Track	Gravity stud
Yield stress (MPa)	Avg.	323.9	308.0	348.3
	Std. Dev.	10.5	8.1	11.5
	COV (%)	3.25	2.62	3.30
Tensile stress (MPa)	Avg.	445.9	443.7	459.5
	Std. Dev.	11.1	8.5	12.2
	COV (%)	2.48	1.91	2.66

Table B.5. Individual coupon test results

Batch	Coupon Location	Thickness [mil]	Coupon Name	Thickness (with coating) [inch]	Thickness (without coating) [inch]	Gauge Width [inch]	Pre-test length across gauge [inch]	Post-test length across gauge [inch]	Net Extension [inch]	Strength [kip]	Loading Rate: Force Controlled Part [kip/min] upto [kip]	Loading Rate: Displacement Controlled Part [inch/min]/[inch/min]	Additional Notes
											Test runs as a force controlled test initially at a defined rate upto a defined load limit, and then switches to a displacement controlled test. Runs at a defined rate of machine head movement until the user switches to a pre-defined faster test (head movement) rate.		
			A1	0.104		0.512	2.019	2.555	0.537	3.7826	1.50 upto 1.50	0.005/0.025	
	SGGS-2 SSW		A2	0.104		0.509	2.002	2.563	0.562	3.5566	1.50 upto 1.50	0.005/0.050	
A1	Chord Stud (Powell)	97	A3	0.103		0.515	2.002	2.624	0.623	3.8411	1.50 upto 1.50	0.005/0.050	
			B1	0.101		0.501	2.011	2.677	0.666	3.3199	1.50 upto 1.50	0.005/0.100	
	SWWS-2 NSW		B2	0.102		0.509	2.005	2.522	0.517	3.2584	1.50 upto 1.50	0.005/0.100	Failure outside gauge length
B2	Chord Stud (Powell)	97	B3	0.101		0.505	2.007	2.641	0.635	3.2154	1.50 upto 1.50	0.005/0.100	
			C1	0.101		0.509	1.996	2.443	0.447	3.4657	1.50 upto 1.50	0.005/0.100	Failure outside gauge length
	SWWS-1 SW		C2	0.101		0.510	2.005	2.393	0.389	3.3588	1.50 upto 1.50	0.005/0.100	Failure outside gauge length
B2	Chord Stud (ESEC)	97	C3	0.102		0.504	2.001	2.564	0.564	3.2887	1.50 upto 1.50	0.005/0.100	
			D1	0.103		0.531	2.008	2.485	0.477	3.9331	1.50 upto 1.50	0.005/0.100	
	SGGS-2		D2	0.103		0.504	1.989	2.493	0.505	3.7507	1.50 upto 1.50	0.005/0.100	
A1	Track (Powell)	97	D3	0.104		0.496	2.011	2.487	0.477	4.2419	1.50 upto 1.50	0.005/0.100	
			E1	0.102		0.499	1.997	2.692	0.696	3.2854	1.50 upto 1.50	0.005/0.100	
	SWWS-2		E2	0.101		0.513	2.001	2.596	0.595	3.3373	1.50 upto 1.50	0.005/0.100	
B2	Window Track (Powell)	97	E3	0.102		0.510	2.008	2.653	0.645	3.3683	1.50 upto 1.50	0.005/0.100	
			F1	0.101		0.517	1.999	2.457	0.459	3.4746	1.50 upto 1.50	0.005/0.100	
	SWWS-1		F2	0.101		0.507	2.004	2.422	0.419	3.2356	1.50 upto 1.50	0.005/0.100	Failure outside gauge length
B2	Track (ESEC)	97	F3	0.101		0.498	2.002	2.356	0.354	3.1534	1.50 upto 1.50	0.005/0.100	Failure outside gauge length
			G1	0.073		0.500	2.003	2.640	0.638	2.7969	1.50 upto 1.50	0.005/0.100	
	SGGS-2		G2	0.072		0.440	1.999	2.271	0.272	2.4941	1.50 upto 1.50	0.005/0.100	Failure outside gauge length
A1	Gravity Stud (Powell)	68	G3	0.072		0.437	2.009	2.252	0.243	2.4087	1.50 upto 1.50	0.005/0.100	Failure outside gauge length
			H1	0.071		0.505	2.025	2.632	0.608	2.4138	1.50 upto 1.50	0.005/0.100	
	SWWS-2		H2	0.071		0.509	2.023	2.657	0.634	2.2839	1.50 upto 1.50	0.005/0.100	
B2	Gravity Stud (Powell)	68	H3	0.071		0.507	1.997	2.603	0.606	2.4551	1.50 upto 1.50	0.005/0.100	
			I1	0.071		0.505	2.004	2.600	0.597	2.4546	1.50 upto 1.50	0.005/0.100	
	SWWS-1		I2	0.071		0.508	2.005	2.634	0.629	2.4145	1.50 upto 1.50	0.005/0.100	
B2	Gravity Stud (ESEC)	68	I3	0.071		0.504	2.007	2.649	0.642	2.3531	1.50 upto 1.50	0.005/0.100	
			J1	0.032		0.503	2.009	2.718	0.709	0.7679	1.50 upto 1.50	0.005/0.100	Test ran as Force controlled test
	SWWS-2 NSW		J2	0.032		0.504	2.010	2.724	0.714	0.7633	0.15 upto 0.30	0.005/0.050	
A2	Sheet 1 (Powell)	30	J3	0.032		0.504	2.006	2.707	0.701	0.7804	0.30 upto 0.30	0.005/0.100	
			K1	0.032		0.500	1.990	2.679	0.689	0.7410	0.30 upto 0.30	0.005/0.100	
	SWWS-1 SW		K2	0.032		0.502	1.991	2.721	0.730	0.7605	0.30 upto 0.30	0.005/0.100	
A2	Sheet (ESEC)	30	K3	0.032		0.497	1.997	2.703	0.706	0.7517	0.30 upto 0.30	0.005/0.100	
			L1	0.032		0.498	2.001	2.736	0.735	0.7354	0.30 upto 0.30	0.005/0.100	
	SGGS-2 SW		L2	0.032		0.498	2.010	2.772	0.762	0.7211	0.30 upto 0.30	0.005/0.100	Extensometer removed after yield
A1	Sheet 1 (ESEC)	30	L3	0.032		0.497	2.000	2.748	0.748	0.7326	0.30 upto 0.30	0.005/0.100	

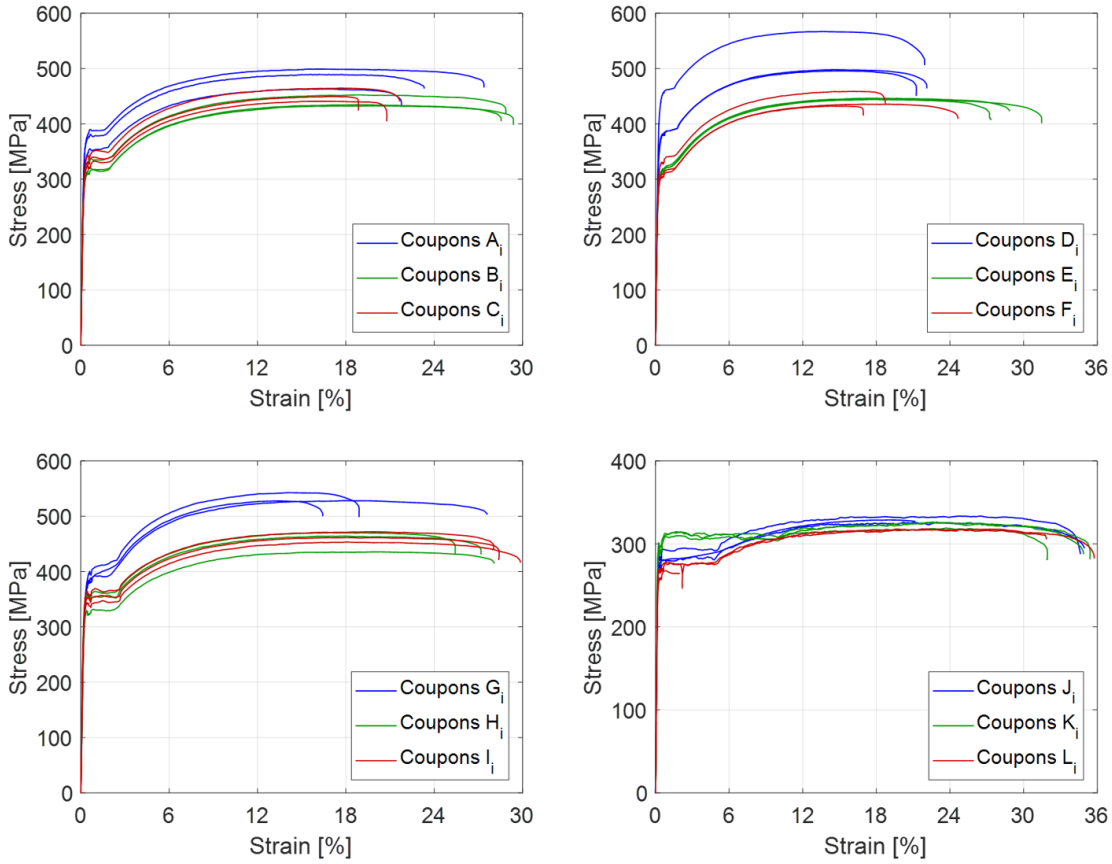


Figure B.1. Stress-strain curve of CFS coupons

B.2 Finish Layer Stucco Compressive Strength Tests

Table B.6 provide the information about the batches of stucco mix used in the two finish layers and the specimens they was applied to. The samples obtained from each batch were tested for their compressive strength. The results from those tests are provided in Tables B.7 and B.8.

B.3 Hold-down Manufacturer Catalog

Figure B.2 provides the hold-down product catalog provided by the manufacturer. Based on the hold-down load requirements, TD15S was chosen from the catalog for installation in specimens SGGS-1HD and SGGS-1HDF during the quasi-static tests. This was also the hold-

Table B.6. Stucco mix batches

Batch	Samples	Wall-line specimen
Finish layer 1		
1	1, 2, 3	GGGG-F
2	1, 2, 3, 4	GGGG-F, SGGS-1HDF
3	1, 2	SGGS-1HDF
4	1, 2	SGGS-2F
5	1, 2	SGGS-2F, SWWS-2F
6	1, 2	SWWS-2F
7	1, 2	SWWS-2F, SGGG-1F
8	1	SGGG-1F
Finish layer 2		
1	1, 2	GGGG-F
2	1	GGGG-F
3	1, 2	SGGS-1HDF, SGGG-1F
4	1, 2	SGGG-1F, SGGS-2F
5	1	SGGS-2F
7	1	SWWS-2F
8	1, 2	SWWS-2F

down with the largest capacity available from the manufacturer.

B.4 Tension Tie-rods Uni-axial Tests

Table B.9 and Figure B.3 provide the material properties obtained for the tension tie-rods obtained by uni-axial tension tests performed on four test rods cut from tie-rods used in dynamic and quasi-static tests.

Figure B.4 and the pages following it provide material and quality certification provided by the manufacturer about the mechanical and chemical properties of the tension tie-rods.

Table B.7. Finish layer 1 compressive strength test

Batch	Sample	Load (kN)	Area (cm^2)	Compressive (MPa)	Average (MPa)
1	1	25.44	20.27	12.55	13.08
	2	26.52	20.27	13.08	
	3	27.60	20.27	13.62	
2	1	24.46	20.27	12.07	13.09
	2	25.00	20.27	12.33	
	3	27.15	20.27	13.39	
	4	29.48	20.27	14.54	
3	1	39.78	20.27	19.63	18.84
	2	36.60	20.27	18.06	
4	1	34.31	20.27	16.93	17.48
	2	36.55	20.27	18.04	
5	1	35.48	20.27	17.50	18.19
	2	38.26	20.27	18.88	
6	1	49.55	20.27	24.45	24.42
	2	49.46	20.27	24.40	
7	1	27.51	20.27	13.57	13.26
	2	26.25	20.27	12.95	
8	1	36.42	20.27	17.97	17.97

Table B.8. Finish layer 2 compressive strength test

Batch	Sample	Load (kN)	Area (cm^2)	Compressive (MPa)	Average (MPa)
1	1	25.18	20.27	12.42	12.89
	2	27.06	20.27	13.35	
2	1	25.26	20.27	12.47	12.47
3	1	45.94	20.27	22.67	22.09
	2	43.59	20.27	21.51	
4	1	32.16	20.27	15.87	17.11
	2	37.18	20.27	18.35	
5	1	32.52	20.27	16.05	16.05
7	1	34.58	20.27	17.06	17.06
8	1	26.97	20.27	13.31	13.79
	2	28.94	20.27	14.28	

The **TD8S, TD10S,** and **TD15S** are high capacity holdowns which are designed for attachment to cold formed steel (CFS) framing members. Holdowns are secured at the base by attachment to an anchor bolt.

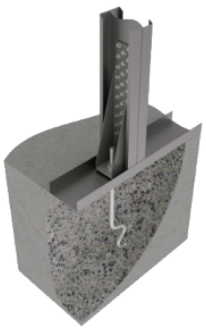
Materials: See chart
Finish: Primer

Installation:

- Use #10 self-tapping screws to attach the back or strap portion of the holdown to a steel stud. Install nut to secure the base of holdown to foundation with anchor bolt of specified diameter.
- A design professional shall specify the type, length, and embedment depth of the anchor bolt.
- Install anchor bolt nut to base of holdown until finger tight, then tighten an additional 1/3 to 1/2 turns with a wrench.



TD10S


Typical TD10S installation

MiTek Stock No.	Ref No.	Steel Thickness		Dimensions (in)			Fastener Schedule			CFS Member			ASD		LRFD		Nominal Tension Load[6] (in)	Code Ref.
							Anchor Bolt[2]	Stud Screws[4]		Stud[1,3]								
		Body	Base (in)	W	L	CL	Dia. (in)	Qty	Type	Plies	Mils	Gr	Tension (Lbs.)	Deflection[5] (in)	Tension (Lbs.)	Deflection[5] (in)		
TD8S	S/HD8S	10	3/8	2-1/2	13-7/8	1-5/8	7/8	24	#10	2	33	33	8250	0.074	13200	0.164	22325	
										2	43	33	10115	0.109	16350	0.242	27650	
										2	54	50	10900	0.091	17435	0.205	29485	
TD10S	S/HD10S	10	3/8	2-1/2	16-1/8	1-5/8	7/8	30	#10	2	33	33	8690	0.071	13900	0.159	24575	
										2	43	33	9310	0.076	14900	0.195	26335	--
										2	54	50	9985	0.058	15975	0.146	28235	
TD15S	S/HD15S	7	1/2	2-5/8	21-1/2	1-11/16	1	48	#10	2	33	33	11780	0.075	18845	0.146	33410	
										2	43	33	13770	0.100	22035	0.192	39065	
										2	54	50	15920	0.096	25475	0.144	45160	

1) Back-to-back stud members are required.
2) The designer must specify anchor bolt type, length, and embedment.
3) Designer shall verify the adequacy of the steel studs to transfer the required load.
4) #10 screws are self-drilling 0.190 inch diameter hardened washer-head screws with a minimum nominal shear strength of 1650 pounds.
5) Holdown deflection at ASD and LRFD static test load includes fastener slip, holdown deflection, and anchor bolt elongation.
6) The nominal tension load is based on the average of the ultimate tested values.

Figure B.2. Hold-down catalog from manufacturer (source: www.mitek-us.com)

Table B.9. Material properties of tension tie-rods

	Young's modulus (GPa)	Yield point (MPa)	Tensile strength (MPa)
Test rod 1	209.32	882.80	1011.87
Test rod 2	205.39	863.29	994.64
Test rod 3	196.02	886.18	959.06
Test rod 4	198.29	874.46	975.40
Average	202.26	876.69	985.24
Std. Dev.	5.35	8.83	19.87
COV (%)	2.64	1.01	2.02

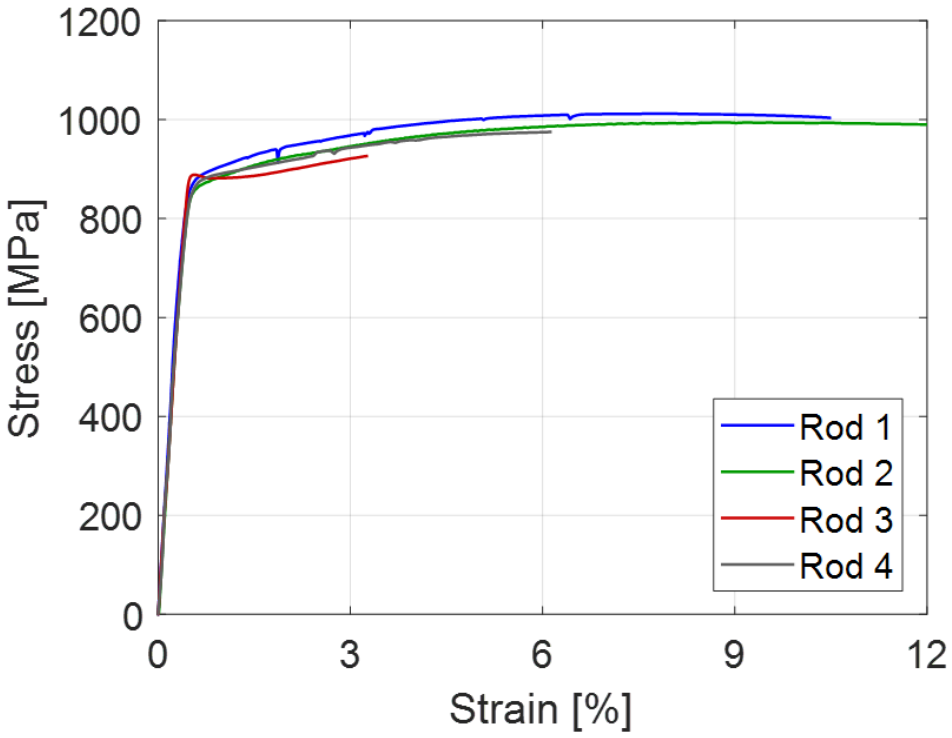
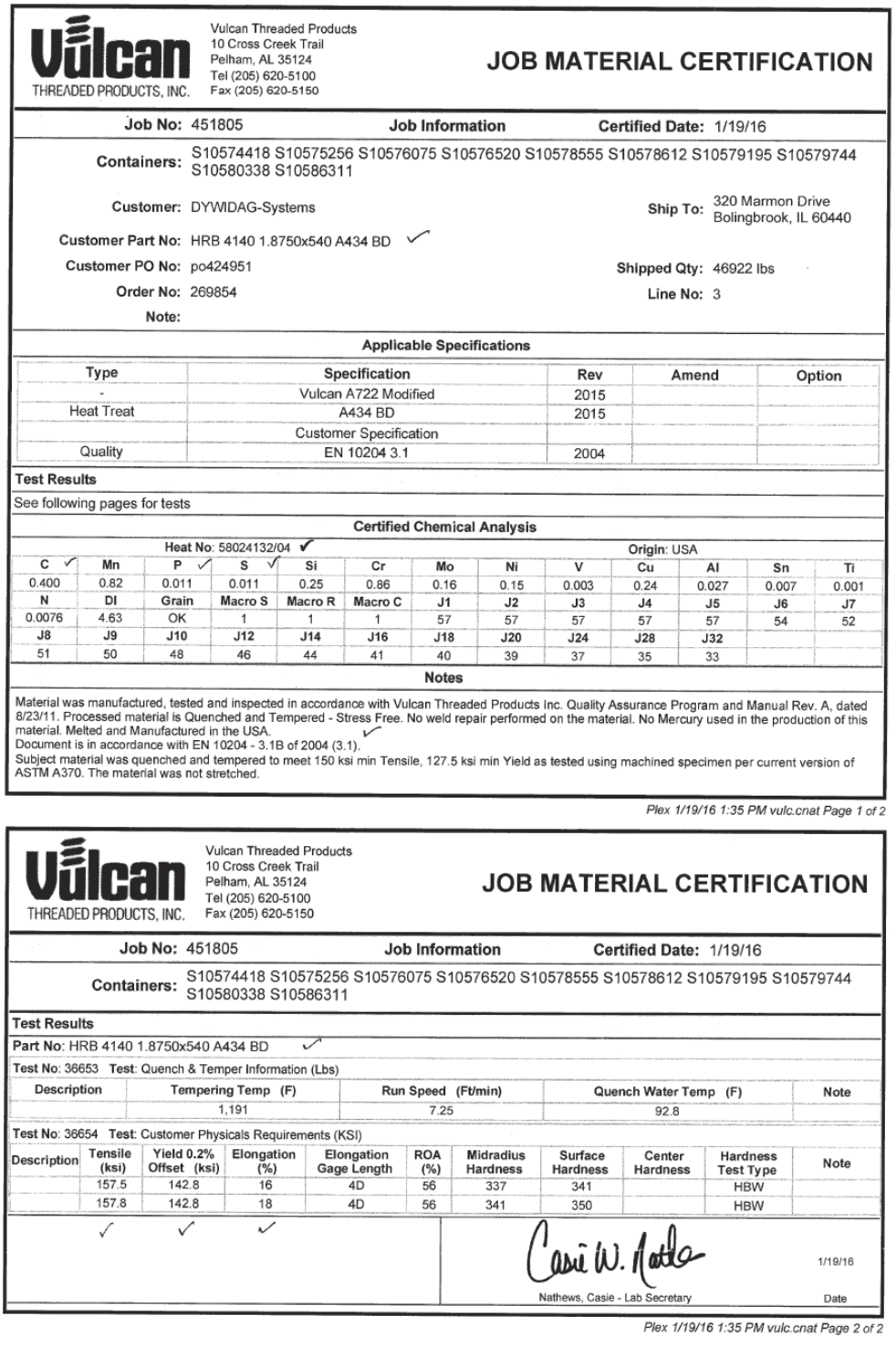


Figure B.3. Stress-strain curve for tension tie-rods



Vulcan
THREADED PRODUCTS, INC.

Vulcan Threaded Products
10 Cross Creek Trail
Pelham, AL 35124
Tel (205) 620-5100
Fax (205) 620-5150

JOB MATERIAL CERTIFICATION

Job No: 451805 **Job Information** **Certified Date:** 1/19/16

Containers: S10574418 S10575256 S10576075 S10576520 S10578555 S10578612 S10579195 S10579744 S10580338 S10586311

Customer: DYWIDAG-Systems **Ship To:** 320 Marmon Drive Bolingbrook, IL 60440

Customer Part No: HRB 4140 1.8750x540 A434 BD ✓

Customer PO No: po424951 **Shipped Qty:** 46922 lbs

Order No: 269854 **Line No:** 3

Note:

Applicable Specifications

Type	Specification	Rev	Amend	Option
-	Vulcan A722 Modified	2015		
Heat Treat	A434 BD	2015		
	Customer Specification			
Quality	EN 10204 3.1	2004		

Test Results

See following pages for tests

Certified Chemical Analysis

Heat No: 58024132/04 ✓ Origin: USA

C ✓	Mn	P ✓	S ✓	Si	Cr	Mo	Ni	V	Cu	Al	Sn	Ti
0.400	0.82	0.011	0.011	0.25	0.86	0.16	0.15	0.003	0.24	0.027	0.007	0.001
N	**DI**	**Grain**	**Macro S**	**Macro R**	**Macro C**	**J1**	**J2**	**J3**	**J4**	**J5**	**J6**	**J7**
0.0076	4.63	OK	1	1	1	57	57	57	57	57	54	52
J8	**J9**	**J10**	**J12**	**J14**	**J16**	**J18**	**J20**	**J24**	**J28**	**J32**		
51	50	48	46	44	41	40	39	37	35	33		

Notes

Material was manufactured, tested and inspected in accordance with Vulcan Threaded Products Inc. Quality Assurance Program and Manual Rev. A, dated 8/23/11. Processed material is Quenched and Tempered - Stress Free. No weld repair performed on the material. No Mercury used in the production of this material. Melted and Manufactured in the USA. ✓
Document is in accordance with EN 10204 - 3.1B of 2004 (3.1).
Subject material was quenched and tempered to meet 150 ksi min Tensile, 127.5 ksi min Yield as tested using machined specimen per current version of ASTM A370. The material was not stretched.

Plex 1/19/16 1:35 PM vulc.cnat Page 1 of 2

Vulcan
THREADED PRODUCTS, INC.

Vulcan Threaded Products
10 Cross Creek Trail
Pelham, AL 35124
Tel (205) 620-5100
Fax (205) 620-5150

JOB MATERIAL CERTIFICATION

Job No: 451805 **Job Information** **Certified Date:** 1/19/16

Containers: S10574418 S10575256 S10576075 S10576520 S10578555 S10578612 S10579195 S10579744 S10580338 S10586311

Test Results

Part No: HRB 4140 1.8750x540 A434 BD ✓

Test No: 36653 **Test:** Quench & Temper Information (Lbs)

Description	Tempering Temp (F)	Run Speed (Ft/min)	Quench Water Temp (F)	Note
	1,191	7.25	92.8	

Test No: 36654 **Test:** Customer Physicals Requirements (KSI)

Description	Tensile (ksi)	Yield 0.2% Offset (ksi)	Elongation (%)	Elongation Gage Length	ROA (%)	Midradius Hardness	Surface Hardness	Center Hardness	Hardness Test Type	Note
	157.5	142.8	16	4D	56	337	341		HBW	
	157.8	142.8	18	4D	56	341	350		HBW	

✓ ✓ ✓

Casie W. Nathews — 1/19/16

Nathews, Casie - Lab Secretary — Date

Plex 1/19/16 1:35 PM vulc.cnat Page 2 of 2

Figure B.4. Material certification for tension tie-rods provided by manufacturer

JIAXING TONGLIN GENERAL EQUIPMENT CO., LTD.

TEST REPORT

COMMODITY\BPW SIZE: BPW-27-6 OS QTY : 2000 MATERIAL : Q235

ORDER NO Z4002946-2843 LOT No : 60 DATE : 2018.5.17

Heat No: 171202

一、CHEMICAL ELEMENTS (%)

	C	Mn	P	S	Si
Standard	0-0.2	0.3-0.7	0.00-0.045	0.00-0.045	0-0.35
TEST REPORT	0.188	0.5	0.038	0.022	0.325

二、PHYSICAL PROPERTIES for SQUARE TUBE

ITEM	Length	Width	Heigth	Small Hole	Big Hole
STANDARD	228.6±1.58	127±1.58	25.4±1.58	9.525±0.0254	39.7±0.025
TEST REPORT	228.5	127	25.3	9.52	39.72

三. paint appearance (Visual)

ITEM	No Burrs	No defects	paint uniformity
TEST REPORT	OK	OK	OK

吴江市永方金属材料有限公司产品质量证明书

Wujiang Yongfang metal materials Co., Ltd.

客户名称 Customer name	嘉兴通林通用设备有限公司												证明书编号 Certificate number	171202
合同编号 Contract number													交货日期 Delivery date	2017/12/4
产品名称 Product name	炉批号 Heat No	钢号 Steel grade	产品规格 Size	交货状态 Delivery status	长度 Length	重量 KG Weight KG	化学成分 (%) Chemical composition						力学性能 Mechanical property	
							C	Mn	Si	P	S		屈服强度 Yield strength	抗拉强度 Tensile strength	伸长率 Elongation	冷弯 Cold bend
钢坯/billet steel	171202	Q235	31.75*82.55	热/Y		7.059	0.182	0.365	0.182	0.035	0.029		320	425	27%	合格/PASS
			19.05*82.55	热/Y		9.473	0.183	0.358	0.18	0.035	0.029					
			12.7*82.55	热/Y		7.47	0.188	0.39	1.177	0.038	0.03					
			15.87*127	热/Y		18.44	0.185	0.355	0.18	0.037	0.027					
			6.35*76.2	热/Y		5.985	0.184	0.381	0.178	0.036	0.026					
			9.525*82.55	热/Y		6.847	0.181	0.391	0.175	0.038	0.027					
			15.87*82.55	热/Y		11.592	0.19	0.384	0.179	0.036	0.026					
			22.2*82.55	热/Y		14.772	0.187	0.396	0.176	0.038	0.03					
			25.4*127	热/Y		52.427	0.184	0.384	0.179	0.037	0.026					
			38.1*88.9	热/Y		6.347	0.189	0.388	0.182	0.035	0.03					
			38.1*127	热/Y		12.872	0.182	0.39	0.175	0.037	0.03					
单项判定 Single decision																
备注 Note	1:本产品质量证明书加盖红色印章生效 2:监督电话：0512-63229188 1: The product quality certificate stamped with the red seal into effect. 2: Supervision telephone: 0512-63229188												产品质位专用章 Special product quality			
符合 Accord	GB 699-88 GB 2101-89 YB4055-1995 GB 700-79 GB 704-88 702-86 标准/Standard												制表人: Lister:		张建超 Jianchao Zhang	

TEST REPORT

PRODUCT: Heavy Hex Coupling Nuts SIZE: 1-1/8" STANDARD: SAE J995 MATERIAL: Gr.8

ORDER NO.: Z4002740 QTY: 1350pcs MARK: Z4 C-9 DATE: Dec.2nd,2017

RAW MATERIAL HEAT No:1110-08873

一、CHEMICAL ELEMENTS (%)

ITEM	C	Mn	Si	P	S	Cr	Ni	Cu
Standard	0.42~0.50	0.50~0.80	0.17~0.37	≤0.035	≤0.035	≤0.25	≤0.25	≤0.25
TEST REPORT	0.450	0.590	0.210	0.014	0.007	0.050	0.010	0.010

二、MECHANICAL PROPERTIES

ITEM	HARDNESS(HRC)	PROOF LOAD(PSI)
STANDARD	26-36	165000
TEST REPORT	28	PASS

三、PHYSICAL PROPERTIES

ITEM	ACROSS FLATS(INCH)	ACROSS CORNERS(INCH)	THICKNESS(INCH)	L1	L1
				GO	NO
STANDARD	1.756-1.812	2.002-2.093	3.34-3.4	通规	止规
TEST REPORT	1.765	2.017	3.357	OK	OK

REPORT:ACCEPT

QUALITY DEPARTMENT

SHANGHAI NANSHI FOREIGN ECONOMIC
COOPERATION & TRADING COMPANY LTD
4/F NO.62 PUSAN RD.PUDONG NEW AREA,SHANGHAI 200125,CHINA
TEL.(021)64326619 FAX.(021)64329337

QUALITY CERTIFICATE

COMMODITY:THREADED RODS SIZE: 1-1/8-7×12FT STANDARD: ASTM A193-06

Order No: 0108-00050861 Q'TY: 1156 (PCS) INVOICE NO.: I18-20131

LOT NO.: PART NO.: 112C144RB7 HEAD MARKS: B7

CHEMICAL ELEMENTS（%） HEAT NO: 17605659 MATERIAL:

CHEMICAL ELEMENT	C	Mn	Si	P	S	Cr	Mo
SPEC	0.37	0.65	0.15	max	max	0.75	0.15
	0.49	1.10	0.35	0.035	0.04	1.20	0.25
TEST REPORT	0.39	0.82	0.21	0.008	0.005	0.95	0.18

MACHINICAL PROPERTIES BATCH NO 4P7051901 TEST NO: A193-06 B7

ITEM	TENSILE STRENGTH min (Mpa)	YIELD STRENGTH min (Mpa)	ELONGATION min (%)	REDUCE min (%)	TEMPERING min (^{0}C)	QUENCHING (^{0}C)	HARDNESS max (HRC)
STANDARD	860	724	16	50	593	820~880	35
TEST REPORT	972	825	19	56	640	860	29

TESTED SIZE

ITEM	LENGTH	MAJORDIA	GO	NO	T/LENGTH	STRAIGHTNESS	ADD
STANDARD	3663.95	28.522	2A	2A		max	
	3651.25	28.141				18.29	
TEST REPORT ①	3657.00	28.30	OK	OK		OK	
②	3656.00	28.35	OK	OK		OK	
③	3656.00	28.29	OK	OK		OK	
PCS: 4 ④	3657.00	28.36	OK	OK		OK	OK

PARTS ARE MANUFACTURED AND TESTED IN ACCORDANCE WITH ASTM A193-06 B7
ALSO MEET THE REQUIREMENTS OF ASME SA-95 SECTION 2 IN YOUR MTR.
ALL TESTS IN ACCORDANCE WITH THE METHODS PRESCRIBED IN THE APPLICABLE ASTM SPECIFICATION.WE CERTIFY THAT THIS DATA IS TRUE REPRESENTATION OF INFORMATION PROVIDED BY THE MATERIAL SUPPLIES AND OUR TESTING LABORATORY.

Signature & Stamp

上海南市对外经济贸易有限公司
SHANGHAI NANSHI FOREIGN ECONOMIC
COOPERATION & TRADING COMPANY LTD

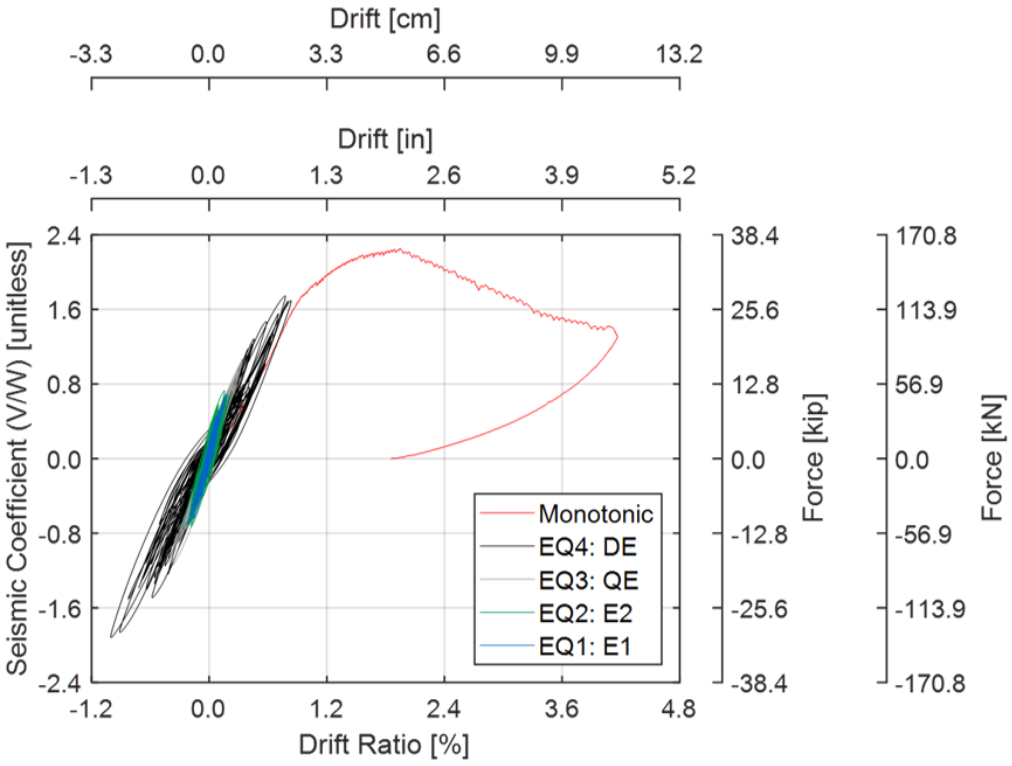
HARDY FRAMES
PO#Z4003156
ORDER#01-00238749
48PCS 1-1/8-7 X 59" ATR A193 B7 PLN
LOT#1807257A-6

Appendix C

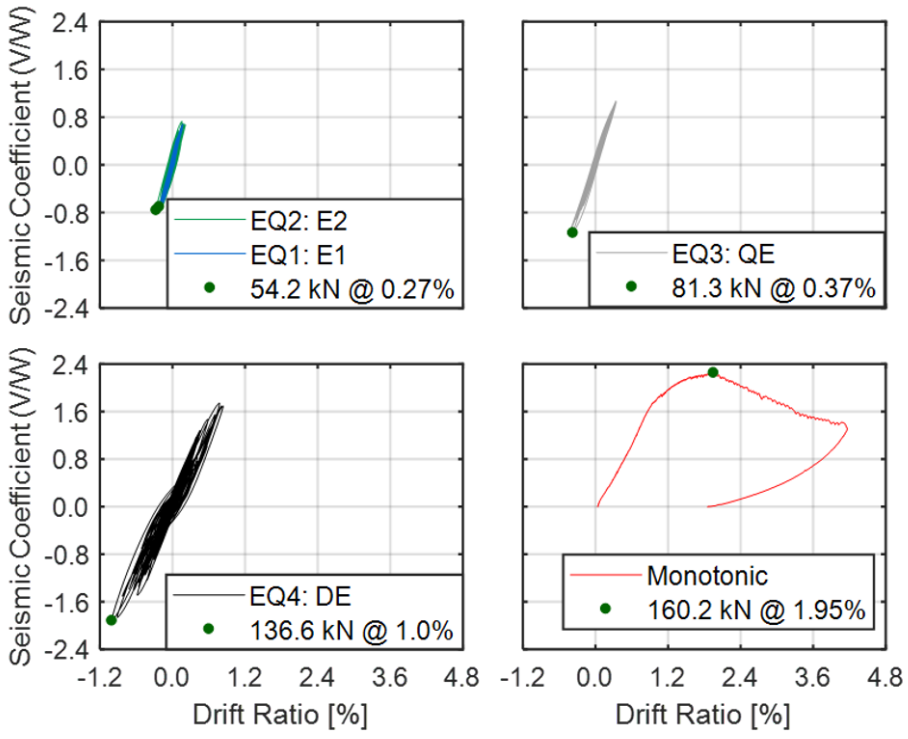
Hysteretic Response of Wall-Line Specimens

Hysteretic response for all the wall-lines tested across the two phases of the CFS-NHERI wall-line experimental program are presented here. Figures C.1-C.8 present the measured lateral response from specimens tested during the shake table test phase.

C.1 Shake Table Test Phase

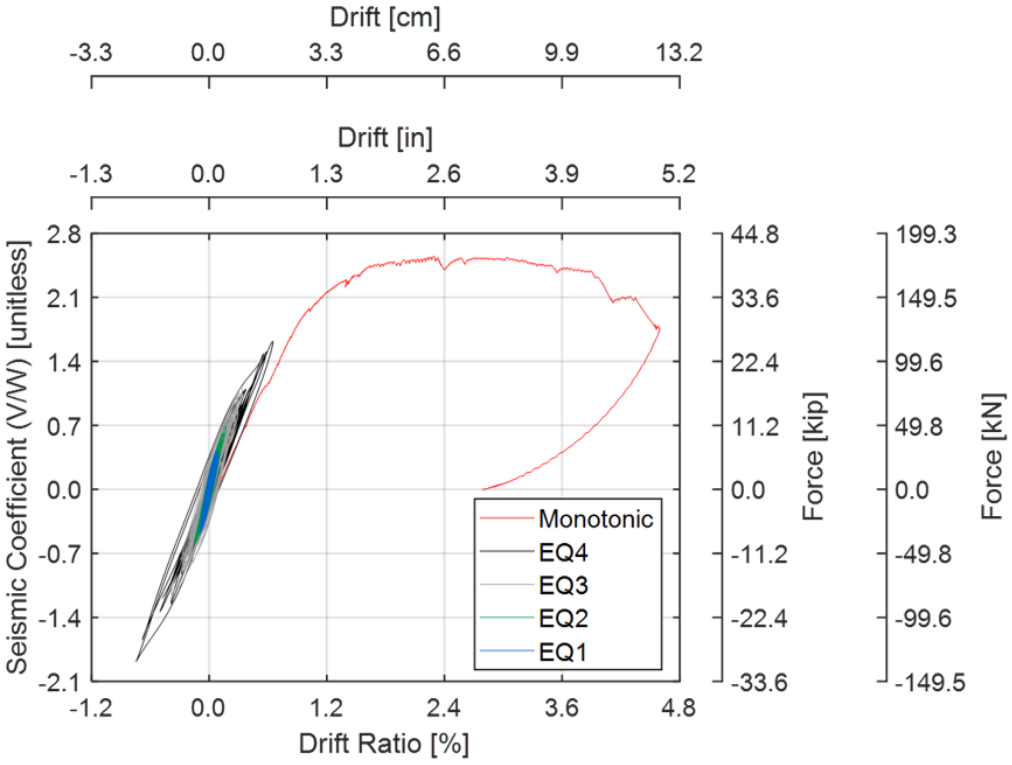


(a)

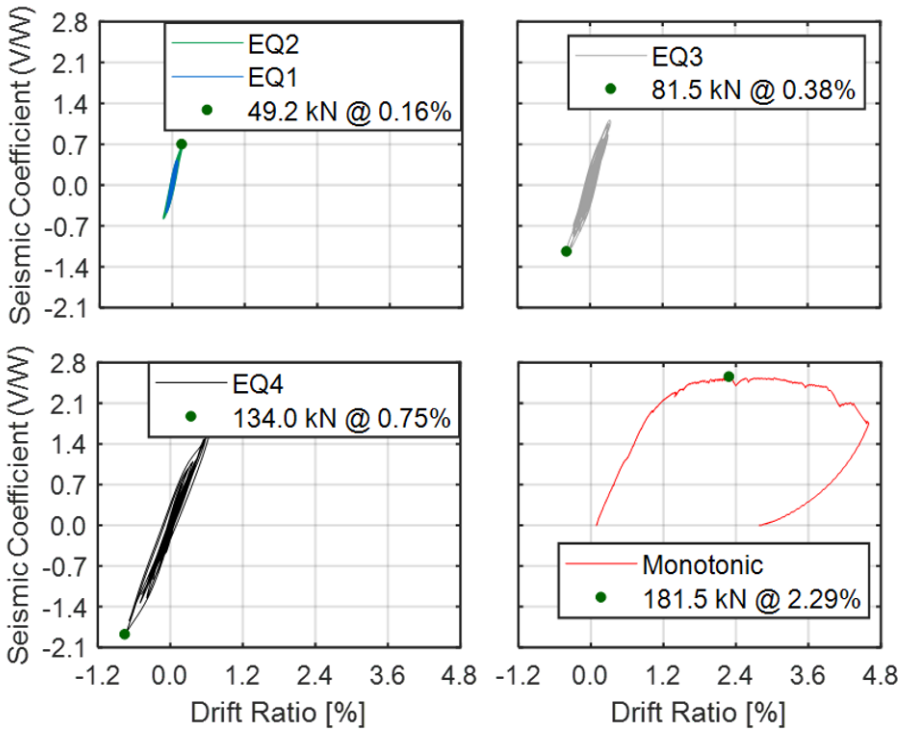


(b)

Figure C.1. Force displacement response of SGGS-1 specimen

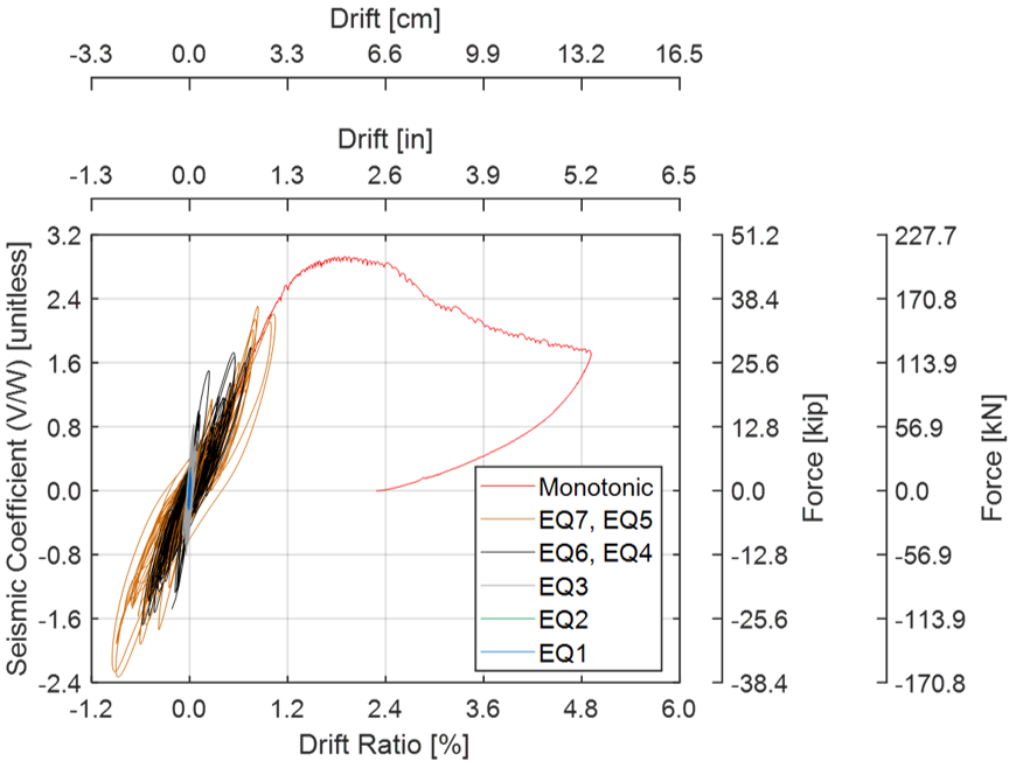


(a)



(b)

Figure C.2. Force displacement response of SGGS-1XS specimen



(a)

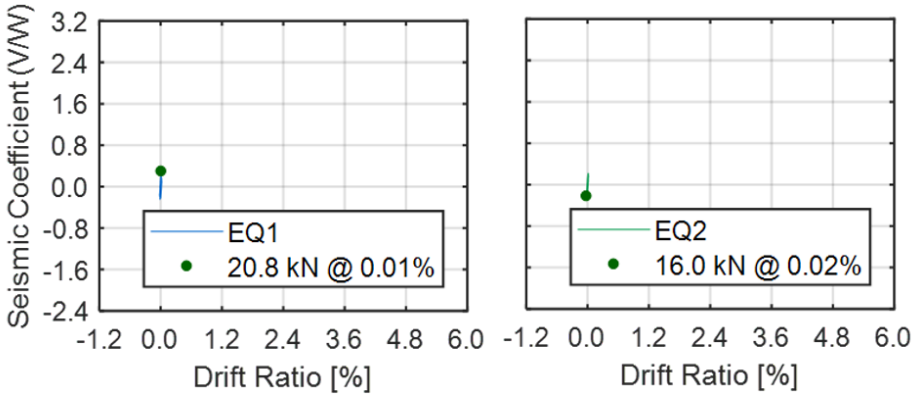
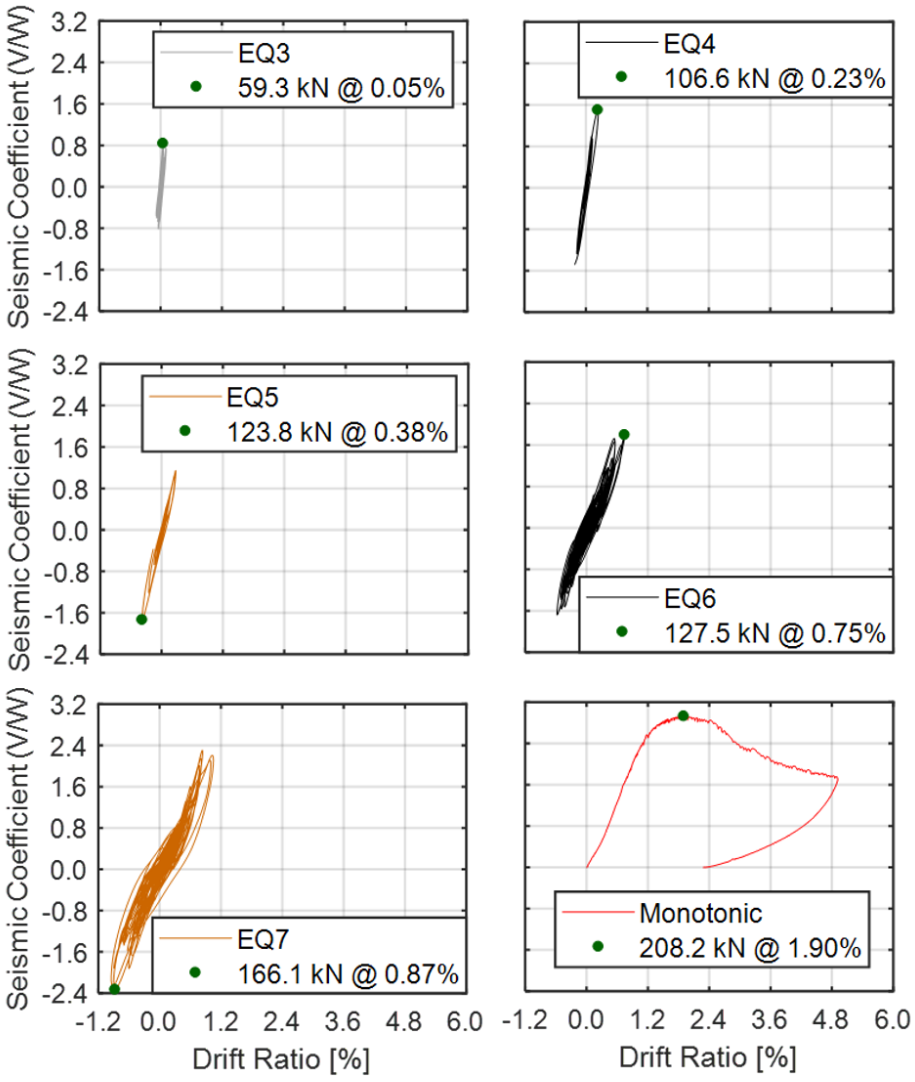
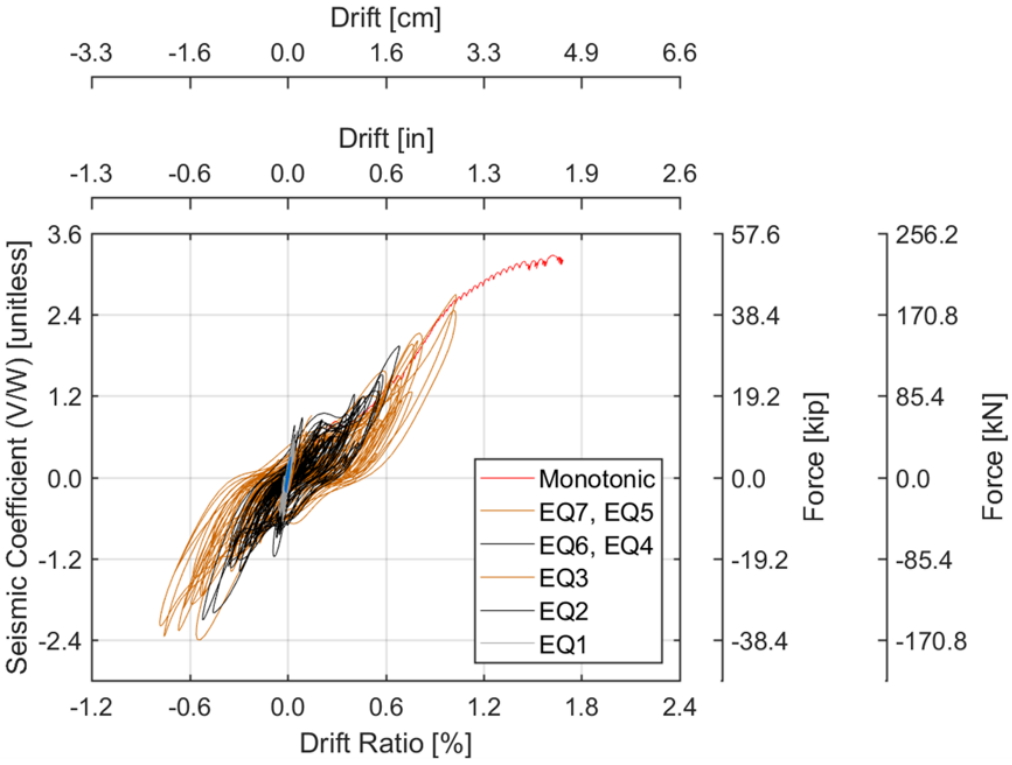


Figure C.3. Force displacement response of SGGS-1F specimen



(b)

Figure C.3. Force displacement response of SGGS-1F specimen (cont.)



(a)

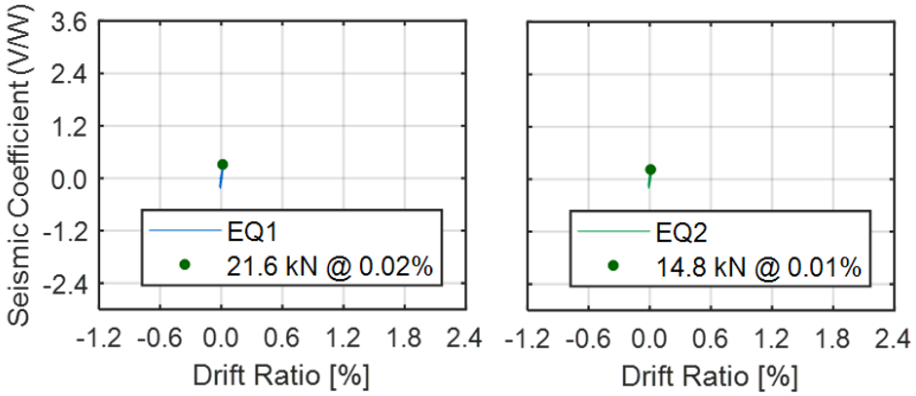
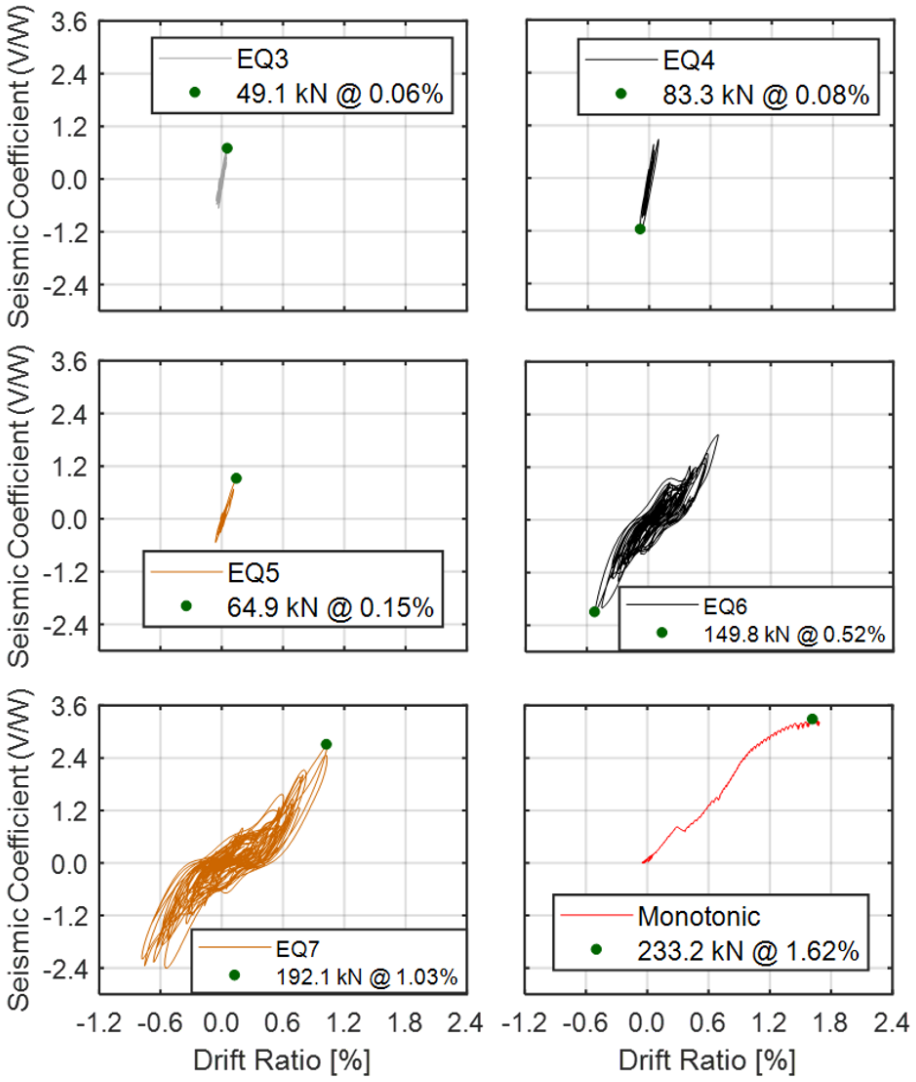
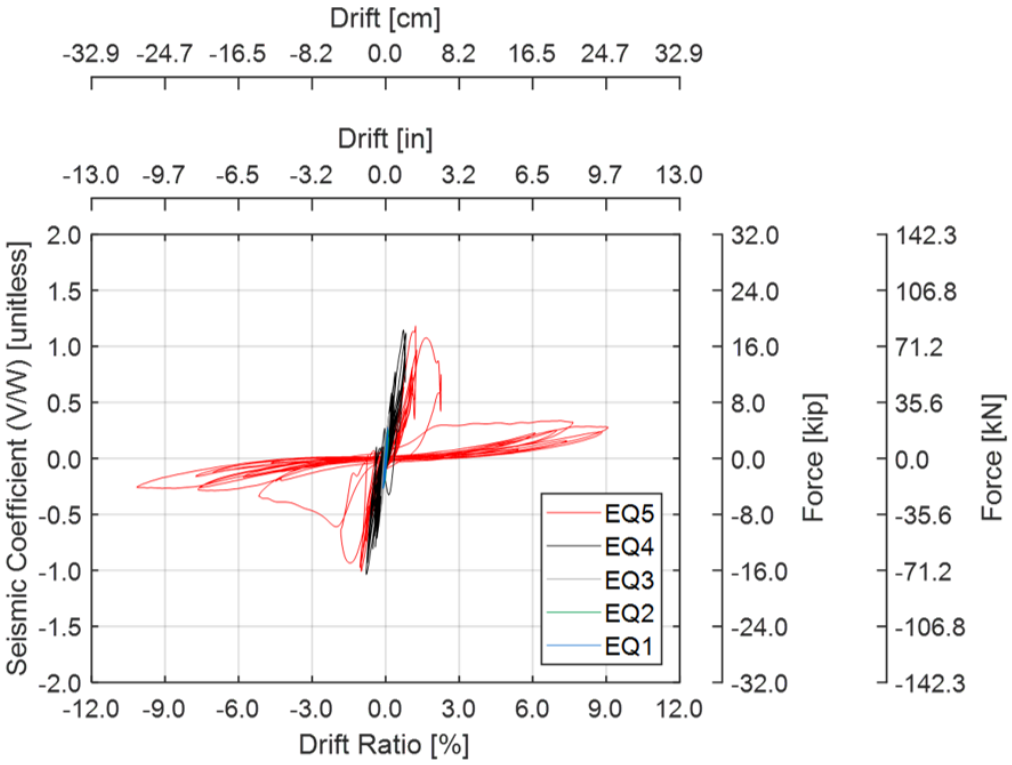


Figure C.4. Force displacement response of SGGS-1SB specimen

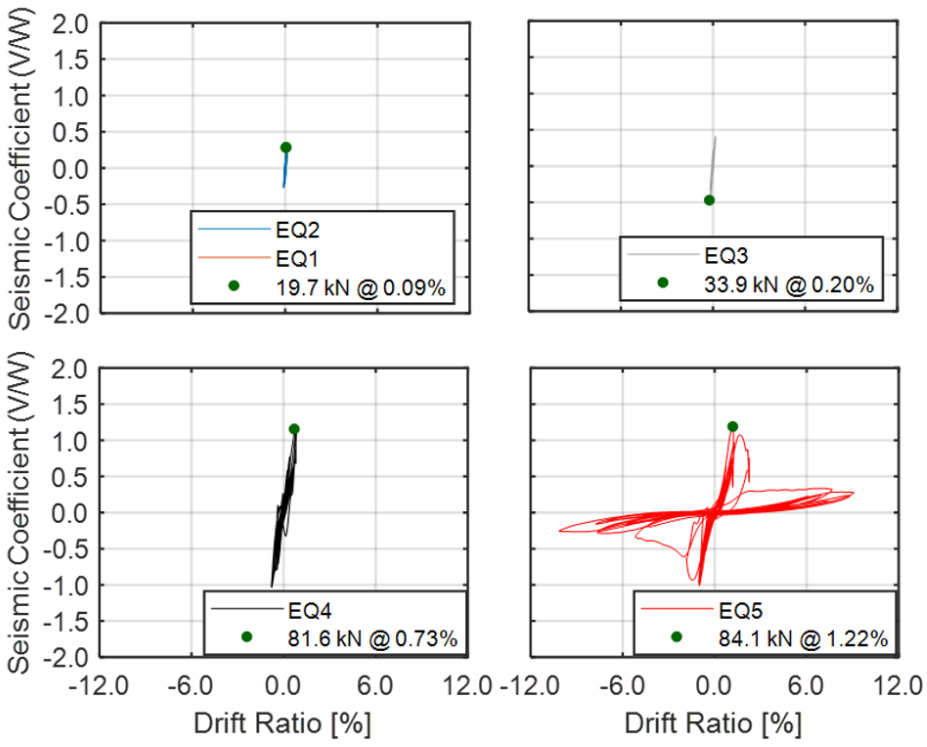


(b)

Figure C.4. Force displacement response of SGGS-1SB specimen (cont.)

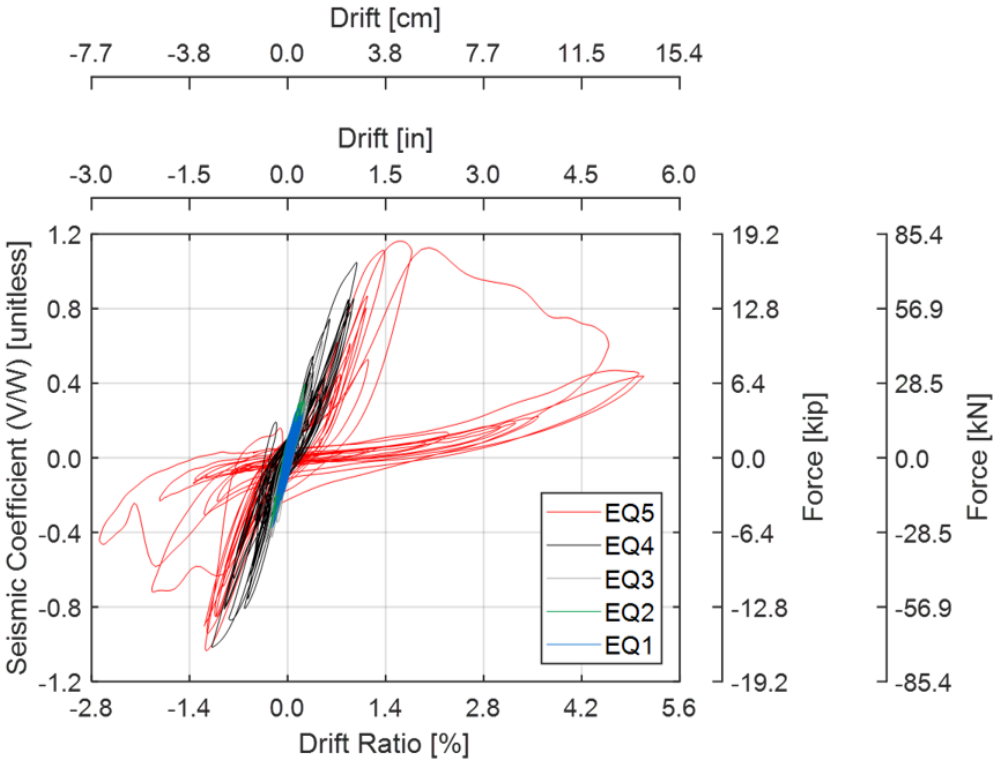


(a)

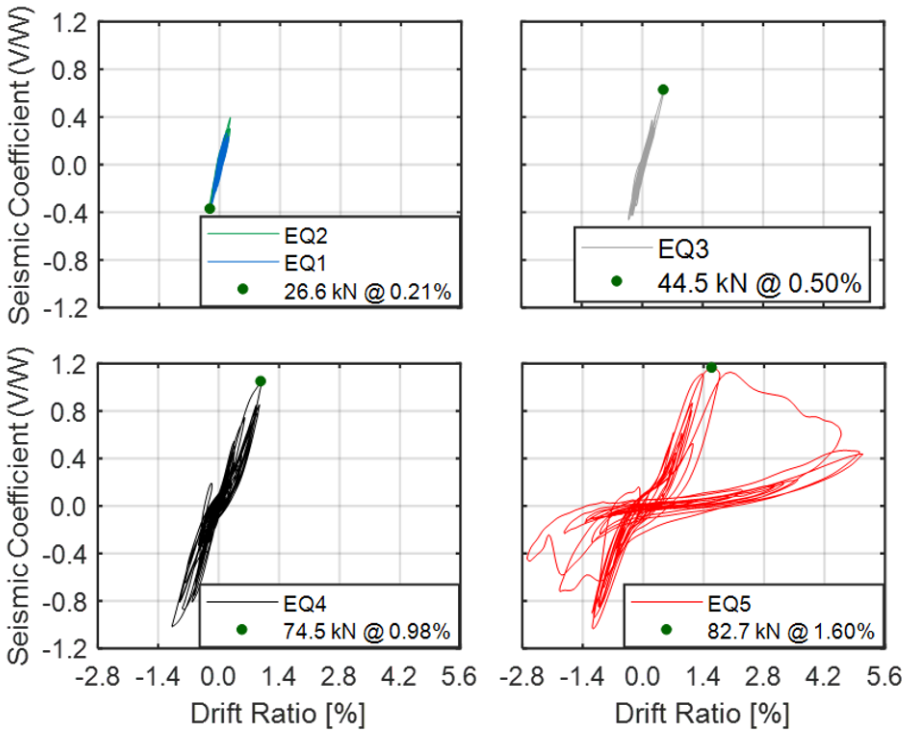


(b)

Figure C.5. Force displacement response of SGGS-2B specimen

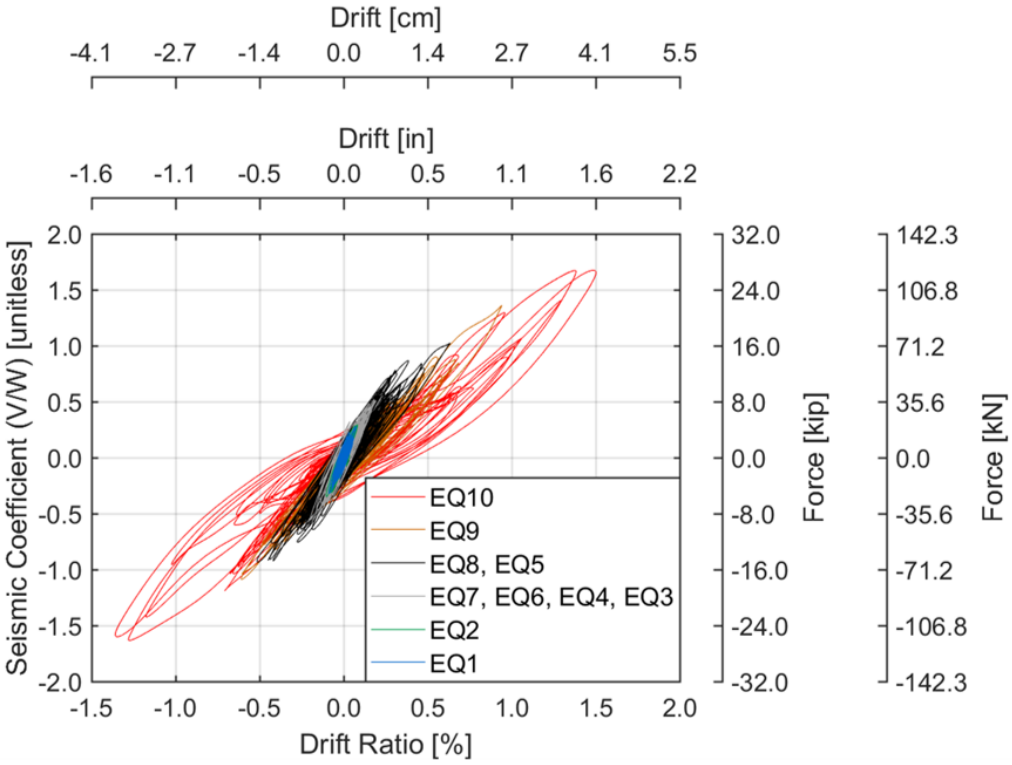


(a)



(b)

Figure C.6. Force displacement response of SGGG-1 specimen



(a)

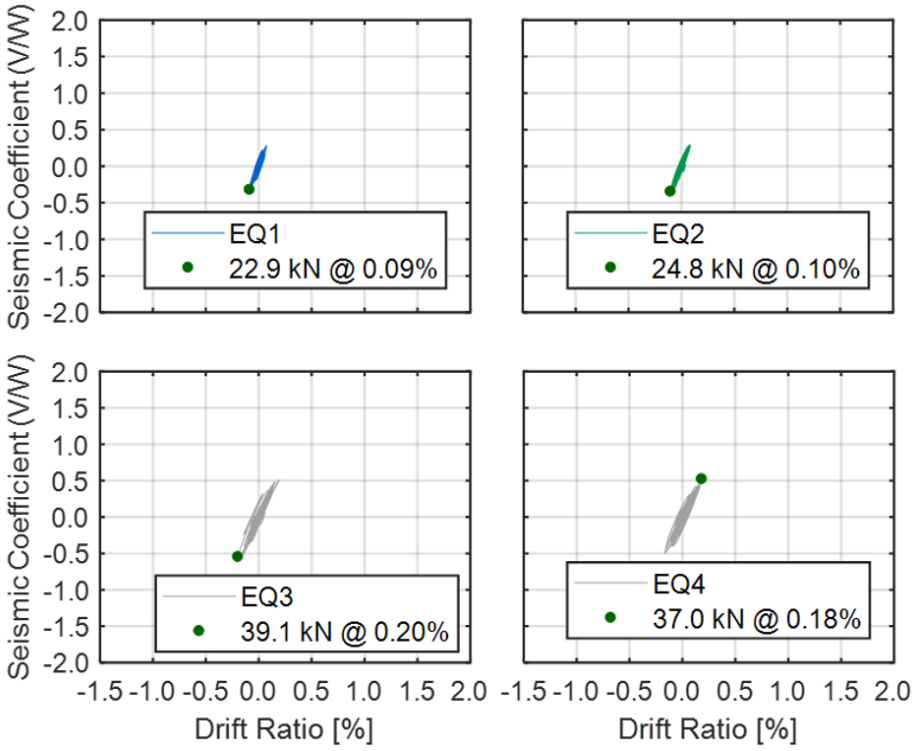
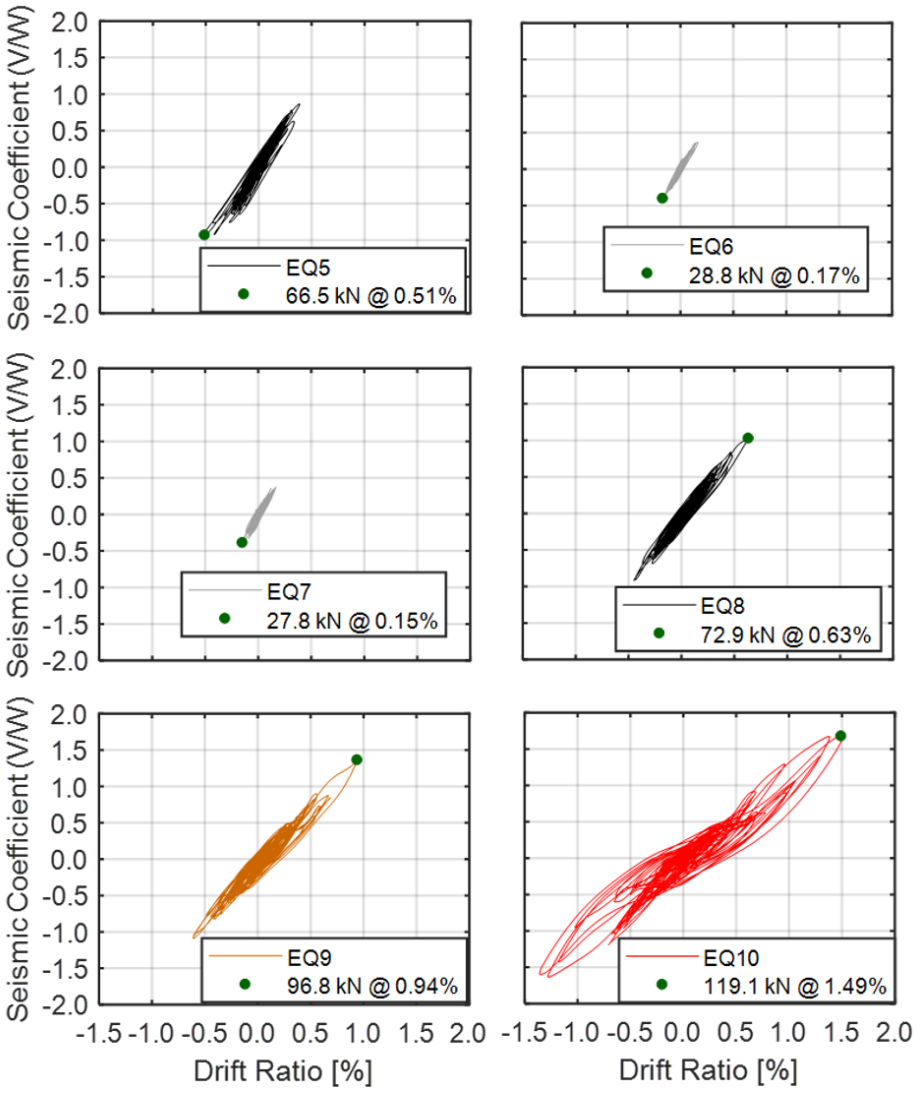
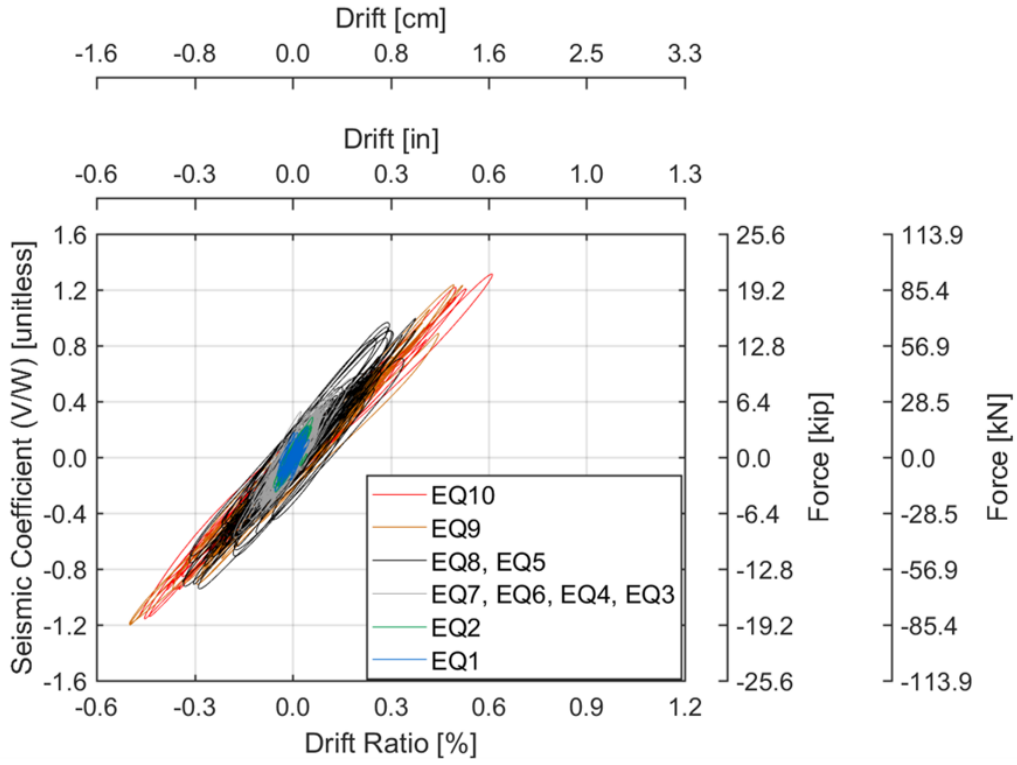


Figure C.7. Force displacement response of SWWS-2 specimen



(b)

Figure C.7. Force displacement response of SWWS-2 specimen (cont.)



(a)

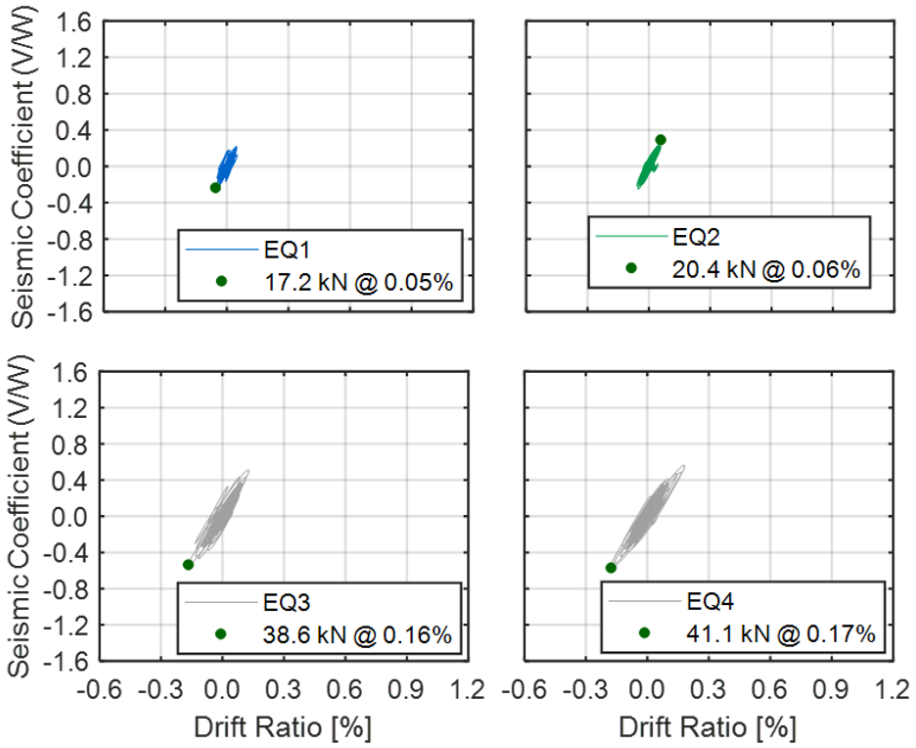
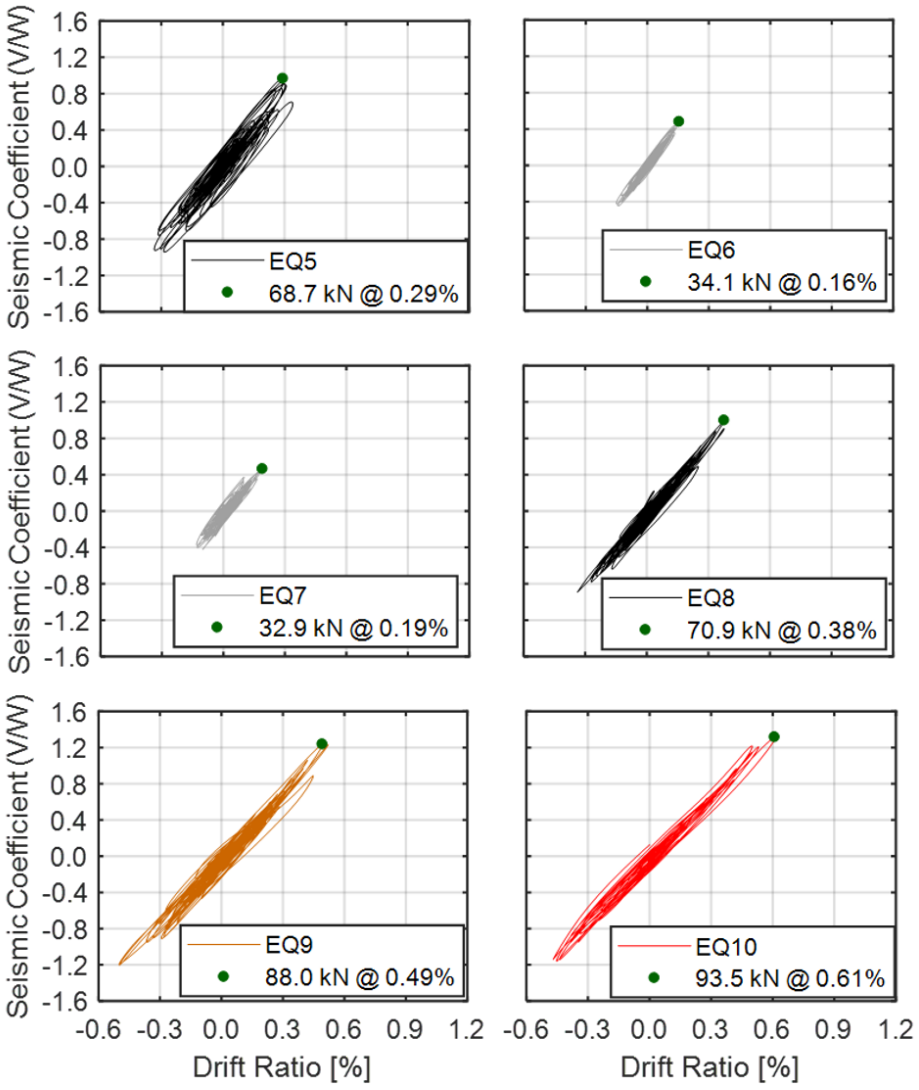


Figure C.8. Force displacement response of SWWS-1 specimen



(b)

Figure C.8. Force displacement response of SWWS-1 specimen (cont.)

C.2 Quasi-Static Test Phase

C.2.1 Force-Displacement Response of Wall-Line Specimens

Figures C.9-C.18 present the measured force vs. displacement response as well as the dissipated hysteretic energy from specimens tested during the quasi-static test phase.

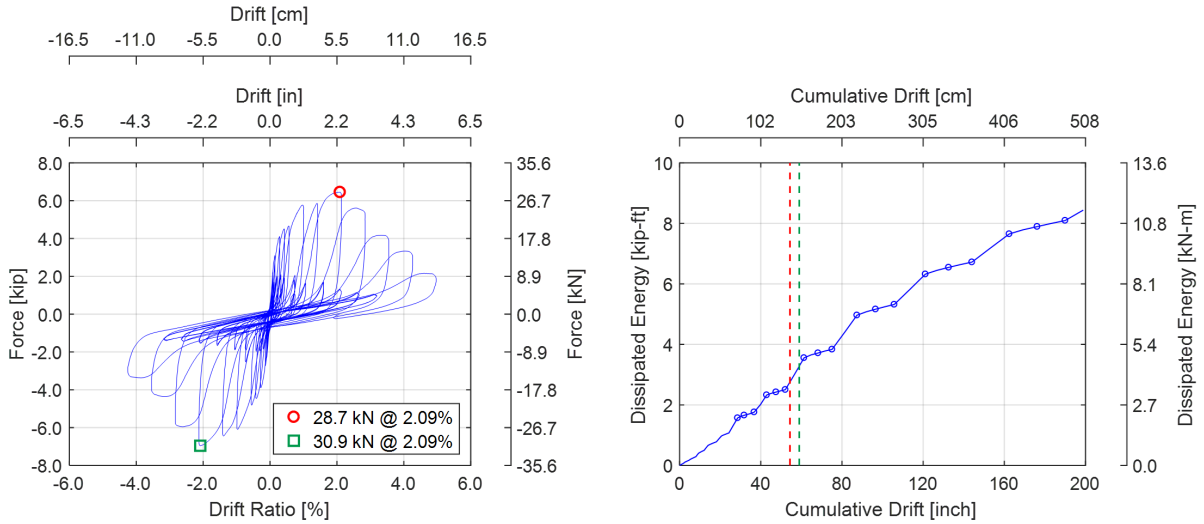


Figure C.9. Force displacement and energy dissipation response of specimen GGGG
Note: Colored markers and lines denote when strength is reached in positive and negative directions.

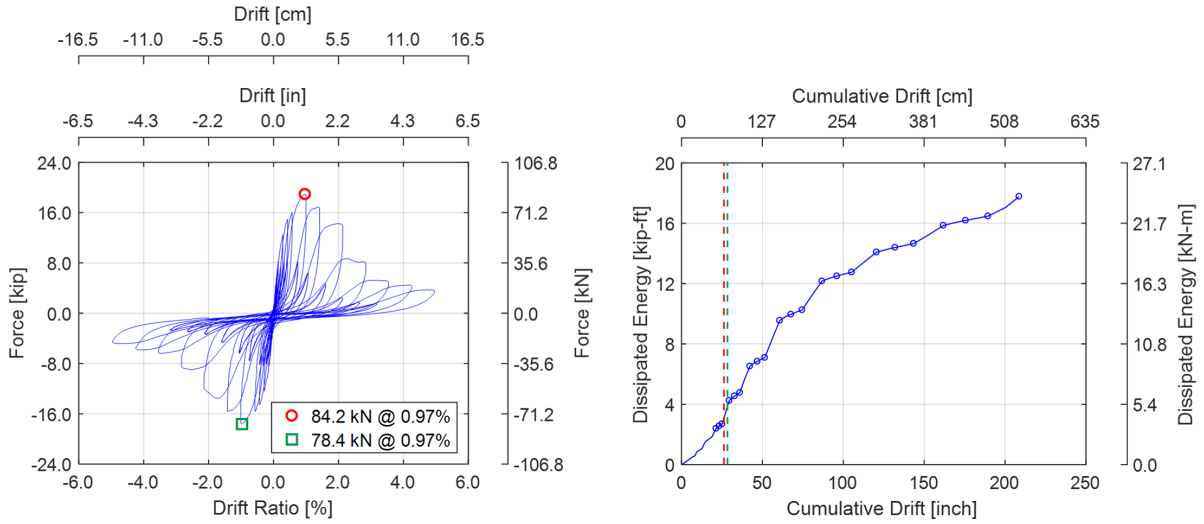


Figure C.10. Force displacement and energy dissipation response of specimen GGGG-F

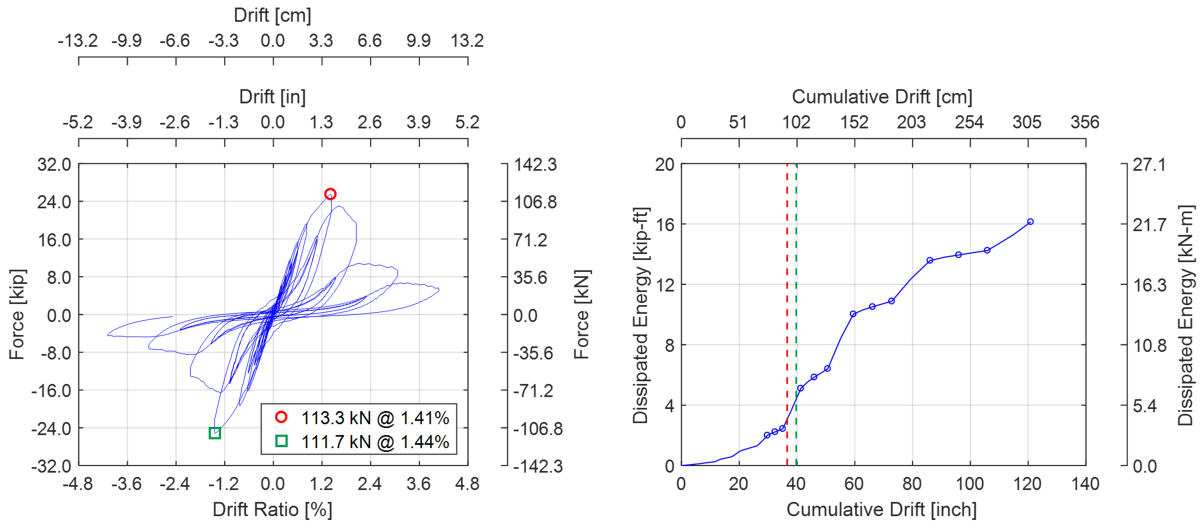


Figure C.11. Force displacement and energy dissipation response of specimen SGGS-2

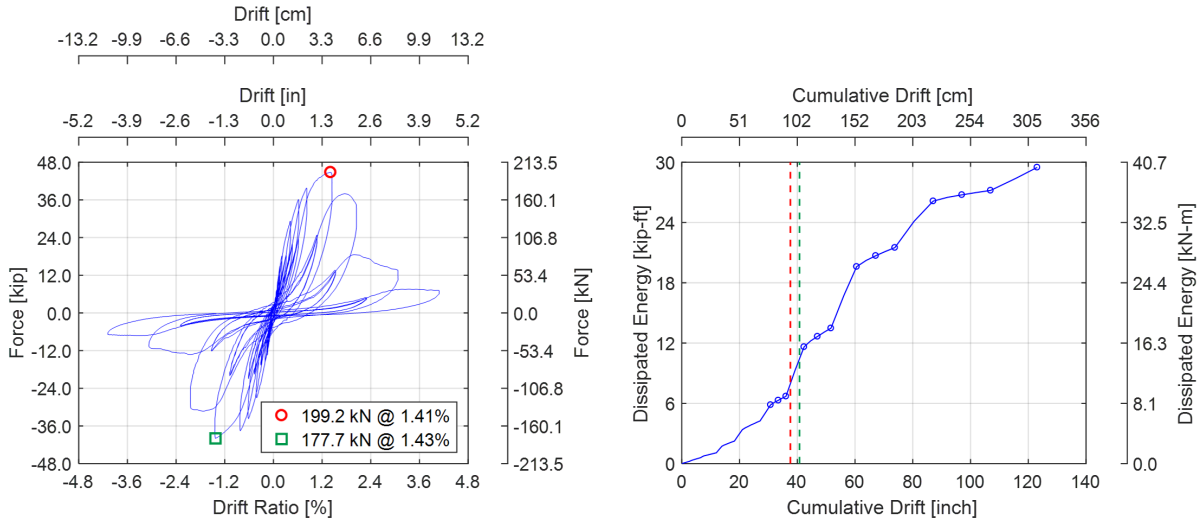


Figure C.12. Force displacement and energy dissipation response of specimen SGGS-2F

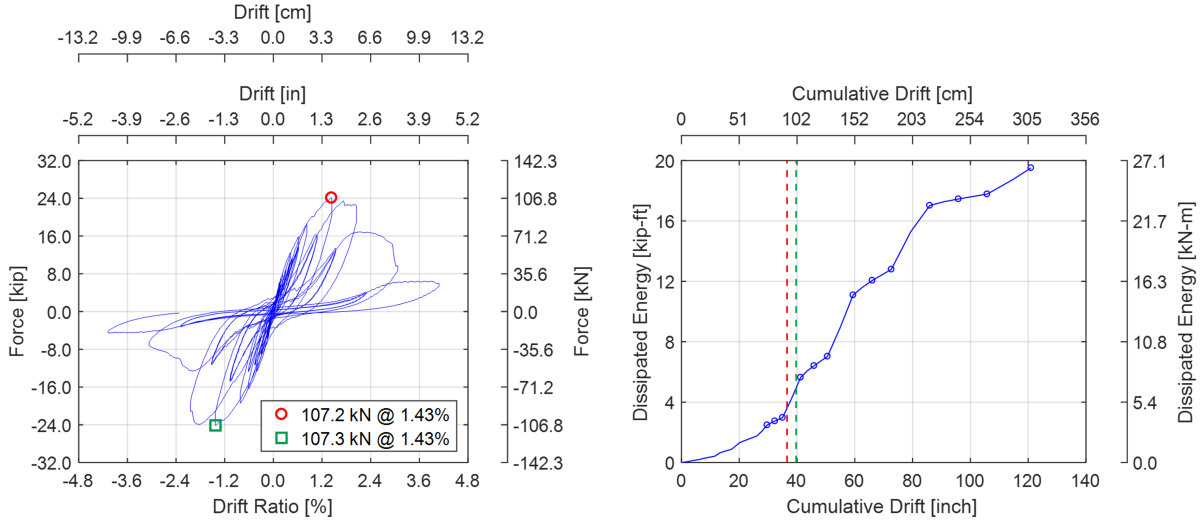


Figure C.13. Force displacement and energy dissipation response of specimen SWWS-2

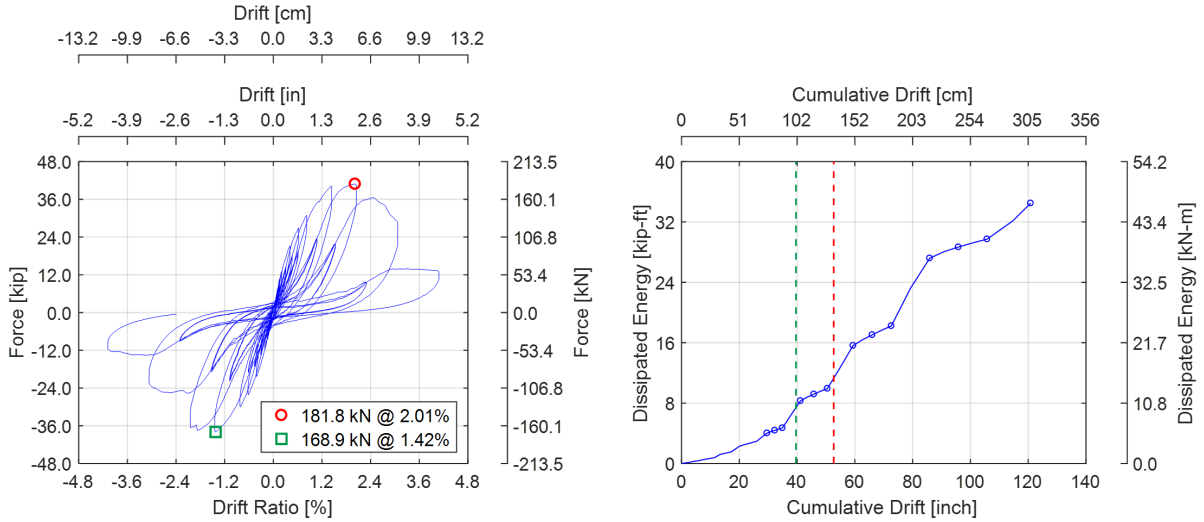


Figure C.14. Force displacement and energy dissipation response of specimen SWWS-2F

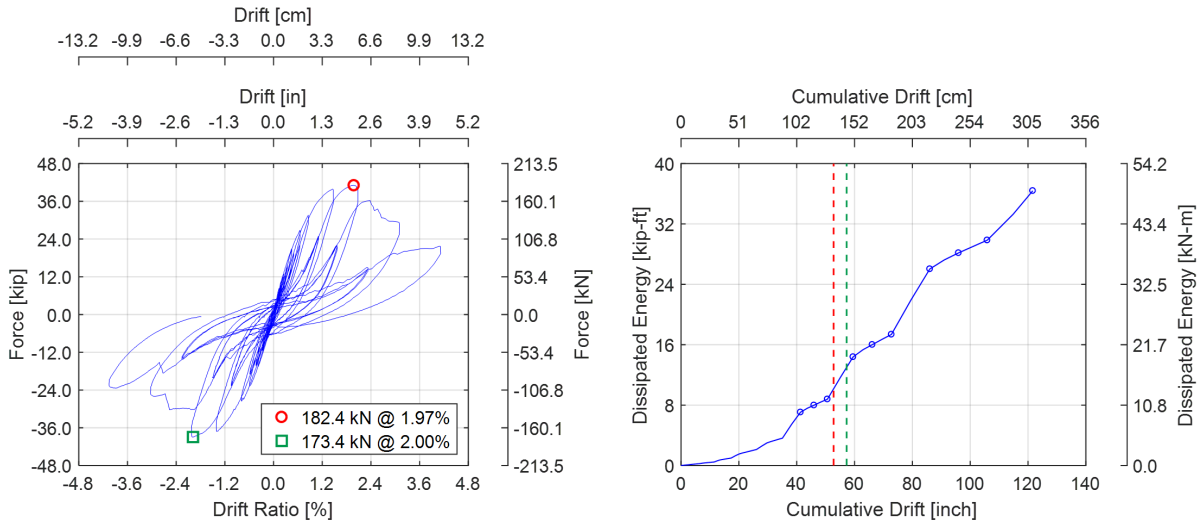


Figure C.15. Force displacement and energy dissipation response of specimen SWWS-1

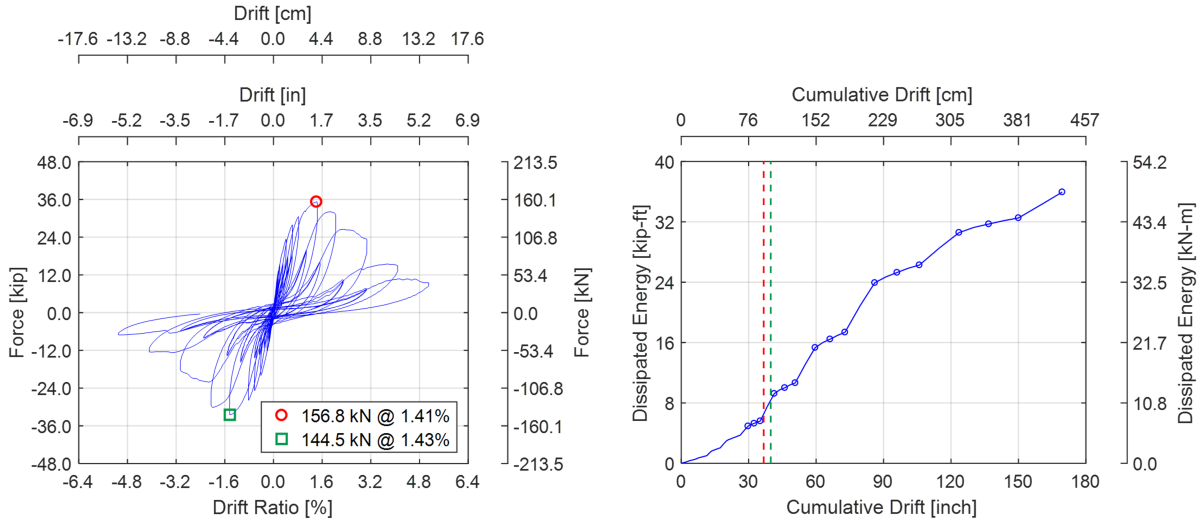


Figure C.16. Force displacement and energy dissipation response of specimen SGGG-1F

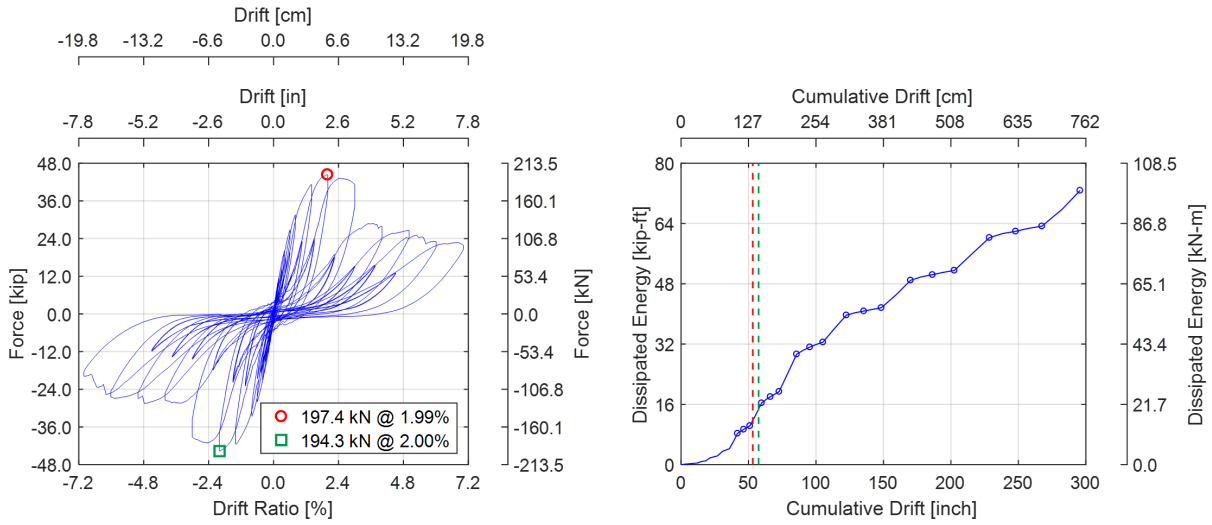


Figure C.17. Force displacement and energy dissipation response of specimen SGGS-1HD

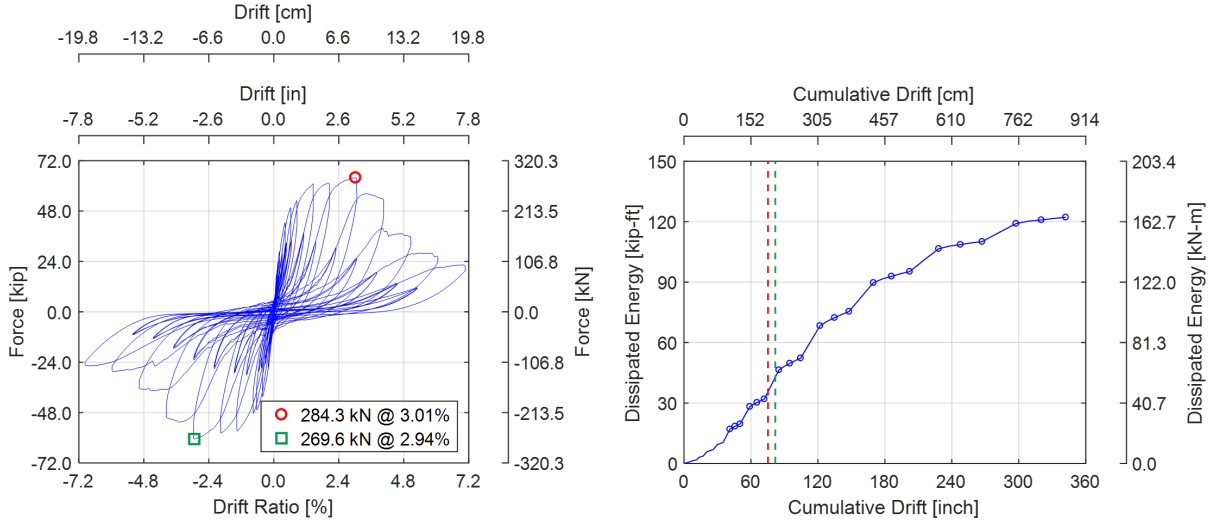


Figure C.18. Force displacement and energy dissipation response of specimen SGGS-1HDF

C.2.2 Equivalent Hysteretic Damping of Wall-Line Specimens

Equivalent hysteretic damping ζ for wall-lines tested during the quasi-static test phase of the CFS-NHERI wall-line experimental program are presented through Figures C.19-C.23. Calculation of equivalent hysteretic damping is shown in Eq. 4.1.

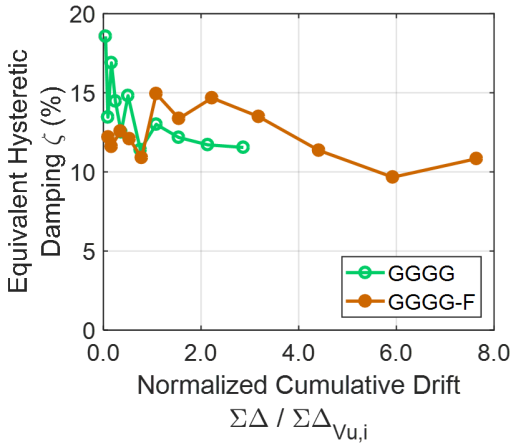


Figure C.19. Equivalent hysteretic damping for specimens GGGG and GGGG-F

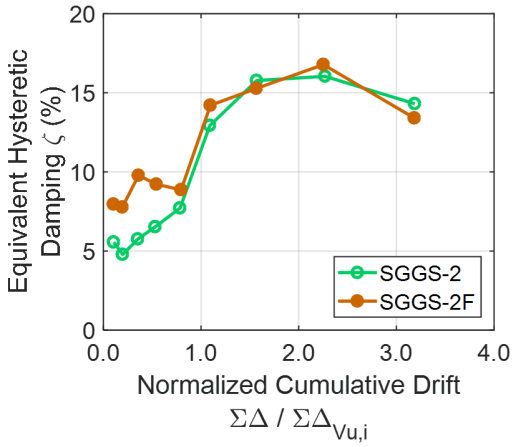


Figure C.20. Equivalent hysteretic damping for specimens SGGS-2 and SGGS-2F

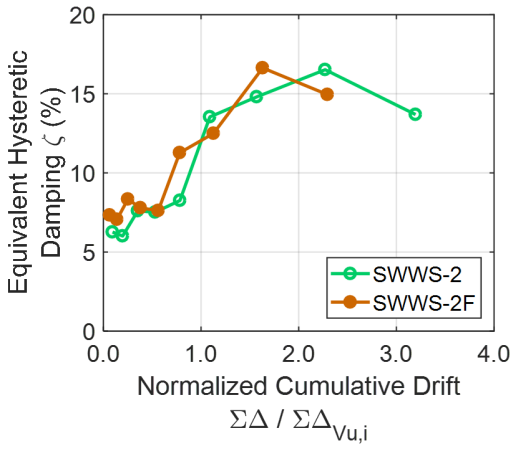


Figure C.21. Equivalent hysteretic damping for specimens SWWS-2 and SWWS-2F

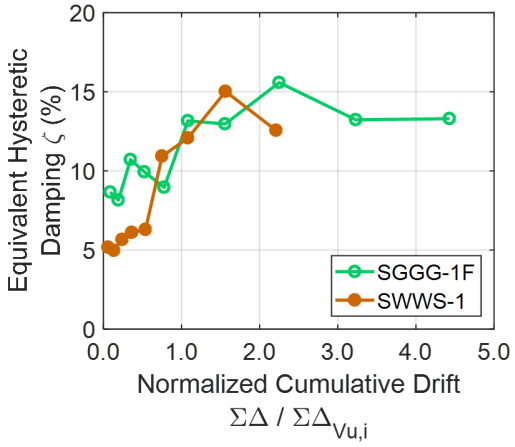


Figure C.22. Equivalent hysteretic damping for specimens SGGG-1F and SWWS-1

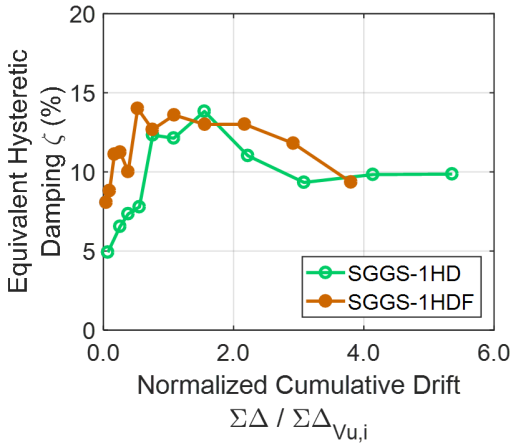


Figure C.23. Equivalent hysteretic damping for specimens SGGS-1HD and SGGS-1HDF

Appendix D

Local Response of Wall-Line Specimens

Local response, i.e. tie-down force, wall uplift, and panel shear distortion, for all the wall-lines tested across the two phases of the CFS-NHERI wall-line experimental program are presented here. Figures D.1-D.16 present the measured response from specimens tested during the shake table test phase. Figures D.17-D.42 present the measured response from specimens tested during the quasi-static test phase.

D.1 Shake Table Test Phase

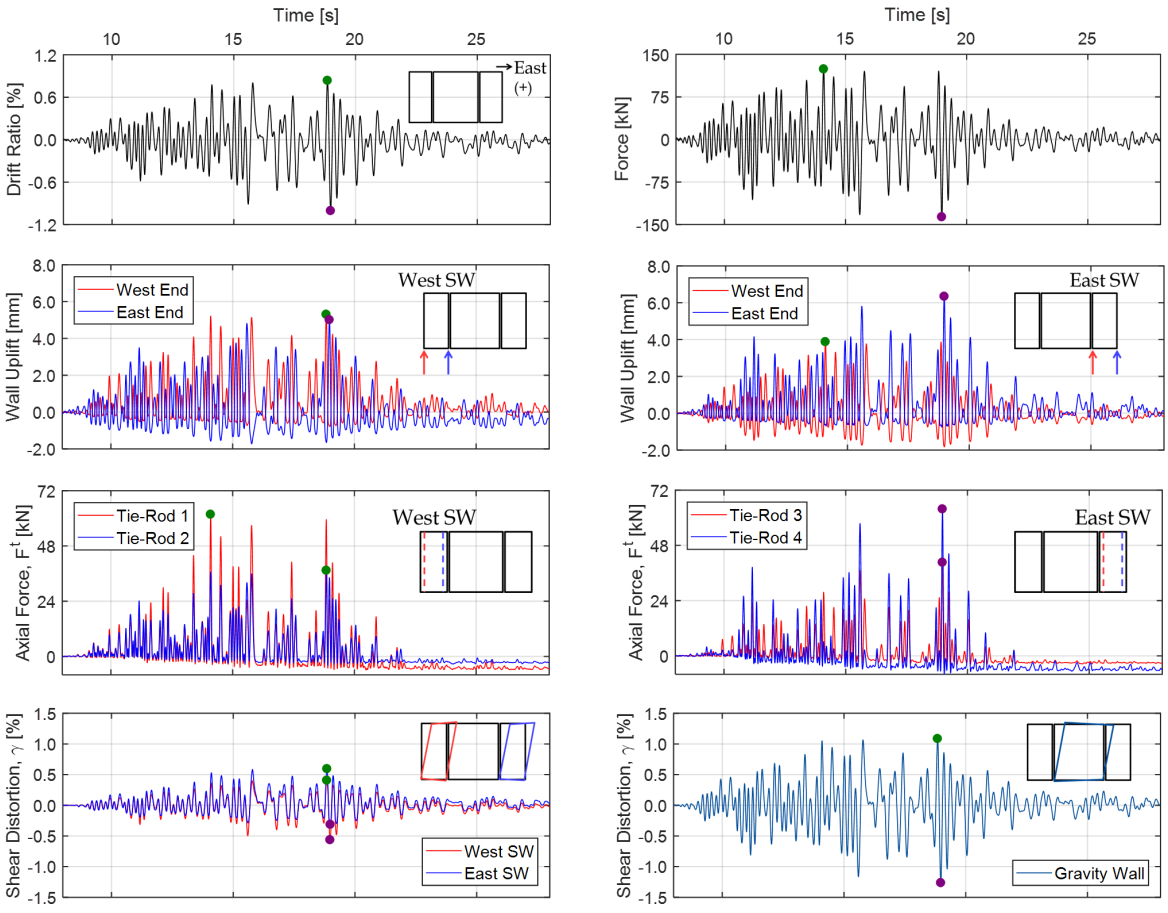


Figure D.1. SGGS-1 specimen local response during design earthquake test
Note: Schematics within subplots indicate location and type of response plotted.

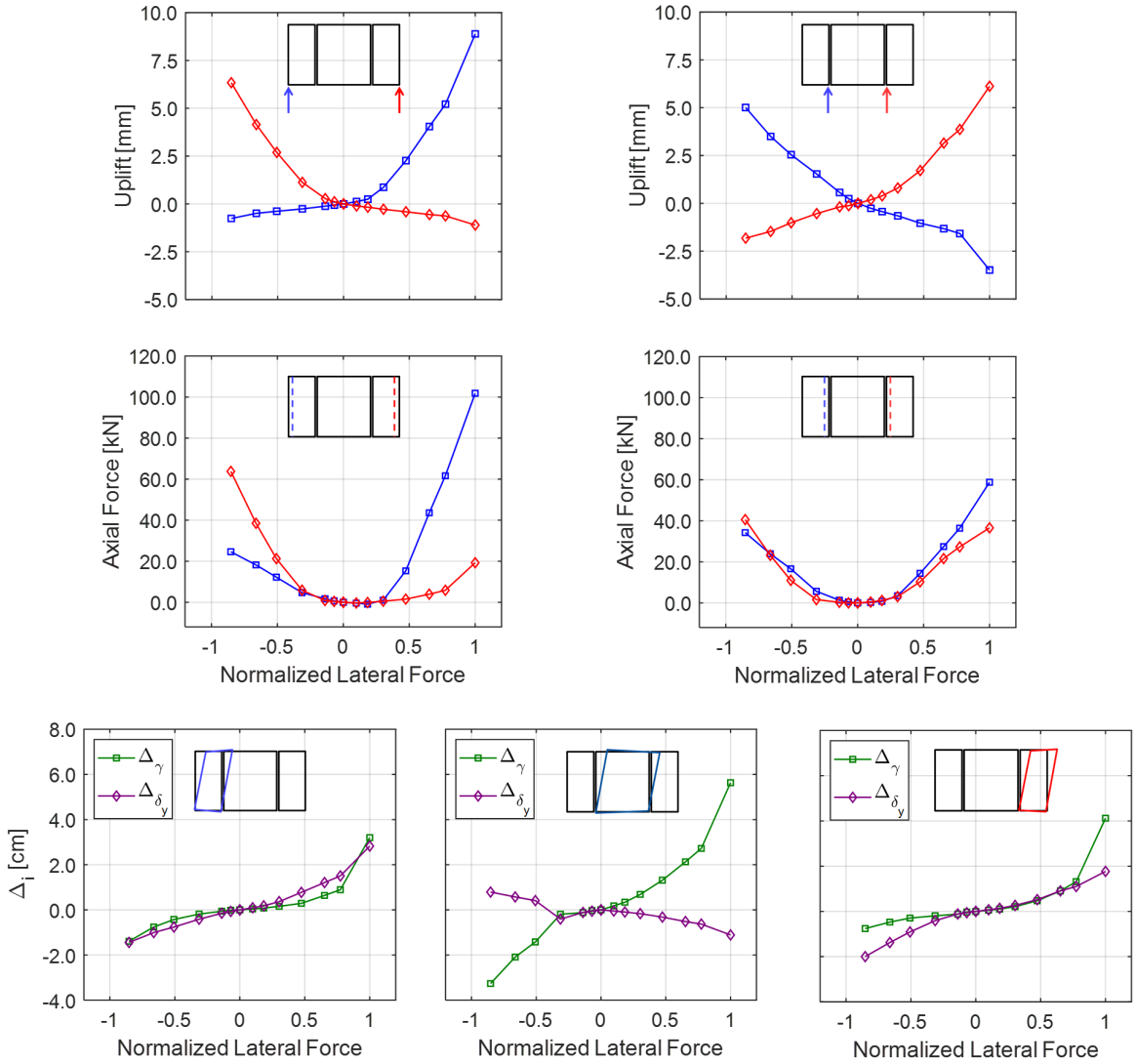


Figure D.2. SGGS-1 specimen local behavior evolution

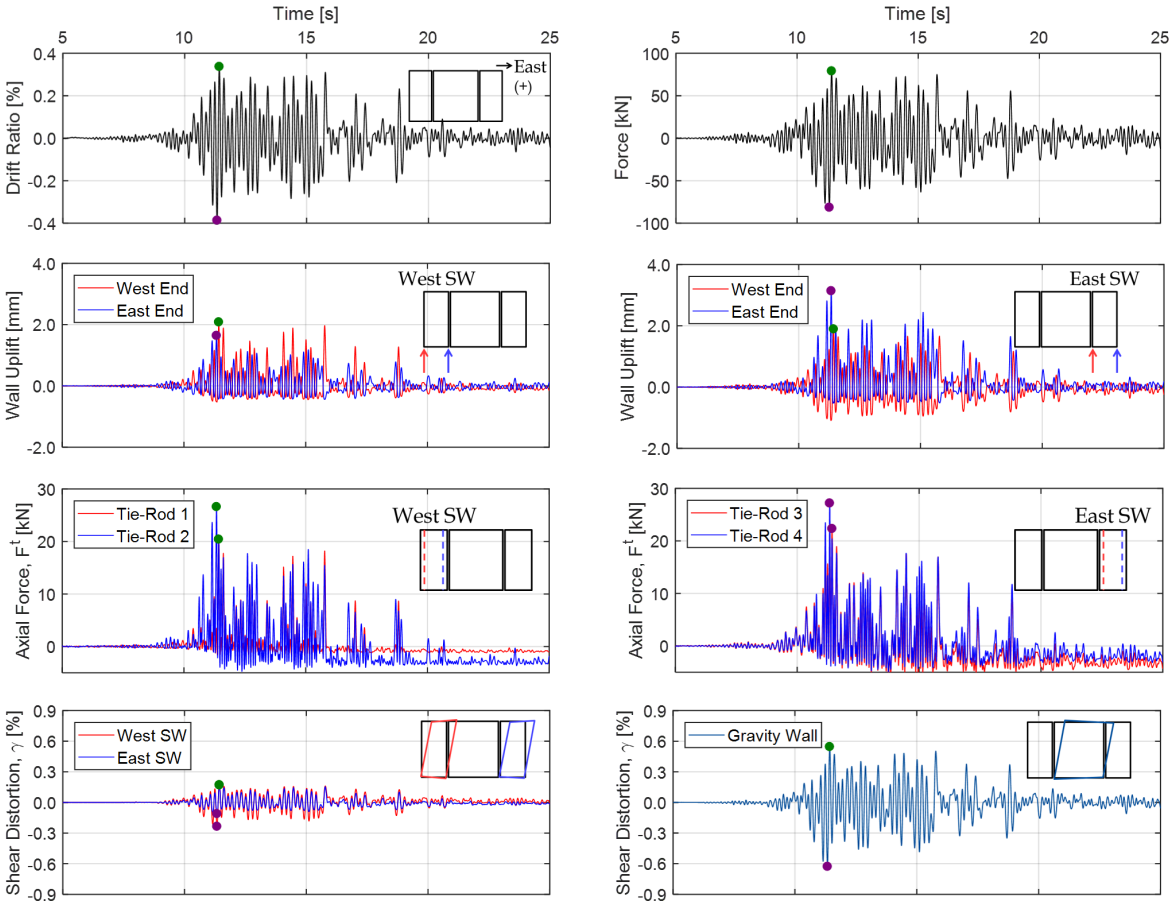


Figure D.3. SGGS-1XS specimen local response during quasi-elastic earthquake test

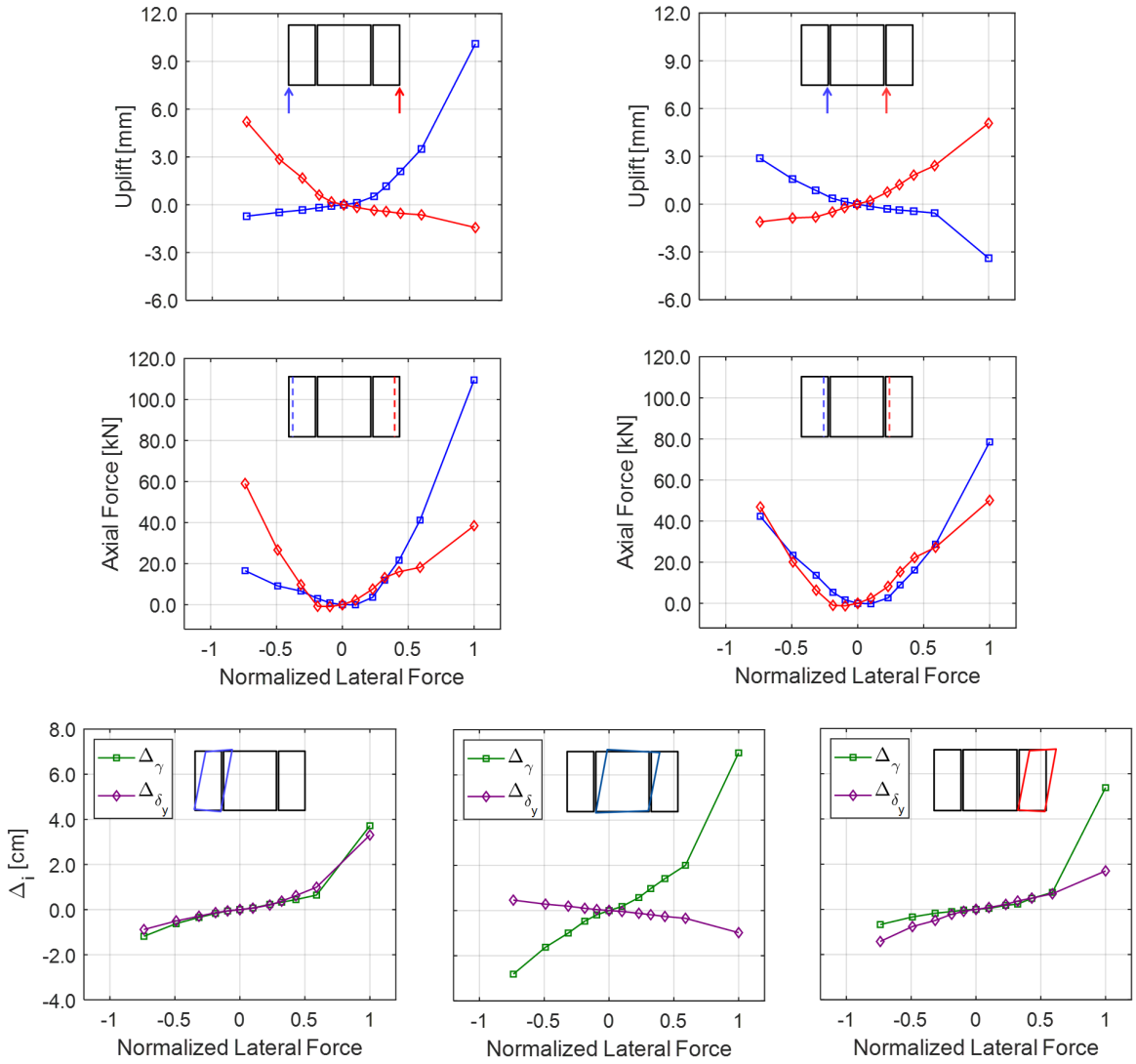


Figure D.4. SGGS-1XS specimen local behavior evolution

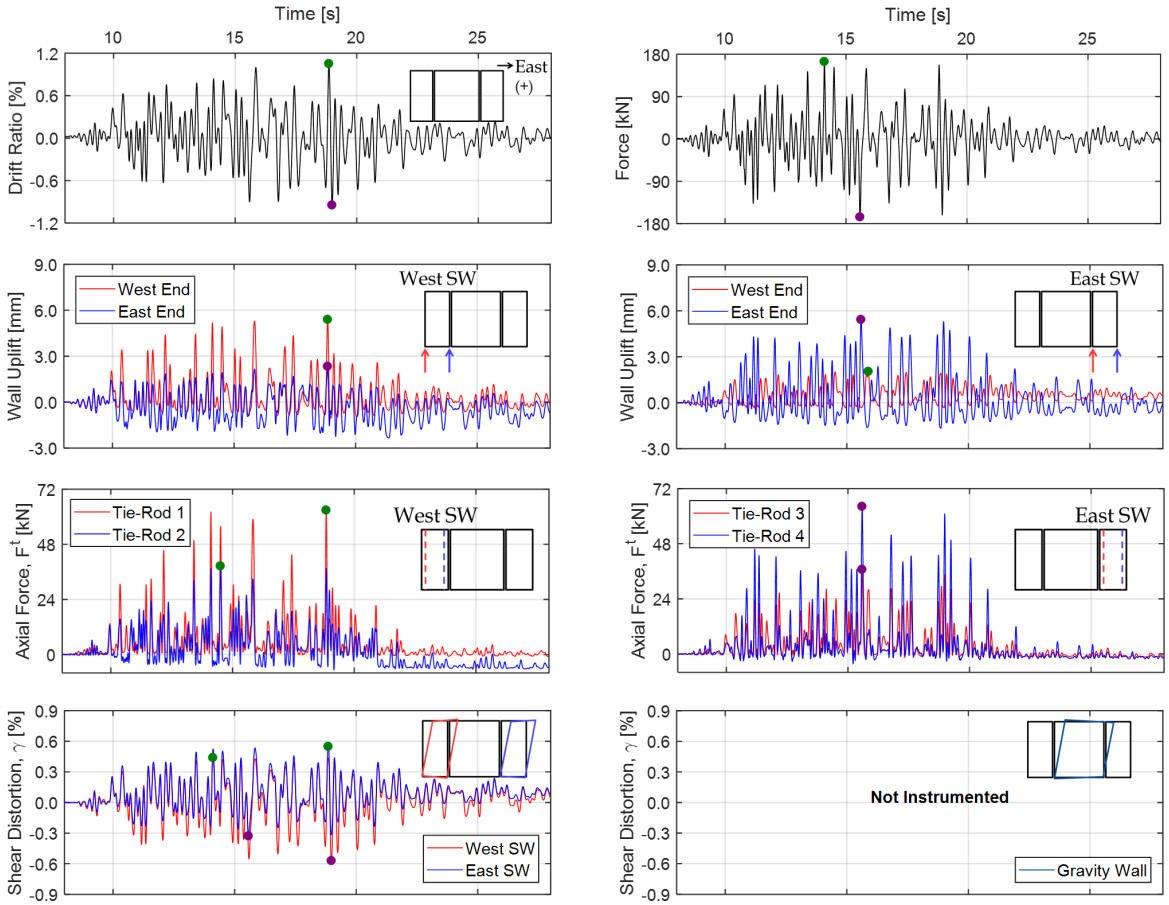


Figure D.5. SGGS-1F specimen local response during quasi-elastic earthquake test

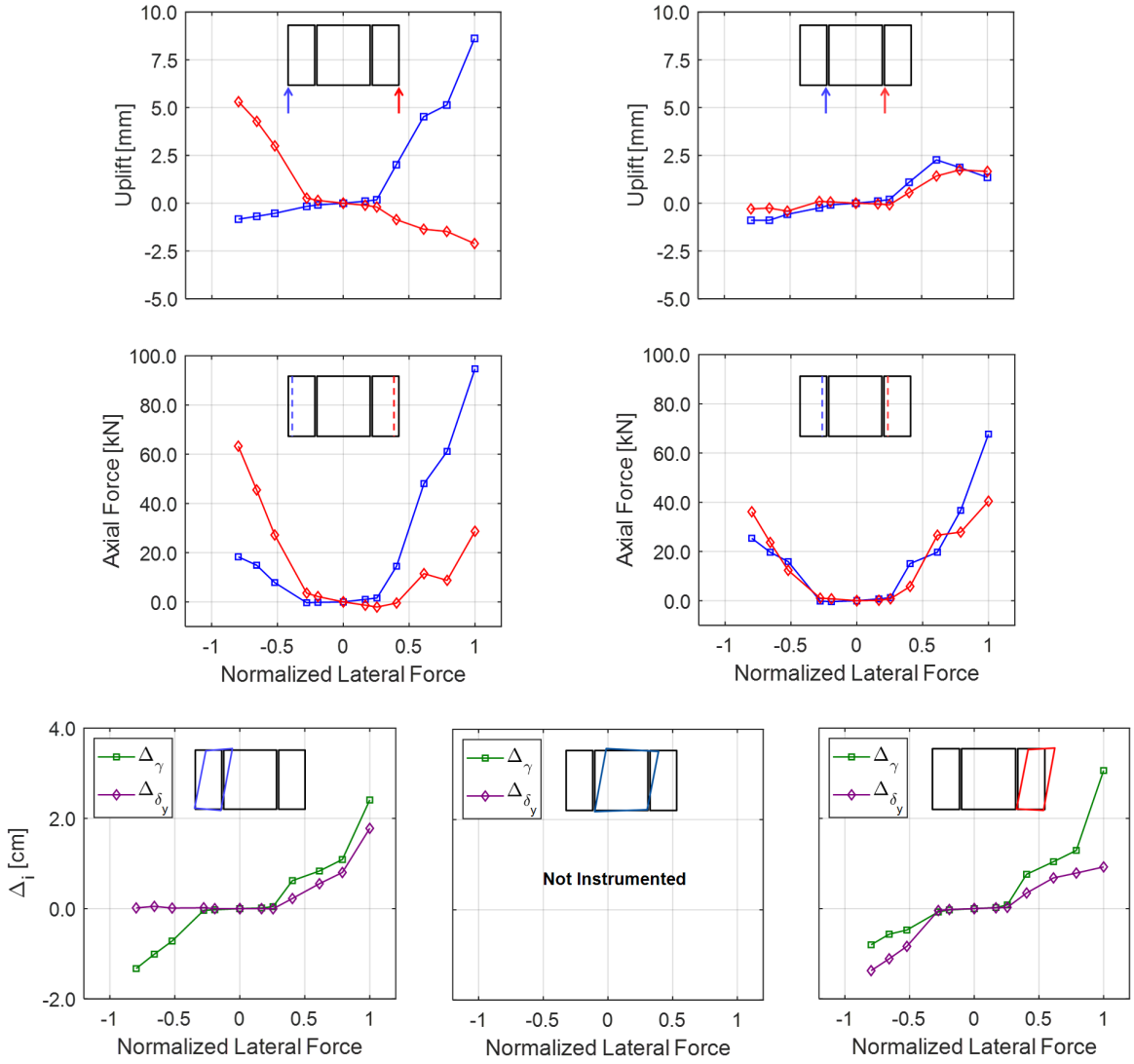


Figure D.6. SGGS-1F specimen local behavior evolution

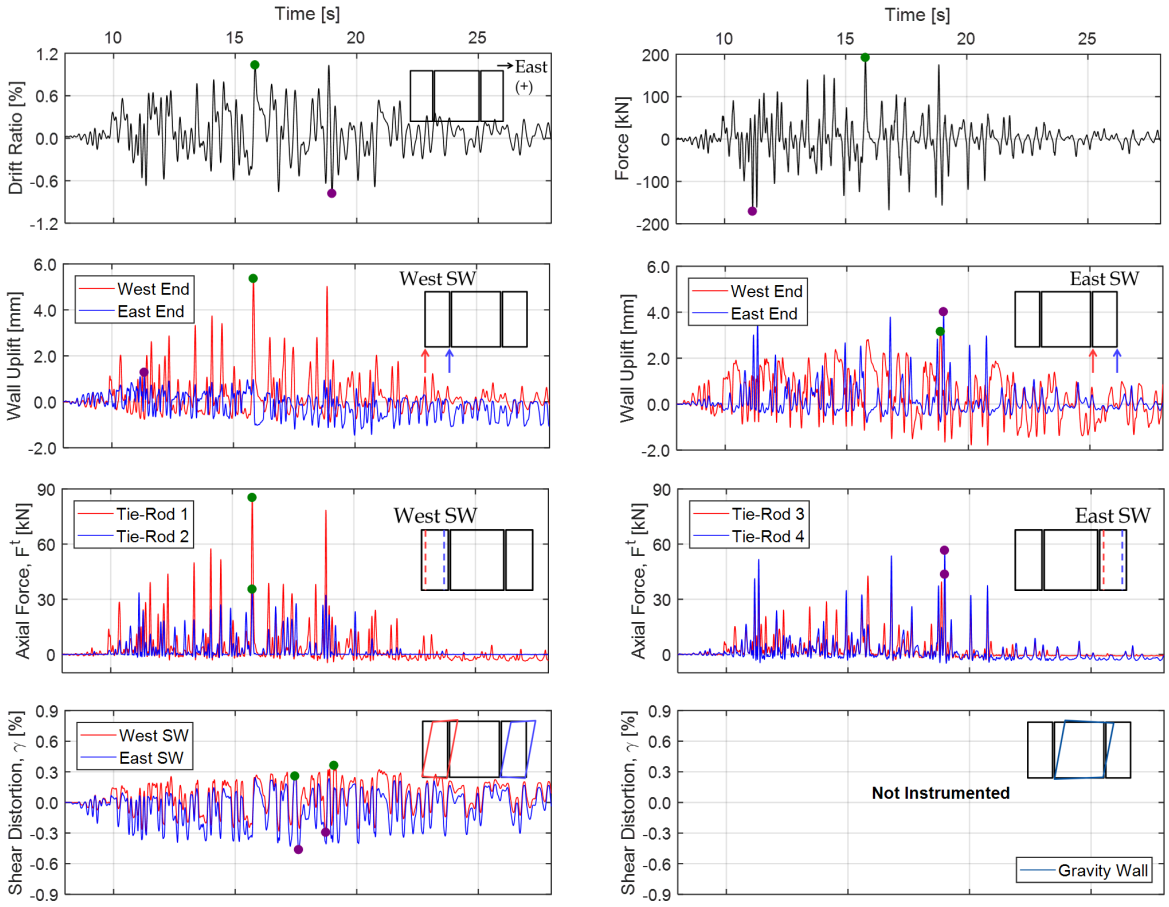


Figure D.7. SGGS-1SB specimen local response during quasi-elastic earthquake test

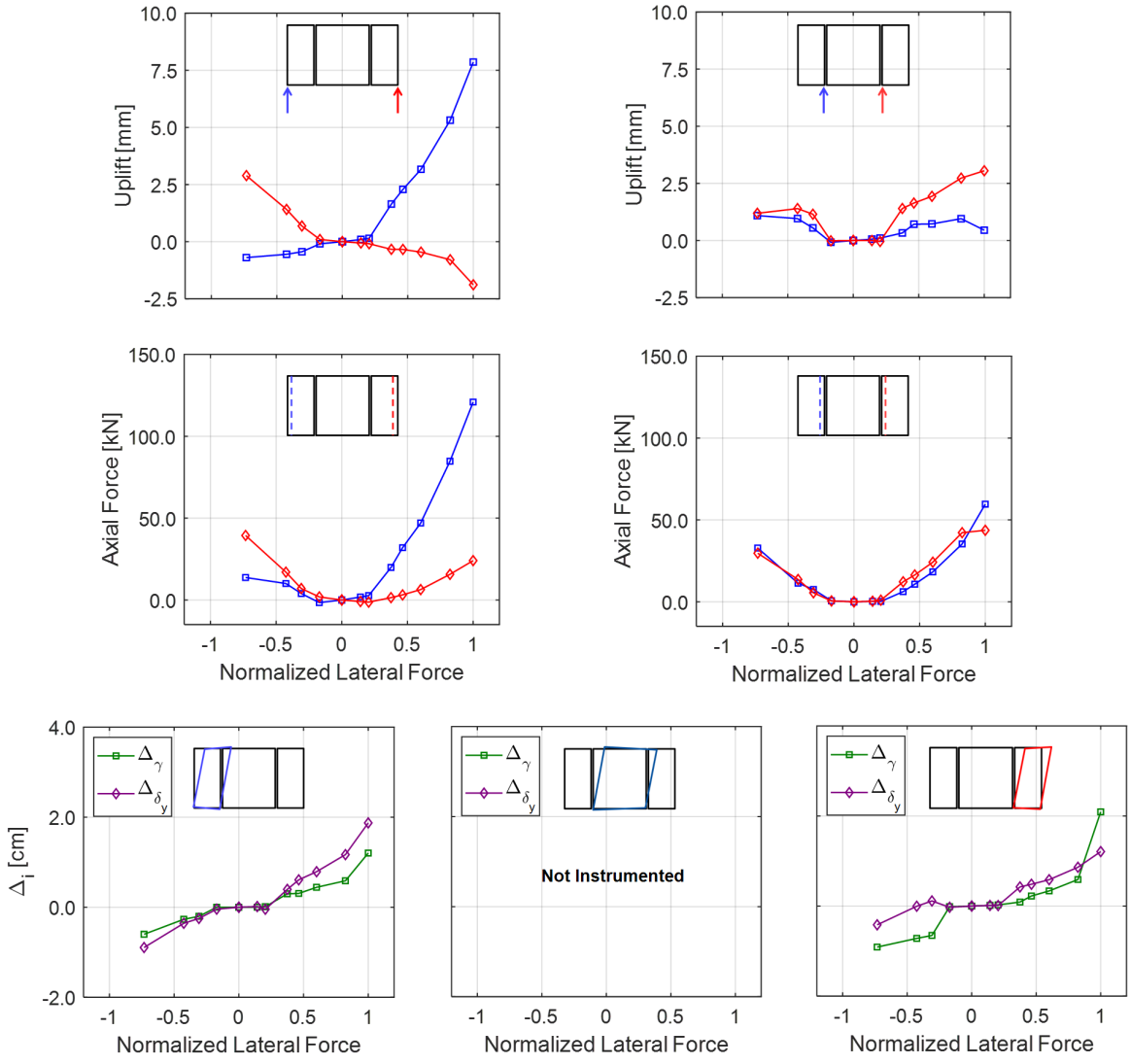


Figure D.8. SGGS-1SB specimen local behavior evolution

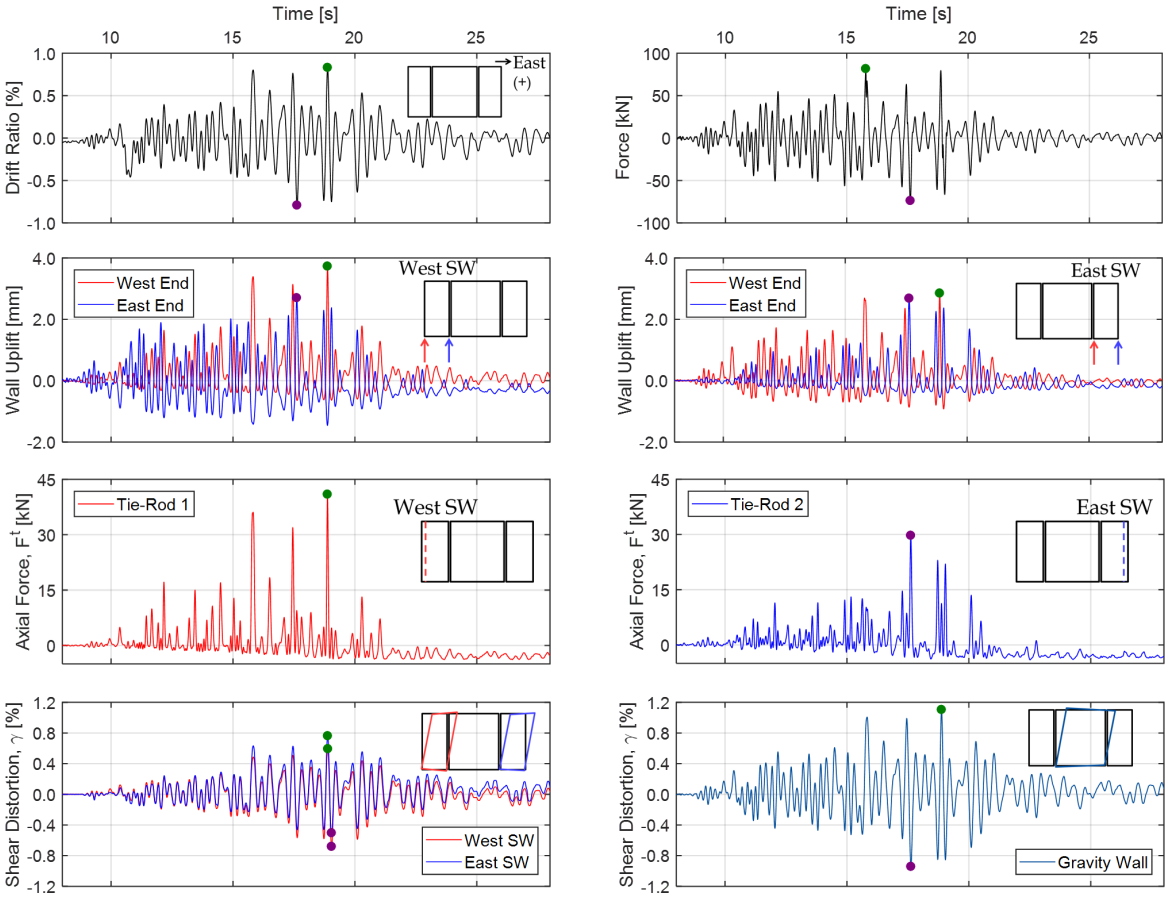


Figure D.9. SGGS-2B specimen local response during design earthquake test

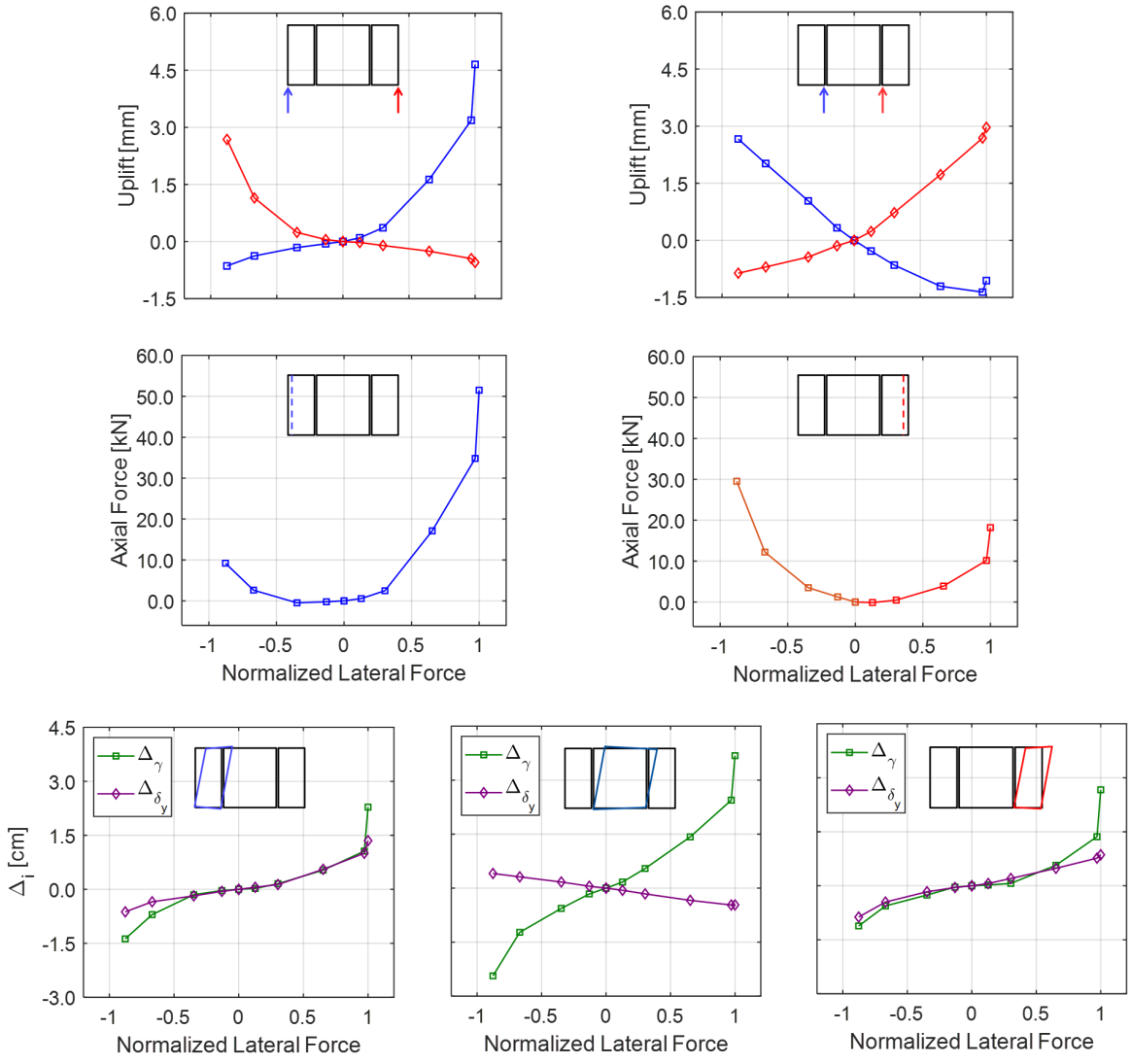


Figure D.10. SGGS-2B specimen local behavior evolution

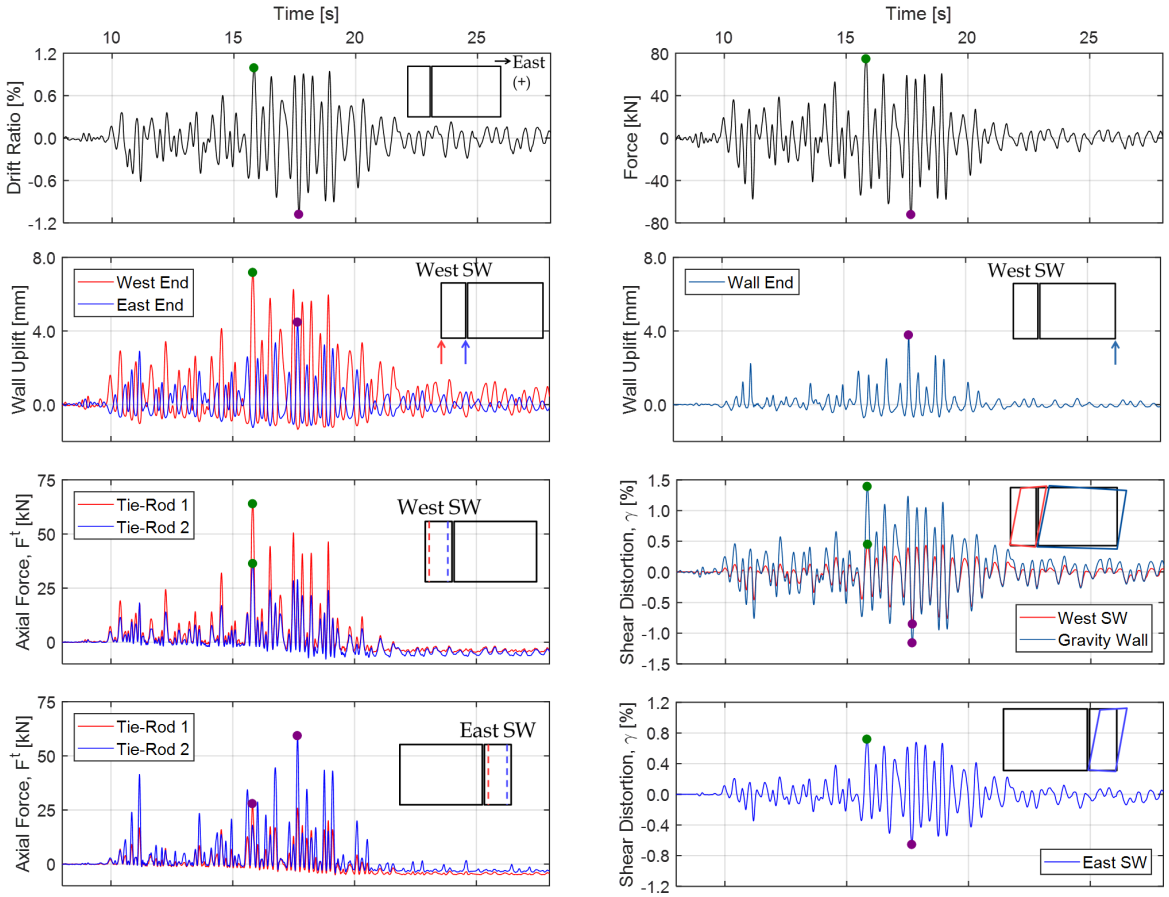


Figure D.11. SGGG-1 specimen local response during design earthquake test

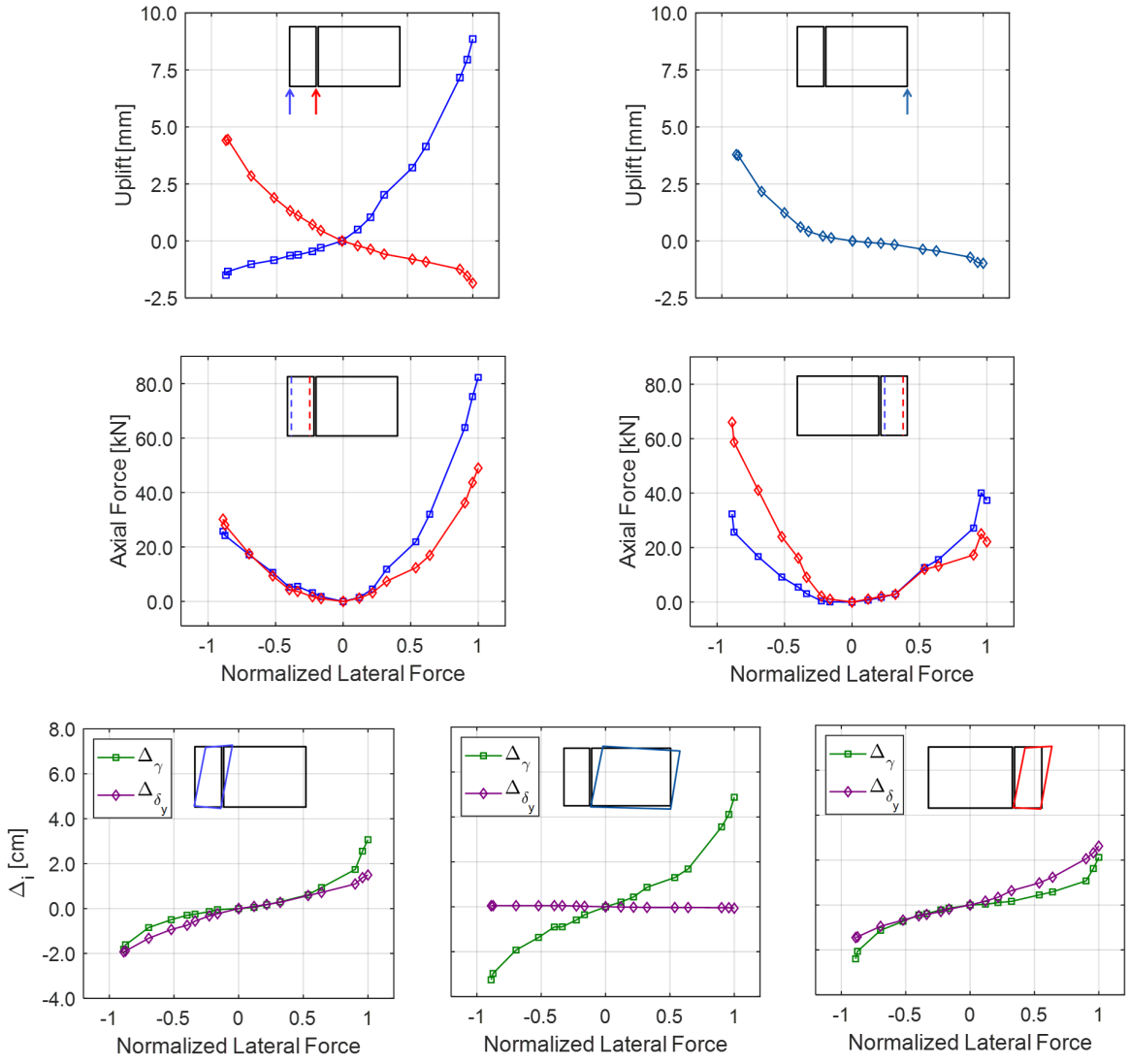


Figure D.12. SGGG-1 specimen local behavior evolution

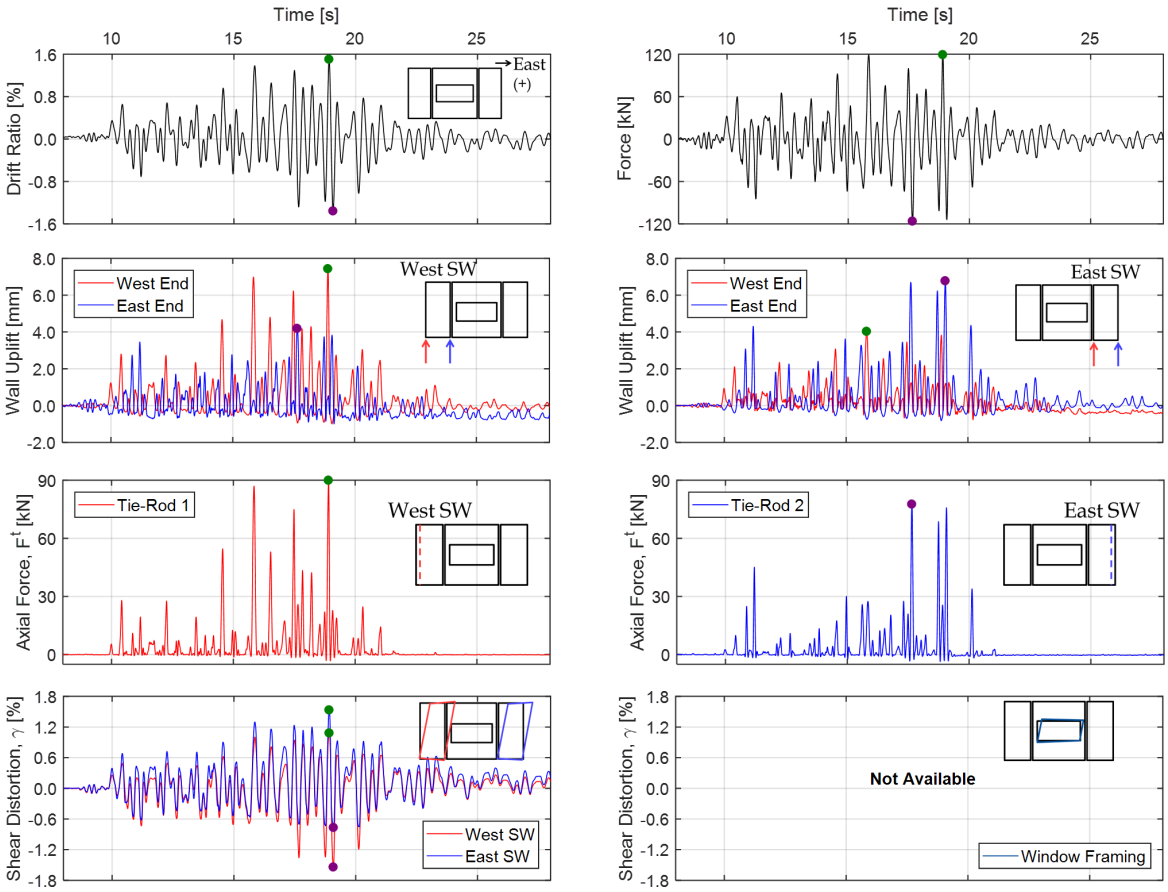


Figure D.13. SWWS-2 specimen local response during above design 2 earthquake test

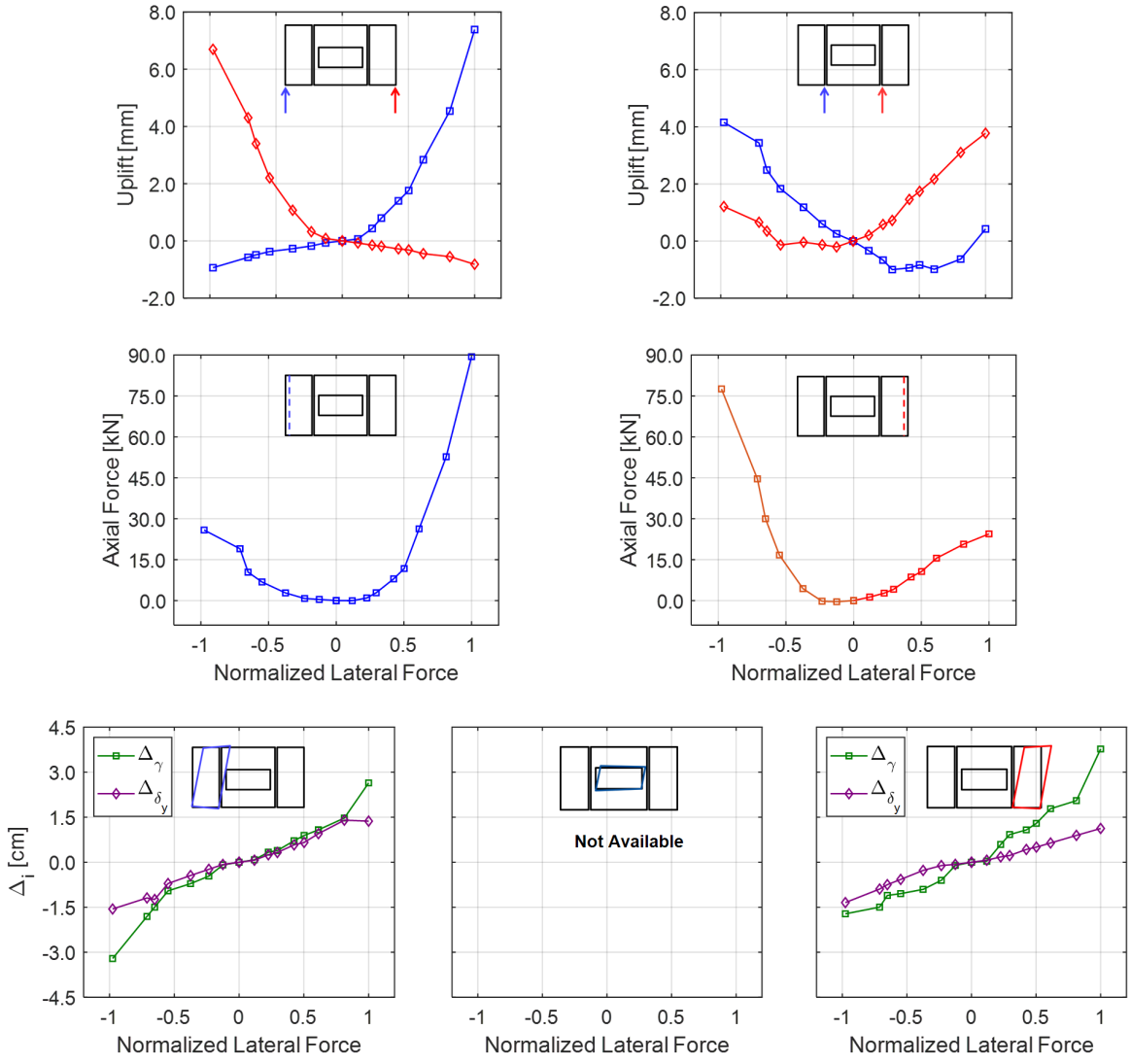


Figure D.14. SWWS-2 specimen local behavior evolution

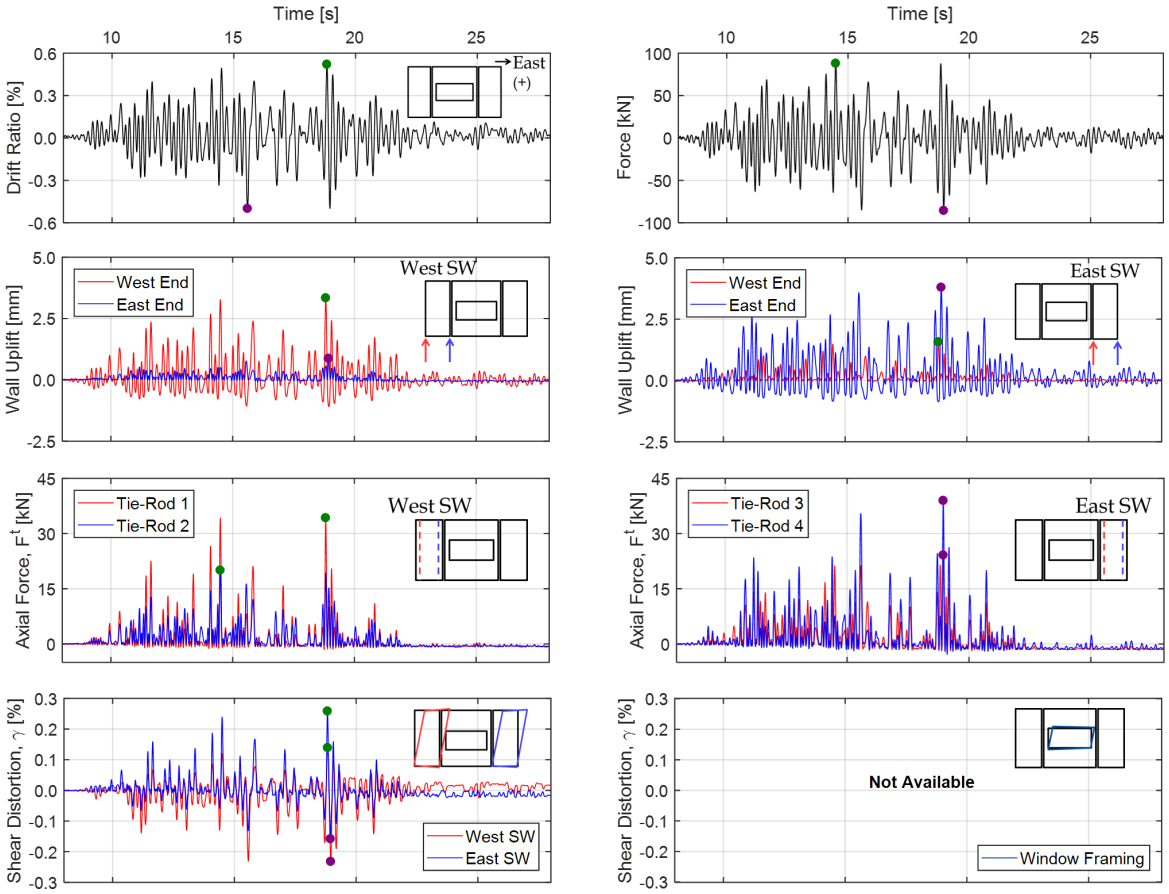


Figure D.15. SWWS-1 specimen local response during above design 1 earthquake test

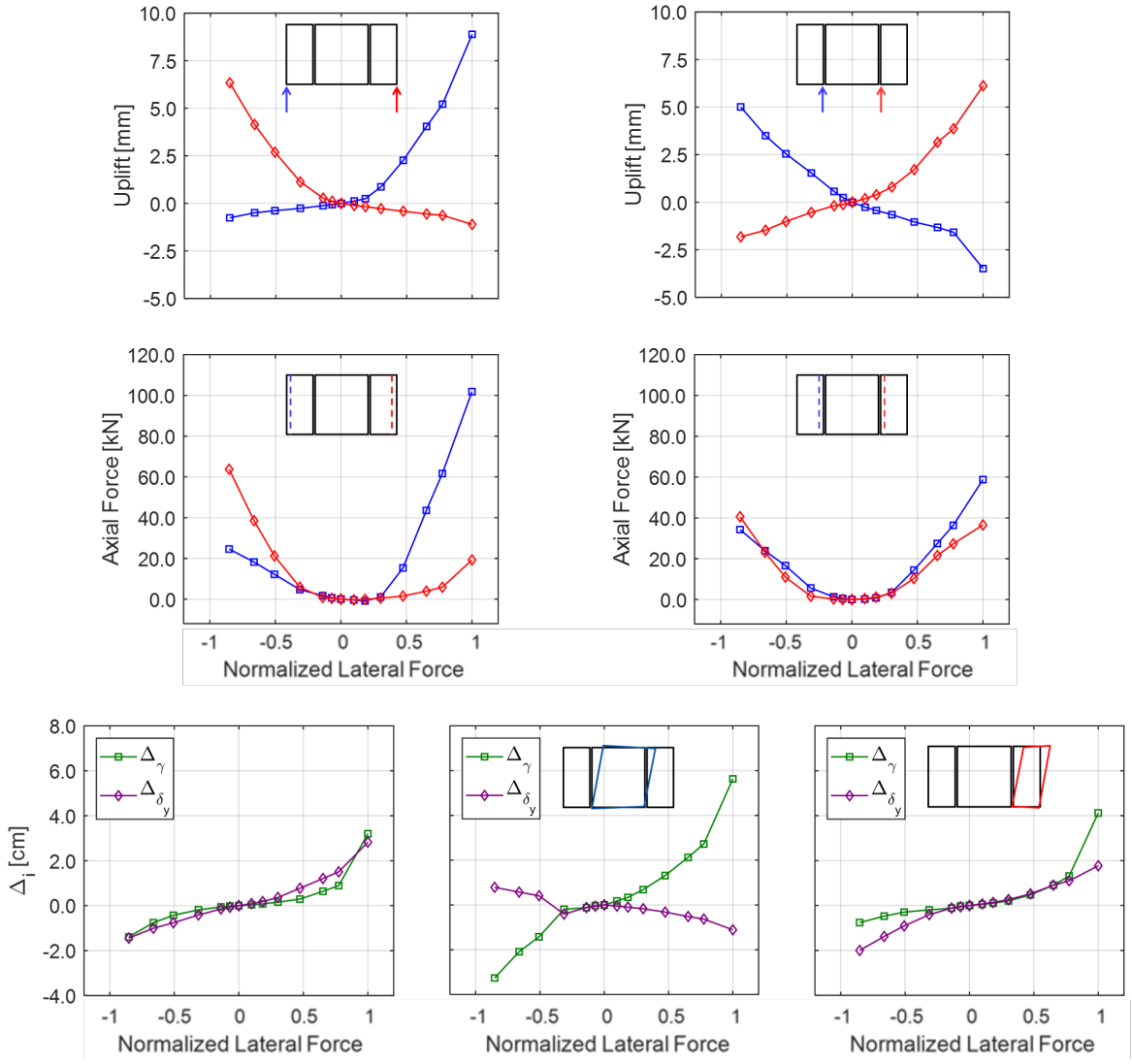


Figure D.16. SWWS-1 specimen local behavior evolution

D.2 Quasi-Static Test Phase

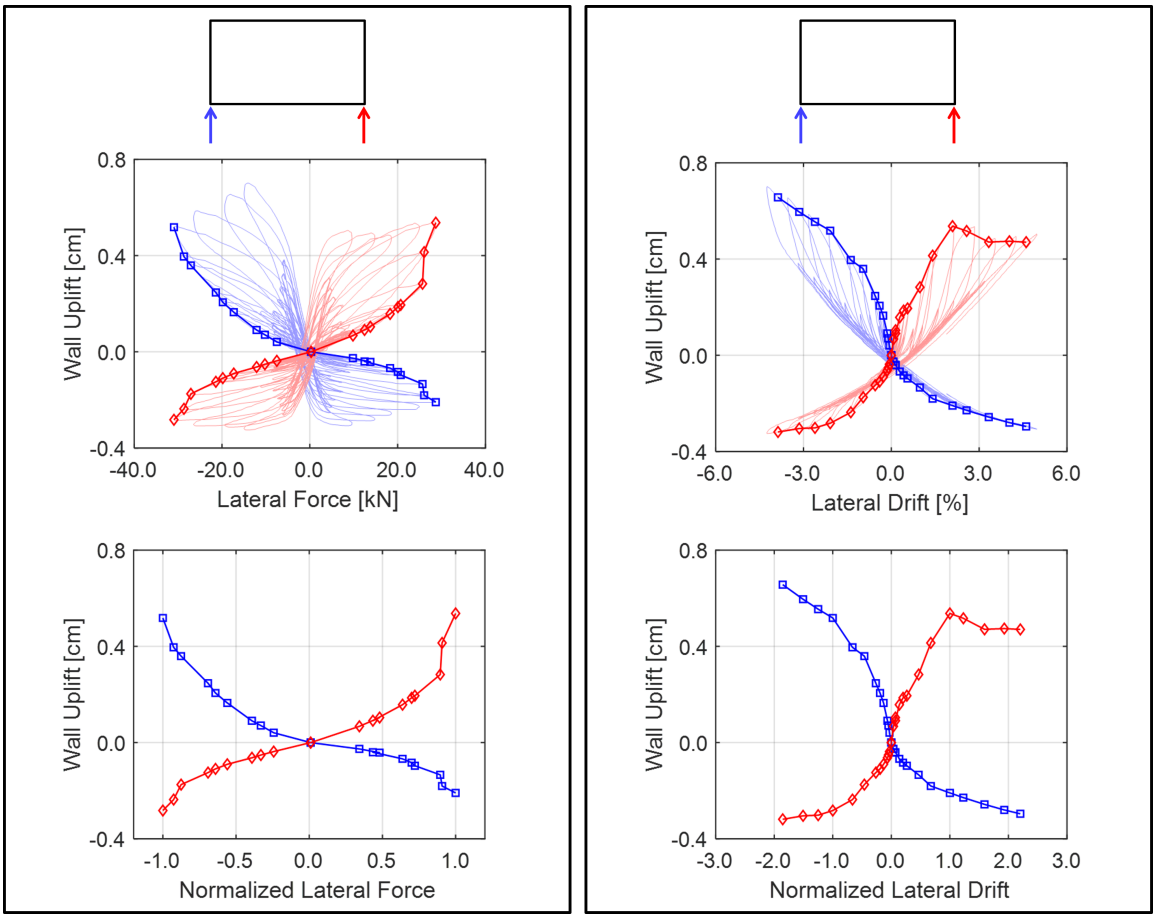


Figure D.17. Wall uplift evolution for specimen GGGG with increase in lateral force and lateral drift

Note: Schematics in subplots show location and type of response plotted. Drift positive towards left.

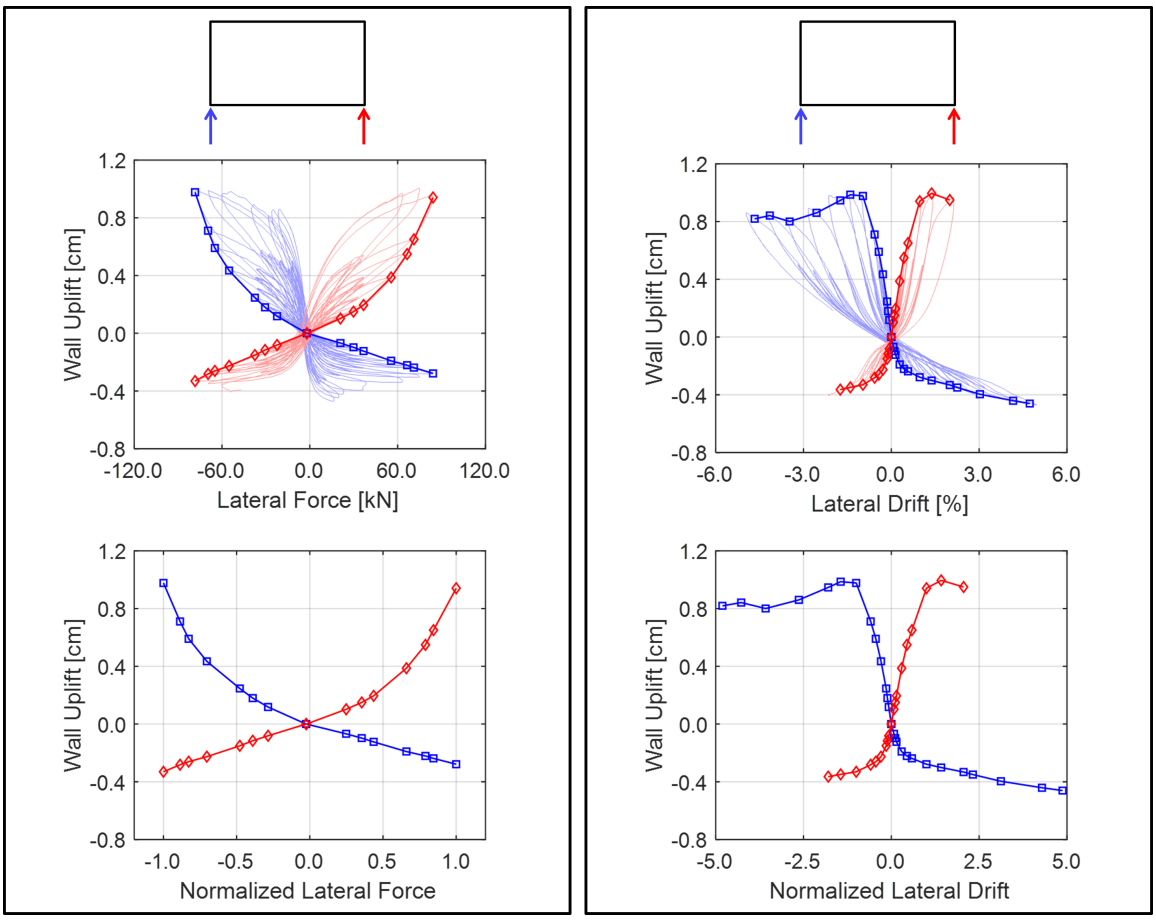


Figure D.18. Wall uplift evolution for specimen GGGG-F with increase in lateral force and lateral drift

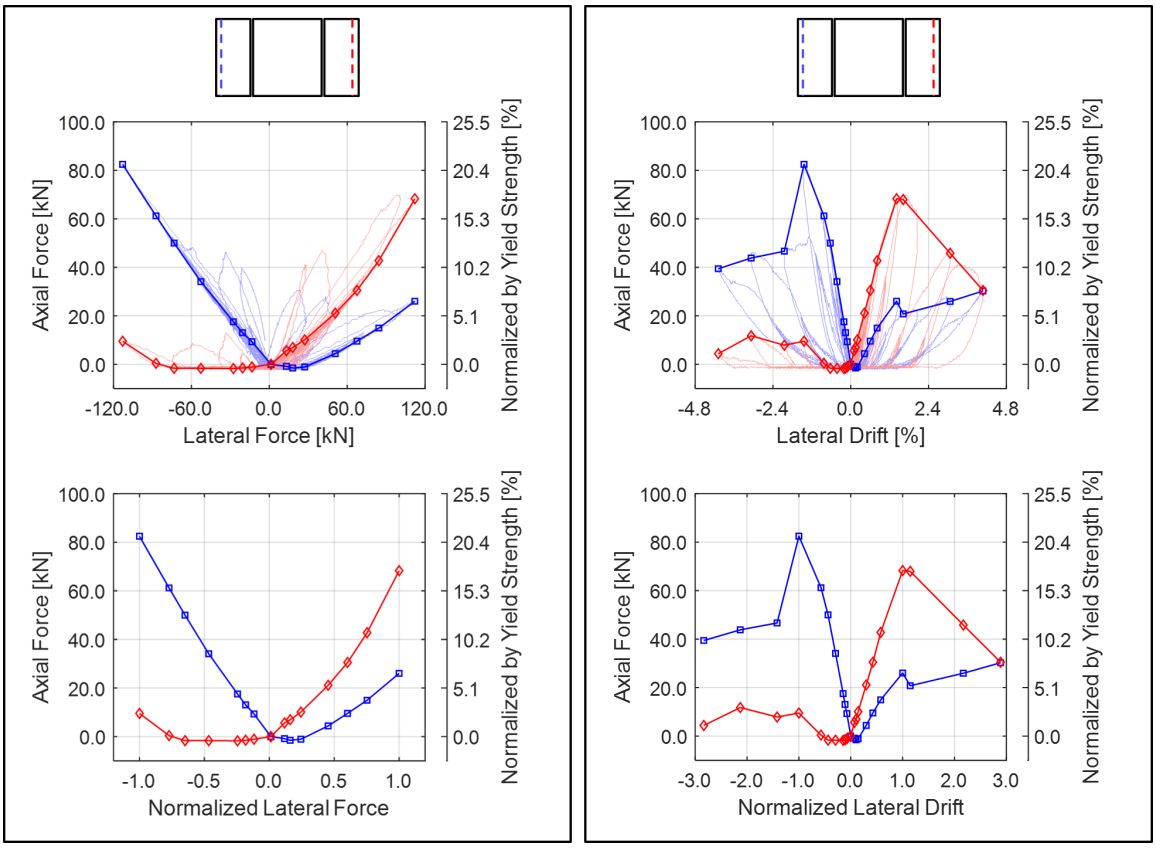
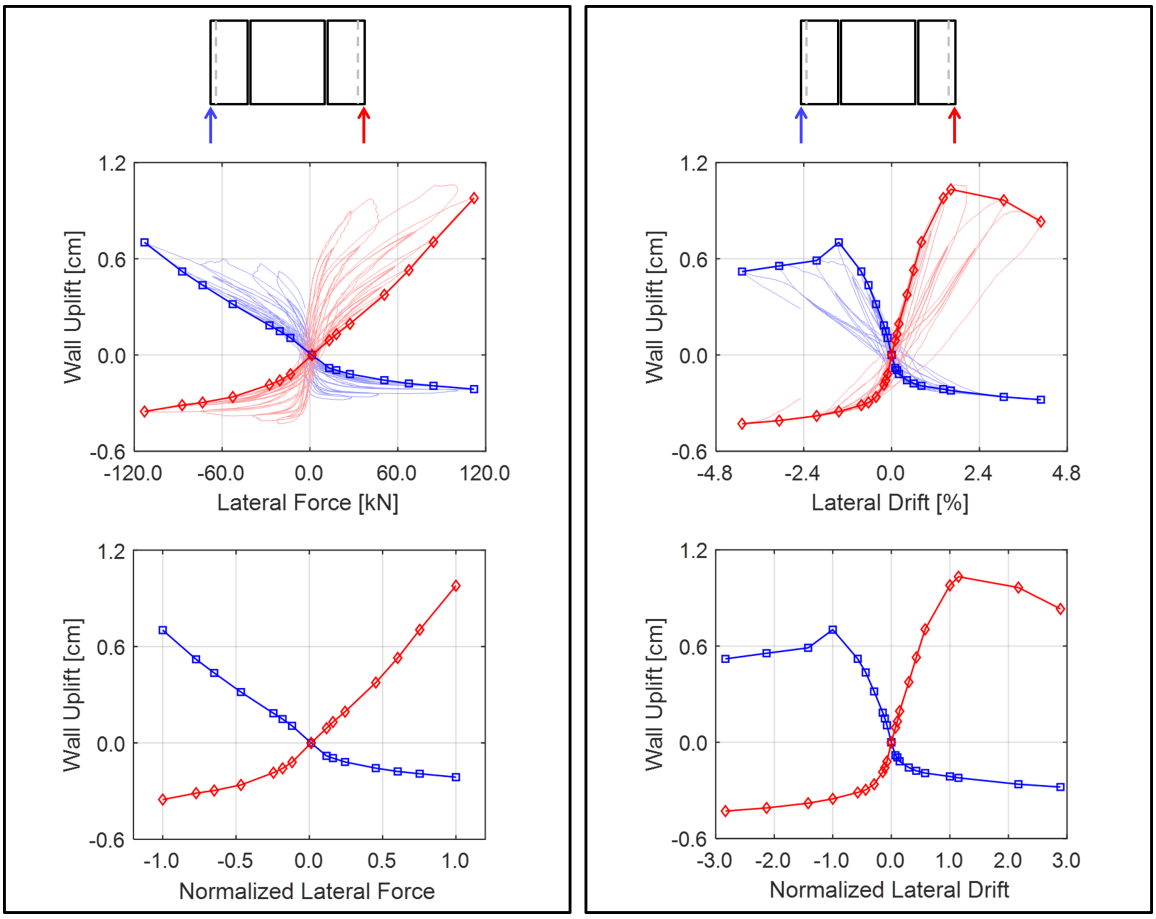
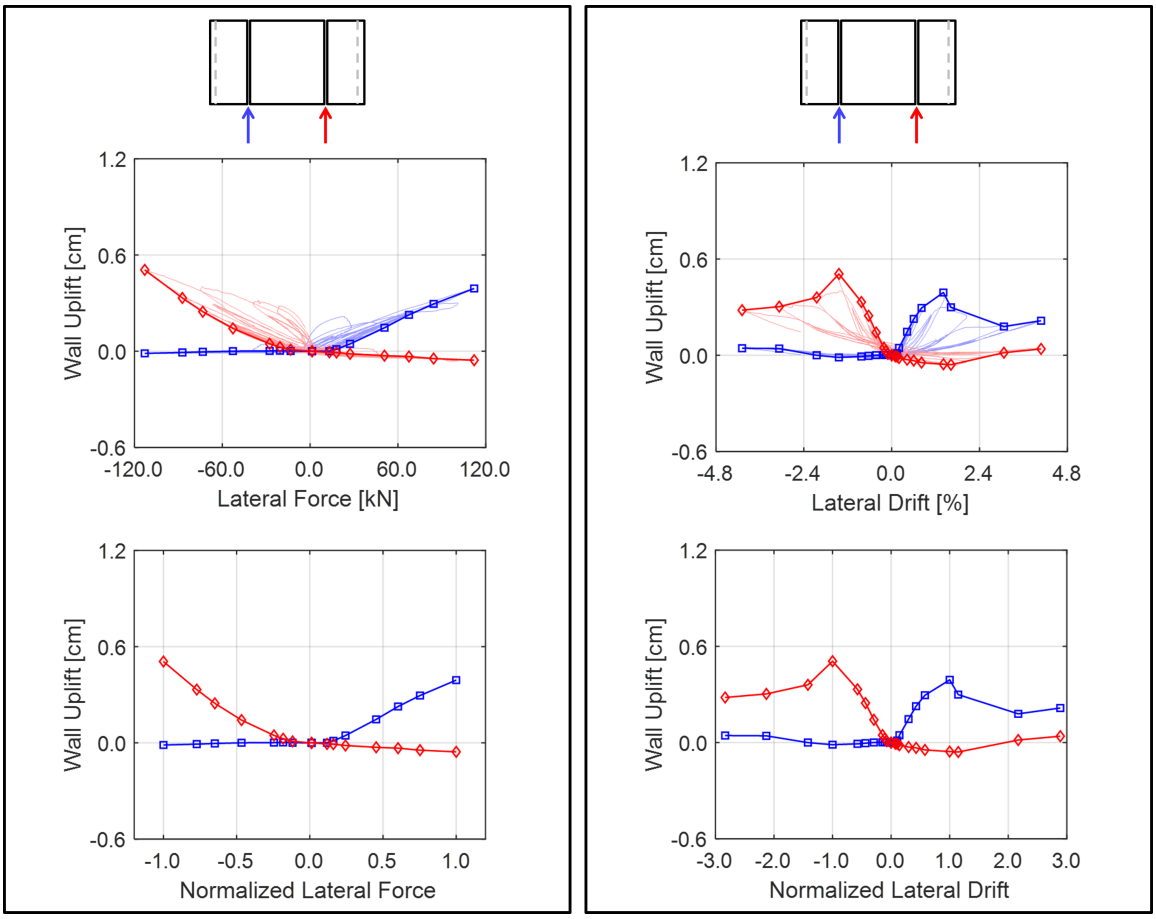


Figure D.19. Tension tie-rod force evolution for specimen SGGS-2 with increase in lateral force and lateral drift



(a)

Figure D.20. Wall uplift evolution for specimen SGGS-2 with increase in lateral force and lateral drift: (a) Wall ends and (b) Gravity bay ends



(b)

Figure D.20. Wall uplift evolution for specimen SGGS-2 with increase in lateral force and lateral drift: (a) Wall ends and (b) Gravity bay ends (cont.)

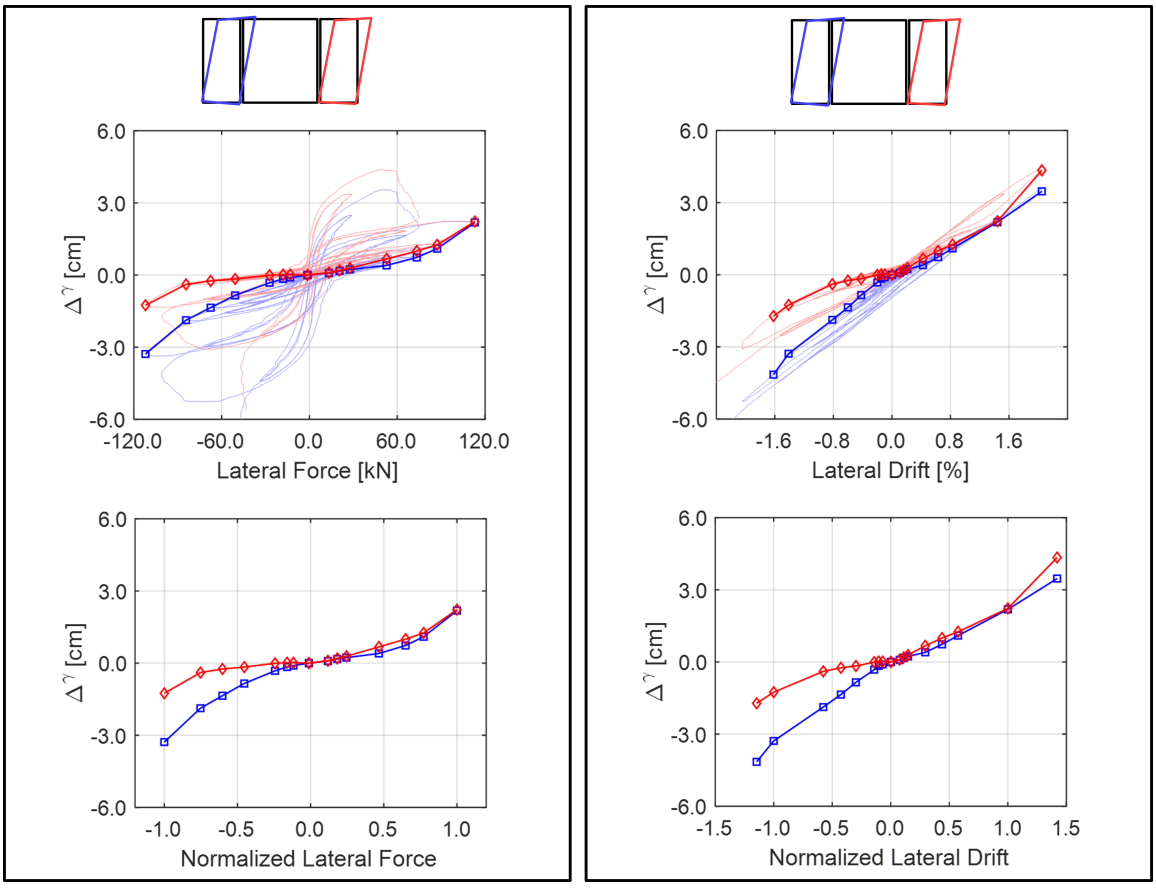


Figure D.21. Shear wall shear distortion evolution for specimen SGGS-2 with increase in lateral force and lateral drift

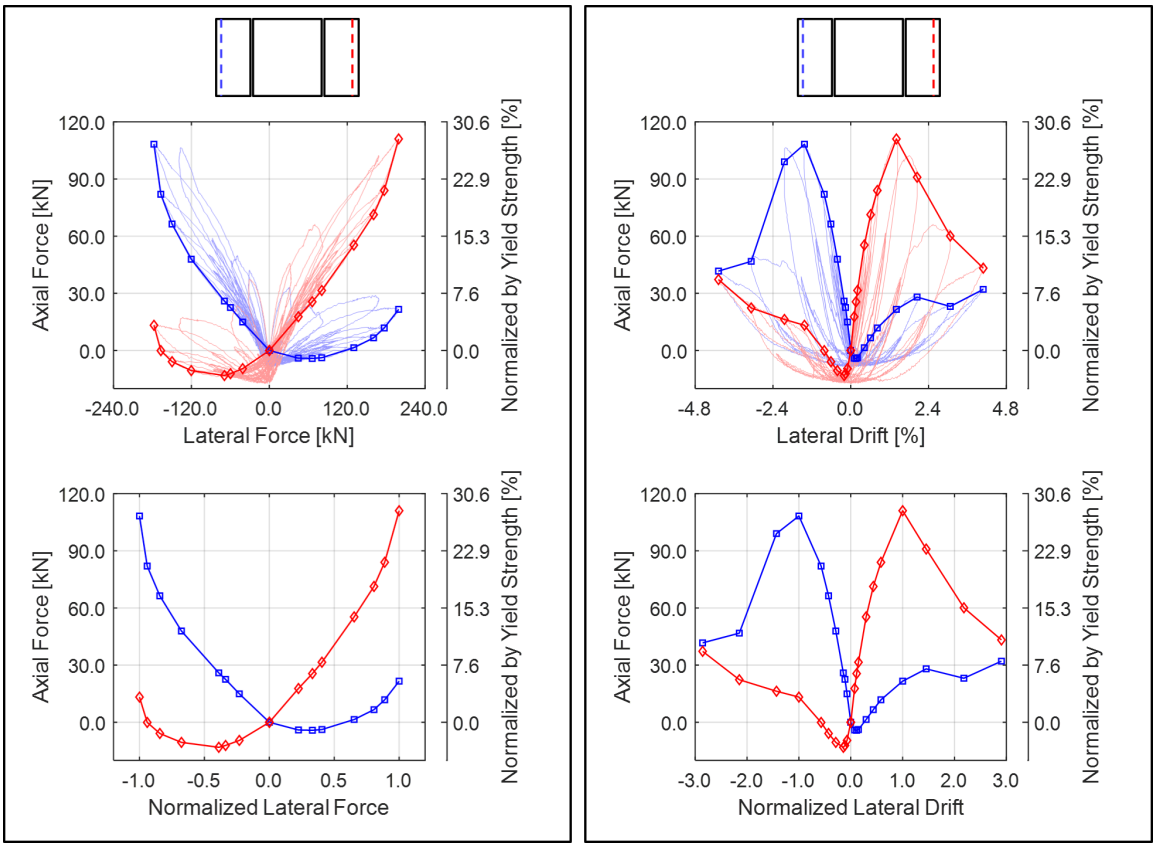
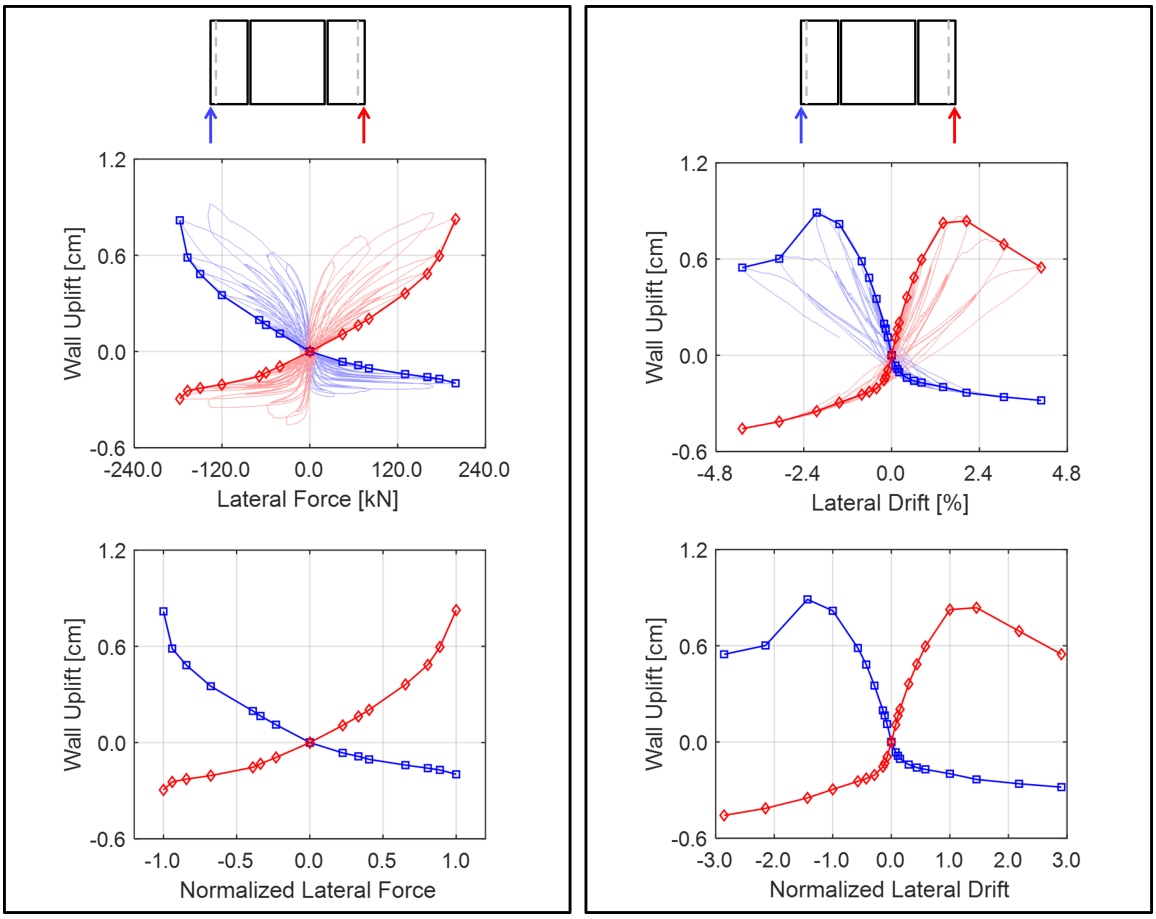
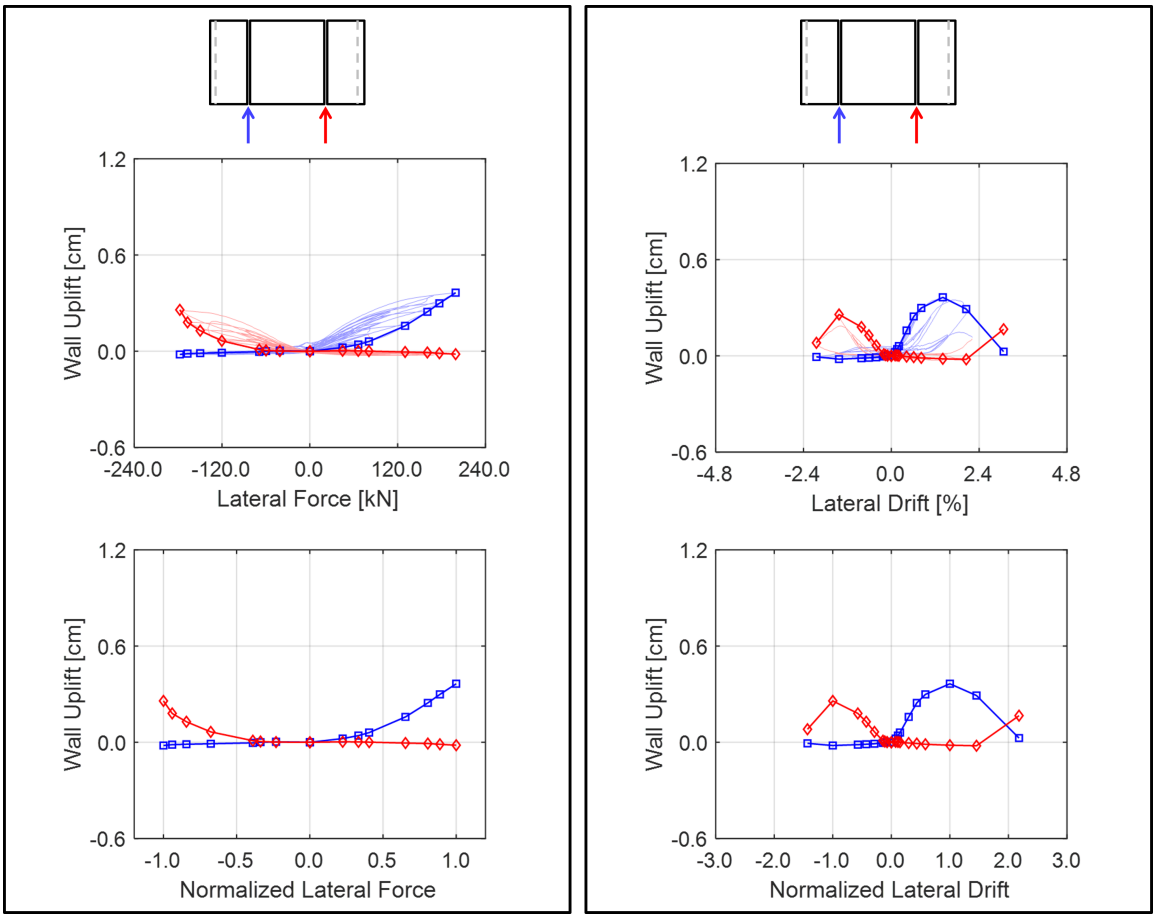


Figure D.22. Tension tie-rod force evolution for specimen SGGS-2F with increase in lateral force and lateral drift



(a)

Figure D.23. Wall uplift evolution for specimen SGGS-2F with increase in lateral force and lateral drift: (a) Wall ends and (b) Gravity bay ends



(b)

Figure D.23. Wall uplift evolution for specimen SGGS-2F with increase in lateral force and lateral drift: (a) Wall ends and (b) Gravity bay ends (cont.)

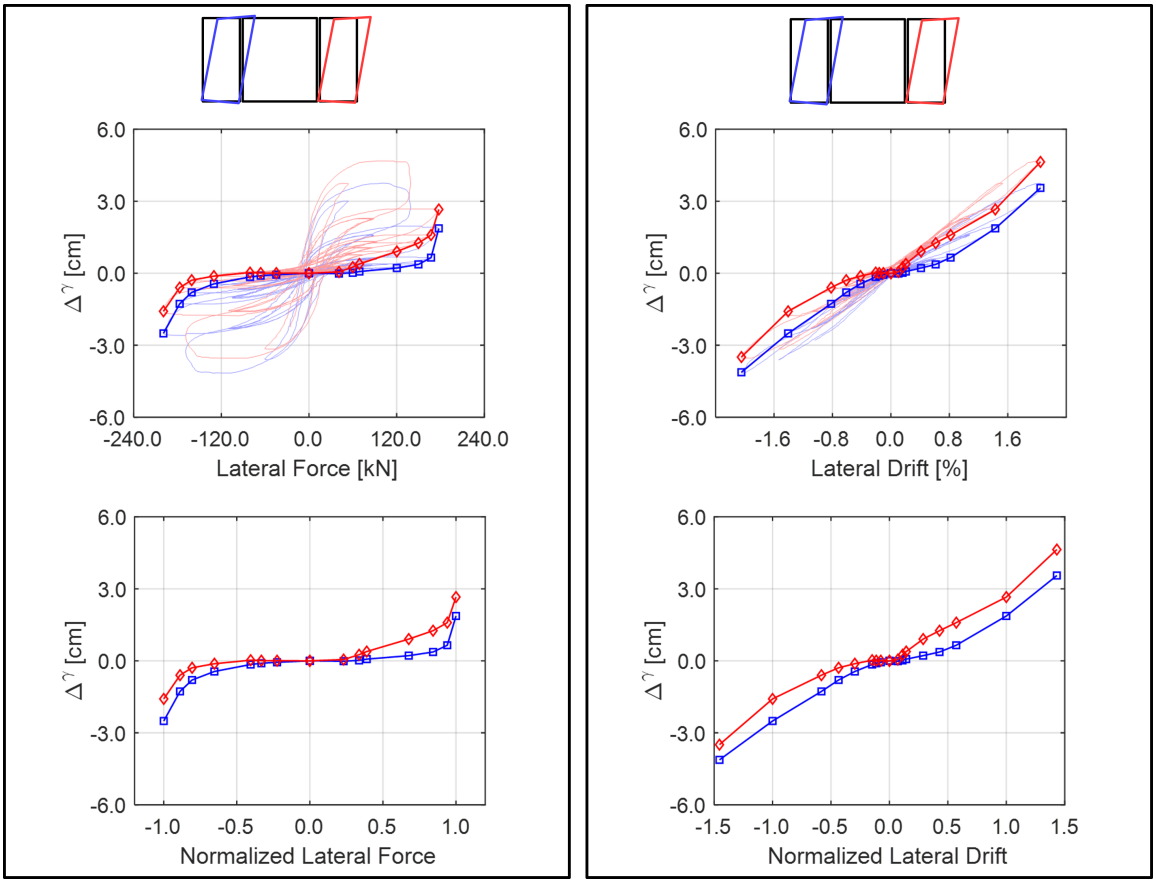


Figure D.24. Shear wall shear distortion evolution for specimen SGGS-2F with increase in lateral force and lateral drift

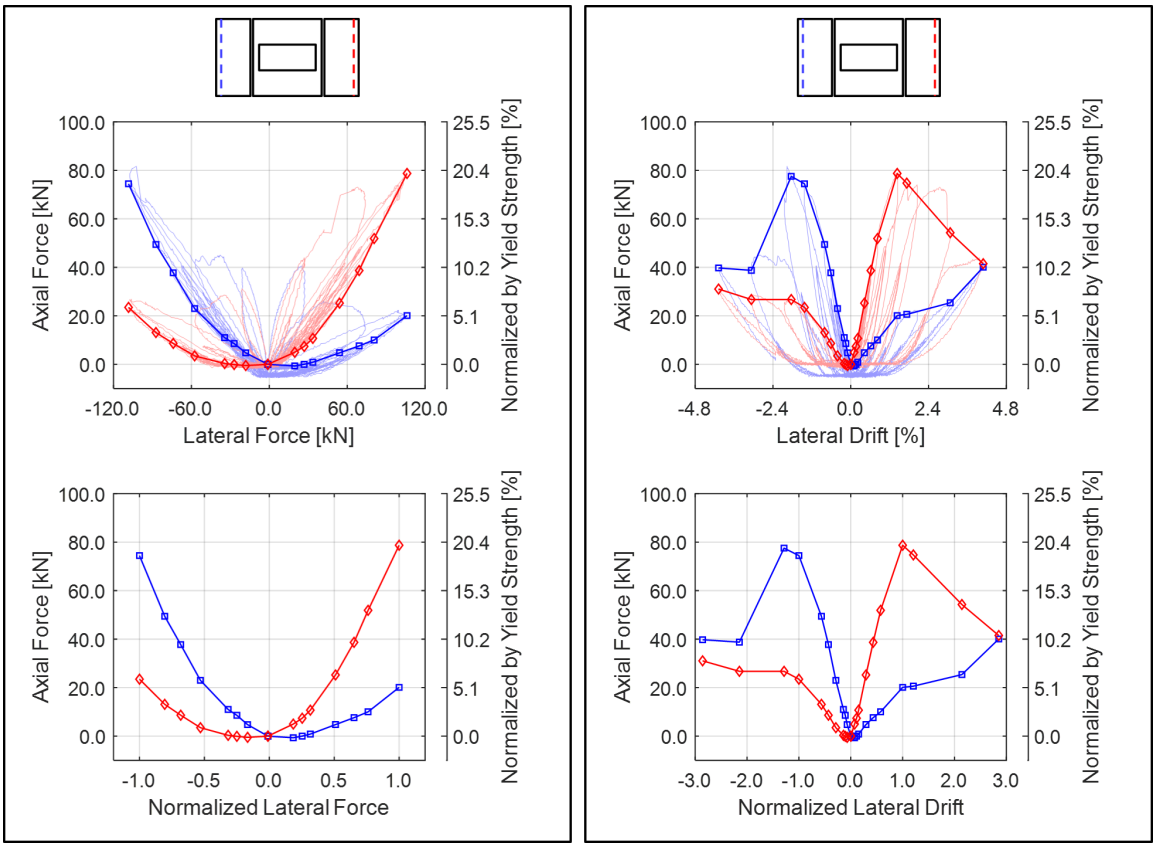
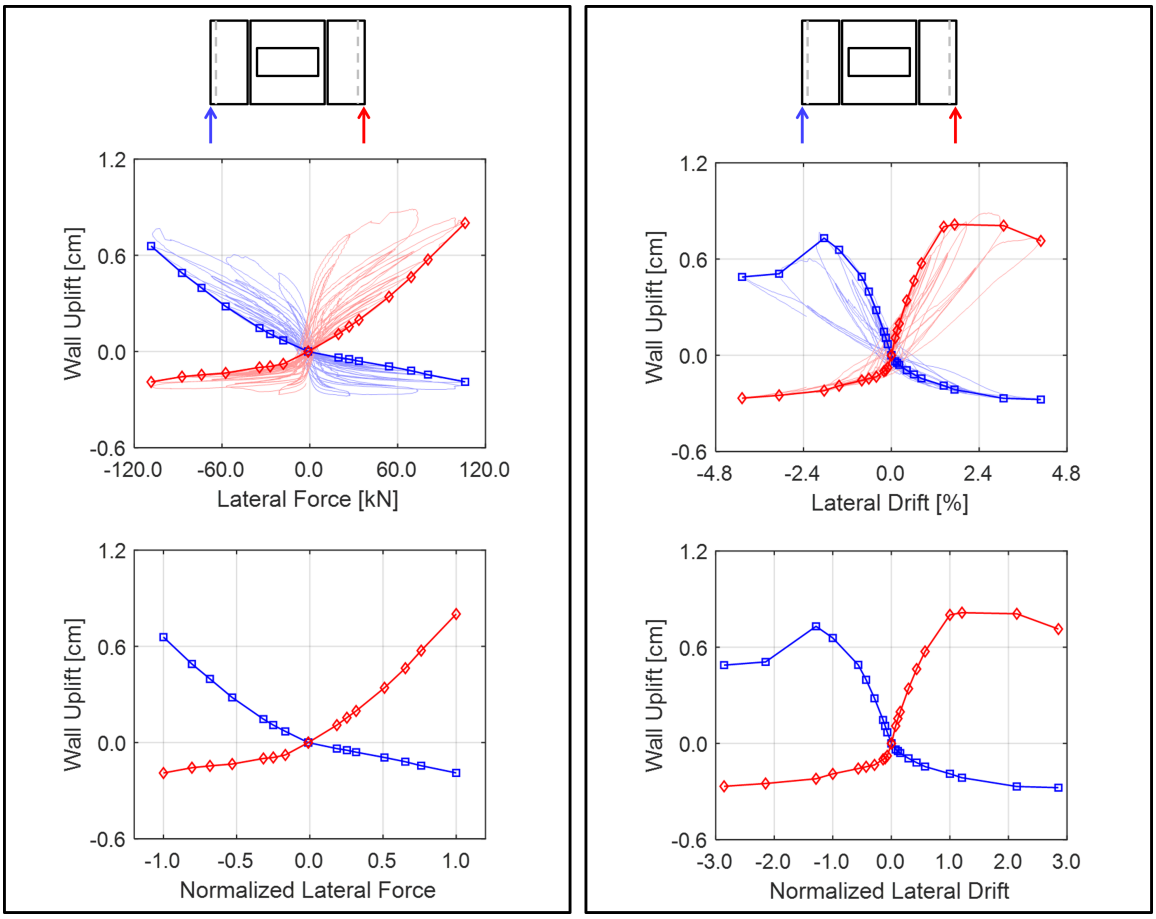
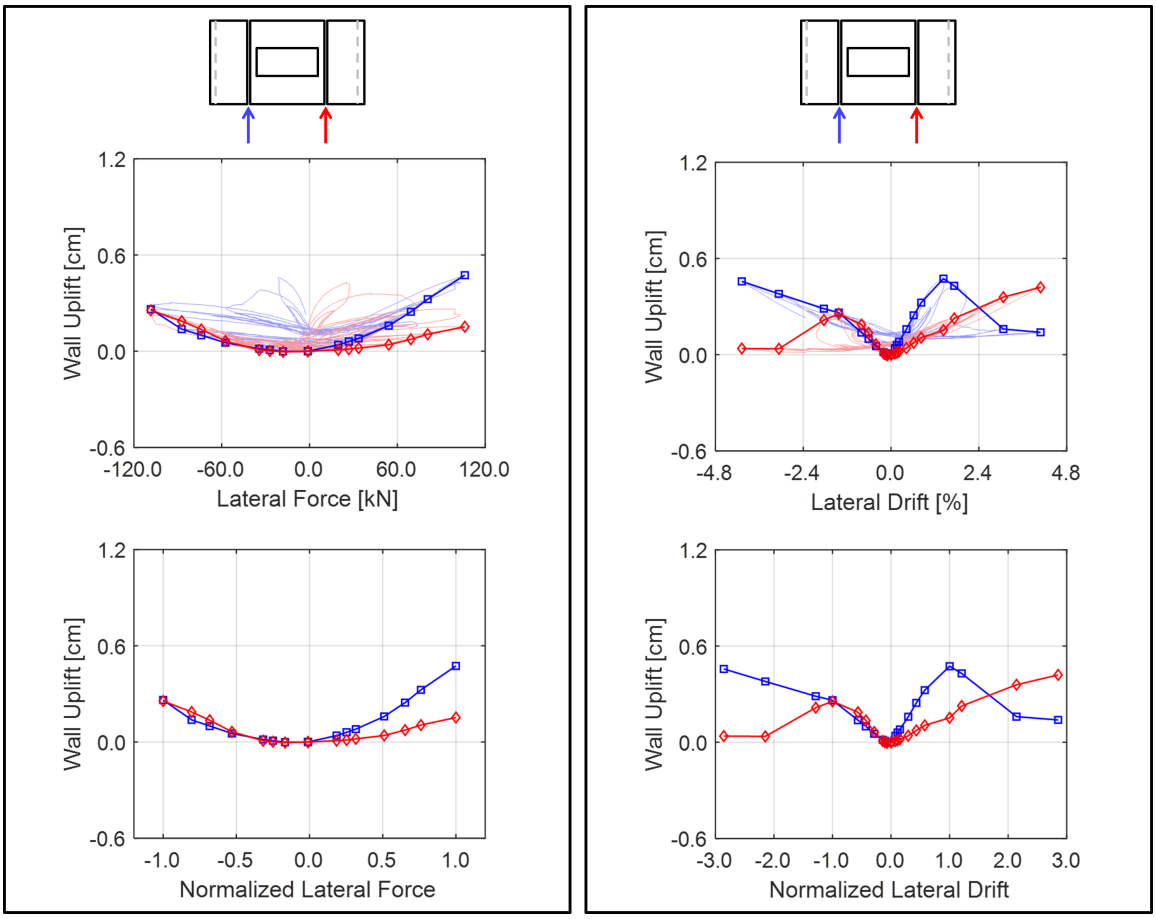


Figure D.25. Tension tie-rod force evolution for specimen SWWS-2 with increase in lateral force and lateral drift



(a)

Figure D.26. Wall uplift evolution for specimen SWWS-2 with increase in lateral force and lateral drift: (a) Wall ends and (b) Window bay ends



(b)

Figure D.26. Wall uplift evolution for specimen SWWS-2 with increase in lateral force and lateral drift: (a) Wall ends and (b) Window bay ends (cont.)

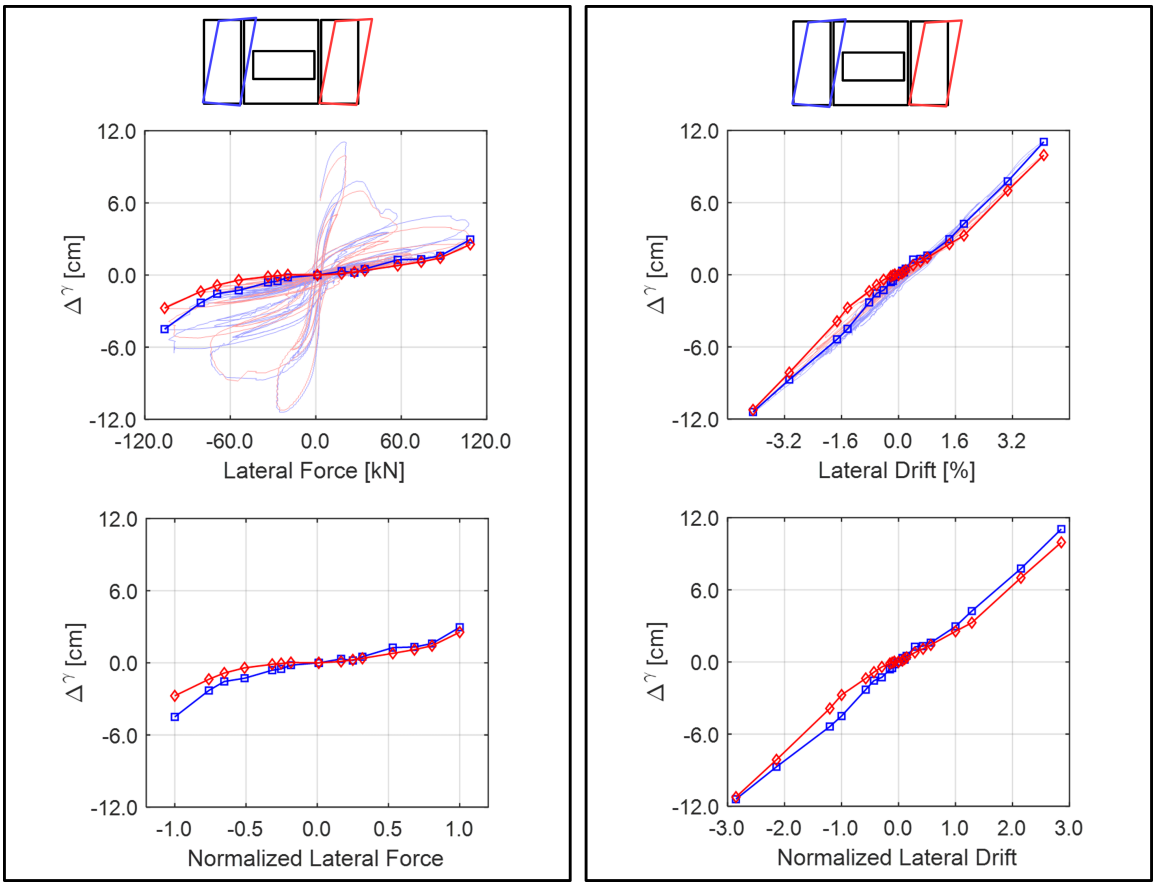


Figure D.27. Shear wall shear distortion evolution for specimen SWWS-2 with increase in lateral force and lateral drift

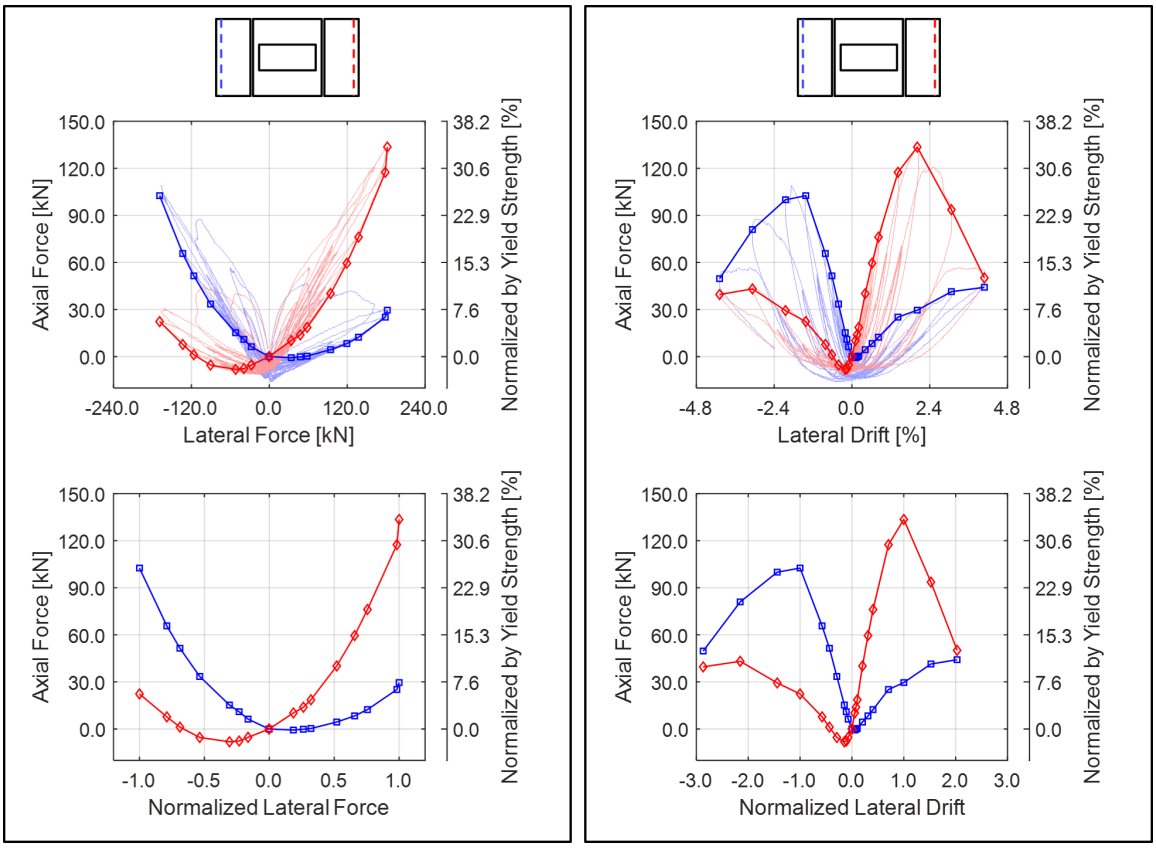
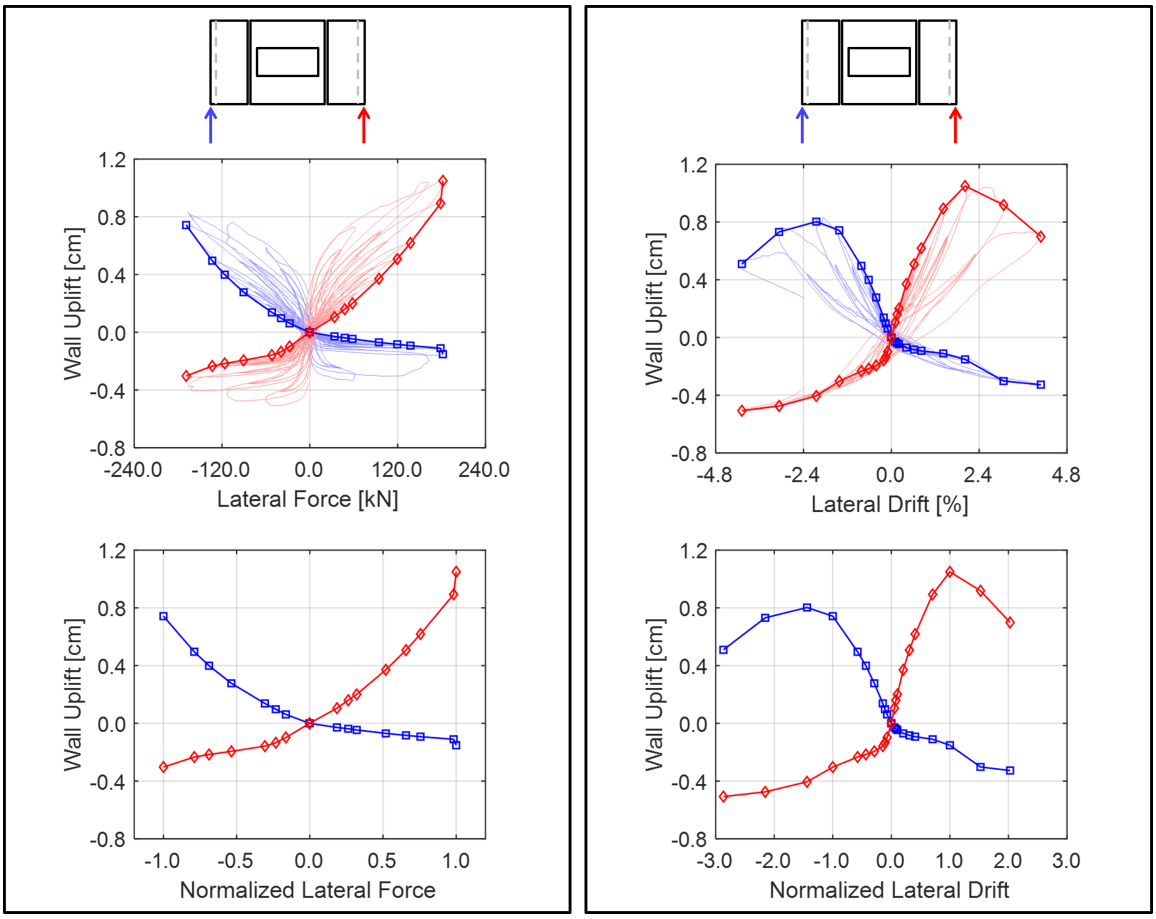
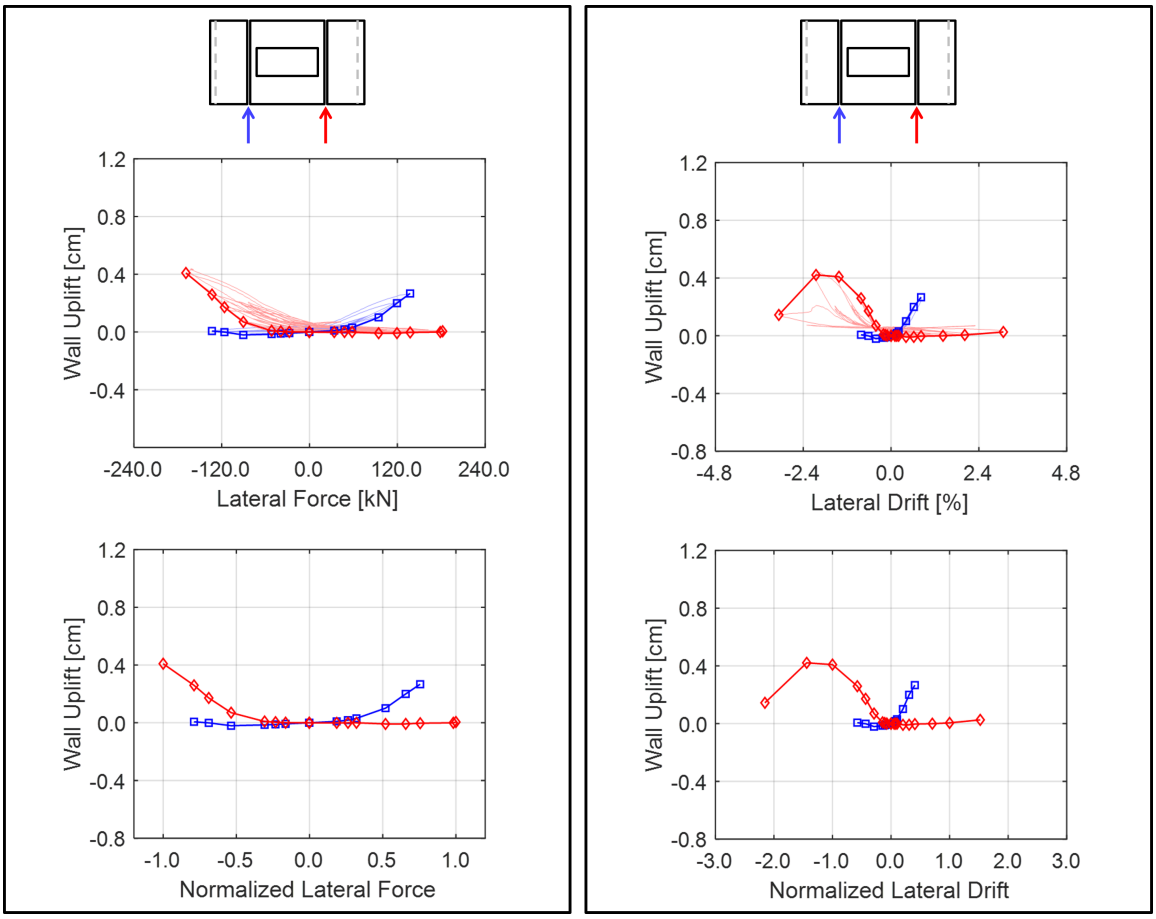


Figure D.28. Tension tie-rod force evolution for specimen SWWS-2F with increase in lateral force and lateral drift



(a)

Figure D.29. Wall uplift evolution for specimen SWWS-2F with increase in lateral force and lateral drift: (a) Wall ends and (b) Window bay ends



(b)

Figure D.29. Wall uplift evolution for specimen SWWS-2F with increase in lateral force and lateral drift: (a) Wall ends and (b) Window bay ends (cont.)

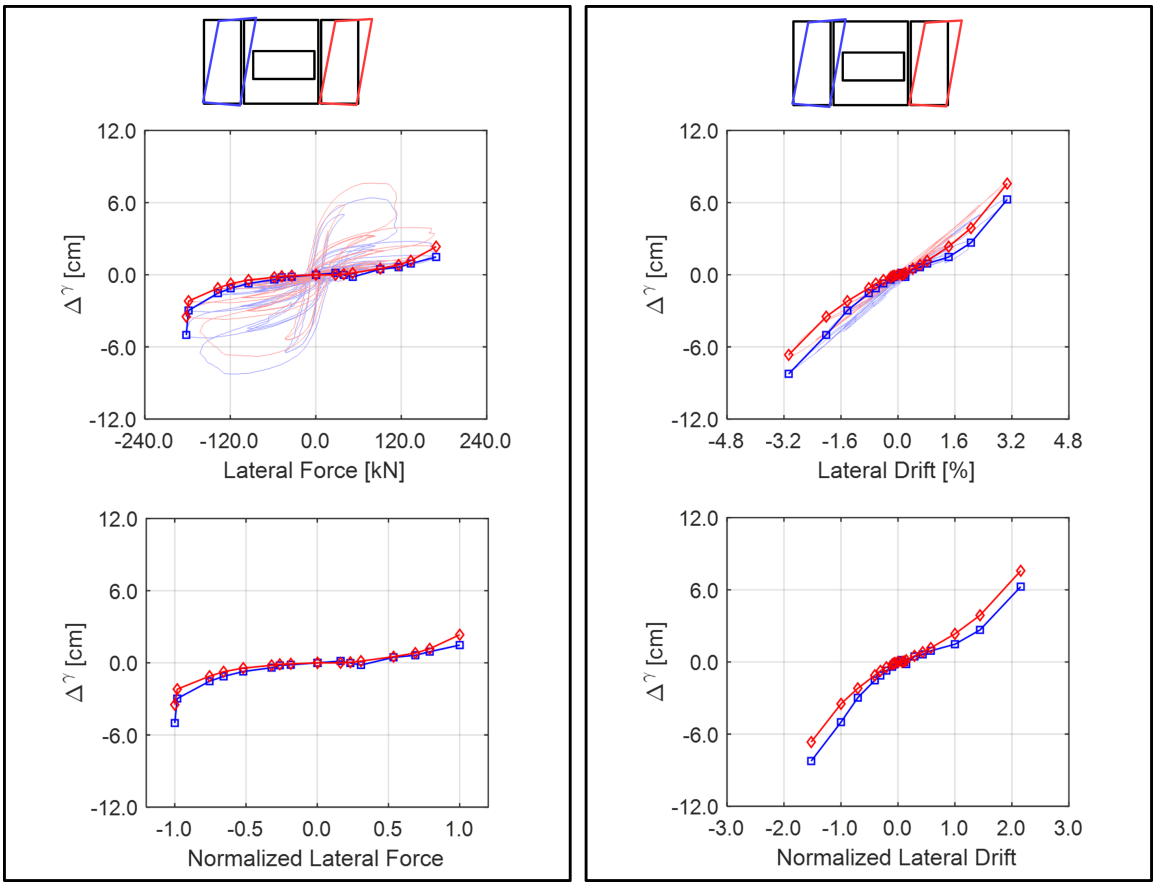
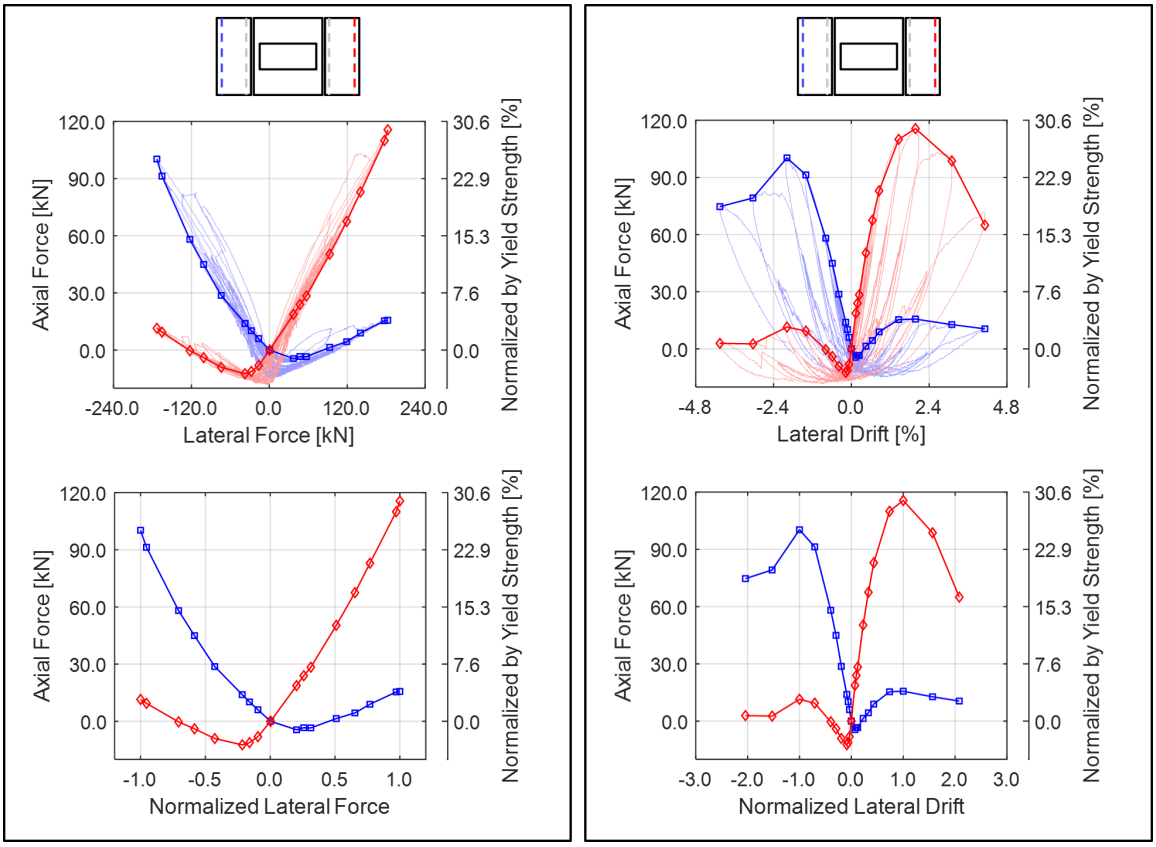
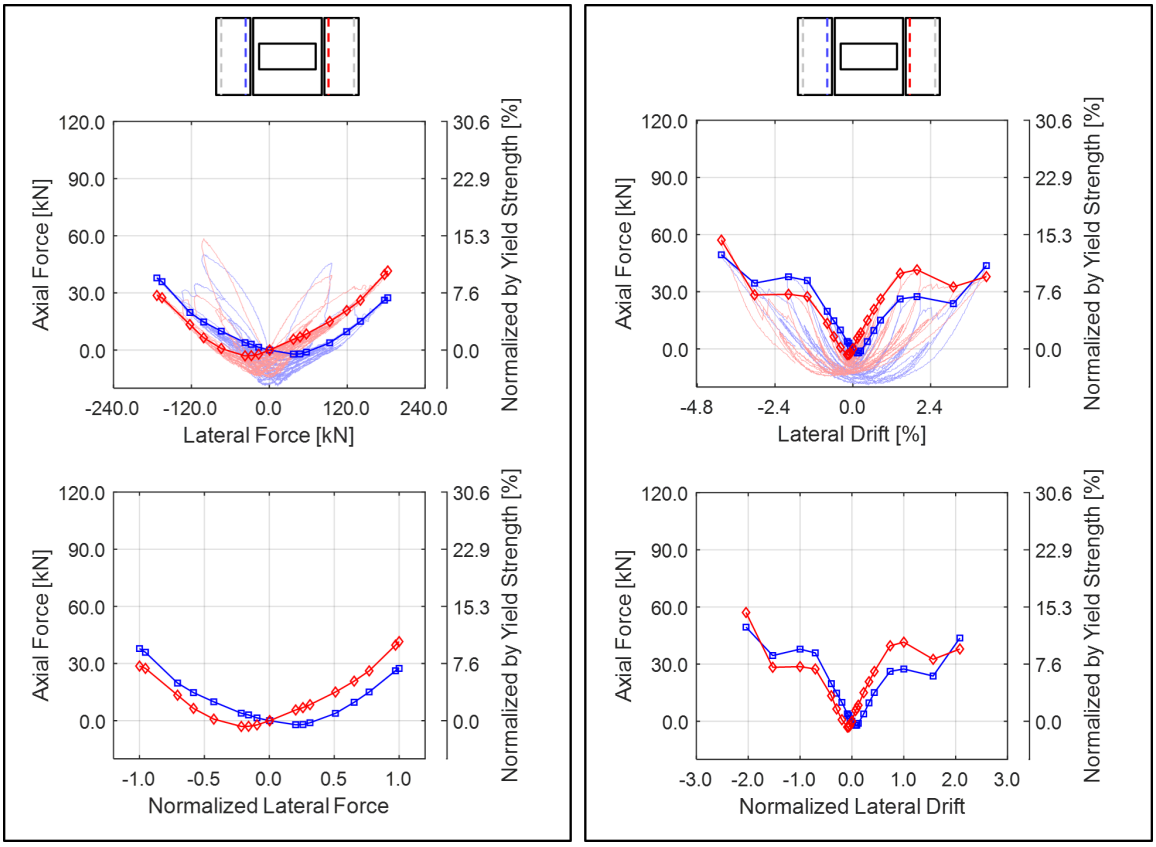


Figure D.30. Shear wall shear distortion evolution for specimen SWWS-2F with increase in lateral force and lateral drift



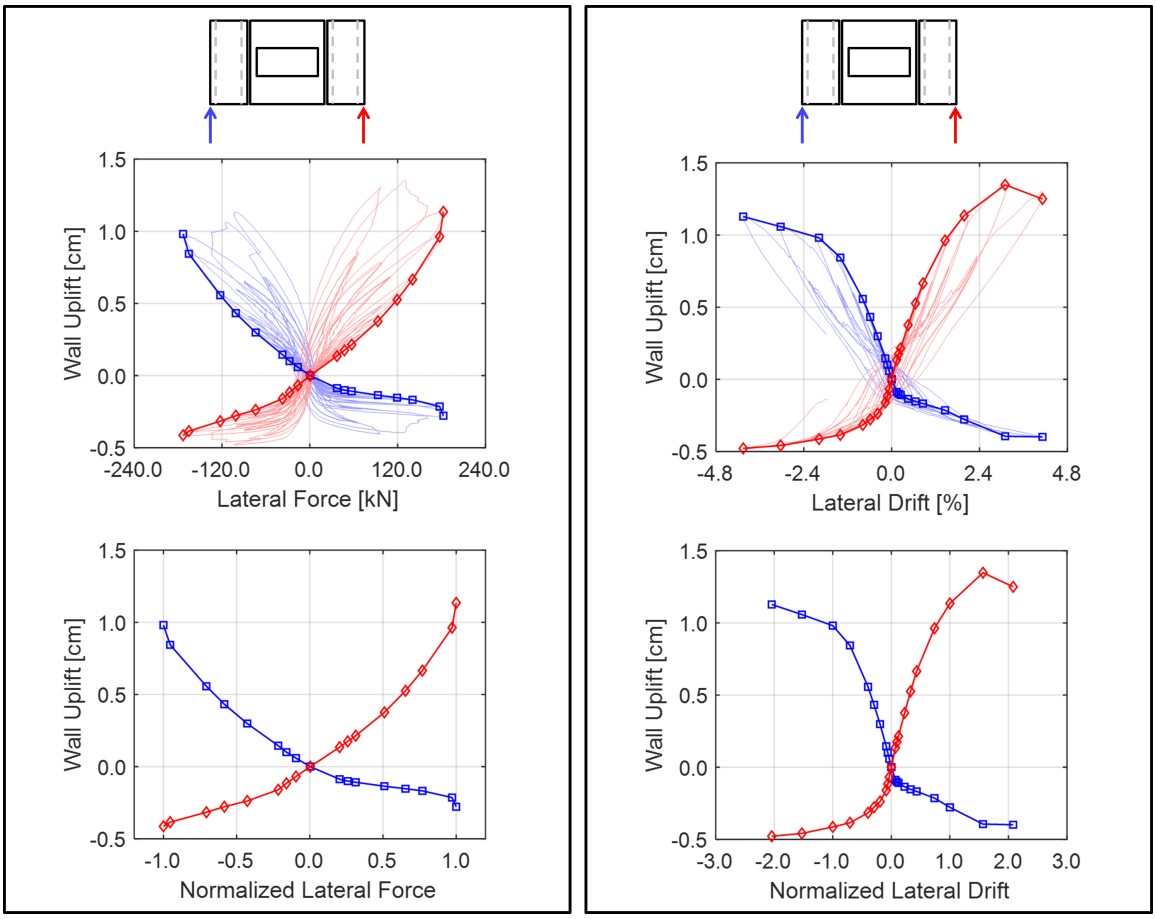
(a)

Figure D.31. Tension tie-rod force evolution for specimen SWWS-1 with increase in lateral force and lateral drift: (a) Exterior rods and (b) Interior rods



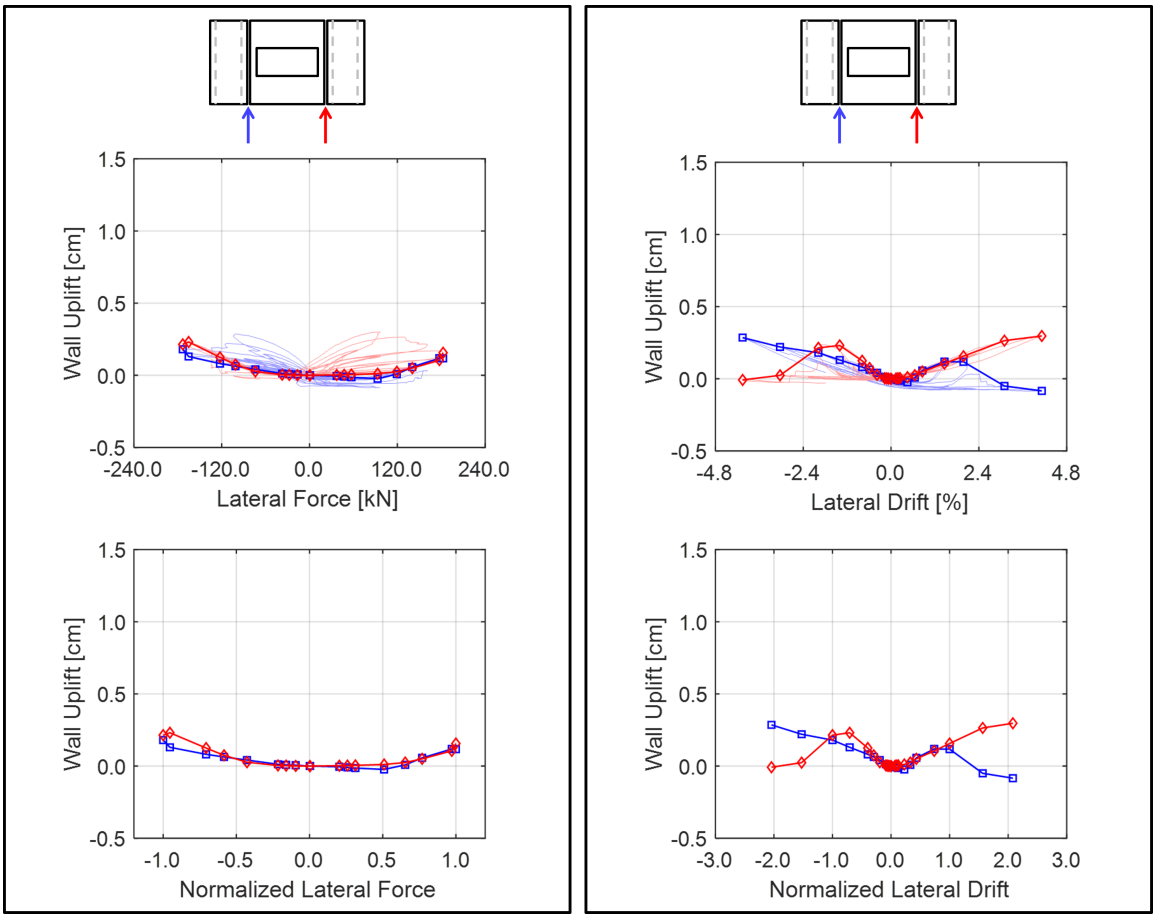
(b)

Figure D.31. Tension tie-rod force evolution for specimen SWWS-1 with increase in lateral force and lateral drift: (a) Exterior rods and (b) Interior rods (cont.)



(a)

Figure D.32. Wall uplift evolution for specimen SWWS-1 with increase in lateral force and lateral drift: (a) Wall ends and (b) Window bay ends



(b)

Figure D.32. Wall uplift evolution for specimen SWWS-1 with increase in lateral force and lateral drift: (a) Wall ends and (b) Window bay ends (cont.)

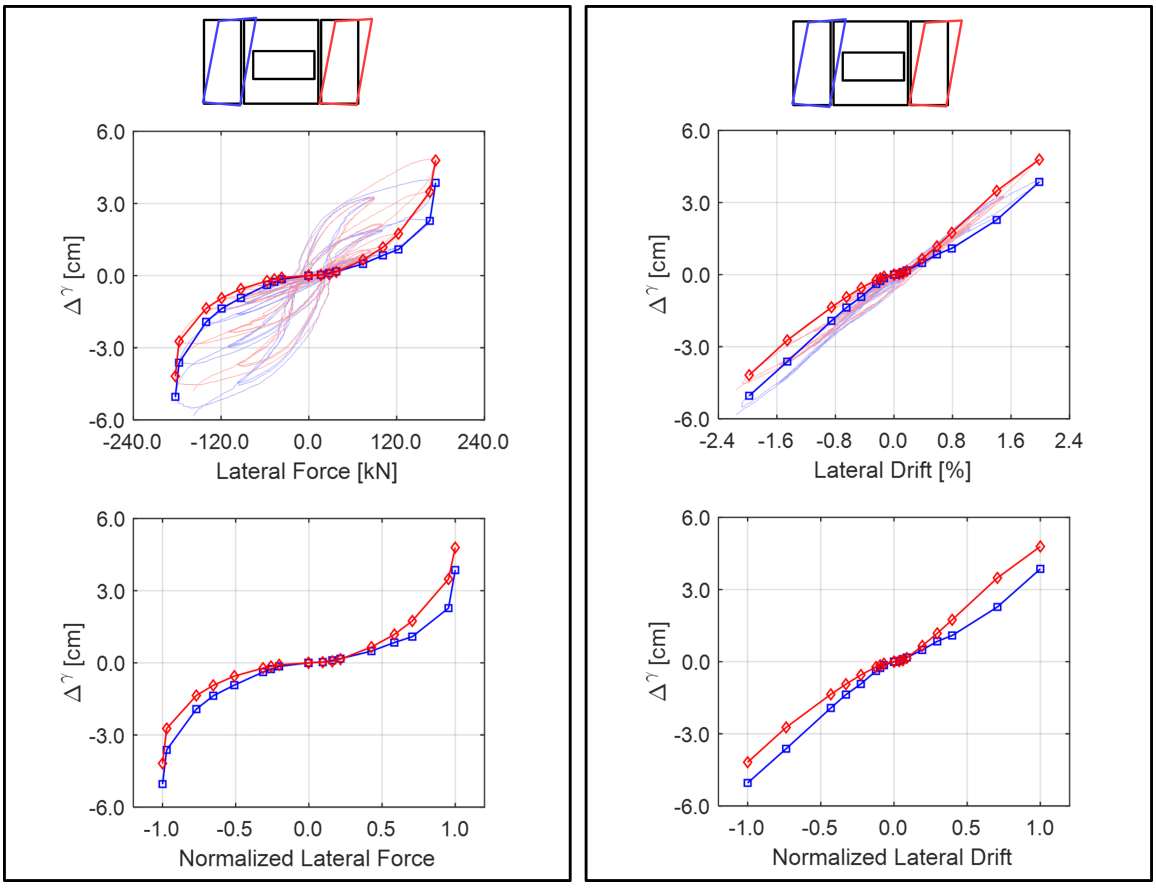


Figure D.33. Shear wall shear distortion evolution for specimen SWWS-1 with increase in lateral force and lateral drift

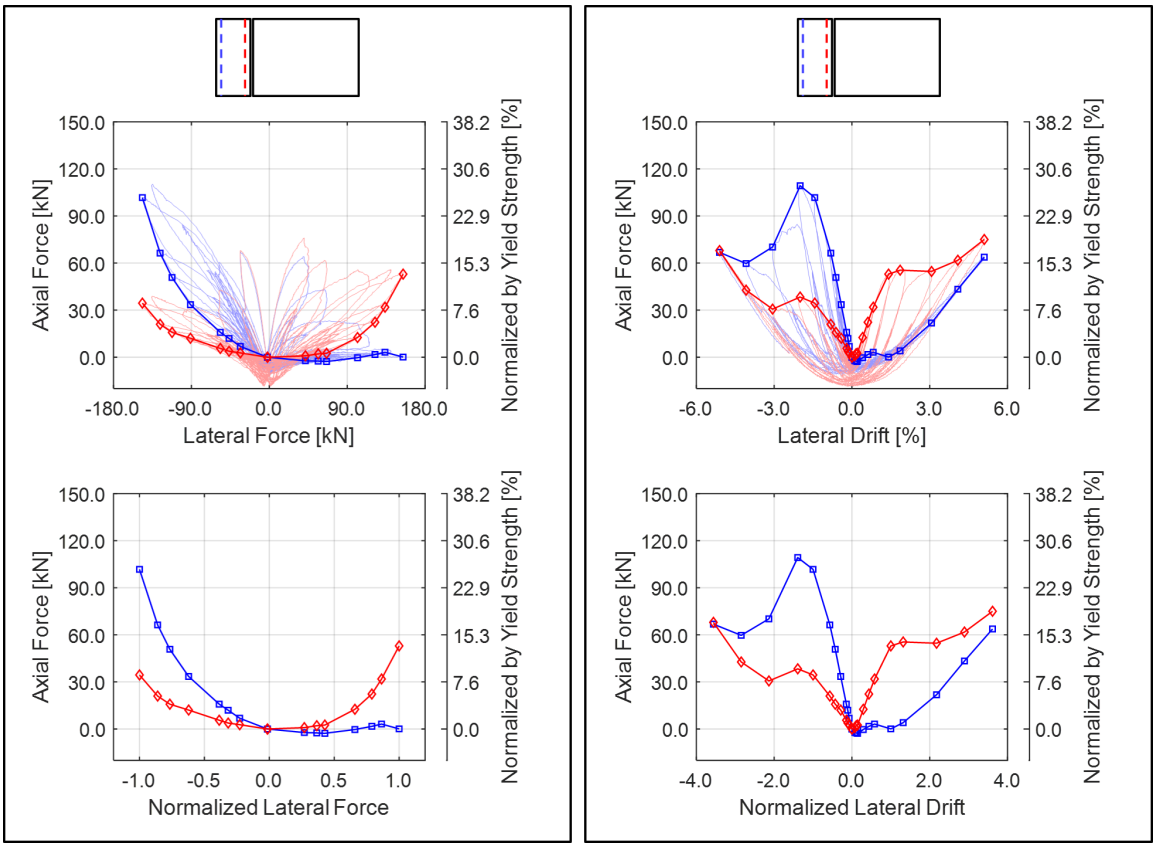
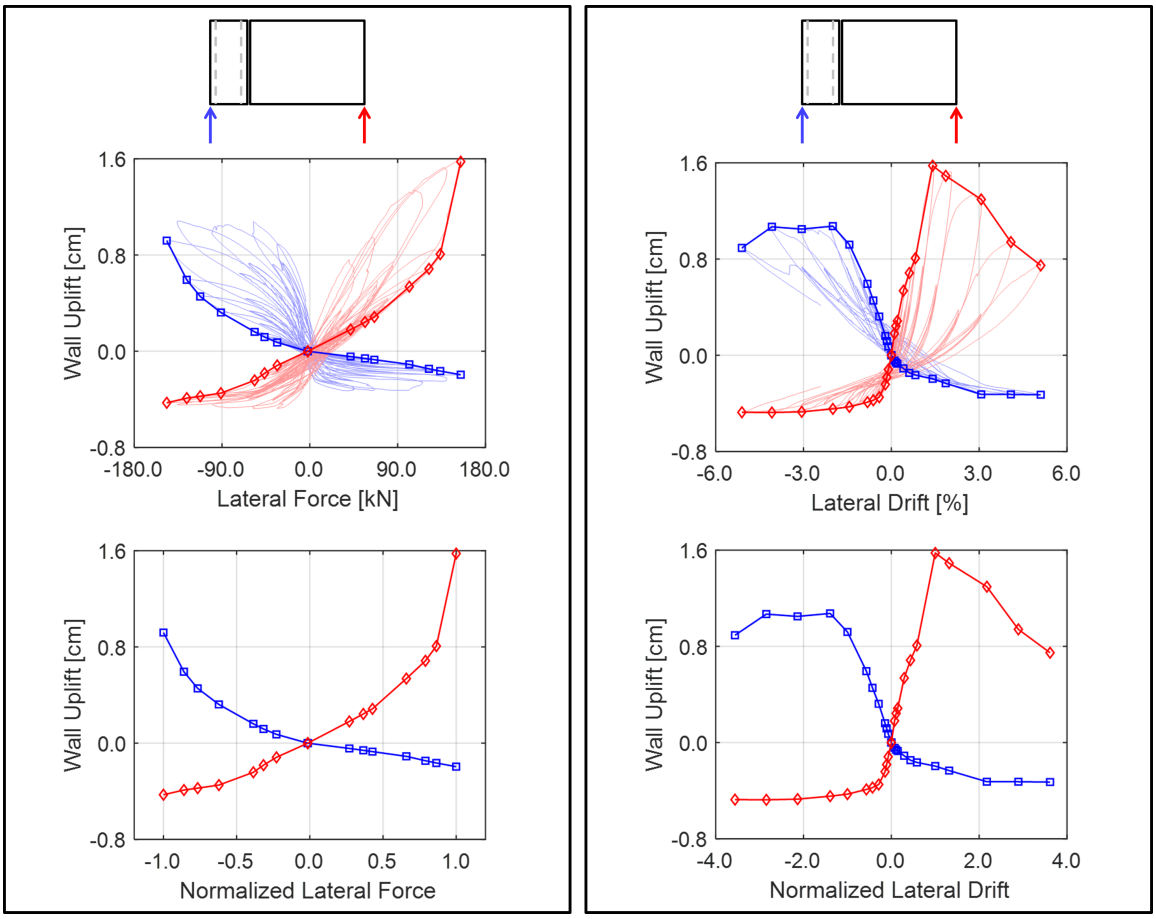
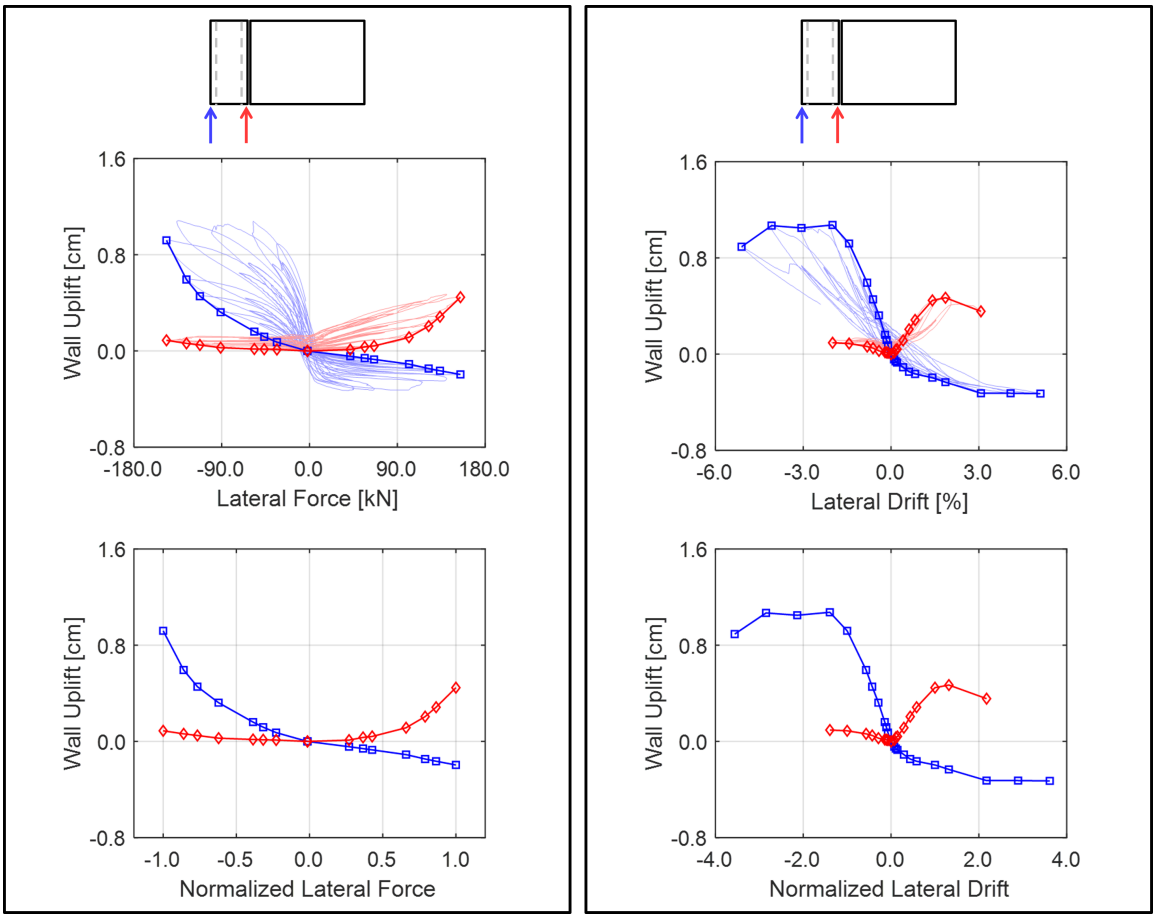


Figure D.34. Tension tie-rod force evolution for specimen SGGG-1F with increase in lateral force and lateral drift



(a)

Figure D.35. Wall uplift evolution for specimen SGGG-1F with increase in lateral force and lateral drift: (a) Wall ends and (b) Shear segment ends



(b)

Figure D.35. Wall uplift evolution for specimen SGGG-1F with increase in lateral force and lateral drift: (a) Wall ends and (b) Shear segment ends (cont.)

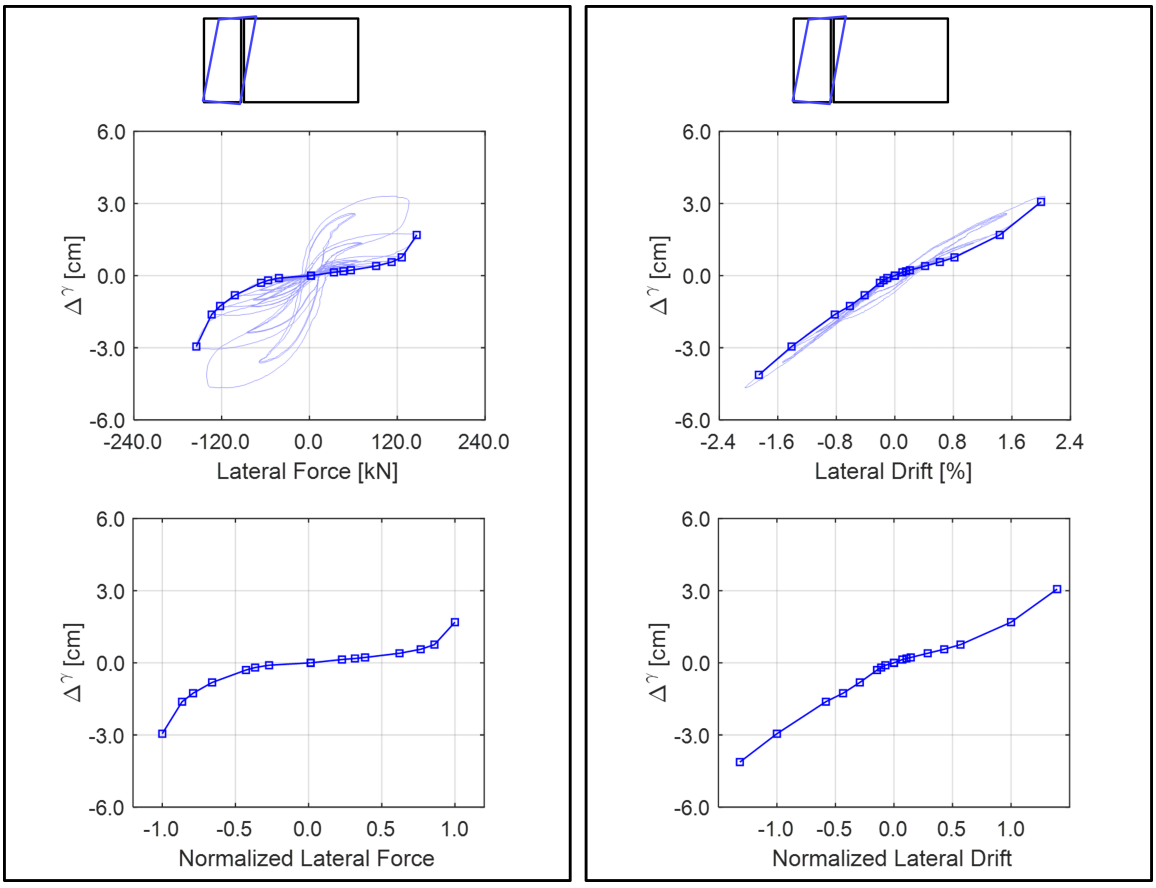


Figure D.36. Shear wall shear distortion evolution for specimen SGGG-1F with increase in lateral force and lateral drift

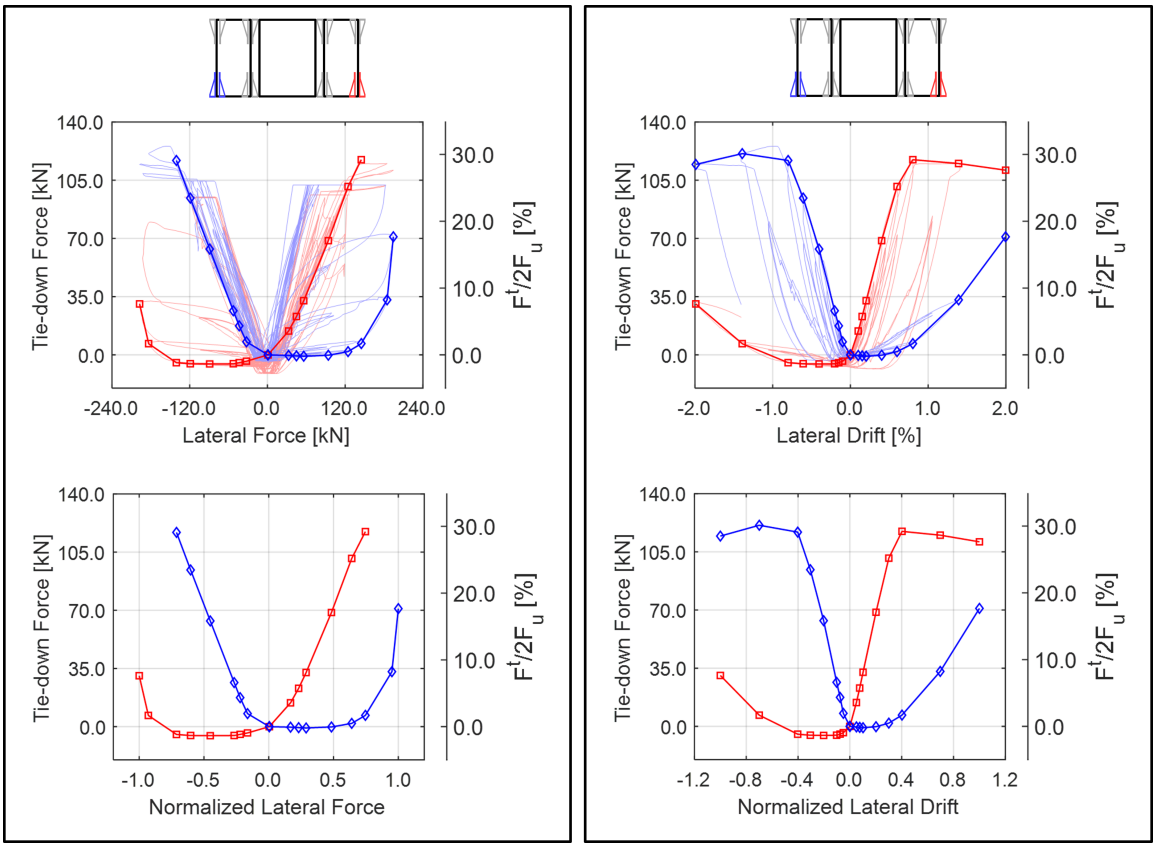
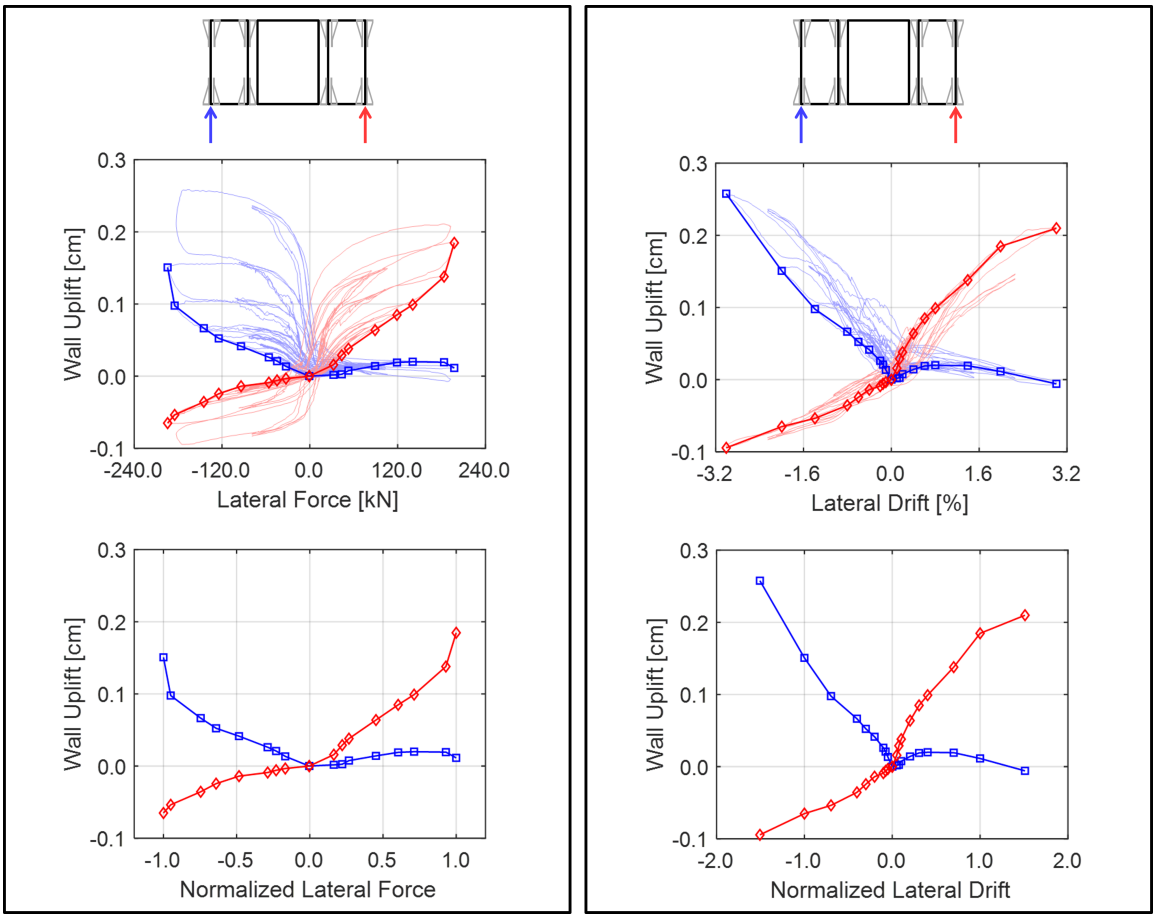
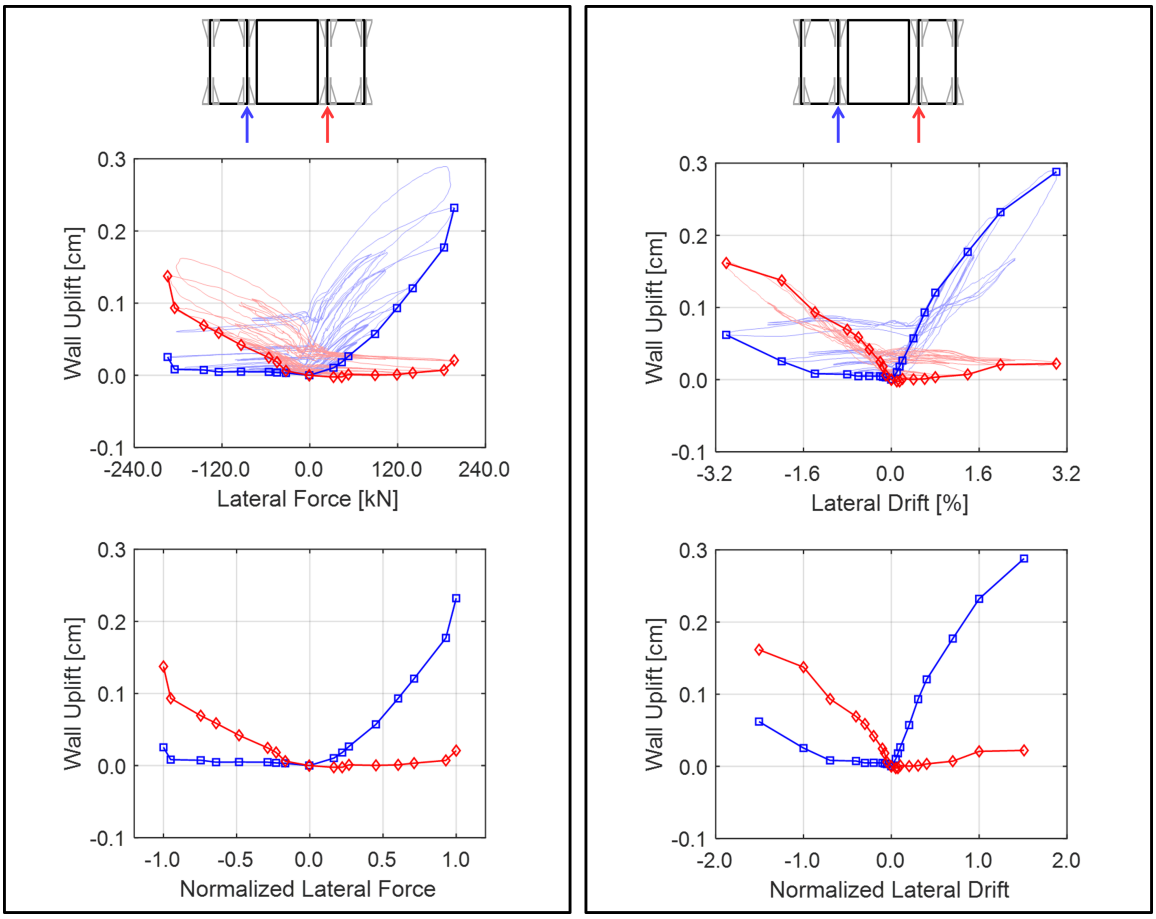


Figure D.37. Hold-down tie-down force evolution for specimen SGGS-1HD with increase in lateral force and lateral drift



(a)

Figure D.38. Wall uplift evolution for specimen SGGS-1HD with increase in lateral force and lateral drift: (a) Wall ends and (b) Gravity bay ends



(b)

Figure D.38. Wall uplift evolution for specimen SGGS-1HD with increase in lateral force and lateral drift: (a) Wall ends and (b) Gravity bay ends (cont.)

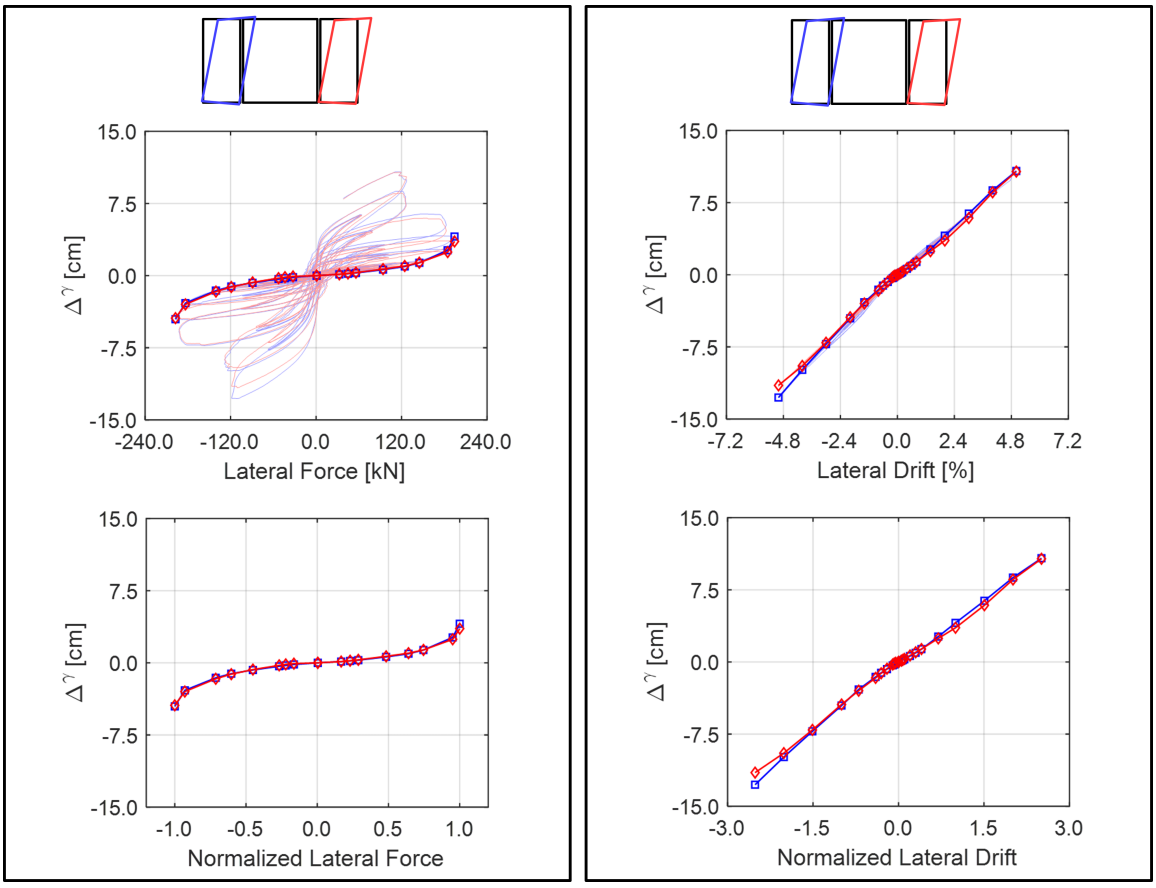


Figure D.39. Shear wall shear distortion evolution for specimen SGGS-1HD with increase in lateral force and lateral drift

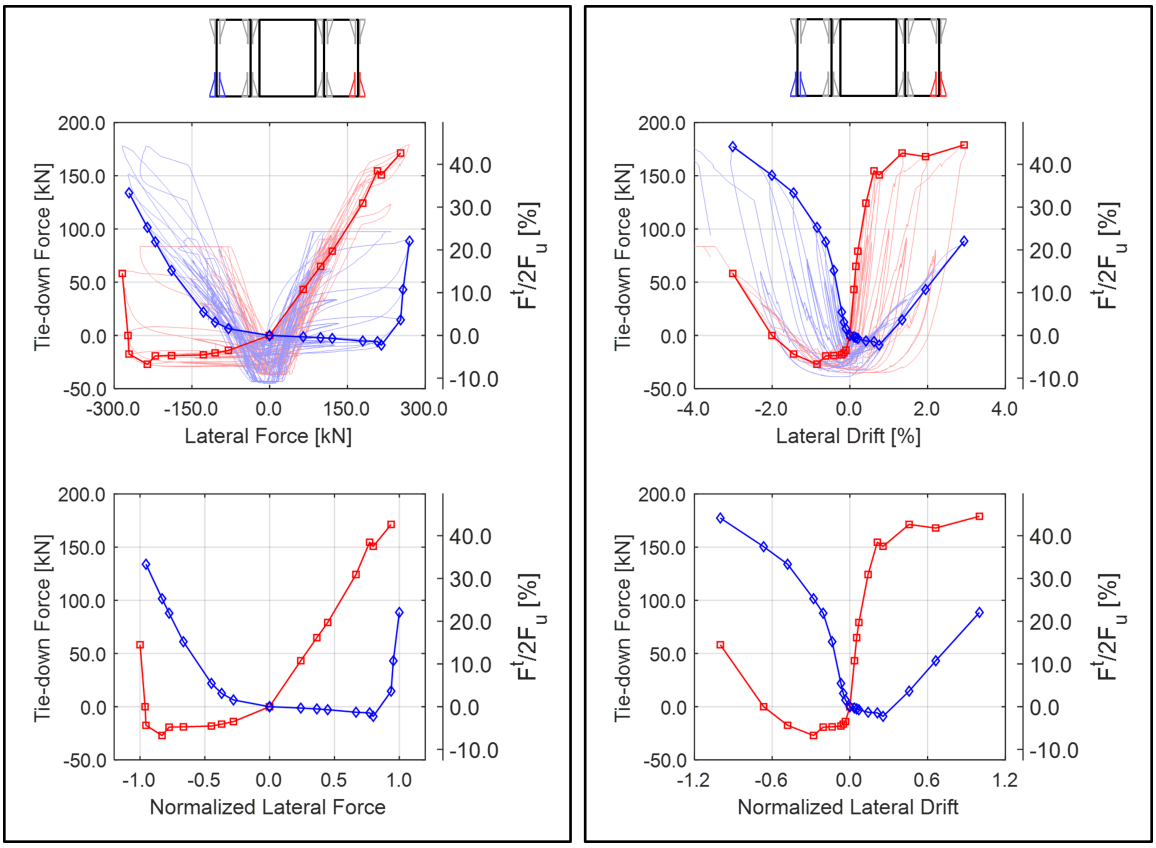
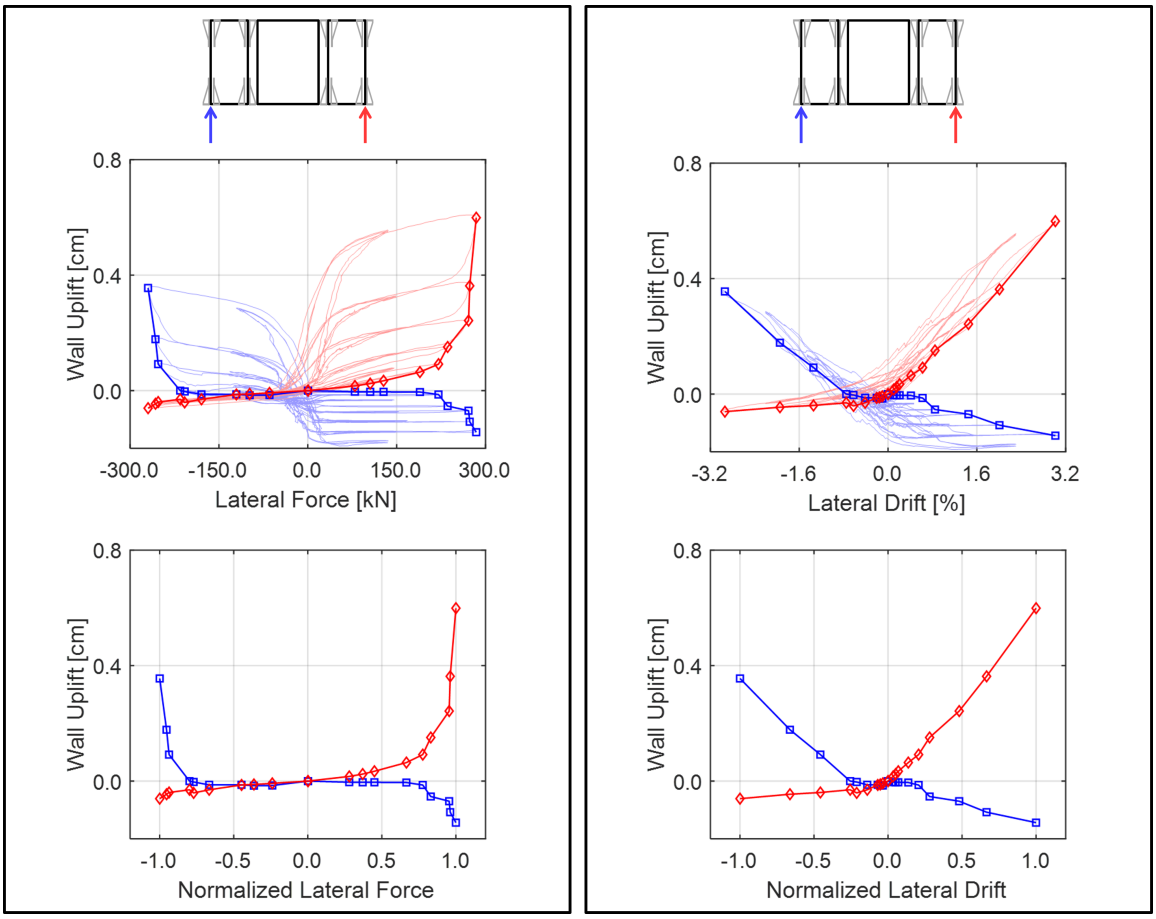
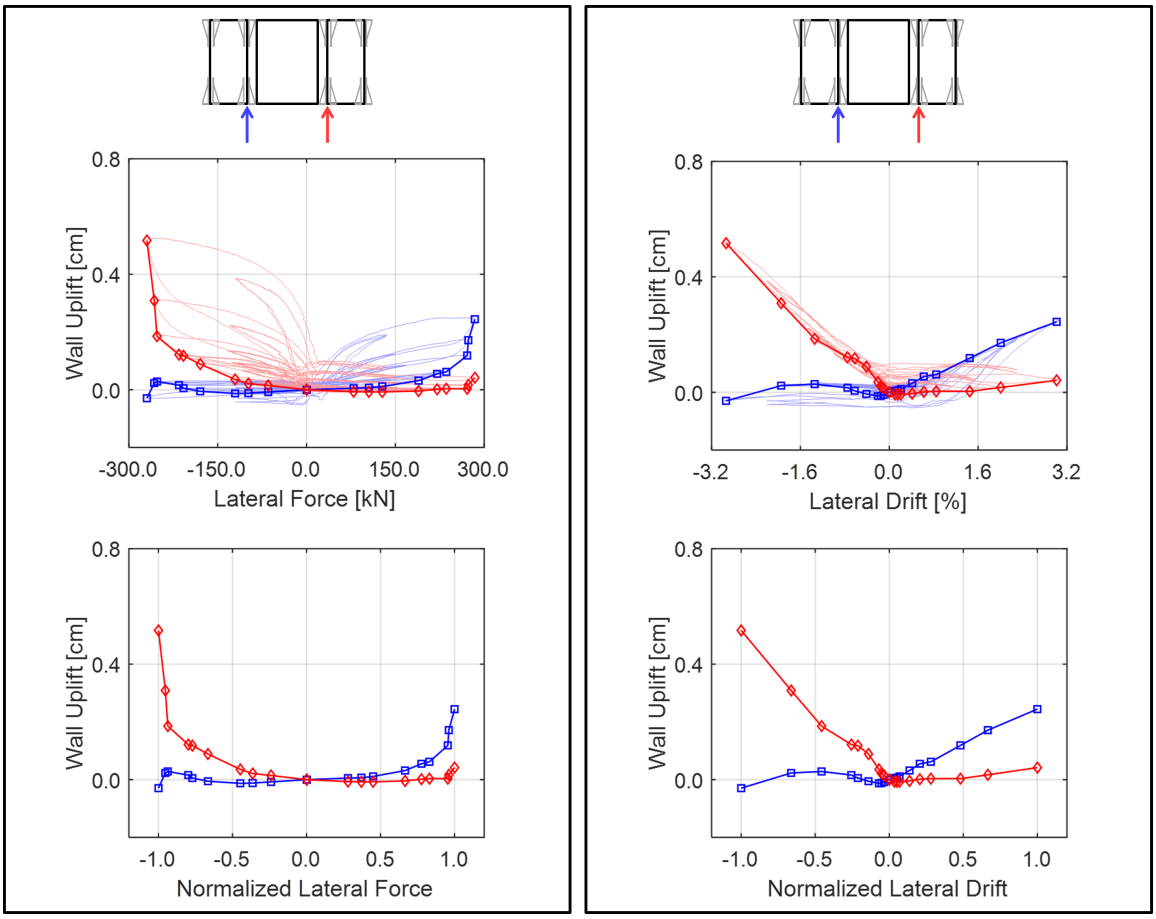


Figure D.40. Hold-down tie-down force evolution for specimen SGGS-1HDF with increase in lateral force and lateral drift



(a)

Figure D.41. Wall uplift evolution for specimen SGGS-1HDF with increase in lateral force and lateral drift: (a) Wall ends and (b) Gravity bay ends



(b)

Figure D.41. Wall uplift evolution for specimen SGGS-1HDF with increase in lateral force and lateral drift: (a) Wall ends and (b) Gravity bay ends (cont.)

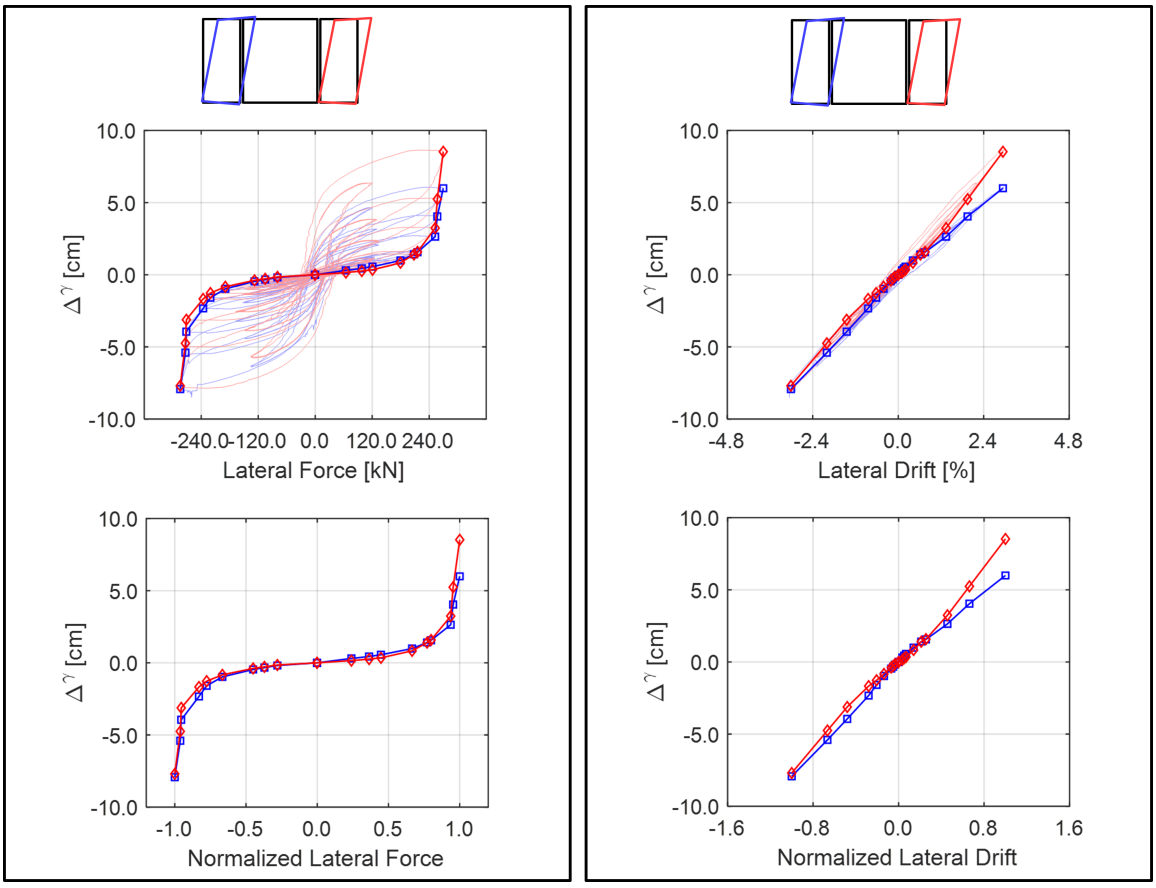


Figure D.42. Shear wall shear distortion evolution for specimen SGGS-1HDF with increase in lateral force and lateral drift

Appendix E

OpenSeesPy Code of Building Numerical Model

The complete OpenSeesPy code of the CFS-HUD test building numerical model has been provided here. This code contains building geometry, material model, element, section, and gravity, eigenvalue and nonlinear time history analyses definitions. The code was compiled in OpenSees version 3.4.0.

```python
# -*- coding: utf-8 -*-
"""
Created on Tue Apr 19 13:21:08 2022

@author: Amanpreet Singh
"""

import openseespy.opensees as ops
import os
import copy
import math
import numpy as np
import matplotlib.pyplot as plt

# ########################################################
#          CFS-HUD 6-story building (June 2016)          #
#            Amanpreet Singh, March 2022                 #
# ########################################################

# INITIALIZATION ----------------------------------------------------------------------
ops.wipe()                                  # clear memory of all past model definitions
ops.model('basic', '-ndm', 3, '-ndf', 6)    # define the model builder, ndm=#dimension, ndf=#dofs
ModelDirectory = "Model"

if not os.path.exists(ModelDirectory):
    os.mkdir(ModelDirectory)

exec(open('UNITS.py').read())    # define units
print("MODEL SET-UP OK")


#               ================================
#                  Global Coordinate System
#               ================================
#                _____________________________________          ^ Y-axis
#           |   _____________________________________|          |
#           |  |                                  | |          |
#           |  |                                  | |          |
#           |  |                                  | |          o--------->  X-axis
#           |  |                                  | |
#           |  |                                  | |
#           |  |                                  | |
#           |  |__________________________________| |
#           |_____________________________________|
#

# SET MODEL PARAMETERS ----------------------------------------------------------------------
nStory = 6                      # number of story
storyH = 10.0*ft                # height of story
buildingHeight = nStory*storyH
nNodesEle = 3                   # number of elements per floor
GravityAnalysisDone = "No"
THAnalysisDone = "No"
DoModalAnalysis = "Yes"
num_modes = 8                   # number of modes
analysisType = "TimeHistory"

ExportID = open(os.path.join(ModelDirectory,'modelData.txt'), 'w')
FrameID = open(os.path.join(ModelDirectory,'modelFrameData.txt'), 'w')

# GEOMETRY ----------------------------------------------------------------------
exec(open('INPUT_nodes.py').read())
print("NODES OK")

# MATERIAL ----------------------------------------------------------------------
exec(open('INPUT_mat.py').read())
print("MATERIAL OK")

# SECTIONS ----------------------------------------------------------------------
exec(open('INPUT_sec.py').read())
```

```
print("SECTIONS OK")

# GEOMETRIC TRANSFORMATIONS -------------------------------------------------------
exec(open('TRANSF.py').read())
print("TRANSFORMATIONS OK")

# ELEMENTS ------------------------------------------------------------------------
exec(open('INPUT_elem.py').read())
print("ELEMENTS OK")

# MASS ----------------------------------------------------------------------------
exec(open('GENERATE_mass.py').read())
print("MASS OK")


if DoModalAnalysis == 'Yes':
    exec(open('Analysis_Modal.py').read())
    print('Modal Analysis Results Pre - Gravity\n')
    print('---------------------------------------\n')
    for i in range(num_modes):
        print('T' + str(i+1) + ' = ' + str(T[i]) + 's\n')

# GRAVITY ANALYSIS ----------------------------------------------------------------------------
exec(open('Analysis_Gravity.py').read())

if DoModalAnalysis == 'Yes':
    exec(open('Analysis_Modal.py').read())
    print('Modal Analysis Results Post - Gravity\n')
    print('---------------------------------------\n')
    for i in range(num_modes):
        print('T' + str(i+1) + ' = ' + str(T[i]) + 's\n')


# ANALYSIS ------------------------------------------------------------------------
if analysisType == 'Cyclic':
    exec(open('Analysis_Cyclic.py').read())
elif analysisType == 'TimeHistory':
    exec(open('Analysis_TimeHistory.py').read())


if DoModalAnalysis == 'Yes' and THAnalysisDone == 'Yes':
    exec(open('Analysis_Modal.py').read())
    print('Modal Analysis Results Post - Time History Analysis\n')
    print('---------------------------------------\n')
    for i in range(num_modes):
        print('T' + str(i+1) + ' = ' + str(T[i]) + 's\n')

ExportID.close()
FrameID.close()
ops.wipe()
```

```
# -*- coding: utf-8 -*-
"""
Created on Tue Apr 19 13:36:22 2022

@author: Amanpreet Singh
"""

# UNITS --------------------------------------------------------------------------------
inch = 1.           # define basic units -- output units
kip = 1.            # define basic units -- output units
sec = 1.            # define basic units -- output units
LunitTXT = "inch"   # define basic-unit text for output
FunitTXT = "kip"    # define basic-unit text for output
TunitTXT = "sec"    # define basic-unit text for output
ft = 12.*inch       # define engineering units
ksi = kip/pow(inch,2)
psi = ksi/1000.
lbf = psi*inch*inch # pounds force
pcf = lbf/pow(ft,3) # pounds per cubic foot
psf = lbf/pow(ft,3) # pounds per square foot
in2 = inch*inch             # inch^2
in4 = inch*inch*inch*inch   # inch^4
cm = inch/2.54      # centimeter, needed for displacement input in MultipleSupport
excitation
cmsec2 = cm/pow(sec,2)  # cm/sec^2, needed for some ground accelerations
m = cm*100          # meter
mm = cm/10          # millimeter
mm2 = mm*mm         # millimeter^2
kN = 0.2247*kip     # kilo newton
MPa = 0.1450*ksi    # mega pascal
GPa = 1000*MPa      # giga pascal
pi = math.pi        # define constants
g = 32.2*ft/pow(sec,2)  # gravitational acceleration
Ubig = 1.e10        # a really large number
Usmall = 1/Ubig     # a really small number

print("BASIC UNITS - in, kip, sec")
```

```
# -*- coding: utf-8 -*-
"""
Created on Tue Apr 19 14:19:28 2022
INPUT_nodes.py
@author: Amanpreet Singh
"""

BuildingCorners = np.array([[0., 0.], [0., 288.], [408., 0.], [408., 288.]])

SW_NS_coord = np.array([[0., 42.], [0., 246.], [408., 42.], [408., 246.]])
GW_NS_coord = np.array([[0., 120.], [0., 168.], [408., 120.], [408., 168.]])
TR1_NS_coord = np.array([[0., 24.], [0., 216.], [408., 24.], [408., 216.]])
TR2_NS_coord = np.array([[0., 72.], [0., 264.], [408., 72.], [408., 264.]])

SW_EW_coord = np.array([[32., 0.], [78., 120.], [78., 168.], [32., 288.], [376., 0.], [342., 120.], [342., 168.], [376., 288.]])
GW_EW_coord = np.array([[202.5, 0.], [193.5, 120.], [193.5, 168.], [202.5, 288.]])
TR1_EW_coord = np.array([[24., 0.], [24., 120.], [24., 168.], [24., 288.], [360., 0.], [288., 120.], [288., 168.], [360., 288.]])
TR2_EW_coord = np.array([[48., 0.], [144., 120.], [144., 168.], [48., 288.], [384., 0.], [384., 120.], [384., 168.], [384., 288.]])

diaphragm_masternodes = np.array([[204., 144.]])

Nodes = []
Nodes_base = []
Nodes_floor = []
Nodes_frame = []
NodesSWX = []
NodesSWY = []
NodesGWX = []
NodesGWY = []
NodesTR1X = []
NodesTR1Y = []
NodesTR2X = []
NodesTR2Y = []

z = 0. # Current node height

# Nodes for all SW elements and Tie rods on levels other than ground
for j in range(nStory):

    z_elenodes = np.array([[0.], [60.], [60.], [120.]])
    # NS Shear wall nodes (Y-axis)----------------------------------------
    for i in range(SW_NS_coord.shape[0]):

        for k in range(nNodesEle+1):

            ops.node(10000*(j+1) + 50*(i+1) + k+1, SW_NS_coord[i][0],
            SW_NS_coord[i][1], z + z_elenodes[k][0])

            Nodes.extend([10000*(j+1) + 50*(i+1) + k+1])
            ExportID.write('node '+ str(10000*(j+1) + 50*(i+1) + k+1) + ' ' +
            str(SW_NS_coord[i][0]) + ' ' + str(SW_NS_coord[i][1]) + ' ' + str(z +
            z_elenodes[k][0]) + '\n')

            if j == 0 and k == 0:
                    ops.fix(10000*(j+1) + 50*(i+1) + k+1, 1, 1, 1, 0, 0, 0)

                    Nodes_base.extend([10000*(j+1) + 50*(i+1) + k+1])
                    ExportID.write('fix '+ str(10000*(j+1) + 50*(i+1) + k+1) + ' 1 1 1
                    0 0 1' + '\n')

            if k != (nNodesEle) and k != 0:
                NodesSWY.extend([10000*(j+1) + 50*(i+1) + k+1])

```

```
            if k == (nNodesEle) or k == 0:
                Nodes_floor.extend([10000*(j+1) + 50*(i+1) + k+1])
                Nodes_frame.extend([10000*(j+1) + 50*(i+1) + k+1])
                FrameID.write('node '+ str(10000*(j+1) + 50*(i+1) + k+1) + ' ' +
                str(SW_NS_coord[i][0]) + ' ' + str(SW_NS_coord[i][1]) + ' ' + str(z +
                z_elenodes[k][0]) + '\n')


    # EW Shear wall nodes (X-axis)-----------------------------------------
    for i in range(SW_EW_coord.shape[0]):

        for k in range(nNodesEle+1):

            ops.node(10000*(j+1) + 50*(i+1 + SW_NS_coord.shape[0]) + k+1,
            SW_EW_coord[i][0], SW_EW_coord[i][1], z + z_elenodes[k][0])

            Nodes.extend([10000*(j+1) + 50*(i+1 + SW_NS_coord.shape[0]) + k+1])
            ExportID.write('node '+ str(10000*(j+1) + 50*(i+1 + SW_NS_coord.shape[0]) +
            k+1) + ' ' + str(SW_EW_coord[i][0]) + ' ' + str(SW_EW_coord[i][1]) + ' ' +
            str(z + z_elenodes[k][0]) + '\n')

            if j == 0 and k == 0:
                    ops.fix(10000*(j+1) + 50*(i+1 + SW_NS_coord.shape[0]) + k+1, 1, 1,
                    1, 0, 0, 0)

                    Nodes_base.extend([10000*(j+1) + 50*(i+1 + SW_NS_coord.shape[0]) +
                    k+1])
                    ExportID.write('fix '+ str(10000*(j+1) + 50*(i+1 +
                    SW_NS_coord.shape[0]) + k+1) + ' 1 1 1 0 0 1' + '\n')

            if k != (nNodesEle) and k != 0:
                NodesSWX.extend([10000*(j+1) + 50*(i+1 + SW_NS_coord.shape[0]) + k+1])

            if k == (nNodesEle) or k == 0:
                Nodes_floor.extend([10000*(j+1) + 50*(i+1 + SW_NS_coord.shape[0]) + k+1])
                Nodes_frame.extend([10000*(j+1) + 50*(i+1 + SW_NS_coord.shape[0]) + k+1])
                FrameID.write('node '+ str(10000*(j+1) + 50*(i+1 +
                SW_NS_coord.shape[0]) + k+1) + ' ' + str(SW_EW_coord[i][0]) + ' ' +
                str(SW_EW_coord[i][1]) + ' ' + str(z + z_elenodes[k][0]) + '\n')


    # NS Gravity wall nodes (Y-axis)---------------------------------------
    for i in range(GW_NS_coord.shape[0]):

        for k in range(nNodesEle+1):

            ops.node(10000*(j+1) + 50*(i+1 + SW_NS_coord.shape[0] +
            SW_EW_coord.shape[0]) + k+1, GW_NS_coord[i][0], GW_NS_coord[i][1], z +
            z_elenodes[k][0])

            Nodes.extend([10000*(j+1) + 50*(i+1 + SW_NS_coord.shape[0] +
            SW_EW_coord.shape[0]) + k+1])
            ExportID.write('node '+ str(10000*(j+1) + 50*(i+1 + SW_NS_coord.shape[0] +
            SW_EW_coord.shape[0]) + k+1) + ' ' + str(GW_NS_coord[i][0]) + ' ' +
            str(GW_NS_coord[i][1]) + ' ' + str(z + z_elenodes[k][0]) + '\n')

            if j == 0 and k == 0:
                    ops.fix(10000*(j+1) + 50*(i+1 + SW_NS_coord.shape[0] +
                    SW_EW_coord.shape[0]) + k+1, 1, 1, 1, 0, 0, 0)

                    Nodes_base.extend([10000*(j+1) + 50*(i+1 + SW_NS_coord.shape[0] +
                    SW_EW_coord.shape[0]) + k+1])
                    ExportID.write('fix '+ str(10000*(j+1) + 50*(i+1 +
                    SW_NS_coord.shape[0] + SW_EW_coord.shape[0]) + k+1) + ' 1 1 1 0 0
                    1' + '\n')

```

```
            if k != (nNodesEle) and k != 0:
                NodesGWY.extend([10000*(j+1) + 50*(i+1 + SW_NS_coord.shape[0] +
                SW_EW_coord.shape[0]) + k+1])

            if k == (nNodesEle) or k == 0:
                Nodes_floor.extend([10000*(j+1) + 50*(i+1 + SW_NS_coord.shape[0] +
                SW_EW_coord.shape[0]) + k+1])
                Nodes_frame.extend([10000*(j+1) + 50*(i+1 + SW_NS_coord.shape[0] +
                SW_EW_coord.shape[0]) + k+1])
                FrameID.write('node '+ str(10000*(j+1) + 50*(i+1 + SW_NS_coord.shape[0]
                + SW_EW_coord.shape[0]) + k+1) + ' ' + str(GW_NS_coord[i][0]) + ' ' +
                str(GW_NS_coord[i][1]) + ' ' + str(z + z_elenodes[k][0]) + '\n')


    # EW Gravity wall nodes (X-axis)-----------------------------------------
    for i in range(GW_EW_coord.shape[0]):

        for k in range(nNodesEle+1):

            ops.node(10000*(j+1) + 50*(i+1 + SW_NS_coord.shape[0] +
            SW_EW_coord.shape[0] + GW_NS_coord.shape[0]) + k+1, GW_EW_coord[i][0],
            GW_EW_coord[i][1], z + z_elenodes[k][0])

            Nodes.extend([10000*(j+1) + 50*(i+1 + SW_NS_coord.shape[0] +
            SW_EW_coord.shape[0] + GW_NS_coord.shape[0]) + k+1])
            ExportID.write('node '+ str(10000*(j+1) + 50*(i+1 + SW_NS_coord.shape[0] +
            SW_EW_coord.shape[0] + GW_NS_coord.shape[0]) + k+1) + ' ' +
            str(GW_EW_coord[i][0]) + ' ' + str(GW_EW_coord[i][1]) + ' ' + str(z +
            z_elenodes[k][0]) + '\n')

            if j == 0 and k == 0:
                    ops.fix(10000*(j+1) + 50*(i+1 + SW_NS_coord.shape[0] +
                    SW_EW_coord.shape[0] + GW_NS_coord.shape[0]) + k+1, 1, 1, 1, 0, 0, 0)

                    Nodes_base.extend([10000*(j+1) + 50*(i+1 + SW_NS_coord.shape[0] +
                    SW_EW_coord.shape[0] + GW_NS_coord.shape[0]) + k+1])
                    ExportID.write('fix '+ str(10000*(j+1) + 50*(i+1 +
                    SW_NS_coord.shape[0] + SW_EW_coord.shape[0] + GW_NS_coord.shape[0])
                    + k+1) + ' 1 1 1 0 0 1' + '\n')

            if k != (nNodesEle) and k != 0:
                NodesGWX.extend([10000*(j+1) + 50*(i+1 + SW_NS_coord.shape[0] +
                SW_EW_coord.shape[0] + GW_NS_coord.shape[0]) + k+1])

            if k == (nNodesEle) or k == 0:
                Nodes_floor.extend([10000*(j+1) + 50*(i+1 + SW_NS_coord.shape[0] +
                SW_EW_coord.shape[0] + GW_NS_coord.shape[0]) + k+1])
                Nodes_frame.extend([10000*(j+1) + 50*(i+1 + SW_NS_coord.shape[0] +
                SW_EW_coord.shape[0] + GW_NS_coord.shape[0]) + k+1])
                FrameID.write('node '+ str(10000*(j+1) + 50*(i+1 + SW_NS_coord.shape[0]
                + SW_EW_coord.shape[0] + GW_NS_coord.shape[0]) + k+1) + ' ' +
                str(GW_EW_coord[i][0]) + ' ' + str(GW_EW_coord[i][1]) + ' ' + str(z +
                z_elenodes[k][0]) + '\n')


    z_elenodes = np.array([[0.], [60.], [60.], [120.]])
    # NS Tie-rod nodes (Y-axis)----------------------------------------------
    for i in range(SW_NS_coord.shape[0]):

        for k in range(nNodesEle+1):

            ops.node(10000*(j+1) + 50*(i+1) + 10 + k+1, TR1_NS_coord[i][0],
            TR1_NS_coord[i][1], z + z_elenodes[k][0])
            ops.node(10000*(j+1) + 50*(i+1) + 14 + k+1, TR2_NS_coord[i][0],
            TR2_NS_coord[i][1], z + z_elenodes[k][0])
```

```
150
151             Nodes.extend([10000*(j+1) + 50*(i+1) + 10 + k+1, 10000*(j+1) + 50*(i+1) +
                14 + k+1])
152             ExportID.write('node '+ str(10000*(j+1) + 50*(i+1) + 10 + k+1) + ' ' +
                str(TR1_NS_coord[i][0]) + ' ' + str(TR1_NS_coord[i][1]) + ' ' + str(z +
                z_elenodes[k][0]) + '\n')
153             ExportID.write('node '+ str(10000*(j+1) + 50*(i+1) + 14 + k+1) + ' ' +
                str(TR2_NS_coord[i][0]) + ' ' + str(TR2_NS_coord[i][1]) + ' ' + str(z +
                z_elenodes[k][0]) + '\n')
154
155             if j == 0 and k == 0:
156                     ops.fix(10000*(j+1) + 50*(i+1) + 10 + k+1, 1, 1, 1, 0, 0, 0)
157                     ops.fix(10000*(j+1) + 50*(i+1) + 14 + k+1, 1, 1, 1, 0, 0, 0)
158
159                     Nodes_base.extend([10000*(j+1) + 50*(i+1) + 10 + k+1, 10000*(j+1) +
                        50*(i+1) + 14 + k+1])
160                     ExportID.write('fix '+ str(10000*(j+1) + 50*(i+1) + 10 + k+1) + ' 1
                        1 1 0 0 1' + '\n')
161                     ExportID.write('fix '+ str(10000*(j+1) + 50*(i+1) + 14 + k+1) + ' 1
                        1 1 0 0 1' + '\n')
162
163             if k != (nNodesEle) and k != 0:
164                 NodesTR1Y.extend([10000*(j+1) + 50*(i+1) + 10 + k+1])
165                 NodesTR2Y.extend([10000*(j+1) + 50*(i+1) + 14 + k+1])
166
167             if k == (nNodesEle) or k == 0:
168                 Nodes_floor.extend([10000*(j+1) + 50*(i+1) + 10 + k+1, 10000*(j+1) +
                    50*(i+1) + 14 + k+1])
169
170
171
172     # EW Tie-rods nodes (X-axis)-----------------------------------------
173     for i in range(SW_EW_coord.shape[0]):
174
175         for k in range(nNodesEle+1):
176
177             ops.node(10000*(j+1) + 50*(i+1 + SW_NS_coord.shape[0]) + 10 + k+1,
                TR1_EW_coord[i][0], TR1_EW_coord[i][1], z + z_elenodes[k][0])
178             ops.node(10000*(j+1) + 50*(i+1 + SW_NS_coord.shape[0]) + 14 + k+1,
                TR2_EW_coord[i][0], TR2_EW_coord[i][1], z + z_elenodes[k][0])
179
180             Nodes.extend([10000*(j+1) + 50*(i+1 + SW_NS_coord.shape[0]) + 10 + k+1,
                10000*(j+1) + 50*(i+1 + SW_NS_coord.shape[0]) + 14 + k+1])
181             ExportID.write('node '+ str(10000*(j+1) + 50*(i+1 + SW_NS_coord.shape[0]) +
                10 + k+1) + ' ' + str(TR1_EW_coord[i][0]) + ' ' + str(TR1_EW_coord[i][1]) +
                ' ' + str(z + z_elenodes[k][0]) + '\n')
182             ExportID.write('node '+ str(10000*(j+1) + 50*(i+1 + SW_NS_coord.shape[0]) +
                14 + k+1) + ' ' + str(TR2_EW_coord[i][0]) + ' ' + str(TR2_EW_coord[i][1]) +
                ' ' + str(z + z_elenodes[k][0]) + '\n')
183
184             if j == 0 and k == 0:
185                     ops.fix(10000*(j+1) + 50*(i+1 + SW_NS_coord.shape[0]) + 10 + k+1,
                        1, 1, 1, 0, 0, 0)
186                     ops.fix(10000*(j+1) + 50*(i+1 + SW_NS_coord.shape[0]) + 14 + k+1,
                        1, 1, 1, 0, 0, 0)
187
188                     Nodes_base.extend([10000*(j+1) + 50*(i+1 + SW_NS_coord.shape[0]) +
                        10 + k+1, 10000*(j+1) + 50*(i+1 + SW_NS_coord.shape[0]) + 14 + k+1])
189                     ExportID.write('fix '+ str(10000*(j+1) + 50*(i+1 +
                        SW_NS_coord.shape[0]) + 10 + k+1) + ' 1 1 1 0 0 1' + '\n')
190                     ExportID.write('fix '+ str(10000*(j+1) + 50*(i+1 +
                        SW_NS_coord.shape[0]) + 14 + k+1) + ' 1 1 1 0 0 1' + '\n')
191
192             if k != (nNodesEle) and k != 0:
193                 NodesTR1X.extend([10000*(j+1) + 50*(i+1 + SW_NS_coord.shape[0]) + 10 +
                    k+1])
```

```
194                 NodesTR2X.extend([10000*(j+1) + 50*(i+1 + SW_NS_coord.shape[0]) + 14 +
                    k+1])
195
196             if k == (nNodesEle) or k == 0:
197                 Nodes_floor.extend([10000*(j+1) + 50*(i+1 + SW_NS_coord.shape[0]) + 10
                    + k+1, 10000*(j+1) + 50*(i+1 + SW_NS_coord.shape[0]) + 14 + k+1])
198
199
200     z = z + storyH
201
202     # Floor corner nodes ----------------------------------------
203     for i in range(BuildingCorners.shape[0]):
204         ops.node(10000*(j+1) + i+1, BuildingCorners[i][0], BuildingCorners[i][1], z)
205         Nodes.extend([10000*(j+1) + i+1])
206         Nodes_floor.extend([10000*(j+1) + i+1])
207         Nodes_frame.extend([10000*(j+1) + i+1])
208         ExportID.write('node '+ str(10000*(j+1) + i+1) + ' ' +
            str(BuildingCorners[i][0]) + ' ' + str(BuildingCorners[i][1]) + ' ' + str(z) +
            '\n')
209         FrameID.write('node '+ str(10000*(j+1) + i+1) + ' ' +
            str(BuildingCorners[i][0]) + ' ' + str(BuildingCorners[i][1]) + ' ' + str(z) +
            '\n')
210
211     # Diaphragm master nodes ------------------------------------
212     for i in range(diaphragm_masternodes.shape[0]):
213         ops.node(10000*(j+1) + i+11, diaphragm_masternodes[i][0],
            diaphragm_masternodes[i][1], z)
214         ops.fix(10000*(j+1) + i+11, 0, 0, 1, 1, 1, 0)
215         Nodes.extend([10000*(j+1) + i+11])
216         Nodes_floor.extend([10000*(j+1) + i+11])
217         ExportID.write('node '+ str(10000*(j+1) + i+11) + ' ' +
            str(diaphragm_masternodes[i][0]) + ' ' + str(diaphragm_masternodes[i][1]) + ' '
            + str(z) + '\n')
218         ExportID.write('fix '+ str(10000*(j+1) + i+11) + ' 0 0 1 1 1 0' + '\n')
219
```

```
# -*- coding: utf-8 -*-
"""
Created on Thu May 12 23:32:54 2022
INPUT_mat.py
@author: Amanpreet Singh
"""

#uniaxialMaterial('Pinching4', matTag, ePf1, ePd1, ePf2, ePd2, ePf3, ePd3, ePf4, ePd4, <eNf1, eNd1, eNf2, eNd2, eNf3, eNd3, eNf4, eNd4>, rDispP, rForceP, uForceP, <rDispN, rForceN, uForceN>, gK1, gK2, gK3, gK4, gKLim, gD1, gD2, gD3, gD4, gDLim, gF1, gF2, gF3, gF4, gFLim, gE, dmgType)
#uniaxialMaterial('ElasticMultiLinear', matTag, eta=0.0, '-strain', *strain, '-stress', *stress)

# SW EW Corridor (West)
ops.uniaxialMaterial('Pinching4', 21, 12.3907333333333, 0.0531141, 49.5627166666667, 0.888394, 61.95345, 1.92983, 21.683675, 3.43206, -12.3907333333333, -0.0531141, -49.5627166666667, -0.888394, -61.95345, -1.92983, -21.683675, -3.43206, 0.165, 0.11, -0.022, 0.165, 0.11, -0.022, 0.1, 0.4, 2, 2, 0.7, 0.5, 0.25, 1, 2, 0.5, 0.4, 0.4, 1.75, 2, 0.5, 10, 'energy')
ops.uniaxialMaterial('Pinching4', 22, 12.0276, 0.0554232, 48.1104, 0.919769, 60.138, 1.92983, 21.0483, 3.43007, -12.0276, -0.0554232, -48.1104, -0.919769, -60.138, -1.92983, -21.0483, -3.43007, 0.165, 0.11, -0.022, 0.165, 0.11, -0.022, 0.1, 0.4, 2, 2, 0.7, 0.5, 0.25, 1, 2, 0.5, 0.4, 0.4, 1.75, 2, 0.5, 10, 'energy')
ops.uniaxialMaterial('Pinching4', 23, 12.0276, 0.0554232, 48.1104, 0.919769, 60.138, 1.92983, 21.0483, 3.43007, -12.0276, -0.0554232, -48.1104, -0.919769, -60.138, -1.92983, -21.0483, -3.43007, 0.165, 0.11, -0.022, 0.165, 0.11, -0.022, 0.1, 0.4, 2, 2, 0.7, 0.5, 0.25, 1, 2, 0.5, 0.4, 0.4, 1.75, 2, 0.5, 10, 'energy')
ops.uniaxialMaterial('Pinching4', 24, 10.9341818181818, 0.0554232, 38.48832, 0.919769, 48.1104, 1.92983, 16.83864, 3.43007, -10.9341818181818, -0.0554232, -38.48832, -0.919769, -48.1104, -1.92983, -16.83864, -3.43007, 0.165, 0.11, -0.022, 0.165, 0.11, -0.022, 0.1, 0.4, 2, 2, 0.7, 0.5, 0.25, 1, 2, 0.5, 0.4, 0.4, 1.75, 2, 0.5, 10, 'energy')
ops.uniaxialMaterial('Pinching4', 25, 9.49218666666667, 0.0609416, 25.5474022916667, 0.569479, 36.4962582291667, 1.472, 10.58390125, 2.5795, -9.49218666666667, -0.0609416, -25.5474022916667, -0.569479, -36.4962582291667, -1.472, -10.58390125, -2.5795, 0.165, 0.11, -0.022, 0.165, 0.11, -0.022, 0.1, 0.4, 2, 2, 0.7, 0.5, 0.25, 1, 2, 0.5, 0.4, 0.4, 1.75, 2, 0.5, 10, 'energy')
ops.uniaxialMaterial('Pinching4', 26, 8.47516666666666, 0.0609416, 24.1013229166667, 0.569479, 34.4304322916667, 1.472, 9.9848125, 2.5795, -8.47516666666666, -0.0609416, -24.1013229166667, -0.569479, -34.4304322916667, -1.472, -9.9848125, -2.5795, 0.165, 0.11, -0.022, 0.165, 0.11, -0.022, 0.1, 0.4, 2, 2, 0.7, 0.5, 0.25, 1, 2, 0.5, 0.4, 0.4, 1.75, 2, 0.5, 10, 'energy')

# SW EW Corridor (East)
ops.uniaxialMaterial('Pinching4', 27, 10.4844666666667, 0.0531141, 41.9376833333333, 0.888394, 52.42215, 1.92983, 18.347725, 3.43206, -10.4844666666667, -0.0531141, -41.9376833333333, -0.888394, -52.42215, -1.92983, -18.347725, -3.43206, 0.165, 0.11, -0.022, 0.165, 0.11, -0.022, 0.1, 0.4, 2, 2, 0.7, 0.5, 0.25, 1, 2, 0.5, 0.4, 0.4, 1.75, 2, 0.5, 10, 'energy')
ops.uniaxialMaterial('Pinching4', 28, 10.1772, 0.0554232, 40.7088, 0.919769, 50.886, 1.92983, 17.8101, 3.43007, -10.1772, -0.0554232, -40.7088, -0.919769, -50.886, -1.92983, -17.8101, -3.43007, 0.165, 0.11, -0.022, 0.165, 0.11, -0.022, 0.1, 0.4, 2, 2, 0.7, 0.5, 0.25, 1, 2, 0.5, 0.4, 0.4, 1.75, 2, 0.5, 10, 'energy')
ops.uniaxialMaterial('Pinching4', 29, 10.1772, 0.0554232, 40.7088, 0.919769, 50.886, 1.92983, 17.8101, 3.43007, -10.1772, -0.0554232, -40.7088, -0.919769, -50.886, -1.92983, -17.8101, -3.43007, 0.165, 0.11, -0.022, 0.165, 0.11, -0.022, 0.1, 0.4, 2, 2, 0.7, 0.5, 0.25, 1, 2, 0.5, 0.4, 0.4, 1.75, 2, 0.5, 10, 'energy')
ops.uniaxialMaterial('Pinching4', 30, 9.252, 0.0554232, 32.56704, 0.919769, 40.7088, 1.92983, 14.24808, 3.43007, -9.252, -0.0554232, -32.56704, -0.919769, -40.7088, -1.92983, -14.24808, -3.43007, 0.165, 0.11, -0.022, 0.165, 0.11, -0.022, 0.1, 0.4, 2, 2, 0.7, 0.5, 0.25, 1, 2, 0.5, 0.4, 0.4, 1.75, 2, 0.5, 10, 'energy')
ops.uniaxialMaterial('Pinching4', 31, 8.03185025641026, 0.0609416, 21.6170327083333, 0.569479, 30.8814492708333, 1.472, 8.95560875, 2.5795, -8.03185025641026, -0.0609416, -21.6170327083333, -0.569479, -30.8814492708333, -1.472, -8.95560875, -2.5795, 0.165, 0.11, -0.022, 0.165, 0.11, -0.022, 0.1, 0.4, 2, 2, 0.7, 0.5, 0.25, 1, 2, 0.5, 0.4, 0.4, 1.75, 2, 0.5, 10, 'energy')
```

```
ops.uniaxialMaterial('Pinching4', 32, 7.17129487179487, 0.0609416, 20.3934270833333, 0.569479, 29.1334427083333, 1.472, 8.4486875, 2.5795, -7.17129487179487, -0.0609416, -20.3934270833333, -0.569479, -29.1334427083333, -1.472, -8.4486875, -2.5795, 0.165, 0.11, -0.022, 0.165, 0.11, -0.022, 0.1, 0.4, 2, 2, 0.7, 0.5, 0.25, 1, 2, 0.5, 0.4, 0.4, 1.75, 2, 0.5, 10, 'energy')

# SW NS Corner
ops.uniaxialMaterial('Pinching4', 1, 5.14160111111111, 0.0609416, 14.6065524137931, 0.569479, 20.866485862069, 1.472, 6.05127310344828, 2.5795, -5.14160111111111, -0.0609416, -14.6065524137931, -0.569479, -20.866485862069, -1.472, -6.05127310344828, -2.5795, 0.165, 0.11, -0.022, 0.165, 0.11, -0.022, 0.1, 0.4, 2, 2, 0.7, 0.5, 0.25, 1, 2, 0.5, 0.4, 0.4, 1.75, 2, 0.5, 10, 'energy')
ops.uniaxialMaterial('Pinching4', 2, 4.94384722222222, 0.0609416, 14.3201494252874, 0.569479, 20.4573390804598, 1.472, 5.93262068965517, 2.5795, -4.94384722222222, -0.0609416, -14.3201494252874, -0.569479, -20.4573390804598, -1.472, -5.93262068965517, -2.5795, 0.165, 0.11, -0.022, 0.165, 0.11, -0.022, 0.1, 0.4, 2, 2, 0.7, 0.5, 0.25, 1, 2, 0.5, 0.4, 0.4, 1.75, 2, 0.5, 10, 'energy')

# SW EW Corner
ops.uniaxialMaterial('Pinching4', 3, 3.85319052823315, 0.0609416, 11.1288018390805, 0.569479, 15.8982749425287, 1.472, 4.61049379310345, 2.5795, -3.85319052823315, -0.0609416, -11.1288018390805, -0.569479, -15.8982749425287, -1.472, -4.61049379310345, -2.5795, 0.165, 0.11, -0.022, 0.165, 0.11, -0.022, 0.1, 0.4, 2, 2, 0.7, 0.5, 0.25, 1, 2, 0.5, 0.4, 0.4, 1.75, 2, 0.5, 10, 'energy')
ops.uniaxialMaterial('Pinching4', 4, 3.70499089253188, 0.0609416, 10.9105900383142, 0.569479, 15.5865440613027, 1.472, 4.52009195402299, 2.5795, -3.70499089253188, -0.0609416, -10.9105900383142, -0.569479, -15.5865440613027, -1.472, -4.52009195402299, -2.5795, 0.165, 0.11, -0.022, 0.165, 0.11, -0.022, 0.1, 0.4, 2, 2, 0.7, 0.5, 0.25, 1, 2, 0.5, 0.4, 0.4, 1.75, 2, 0.5, 10, 'energy')

# Tie Rods Corridor and Corners
# Above SLE
ops.uniaxialMaterial('ElasticMultiLinear', 11, 0.0, '-strain', -0.35, 0, 0.055, 0.35, '-stress', -963.959090909091, 0, 8.31581298701299, 84.2242597402597)
ops.uniaxialMaterial('ElasticMultiLinear', 12, 0.0, '-strain', -0.35, 0, 0.055, 0.35, '-stress', -904.166666666667, 0, 7.8, 79)
ops.uniaxialMaterial('ElasticMultiLinear', 13, 0.0, '-strain', -0.35, 0, 0.055, 0.35, '-stress', -588.436363636364, 0, 5.07628051948052, 51.4136103896104)
ops.uniaxialMaterial('ElasticMultiLinear', 14, 0.0, '-strain', -0.35, 0, 0.055, 0.35, '-stress', -389.566666666667, 0, 3.36068571428571, 34.0377142857143)
ops.uniaxialMaterial('ElasticMultiLinear', 15, 0.0, '-strain', -0.35, 0, 0.055, 0.35, '-stress', -389.566666666667, 0, 3.36068571428571, 34.0377142857143)
ops.uniaxialMaterial('ElasticMultiLinear', 16, 0.0, '-strain', -0.35, 0, 0.055, 0.35, '-stress', -117.095454545455, 0, 1.01015064935065, 10.231012987013)

ops.uniaxialMaterial('ElasticMultiLinear', 17, 0.0, '-strain', -0.35, 0, 0.055, 0.35, '-stress', -963.959090909091, 0, 8.31581298701299, 84.2242597402597)
ops.uniaxialMaterial('ElasticMultiLinear', 18, 0.0, '-strain', -0.35, 0, 0.055, 0.35, '-stress', -389.566666666667, 0, 3.36068571428571, 34.0377142857143)
ops.uniaxialMaterial('ElasticMultiLinear', 19, 0.0, '-strain', -0.35, 0, 0.055, 0.35, '-stress', -308.590909090909, 0, 2.66212987012987, 26.9625974025974)
ops.uniaxialMaterial('ElasticMultiLinear', 20, 0.0, '-strain', -0.35, 0, 0.055, 0.35, '-stress', -171.533333333333, 0, 1.47977142857143, 14.9874285714286)

# SLE
# ops.uniaxialMaterial('ElasticMultiLinear', 11, 0.0, '-strain', -0.35, 0, 0.35, '-stress', -963.959090909091, 0, 173.590375)
# ops.uniaxialMaterial('ElasticMultiLinear', 12, 0.0, '-strain', -0.35, 0, 0.35, '-stress', -904.166666666667, 0, 162.822916666667)
# ops.uniaxialMaterial('ElasticMultiLinear', 13, 0.0, '-strain', -0.35, 0, 0.35, '-stress', -588.436363636364, 0, 105.966)
# ops.uniaxialMaterial('ElasticMultiLinear', 14, 0.0, '-strain', -0.35, 0, 0.35, '-stress', -389.566666666667, 0, 70.1534166666667)
# ops.uniaxialMaterial('ElasticMultiLinear', 15, 0.0, '-strain', -0.35, 0, 0.35, '-stress', -389.566666666667, 0, 70.1534166666667)
# ops.uniaxialMaterial('ElasticMultiLinear', 16, 0.0, '-strain', -0.35, 0, 0.35,
```

```
    '-stress', -117.095454545455, 0, 21.086625)
56
57  # ops.uniaxialMaterial('ElasticMultiLinear', 17, 0.0, '-strain', -0.35, 0, 0.35,
    '-stress', -963.959090909091, 0, 173.590375)
58  # ops.uniaxialMaterial('ElasticMultiLinear', 18, 0.0, '-strain', -0.35, 0, 0.35,
    '-stress', -389.566666666667, 0, 70.1534166666667)
59  # ops.uniaxialMaterial('ElasticMultiLinear', 19, 0.0, '-strain', -0.35, 0, 0.35,
    '-stress', -308.590909090909, 0, 55.57125)
60  # ops.uniaxialMaterial('ElasticMultiLinear', 20, 0.0, '-strain', -0.35, 0, 0.35,
    '-stress', -171.533333333333, 0, 30.8898333333333)
61
62  # GW NS
63  ops.uniaxialMaterial('Pinching4', 5, 1.295271, 0.105110444444444, 2.59054875,
    0.511475555555556, 3.2381775, 1.16454444444444, 0.97145325, 3.69948888888889,
    -1.295271, -0.105110444444444, -2.59054875, -0.511475555555556, -3.2381775,
    -1.16454444444444, -0.97145325, -3.69948888888889, 0.35, 0.16, -0.065, 0.35, 0.16,
    -0.065, 0.1, 0.5, 3, 1.2, 0.6, 0.1, 0.5, 3, 1.1, 0.6, 0.4, 0.4, 3, 1.2, 0.5, 10,
    'energy')
64
65  # GW EW
66  ops.uniaxialMaterial('Pinching4', 6, 5.43294225, 0.105110444444444, 10.8659128125,
    0.511475555555556, 13.582355625, 1.16454444444444, 4.0747066875, 3.69948888888889,
    -5.43294225, -0.105110444444444, -10.8659128125, -0.511475555555556, -13.582355625,
    -1.16454444444444, -4.0747066875, -3.69948888888889, 0.35, 0.16, -0.065, 0.35, 0.16,
    -0.065, 0.1, 0.5, 3, 1.2, 0.6, 0.1, 0.5, 3, 1.1, 0.6, 0.4, 0.4, 3, 1.2, 0.5, 10,
    'energy')
67  ops.uniaxialMaterial('Pinching4', 7, 1.9794375, 0.117288888888889, 3.9589453125,
    0.922633333333333, 4.9486640625, 2.50666666666667, 1.9794375, 5.10755555555556,
    -1.9794375, -0.117288888888889, -3.9589453125, -0.922633333333333, -4.9486640625,
    -2.50666666666667, -1.9794375, -5.10755555555556, 0.35, 0.15, -0.075, 0.35, 0.15,
    -0.075, 0.1, 0.5, 3, 1.2, 0.6, 0.1, 0.5, 3, 1.1, 0.6, 0.4, 0.4, 3, 1.2, 0.5, 10,
    'energy')
68
69  ops.uniaxialMaterial('Elastic', 10, 1e7, 0.0, 1e7)
```

```
# -*- coding: utf-8 -*-
"""
Created on Wed Apr 20 09:40:37 2022
INPUT_sec.py
@author: Amanpreet Singh
"""

# RIGID ELEMENT COLUMN SECTION PROPERTIES --------------------------------
E = 1e6
G = 1e6
ARigid = 1e10
JRigid = 1e10
IyRigid = 1e10
IzRigid = 1e10


# RIGID ELEMENT BEAM SECTION PROPERTIES --------------------------------
Eb = 1e5
Gb = 1e5
AbRigid = 1e8
JbRigid = 1e8
IybRigid = 1e8
IzbRigid = 1e8
```

```
# -*- coding: utf-8 -*-
"""
Created on Wed Apr 20 09:42:22 2022
TRANSF.py
@author: Amanpreet Singh
"""

# TRANSFORMATIONS FOR RIGID ELEMENTS ------------------------------------------
# geomTransf(transfType, transfTag, *transfArgs)
transfTagVertRig = 1                    # associate a tag to the transformation
VertRiglist = [1, 0, 0]
ops.geomTransf('Linear', transfTagVertRig, *VertRiglist)    # geometric transformation of beam stiffness and resisting force from the basic system to the global-coordinate system
transfTagHorizRig = 2               # associate a tag to the transformation
HorizRiglist = [0, 0, 1]
ops.geomTransf('Linear', transfTagHorizRig, *HorizRiglist)  # geometric transformation of beam stiffness and resisting force from the basic system to the global-coordinate system

str1 = ' '.join(str(e) for e in VertRiglist)
ExportID.write('geomTransf Linear ' + str(transfTagVertRig) + ' ' + str1 + '\n')
str1 = ' '.join(str(e) for e in HorizRiglist)
ExportID.write('geomTransf Linear ' + str(transfTagHorizRig) + ' ' + str1 + '\n')

```

```
# -*- coding: utf-8 -*-
"""
Created on Wed May 11 17:22:32 2022
INPUT_elem.py
@author: Amanpreet Singh
"""

# element('elasticBeamColumn', eleTag, *eleNodes, Area, E_mod, G_mod, Jxx, Iy, Iz, transfTag, <'-mass', mass>, <'-cMass'>)
# element('zeroLength', eleTag, *eleNodes, '-mat', *matTags, '-dir', *dirs, <'-doRayleigh', rFlag=0>, <'-orient', *vecx, *vecyp>)
# rigidDiaphragm(perpDirn, rNodeTag, *cNodeTags)

mat_NS_SW = [1, 1, 1, 1], [2, 2, 2, 2], [2, 2, 2, 2], [2, 2, 2, 2], [2, 2, 2, 2], [2, 2, 2, 2]
mat_EW_SW = [3, 21, 21, 3, 3, 27, 27, 3], [4, 22, 22, 4, 4, 28, 28, 4], [4, 23, 23, 4, 4, 29, 29, 4], [4, 24, 24, 4, 4, 30, 30, 4], [4, 25, 25, 4, 4, 31, 31, 4], [4, 26, 26, 4, 4, 32, 32, 4]

mat_NS_GW = [5, 5, 5, 5], [5, 5, 5, 5], [5, 5, 5, 5], [5, 5, 5, 5], [5, 5, 5, 5], [5, 5, 5, 5]
mat_EW_GW = [6, 7, 7, 6], [6, 7, 7, 6], [6, 7, 7, 6], [6, 7, 7, 6], [6, 7, 7, 6], [6, 7, 7, 6]

mat_NS_TR = [17, 17, 17, 17], [18, 18, 18, 18], [19, 19, 19, 19], [20, 20, 20, 20], [16, 16, 16, 16], [16, 16, 16, 16]
mat_EW_TR = [17, 11, 11, 17, 17, 11, 11, 17], [18, 12, 12, 18, 18, 12, 12, 18], [19, 13, 13, 19, 19, 13, 13, 19], [20, 14, 14, 20, 20, 14, 14, 20], [16, 15, 15, 16, 16, 15, 15, 16], [16, 16, 16, 16, 16, 16, 16, 16]


dofs_shearelem = [4, 5, 6]
dofs_upliftelem = [4, 5, 6]

EleSWX = []
EleSWY = []
EleGWX = []
EleGWY = []
EleTR1X = []
EleTR1Y = []
EleTR2X = []
EleTR2Y = []

EleXTrack = []
EleYTrack = []
EleSWXVert = []
EleSWYVert = []
EleGWXVert = []
EleGWYVert = []
EleTR1XVert = []
EleTR1YVert = []
EleTR2XVert = []
EleTR2YVert = []

# Vertical elements for SWs and Tie-rods
for j in range(nStory):

    # NS Shear wall elements ------------------------------------------
    for i in range(SW_NS_coord.shape[0]):

        # Shear wall
        ops.element('elasticBeamColumn', 10000*(j+1) + 50*(i+1) + 1, 10000*(j+1) + 50*(i+1) + 1, 10000*(j+1) + 50*(i+1) + 2, ARigid, E, G, JRigid, IyRigid, IzRigid, transfTagVertRig)
        ops.element('elasticBeamColumn', 10000*(j+1) + 50*(i+1) + 2, 10000*(j+1) + 50*(i+1) + 3, 10000*(j+1) + 50*(i+1) + 4, ARigid, E, G, JRigid, IyRigid,
```

```
            IzRigid, transfTagVertRig)
54          ops.element('zeroLength', 10000*(j+1) + 50*(i+1) + 3, 10000*(j+1) + 50*(i+1) +
            2, 10000*(j+1) + 50*(i+1) + 3, '-mat', mat_NS_SW[j][i], '-dir', 2)
55          ops.equalDOF(10000*(j+1) + 50*(i+1) + 2, 10000*(j+1) + 50*(i+1) + 3,
            *dofs_shearelem)
56
57          # Tie-rod 1
58          ops.element('elasticBeamColumn', 10000*(j+1) + 50*(i+1) + 11, 10000*(j+1) +
            50*(i+1) + 11, 10000*(j+1) + 50*(i+1) + 12, ARigid, E, G, JRigid, IyRigid,
            IzRigid, transfTagVertRig)
59          ops.element('elasticBeamColumn', 10000*(j+1) + 50*(i+1) + 12, 10000*(j+1) +
            50*(i+1) + 13, 10000*(j+1) + 50*(i+1) + 14, ARigid, E, G, JRigid, IyRigid,
            IzRigid, transfTagVertRig)
60          ops.element('zeroLength', 10000*(j+1) + 50*(i+1) + 13, 10000*(j+1) + 50*(i+1) +
            12, 10000*(j+1) + 50*(i+1) + 13, '-mat', mat_NS_TR[j][i], '-dir', 3)
61          ops.equalDOF(10000*(j+1) + 50*(i+1) + 12, 10000*(j+1) + 50*(i+1) + 13,
            *dofs_upliftelem)
62
63          # Tie-rod 2
64          ops.element('elasticBeamColumn', 10000*(j+1) + 50*(i+1) + 16, 10000*(j+1) +
            50*(i+1) + 15, 10000*(j+1) + 50*(i+1) + 16, ARigid, E, G, JRigid, IyRigid,
            IzRigid, transfTagVertRig)
65          ops.element('elasticBeamColumn', 10000*(j+1) + 50*(i+1) + 17, 10000*(j+1) +
            50*(i+1) + 17, 10000*(j+1) + 50*(i+1) + 18, ARigid, E, G, JRigid, IyRigid,
            IzRigid, transfTagVertRig)
66          ops.element('zeroLength', 10000*(j+1) + 50*(i+1) + 18, 10000*(j+1) + 50*(i+1) +
            16, 10000*(j+1) + 50*(i+1) + 17, '-mat', mat_NS_TR[j][i], '-dir', 3)
67          ops.equalDOF(10000*(j+1) + 50*(i+1) + 16, 10000*(j+1) + 50*(i+1) + 17,
            *dofs_upliftelem)
68
69          # Wall "top track"
70          ops.element('elasticBeamColumn', 10000*(j+1) + 50*(i+1) + 5, 10000*(j+1) +
            50*(i+1) + 14, 10000*(j+1) + 50*(i+1) + 4, AbRigid, Eb, Gb, JbRigid, IybRigid,
            IzbRigid, transfTagHorizRig)
71          ops.element('elasticBeamColumn', 10000*(j+1) + 50*(i+1) + 6, 10000*(j+1) +
            50*(i+1) + 4, 10000*(j+1) + 50*(i+1) + 18, AbRigid, Eb, Gb, JbRigid, IybRigid,
            IzbRigid, transfTagHorizRig)
72
73          if j > 0:
74              ops.element('zeroLength', 10000*(j+1) + 50*(i+1) + 4, 10000*(j) + 50*(i+1)
                + 4, 10000*(j+1) + 50*(i+1) + 1, '-mat', *[10, 10, 10], '-dir', *[1, 2, 3])
75              ops.element('zeroLength', 10000*(j+1) + 50*(i+1) + 14, 10000*(j) + 50*(i+1)
                + 14, 10000*(j+1) + 50*(i+1) + 11, '-mat', *[10, 10, 10], '-dir', *[1, 2, 3])
76              ops.element('zeroLength', 10000*(j+1) + 50*(i+1) + 19, 10000*(j) + 50*(i+1)
                + 18, 10000*(j+1) + 50*(i+1) + 15, '-mat', *[10, 10, 10], '-dir', *[1, 2, 3])
77
78          EleSWY.extend([10000*(j+1) + 50*(i+1) + 3])
79          EleTR1Y.extend([10000*(j+1) + 50*(i+1) + 13])
80          EleTR2Y.extend([10000*(j+1) + 50*(i+1) + 18])
81
82          EleSWYVert.extend([10000*(j+1) + 50*(i+1) + 1, 10000*(j+1) + 50*(i+1) + 2])
83          EleTR1YVert.extend([10000*(j+1) + 50*(i+1) + 11, 10000*(j+1) + 50*(i+1) + 12])
84          EleTR2YVert.extend([10000*(j+1) + 50*(i+1) + 16, 10000*(j+1) + 50*(i+1) + 17])
85          EleYTrack.extend([10000*(j+1) + 50*(i+1) + 5, 10000*(j+1) + 50*(i+1) + 6])
86
87          str1 = ' '.join(str(e) for e in dofs_shearelem)
88          ExportID.write('element elasticBeamColumn '+ str(10000*(j+1) + 50*(i+1) + 1) +
            ' ' + str(10000*(j+1) + 50*(i+1) + 1) + ' ' + str(10000*(j+1) + 50*(i+1) + 2) +
            ' ' + str(ARigid) + ' ' + str(E) + ' ' + str(G) + ' ' + str(JRigid) + ' ' +
            str(IyRigid) + ' ' + str(IzRigid) + ' ' + str(transfTagVertRig) + '\n')
89          ExportID.write('element elasticBeamColumn '+ str(10000*(j+1) + 50*(i+1) + 2) +
            ' ' + str(10000*(j+1) + 50*(i+1) + 3) + ' ' + str(10000*(j+1) + 50*(i+1) + 4) +
            ' ' + str(ARigid) + ' ' + str(E) + ' ' + str(G) + ' ' + str(JRigid) + ' ' +
            str(IyRigid) + ' ' + str(IzRigid) + ' ' + str(transfTagVertRig) + '\n')
90          ExportID.write('element zeroLength '+ str(10000*(j+1) + 50*(i+1) + 3) + ' ' +
            str(10000*(j+1) + 50*(i+1) + 2) + ' ' + str(10000*(j+1) + 50*(i+1) + 3) + '
```

```
            -mat ' + str(mat_NS_SW[j][i]) + ' -dir 2' + '\n')
91          ExportID.write('equalDOF '+ str(10000*(j+1) + 50*(i+1) + 2) + ' ' +
            str(10000*(j+1) + 50*(i+1) + 3) + ' ' + str1 + '\n')
92          FrameID.write('element elasticBeamColumn '+ str(10000*(j+1) + 50*(i+1) + 2) + '
            ' + str(10000*(j+1) + 50*(i+1) + 1) + ' ' + str(10000*(j+1) + 50*(i+1) + 4) + '
            ' + str(ARigid) + ' ' + str(E) + ' ' + str(G) + ' ' + str(JRigid) + ' ' +
            str(IyRigid) + ' ' + str(IzRigid) + ' ' + str(transfTagVertRig) + '\n')
93
94          str2 = ' '.join(str(e) for e in dofs_upliftelem)
95          ExportID.write('element elasticBeamColumn '+ str(10000*(j+1) + 50*(i+1) + 11) +
            ' ' + str(10000*(j+1) + 50*(i+1) + 11) + ' ' + str(10000*(j+1) + 50*(i+1) + 12)
            + ' ' + str(ARigid) + ' ' + str(E) + ' ' + str(G) + ' ' + str(JRigid) + ' ' +
            str(IyRigid) + ' ' + str(IzRigid) + ' ' + str(transfTagVertRig) + '\n')
96          ExportID.write('element elasticBeamColumn '+ str(10000*(j+1) + 50*(i+1) + 12) +
            ' ' + str(10000*(j+1) + 50*(i+1) + 13) + ' ' + str(10000*(j+1) + 50*(i+1) + 14)
            + ' ' + str(ARigid) + ' ' + str(E) + ' ' + str(G) + ' ' + str(JRigid) + ' ' +
            str(IyRigid) + ' ' + str(IzRigid) + ' ' + str(transfTagVertRig) + '\n')
97          ExportID.write('element zeroLength '+ str(10000*(j+1) + 50*(i+1) + 13) + ' ' +
            str(10000*(j+1) + 50*(i+1) + 12) + ' ' + str(10000*(j+1) + 50*(i+1) + 13) + '
            -mat ' + str(mat_NS_TR[j][i]) + ' -dir 3' + '\n')
98          ExportID.write('equalDOF '+ str(10000*(j+1) + 50*(i+1) + 12) + ' ' +
            str(10000*(j+1) + 50*(i+1) + 13) + ' ' + str2 + '\n')
99
100         ExportID.write('element elasticBeamColumn '+ str(10000*(j+1) + 50*(i+1) + 16) +
            ' ' + str(10000*(j+1) + 50*(i+1) + 15) + ' ' + str(10000*(j+1) + 50*(i+1) + 16)
            + ' ' + str(ARigid) + ' ' + str(E) + ' ' + str(G) + ' ' + str(JRigid) + ' ' +
            str(IyRigid) + ' ' + str(IzRigid) + ' ' + str(transfTagVertRig) + '\n')
101         ExportID.write('element elasticBeamColumn '+ str(10000*(j+1) + 50*(i+1) + 17) +
            ' ' + str(10000*(j+1) + 50*(i+1) + 17) + ' ' + str(10000*(j+1) + 50*(i+1) + 18)
            + ' ' + str(ARigid) + ' ' + str(E) + ' ' + str(G) + ' ' + str(JRigid) + ' ' +
            str(IyRigid) + ' ' + str(IzRigid) + ' ' + str(transfTagVertRig) + '\n')
102         ExportID.write('element zeroLength '+ str(10000*(j+1) + 50*(i+1) + 18) + ' ' +
            str(10000*(j+1) + 50*(i+1) + 16) + ' ' + str(10000*(j+1) + 50*(i+1) + 17) + '
            -mat ' + str(mat_NS_TR[j][i]) + ' -dir 3' + '\n')
103         ExportID.write('equalDOF '+ str(10000*(j+1) + 50*(i+1) + 16) + ' ' +
            str(10000*(j+1) + 50*(i+1) + 17) + ' ' + str2 + '\n')
104
105         ExportID.write('element elasticBeamColumn '+ str(10000*(j+1) + 50*(i+1) + 5) +
            ' ' + str(10000*(j+1) + 50*(i+1) + 14) + ' ' + str(10000*(j+1) + 50*(i+1) + 4)
            + ' ' + str(ARigid) + ' ' + str(E) + ' ' + str(G) + ' ' + str(JRigid) + ' ' +
            str(IyRigid) + ' ' + str(IzRigid) + ' ' + str(transfTagHorizRig) + '\n')
106         ExportID.write('element elasticBeamColumn '+ str(10000*(j+1) + 50*(i+1) + 6) +
            ' ' + str(10000*(j+1) + 50*(i+1) + 4) + ' ' + str(10000*(j+1) + 50*(i+1) + 18)
            + ' ' + str(ARigid) + ' ' + str(E) + ' ' + str(G) + ' ' + str(JRigid) + ' ' +
            str(IyRigid) + ' ' + str(IzRigid) + ' ' + str(transfTagHorizRig) + '\n')
107
108
109     # EW Shear wall elements ------------------------------------------
110     for i in range(SW_EW_coord.shape[0]):
111
112         # Shear wall
113         ops.element('elasticBeamColumn', 10000*(j+1) + 50*(i+1 + SW_NS_coord.shape[0])
            + 1, 10000*(j+1) + 50*(i+1 + SW_NS_coord.shape[0]) + 1, 10000*(j+1) + 50*(i+1 +
            SW_NS_coord.shape[0]) + 2, ARigid, E, G, JRigid, IyRigid, IzRigid,
            transfTagVertRig)
114         ops.element('elasticBeamColumn', 10000*(j+1) + 50*(i+1 + SW_NS_coord.shape[0])
            + 2, 10000*(j+1) + 50*(i+1 + SW_NS_coord.shape[0]) + 3, 10000*(j+1) + 50*(i+1 +
            SW_NS_coord.shape[0]) + 4, ARigid, E, G, JRigid, IyRigid, IzRigid,
            transfTagVertRig)
115         ops.element('zeroLength', 10000*(j+1) + 50*(i+1 + SW_NS_coord.shape[0]) + 3,
            10000*(j+1) + 50*(i+1 + SW_NS_coord.shape[0]) + 2, 10000*(j+1) + 50*(i+1 +
            SW_NS_coord.shape[0]) + 3, '-mat', mat_EW_SW[j][i], '-dir', 1)
116         ops.equalDOF(10000*(j+1) + 50*(i+1 + SW_NS_coord.shape[0]) + 2, 10000*(j+1) +
            50*(i+1 + SW_NS_coord.shape[0]) + 3, *dofs_shearelem)
117
118         # Tie-rod 1
```

```
        ops.element('elasticBeamColumn', 10000*(j+1) + 50*(i+1 + SW_NS_coord.shape[0])
        + 11, 10000*(j+1) + 50*(i+1 + SW_NS_coord.shape[0]) + 11, 10000*(j+1) + 50*(i+1
        + SW_NS_coord.shape[0]) + 12, ARigid, E, G, JRigid, IyRigid, IzRigid,
        transfTagVertRig)
        ops.element('elasticBeamColumn', 10000*(j+1) + 50*(i+1 + SW_NS_coord.shape[0])
        + 12, 10000*(j+1) + 50*(i+1 + SW_NS_coord.shape[0]) + 13, 10000*(j+1) + 50*(i+1
        + SW_NS_coord.shape[0]) + 14, ARigid, E, G, JRigid, IyRigid, IzRigid,
        transfTagVertRig)
        ops.element('zeroLength', 10000*(j+1) + 50*(i+1 + SW_NS_coord.shape[0]) + 13,
        10000*(j+1) + 50*(i+1 + SW_NS_coord.shape[0]) + 12, 10000*(j+1) + 50*(i+1 +
        SW_NS_coord.shape[0]) + 13, '-mat', mat_EW_TR[j][i], '-dir', 3)
        ops.equalDOF(10000*(j+1) + 50*(i+1 + SW_NS_coord.shape[0]) + 12, 10000*(j+1) +
        50*(i+1 + SW_NS_coord.shape[0]) + 13, *dofs_upliftelem)

        # Tie-rod 2
        ops.element('elasticBeamColumn', 10000*(j+1) + 50*(i+1 + SW_NS_coord.shape[0])
        + 16, 10000*(j+1) + 50*(i+1 + SW_NS_coord.shape[0]) + 15, 10000*(j+1) + 50*(i+1
        + SW_NS_coord.shape[0]) + 16, ARigid, E, G, JRigid, IyRigid, IzRigid,
        transfTagVertRig)
        ops.element('elasticBeamColumn', 10000*(j+1) + 50*(i+1 + SW_NS_coord.shape[0])
        + 17, 10000*(j+1) + 50*(i+1 + SW_NS_coord.shape[0]) + 17, 10000*(j+1) + 50*(i+1
        + SW_NS_coord.shape[0]) + 18, ARigid, E, G, JRigid, IyRigid, IzRigid,
        transfTagVertRig)
        ops.element('zeroLength', 10000*(j+1) + 50*(i+1 + SW_NS_coord.shape[0]) + 18,
        10000*(j+1) + 50*(i+1 + SW_NS_coord.shape[0]) + 16, 10000*(j+1) + 50*(i+1 +
        SW_NS_coord.shape[0]) + 17, '-mat', mat_EW_TR[j][i], '-dir', 3)
        ops.equalDOF(10000*(j+1) + 50*(i+1 + SW_NS_coord.shape[0]) + 16, 10000*(j+1) +
        50*(i+1 + SW_NS_coord.shape[0]) + 17, *dofs_upliftelem)

        # Wall "top track"
        ops.element('elasticBeamColumn', 10000*(j+1) + 50*(i+1 + SW_NS_coord.shape[0])
        + 5, 10000*(j+1) + 50*(i+1 + SW_NS_coord.shape[0]) + 14, 10000*(j+1) + 50*(i+1
        + SW_NS_coord.shape[0]) + 4, AbRigid, Eb, Gb, JbRigid, IybRigid, IzbRigid,
        transfTagHorizRig)
        ops.element('elasticBeamColumn', 10000*(j+1) + 50*(i+1 + SW_NS_coord.shape[0])
        + 6, 10000*(j+1) + 50*(i+1 + SW_NS_coord.shape[0]) + 4, 10000*(j+1) + 50*(i+1 +
        SW_NS_coord.shape[0]) + 18, AbRigid, Eb, Gb, JbRigid, IybRigid, IzbRigid,
        transfTagHorizRig)

        if j > 0:
            ops.element('zeroLength', 10000*(j+1) + 50*(i+1 + SW_NS_coord.shape[0]) +
            4, 10000*(j) + 50*(i+1 + SW_NS_coord.shape[0]) + 4, 10000*(j+1) + 50*(i+1 +
            SW_NS_coord.shape[0]) + 1, '-mat', *[10, 10, 10], '-dir', *[1, 2, 3])
            ops.element('zeroLength', 10000*(j+1) + 50*(i+1 + SW_NS_coord.shape[0]) +
            14, 10000*(j) + 50*(i+1 + SW_NS_coord.shape[0]) + 14, 10000*(j+1) + 50*(i+1
            + SW_NS_coord.shape[0]) + 11, '-mat', *[10, 10, 10], '-dir', *[1, 2, 3])
            ops.element('zeroLength', 10000*(j+1) + 50*(i+1 + SW_NS_coord.shape[0]) +
            19, 10000*(j) + 50*(i+1 + SW_NS_coord.shape[0]) + 18, 10000*(j+1) + 50*(i+1
            + SW_NS_coord.shape[0]) + 15, '-mat', *[10, 10, 10], '-dir', *[1, 2, 3])

        EleSWX.extend([10000*(j+1) + 50*(i+1 + SW_NS_coord.shape[0]) + 3])
        EleTR1X.extend([10000*(j+1) + 50*(i+1 + SW_NS_coord.shape[0]) + 13])
        EleTR2X.extend([10000*(j+1) + 50*(i+1 + SW_NS_coord.shape[0]) + 18])

        EleSWXVert.extend([10000*(j+1) + 50*(i+1 + SW_NS_coord.shape[0]) + 1,
        10000*(j+1) + 50*(i+1 + SW_NS_coord.shape[0]) + 2])
        EleTR1XVert.extend([10000*(j+1) + 50*(i+1 + SW_NS_coord.shape[0]) + 11,
        10000*(j+1) + 50*(i+1 + SW_NS_coord.shape[0]) + 12])
        EleTR2XVert.extend([10000*(j+1) + 50*(i+1 + SW_NS_coord.shape[0]) + 16,
        10000*(j+1) + 50*(i+1 + SW_NS_coord.shape[0]) + 17])
        EleXTrack.extend([10000*(j+1) + 50*(i+1 + SW_NS_coord.shape[0]) + 5,
        10000*(j+1) + 50*(i+1 + SW_NS_coord.shape[0]) + 6])

        ExportID.write('element elasticBeamColumn '+ str(10000*(j+1) + 50*(i+1 +
        SW_NS_coord.shape[0]) + 1) + ' ' + str(10000*(j+1) + 50*(i+1 +
        SW_NS_coord.shape[0]) + 1) + ' ' + str(10000*(j+1) + 50*(i+1 +
```

```
        SW_NS_coord.shape[0]) + 2) + ' ' + str(ARigid) + ' ' + str(E) + ' ' + str(G) +
        ' ' + str(JRigid) + ' ' + str(IyRigid) + ' ' + str(IzRigid) + ' ' +
        str(transfTagVertRig) + '\n')
149     ExportID.write('element elasticBeamColumn '+ str(10000*(j+1) + 50*(i+1 +
        SW_NS_coord.shape[0]) + 2) + ' ' + str(10000*(j+1) + 50*(i+1 +
        SW_NS_coord.shape[0]) + 3) + ' ' + str(10000*(j+1) + 50*(i+1 +
        SW_NS_coord.shape[0]) + 4) + ' ' + str(ARigid) + ' ' + str(E) + ' ' + str(G) +
        ' ' + str(JRigid) + ' ' + str(IyRigid) + ' ' + str(IzRigid) + ' ' +
        str(transfTagVertRig) + '\n')
150     ExportID.write('element zeroLength '+ str(10000*(j+1) + 50*(i+1 +
        SW_NS_coord.shape[0]) + 3) + ' ' + str(10000*(j+1) + 50*(i+1 +
        SW_NS_coord.shape[0]) + 2) + ' ' + str(10000*(j+1) + 50*(i+1 +
        SW_NS_coord.shape[0]) + 3) + ' -mat ' + str(mat_EW_SW[j][i]) + ' -dir 1' + '\n')
151     ExportID.write('equalDOF '+ str(10000*(j+1) + 50*(i+1 + SW_NS_coord.shape[0]) +
        2) + ' ' + str(10000*(j+1) + 50*(i+1 + SW_NS_coord.shape[0]) + 3) + ' ' + str1
        + '\n')
152     FrameID.write('element elasticBeamColumn '+ str(10000*(j+1) + 50*(i+1 +
        SW_NS_coord.shape[0]) + 1) + ' ' + str(10000*(j+1) + 50*(i+1 +
        SW_NS_coord.shape[0]) + 1) + ' ' + str(10000*(j+1) + 50*(i+1 +
        SW_NS_coord.shape[0]) + 4) + ' ' + str(ARigid) + ' ' + str(E) + ' ' + str(G) +
        ' ' + str(JRigid) + ' ' + str(IyRigid) + ' ' + str(IzRigid) + ' ' +
        str(transfTagVertRig) + '\n')
153
154     ExportID.write('element elasticBeamColumn '+ str(10000*(j+1) + 50*(i+1 +
        SW_NS_coord.shape[0]) + 11) + ' ' + str(10000*(j+1) + 50*(i+1 +
        SW_NS_coord.shape[0]) + 11) + ' ' + str(10000*(j+1) + 50*(i+1 +
        SW_NS_coord.shape[0]) + 12) + ' ' + str(ARigid) + ' ' + str(E) + ' ' + str(G) +
        ' ' + str(JRigid) + ' ' + str(IyRigid) + ' ' + str(IzRigid) + ' ' +
        str(transfTagVertRig) + '\n')
155     ExportID.write('element elasticBeamColumn '+ str(10000*(j+1) + 50*(i+1 +
        SW_NS_coord.shape[0]) + 12) + ' ' + str(10000*(j+1) + 50*(i+1 +
        SW_NS_coord.shape[0]) + 13) + ' ' + str(10000*(j+1) + 50*(i+1 +
        SW_NS_coord.shape[0]) + 14) + ' ' + str(ARigid) + ' ' + str(E) + ' ' + str(G) +
        ' ' + str(JRigid) + ' ' + str(IyRigid) + ' ' + str(IzRigid) + ' ' +
        str(transfTagVertRig) + '\n')
156     ExportID.write('element zeroLength '+ str(10000*(j+1) + 50*(i+1 +
        SW_NS_coord.shape[0]) + 13) + ' ' + str(10000*(j+1) + 50*(i+1 +
        SW_NS_coord.shape[0]) + 12) + ' ' + str(10000*(j+1) + 50*(i+1 +
        SW_NS_coord.shape[0]) + 13) + ' -mat ' + str(mat_EW_TR[j][i]) + ' -dir 3' + '\n')
157     ExportID.write('equalDOF '+ str(10000*(j+1) + 50*(i+1 + SW_NS_coord.shape[0]) +
        12) + ' ' + str(10000*(j+1) + 50*(i+1 + SW_NS_coord.shape[0]) + 13) + ' ' +
        str2 + '\n')
158
159     ExportID.write('element elasticBeamColumn '+ str(10000*(j+1) + 50*(i+1 +
        SW_NS_coord.shape[0]) + 16) + ' ' + str(10000*(j+1) + 50*(i+1 +
        SW_NS_coord.shape[0]) + 15) + ' ' + str(10000*(j+1) + 50*(i+1 +
        SW_NS_coord.shape[0]) + 16) + ' ' + str(ARigid) + ' ' + str(E) + ' ' + str(G) +
        ' ' + str(JRigid) + ' ' + str(IyRigid) + ' ' + str(IzRigid) + ' ' +
        str(transfTagVertRig) + '\n')
160     ExportID.write('element elasticBeamColumn '+ str(10000*(j+1) + 50*(i+1 +
        SW_NS_coord.shape[0]) + 17) + ' ' + str(10000*(j+1) + 50*(i+1 +
        SW_NS_coord.shape[0]) + 17) + ' ' + str(10000*(j+1) + 50*(i+1 +
        SW_NS_coord.shape[0]) + 18) + ' ' + str(ARigid) + ' ' + str(E) + ' ' + str(G) +
        ' ' + str(JRigid) + ' ' + str(IyRigid) + ' ' + str(IzRigid) + ' ' +
        str(transfTagVertRig) + '\n')
161     ExportID.write('element zeroLength '+ str(10000*(j+1) + 50*(i+1 +
        SW_NS_coord.shape[0]) + 18) + ' ' + str(10000*(j+1) + 50*(i+1 +
        SW_NS_coord.shape[0]) + 16) + ' ' + str(10000*(j+1) + 50*(i+1 +
        SW_NS_coord.shape[0]) + 17) + ' -mat ' + str(mat_EW_TR[j][i]) + ' -dir 3' + '\n')
162     ExportID.write('equalDOF '+ str(10000*(j+1) + 50*(i+1 + SW_NS_coord.shape[0]) +
        16) + ' ' + str(10000*(j+1) + 50*(i+1 + SW_NS_coord.shape[0]) + 17) + ' ' +
        str2 + '\n')
163
164     ExportID.write('element elasticBeamColumn '+ str(10000*(j+1) + 50*(i+1 +
        SW_NS_coord.shape[0]) + 5) + ' ' + str(10000*(j+1) + 50*(i+1 +
        SW_NS_coord.shape[0]) + 14) + ' ' + str(10000*(j+1) + 50*(i+1 +
```

```
            SW_NS_coord.shape[0]) + 4) + ' ' + str(ARigid) + ' ' + str(E) + ' ' + str(G) +
            ' ' + str(JRigid) + ' ' + str(IyRigid) + ' ' + str(IzRigid) + ' ' +
            str(transfTagHorizRig) + '\n')
165         ExportID.write('element elasticBeamColumn '+ str(10000*(j+1) + 50*(i+1 +
            SW_NS_coord.shape[0]) + 6) + ' ' + str(10000*(j+1) + 50*(i+1 +
            SW_NS_coord.shape[0]) + 4) + ' ' + str(10000*(j+1) + 50*(i+1 +
            SW_NS_coord.shape[0]) + 18) + ' ' + str(ARigid) + ' ' + str(E) + ' ' + str(G) +
            ' ' + str(JRigid) + ' ' + str(IyRigid) + ' ' + str(IzRigid) + ' ' +
            str(transfTagHorizRig) + '\n')
166
167
168     # NS Gravity wall elements -----------------------------------------
169     for i in range(GW_NS_coord.shape[0]):
170
171         ops.element('elasticBeamColumn', 10000*(j+1) + 50*(i+1 + SW_NS_coord.shape[0] +
            SW_EW_coord.shape[0]) + 1, 10000*(j+1) + 50*(i+1 + SW_NS_coord.shape[0] +
            SW_EW_coord.shape[0]) + 1, 10000*(j+1) + 50*(i+1 + SW_NS_coord.shape[0] +
            SW_EW_coord.shape[0]) + 2, ARigid, E, G, JRigid, IyRigid, IzRigid,
            transfTagVertRig)
172         ops.element('elasticBeamColumn', 10000*(j+1) + 50*(i+1 + SW_NS_coord.shape[0] +
            SW_EW_coord.shape[0]) + 2, 10000*(j+1) + 50*(i+1 + SW_NS_coord.shape[0] +
            SW_EW_coord.shape[0]) + 3, 10000*(j+1) + 50*(i+1 + SW_NS_coord.shape[0] +
            SW_EW_coord.shape[0]) + 4, ARigid, E, G, JRigid, IyRigid, IzRigid,
            transfTagVertRig)
173         ops.element('zeroLength', 10000*(j+1) + 50*(i+1 + SW_NS_coord.shape[0] +
            SW_EW_coord.shape[0]) + 3, 10000*(j+1) + 50*(i+1 + SW_NS_coord.shape[0] +
            SW_EW_coord.shape[0]) + 2, 10000*(j+1) + 50*(i+1 + SW_NS_coord.shape[0] +
            SW_EW_coord.shape[0]) + 3, '-mat', mat_NS_GW[j][i], '-dir', 2)
174         ops.equalDOF(10000*(j+1) + 50*(i+1 + SW_NS_coord.shape[0] +
            SW_EW_coord.shape[0]) + 2, 10000*(j+1) + 50*(i+1 + SW_NS_coord.shape[0] +
            SW_EW_coord.shape[0]) + 3, *dofs_shearelem)
175
176         if j > 0:
177             ops.element('zeroLength', 10000*(j+1) + 50*(i+1 + SW_NS_coord.shape[0] +
                SW_EW_coord.shape[0]) + 4, 10000*(j) + 50*(i+1 + SW_NS_coord.shape[0] +
                SW_EW_coord.shape[0]) + 4, 10000*(j+1) + 50*(i+1 + SW_NS_coord.shape[0] +
                SW_EW_coord.shape[0]) + 1, '-mat', *[10, 10, 10], '-dir', *[1, 2, 3])
178
179         EleGWY.extend([10000*(j+1) + 50*(i+1 + SW_NS_coord.shape[0] +
            SW_EW_coord.shape[0]) + 3])
180
181         EleGWYVert.extend([10000*(j+1) + 50*(i+1 + SW_NS_coord.shape[0] +
            SW_EW_coord.shape[0]) + 1, 10000*(j+1) + 50*(i+1 + SW_NS_coord.shape[0] +
            SW_EW_coord.shape[0]) + 2])
182
183         ExportID.write('element elasticBeamColumn '+ str(10000*(j+1) + 50*(i+1 +
            SW_NS_coord.shape[0] + SW_EW_coord.shape[0]) + 1) + ' ' + str(10000*(j+1) +
            50*(i+1 + SW_NS_coord.shape[0] + SW_EW_coord.shape[0]) + 1) + ' ' +
            str(10000*(j+1) + 50*(i+1 + SW_NS_coord.shape[0] + SW_EW_coord.shape[0]) + 2) +
            ' ' + str(ARigid) + ' ' + str(E) + ' ' + str(G) + ' ' + str(JRigid) + ' ' +
            str(IyRigid) + ' ' + str(IzRigid) + ' ' + str(transfTagVertRig) + '\n')
184         ExportID.write('element elasticBeamColumn '+ str(10000*(j+1) + 50*(i+1 +
            SW_NS_coord.shape[0] + SW_EW_coord.shape[0]) + 2) + ' ' + str(10000*(j+1) +
            50*(i+1 + SW_NS_coord.shape[0] + SW_EW_coord.shape[0]) + 3) + ' ' +
            str(10000*(j+1) + 50*(i+1 + SW_NS_coord.shape[0] + SW_EW_coord.shape[0]) + 4) +
            ' ' + str(ARigid) + ' ' + str(E) + ' ' + str(G) + ' ' + str(JRigid) + ' ' +
            str(IyRigid) + ' ' + str(IzRigid) + ' ' + str(transfTagVertRig) + '\n')
185         ExportID.write('element zeroLength '+ str(10000*(j+1) + 50*(i+1 +
            SW_NS_coord.shape[0] + SW_EW_coord.shape[0]) + 3) + ' ' + str(10000*(j+1) +
            50*(i+1 + SW_NS_coord.shape[0] + SW_EW_coord.shape[0]) + 2) + ' ' +
            str(10000*(j+1) + 50*(i+1 + SW_NS_coord.shape[0] + SW_EW_coord.shape[0]) + 3) +
            ' -mat ' + str(mat_NS_GW[j][i]) + ' -dir 2' + '\n')
186         ExportID.write('equalDOF '+ str(10000*(j+1) + 50*(i+1 + SW_NS_coord.shape[0] +
            SW_EW_coord.shape[0]) + 2) + ' ' + str(10000*(j+1) + 50*(i+1 +
            SW_NS_coord.shape[0] + SW_EW_coord.shape[0]) + 3) + ' ' + str1 + '\n')
187         FrameID.write('element elasticBeamColumn '+ str(10000*(j+1) + 50*(i+1 +
```

```
            SW_NS_coord.shape[0] + SW_EW_coord.shape[0]) + 1) + ' ' + str(10000*(j+1) +
            50*(i+1 + SW_NS_coord.shape[0] + SW_EW_coord.shape[0]) + 1) + ' ' +
            str(10000*(j+1) + 50*(i+1 + SW_NS_coord.shape[0] + SW_EW_coord.shape[0]) + 4) +
            ' ' + str(ARigid) + ' ' + str(E) + ' ' + str(G) + ' ' + str(JRigid) + ' ' +
            str(IyRigid) + ' ' + str(IzRigid) + ' ' + str(transfTagVertRig) + '\n')
188
189
190         # EW Gravity wall elements ------------------------------------------
191         for i in range(GW_EW_coord.shape[0]):
192
193             ops.element('elasticBeamColumn', 10000*(j+1) + 50*(i+1 + SW_NS_coord.shape[0] +
            SW_EW_coord.shape[0] + GW_NS_coord.shape[0]) + 1, 10000*(j+1) + 50*(i+1 +
            SW_NS_coord.shape[0] + SW_EW_coord.shape[0] + GW_NS_coord.shape[0]) + 1,
            10000*(j+1) + 50*(i+1 + SW_NS_coord.shape[0] + SW_EW_coord.shape[0] +
            GW_NS_coord.shape[0]) + 2, ARigid, E, G, JRigid, IyRigid, IzRigid,
            transfTagVertRig)
194             ops.element('elasticBeamColumn', 10000*(j+1) + 50*(i+1 + SW_NS_coord.shape[0] +
            SW_EW_coord.shape[0] + GW_NS_coord.shape[0]) + 2, 10000*(j+1) + 50*(i+1 +
            SW_NS_coord.shape[0] + SW_EW_coord.shape[0] + GW_NS_coord.shape[0]) + 3,
            10000*(j+1) + 50*(i+1 + SW_NS_coord.shape[0] + SW_EW_coord.shape[0] +
            GW_NS_coord.shape[0]) + 4, ARigid, E, G, JRigid, IyRigid, IzRigid,
            transfTagVertRig)
195             ops.element('zeroLength', 10000*(j+1) + 50*(i+1 + SW_NS_coord.shape[0] +
            SW_EW_coord.shape[0] + GW_NS_coord.shape[0]) + 3, 10000*(j+1) + 50*(i+1 +
            SW_NS_coord.shape[0] + SW_EW_coord.shape[0] + GW_NS_coord.shape[0]) + 2,
            10000*(j+1) + 50*(i+1 + SW_NS_coord.shape[0] + SW_EW_coord.shape[0] +
            GW_NS_coord.shape[0]) + 3, '-mat', mat_EW_GW[j][i], '-dir', 1)
196             ops.equalDOF(10000*(j+1) + 50*(i+1 + SW_NS_coord.shape[0] +
            SW_EW_coord.shape[0] + GW_NS_coord.shape[0]) + 2, 10000*(j+1) + 50*(i+1 +
            SW_NS_coord.shape[0] + SW_EW_coord.shape[0] + GW_NS_coord.shape[0]) + 3,
            *dofs_shearelem)
197
198             if j > 0:
199                 ops.element('zeroLength', 10000*(j+1) + 50*(i+1 + SW_NS_coord.shape[0] +
                SW_EW_coord.shape[0] + GW_NS_coord.shape[0]) + 4, 10000*(j) + 50*(i+1 +
                SW_NS_coord.shape[0] + SW_EW_coord.shape[0] + GW_NS_coord.shape[0]) + 4,
                10000*(j+1) + 50*(i+1 + SW_NS_coord.shape[0] + SW_EW_coord.shape[0] +
                GW_NS_coord.shape[0]) + 1, '-mat', *[10, 10, 10], '-dir', *[1, 2, 3])
200
201             EleGWX.extend([10000*(j+1) + 50*(i+1 + SW_NS_coord.shape[0] +
            SW_EW_coord.shape[0] + GW_NS_coord.shape[0]) + 3])
202
203             EleGWXVert.extend([10000*(j+1) + 50*(i+1 + SW_NS_coord.shape[0] +
            SW_EW_coord.shape[0] + GW_NS_coord.shape[0]) + 1, 10000*(j+1) + 50*(i+1 +
            SW_NS_coord.shape[0] + SW_EW_coord.shape[0] + GW_NS_coord.shape[0]) + 2])
204
205             ExportID.write('element elasticBeamColumn '+ str(10000*(j+1) + 50*(i+1 +
            SW_NS_coord.shape[0] + SW_EW_coord.shape[0] + GW_NS_coord.shape[0]) + 1) + ' '
            + str(10000*(j+1) + 50*(i+1 + SW_NS_coord.shape[0] + SW_EW_coord.shape[0] +
            GW_NS_coord.shape[0]) + 1) + ' ' + str(10000*(j+1) + 50*(i+1 +
            SW_NS_coord.shape[0] + SW_EW_coord.shape[0] + GW_NS_coord.shape[0]) + 2) + ' '
            + str(ARigid) + ' ' + str(E) + ' ' + str(G) + ' ' + str(JRigid) + ' ' +
            str(IyRigid) + ' ' + str(IzRigid) + ' ' + str(transfTagVertRig) + '\n')
206             ExportID.write('element elasticBeamColumn '+ str(10000*(j+1) + 50*(i+1 +
            SW_NS_coord.shape[0] + SW_EW_coord.shape[0] + GW_NS_coord.shape[0]) + 2) + ' '
            + str(10000*(j+1) + 50*(i+1 + SW_NS_coord.shape[0] + SW_EW_coord.shape[0] +
            GW_NS_coord.shape[0]) + 3) + ' ' + str(10000*(j+1) + 50*(i+1 +
            SW_NS_coord.shape[0] + SW_EW_coord.shape[0] + GW_NS_coord.shape[0]) + 4) + ' '
            + str(ARigid) + ' ' + str(E) + ' ' + str(G) + ' ' + str(JRigid) + ' ' +
            str(IyRigid) + ' ' + str(IzRigid) + ' ' + str(transfTagVertRig) + '\n')
207             ExportID.write('element zeroLength '+ str(10000*(j+1) + 50*(i+1 +
            SW_NS_coord.shape[0] + SW_EW_coord.shape[0] + GW_NS_coord.shape[0]) + 3) + ' '
            + str(10000*(j+1) + 50*(i+1 + SW_NS_coord.shape[0] + SW_EW_coord.shape[0] +
            GW_NS_coord.shape[0]) + 2) + ' ' + str(10000*(j+1) + 50*(i+1 +
            SW_NS_coord.shape[0] + SW_EW_coord.shape[0] + GW_NS_coord.shape[0]) + 3) + '
            -mat ' + str(mat_EW_GW[j][i]) + ' -dir 1' + '\n')
```

```
208             ExportID.write('equalDOF '+ str(10000*(j+1) + 50*(i+1 + SW_NS_coord.shape[0] +
                SW_EW_coord.shape[0] + GW_NS_coord.shape[0]) + 2) + ' ' + str(10000*(j+1) +
                50*(i+1 + SW_NS_coord.shape[0] + SW_EW_coord.shape[0] + GW_NS_coord.shape[0]) +
                3) + ' ' + str1 + '\n')
209             FrameID.write('element elasticBeamColumn '+ str(10000*(j+1) + 50*(i+1 +
                SW_NS_coord.shape[0] + SW_EW_coord.shape[0] + GW_NS_coord.shape[0]) + 1) + ' '
                + str(10000*(j+1) + 50*(i+1 + SW_NS_coord.shape[0] + SW_EW_coord.shape[0] +
                GW_NS_coord.shape[0]) + 1) + ' ' + str(10000*(j+1) + 50*(i+1 +
                SW_NS_coord.shape[0] + SW_EW_coord.shape[0] + GW_NS_coord.shape[0]) + 4) + ' '
                + str(ARigid) + ' ' + str(E) + ' ' + str(G) + ' ' + str(JRigid) + ' ' +
                str(IyRigid) + ' ' + str(IzRigid) + ' ' + str(transfTagVertRig) + '\n')
210
211
212         # Floor corridor rigid elements ----------------------------------------
213         # NS wall lines
214         ops.element('elasticBeamColumn', 10000*(j+1) + 1, 10000*(j+1) + 1, 10000*(j+1) +
            50*(1) + 14, AbRigid, Eb, Gb, JbRigid, IybRigid, IzbRigid, transfTagHorizRig)
215         ops.element('elasticBeamColumn', 10000*(j+1) + 2, 10000*(j+1) + 50*(1) + 18,
            10000*(j+1) + 50*(13) + 4, AbRigid, Eb, Gb, JbRigid, IybRigid, IzbRigid,
            transfTagHorizRig)
216         ops.element('elasticBeamColumn', 10000*(j+1) + 3, 10000*(j+1) + 50*(13) + 4,
            10000*(j+1) + 50*(14) + 4, AbRigid, Eb, Gb, JbRigid, IybRigid, IzbRigid,
            transfTagHorizRig)
217         ops.element('elasticBeamColumn', 10000*(j+1) + 4, 10000*(j+1) + 50*(14) + 4,
            10000*(j+1) + 50*(2) + 14, AbRigid, Eb, Gb, JbRigid, IybRigid, IzbRigid,
            transfTagHorizRig)
218         ops.element('elasticBeamColumn', 10000*(j+1) + 5, 10000*(j+1) + 50*(2) + 18,
            10000*(j+1) + 2, AbRigid, Eb, Gb, JbRigid, IybRigid, IzbRigid, transfTagHorizRig)
219
220         ops.element('elasticBeamColumn', 10000*(j+1) + 6, 10000*(j+1) + 3, 10000*(j+1) +
            50*(3) + 14, AbRigid, Eb, Gb, JbRigid, IybRigid, IzbRigid, transfTagHorizRig)
221         ops.element('elasticBeamColumn', 10000*(j+1) + 7, 10000*(j+1) + 50*(3) + 18,
            10000*(j+1) + 50*(15) + 4, AbRigid, Eb, Gb, JbRigid, IybRigid, IzbRigid,
            transfTagHorizRig)
222         ops.element('elasticBeamColumn', 10000*(j+1) + 8, 10000*(j+1) + 50*(15) + 4,
            10000*(j+1) + 50*(16) + 4, AbRigid, Eb, Gb, JbRigid, IybRigid, IzbRigid,
            transfTagHorizRig)
223         ops.element('elasticBeamColumn', 10000*(j+1) + 9, 10000*(j+1) + 50*(16) + 4,
            10000*(j+1) + 50*(4) + 14, AbRigid, Eb, Gb, JbRigid, IybRigid, IzbRigid,
            transfTagHorizRig)
224         ops.element('elasticBeamColumn', 10000*(j+1) + 10, 10000*(j+1) + 50*(4) + 18,
            10000*(j+1) + 4, AbRigid, Eb, Gb, JbRigid, IybRigid, IzbRigid, transfTagHorizRig)
225
226         EleYTrack.extend([10000*(j+1) + 1, 10000*(j+1) + 2, 10000*(j+1) + 3, 10000*(j+1) +
            4, 10000*(j+1) + 5, 10000*(j+1) + 6, 10000*(j+1) + 7, 10000*(j+1) + 8, 10000*(j+1)
            + 9, 10000*(j+1) + 10])
227
228         ExportID.write('element elasticBeamColumn '+ str(10000*(j+1) + 1) + ' ' +
            str(10000*(j+1) + 1) + ' ' + str(10000*(j+1) + 50*(1) + 14) + ' ' + str(ARigid) + '
            ' + str(E) + ' ' + str(G) + ' ' + str(JRigid) + ' ' + str(IyRigid) + ' ' +
            str(IzRigid) + ' ' + str(transfTagHorizRig) + '\n')
229         ExportID.write('element elasticBeamColumn '+ str(10000*(j+1) + 2) + ' ' +
            str(10000*(j+1) + 50*(1) + 18) + ' ' + str(10000*(j+1) + 50*(13) + 4) + ' ' +
            str(ARigid) + ' ' + str(E) + ' ' + str(G) + ' ' + str(JRigid) + ' ' + str(IyRigid)
            + ' ' + str(IzRigid) + ' ' + str(transfTagHorizRig) + '\n')
230         ExportID.write('element elasticBeamColumn '+ str(10000*(j+1) + 3) + ' ' +
            str(10000*(j+1) + 50*(13) + 4) + ' ' + str(10000*(j+1) + 50*(14) + 4) + ' ' +
            str(ARigid) + ' ' + str(E) + ' ' + str(G) + ' ' + str(JRigid) + ' ' + str(IyRigid)
            + ' ' + str(IzRigid) + ' ' + str(transfTagHorizRig) + '\n')
231         ExportID.write('element elasticBeamColumn '+ str(10000*(j+1) + 4) + ' ' +
            str(10000*(j+1) + 50*(14) + 4) + ' ' + str(10000*(j+1) + 50*(2) + 14) + ' ' +
            str(ARigid) + ' ' + str(E) + ' ' + str(G) + ' ' + str(JRigid) + ' ' + str(IyRigid)
            + ' ' + str(IzRigid) + ' ' + str(transfTagHorizRig) + '\n')
232         ExportID.write('element elasticBeamColumn '+ str(10000*(j+1) + 5) + ' ' +
            str(10000*(j+1) + 50*(2) + 18) + ' ' + str(10000*(j+1) + 2) + ' ' + str(ARigid) + '
            ' + str(E) + ' ' + str(G) + ' ' + str(JRigid) + ' ' + str(IyRigid) + ' ' +
```

```
        str(IzRigid) + ' ' + str(transfTagHorizRig) + '\n')
233
234     ExportID.write('element elasticBeamColumn '+ str(10000*(j+1) + 6) + ' ' +
        str(10000*(j+1) + 3) + ' ' + str(10000*(j+1) + 50*(3) + 14) + ' ' + str(ARigid) + '
        ' + str(E) + ' ' + str(G) + ' ' + str(JRigid) + ' ' + str(IyRigid) + ' ' +
        str(IzRigid) + ' ' + str(transfTagHorizRig) + '\n')
235     ExportID.write('element elasticBeamColumn '+ str(10000*(j+1) + 7) + ' ' +
        str(10000*(j+1) + 50*(3) + 18) + ' ' + str(10000*(j+1) + 50*(15) + 4) + ' ' +
        str(ARigid) + ' ' + str(E) + ' ' + str(G) + ' ' + str(JRigid) + ' ' + str(IyRigid)
        + ' ' + str(IzRigid) + ' ' + str(transfTagHorizRig) + '\n')
236     ExportID.write('element elasticBeamColumn '+ str(10000*(j+1) + 8) + ' ' +
        str(10000*(j+1) + 50*(15) + 4) + ' ' + str(10000*(j+1) + 50*(16) + 4) + ' ' +
        str(ARigid) + ' ' + str(E) + ' ' + str(G) + ' ' + str(JRigid) + ' ' + str(IyRigid)
        + ' ' + str(IzRigid) + ' ' + str(transfTagHorizRig) + '\n')
237     ExportID.write('element elasticBeamColumn '+ str(10000*(j+1) + 9) + ' ' +
        str(10000*(j+1) + 50*(16) + 4) + ' ' + str(10000*(j+1) + 50*(4) + 14) + ' ' +
        str(ARigid) + ' ' + str(E) + ' ' + str(G) + ' ' + str(JRigid) + ' ' + str(IyRigid)
        + ' ' + str(IzRigid) + ' ' + str(transfTagHorizRig) + '\n')
238     ExportID.write('element elasticBeamColumn '+ str(10000*(j+1) + 10) + ' ' +
        str(10000*(j+1) + 50*(4) + 18) + ' ' + str(10000*(j+1) + 4) + ' ' + str(ARigid) + '
        ' + str(E) + ' ' + str(G) + ' ' + str(JRigid) + ' ' + str(IyRigid) + ' ' +
        str(IzRigid) + ' ' + str(transfTagHorizRig) + '\n')
239
240     FrameID.write('element elasticBeamColumn '+ str(10000*(j+1) + 1) + ' ' +
        str(10000*(j+1) + 1) + ' ' + str(10000*(j+1) + 50*(1) + 4) + ' ' + str(ARigid) + '
        ' + str(E) + ' ' + str(G) + ' ' + str(JRigid) + ' ' + str(IyRigid) + ' ' +
        str(IzRigid) + ' ' + str(transfTagHorizRig) + '\n')
241     FrameID.write('element elasticBeamColumn '+ str(10000*(j+1) + 2) + ' ' +
        str(10000*(j+1) + 50*(1) + 4) + ' ' + str(10000*(j+1) + 50*(13) + 4) + ' ' +
        str(ARigid) + ' ' + str(E) + ' ' + str(G) + ' ' + str(JRigid) + ' ' + str(IyRigid)
        + ' ' + str(IzRigid) + ' ' + str(transfTagHorizRig) + '\n')
242     FrameID.write('element elasticBeamColumn '+ str(10000*(j+1) + 3) + ' ' +
        str(10000*(j+1) + 50*(13) + 4) + ' ' + str(10000*(j+1) + 50*(14) + 4) + ' ' +
        str(ARigid) + ' ' + str(E) + ' ' + str(G) + ' ' + str(JRigid) + ' ' + str(IyRigid)
        + ' ' + str(IzRigid) + ' ' + str(transfTagHorizRig) + '\n')
243     FrameID.write('element elasticBeamColumn '+ str(10000*(j+1) + 4) + ' ' +
        str(10000*(j+1) + 50*(14) + 4) + ' ' + str(10000*(j+1) + 50*(2) + 4) + ' ' +
        str(ARigid) + ' ' + str(E) + ' ' + str(G) + ' ' + str(JRigid) + ' ' + str(IyRigid)
        + ' ' + str(IzRigid) + ' ' + str(transfTagHorizRig) + '\n')
244     FrameID.write('element elasticBeamColumn '+ str(10000*(j+1) + 5) + ' ' +
        str(10000*(j+1) + 50*(2) + 4) + ' ' + str(10000*(j+1) + 2) + ' ' + str(ARigid) + '
        ' + str(E) + ' ' + str(G) + ' ' + str(JRigid) + ' ' + str(IyRigid) + ' ' +
        str(IzRigid) + ' ' + str(transfTagHorizRig) + '\n')
245
246     FrameID.write('element elasticBeamColumn '+ str(10000*(j+1) + 6) + ' ' +
        str(10000*(j+1) + 3) + ' ' + str(10000*(j+1) + 50*(3) + 4) + ' ' + str(ARigid) + '
        ' + str(E) + ' ' + str(G) + ' ' + str(JRigid) + ' ' + str(IyRigid) + ' ' +
        str(IzRigid) + ' ' + str(transfTagHorizRig) + '\n')
247     FrameID.write('element elasticBeamColumn '+ str(10000*(j+1) + 7) + ' ' +
        str(10000*(j+1) + 50*(3) + 4) + ' ' + str(10000*(j+1) + 50*(15) + 4) + ' ' +
        str(ARigid) + ' ' + str(E) + ' ' + str(G) + ' ' + str(JRigid) + ' ' + str(IyRigid)
        + ' ' + str(IzRigid) + ' ' + str(transfTagHorizRig) + '\n')
248     FrameID.write('element elasticBeamColumn '+ str(10000*(j+1) + 8) + ' ' +
        str(10000*(j+1) + 50*(15) + 4) + ' ' + str(10000*(j+1) + 50*(16) + 4) + ' ' +
        str(ARigid) + ' ' + str(E) + ' ' + str(G) + ' ' + str(JRigid) + ' ' + str(IyRigid)
        + ' ' + str(IzRigid) + ' ' + str(transfTagHorizRig) + '\n')
249     FrameID.write('element elasticBeamColumn '+ str(10000*(j+1) + 9) + ' ' +
        str(10000*(j+1) + 50*(16) + 4) + ' ' + str(10000*(j+1) + 50*(4) + 4) + ' ' +
        str(ARigid) + ' ' + str(E) + ' ' + str(G) + ' ' + str(JRigid) + ' ' + str(IyRigid)
        + ' ' + str(IzRigid) + ' ' + str(transfTagHorizRig) + '\n')
250     FrameID.write('element elasticBeamColumn '+ str(10000*(j+1) + 10) + ' ' +
        str(10000*(j+1) + 50*(4) + 4) + ' ' + str(10000*(j+1) + 4) + ' ' + str(ARigid) + '
        ' + str(E) + ' ' + str(G) + ' ' + str(JRigid) + ' ' + str(IyRigid) + ' ' +
        str(IzRigid) + ' ' + str(transfTagHorizRig) + '\n')
251
252
```

```
253     # EW wall lines
254     ops.element('elasticBeamColumn', 10000*(j+1) + 11, 10000*(j+1) + 1, 10000*(j+1) +
        50*(5) + 14, AbRigid, Eb, Gb, JbRigid, IybRigid, IzbRigid, transfTagHorizRig)
255     ops.element('elasticBeamColumn', 10000*(j+1) + 12, 10000*(j+1) + 50*(5) + 18,
        10000*(j+1)+ 50*(17) + 4, AbRigid, Eb, Gb, JbRigid, IybRigid, IzbRigid,
        transfTagHorizRig)
256     ops.element('elasticBeamColumn', 10000*(j+1) + 13, 10000*(j+1) + 50*(17) + 4,
        10000*(j+1)+ 50*(9) + 14, AbRigid, Eb, Gb, JbRigid, IybRigid, IzbRigid,
        transfTagHorizRig)
257     ops.element('elasticBeamColumn', 10000*(j+1) + 14, 10000*(j+1) + 50*(9) + 18,
        10000*(j+1) + 3, AbRigid, Eb, Gb, JbRigid, IybRigid, IzbRigid, transfTagHorizRig)
258
259     ops.element('elasticBeamColumn', 10000*(j+1) + 15, 10000*(j+1) + 50*(13) + 4,
        10000*(j+1) + 50*(6) + 14, AbRigid, Eb, Gb, JbRigid, IybRigid, IzbRigid,
        transfTagHorizRig)
260     ops.element('elasticBeamColumn', 10000*(j+1) + 16, 10000*(j+1) + 50*(6) + 18,
        10000*(j+1)+ 50*(18) + 4, AbRigid, Eb, Gb, JbRigid, IybRigid, IzbRigid,
        transfTagHorizRig)
261     ops.element('elasticBeamColumn', 10000*(j+1) + 17, 10000*(j+1) + 50*(18) + 4,
        10000*(j+1)+ 50*(10) + 14, AbRigid, Eb, Gb, JbRigid, IybRigid, IzbRigid,
        transfTagHorizRig)
262     ops.element('elasticBeamColumn', 10000*(j+1) + 18, 10000*(j+1) + 50*(10) + 18,
        10000*(j+1) + 50*(15) + 4, AbRigid, Eb, Gb, JbRigid, IybRigid, IzbRigid,
        transfTagHorizRig)
263
264     ops.element('elasticBeamColumn', 10000*(j+1) + 19, 10000*(j+1) + 50*(14) + 4,
        10000*(j+1) + 50*(7) + 14, AbRigid, Eb, Gb, JbRigid, IybRigid, IzbRigid,
        transfTagHorizRig)
265     ops.element('elasticBeamColumn', 10000*(j+1) + 20, 10000*(j+1) + 50*(7) + 18,
        10000*(j+1)+ 50*(19) + 4, AbRigid, Eb, Gb, JbRigid, IybRigid, IzbRigid,
        transfTagHorizRig)
266     ops.element('elasticBeamColumn', 10000*(j+1) + 21, 10000*(j+1) + 50*(19) + 4,
        10000*(j+1)+ 50*(11) + 14, AbRigid, Eb, Gb, JbRigid, IybRigid, IzbRigid,
        transfTagHorizRig)
267     ops.element('elasticBeamColumn', 10000*(j+1) + 22, 10000*(j+1) + 50*(11) + 18,
        10000*(j+1) + 50*(16) + 4, AbRigid, Eb, Gb, JbRigid, IybRigid, IzbRigid,
        transfTagHorizRig)
268
269     ops.element('elasticBeamColumn', 10000*(j+1) + 23, 10000*(j+1) + 2, 10000*(j+1) +
        50*(8) + 14, AbRigid, Eb, Gb, JbRigid, IybRigid, IzbRigid, transfTagHorizRig)
270     ops.element('elasticBeamColumn', 10000*(j+1) + 24, 10000*(j+1) + 50*(8) + 18,
        10000*(j+1)+ 50*(20) + 4, AbRigid, Eb, Gb, JbRigid, IybRigid, IzbRigid,
        transfTagHorizRig)
271     ops.element('elasticBeamColumn', 10000*(j+1) + 25, 10000*(j+1) + 50*(20) + 4,
        10000*(j+1)+ 50*(12) + 14, AbRigid, Eb, Gb, JbRigid, IybRigid, IzbRigid,
        transfTagHorizRig)
272     ops.element('elasticBeamColumn', 10000*(j+1) + 26, 10000*(j+1) + 50*(12) + 18,
        10000*(j+1) + 4, AbRigid, Eb, Gb, JbRigid, IybRigid, IzbRigid, transfTagHorizRig)
273
274     EleXTrack.extend([10000*(j+1) + 11, 10000*(j+1) + 12, 10000*(j+1) + 13, 10000*(j+1)
        + 14, 10000*(j+1) + 15, 10000*(j+1) + 16, 10000*(j+1) + 17, 10000*(j+1) + 18,
        10000*(j+1) + 19, 10000*(j+1) + 20, 10000*(j+1) + 21, 10000*(j+1) + 22, 10000*(j+1)
        + 23, 10000*(j+1) + 24, 10000*(j+1) + 25, 10000*(j+1) + 26])
275
276     ExportID.write('element elasticBeamColumn '+ str(10000*(j+1) + 11) + ' ' +
        str(10000*(j+1) + 1) + ' ' + str(10000*(j+1) + 50*(5) + 14) + ' ' + str(ARigid) + '
        ' + str(E) + ' ' + str(G) + ' ' + str(JRigid) + ' ' + str(IyRigid) + ' ' +
        str(IzRigid) + ' ' + str(transfTagHorizRig) + '\n')
277     ExportID.write('element elasticBeamColumn '+ str(10000*(j+1) + 12) + ' ' +
        str(10000*(j+1) + 50*(5) + 18) + ' ' + str(10000*(j+1) + 50*(17) + 4) + ' ' +
        str(ARigid) + ' ' + str(E) + ' ' + str(G) + ' ' + str(JRigid) + ' ' + str(IyRigid)
        + ' ' + str(IzRigid) + ' ' + str(transfTagHorizRig) + '\n')
278     ExportID.write('element elasticBeamColumn '+ str(10000*(j+1) + 13) + ' ' +
        str(10000*(j+1) + 50*(17) + 4) + ' ' + str(10000*(j+1) + 50*(9) + 14) + ' ' +
        str(ARigid) + ' ' + str(E) + ' ' + str(G) + ' ' + str(JRigid) + ' ' + str(IyRigid)
        + ' ' + str(IzRigid) + ' ' + str(transfTagHorizRig) + '\n')
```

```
279         ExportID.write('element elasticBeamColumn '+ str(10000*(j+1) + 14) + ' ' +
            str(10000*(j+1) + 50*(9) + 18) + ' ' + str(10000*(j+1) + 3) + ' ' + str(ARigid) + '
            ' + str(E) + ' ' + str(G) + ' ' + str(JRigid) + ' ' + str(IyRigid) + ' ' +
            str(IzRigid) + ' ' + str(transfTagHorizRig) + '\n')
280
281         ExportID.write('element elasticBeamColumn '+ str(10000*(j+1) + 15) + ' ' +
            str(10000*(j+1) + 50*(13) + 4) + ' ' + str(10000*(j+1) + 50*(6) + 14) + ' ' +
            str(ARigid) + ' ' + str(E) + ' ' + str(G) + ' ' + str(JRigid) + ' ' + str(IyRigid)
            + ' ' + str(IzRigid) + ' ' + str(transfTagHorizRig) + '\n')
282         ExportID.write('element elasticBeamColumn '+ str(10000*(j+1) + 16) + ' ' +
            str(10000*(j+1) + 50*(6) + 18) + ' ' + str(10000*(j+1) + 50*(18) + 4) + ' ' +
            str(ARigid) + ' ' + str(E) + ' ' + str(G) + ' ' + str(JRigid) + ' ' + str(IyRigid)
            + ' ' + str(IzRigid) + ' ' + str(transfTagHorizRig) + '\n')
283         ExportID.write('element elasticBeamColumn '+ str(10000*(j+1) + 17) + ' ' +
            str(10000*(j+1) + 50*(18) + 4) + ' ' + str(10000*(j+1) + 50*(10) + 14) + ' ' +
            str(ARigid) + ' ' + str(E) + ' ' + str(G) + ' ' + str(JRigid) + ' ' + str(IyRigid)
            + ' ' + str(IzRigid) + ' ' + str(transfTagHorizRig) + '\n')
284         ExportID.write('element elasticBeamColumn '+ str(10000*(j+1) + 18) + ' ' +
            str(10000*(j+1) + 50*(10) + 18) + ' ' + str(10000*(j+1) + 50*(15) + 4) + ' ' +
            str(ARigid) + ' ' + str(E) + ' ' + str(G) + ' ' + str(JRigid) + ' ' + str(IyRigid)
            + ' ' + str(IzRigid) + ' ' + str(transfTagHorizRig) + '\n')
285
286         ExportID.write('element elasticBeamColumn '+ str(10000*(j+1) + 19) + ' ' +
            str(10000*(j+1) + 50*(14) + 4) + ' ' + str(10000*(j+1) + 50*(7) + 14) + ' ' +
            str(ARigid) + ' ' + str(E) + ' ' + str(G) + ' ' + str(JRigid) + ' ' + str(IyRigid)
            + ' ' + str(IzRigid) + ' ' + str(transfTagHorizRig) + '\n')
287         ExportID.write('element elasticBeamColumn '+ str(10000*(j+1) + 20) + ' ' +
            str(10000*(j+1) + 50*(7) + 18) + ' ' + str(10000*(j+1) + 50*(19) + 4) + ' ' +
            str(ARigid) + ' ' + str(E) + ' ' + str(G) + ' ' + str(JRigid) + ' ' + str(IyRigid)
            + ' ' + str(IzRigid) + ' ' + str(transfTagHorizRig) + '\n')
288         ExportID.write('element elasticBeamColumn '+ str(10000*(j+1) + 21) + ' ' +
            str(10000*(j+1) + 50*(19) + 4) + ' ' + str(10000*(j+1) + 50*(11) + 14) + ' ' +
            str(ARigid) + ' ' + str(E) + ' ' + str(G) + ' ' + str(JRigid) + ' ' + str(IyRigid)
            + ' ' + str(IzRigid) + ' ' + str(transfTagHorizRig) + '\n')
289         ExportID.write('element elasticBeamColumn '+ str(10000*(j+1) + 22) + ' ' +
            str(10000*(j+1) + 50*(11) + 18) + ' ' + str(10000*(j+1) + 50*(16) + 4) + ' ' +
            str(ARigid) + ' ' + str(E) + ' ' + str(G) + ' ' + str(JRigid) + ' ' + str(IyRigid)
            + ' ' + str(IzRigid) + ' ' + str(transfTagHorizRig) + '\n')
290
291         ExportID.write('element elasticBeamColumn '+ str(10000*(j+1) + 23) + ' ' +
            str(10000*(j+1) + 2) + ' ' + str(10000*(j+1) + 50*(8) + 14) + ' ' + str(ARigid) + '
            ' + str(E) + ' ' + str(G) + ' ' + str(JRigid) + ' ' + str(IyRigid) + ' ' +
            str(IzRigid) + ' ' + str(transfTagHorizRig) + '\n')
292         ExportID.write('element elasticBeamColumn '+ str(10000*(j+1) + 24) + ' ' +
            str(10000*(j+1) + 50*(8) + 18) + ' ' + str(10000*(j+1) + 50*(20) + 4) + ' ' +
            str(ARigid) + ' ' + str(E) + ' ' + str(G) + ' ' + str(JRigid) + ' ' + str(IyRigid)
            + ' ' + str(IzRigid) + ' ' + str(transfTagHorizRig) + '\n')
293         ExportID.write('element elasticBeamColumn '+ str(10000*(j+1) + 25) + ' ' +
            str(10000*(j+1) + 50*(20) + 4) + ' ' + str(10000*(j+1) + 50*(12) + 14) + ' ' +
            str(ARigid) + ' ' + str(E) + ' ' + str(G) + ' ' + str(JRigid) + ' ' + str(IyRigid)
            + ' ' + str(IzRigid) + ' ' + str(transfTagHorizRig) + '\n')
294         ExportID.write('element elasticBeamColumn '+ str(10000*(j+1) + 26) + ' ' +
            str(10000*(j+1) + 50*(12) + 18) + ' ' + str(10000*(j+1) + 4) + ' ' + str(ARigid) +
            ' ' + str(E) + ' ' + str(G) + ' ' + str(JRigid) + ' ' + str(IyRigid) + ' ' +
            str(IzRigid) + ' ' + str(transfTagHorizRig) + '\n')
295
296         FrameID.write('element elasticBeamColumn '+ str(10000*(j+1) + 11) + ' ' +
            str(10000*(j+1) + 1) + ' ' + str(10000*(j+1) + 50*(5) + 4) + ' ' + str(ARigid) + '
            ' + str(E) + ' ' + str(G) + ' ' + str(JRigid) + ' ' + str(IyRigid) + ' ' +
            str(IzRigid) + ' ' + str(transfTagHorizRig) + '\n')
297         FrameID.write('element elasticBeamColumn '+ str(10000*(j+1) + 12) + ' ' +
            str(10000*(j+1) + 50*(5) + 4) + ' ' + str(10000*(j+1) + 50*(17) + 4) + ' ' +
            str(ARigid) + ' ' + str(E) + ' ' + str(G) + ' ' + str(JRigid) + ' ' + str(IyRigid)
            + ' ' + str(IzRigid) + ' ' + str(transfTagHorizRig) + '\n')
298         FrameID.write('element elasticBeamColumn '+ str(10000*(j+1) + 13) + ' ' +
            str(10000*(j+1) + 50*(17) + 4) + ' ' + str(10000*(j+1) + 50*(9) + 4) + ' ' +
```

```
        str(ARigid) + ' ' + str(E) + ' ' + str(G) + ' ' + str(JRigid) + ' ' + str(IyRigid)
        + ' ' + str(IzRigid) + ' ' + str(transfTagHorizRig) + '\n')
299     FrameID.write('element elasticBeamColumn '+ str(10000*(j+1) + 14) + ' ' +
        str(10000*(j+1) + 50*(9) + 4) + ' ' + str(10000*(j+1) + 3) + ' ' + str(ARigid) + '
        ' + str(E) + ' ' + str(G) + ' ' + str(JRigid) + ' ' + str(IyRigid) + ' ' +
        str(IzRigid) + ' ' + str(transfTagHorizRig) + '\n')
300
301     FrameID.write('element elasticBeamColumn '+ str(10000*(j+1) + 15) + ' ' +
        str(10000*(j+1) + 50*(13) + 4) + ' ' + str(10000*(j+1) + 50*(6) + 4) + ' ' +
        str(ARigid) + ' ' + str(E) + ' ' + str(G) + ' ' + str(JRigid) + ' ' + str(IyRigid)
        + ' ' + str(IzRigid) + ' ' + str(transfTagHorizRig) + '\n')
302     FrameID.write('element elasticBeamColumn '+ str(10000*(j+1) + 16) + ' ' +
        str(10000*(j+1) + 50*(6) + 4) + ' ' + str(10000*(j+1) + 50*(18) + 4) + ' ' +
        str(ARigid) + ' ' + str(E) + ' ' + str(G) + ' ' + str(JRigid) + ' ' + str(IyRigid)
        + ' ' + str(IzRigid) + ' ' + str(transfTagHorizRig) + '\n')
303     FrameID.write('element elasticBeamColumn '+ str(10000*(j+1) + 17) + ' ' +
        str(10000*(j+1) + 50*(18) + 4) + ' ' + str(10000*(j+1) + 50*(10) + 4) + ' ' +
        str(ARigid) + ' ' + str(E) + ' ' + str(G) + ' ' + str(JRigid) + ' ' + str(IyRigid)
        + ' ' + str(IzRigid) + ' ' + str(transfTagHorizRig) + '\n')
304     FrameID.write('element elasticBeamColumn '+ str(10000*(j+1) + 18) + ' ' +
        str(10000*(j+1) + 50*(10) + 4) + ' ' + str(10000*(j+1) + 50*(15) + 4) + ' ' +
        str(ARigid) + ' ' + str(E) + ' ' + str(G) + ' ' + str(JRigid) + ' ' + str(IyRigid)
        + ' ' + str(IzRigid) + ' ' + str(transfTagHorizRig) + '\n')
305
306     FrameID.write('element elasticBeamColumn '+ str(10000*(j+1) + 19) + ' ' +
        str(10000*(j+1) + 50*(14) + 4) + ' ' + str(10000*(j+1) + 50*(7) + 4) + ' ' +
        str(ARigid) + ' ' + str(E) + ' ' + str(G) + ' ' + str(JRigid) + ' ' + str(IyRigid)
        + ' ' + str(IzRigid) + ' ' + str(transfTagHorizRig) + '\n')
307     FrameID.write('element elasticBeamColumn '+ str(10000*(j+1) + 20) + ' ' +
        str(10000*(j+1) + 50*(7) + 4) + ' ' + str(10000*(j+1) + 50*(19) + 4) + ' ' +
        str(ARigid) + ' ' + str(E) + ' ' + str(G) + ' ' + str(JRigid) + ' ' + str(IyRigid)
        + ' ' + str(IzRigid) + ' ' + str(transfTagHorizRig) + '\n')
308     FrameID.write('element elasticBeamColumn '+ str(10000*(j+1) + 21) + ' ' +
        str(10000*(j+1) + 50*(19) + 4) + ' ' + str(10000*(j+1) + 50*(11) + 4) + ' ' +
        str(ARigid) + ' ' + str(E) + ' ' + str(G) + ' ' + str(JRigid) + ' ' + str(IyRigid)
        + ' ' + str(IzRigid) + ' ' + str(transfTagHorizRig) + '\n')
309     FrameID.write('element elasticBeamColumn '+ str(10000*(j+1) + 22) + ' ' +
        str(10000*(j+1) + 50*(11) + 4) + ' ' + str(10000*(j+1) + 50*(16) + 4) + ' ' +
        str(ARigid) + ' ' + str(E) + ' ' + str(G) + ' ' + str(JRigid) + ' ' + str(IyRigid)
        + ' ' + str(IzRigid) + ' ' + str(transfTagHorizRig) + '\n')
310
311     FrameID.write('element elasticBeamColumn '+ str(10000*(j+1) + 23) + ' ' +
        str(10000*(j+1) + 2) + ' ' + str(10000*(j+1) + 50*(8) + 4) + ' ' + str(ARigid) + '
        ' + str(E) + ' ' + str(G) + ' ' + str(JRigid) + ' ' + str(IyRigid) + ' ' +
        str(IzRigid) + ' ' + str(transfTagHorizRig) + '\n')
312     FrameID.write('element elasticBeamColumn '+ str(10000*(j+1) + 24) + ' ' +
        str(10000*(j+1) + 50*(8) + 4) + ' ' + str(10000*(j+1) + 50*(20) + 4) + ' ' +
        str(ARigid) + ' ' + str(E) + ' ' + str(G) + ' ' + str(JRigid) + ' ' + str(IyRigid)
        + ' ' + str(IzRigid) + ' ' + str(transfTagHorizRig) + '\n')
313     FrameID.write('element elasticBeamColumn '+ str(10000*(j+1) + 25) + ' ' +
        str(10000*(j+1) + 50*(20) + 4) + ' ' + str(10000*(j+1) + 50*(12) + 4) + ' ' +
        str(ARigid) + ' ' + str(E) + ' ' + str(G) + ' ' + str(JRigid) + ' ' + str(IyRigid)
        + ' ' + str(IzRigid) + ' ' + str(transfTagHorizRig) + '\n')
314     FrameID.write('element elasticBeamColumn '+ str(10000*(j+1) + 26) + ' ' +
        str(10000*(j+1) + 50*(12) + 4) + ' ' + str(10000*(j+1) + 4) + ' ' + str(ARigid) + '
        ' + str(E) + ' ' + str(G) + ' ' + str(JRigid) + ' ' + str(IyRigid) + ' ' +
        str(IzRigid) + ' ' + str(transfTagHorizRig) + '\n')
315
316
317     # Floor rigid diaphragm elements ----------------------------------------
318     diaphragm1_slavenodes = [10000*(j+1) + 1, 10000*(j+1) + 50*(1) + 14, 10000*(j+1) +
        50*(1) + 4, 10000*(j+1) + 50*(1) + 18, 10000*(j+1) + 50*(13) + 4, \
319                              10000*(j+1) + 50*(14) + 4, 10000*(j+1) + 50*(2) + 14,
                             10000*(j+1) + 50*(2) + 4, 10000*(j+1) + 50*(2) + 18,
                             10000*(j+1) + 2, \
320                          10000*(j+1) + 50*(8) + 14, 10000*(j+1) + 50*(8) + 4,
```

```
                                10000*(j+1) + 50*(8) + 18, 10000*(j+1) + 50*(20) + 4,
                                10000*(j+1) + 50*(12) + 14, 10000*(j+1) + 50*(12) + 4,
                                10000*(j+1) + 50*(12) + 18, \
321                             10000*(j+1) + 4, 10000*(j+1) + 50*(4) + 18, 10000*(j+1) +
                                50*(4) + 4, 10000*(j+1) + 50*(4) + 14, 10000*(j+1) +
                                50*(16) + 4, \
322                             10000*(j+1) + 50*(15) + 4, 10000*(j+1) + 50*(3) + 18,
                                10000*(j+1) + 50*(3) + 4, 10000*(j+1) + 50*(3) + 14,
                                10000*(j+1) + 3, \
323                             10000*(j+1) + 50*(9) + 18, 10000*(j+1) + 50*(9) + 4,
                                10000*(j+1) + 50*(9) + 14, 10000*(j+1) + 50*(17) + 4,
                                10000*(j+1) + 50*(5) + 18, 10000*(j+1) + 50*(5) + 4,
                                10000*(j+1) + 50*(5) + 14]
324
325         ops.rigidDiaphragm(3, 10000*(j+1) + 11, *diaphragm1_slavenodes)
326         str1 = ' '.join(str(e) for e in diaphragm1_slavenodes)
327         ExportID.write('rigidDiaphragm 3 ' + str(10000*(j+1) + 11) + ' ' + str1 + '\n')
328
329         diaphragm1corner_slavenodes = [10000*(j+1) + 1, 10000*(j+1) + 2, 10000*(j+1) + 4,
            10000*(j+1) + 3]
330         str1 = ' '.join(str(e) for e in diaphragm1corner_slavenodes)
331         FrameID.write('rigidDiaphragm 3 ' + str(10000*(j+1) + 11) + ' ' + str1 + '\n')
332
333
```

```
# -*- coding: utf-8 -*-
"""
Created on Tue Jun 14 18:52:17 2022
GENERATE_mass.py
@author: Amanpreet Singh
"""

SW_NS_Weight = [0.83781, 0.85065, 0.83781, 0.83781, 0.83781, 0.62488]
SW_EW_Corridor_Weight = [4.286247259, 4.837600634, 4.286247259, 4.286247259, 4.286247259, 4.450566348]
SW_EW_Edge_Weight = [1.631397411, 1.804136466, 1.631397411, 1.631397411, 1.631397411, 1.632121228]

GW_NS_Weight = [0.359061429, 0.364564286, 0.359061429, 0.359061429, 0.359061429, 0.267805714]
GW_EW_Corridor_Weight = [1.633243936, 1.920407152, 1.633243936, 1.633243936, 1.633243936, 1.718826794]
GW_EW_Edge_Weight = [3.585508867, 3.993065077, 3.585508867, 3.585508867, 3.585508867, 3.587216624]

TR_Weight = [0.06460125, 0.0393225, 0.02527875, 0.018725, 0.01217125, 0.]


k = nNodesEle
#mass(nodeTag, *massValues)
for j in range(nStory):

    # NS Shear wall node mass (Y-axis)-------------------------------------
    for i in range(SW_NS_coord.shape[0]):

        ops.mass(10000*(j+1) + 50*(i+1) + k+1, *[SW_NS_Weight[j]/g, SW_NS_Weight[j]/g, 0, 0, 0, 0])
        ops.mass(10000*(j+1) + 50*(i+1) + 10 + k+1, *[TR_Weight[j]/g, TR_Weight[j]/g, 0, 0, 0, 0])
        ops.mass(10000*(j+1) + 50*(i+1) + 14 + k+1, *[TR_Weight[j]/g, TR_Weight[j]/g, 0, 0, 0, 0])

    # EW Shear wall node mass (X-axis)-------------------------------------
    for i in range(SW_EW_coord.shape[0]):

        if i == 0 or i == 3 or i == 4 or i == 7:
            ops.mass(10000*(j+1) + 50*(i+1 + SW_NS_coord.shape[0]) + k+1,
            *[SW_EW_Edge_Weight[j]/g, SW_EW_Edge_Weight[j]/g, 0, 0, 0, 0])
        if i == 1 or i == 2 or i == 5 or i == 6:
            ops.mass(10000*(j+1) + 50*(i+1 + SW_NS_coord.shape[0]) + k+1,
            *[SW_EW_Corridor_Weight[j]/g, SW_EW_Corridor_Weight[j]/g, 0, 0, 0, 0])

        ops.mass(10000*(j+1) + 50*(i+1 + SW_NS_coord.shape[0]) + 10 + k+1,
        *[TR_Weight[j]/g, TR_Weight[j]/g, 0, 0, 0, 0])
        ops.mass(10000*(j+1) + 50*(i+1 + SW_NS_coord.shape[0]) + 14 + k+1,
        *[TR_Weight[j]/g, TR_Weight[j]/g, 0, 0, 0, 0])

    # NS Gravity wall nodes (Y-axis)---------------------------------------
    for i in range(GW_NS_coord.shape[0]):

        ops.mass(10000*(j+1) + 50*(i+1 + SW_NS_coord.shape[0] + SW_EW_coord.shape[0]) +
        k+1, *[GW_NS_Weight[j]/g, GW_NS_Weight[j]/g, 0, 0, 0, 0])

    # EW Gravity wall nodes (X-axis)---------------------------------------
    for i in range(GW_EW_coord.shape[0]):

        if i == 0 or i == 3:
            ops.mass(10000*(j+1) + 50*(i+1 + SW_NS_coord.shape[0] +
            SW_EW_coord.shape[0] + GW_NS_coord.shape[0]) + k+1,
            *[GW_EW_Edge_Weight[j]/g, GW_EW_Edge_Weight[j]/g, 0, 0, 0, 0])
        if i == 1 or i == 2:
```

```
52              ops.mass(10000*(j+1) + 50*(i+1 + SW_NS_coord.shape[0] +
                SW_EW_coord.shape[0] + GW_NS_coord.shape[0]) + k+1,
                *[GW_EW_Corridor_Weight[j]/g, GW_EW_Corridor_Weight[j]/g, 0, 0, 0, 0])
53
54
```

```
# -*- coding: utf-8 -*-
"""
Created on Mon Jun 13 11:52:15 2022
Analysis_Modal.py
@author: Amanpreet Singh
"""

ModalAnalysisDirectory = "ModalAnalysis"
ModeShapePreGravDirectory = "PreGravity"
ModeShapePostGravDirectory = "PostGravity"
ModeShapePostTHADirectory = "PostTHA"

if not os.path.exists(ModalAnalysisDirectory):
    os.mkdir(ModalAnalysisDirectory)
    os.makedirs(os.path.join(ModalAnalysisDirectory,ModeShapePreGravDirectory),
    exist_ok = True)
    os.makedirs(os.path.join(ModalAnalysisDirectory,ModeShapePostGravDirectory),
    exist_ok = True)
    os.makedirs(os.path.join(ModalAnalysisDirectory,ModeShapePostTHADirectory),
    exist_ok = True)

omega = []
F = []
T = []
#lambda_eig = ops.eigen('-fullGenLapack', num_modes)
lambda_eig = ops.eigen('-genBandArpack', num_modes)
ops.modalProperties("-print", "-file", "ModalReport.txt", "-unorm") # perform modal
analysis, and print results

for lam in lambda_eig:
    omega.extend([math.sqrt(lam)])
    F.extend([math.sqrt(lam)/(2*pi)])
    T.extend([(2*pi)/math.sqrt(lam)])

if GravityAnalysisDone == 'No' or GravityAnalysisDone == 'no' or GravityAnalysisDone ==
'NO':
    PeriodFile =
    open(os.path.join(ModalAnalysisDirectory,ModeShapePreGravDirectory,'TimePeriods.txt')
    , 'w')
    PeriodFile.write(' '.join(str(e) for e in T))
elif GravityAnalysisDone == 'Yes' and THAnalysisDone != 'Yes':
    PeriodFile =
    open(os.path.join(ModalAnalysisDirectory,ModeShapePostGravDirectory,'TimePeriods.txt'
    ), 'w')
    PeriodFile.write(' '.join(str(e) for e in T))
elif THAnalysisDone == 'Yes':
    PeriodFile =
    open(os.path.join(ModalAnalysisDirectory,ModeShapePostTHADirectory,'TimePeriods.txt')
    , 'w')
    PeriodFile.write(' '.join(str(e) for e in T))


PeriodFile.close()


for iMode in range(num_modes):

    if GravityAnalysisDone == 'No' or GravityAnalysisDone == 'no' or
    GravityAnalysisDone == 'NO':
        modeFile =
        open(os.path.join(ModalAnalysisDirectory,ModeShapePreGravDirectory,'ModeShape_'
        + str(iMode+1) + '.txt'), 'w')
    elif GravityAnalysisDone == 'Yes' and THAnalysisDone != 'Yes':
        modeFile =
        open(os.path.join(ModalAnalysisDirectory,ModeShapePostGravDirectory,'ModeShape_'
        + str(iMode+1) + '.txt'), 'w')
```

```
51      elif THAnalysisDone == 'Yes':
52          modeFile =
            open(os.path.join(ModalAnalysisDirectory,ModeShapePostTHADirectory,'ModeShape_'
            + str(iMode+1) + '.txt'), 'w')
53
54      for i in range(len(Nodes)):
55          vector = ops.nodeEigenvector(Nodes[i], iMode+1)
56          modeFile.write(str(Nodes[i]) + ' ' + ' '.join(str(e) for e in vector) + '\n')
57
58      modeFile.close()
59
```

```
# -*- coding: utf-8 -*-
"""
Created on Tue Jun 14 10:51:40 2022
Analysis_Gravity.py
@author: Amanpreet Singh
"""

TR_EWCor_Weight = [0.436553422, 0.45296082, 0.397230922, 0.390677172, 0.384123422, 0.175851284]
TR_EWExt_Weight = [0.294857357, 0.295384317, 0.255534857, 0.248981107, 0.242427357, 0.175851284]
TR_NS_Weight = [0.294857357, 0.295384317, 0.255534857, 0.248981107, 0.242427357, 0.175851284]

patternTagGravity = 1
ops.timeSeries('Constant', 1)
ops.pattern('Plain', patternTagGravity, 1)

k = nNodesEle
#load(nodeTag, *loadValues)
for j in range(nStory):

    # NS Shear wall node mass (Y-axis)-------------------------------------
    for i in range(SW_NS_coord.shape[0]):

        ops.load(10000*(j+1) + 50*(i+1) + 10 + k+1, *[0, 0, -TR_NS_Weight[j], 0, 0, 0])
        ops.load(10000*(j+1) + 50*(i+1) + 14 + k+1, *[0, 0, -TR_NS_Weight[j], 0, 0, 0])


    # EW Shear wall node mass (X-axis)-------------------------------------
    for i in range(SW_EW_coord.shape[0]):

        if i == 0 or i == 3 or i == 4 or i == 7:
            ops.load(10000*(j+1) + 50*(i+1 + SW_NS_coord.shape[0]) + 10 + k+1, *[0, 0, -TR_EWExt_Weight[j], 0, 0, 0])
            ops.load(10000*(j+1) + 50*(i+1 + SW_NS_coord.shape[0]) + 14 + k+1, *[0, 0, -TR_EWExt_Weight[j], 0, 0, 0])
        if i == 1 or i == 2 or i == 5 or i == 6:
            ops.load(10000*(j+1) + 50*(i+1 + SW_NS_coord.shape[0]) + 10 + k+1, *[0, 0, -TR_EWCor_Weight[j], 0, 0, 0])
            ops.load(10000*(j+1) + 50*(i+1 + SW_NS_coord.shape[0]) + 14 + k+1, *[0, 0, -TR_EWCor_Weight[j], 0, 0, 0])


# Define analysis parameters
NStepGravity = 10
lambdaGravity = 1./NStepGravity
ops.integrator('LoadControl', lambdaGravity)
ops.system('BandGeneral')
ops.test('NormDispIncr', 1e-06, 500, 0)
ops.numberer('Plain')
ops.constraints('Transformation')
ops.algorithm('Newton')
ops.analysis('Static')
ok = ops.analyze(NStepGravity)

if ok != 0:
    print('NOT CONVERGED for Gravity.\n')
else:
    print('GRAVITY ANALYSIS DONE!!\n')

ops.loadConst('-time', 0.0)
ops.wipeAnalysis()
GravityAnalysisDone = 'Yes'
```

```
# -*- coding: utf-8 -*-
"""
Created on Mon Jun 13 22:31:07 2022
Analysis_TimeHistory.py
@author: Amanpreet Singh
"""

GMdirectionX = 1            # ground-motion direction in global coordinates
GMdirectionY = 2            # ground-motion direction in global coordinates

GMfactX = 1.*g              # GM scaling factor in X direction
GMfactY = 1.*g              # GM scaling factor in Y direction

# Read ground-motion-analysis parameters
dt = 1/240*sec
gmX_file = 'Eq25_gAccX.txt'
gmY_file = 'Eq25_gAccY.txt'
f = open(gmX_file, 'r')   # GM input filename in X direction
GMData = f.readlines()
GMDataAllX = copy.deepcopy(GMData)
f.close()

f = open(gmY_file, 'r')   # GM input filename in Y direction
GMData = f.readlines()
GMDataAllY = copy.deepcopy(GMData)
f.close()

NPTS_X = len(GMDataAllX)
NPTS_Y = len(GMDataAllY)
NPTS = min(NPTS_X,NPTS_Y)     # number of ground acceleration data points
DtAnalysis = dt         # time-step Dt for lateral analysis
TmaxAnalysis = dt*NPTS  # duration of earthquake

# ########################################
# ############# ASSIGN DAMPING ############
# ########################################

if DoModalAnalysis == 'Yes':
    w1 = omega[0]
    w2 = omega[1]
else:
    exec(open('Analysis_Modal.py').read())
    print('Modal Analysis Results Post - Gravity\n')
    print('---------------------------------------\n')
    for i in range(num_modes):
        print('T' + str(i+1) + ' = ' + str(T[i]) + 's\n')
    w1 = omega[0] # Mode 1
    w2 = omega[1] # Mode 2


# define DAMPING
# D=alphaM*M + betaKcurr*Kcurrent + betaKcomm*KlastCommit + beatKinit*Kinitial
chi = 0.05 # 5% damping ratio
alphaM = 2.*chi*w1*w2/(w1+w2)
betaKinit = 2.*chi/(w1+w2)
betaKcurr = 0.0
betaKcomm = 0.0
ops.rayleigh(alphaM, betaKcurr, betaKinit, betaKcomm)


#  Set up timeSeries and UniformExcitation patterns
TSTagX = 3
TSTagY = 4

ops.timeSeries('Path', TSTagX, '-dt', dt, '-filePath', gmX_file, '-factor', GMfactX)
ops.timeSeries('Path', TSTagY, '-dt', dt, '-filePath', gmY_file, '-factor', GMfactY)
```

```
67
68  IDloadTag_TH_X = 4  # LoadTag for Uniform ground motion excitation
69  IDloadTag_TH_Y = 5  # LoadTag for Uniform ground motion excitation
70
71  ops.pattern('UniformExcitation', IDloadTag_TH_X, GMdirectionX, '-accel', TSTagX)    #
    create Uniform excitation
72  ops.pattern('UniformExcitation', IDloadTag_TH_Y, GMdirectionY, '-accel', TSTagY)    #
    create Uniform excitation
73
74
75  # ############# SET ANALYSIS PARAMETERS ############
76  NewmarkGamma = 0.50 # Newmark-integrator gamma parameter (also HHT)
77  NewmarkBeta = 0.25  # Newmark-integrator beta parameter
78  TolDynamic = 1.e-6
79  maxNumIterDynamic = 200
80
81  ops.integrator('Newmark', NewmarkGamma, NewmarkBeta)
82  ops.system('BandGeneral')
83  ops.test('EnergyIncr', TolDynamic, maxNumIterDynamic, 0)
84  ops.numberer('Plain')
85  ops.constraints('Transformation')
86  ops.algorithm('Newton')
87  ops.analysis('Transient')
88
89  exec(open('Recorders_dyn.py').read())
90
91
92  # ############# RUN ANALYSIS ############
93  NSteps = int(TmaxAnalysis/DtAnalysis)
94  tCurrent = ops.getTime()
95  ok = 0
96
97  while tCurrent<=TmaxAnalysis and ok==0:
98      ok = ops.analyze(1, DtAnalysis)
99      if ok == 0:
100         print('TIME: ' + str(tCurrent) + ' >> CONVERGED\n')
101     tCurrent = ops.getTime()
102     if ok != 0:
103         print('Test Relative Force\n')
104         ops.test('RelativeNormUnbalance', TolDynamic, maxNumIterDynamic, 0)
105         ok = ops.analyze(1, DtAnalysis)
106     if ok != 0:
107         print('Test Relative Displacement\n')
108         ops.test('RelativeNormDispIncr', TolDynamic, maxNumIterDynamic, 0)
109         ok = ops.analyze(1, DtAnalysis)
110     if ok != 0:
111         print('ModifiedNewton\n')
112         ops.algorithm('ModifiedNewton', False, False) #algorithm('ModifiedNewton',
            secant=False, initial=False)
113         ok = ops.analyze(1, DtAnalysis)
114     if ok != 0:
115         print('Test Relative Energy\n')
116         ops.algorithm('Newton', False, True, False)
117         ops.test('RelativeEnergyIncr', TolDynamic, maxNumIterDynamic, 0)
118         ok = ops.analyze(1, DtAnalysis)
119     if ok != 0:
120         print('Newton Modified -initial\n')
121         ops.algorithm('ModifiedNewton', False, True) #algorithm('ModifiedNewton',
            secant=False, initial=False)
122         ops.test('RelativeEnergyIncr', TolDynamic, maxNumIterDynamic, 0)
123         ok = ops.analyze(1, DtAnalysis)
124     if ok != 0:
125         print('Test Relative Force\n')
126         ops.algorithm('Newton', False, True, False)
127         ops.test('RelativeNormUnbalance', TolDynamic, maxNumIterDynamic, 0)
128         ok = ops.analyze(1, DtAnalysis)
```

```
129         if ok != 0:
130             print('Test Relative Displ\n')
131             ops.test('RelativeNormDispIncr', TolDynamic, maxNumIterDynamic, 0)
132             ok = ops.analyze(1, DtAnalysis)
133         if ok != 0:
134             print('Broyden\n')
135             ops.algorithm('Broyden', False, False, 8) #algorithm('Broyden', secant=False,
                initial=False, count=10)
136             ok = ops.analyze(1, DtAnalysis)
137         if ok != 0:
138             print('Newton Line Search\n')
139             ops.algorithm('NewtonLineSearch', False, False, False, False, 0.8, 10, 0.1,
                10.0) #algorithm('NewtonLineSearch', Bisection=False, Secant=False,
                RegulaFalsi=False, InitialInterpolated=False, tol=0.8, maxIter=10, minEta=0.1,
                maxEta=10.0)
140             ok = ops.analyze(1, DtAnalysis)
141         if ok != 0:
142             print('BFGS\n')
143             ops.algorithm('BFGS')
144             ok = ops.analyze(1, DtAnalysis)
145
146     print('\nTime-history response analysis complete\n')
147     ops.wipeAnalysis()
148     THAnalysisDone = 'Yes'
```

```
# -*- coding: utf-8 -*-
"""
Created on Tue Jun 14 00:40:01 2022
Recorders_dyn.py
@author: Amanpreet Singh
"""

ResultsDirectory = "Results_EQ25alt"
if not os.path.exists(ResultsDirectory):
    os.mkdir(ResultsDirectory)

ops.recorder('Node', '-file', str(ResultsDirectory) + '/absacclnX.txt', '-timeSeries', 3, '-time', '-node', *Nodes_frame, '-dof', 1, 'accel')
ops.recorder('Node', '-file', str(ResultsDirectory) + '/absacclnY.txt', '-timeSeries', 4, '-time', '-node', *Nodes_frame, '-dof', 2, 'accel')
#ops.recorder('Node', '-file', str(ResultsDirectory) + '/absacclnZ.txt', '-time', '-node', *Nodes_frame, '-dof', 3, 'accel')

ops.recorder('Node', '-file', str(ResultsDirectory) + '/SWX_dispX.txt', '-node', *NodesSWX, '-dof', 1, 'disp')
#ops.recorder('Node', '-file', str(ResultsDirectory) + '/SWX_dispY.txt', '-node', *NodesSWX, '-dof', 2, 'disp')
ops.recorder('Element', '-file', str(ResultsDirectory) + '/SWX_force.txt', '-ele', *EleSWX, 'force')
#ops.recorder('Element', '-file', str(ResultsDirectory) + '/SWX_elemdisp.txt', '-ele', *EleSWX, 'basicDisplacement')

ops.recorder('Node', '-file', str(ResultsDirectory) + '/GWX_dispX.txt', '-node', *NodesGWX, '-dof', 1, 'disp')
#ops.recorder('Node', '-file', str(ResultsDirectory) + '/GWX_dispY.txt', '-node', *NodesGWX, '-dof', 2, 'disp')
ops.recorder('Element', '-file', str(ResultsDirectory) + '/GWX_force.txt', '-ele', *EleGWX, 'force')
#ops.recorder('Element', '-file', str(ResultsDirectory) + '/GWX_elemdisp.txt', '-ele', *EleGWX, 'basicDisplacement')

ops.recorder('Node', '-file', str(ResultsDirectory) + '/TR1X_dispZ.txt', '-node', *NodesTR1X, '-dof', 3, 'disp')
ops.recorder('Node', '-file', str(ResultsDirectory) + '/TR2X_dispZ.txt', '-node', *NodesTR2X, '-dof', 3, 'disp')
ops.recorder('Element', '-file', str(ResultsDirectory) + '/TR1X_force.txt', '-ele', *EleTR1X, 'force')
ops.recorder('Element', '-file', str(ResultsDirectory) + '/TR2X_force.txt', '-ele', *EleTR2X, 'force')

ops.recorder('Node', '-file', str(ResultsDirectory) + '/TR1Y_dispZ.txt', '-node', *NodesTR1Y, '-dof', 3, 'disp')
ops.recorder('Node', '-file', str(ResultsDirectory) + '/TR2Y_dispZ.txt', '-node', *NodesTR2Y, '-dof', 3, 'disp')
ops.recorder('Element', '-file', str(ResultsDirectory) + '/TR1Y_force.txt', '-ele', *EleTR1Y, 'force')
ops.recorder('Element', '-file', str(ResultsDirectory) + '/TR2Y_force.txt', '-ele', *EleTR2Y, 'force')

for i in range(len(Nodes_frame)):
    ops.recorder('Node', '-file', str(ResultsDirectory) + '/dispNode_' + str(Nodes_frame[i]) + '.txt', '-time', '-node', Nodes_frame[i], '-dof', *[1, 2, 3], 'disp')

#ops.recorder('Node', '-file', str(ResultsDirectory) + '/reactionX.txt', '-node', *Nodes_base, '-dof', 1, 'reaction')
#ops.recorder('Node', '-file', str(ResultsDirectory) + '/reactionY.txt', '-node', *Nodes_base, '-dof', 2, 'reaction')
#ops.recorder('Node', '-file', str(ResultsDirectory) + '/reactionZ.txt', '-node', *Nodes_base, '-dof', 3, 'reaction')

```

```
43  #ops.recorder('Node', '-file', str(ResultsDirectory) + '/SWY_dispX.txt', '-node',
    *NodesSWY, '-dof', 1, 'disp')
44  ops.recorder('Node', '-file', str(ResultsDirectory) + '/SWY_dispY.txt', '-node',
    *NodesSWY, '-dof', 2, 'disp')
45  ops.recorder('Element', '-file', str(ResultsDirectory) + '/SWY_force.txt', '-ele',
    *EleSWY, 'force')
46
47  #ops.recorder('Node', '-file', str(ResultsDirectory) + '/GWY_dispX.txt', '-node',
    *NodesGWY, '-dof', 1, 'disp')
48  ops.recorder('Node', '-file', str(ResultsDirectory) + '/GWY_dispY.txt', '-node',
    *NodesGWY, '-dof', 2, 'disp')
49  ops.recorder('Element', '-file', str(ResultsDirectory) + '/GWY_force.txt', '-ele',
    *EleGWY, 'force')
50
51
```

Bibliography

ABAQUS (2014). "Abaqus theory guide", Version 6.14, Dassault Systems Simulia Corp, USA.

AISI (2007). "North American standard for cold-formed steel farming—Lateral design." *AISI S213-07*, American Iron and Steel Institute, Washington, D.C.

AISI (2012). "North American specification for the design of cold-formed steel structural members." *AISI S100-12*, American Iron and Steel Institute, Washington, D.C.

AISI (2017). "Cold-formed steel design manual." *AISI D100-17*, American Iron and Steel Institute, Washington, D.C.

AISI (2020a). "North American specification for the design of cold-formed steel structural members." *AISI S100-20*, American Iron and Steel Institute, Washington, D.C.

AISI (2020b). "North American standard for cold-formed steel structural framing." *AISI S240-20*, American Iron and Steel Institute, Washington, D.C.

AISI (2020c). "North American standard for seismic design of cold-formed steel structural systems." *AISI S400-20*, American Iron and Steel Institute, Washington, D.C.

ASCE/SEI (2010). "Minimum design loads for buildings and other structures." *ASCE/SEI 7-10*, American Society of Civil Engineers / Structural Engineering Institute, Reston, VA.

ASCE/SEI (2016). "Minimum design loads for buildings and other structures." *ASCE/SEI 7-16*, American Society of Civil Engineers / Structural Engineering Institute, Reston, VA.

ASCE/SEI (2017). "Seismic evaluation and retrofit of existing buildings." *ASCE/SEI 41-17*, American Society of Civil Engineers / Structural Engineering Institute, Reston, VA.

ASCE/SEI (2022). "Minimum design loads for buildings and other structures." *ASCE/SEI 7-22*, American Society of Civil Engineers / Structural Engineering Institute, Reston, VA.

ASTM (2014). "Standard specification for carbon structural steel." *A36/A36M-14*, ASTM, West Conshohocken, PA.

ASTM (2015a). "Standard specification for alloy-steel and stainless steel bolting for high temperature or high pressure service and other special purpose applications." *ASTM A193/A193M-15*, ASTM, West Conshohocken, PA.

ASTM (2015b). "Standard specification for high-strength steel bars for prestressed concrete." *ASTM A722/A722M-15*, ASTM, West Conshohocken, PA.

ASTM (2017). "Standard specification for steel sheet, zinc-coated (galvanized) or zinc-iron alloy-coated (galvannealed) by the hot-dip process." *ASTM A653/A653M-17*, ASTM, West Conshohocken, PA.

Balh, N., DaBreo, J., Ong-Tone, C., El-Saloussy, K., Yu, C., and Rogers, C. (2014). "Design of steel sheathed cold-formed steel framed shear walls." *Thin-Walled Structures*, 75, 76–86. DOI: 10.1016/j.tws.2013.10.023.

Bian, G., Padilla-Llano, D., Buonopane, S., Moen, C., and Schafer, B. (2015). "Opensees modeling of wood sheathed cold-formed steel framed shear walls." *Proceedings of Annual Stability Conference Structural Stability Research Council*, Nashville, TN.

Briere, V. and Rogers, C. (2017). "Higher capacity cold-formed steel sheathed and framed shear walls for mid-rise buildings: part 2." *Research Report RP17-6*, Department of Civil Engineering and Applied Mechanics, McGill University, Montréal, Canada.

Brière, V., Santos, V., and Rogers, C. (2018). "Cold-formed steel centre-sheathed (mid-ply) shear walls." *Soil Dynamics and Earthquake Engineering*, 114, 253–266. DOI: 10.1016/j.soildyn.2018.07.008.

Buonopane, S., Tun, T., and Schafer, B. (2014). "Fastener-based computational models for prediction of seismic behavior of cfs shear walls." *Proceedings of the 10th National Conference in Earthquake Engineering*, Anchorage, AK, Earthquake Engineering Research Institute.

Campiche, A., Fiorino, L., and Landolfo, R. (2020). "Numerical modelling of cfs two-storey sheathing-braced building under shaking-table excitations." *Journal of Constructional Steel Research*, 170, 106110. DOI: 10.1016/j.jcsr.2020.106110.

DaBreo, J., Balh, N., Ong-Tone, C., and Rogers, C. (2014). "Steel sheathed cold-formed steel framed shear walls subjected to lateral and gravity loading." *Thin-Walled Structures*, 74, 232–245. DOI: 10.1016/j.tws.2013.10.006.

Derveni, F., Gerasimidis, S., and Peterman, K. (2020). "Behavior of cold-formed steel shear walls sheathed with high-capacity sheathing." *Engineering Structures*, 225, 111280. DOI: 10.1016/j.engstruct.2020.111280.

ETABS (2023). "Building analysis and design", Computers & Structures, Inc., Berkeley, CA,

<https://www.csiamerica.com/products/etabs>.

Filiatrault, A., Fischer, D., Folz, B., and Uang, C. (2002). "Seismic testing of two-story woodframe house: Influence of wall finish materials." *ASCE Journal of Structural Engineering*, 128(10), 1337–1345. DOI: 10.1061/(ASCE)0733-9445(2002)128:10(1337).

Fiorino, L., Macillo, V., and Landolfo, R. (2017). "Shake table tests of a full-scale two-story sheathing-braced cold-formed steel building." *Engineering Structures*, 151, 633–647. DOI: 10.1016/j.engstruct.2017.08.056.

Folz, B. and Filiatrault, A. (2004). "Seismic analysis of woodframe structures. I: Model formulation." *ASCE Journal of Structural Engineering*, 130(9), 1353–1360. DOI: 10.1061/(ASCE)0733-9445(2004)130:9(1353).

Franklin, N., Ahmed, A., Teh, L., Heffernan, E., and McCarthy, T. (2019). "Efficient 3D lateral analysis of cold-formed steel buildings." *Journal of Constructional Steel Research*, 160, 16–22. DOI: 10.1016/j.jcsr.2019.05.029.

Gatto, K. and Uang, C. (2003). "Effects of finish materials and dynamic loading on the cyclic response of woodframe shearwalls." *ASCE Journal of Structural Engineering*, 129(10), 1384–1393. DOI: 10.1061/(ASCE)0733-9445(2003)129:10(1384).

Haghpanah, F. and Schafer, B. (2021). "Updated seismic fragility functions for cold-formed steel framed shear walls per FEMA P-58 methodology." *Engineering Structures*, 244, 112753. DOI: 10.1016/j.engstruct.2021.112753.

Hancock, J. and Bommer, J. (2005). "The effective number of cycles of earthquake ground motion." *Earthquake Engineering & Structural Dynamics*, 34(6), 637–664. DOI: 10.1002/eqe.437.

Hikita, K. (2006). "Impact of gravity loads on the lateral performance of light gauge steel frame / wood panel shear walls." Master thesis, Department of Civil Engineering and Applied Mechanics, McGill University, Montréal, Canada.

Hoehler, M., Smith, C., Hutchinson, T., Wang, X., Meacham, B., and Kamath, P. (2017). "Behavior of steel-sheathed shear walls subjected to seismic and fire loads." *Fire safety journal*, 91, 524–531. DOI: 10.1016/j.firesaf.2017.03.021.

Hutchinson, T., Wang, X., Hegemier, G., Kamath, P., and Meacham, B. (2021). "Earthquake and postearthquake fire testing of a midrise cold-formed steel-framed building. I: Building response and physical damage." *ASCE Journal of Structural Engineering*, 147(9), 04021125. DOI: 10.1061/(ASCE)ST.1943-541X.0003097.

Hutchinson, T., Wang, X., Hegemier, G., Meacham, B., Kamath, P., Sesma, F., and Holcomb,

K. (2017). "Earthquake and post-earthquake fire performance of a mid-rise cold-formed steel framed building." *Proceedings of 2017 SEAOC Convention*, San Diego, CA, Structural Engineers Association of California.

IBC (2018a). "IBC SEAOC Structural/Seismic Design Manual Vol. 2: Four story wood light-frame structure." International Code Council.

IBC (2018b). "International Building Code." International Code Council.

Kechidi, S. and Bourahla, N. (2016). "Deteriorating hysteresis model for cold-formed steel shear wall panel based on its physical and mechanical characteristics." *Thin-Walled Structures*, 98, 421–430. DOI: 10.1016/j.tws.2015.09.022.

Krawinkler, H., Parisi, F., Ibarra, L., Ayoub, A., and Medina, R. (2001). "Development of a testing protocol for woodframe structures." *CUREE Publication No. W-02*, Consortium of Universities for Research in Earthquake Engineering, Richmond, CA.

Landolfo, R., Iuorio, O., and Fiorino, L. (2018). "Experimental seismic performance evaluation of modular lightweight steel buildings within the ELISSA project." *Earthquake Engineering & Structural Dynamics*, 47(15), 2921–2943. DOI: 10.1002/eqe.3114.

Lee, T., Kato, M., Matsumiya, T., Suita, K., and Nakashima, M. (2007). "Seismic performance evaluation of non-structural components: drywall partitions." *Earthquake Engineering & Structural Dynamics*, 36(3), 367–382. DOI: 10.1002/eqe.638.

Leng, J., Peterman, K., Bian, G., Buonopane, S., and Schafer, B. (2017). "Modeling seismic response of a full-scale cold-formed steel-framed building." *Engineering Structures*, 153, 146–165. DOI: 10.1016/j.engstruct.2017.10.008.

Liu, P., Peterman, K., and Schafer, B. (2014). "Impact of construction details on osb-sheathed cold-formed steel framed shear walls." *Journal of Constructional Steel Research*, 101, 114–123. DOI: 10.1016/j.jcsr.2014.05.003.

Liu, P., Peterman, K., Yu, C., and Schafer, B. (2012). "Characterization of cold-formed steel shear wall behavior under cyclic loading for the CFS-NEES building." *Proceedings of International Specialty Conference on Cold-Formed Steel Structures*, St. Louis, MO, Missouri University of Science and Technology.

Lowes, L. and Altoontash, A. (2003). "Modeling reinforced-concrete beam-column joints subjected to cyclic loading." *ASCE Journal of Structural Engineering*, 129(12), 1686–1697. DOI: 10.1061/(ASCE)0733-9445(2003)129:12(1686).

Lu, S. (2015). "Influence of gypsum panels on the response of cold-formed steel framed shear walls." Master thesis, Department of Civil Engineering and Applied Mechanics, McGill

University, Montréal, Canada.

Macillo, V., Fiorino, L., and Landolfo, R. (2017). "Seismic response of cfs shear walls sheathed with nailed gypsum panels: Experimental tests." *Thin-Walled Structures*, 120, 161–171. DOI: 10.1016/j.tws.2017.08.022.

Madsen, R., Nakata, N., and Schafer, B. (2011). "Cfs-nees building structural design narrative." *Research Report RR01*, Johns Hopkins University, Baltimore, MD.

McKenna, F. (2011). "Opensees: a framework for earthquake engineering simulation." *Computing in Science & Engineering*, 13(4), 58–66.

McMullin, K. and Merrick, D. (2007). "Seismic damage thresholds for gypsum wallboard partition walls." *ASCE Journal of Structural Engineering*, 13(1), 22–29. DOI: 10.1061/(ASCE)ST.1943-541X.0001577.

Morello, D. (2009). "Seismic performance of multi-storey structures with cold-formed steel wood sheathed shear walls." Master thesis, Department of Civil Engineering and Applied Mechanics, McGill University, Montréal, Canada.

Morgan, K., Sorhouet, M., and Serrette, R. (2002). "Performance of CFS framed shear walls - alternative configurations." *Research Report LGSRG-06-02*, Department of Civil Engineering, Santa Clara University, Santa Clara, CA.

NAHB Research Center (1997). *Monotonic tests of cold-formed steel shear walls with openings*. Research Report RP97-1, Upper Marlboro, MD.

Nguyen, H., Hall, G., and Serrette, R. (1996). "Shear wall values for light weight steel framing." *Research Report LGSRG-3-96*, Department of Civil Engineering, Santa Clara University, Santa Clara, CA.

Ong-Tone, C. (2009). "Tests and evaluation of cold-formed steel frame / steel sheathed shear walls." Master thesis, Department of Civil Engineering and Applied Mechanics, McGill University, Montréal, Canada.

Pali, T., Macillo, V., Terracciano, M., Bucciero, B., Fiorino, L., and Landolfo, R. (2018). "In-plane quasi-static cyclic tests of nonstructural lightweight steel drywall partitions for seismic performance evaluation." *Earthquake Engineering & Structural Dynamics*, 47(6), 1566–1588. DOI: 10.1002/eqe.3031.

Pei, S. and Van de Lindt, J. (2009). "Coupled shear-bending formulation for seismic analysis of stacked wood shear wall systems." *Earthquake Engineering & Structural Dynamics*, 38(14), 1631–1647. DOI: 10.1002/eqe.926.

Pei, S. and van de Lindt, J. (2010). "Seismic Analysis Package for Wood frame Structures—Version 2.0: Users Manual for SAPWood for Windows", Colorado State University, Fort Collins, CO.

Pei, S. and Van de Lindt, J. (2011). "Seismic numerical modeling of a six-story light-frame wood building: Comparison with experiments." *Journal of Earthquake Engineering*, 15(6), 924–941. DOI: 10.1080/13632469.2010.544840.

Peterman, K. (2014). "Behavior of full-scale cold-formed steel buildings under seismic excitations." Doctoral dissertation, Johns Hopkins University, Baltimore, MD.

Peterman, K., Stehman, M., Madsen, R., Buonopane, S., Nakata, N., and Schafer, B. (2013). "Experimental seismic fragility of cold-formed steel framed gypsum partition walls." *ASCE Journal of Structural Engineering*, 139(8), 1285–1293. DOI: 10.1061/(ASCE)ST.1943-541X.0000657.

Peterman, K., Stehman, M., Madsen, R., Buonopane, S., Nakata, N., and Schafer, B. (2016). "Experimental seismic response of a full-scale cold-formed steel-framed building. I: System-level response." *ASCE Journal of Structural Engineering*, 142(12), 04016127. DOI: 10.1061/(ASCE)ST.1943-541X.0001577.

Petrone, C., Magliulo, G., Lopez, P., and Manfredi, G. (2015). "Seismic fragility of plasterboard partitions via in-plane quasi-static tests." *Earthquake Engineering & Structural Dynamics*, 44(14), 2589–2606. DOI: 10.1002/eqe.2600.

Rathje, E., Dawson, C., Padgett, J., Pinelli, J.-P., Stanzione, D., Adair, A., Arduino, P., Brandenberg, S., Cockerill, T., Dey, C., Esteva, M., Haan, Jr., F., Hanlon, M., Kareem, A., Lowes, L., Mock, S., and Mosqueda, G. (2017). "Designsafe: New cyberinfrastructure for natural hazards engineering." *ASCE Natural Hazards Review*, 18(3), 06017001. DOI: 10.1061/(ASCE)NH.1527-6996.0000246.

Restrepo, J. and Bersofsky, A. (2011). "Performance characteristics of light gage steel stud partition walls." *Thin-Walled Structures*, 49(2), 317–324. DOI: 10.1016/j.tws.2010.10.001.

Rizk, R. and Rogers, C. (2017). "Higher strength cold-formed steel framed / steel shear walls for mid-rise construction." *Research Report RP17-4*, Department of Civil Engineering and Applied Mechanics, McGill University, Montréal, Canada.

Salenikovich, A., Dolan, D., and Easterling, S. (2000). "Racking performance of long steel-frame shear walls." *Proceedings of Fifteenth International Specialty Conference on Cold-Formed Steel Structures*, St. Louis, MO, Missouri University of Science and Technology.

Santos, V. and Rogers, C. (2017). "Higher capacity cold-formed steel sheathed and framed shear walls for mid-rise buildings: part 1." *Research Report RP17-5*, Department of Civil

Engineering and Applied Mechanics, McGill University, Montréal, Canada.

SAP2000 (2023). "Structural analysis and design", Computers & Structures, Inc., Berkeley, CA, <https://www.csiamerica.com/products/sap2000>.

Schafer, B. (2019). "CUFSM 5.04 – Finite Strip Buckling Analysis of Thin-Walled Members", Department of Civil Engineering, Johns Hopkins University, Baltimore, USA, <https://www.ce.jhu.edu/cufsm>.

Schafer, B., Zhang, Z., and Haghpanah, F. (2020). "Overstrength in seismic design of cold-formed steel framed shear walls." *Proceedings of the Cold-Formed Steel Research Consortium Colloquium*, Baltimore, MD, Johns Hopkins University.

Schafer, B. W. (2011). "Cold-formed steel structures around the world: A review of recent advances in applications, analysis and design." *Steel Construction*, 4(3), 141–149. DOI: 10.1002/stco.201110019.

Serrette, R. (1997). "Additional shear wall values for light weight steel framing." *Report No. LGSRG-1-97*, Department of Civil Engineering, Santa Clara University, Santa Clara, CA.

Serrette, R., Encalada, J., Juadines, M., and Nguyen, H. (1997). "Static racking behavior of plywood, osb, gypsum, and fiberbond walls with metal framing." *ASCE Journal of Structural Engineering*, 123(8), 1079–1086. DOI: 10.1061/(ASCE)0733-9445(1997)123:8(1079).

Shamim, I., DaBreo, J., and Rogers, C. A. (2013). "Dynamic testing of single-and double-story steel-sheathed cold-formed steel-framed shear walls." *ASCE Journal of Structural Engineering*, 139(5), 807–817. DOI: 10.1061/(ASCE)ST.1943-541X.0000594.

Shamim, I. and Rogers, C. (2013). "Steel sheathed/CFS framed shear walls under dynamic loading: numerical modelling and calibration." *Thin-Walled Structures*, 71, 57–71. DOI: 10.1016/j.tws.2013.05.007.

Singh, A. and Hutchinson, T. (2018). "Finite element modeling and validation of steel sheathed cold-formed steel framed shear walls." *Proceedings of International Specialty Conference on Cold-Formed Steel Structures*, St. Louis, MO, Missouri University of Science and Technology.

Singh, A., Hutchinson, T., Torabian, S., Schafer, B., Peterman, K., Padgett, L., and Jones, H. (2022a). "Structural design narrative of the cfs-nheri 10-story test building for multi-dimensional shake table testing." *Proceedings of the Cold-Formed Steel Research Consortium Colloquium*, Baltimore, MD.

Singh, A., Hutchinson, T., Wang, X., Zhang, Z., Schafer, B., Derveni, F., Castaneda, H., and Peterman, K. (2021a). "Wall line tests: Phase 1 – shake table tests." *CFS-NHERI: Seismic Resiliency of Repetitively Framed Mid-Rise Cold-Formed Steel Buildings*, DesignSafe-CI.

DOI: 10.17603/ds2-mvj8-8386.

Singh, A., Hutchinson, T., Wang, X., Zhang, Z., Schafer, B., Derveni, F., Castaneda, H., and Peterman, K. (2022b). "Wall line tests: Phase 2 – quasi-static tests." *CFS-NHERI: Seismic Resiliency of Repetitively Framed Mid-Rise Cold-Formed Steel Buildings*, DesignSafe-CI. DOI: 10.17603/ds2-encf-vj32.

Singh, A. and Hutchinson, T. C. (2022). "Lateral response of cold-formed steel framed steel sheathed in-line wall systems detailed for mid-rise buildings. Part II: Quasi-static test phase." *Structural Systems Research Project Report SSRP-19/06*, University of California, San Diego, La Jolla, CA.

Singh, A., Wang, X., and Hutchinson, T. C. (2021b). "Lateral response of cold-formed steel framed steel sheathed in-line wall systems detailed for mid-rise buildings. Part I: Shake table test phase." *Structural Systems Research Project Report SSRP-19/05*, University of California, San Diego, La Jolla, CA.

Singh, A., Wang, X., Zhang, Z., Derveni, F., Castaneda, H., Peterman, K., Schafer, B., and Hutchinson, T. (2022c). "Steel sheet sheathed cold-formed steel framed in-line wall systems. I: Impact of structural detailing." *ASCE Journal of Structural Engineering*, 148(12), 04022193. DOI: 10.1061/(ASCE)ST.1943-541X.0003433.

Singh, A., Wang, X., Zhang, Z., Derveni, F., Castaneda, H., Peterman, K., Schafer, B., and Hutchinson, T. (2022d). "Steel sheet sheathed cold-formed steel framed in-line wall systems. II: Impact of nonstructural detailing." *ASCE Journal of Structural Engineering*, 148(12), 04022194. DOI: 10.1061/(ASCE)ST.1943-541X.0003434.

Torabian, S., Nia, Z., and Schafer, B. (2016a). "An archetype mid-rise building for novel complete cold-formed steel buildings." *Proceedings of International Specialty Conference on Cold-Formed Steel Structures*, Baltimore, MD, Missouri University of Science and Technology.

Torabian, S., Zheng, B. Shifferaw, Y., and Schafer, B. (2016b). "Direct strength prediction of cold-formed steel beam-columns." *Research Report RP16-3*, American Iron and Steel Institute, Washington, D.C.

Uang, C. and Gatto, K. (2003). "Effects of finish materials and dynamic loading on the cyclic response of woodframe shearwalls." *ASCE Journal of Structural Engineering*, 129(10), 1394–1402. DOI: 10.1061/(ASCE)0733-9445(2003)129:10(1394).

van de Lindt, J., Pei, S., Liu, H., and Filiatrault, A. (2010). "Three-dimensional seismic response of a full-scale light-frame wood building: Numerical study." *ASCE Journal of Structural Engineering*, 136(1), 56–65. DOI: 10.1061/(ASCE)ST.1943-541X.0000086.

Wang, X. and Hutchinson, T. (2020). "Evolution of modal characteristics of a mid-rise cold-

formed steel building during construction and earthquake testing." *Earthquake Engineering & Structural Dynamics*, 49(14), 1539–1558. DOI: 10.1002/eqe.3316.

Wang, X. and Hutchinson, T. (2021). "Earthquake and postearthquake fire testing of a midrise cold-formed steel-framed building. II: Shear wall behavior and design implications." *ASCE Journal of Structural Engineering*, 147(9), 04021126. DOI: 10.1061/(ASCE)ST.1943-541X.0003098.

Wang, X., Hutchinson, T. C., Hegemeir, G., and Gunisetty, S. (2018a). "Earthquake and post-earthquake fire performance of a mid-rise cold-formed steel framed building – supplemental materials: Final report." *Structural Systems Research Project Rep. No. SSRP-16/09*, University of California, San Diego, La Jolla, CA.

Wang, X., Hutchinson, T. C., Hegemeir, G., Gunisetty, S., Kamath, P., and Meacham, B. (2018b). "Earthquake and post-earthquake fire performance of a mid-rise cold-formed steel framed building – test program and test results: Final report." *Structural Systems Research Project Rep. No. SSRP-16/08*, University of California, San Diego, La Jolla, CA.

Wang, X., Lo, E., De Vivo, L., Hutchinson, T., and Kuester, F. (2022). "Monitoring the earthquake response of full-scale structures using uav vision-based techniques." *Structural Control and Health Monitoring*, 29(1), e2862. DOI: 10.1002/stc.2862.

Wang, X., Singh, A., and Hutchinson, T. (2023). "Development of an adaptive shake table test protocol for seismic performance evaluation." *Journal of Earthquake Engineering* In review.

Wang, X., Wittich, C., Hutchinson, T., Bock, Y., Goldberg, D., Lo, E., and Kuester, F. (2020). "Methodology and validation of uav-based video analysis approach for tracking earthquake-induced building displacements." *ASCE Journal of Computing in Civil Engineering*, 34(6), 04020045. DOI: 10.1061/(ASCE)CP.1943-5487.0000928.

Yu, C. (2010). "Shear resistance of cold-formed steel framed shear walls with 0.686 mm, 0.762 mm, and 0.838 mm steel sheet sheathing." *Engineering Structures*, 32(6), 1522–1529. DOI: 10.1016/j.engstruct.2010.01.029.

Yu, C. and Chen, Y. (2009). "Steel sheet sheathing options for cold-formed steel framed shear wall assemblies providing shear resistance - phase 2." *Report No. UNT-G70752*, Department of Engineering Technology, University of North Texas, Denton, USA.

Yu, C., Vora, H., Dainard, T., Tucker, J., and Veetvkuri, P. (2007). "Steel sheet sheathing options for cold-formed steel framed shear wall assemblies providing shear resistance." *Report No. UNT-G76234*, Department of Engineering Technology, University of North Texas, Denton, USA.

Zhang, Z. (2023). "Simulation and performance of steel sheet sheathed shear walls in cfs-framed

building systems." Doctoral dissertation, Department of Civil and Systems Engineering, Johns Hopkins University, Baltimore, MD.

Zhang, Z., Eladly, M., Rogers, C., and Schafer, B. (2022a). "Cold-formed steel framed shear wall database." *CFS-NHERI: Seismic Resiliency of Repetitively Framed Mid-Rise Cold-Formed Steel Buildings*, DesignSafe-CI. DOI: 10.17603/ds2-ag1e-6m27.

Zhang, Z. and Schafer, B. (2019). "Simulation of steel sheet sheathed cold-formed steel framed shear walls." *Proceedings of Annual Stability Conference Structural Stability Research Council*, St. Louis, MO.

Zhang, Z., Singh, A., Derveni, F., Torabian, S., Peterman, K., Hutchinson, T., and Schafer, B. (2021). "Cyclic experiments on isolated steel sheet connections for cfs framed steel sheet sheathed shear walls with new configurations." *Engineering Structures*, 244, 112805. DOI: 10.1016/j.engstruct.2021.112805.

Zhang, Z., Singh, A., Derveni, F., Torabian, S., Peterman, K., Hutchinson, T., and Schafer, B. (2022b). "Earthquake and postearthquake fire testing of a midrise cold-formed steel-framed building. II: Shear wall behavior and design implications." *ASCE Journal of Structural Engineering*, 148(2), 04021261. DOI: 10.1061/(ASCE)ST.1943-541X.0003233.

Zhang, Z., Speicher, M., Singh, A., Hutchinson, T., and Schafer, B. (2022c). "Effects of modeling decisions on the lateral performance of cold-formed steel framed walls." *Proceedings of the Cold-Formed Steel Research Consortium Colloquium*, Baltimore, MD.

Zhang, Z., Speicher, M., Singh, A., Hutchinson, T., and Schafer, B. (2022d). "Impact of detailing on the lateral performance of cold-formed steel framed walls." *Proceedings of the 12th National Conference in Earthquake Engineering*, Salt Lake City, UT, Earthquake Engineering Research Institute.

Zhou, X., Yao, X., Xu, L., Shi, Y., Ke, K., and Liu, L. (2022). "Shake table tests on a full-scale six-storey cold-formed thin-walled steel-steel plate shear wall structure." *Thin-Walled Structures*, 181, 110009. DOI: 10.1016/j.tws.2022.110009.

Zhu, M., McKenna, F., and Scott, M. (2018). "Openseespy: Python library for the opensees finite element framework." *SoftwareX*, 7, 6–11.